IAEA TECDOC SERIES

IAEA-TECDOC-1746

Heat Transfer Behaviour and Thermohydraulics Code Testing for Supercritical Water Cooled Reactors (SCWRs)

IAEA
International Atomic Energy Agency

HEAT TRANSFER BEHAVIOUR AND THERMOHYDRAULICS CODE TESTING FOR SUPERCRITICAL WATER COOLED REACTORS (SCWRs)

The following States are Members of the International Atomic Energy Agency:

AFGHANISTAN
ALBANIA
ALGERIA
ANGOLA
ARGENTINA
ARMENIA
AUSTRALIA
AUSTRIA
AZERBAIJAN
BAHAMAS
BAHRAIN
BANGLADESH
BELARUS
BELGIUM
BELIZE
BENIN
BOLIVIA
BOSNIA AND HERZEGOVINA
BOTSWANA
BRAZIL
BRUNEI DARUSSALAM
BULGARIA
BURKINA FASO
BURUNDI
CAMBODIA
CAMEROON
CANADA
CENTRAL AFRICAN REPUBLIC
CHAD
CHILE
CHINA
COLOMBIA
CONGO
COSTA RICA
CÔTE D'IVOIRE
CROATIA
CUBA
CYPRUS
CZECH REPUBLIC
DEMOCRATIC REPUBLIC OF THE CONGO
DENMARK
DOMINICA
DOMINICAN REPUBLIC
ECUADOR
EGYPT
EL SALVADOR
ERITREA
ESTONIA
ETHIOPIA
FIJI
FINLAND
FRANCE
GABON
GEORGIA
GERMANY
GHANA
GREECE
GUATEMALA
HAITI
HOLY SEE
HONDURAS
HUNGARY
ICELAND
INDIA
INDONESIA
IRAN, ISLAMIC REPUBLIC OF
IRAQ
IRELAND
ISRAEL
ITALY
JAMAICA
JAPAN
JORDAN
KAZAKHSTAN
KENYA
KOREA, REPUBLIC OF
KUWAIT
KYRGYZSTAN
LAO PEOPLE'S DEMOCRATIC REPUBLIC
LATVIA
LEBANON
LESOTHO
LIBERIA
LIBYA
LIECHTENSTEIN
LITHUANIA
LUXEMBOURG
MADAGASCAR
MALAWI
MALAYSIA
MALI
MALTA
MARSHALL ISLANDS
MAURITANIA
MAURITIUS
MEXICO
MONACO
MONGOLIA
MONTENEGRO
MOROCCO
MOZAMBIQUE
MYANMAR
NAMIBIA
NEPAL
NETHERLANDS
NEW ZEALAND
NICARAGUA
NIGER
NIGERIA
NORWAY
OMAN
PAKISTAN
PALAU
PANAMA
PAPUA NEW GUINEA
PARAGUAY
PERU
PHILIPPINES
POLAND
PORTUGAL
QATAR
REPUBLIC OF MOLDOVA
ROMANIA
RUSSIAN FEDERATION
RWANDA
SAN MARINO
SAUDI ARABIA
SENEGAL
SERBIA
SEYCHELLES
SIERRA LEONE
SINGAPORE
SLOVAKIA
SLOVENIA
SOUTH AFRICA
SPAIN
SRI LANKA
SUDAN
SWAZILAND
SWEDEN
SWITZERLAND
SYRIAN ARAB REPUBLIC
TAJIKISTAN
THAILAND
THE FORMER YUGOSLAV REPUBLIC OF MACEDONIA
TOGO
TRINIDAD AND TOBAGO
TUNISIA
TURKEY
UGANDA
UKRAINE
UNITED ARAB EMIRATES
UNITED KINGDOM OF GREAT BRITAIN AND NORTHERN IRELAND
UNITED REPUBLIC OF TANZANIA
UNITED STATES OF AMERICA
URUGUAY
UZBEKISTAN
VENEZUELA
VIET NAM
YEMEN
ZAMBIA
ZIMBABWE

The Agency's Statute was approved on 23 October 1956 by the Conference on the Statute of the IAEA held at United Nations Headquarters, New York; it entered into force on 29 July 1957. The Headquarters of the Agency are situated in Vienna. Its principal objective is "to accelerate and enlarge the contribution of atomic energy to peace, health and prosperity throughout the world''.

IAEA-TECDOC-1746

HEAT TRANSFER BEHAVIOUR AND THERMOHYDRAULICS CODE TESTING FOR SUPERCRITICAL WATER COOLED REACTORS (SCWRs)

INTERNATIONAL ATOMIC ENERGY AGENCY
VIENNA, 2014

COPYRIGHT NOTICE

For further information on this publication, please contact:

Nuclear Power Technology Development Section
International Atomic Energy Agency
Vienna International Centre
PO Box 100
1400 Vienna, Austria
Email: Official.Mail@iaea.org

Printed by the IAEA in Austria
August 2014

IAEA Library Cataloguing in Publication Data

Heat transfer behaviour and thermohydraulics code testing for supercritical water cooled reactors (SCWRs). — Vienna : International Atomic Energy Agency, 2014.
p. ; 30 cm. — (IAEA-TECDOC series, ISSN 1011–4289 ; no. 1746)
ISBN 978–92–0–107614–4
Includes bibliographical references.

1. Water cooled reactors — Design and construction. 2. Nuclear reactors — Technological innovations. 3. Nuclear reactors — Thermal properties. I. International Atomic Energy Agency. II. Series.

IAEAL 14–00921

FOREWORD

The supercritical water cooled reactor (SCWR) is an innovative water cooled reactor concept which uses water pressurized above its thermodynamic critical pressure as the reactor coolant. This concept offers high thermal efficiencies and a simplified reactor system, and is hence expected to help to improve economic competitiveness. Various kinds of SCWR concepts have been developed, with varying combinations of reactor type (pressure vessel or pressure tube) and core spectrum (thermal, fast or mixed). There is great interest in both developing and developed countries in the research and development (R&D) and conceptual design of SCWRs.

Considering the high interest shown in a number of Member States, the IAEA established in 2008 the Coordinated Research Project (CRP) on Heat Transfer Behaviour and Thermo-hydraulics Code Testing for SCWRs. The aim was to foster international collaboration in the R&D of SCWRs in support of Member States' efforts and under the auspices of the IAEA Nuclear Energy Department's Technical Working Groups on Advanced Technologies for Light Water Reactors (TWG-LWR) and Heavy Water Reactors (TWG-HWR).

The two key objectives of the CRP were to establish accurate databases on the thermohydraulics of supercritical pressure fluids and to test analysis methods for SCWR thermohydraulic behaviour to identify code development needs. In total, 16 institutes from nine Member States and two international organizations were involved in the CRP. The thermohydraulics phenomena investigated in the CRP included heat transfer and pressure loss characteristics of supercritical pressure fluids, development of new heat transfer prediction methods, critical flow during depressurization from supercritical conditions, flow stability and natural circulation in supercritical pressure systems. Two code testing benchmark exercises were performed for steady state heat transfer and flow stability in a heated channel. The CRP was completed with the planned outputs in 2012.

This publication consists of the background and objectives, descriptions of current SCWR design concepts, and major technical achievements from the CRP tasks based on the results of R&D at participating institutes and through their close collaboration. It provides researchers and engineers with a comprehensive and reliable database, and the current status of prediction methods in the area of thermohydraulics of supercritical pressure fluids relevant to SCWRs.

The IAEA appreciates the contributions of N. Aksan (Switzerland) and R. Duffey (Canada), the chairpersons of the CRP and the chief scientific investigators from all CRP participating institutes. The IAEA officer responsible for this publication was K. Yamada of the Division of Nuclear Power.

EDITORIAL NOTE

This publication has been prepared from the original material as submitted by the contributors and has not been edited by the editorial staff of the IAEA. The views expressed remain the responsibility of the contributors and do not necessarily represent the views of the IAEA or its Member States.

Neither the IAEA nor its Member States assume any responsibility for consequences which may arise from the use of this publication. This publication does not address questions of responsibility, legal or otherwise, for acts or omissions on the part of any person.

The use of particular designations of countries or territories does not imply any judgement by the publisher, the IAEA, as to the legal status of such countries or territories, of their authorities and institutions or of the delimitation of their boundaries.

The mention of names of specific companies or products (whether or not indicated as registered) does not imply any intention to infringe proprietary rights, nor should it be construed as an endorsement or recommendation on the part of the IAEA.

The IAEA has no responsibility for the persistence or accuracy of URLs for external or third party Internet web sites referred to in this publication and does not guarantee that any content on such web sites is, or will remain, accurate or appropriate.

CONTENTS

SUMMARY

In support of Member States' efforts, the IAEA started the Coordinated Research Project (CRP) on heat transfer behaviour and thermo-hydraulics code testing for supercritical water-cooled reactors in 2008, and it was successfully completed in 2012. Sixteen (16) institutes from 11 Member States and 2 international organizations participated in the CRP. The chief scientific investigators shared experimental data, prediction methods, and experience in understanding thermo-hydraulic behaviour at supercritical pressure conditions of interest in the design and safety analyses of SCWRs. A large number of experimental data have been contributed to databases of various thermo-hydraulic parameters. Recently developed prediction methods for heat transfer, pressure drop, and instability have been described and will be directly applicable in design and safety analyses. This TECDOC synthesizes the results and technology advancements achieved from the CRP.

In Section 1, an introduction on the CRP and on this TECDOC is given. The objectives and activities are stated. A brief explanation of each section is described.

In Section 2, several SCWR design concepts under development in the international community are presented. One of these concepts evolves from the pressurized heavy-water reactor design and the others from the light water reactor designs. All concepts use supercritical pressure light water as the reactor coolant and utilize the direct thermal cycle that leads to design simplification and cost reduction. Operating pressures of these concepts are close to 25 MPa, but the inlet and outlet coolant temperatures vary. These concepts can generate a range of thermal powers from 1600 to 4000 MW at thermal efficiencies higher than 43%.

Most of these concepts are designed at the thermal neutron spectrum but a couple of concepts are at the fast neutron spectrum. One design concept exhibits two zones; one at thermal spectrum and another at fast spectrum. Uranium oxide fuel is adopted in most thermal spectrum cores but plutonium-thorium fuel has been selected for one of the thermal-spectrum cores. Mixed oxide fuel has been used in the fast spectrum cores. The fuel-rod diameter of these concepts varies from 7 to 13 mm, and stainless steel appears to be the most common cladding material (austenitic alloy has been adopted in one concept).

The reactor core size differs for all design concepts, depending on the power generation and the core spectrum. The maximum active core height is about 5 metres and the core diameter is about 4.5 metres. The majority of these concepts employ light water as the moderator, but two concepts adopt the solid moderator of ZrH2. Another concept uses heavy water as the moderator. Safety system designs are described for most concepts.

Despite of the differences in design and core configuration, some similarities have emerged for the thermal spectrum cores. Most design concepts are still facing challenges, particularly cladding material selection to withstand high temperatures during normal operations and postulated accident scenarios. Improvement in heat-transfer prediction accuracy would provide a realistic estimation of cladding temperature, which may ease the cladding material requirement.

In Section 3, heat transfer characteristics of supercritical water are described. Large amounts of experimental data are available for vertical upward flow of water and surrogate fluids in tubes. These data cover a wide range of flow conditions. However, the amount of data remains limited for relevant conditions to current SCWR design concepts. Nevertheless, these data were applied in the development of methods for calculating supercritical pressure heat transfer coefficients.

Assessments of such methods against a subset of the database show reasonably good agreement for conditions of normal heat transfer. None of the calculation methods appears to capture the deteriorated

heat transfer phenomena observed with vertical tubes. Improved methods (in the form of correlations or look-up tables) have been developed and will be discussed in Section 6. Validation of these methods is required against reliable experimental data.

Calculation methods for supercritical heat-transfer coefficients based on tube data are often applied in subchannel analyses for SCWR fuel bundles, making the assumption that a subchannel can be represented by an equivalent tubular channel. Comparison of experimental data from tubular channel and bundle subassemblies has enabled the differing heat transfer characteristics between these two types of test sections to be identified. A noticeable difference is the apparent absence of (or a diminished effect of) deteriorated heat transfer in bundles. This can probably be attributed to the mixing between subchannels and turbulence enhancement by the spacing devices used in bundles improving the effectiveness of heat transfer from the fuel pin surfaces.

Separate effects on supercritical heat transfer have been identified for SCWR fuel and core analyses. Surveys of experimental studies revealed that experimental data are available for several different separate effects. Most of these data were obtained with tubes and annuli, and the observed effect may not be applicable in bundle analyses. Therefore, additional experimental data are required to understand such phenomena better and for the development of calculation methods for describing observed behaviour.

In Section 4, pressure loss characteristics of supercritical water are described. Pressure loss calculations in heat transport systems are required in design and safety analyses. Predictions of the pressure loss over the SCWR core region are quite complex, due to the fact that fluid properties vary considerably (drastically near the pseudo-critical point) along the fuel assembly. A two-region approach is recommended to minimize the impact of rapid fluid property changes at the pseudo-critical point.

A number of friction factor equations have been reported in literature. Applying these equations is often difficult as the key information (such as surface roughness) was not provided in the literature to support their applicable range. In most cases, the Colebrook-White equation appears to be applicable.

The effect of surface heating (or cooling) on frictional pressure loss is noticeable. A reduction in pressure loss has been observed with the surface in heating mode. On the other hand, the pressure loss appears higher with the surface in cooling mode than in adiabatic mode. The observation is not considered conclusive as the uncertainties remain high among the calculated friction pressure losses and the surface roughness.

Establishment of form loss coefficients rely on experimental data obtained specifically for the piping component and the fuel assembly appendage designs in supercritical flows. The lack of relevant experimental data affects significantly the calculation accuracy of the overall pressure loss and in particular the pressure loss over the fuel assembly.

In Section 5, test facilities available for supercritical heat transfer experiments using water or surrogate fluids as coolant are described. Most of these facilities have relatively small capacity and hence are applicable for experiments with simple test sections and small bundle subassemblies. A new water test facility and two surrogate fluid test facilities have recently been constructed. These facilities are equipped with advanced instrumentation minimizing the measurement uncertainty.

Experiments have been planned using simple test sections (mainly tubes for loop commissioning) and small bundle assemblies. These data are essential for establishing the bundle effect on supercritical heat transfer and for validating the subchannel code and computational fluid dynamic tools.

The planned experiments cover simple bundle subassemblies (either 3 rods or 4 rods only). Experimental data may not be applicable to complex bundle effect in large assemblies. In addition, all rods in the

bundles are uniformly heated. Therefore, experimental data on separate effects, such as axial and radial power profiles, will still be required.

Section 6 deals with development of new correlations for heat transfer to supercritical pressure fluids. It begins with introductory material which provides readers with a picture of early developments and sets the scene for the work on the development of the new heat transfer correlations reported subsequently in the section.

The development of a trans-critical heat transfer look-up table using a large databank which has been subjected to a thorough screening process is described. An assessment of a number of correlation equations in which a detailed error analysis and an examination of parametric trends was carried out for the most promising correlations is then presented.

A new correlation equation is described which has been designed to combine simplicity of structure, explicit connection with physically-based phenomena and avoidance of direct dependence of heat transfer coefficient on wall temperature, whilst being able to cover both normal and deteriorated heat transfer conditions. Then, the performance of this correlation equation and several others is assessed.

An evaluation is presented of four heat transfer correlations for mixed convection using results from a recent study of heat transfer to carbon dioxide at supercritical pressure and also some earlier data for water.

Two physically-based, semi-empirical models are presented which are designed to account for influences of buoyancy and flow acceleration in fluids at supercritical pressure.

In Section 7, critical flow during depressurization from supercritical pressure is described. Critical flow could occur in a LOCA of nuclear reactors, and is of vital importance to the reactor safety. It leads to drastic depressurization and vaporization, and the flow rate is heavily dominated by the content of vapor. This is related to various factors, e.g., the pressure, quality, geometry, etc. Significant complexity of the phenomenon comes from the non-homogeneous and non-equilibrium between phases. Various equilibrium and non-equilibrium models with variable slip ratio and/or thermal non-equilibrium parameter are available. They provide flexible methods for successful prediction of critical flow rate for different conditions. Further work is needed for correlating these parameters over wide range of conditions.

Depressurization transients from supercritical to subcritical water conditions represent a real challenge for system codes in terms of physics and numerical methods. Three system codes (RELAP5, CATHARE and APROS) have been modified and improved to be able to withstand such transients. All three codes maintain the essentials of the two-phase flow balance equations but introduce a pseudo void fraction in the supercritical region. It was necessary to increase the number of discretization points in the water steam tables across the pseudo-critical line in order to achieve good results in the simulations.

The supercritical Edwards' blow-down benchmark tests were successfully run by the three codes, showing similar results. Some discrepancies were attributed to the individual constitutive equations. The extension of the validity of the sub-critical choked flow models in supercritical conditions must be evaluated and improved upon. However as mentioned this affects the very beginning of the transient since the pressure quickly drops below the saturation line. There is definite need for further work in this area to validate the models against the new experiments with data near and above the pseudo critical point. Additional data with a wide variety of L/D ratios and different scale openings are needed to fully understand the effects of depressurization from a SCWR. However it appears that most of the instability and complication occurs in the two phase region, which has been well studied for current reactor systems. This gives a reasonable assurance that existing codes should be able to predict the overall transient

depressurization.

Section 8 collects and describes the issues relevant to stability and natural circulation with fluids at supercritical pressure. In particular, the following considerations are made.

The experimental facilities available at the University of Manitoba, at the Bhabha Atomic Research Centre and at the China Institute for Atomic Energy testify for activities planned or already in progress for collecting experimental data in relation to natural circulation in simple loop configurations. As it can be noted, efforts are spent in particular to establish the boundaries of stable operation of the loops, trying to answer fundamental questions about the causes of instabilities. In this regard, unstable behaviour was observed only in the horizontal heater and horizontal cooler configuration (HHHC) for the BARC facility, confirming the known conclusion that vertical heater and/or cooler tend to favour stability, at least against a Welander's type instability mechanism. On the other hand, the unstable behaviour observed in the China Institute of Atomic Energy (CIAE) facility with vertical heater suggests that at sufficiently high power-to-flow ratios also such configurations may undergo unstable behaviour.

In this perspective, considering the available literature on the subject of natural circulation stability, it appears that there is no complete consensus about the location of the unstable operating regions in the parameter space for a closed loop, except for a generic indication that instabilities are often predicted or observed close to the maximum of the flow vs. power curve. Since this maximum occurs mostly simultaneously with the transition through the pseudo-critical temperature, when a considerable density difference is produced, this transition could be considered at the root of the most probable unstable behaviour. This observation must be anyway contrasted by the consideration that Welander's type instability mechanisms occur also in single-phase loops, where the density difference between hot and cold fluid regions is so small that the Boussinesq fluid model can be safely adopted.

On the basis of the above considerations it can be concluded that a thorough investigation about the mechanisms leading to instability must be made, e.g. to distinguish between possible different unstable modes. In this regard, the presented model results are partly encouraging, showing that system codes and in-house models are able at least to mimic the observed unstable behaviour. However, at the time of writing the role of some plant features, as the heating and passive structures, is not completely clear, being mostly disregarded in simulations; in turn, the effect of heating structures on stability calls into play the prediction of fluid-to-wall heat transfer phenomena, which decide the extent of dynamic coupling between fluid and structures. In this respect, the inability of the reported CFD analysis to predict the unstable behaviour observed in rather specific conditions in the BARC loop does not support firm conclusions about model suitability in predicting instabilities.

On the other hand, the reported work mainly concerns natural circulation stability, giving no experimental contribution to the discussion about the prediction of the stability of simple heated channels containing fluids at supercritical pressures. This issue, discussed in detail in Section 9.2, indeed requires specific investigations, allowing for a step forth with respect to simple model prediction as those reported in the related code-to-code benchmarking activities.

In summary, the results collected in the frame of this CRP on natural circulation and stability are extremely helpful in indicating the potential that experimental activities have in contributing to clarify these phenomena. This happens to be the case also because the presented data, though indicating possible explanations for the addressed mechanisms, clearly show that phenomena occurring in even simple experimental apparatuses are not amenable to too simplistic interpretations, requesting for more in depth analyses to be soundly explained. These analyses are already going on in cooperation between CRP Participants and may constitute a future long lasting product of the above described efforts.

Section 9 deals with thermohydraulics code testing for SCWR conditions. Two code-testing

benchmarking exercises have been performed, and they concerns two important aspects to be considered in the design of SCWRs. A considerable number of research activities are going on worldwide for collecting data suitable for performing an in depth assessment of code capabilities concerning the prediction of heat transfer and stability; these activities will probably provide in the next future a better basis than was available here to draw conclusions and identify areas needing developments.

Relatively simple cases are considered as benchmark conditions, limiting the attention to circular pipe geometries and disregarding many detailed features that are known to have an effect on heat transfer and stability as well. Among these aspects are the presence of spacer grids, heat capacitance of walls and boundary conditions other that those specified for the problems. However, the obtained results are sufficiently interesting to provide a clear perspective of the present capabilities and difficulties.

Major findings can be summarized as follows:

• in relation to heat transfer:

  o system codes need the qualification of suitable correlations for heat transfer prediction in the case of deterioration; despite the number of already proposed correlations, work must still be made in this regard, also considering the flexibility that system code should allow in detecting the proper range of applicability of each implemented correlation (e.g., for vertical upward and downward flows and for horizontal flow);

  o CFD codes, even using low-Reynolds number approaches, are still incompletely satisfactory in their predictions; studies in progress at the time of writing report for possible improvements to be achieved at the price of a greater complexity of turbulence models (e.g., four equation models), whose general applicability is anyway questionable;

• in relation to stability:

  o many of the available system codes make use of first order numerical discretization schemes, which are inherently diffusive and need care to be taken in defining a discretization introducing only limited numerical diffusion effects;

  o the interaction of the adopted correlations for heat transfer with those for friction suggests that both problems should be solved simultaneously in view of a reliable prediction of stability;

  o though different simplifications were adopted in the present analyses (e.g., the neglect of spacer grids and of heat capacitance of the walls) the experience in the analysis of boiling channel stability suggests that studying the pure hydrodynamic phenomenon is only part of the needed model qualification.

In view of these challenges, one of the certain merits of the activities performed so far in the CRP consists in having started a useful cooperation among CRP participants, joining efforts and stimulating a greater awareness of the difficulties to be faced and of the potential to develop better understanding and more accurate predictive tools by common activities.

In Section 10, concluding remarks are provided.

1. INTRODUCTION

One of the IAEA's key functions is to "foster the exchange of scientific and technical information on peaceful uses of atomic energy"[1-1]. To implement this function in practice, coordinated research projects (CRPs) have been established to encourage and assist research and development, which allow the sharing of effort on an international basis, foster team-building and benefit from the experience and expertise of researchers from all participating institutes [1-2].

Advanced designs of nuclear power plants (NPPs) are being considered for future deployment. A group of 10 countries established the Generation-IV International Forum (GIF) to examine new design concepts in 2000 [1-4]. In 2002, these countries signed the GIF Charter, which covered an agreement on the framework to develop advanced nuclear reactor systems by 2030 [1-4]. The main design goals for the Generation IV nuclear system concept are to improve economic, enhance safety, extend sustainability, and strengthen proliferation resistance. Among the large number of potential designs considered, six prominent concepts were selected for participating countries to collaborate in relevant R&D work towards the design. Since the signing of the GIF Charter in 2002, several additional countries have joined GIF to collaborate in the system development and there are 13 signatories in the current GIF Charter.

Among the six selected concepts, the supercritical water cooled reactor (SCWR) is the only one that has directly evolved from the current generation of water cooled NPPs. The main advantages of using supercritical water (SCW) in nuclear reactors are to increase the efficiency of modern NPPs, decrease capital and operational costs, and finally decrease electrical energy costs. The last two advantages are achieved by the simplification of plant components, systems and layout (such as eliminating heat exchangers, steam generators, steam dryers, and moisture separator reheaters), and the introduction of advanced fuel cycles and optimized fuel design.

Using advances made in the fossil power and thermal plant industry, there is a potential to significantly improve nuclear plant cycle efficiency for the 21st century. Benefits from plant-cycle efficiency improvements are threefold:

- Increasing the power output for the same fuel input (specific fuel utilization);
- Reducing waste heat from turbines and condensers (environmental discharges);
- Building fewer plants for meeting demand (capital and operating cost savings).

Reaching 50% efficiency[1] can yield over 40% more electrical output for the same fuel input. In addition, the waste heat rejection is reduced by 30% and there are opportunities for co-generation. In general, the total thermal efficiency of a modern thermal power plant with subcritical steam conditions is about 36–38%; with supercritical parameters about 45-50%; and with ultra-supercritical (USC) parameters 50% or more. The highest total thermal efficiency achieved in today's thermal power industry is about 56–58% with the combined cycle of gas turbine – steam turbine. To improve the cycle efficiency to 45-50%, SCW NPPs would operate at higher operating parameters (i.e., pressures at or near 25 MPa and outlet temperatures up to 625°C) than the current NPPs. Figure 1.1 compares the operating temperature-pressure conditions of current water cooled NPPs and SCWRs (which cover both the pressure vessel (PV) and pressure-tube (PT) types of design concept).

[1] Defined as the percentage of power produced by nuclear reactions that is converted to grid power.

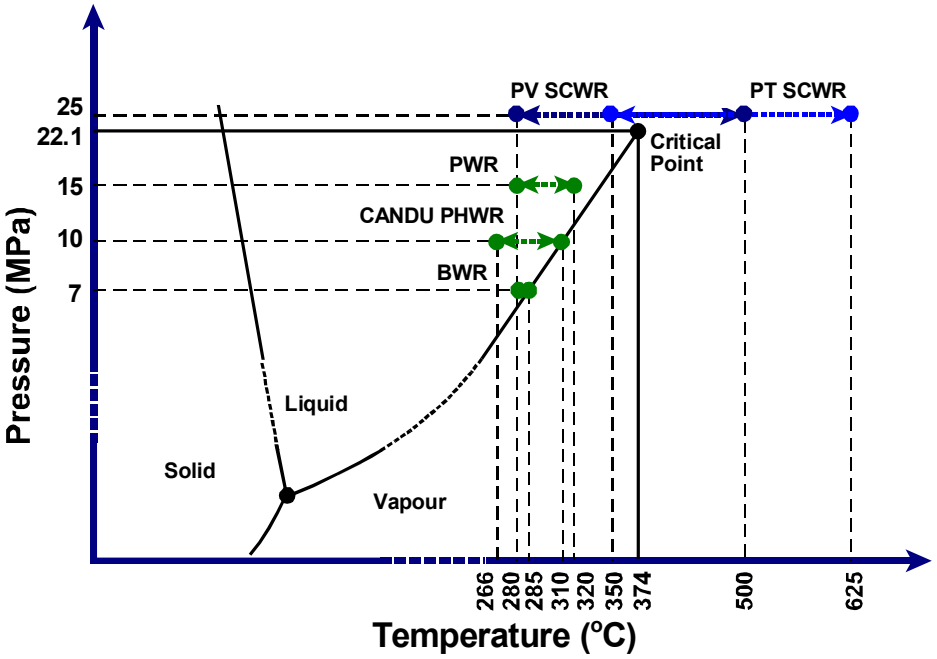

FIG. 1.1. Operating conditions of reactor cores.

The use of supercritical water in fossil power plants is the largest application of fluid at supercritical pressures in the world. Temperatures at the boiler exit were initially around 550°C, but recent advances in materials and turbine technology have led to units using 625°C at 25 MPa, and R&D is proceeding towards adopting outlet temperatures of over 750°C at the pressure of 35 MPa [15]. The USC turbine manufacturers now claim [16] that developments in thermal (coal-fired) power plants will lead to thermal cycle efficiencies of greater than 50%.

The design of SCW nuclear reactors can therefore be seen as the natural and ultimate evolution of today's conventional modern light water reactors (LWRs) and heavy water reactors (HWRs). While the design can be a pressurized-vessel type, a pressurized-channel type, or a hybrid design, the overall design approach is to match the reactor core operating conditions to those of existing supercritical turbines, avoiding the need for a new turbine development effort. Therefore, the typical outlet temperatures of the SCWR designs vary from 550°C to 625°C.

1.1. OVERVIEW OF THE COORDINATED RESEARCH PROJECT

There is high interest internationally in both developing and industrialized countries in the design of innovative SCWRs (attributing to the high thermal efficiencies (45-50%) and improved economic competitiveness). While countries participating in GIF SCWR design concepts are collaborating in the SCWR R&D effort, other countries are working on their SCWR concept design individually. There is a need to expand the collaboration so that duplication of R&D work can be minimized and benefit can be maximized achieving the key development goals of SCWR (i.e., improving economics and safety). In support of Member States' efforts in developing the SCWRs, the IAEA discussed with international experts to explore collaboration opportunity on key R&D areas.

Participants in the GIF SCWR design concepts prepared a System Research Plan (SRP) to guide R&D towards the construction of a SCWR Prototype-of-A-Kind (POAK) [17]. They identified several critical paths impacting the viability of the design concept: System Integration and Assessment, Thermo-

hydraulics and Safety, and Materials and Chemistry. Three projects have been established among GIF SCWR participants to jointly define R&D needs, schedule, and deliverables for each critical-path research topic [18].

Thermo-hydraulic characteristics at supercritical water-flow conditions are required in support of the design and qualification of the fuel bundle and safety analyses for SCWRs. The lack of qualified experimental data on heat transfer and pressure drop for supercritical water flow in rod bundles has been identified as a significant challenge to the SCWR design. This is due to the possible drastic deterioration of heat-transfer characteristic at the vicinity of the critical point.

Based on the consultation with international experts, the IAEA started a Coordinated Research Project (CRP) on Heat Transfer Behaviour and Thermo-hydraulics Codes Testing for SCWRs in 2008. This IAEA CRP promotes international collaboration among IAEA Member States (including participants in the GIF SCWR design concept) for the development of SCWRs in the areas of thermo-hydraulics and heat transfer, including the collection and gathering of experimental data relevant to supercritical fluid behaviour as well as the development and testing of the associated computer methods.

The high coolant temperatures proposed for SCWR systems imply fuel cladding temperatures greater than current water cooled nuclear reactor operating experience. Because of enhanced heat transfer for supercritical flows and the use of new cladding materials with low corrosion rates, it is necessary to have precise information for establishing both the neutronic and thermal limits. In addition, it is considered desirable to match the inlet conditions of existing and proven supercritical turbines.

Consequently, developing SCWR designs requires experimental data for the convective heat transfer from fuel rod bundles to coolant covering relevant ranges of flow rates, pressures and fluid temperatures. The collection, evaluation and assimilation of existing and new data are necessary to establish accurate methods and techniques for the prediction of heat transfer in SCWR cores.

Validated thermo-hydraulic codes are required for the design and safety analyses of SCWR concepts. Existing codes for water cooled reactors need to be extended in their application and improved to model phenomena such as pressure drop, critical flow, flow instability behaviour and transition from super-critical to two-phase conditions. The appropriate predictive models for computing the heat transfer to super-critical fluids need to be incorporated into the codes, and the codes need to be tested and validated.

The CRP has been planned on the advice and with the support of the IAEA Nuclear Energy Department's Technical Working Groups on Advanced Technologies for Light Water Reactors (TWG-LWRs) and Heavy Water Reactors (TWG-HWR). The Gen-IV SCWR System Steering Committee (SSC) provided comments and support in developing the CRP Plan. Coordination has been agreed with the OECD/NEA, which also provides the Technical Secretariat services to GIF. Figure 1.2 illustrates the structure of this CRP.

1.2. OBJECTIVES

Two key objectives of this CRP are:

- To establish accurate databases for heat transfer, pressure drop, blowdown, natural circulation, and stability for conditions relevant to super-critical fluids;
- To test analysis methods for SCWR thermo-hydraulic behaviour, and identify code development needs.

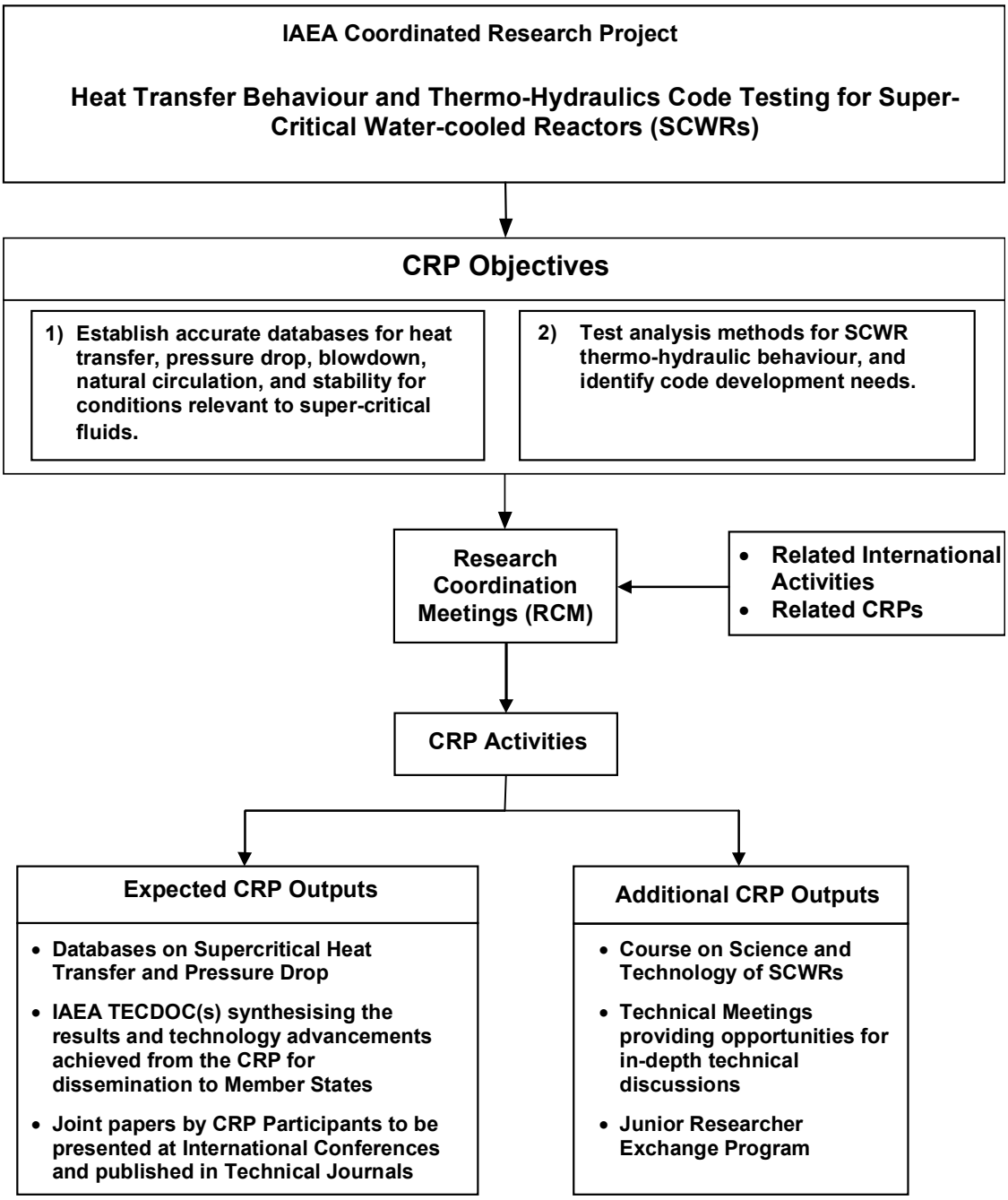

FIG. 1.2. Flow chart for CRP on heat transfer behaviour and thermohydraulics code testing for SCWRs.

1.3. ACTIVITIES

The activities to be carried out collaboratively within the framework of the CRP to meet these needs are listed below:

Activity 1 – collect and share sets of typical SCWR core design parameters such as hydraulic diameter, mass flux, fluid bulk temperature, heat flux; and update information as design of SCWR concepts advance.

- Various SCWR design concepts have been compiled from contributions of CRP participants. Key components of these concepts (such as core configuration, fuel design, etc.) are described in Section 2, which includes a tabulation of design parameters.

Activity 2 – collect, share and analyse existing data for heat transfer and pressure drop for supercritical working fluids (e.g. CO_2, Freon, CF_2Cl_2, He, etc.) for appropriate geometry, flow and heating conditions, and collaboratively assess correlations and relationships, including accuracies and ranges of application.

- CRP participants have contributed their compilation of surrogate-fluid databases on heat transfer in tubes, annuli, and bundle subassemblies. These databases are described in Section 3 and have been uploaded to the NEA database. Little work has been performed to assess heat-transfer correlations against individual database. This is attributed to the applications of fluid-to-fluid modelling parameters since the majority of heat-transfer correlations were developed using water databases. Recent assessments performed within the CRP duration against the database are described in Section 6. Information on pressure drop has been quite limited, primarily due to the fact that pressure-drop data were obtained mostly as a by-product in heat-transfer experiments. These data covered both the liquid-like and vapour-like regions, which would have noticeable differences in hydraulic-resistance characteristics. Nevertheless, a few pressure-drop databases for surrogate fluids have been compiled and described in Section 4.

Activity 3 collect, share and analyse existing data for heat transfer and pressure drop for supercritical water for appropriate geometry (including several rod-array sections), flow and heating conditions, and collaboratively assess correlations and relationships, and including accuracies and ranges of application.

- Large databases on supercritical water heat transfer in tubes and annuli have been compiled and described in Section 3, which includes detailed tabulation on the test flow conditions and geometry (including the flow direction). These databases have been uploaded to the NEA database. Results of several assessments of heat-transfer correlations against individual database are presented in Section 3. Recent assessments performed within the CRP duration against the database are described in Section 6. Information on pressure drop in supercritical water is limited. Further work is needed in the compilation and separation of pressure-drop data for the liquid-like and vapour-like regions.

Activity 4 – perform collaborative fluid-to-fluid scaling analyses so that data from other supercritical working fluids can be used to predict phenomena (for example, heat transfer) in water.

- Fluid-to-fluid scaling parameters for heat transfer in supercritical fluids have been described in Section 3. Assessment results of surrogate-fluid heat-transfer data are presented against water heat-transfer data using the proposed fluid-to-fluid modelling parameters in the section. Non-dimensional parameters applied in correlating hydraulic-resistant data are generally applicable to various fluid types. No additional modelling parameters have been introduced for pressure-drop calculations. Section 8 described the fluid-to-fluid modelling parameters for stability analyses of supercritical fluids. As for hydraulics resistance calculations, non-dimensional parameters for stability appear applicable to various fluid types.

Activity 5 - compare existing heat transfer and pressure drop database with needs, and identify needs for further experiments in annuli, rod bundles, etc.

- Based on the assessment results of heat-transfer correlations against the compiled databases, planned experiments have been described in Section 5 to obtain heat transfer and pressure-drop data for further enhancement of the database. Section 3 identifies also the lack of experimental data on separate effects on heat transfer, which will be covered in several planned experiments.

Activity 6 – collect, share and analyse existing data for critical flow during blowdown from super-critical pressures, and collaboratively develop correlations and relationships.

- Databases on critical flow during blowdown from supercritical to subcritical pressures have been compiled and described in Section 7. These databases were analysed separately and compared against existing prediction models developed for subcritical pressures. General conclusions were presented.

Activity 7 – collaboratively define and potentially conduct new experiments to obtain necessary generic heat transfer and pressure drop data at super-critical conditions with surrogate fluids and with water (for various geometries including rod bundles, grid spacer designs, axial power profiles and coolant velocities) and share results. These experiments would include measurement of wall temperature distributions and pressure drops, as well as other pertinent measurements, for various conditions.

- Planned experiments have been described in Section 5 to obtain heat transfer and pressure-drop data for correlation development and validation. Due to tight scheduling of experimental programs in various available facilities, conducting new experiments collaboratively within the CRP duration is not feasible. An extension of the CRP is recommended to IAEA facilitating the planning and executing experiments in various facilities to collect data on heat transfer (both forced and natural convections), critical flow, and stability.

Activity 8 - collaboratively develop physical models, correlations and relationships for heat transfer and pressure drop (both friction and local pressure loss coefficients), including accuracies and ranges of application based on new data.

- Section 6 describes recent development in a semi-analytical model, correlations, and a look-up table for heat-transfer predictions within the CRP duration. The development of these prediction methods has been led by individual CRP participant, but all CRP participants have provided comments and suggestions for improving these methodologies. No additional work was performed on the prediction of hydraulic resistance. This is attributed to insufficient data compilation (particularly for specific liquid-like and vapour-like regions) and the relatively minor effect of hydraulic-resistance calculation on cladding-temperature predictions).

Activity 9 – conduct experimental and analytical investigations of power-flow instability, with the goal of achieving the ability to predict the onset of instabilities as well as the amplitude of unstable oscillations beyond onset.

- Experimental and analytical information on instability have been described in Section 8. Several prediction methods for stability boundaries are compiled and presented for static and oscillatory instability.

Activity 10 - conduct experiments with supercritical natural circulation investigating steady state performance (flow rate as a function of heater power; pressure drop as a function of flow rate; heat transfer as a function of power, flow and geometry) and investigating transient performance and stability. Share results and compare experimental measurements with analytical predictions.

- Section 8 presents experiments and data obtained for natural circulation within the CRP duration. Prediction models and system codes were assessed against these data. The assessment results have also been described in the section.

Activity 11 - collaboratively define ‘standard problems’ for conditions in which codes used in different countries can be used to model the same physical problems and the results can be compared. These could include, for example, a pipe blowdown from super critical conditions; flow behaviour in a heated test section and in a fuel assembly at different power levels with sufficient specification of conditions (geometry, boundary conditions, and materials) such that extraneous assumptions are eliminated as a source of differences in results.

- Two ‘standard problems’, one on heat transfer and another on stability, have been defined collaboratively among CRP participants, and are described in Section 9. A number of analytical tools have been used to solve the proposed ‘standard problems’. Predictions of these tools were compared and their adequacy was assessed.

Activity 12 – conduct experiments as necessary to support the standard problems of the previous activity, and share results.

- The ‘standard problems’ were established from well-documented experiments, which are described in Section 9. Conducting separate experiments within the CRP duration is not feasible due to tight scheduling of facilities. This will be considered and planned in the next phase of the CRP.

Activity 13 – conduct comparisons of analyses and numerical predictions against theoretical estimates and experimental data, and collaboratively identify areas where further development is required.

- Predictions using computational fluid dynamic tools have been compared against experimental data in the bench-marking exercises. Results from these comparisons are described in Section 9. Experimental data were not compared against theoretical models due mainly to the high uncertainty for the latter.

Activity 14 – conduct analyses with system analysis codes for more complex integral test supercritical system configurations for normal operation and for transients and accidents, and compare results.

- This activity had not been performed due mainly to the design specific information required in the analyses. Furthermore, there is a lack of transient experimental data for verification/validation of code predictions, making it difficult to qualify the analytical results conclusively.

Activity 15 - Establishment of the data base:
The IAEA will share the data obtained within the CRP with the OECD/NEA for the purpose of establishing the data-base. The OECD/NEA has agreed to establish the data base at NEA, and that the data base can be open to organizations participating in the CRP. The data base will include: (a) openly available data including results of work conducted by institutes holding Research or Technical Contracts with the Agency; and data provided to the IAEA by institutes holding Research Agreements with the Agency for those cases where the Agreement holder indicates that the contributed data can be made openly available; (b) data provided by institutes holding Research Agreements with the Agency for those cases where the Agreement holder indicates that the data may be shared among the organizations participating within the CRP; and (c) summary level information about experimental facilities and associated data that could be shared bi-laterally under appropriate agreements between countries.

Activity 16:
As the CRP is being completed, the IAEA together with the participating organizations will prepare a TECDOC synthesising the openly available data, and the results and technology advancements achieved by the CRP for dissemination to Member States. The content of the TECDOC will be planned during the CRP as the extent and nature of the data, and the technology advancement achieved, become clear.

Organizations which have been granted Research Agreements / Contracts are expected to utilize the IAEA Guidance 50-C-Q/SG-8 on Quality Assurance in Research and Development. A Task Group will be formed to review information and data proposed for inclusion into the SCWR database. The task group shall develop criteria and guidance for qualifying the data. It is recognized that there may be very useful data for heat transfer to super-critical water (e.g. for supercritical fossil units) and to surrogate fluids that have been developed in the past with varying levels of quality assurance. These data should not be neglected if their Quality Assurance /Quality Management would not meet current guidance. Participating institutes are encouraged to contribute these data and to examine them collaboratively with regard to

learning as much as possible regarding heat transfer to supercritical fluids.

1.4. DELIVERABLES

The following deliverables have been created as a result of the work performed for the CRP:

- Databases on super-critical heat transfer and pressure drop;
- IAEA reports synthesizing the results and technology advancements achieved from the CRP for dissemination to Member States; and
- Joint papers by CRP participants to be presented at international conferences and published in technical journals.

The databases have been developed as a tool for the CRP participants to share their data and to accelerate their research. At present, the databases contain heat transfer and pressure drop data of various supercritical fluids, critical flow (or depressurization) data of supercritical water and carbon dioxide, natural circulation and flow instability data of supercritical water and carbon dioxide and so on. Several organizations have contributed their original experimental data to the database, and others contributed their analysis results of open data. The databases are hosted by the OECD/NEA, which has accumulated experiences on database management.

This IAEA-TECDOC is one of the deliverables of the CRP summarizing the results obtained through the collaboration among participating organizations.

Many joint papers have been presented at international conferences and published in journals, and some others will be presented and published after the completion of the CRP.

1.5. RESEARCH COORDINATION MEETINGS

The first Research Coordination Meeting (RCM) of the CRP was held at IAEA Headquarters, Vienna, Austria, 22-25 July 2008. During this first RCM the participants developed an Integrated Research Plan (IRP) that indicated how the participating organizations were to collaborate during the CRP and that specified their contributions to the various activities of the CRP.

The second RCM took place on 25–28 August 2009, also at the IAEA Headquarters in Vienna, Austria. The objective of this RCM was to review the progress on the IRP and to update it as needed for the remainder of the CRP. In addition, the RCM evaluated several proposals such as the development of a short technical course on SCWRs, the establishment of a young researcher exchange program, and the organization of an IAEA Technical Meeting on SCWRs.

The third RCM was held at the Institute of Physics and Power Engineering (IPPE) in Obninsk, Russia, 23–27 August 2010. The largest portion of the RCM was scheduled to reviewing work done towards the assembly of the CRP summary report. A detailed plan for the completion of each section was established. Results of the two benchmarking exercises conducted under the framework of the CRP were discussed. Leaders of these exercises requested additional information from some benchmark participants to complete the analyses. Several CRP participants and observers presented SCWR related research activities being carried out at their institutes. The RCM reviewed the outcomes of the technical meeting on heat transfer, thermo-hydraulics and system design for supercritical pressure water cooled reactors that took place in Pisa, Italy on 5–8 July 2010. The consensus was that the technical meeting was an extremely successful and energizing meeting. An extension of the CRP for two more years was proposed to capture new (more relevant) experimental data into the OECD/NEA database and to validate the proposed correlations against these new data. The extension would also permit the execution of more benchmarking exercises providing the SCWR community a very important networking opportunity to collaborate and exchange information.

The fourth RCM was held at the office of Atomic Energy of Canada Limited in Mississauga, Canada, 19-23 September 2011. Two new CRP members from Canada (i.e., McMaster University and University of Ontario Institute of Technology) were welcomed to the meeting. All participants presented the latest advance in thermo-hydraulic and safety code development at their organization. Each leader guided the group to review their draft section of the TECDOC. Participants provided preliminary comments. Reviewers of each draft section were identified. A publication schedule of the TECDOC was established. The CRP has been extended for one year to capture the latest information and experimental databases. Activities and responsibilities were identified among all CRP participants. The possibility of initiating a second CRP on SCWR thermo-hydraulics and safety analyses was discussed. Several participants highlighted the experimental and correlation development work in progress, which would be of interest to IAEA member states (with or without the SCWR program). All participants agreed submitting a proposal to IAEA for the second CRP. The IAEA reported the survey results from participants of the Joint ICTP-IAEA Course on Science and Technology of SCWRs. Overall, the students' ratings have been quite high on the course and many suggestions for improvement have been identified. All participants supported holding the 2nd course next year. The IAEA summarized the Technical Meeting on SCWR Materials, participated by experts of many IAEA member states. The meeting conclusion highlighted the need to establish a CRP for closer interaction and sharing of information among participants.

The fifth RCM was hosted by CIAE and held at Minzu Hotel in Beijing, China, 3–6 September 2012. The objective of the RCM was to review the progress at each institution, to review and finalize the draft of TECDOC on the results achieved under the framework of the CRP, and to discuss future activities relating to the CRP. The progress during the last year and the summary of major activities during the CRP was presented by each representative and discussed among the participants. The draft of TECDOC was discussed, reviewed and finalized. Several institutions have decided to continue collaboration on a bi-lateral or multi-lateral basis even after the completion of the CRP. The database hosted by OECD/NEA will be utilized among the participants until the end of 2016.

Two Consultancy Meetings (CMs) were held to develop, review and compile the TECDOC of the CRP. The First CM was held at the NRC Institute for Fuel Cell Innovation in Vancouver, Canada, on 17–18 March 2011. The objective of this meeting was to advance the preparation of the final report of the CRP. The Second CM was held at University of Wisconsin - Madison, 21–22 June 2012. Section Leads discussed and finalized the draft of the TECDOC for final review of all participants.

1.6. SECTION DESCRIPTIONS

Section 2 summarizes the current SCWR design concepts including selected design parameters. It focuses mainly on the thermodynamic cycle, core design, fuel design, and safety system design of each concept.

Section 3 summarizes the latest experimental data and analytical information available for supercritical heat transfer. This information is considered supplemental to recent literature surveys and state of the art reports.

The pressure drop evaluation approach for supercritical flow is described in Section 4. It is similar to that for single-phase flow but can be separated into the pseudo-liquid and pseudo-vapour regions contacting the heated surface based on the pseudo-critical point. Effects of heating and cooling at the coolant contacting surface have been quantified.

Section 5 describes the supercritical-flow test facilities available in the global research community. These facilities can incorporate simple test sections, such as tubes and annuli, and bundle subassemblies. Working fluids are water and surrogate fluids. Several experiments being planned for these facilities are briefly described.
Section 6 describes the development of physically-based, semi-empirical models aimed at extending

equations for forced convection heat transfer to account for influences of buoyancy and flow acceleration arising as a result of the strong dependence on temperature of density in the vicinity of the pseudo-critical value. A recently proposed equation, which has been specifically designed to combine simplicity of structure and explicit connection with physically-based phenomena, is described. The equation avoids direct dependence of heat transfer coefficient on wall temperature, whilst being able to cover both normal and deteriorated heat transfer conditions. Finally, the development of a trans-critical look-up table, which is ultimately aimed at covering the region near the critical point where conventional single-phase correlations do not apply, is described.

Section 7 describes the critical flow rate during depressurization from supercritical water conditions. Estimation of the depressurization rate is crucial to understand possible transients that may occur if the reactor system undergoes a LOCA (loss of coolant accident) as a result of a pipe break, valve failure or other uncontrolled event. Descriptions of experimental facilities and data measuring critical flow rates from water and surrogate fluids (S-CO2) are presented along with conclusions with regard to model recommendations for the prediction of the depressurization rate. Initial calculations with system codes such as RELAP and CATHARE are discussed with some conclusions with regard to the accuracy of their predicative capability. This section also summarizes details of new facilities that are being constructed at the time this document was written.

After a short overview of presently available information about instability and natural circulation phenomena related to supercritical fluids, Section 8 summarizes the specific contribution provided by CRP participants in the two fields. Available experimental facilities are described together with experimental data obtained up to now and examples of code applications.

Section 9 describes the specifications and the results obtained by Participants for two code-to-code comparison benchmark exercises related to heat transfer (Section 9.1) and flow stability (Section 9.2). The two Code Testing Benchmarks (CTBs) provided an interesting opportunity to compare different methodologies of analysing these phenomena having great relevance for the design of supercritical water reactors. These CTBs correspond to:

- CTB No.1 on Steady State Flow in a Heated Pipe, aimed at assessing the code capabilities in the prediction of heat transfer in front of experimental data;
- CTB No.2 on Benchmark on Flow Stability, aimed at performing a code-to-code comparison of flow stability predictions in a simple heated channel.

REFERENCES FOR SECTION 1

[1-1] INTERNATIONAL ATOMIC ENERGY AGENCY, IAEA website, The Statute of the IAEA, Article III, http://www.iaea.org/About/statute_text.html.

[1-2] INTERNATIONAL ATOMIC ENERGY AGENCY, IAEA website, Coordinated Research Projects, http://www-crp.iaea.org/default.asp

[1-3] INTERNATIONAL ATOMIC ENERGY AGENCY, Thermohydraulic Relationships for Advanced Water Cooled Reactors, IAEA-TECDOC-1023, Vienna, April (2001).

[1-4] Charter of the Generation IV International Forum, Generation IV International Forum Document (www.gen-4.org/PDFs/GIFcharter.pdf), February (2002).

[1-5] DOE, 2009, Materials for Ultra-Supercritical Steam Turbines, ORNL and NETL (www.ms.ornl.gov), and Ultra Supercritical Steam Corrosion, G. Holcomb, et al., (www.osti.gov).

[1-6] WORLD COAL INSTITUTE, Improving Efficiencies (www.worldcoal.org) (2010).

[1-7] IDAHO NATIONAL LABORATORY, Generation IV Nuclear Energy Systems Ten-Year Program Plan – Fiscal Year 2007, Idaho National Laboratory Report, Volume I, September (2007).

[1-8] IDAHO NATIONAL LABORATORY, Supercritical-Water-Cooled Reactor, Appendix 2.0 of Generation IV Nuclear Energy Systems Ten-Year Program Plan – Fiscal Year 2007, Idaho National Laboratory Report, Volume I, September (2007).

2. DESCRIPTION OF SCWR DESIGN CONCEPTS

A number of countries are pursuing the SCWR design concepts, which have been evolved from the current fleet of reactors (i.e., boiling-water reactors (BWRs), pressurized-water reactors (PWRs), or pressurized heavy-water reactors (PHWRs)). The majority of these concepts are the reactor pressure-vessel (RPV) type but one of these concepts is the pressure-tube (PT) type. While the reactor size and operating conditions differ for each concept, all concepts are designed for the operating pressure of 25 MPa (with one at 24.5 MPa). Table 2.1 summarizes the primary design parameters for each concept. A number of these parameters are still evolving with better understanding through the design process. Detailed descriptions of these concepts are presented in the following sections; the SCWR concept of the United States (US) of America is described in the report of the Idaho National Laboratory [2-1] and is not repeated here.

TABLE 2.1. SUMMARY OF DESIGN PARAMETERS FOR SCWR CONCEPTS

Parameters	Unit	Canadian SCWR	SCWR-M	HPLWR	JSCWR	Super Fast Reactor	SCWR-SM	VVER-SCP	US SCWR
Country	–	Canada	China	EU	Japan		Korea	Russia	US
Organization	–	AECL	SJTU	EU-JRC	Japanese Consortium	University of Tokyo	KAERI	OKB Gidropress, IPPE	INEEL
Reactor type	–	PT	RPV	RPV	RPV	RPV	RPV	RPV	RPV
Spectrum	–	Thermal	Mixed	Thermal	Thermal	Fast	Thermal	Fast-resonance	Thermal
Power thermal	MW_{th}	2540	3800	2300	4039	1602	3182	3830	3575
Linear heat rate max/av.	kW/m	37/22	39/18	35/14, 8, 4.5 (a)	-/13.5		39/14.26	-/15.6	39/19.2
Thermal efficiency	%	48	~44	43.5	42.7	~44		43-45	45
Pressure	MPa	25	25	25	25	25	25	24.5	25
T_{in} coolant	ºC	350	280	280	290	280	280	290	280
T_{out} coolant	ºC	625	510	500	510	508	510	540	500
Flow rate	kg/s	1512	1927	1179	2105	820		1890	1843
Active core height	m	5.0	4.5	4.2	4.2	2	3.66	4.05	4.27
Equiv. core diameter	m	~5.5	3.4	3.8	3.34	1.86		3.6	3.93
Fuel	–	Pu-Th	UO_2/MOX	UO_2	UO_2	MOX	UO_2	MOX	UO_2
Cladding material	–	SS	SS	316SS	310SS	SS		austenitic alloy (ChS-68, EP-172)	SS
# of FA		336	284	1404	372	162/73	193	241	145
# of FR in FA		78	180/324	40	192	252/127	316	252	300
D_{rod}	mm	7/12.4/12.4 (b)	8	8	7	5.5	9.516	10.7	10.2
Pitch	mm	vary	9.6/9.6	9.44		6.55	11.5	12	11.2
T_{max} cladding	ºC	850	Not specified	620	700	643	Not specified	Not specified	Not specified
Moderator	–	D_2O	H_2O/---	H_2O	H_2O	-/ZrH	ZrH_2	H_2O	H_2O

(a) Evaporator, Superheater 1, Superheater 2 (b) Outer, Middle, Inner rings

2.1. SCWR CONCEPT IN CANADA

AECL is designing the Canadian SCWR concept, which has evolved from the well-established pressure-tube type CANDU® reactor [2-2]. The Canadian SCWR is designed to produce electrical energy as the main product, plus process heat, hydrogen, industrial isotopes, and drinking water (through the desalination process) as supplementary products, all within a more compact reactor building. Another potential application of the available co-generated process heat is the extraction and refining of oil sands, which is presently achieved using co-generation with natural gas turbines and process heat. The extraction and upgrading process requires: thermal power to lower the viscosity and extract the oil; electric power for separation and refining equipment; and hydrogen gas for upgrading the oil product prior to transport [2-3].

A National Program has been established in Canada to support R&D studies for the Canadian SCWR design [2-4]. It covers key areas of interest (such as thermal hydraulics, safety, materials, and chemistry) to participants in the Generation-IV International Forum (GIF) SCWR designs. Results generated from the program are contributed to the GIF SCWR project management boards (PMBs). For example, heat transfer correlations have been derived using experimental data primarily obtained from fossil-plant related studies (which were started as early as 1930s [2-5], [2-6], [2-7]). Materials and chemistry studies have evolved from operating experience of fossil-fired power plants to a) develop, and perform targeted testing of, materials for key components, in particular in-core reactor components that will be exposed to conditions not encountered in a fossil-fired boiler (such as irradiation and water radiolysis), and b) develop a suitable water chemistry to minimize corrosion and corrosion product transport.

Some of the advanced features of the proposed Canadian SCWR are as follows:

- (Improved) passive safety - passive decay heat removal based on natural circulation and radiation cooling is used to mitigate accident scenarios. The design goal for ensuring 'no-core-melt' is likely achievable by using passive decay heat removal, thus assuring that fuel melting does not occur, even if all emergency injection systems fail, and containment integrity is not challenged;
- (Sustainable and proliferation resistant) thorium fuel cycle – The Canadian SCWR is being specifically designed with the capability to operate with sustainable fuels, namely thorium-uranium-233, and thorium-plutonium reference fuel cycles, while burning up excess plutonium and significantly reducing spent fuel amounts and heat loads in a proliferation resistant fuel cycle;
- (Improved) economics – at SCW operating conditions, thermodynamic cycle efficiency increases significantly. Up to 50% increase in cycle efficiency (i.e., from about 33% to 50%) as compared to current nuclear power plants is possible, resulting in reduced generating cost.

2.1.1. Thermodynamic cycle

The proposed thermodynamic cycle of the Canadian SCWR closely matches the current advanced turbine configuration of SCW fossil power plants. High-pressure SCW from the reactor core is directly fed into SCW turbines. This direct cycle is also used in boiling-water reactors (BWRs) at lower pressures and temperatures. The direct cycle facilitates the implementation of high pressures and temperatures leading to improved thermodynamic efficiency. It also simplifies the system by eliminating the need to transfer energy to a secondary cycle via a steam generator and its associated components. The Canadian SCWR thermodynamic cycle is designed for high-pressure turbines operating at a pressure of 25 MPa and temperature of 625°C [2-8]. Variants of the SCWR thermodynamic cycle currently under consideration include a direct cycle either with or without the option for reheat channels, and a dual cycle which could also be used with or without the reheat option. These variants are discussed below.

The direct cycle is equipped with a moisture separator reheater (MSR) to reduce the steam moisture inside the low pressure turbines. A schematic diagram of the direct cycle is shown in Fig. 2.1 [2-9]. The heat

transport system (HTS) coolant (i.e., SCW) flows directly to the high pressure and intermediate-pressure turbines. Some moisture is anticipated at the exhaust of the intermediate-pressure turbine. An MSR is installed at locations between the intermediate pressure and low-pressure turbines. It separates the moisture from the steam and reheats the steam to ensure an acceptable moisture level at the inlet of the low-pressure turbine. The temperature and pressure of the coolant at various stages in the cycle are also shown in Fig. 2.1.

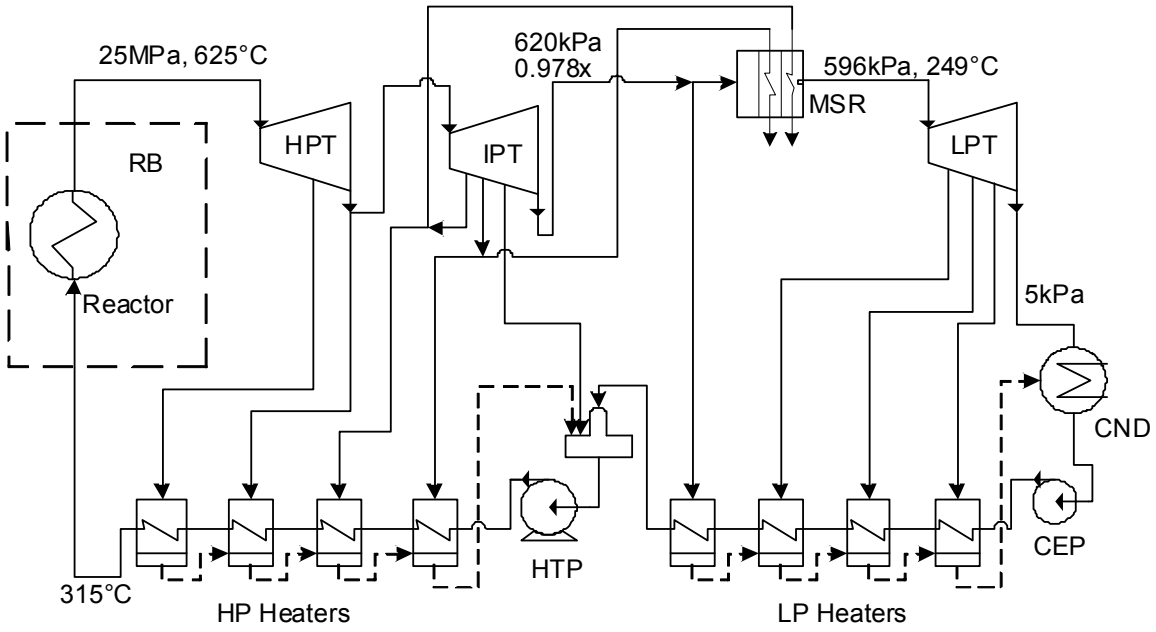

FIG. 2.1. Schematic of direct steam cycle with an MSR in an SCWR plant.

It is envisioned that the Canadian SCWR thermodynamic cycle design will eventually take full advantage of the steam reheat option used in fossil power plants, raising the outlet steam temperature of the reheat channels to the 625°C range at a lower pressure of 6.2 MPa prior to entering the intermediate pressure turbine. This reheat core pass increases the efficiency further and eliminates the need for the MSR. Figure 2.2 illustrates the SCWR layout and thermal cycle with the reheat option and shows the temperature and pressure of the coolant at various stages in the cycle.

To match a SCWR to a reheat SCW turbine, the flow from the back end of the high-pressure turbine must be returned at a lower pressure through the core in the second pass. The steam is then reheated to the required superheat and fed to the intermediate-pressure section of the turbine. At the exit of a pressure-tube type reactor, the target HTS coolant temperature can be established by either extending the channel length or increasing the number of passes through the core. Superheat channels are placed at the periphery of the reactor core and have about 1.5 times lower heat fluxes compared to the average heat flux.

The sizes of the high-pressure and intermediate-pressure turbines are relatively small compared to the low-pressure turbine. This provides an opportunity to simplify the layout, with all high-pressure sections placed inside the reactor building, while the low pressure turbine can be located outside the main containment or reactor building.

Other than the direct cycle configuration, an indirect (or dual) cycle can also be implemented using a heat exchanger that separates the primary side fluid from the secondary side fluid [2-10]. Overall thermal efficiencies for various configurations are compared in Table 2.2 for a typical SCWR of 2540 MWth output. A maximum calculated efficiency of 50% is achievable using the direct cycle with reheat option.

This represents an improvement of about 40% in efficiency over current LWR designs (about 33-35% efficiency).

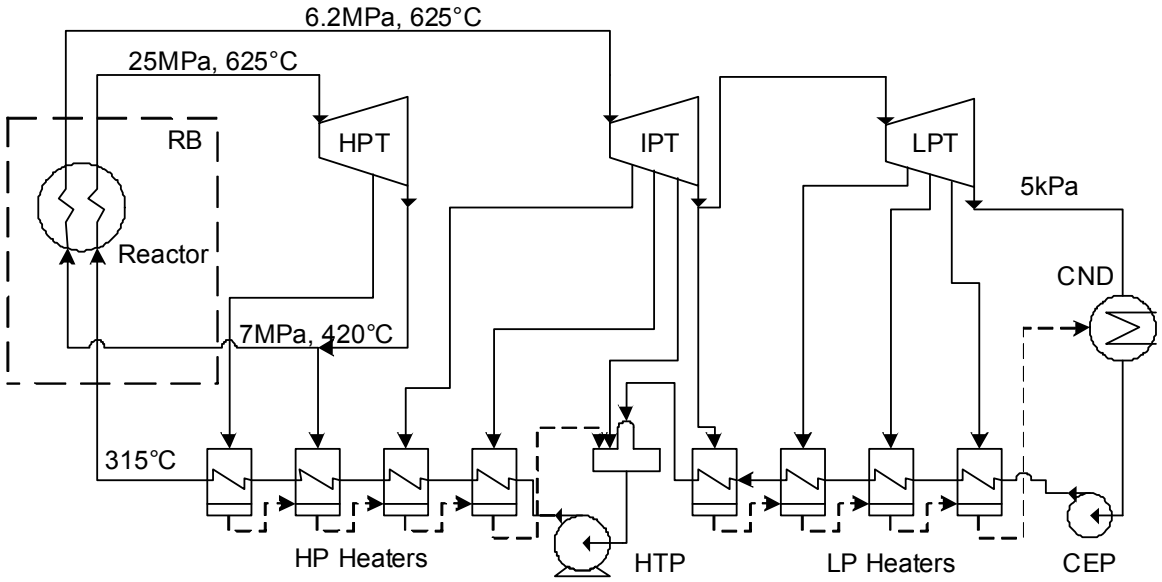

FIG. 2.2. Schematic of direct steam cycle with reheat in an SCWR plant.

TABLE 2.2. SUMMARY OF TYPICAL PREDICTED EFFICIENCIES (25 MPA/625°C/2540 MW(TH))

Cycle	Direct	Direct	Dual	Dual
Option	Reheat	MSR	Reheat	MSR
Reheat (MPa/°C)	6.1/625		6.1/625	
Efficiency %	50	49	49	47

2.1.2. Pre-conceptual core design

The pre-conceptual Canadian SCWR maintains a modular design with separated coolant and moderator, as in current CANDU reactors. For this reactor, the current CANDU practice of on-line refuelling is extremely challenging because of the significantly higher operating pressure and temperatures. Therefore, batch refuelling has been adopted, which leads to a simplified vertical core design with vertical fuel channels, each containing a fuel assembly. Figure 2.3 illustrates schematically the pre-conceptual Canadian SCWR core design.

The pre-conceptual Canadian SCWR design consists of 336 fuel channels, each housing a 5-m long fuel assembly. It is designed to generate 2540 MW of thermal power and about 1200 MW of electric power (assuming a 48% thermodynamic cycle efficiency of the plant). The average fuel channel power is 6.5 MWth and the core radial power profile factor is estimated to be 1.28. The lattice pitch of the channels is selected to be 250 mm based on recent optimization results for the fuel to moderator ratio to achieve a negative void coefficient, and high fuel burnup [2-11]. Figure 2.4 illustrates the cross-section view of the Canadian SCWR core and Fig. 2.5 shows the layout of fuel channels. Some fuel channels at the outer region of the core could be used for the reheat option.

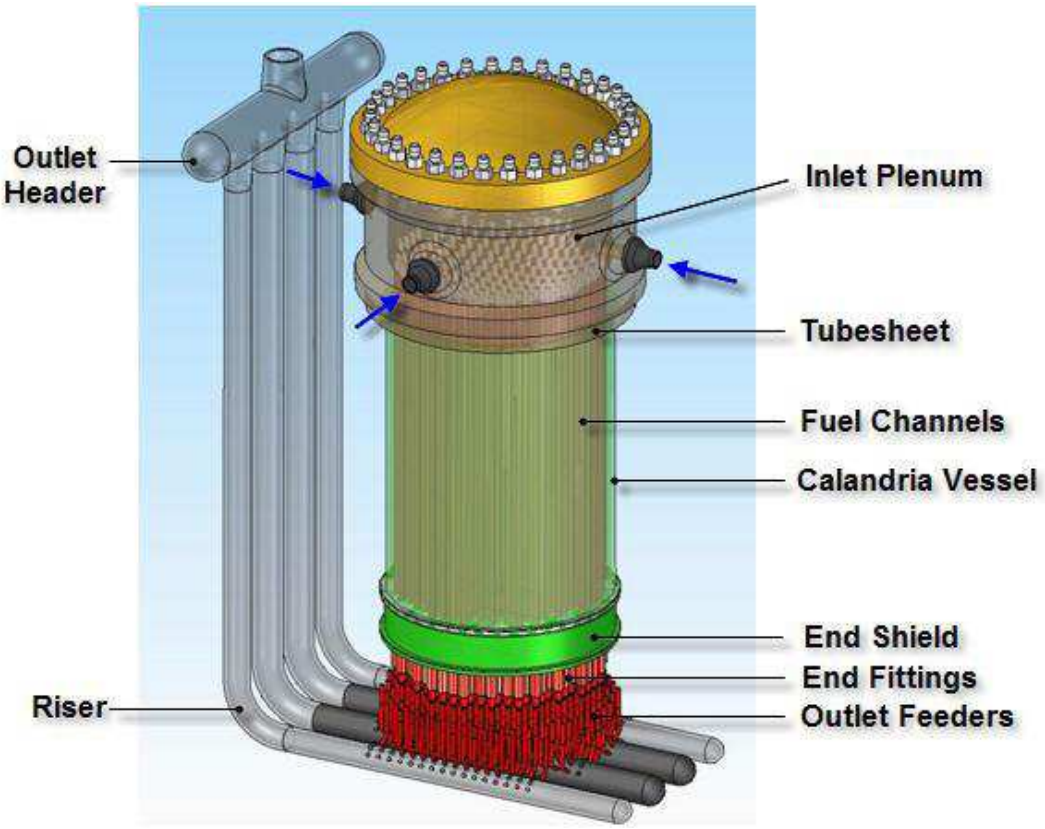

FIG. 2.3. Schematic diagram of the pre-conceptual Canadian SCWR design.

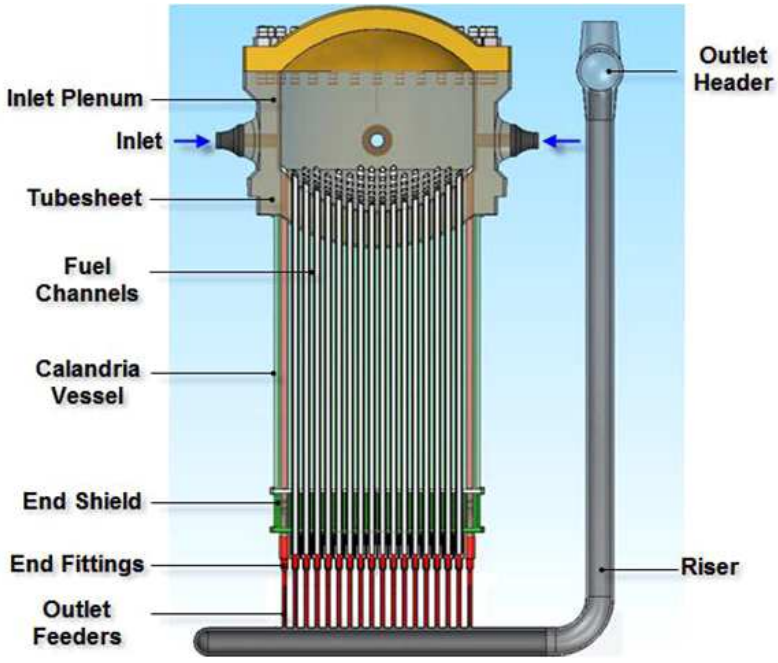

FIG. 2.4. Cross sectional view of the pre-conceptual Canadian SCWR design.

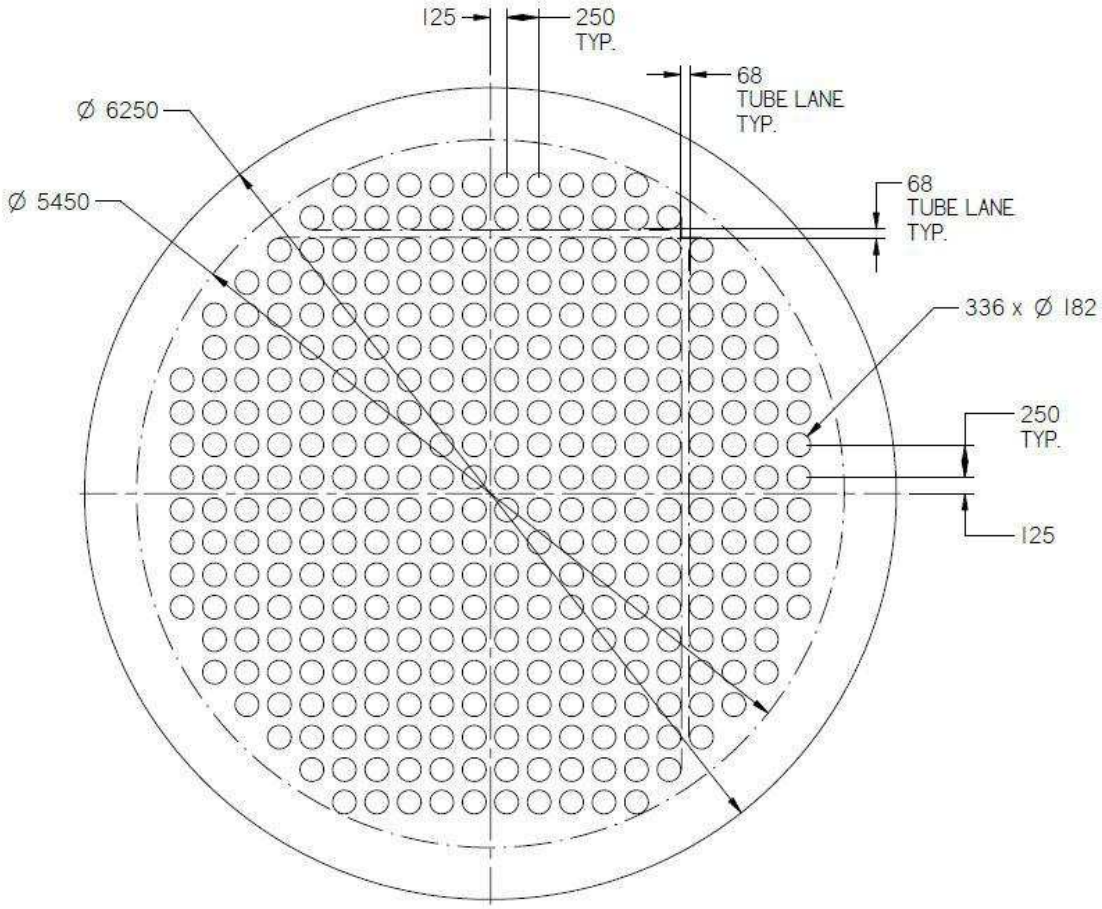

FIG. 2.5. Cross-section layout of fuel channels in the Canadian SCWR core.

As shown in Fig. 2.4, the light water coolant enters the inlet plenum, through inlet nozzles (inlet pipes are not shown) and then enters the fuel channels, which are connected to the tubesheet at the bottom of the inlet plenum. A plenum is feasible for the core inlet due to the relatively low coolant temperature despite the high pressure. The top of the inlet plenum is removable for refuelling. The tubesheet at the bottom of the inlet plenum is machined to form a square array of holes about the same size as the pressure tubes. The pressure tubes, made of a zirconium alloy, are attached to the tubesheet using a well-established rolled joint technique [2-12], which provides a leak-tight connection.

Because the pressure losses in fuel channels are significantly larger than in the inlet plenum, inlet coolant will tend to divide reasonably uniformly into the fuel channels. Finer control of the flow rates in each individual channel would be achieved using orifices in the fuel channels for the purpose of achieving a more uniform exit temperature distribution. Light water coolant from inlet plenum flows down the fuel channel, cooling the fuel assembly and extracting heat. A down-flow configuration for the fuel channel is selected to simplify the refuelling process while avoiding the plenum from getting exposed to hot and potentially oxidizing exit coolant conditions. The coolant exiting from the fuel channels is collected in the outlet header at an average temperature of 625ºC chosen specifically to match SCW turbines being used and developed for thermal power plants.

The calandria vessel holds the low-pressure and low-temperature heavy-water moderator surrounding the fuel channels. It is a relatively low-pressure tank containing the fuel channels, moderator, reactivity control mechanisms and emergency shutdown devices. Control and shut-down rods are installed from the

side of the calandria vessel. When necessary, these rods would be inserted downward due to gravity at an angle toward the other side of the vessel (a spring-assisted inserting movement is also being considered). A second shut-down system would also be installed providing gadolinium injection at various levels of the calandria vessel. The conceptual development and positioning of the control rods, shut-down rods, and gadolinium injection nozzles are in progress. The end shield at the bottom of the reactor is a neutron reflector filled with spherical steel balls as in current CANDU designs.

The reference fuel-channel design consists of a pressure tube, an insulator, and a liner tube (Fig. 2.6). This fuel channel design is called the high-efficiency channel (HEC) [2-13]. The current reference fuel channel dimensions are listed in Table 2.3. The pressure tube is designed to withstand the high coolant pressure, but directly contacts the moderator, thereby maintaining it at a low temperature (~100 °C). This allows the use of the zirconium alloy Excel for the pressure tube. This alloy has superior properties at low temperatures compared to other zirconium alloys. A stainless-steel liner is placed between the fuel bundle and the insulator, minimizing potential damage to the insulator by the bundle. The insulator thermally protects the pressure tube from the higher temperature bulk fluid flowing through the fuel bundle. It is made of Yttrium-Stabilized Zirconia (YSZ), which is refractory, has low neutron absorption properties and excellent resistance to neutron damage. One of the possible benefits of using the HEC is that in the event of a loss of coolant accident (LOCA) without emergency core cooling, the fuel may not melt because of passive heat rejection through the insulator into the moderator [2-14]. That is, the heat in the fuel will be transferred through radiation to the liner tube and conducted to the moderator, maintaining the fuel cladding below its melting point. To achieve this safety goal, the fuel channel requires further optimization of its geometry, strength, corrosion resistance, creep resistance, thermal resistance and mechanical properties to ensure sufficient decay heat removal during accidents conditions while minimizing heat loss during normal operating conditions.

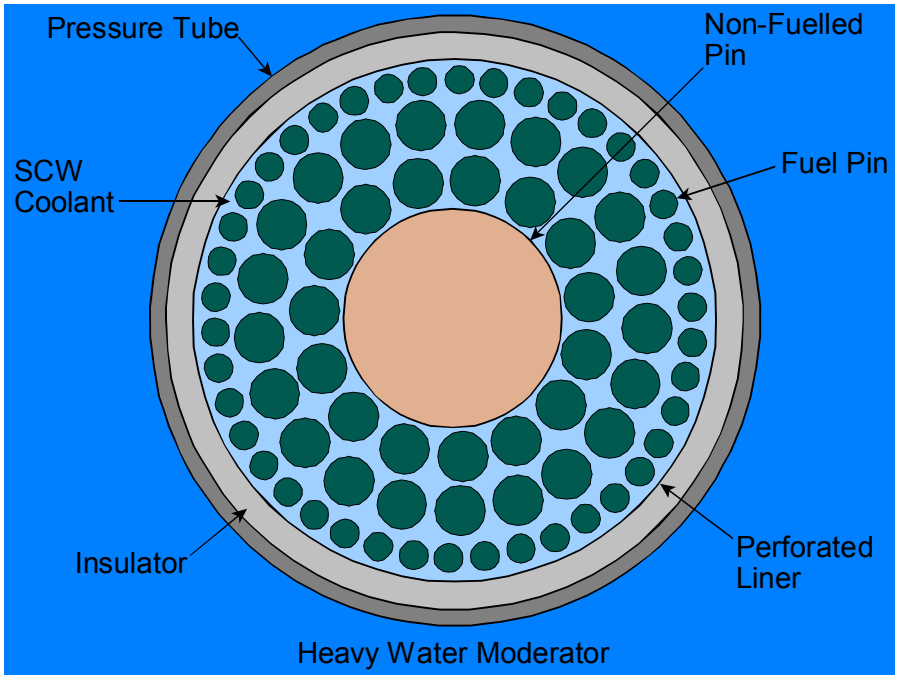

FIG. 2.6. Schematic diagram of the high efficiency channel.

TABLE 2.3. PRE-CONCEPTUAL HEC DIMENSIONS

	Fuel Channel Dimensions
Liner Inside Diameter (mm)	136
Liner Thickness (mm)	0.7
Insulator Thickness (mm)	10
Pressure Tube Thickness (mm)	12
Pressure Tube Outside Diameter (mm)	181.4

The fuel channel outlets are connected to small diameter outlet feeder pipes through transition pieces that are rolled into the pressure tube on one end and welded to the outlet feeder pipes on the other end. The rolled joint is placed inside the calandria vessel and is in direct contact with the moderator to keep it cool. The YSZ insulator extends about 300 mm beyond the rolled joint to ensure that there is a reasonable temperature gradient between the region where the HTS coolant exits past the insulator and the region/elevation of the rolled joint. An expansion bellow at the end of the fuel channel allows for axial thermal expansion and creep growth of the fuel channel.

Outlet feeder pipes provide flexibility to the fuel channel/outlet pipe structures to accommodate any differential growth of the fuel channel due to material creep and thermal expansion. The large diameter outlet pipes, called risers, are anchored such that their downward thermal expansion is about the same as the thermal expansion of fuel channels. This configuration minimizes in-service stresses of both the outlet piping and the fuel channels. Outlet flow from risers is collected in the headers before it is transported to the turbines. Possible candidate materials for the outlet feeders include the T/P91 and T/P92 classes of high-temperature alloys commonly used in conventional supercritical coal plants. However, flow accelerated corrosion may be an issue with these classes of materials. As an alternative, nickel based high temperature super alloys are considered.

Since the SCWR is a water cooled reactor, a key challenge will be to define a water chemistry control strategy. The properties of water change significantly as it passes through the critical point, and while there is a large water chemistry experience base in the fossil-fired SCW power generation industry, the significant structural and operational differences between a fossil-fired boiler and an SCWR core make the direct adoption of fossil plant practices problematic. The key chemistry issues are a) water radiolysis, which can produce oxidizing species that can increase the corrosion of reactor components in-core and immediately downstream of the core, and b) corrosion product deposition on in-core materials, which can lead to overheating and fuel failure [2-15]. These issues are the subject of a number of research programs now underway in Canada.

2.1.3. Advanced fuel cycles

The GIF goals for the development of next-generation reactors include enhanced safety, resource sustainability, economic benefit and proliferation resistance. Each of these goals can be addressed through the implementation of thorium fuel cycles. In particular, there is great potential for enhancing the sustainability of the nuclear fuel cycle by extending the availability of current resources through the use of thorium fuel cycles. Thorium fuel had only been used in research reactors and demonstration irradiations were performed in power reactors. Recent studies of thorium-based fuel cycles in contemporary CANDU reactors demonstrate the possibility for substantial reductions in natural uranium (NU) requirements of the fuel cycle via the recycle of U-233 bred from thorium [2-16]-[2-19]. As thorium itself does not contain a fissile isotope, neutrons must be provided by adding a fissile material, either within or outside of the thorium-based fuel. This fissile isotope is typically enriched uranium, U-233 (which is bred from an earlier thorium cycle) or reactor-grade plutonium.

Thorium fuel cycles are categorized by the type of added fissile material and are also significantly influenced by the way in which the fissile and fertile materials are distributed within the fuel bundle and within the core. The simplest of these fuel cycles are based on homogeneous thorium fuel designs, where the fissile material is mixed uniformly with the fertile thorium. These fuel cycles can be competitive in resource utilization with the best uranium-based fuel cycles, while building up an inventory of U-233 in the spent fuel for possible recycle in thermal reactors. When U-233 is recycled from the spent fuel, thorium-based fuel cycles can provide substantial improvements in the efficiency of energy production from existing fissile resources. Options for once-through and U-233 recycle thorium fuel cycles are currently being investigated and optimized for the Canadian SCWR design [2-20].

The proposed refuelling scheme for the SCWR is a three-batch scheme, i.e., one third of the core is replaced with fresh fuel at the end of each operating cycle, another third of the core contains once-irradiated assemblies, and the remaining third contains assemblies that have been in core for two cycles. Locations of these fresh, one cycle and two-cycle assemblies are determined by a fuel loading scheme. A typical goal of designing such a scheme is to ensure an even power distribution radially across the core, that is, reducing the radial power peaking factor (PPF), defined as the ratio of maximum channel power to average channel power for the reactor [2-11].

At this stage of research and development, no reactivity devices have been modelled nor has any burnable neutron absorber (BNA) been added to fresh fuel or moderator for reactivity suppression. Figure 2.7 shows the refuelling scheme used for the analysis. This scheme produces a relatively even radial power distribution with power peaking factor of 1.28 and was used in the subsequent linear-element rating (LER) analysis. It is expected that further refinement to the fuelling scheme, in combination with BNA addition to fresh fuel and reactivity devices will reduce the radial power peaking further.

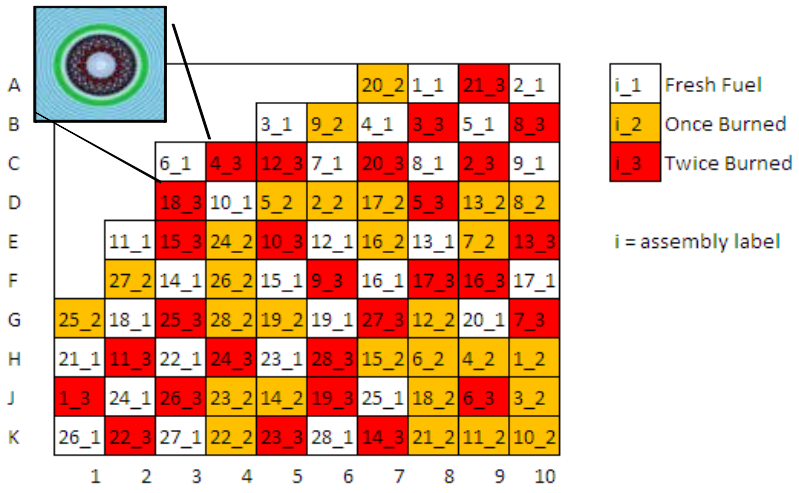

FIG. 2.7. Quarter core fuel loading pattern.

The axial power profile used for the LER analysis of the high power channel is shown in Fig. 2.8. Local powers were established along the fuel channel. The fuel assembly was separated into 10 bundle segments, with the first one located at the inlet and the last one at the outlet of the flow direction in the channel. This selected channel corresponded to the highest LERs in the reactor. The power of this channel is 9648 kW at the beginning of cycle (BOC). The peak-power location shifts from the inlet at BOC to the outlet of the channel at the end of cycle (EOC).

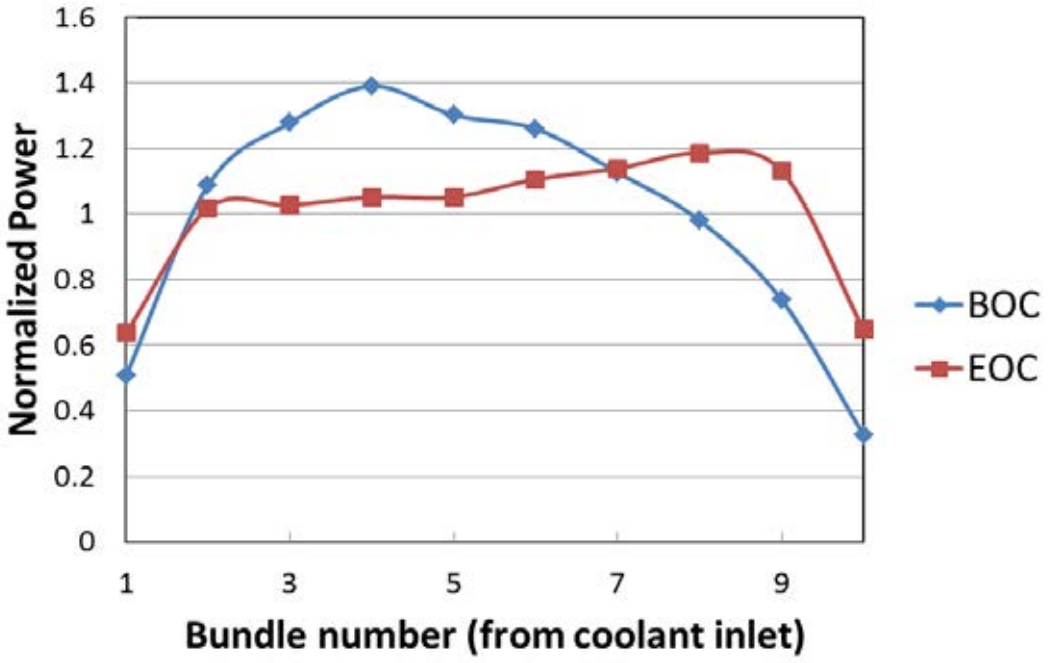

FIG. 2.8. Axial power profiles of maximum power channel.

The refuelling scheme and axial power profiles from the Reactor Fuelling Simulation Program (RFSP) code were used to create a power profile to feed back into the AECL version of the Winfrith Improved Multigroup Scheme (WIMS-AECL) code to calculate linear element ratings. Twelve power values were used in time, for each of five modelled axial positions, as shown in Fig. 2.9. Pencer and Hyland [2-21] provided more details of the physics aspects of the pressure tube type SCWR pre-conceptual design.

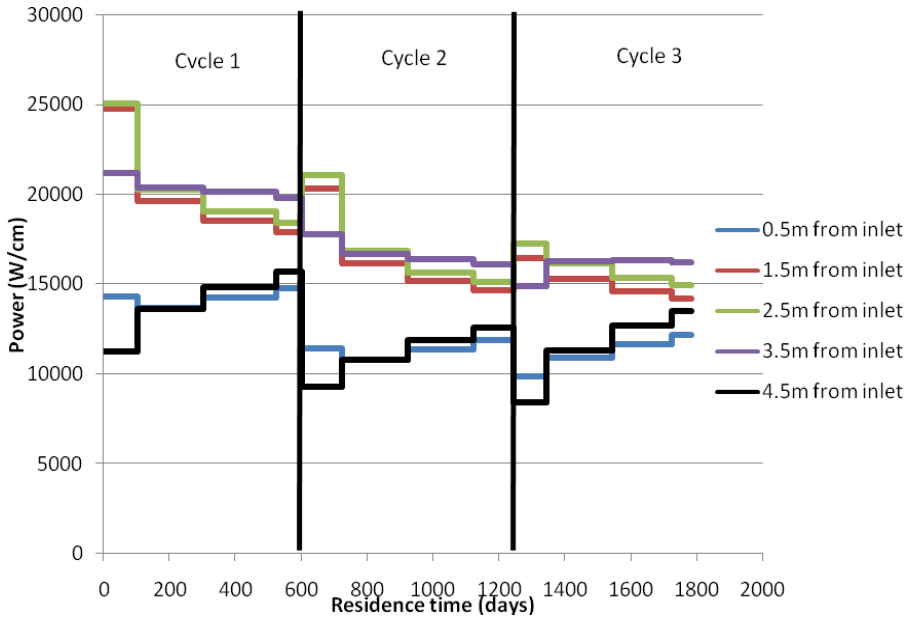

FIG. 2.9. Power profile applied to each axial position.

2.1.4. Conceptual fuel design

The limit on the SCWR outlet temperature is effectively set by the mechanical and corrosion properties of the fuel cladding. Properties such as the strength and corrosion resistance decrease with increasing temperature. The mechanical and corrosion properties of currently available zirconium-based fuel cladding alloys, which have been the mainstay of the current fleet of commercial nuclear power plants, are such that they cannot be used in an SCWR. As a result, various iron and nickel-based alloys are being considered for the fuel cladding of the Canadian SCWR, including austenitic stainless steels, ferritic/martensitic steels, and oxide dispersion strengthened (ODS) steels [2-23]. The cladding material must be able to withstand the peak cladding temperature, which will be some 20% higher than the average cladding temperature. While no alloy has yet been shown to possess all required properties for use at the proposed Canadian SCWR temperatures, there are a number of promising candidates. The modified stainless steel is the reference candidate for fuel cladding material. A number of research and development programs are underway to develop a suitable fuel cladding material for use in the Canadian SCWR. However, the use of these alloys results in some losses in fuel efficiency due to their higher neutron absorption compared to zirconium-based alloys. This is offset by the optimized bundle design where peak fuel cladding temperature is reasonable uniform across the fuel bundle leading to an increase in the allowable outlet temperature and hence efficiency [2-24], [2-25].

The Canadian SCWR fuel bundle design has three concentric rings of fuel with 15, 21, and 42 fuel elements (Fig. 2.6). This bundle has a large non-fuel element in the centre. The removal of fuel from the central region of the bundle has the effect of significantly reducing the coolant void reactivity without requiring burnable neutron absorbers. The fuel composition for the bundle is 13% plutonium in thorium. Table 2.4 lists the dimensions for the current conceptual Canadian SCWR fuel design. Further optimization of the fuel geometry is in progress to enhance the heat transfer.

TABLE 2.4. GEOMETRY PARAMETERS FOR CONCEPTUAL CANADIAN SCWR FUEL DESIGN

Parameter	Value
Elements per bundle	78
Elements in rings 1, 2, 3	15, 21, 42
Pitch circle radius, ring 1	3.655 cm
Pitch circle radius, ring 2	5.11 cm
Pitch circle radius, ring 3	6.295 cm
Radius of central pin	2.82 cm
Outer radius of central pin cladding	2.88 cm
Radius of pins in ring 1 and 2	0.62 cm
Outer radius of ring 1 and 2 pin cladding	0.68 cm
Radius of pins in ring 3	0.35 cm
Outer radius of ring 3 pin cladding	0.41 cm

2.1.5. Safety system design

The safety concepts for the Canadian SCWR are generally similar to those developed for modern nuclear reactors, but specific considerations are necessary to cover the transition through the pseudo-critical temperature. Passive safety concepts have been incorporated to support the ‘inherent safety’ goals required in next generation nuclear reactors.

- The Canadian SCWR fuel is designed to exhibit a negative coolant void reactivity coefficient throughout the residence time in the core. Therefore, a large power pulse will not be encountered under the postulated large-break LOCA scenario;
- One of the inherent safety characteristics of the CANDU reactor is the separation of the primary coolant from the moderator. This feature provides a large heat sink (moderator) in case of LOCA within the primary HTS;
- One of the possible benefits of using the HEC is that in the event of a LOCA without emergency core cooling, the fuel may not melt because of passive heat rejection through the insulator into the moderator [2-14]. That is, the heat in the fuel will be transferred through radiation to the liner tube and conducted to the moderator, maintaining the fuel cladding (modified stainless steel is considered as reference) below its melting point. Work is proceeding to optimize and demonstrate HEC performance for normal operating and accident conditions;
- To ensure the effectiveness of long-term cooling, a passive moderator cooling system has been introduced to remove decay heat from the fuel in a large-break LOCA event (see Fig. 2.10). This system could potentially meet the moderator heat removal requirements for both normal operating and accident conditions. The effectiveness of the passive moderator cooling system has been verified experimentally in a small-scale test facility [2-26]. A large-scale test facility is being designed to qualify the system.

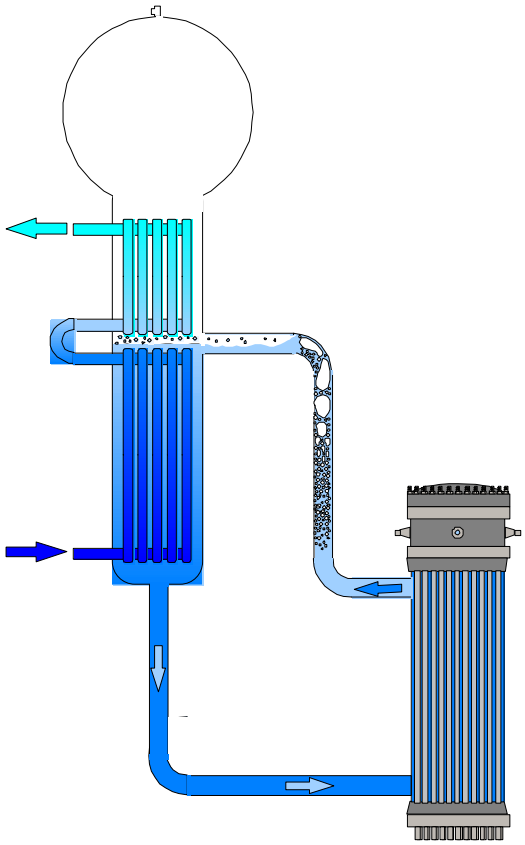

FIG. 2.10. Schematic diagram of the passive moderator cooling system.

2.2. SCWR CONCEPT IN CHINA

To avoid the mechanical and safety problems in both thermal and fast SCWR design, and in the other hand to achieve a high temperature at the reactor exit, a mixed core design with multi-layer fuel assembly has been proposed by the Shanghai Jiao Tong University [2-27]. The core consists of two zones with different neutron spectra, one with thermal and the other with fast spectrum. In the thermal zone, a co-current downward flow is applied with an exit temperature over the pseudo-critical point. The downward flow in the thermal fuel assembly will provide an effective cooling of the fuel rods. As a result, the cladding temperature will be kept at a low value. In the forthcoming fast zone a high exit temperature is achieved. Due to the high coolant inlet temperature over the pseudo-critical point, the heat transfer deterioration phenomenon will be eliminated in this upward flowing area. The low density in the fast zone can provide a hard neutron spectrum with a wide lattice structure, which can mitigate the non-uniformity of the circumferential heat transfer at the cladding surface and ensure a big inventory of water in the core. Consequently, with a hard neutron spectrum and the multi-layer fuel assembly, a conversion ratio close to 1.0 can be achieved.

2.2.1. Thermodynamic cycle

Based on BWR conception and supercritical pressure fossil-fired power plant, a preliminary steam and power conversion system is established. As shown in Fig. 2.11, steam generated in the reactor is supplied to the high pressure turbine, to the second stage re-heater, enters the intermediate-pressure turbine and the low-pressure turbines. Steam exhausted from the low-pressure turbines is condensed in the condenser. The condensate pumps take suction from the condenser hot-well and deliver the condensate water to the low-pressure feed-water heaters. Three parallel and independent strings of four low-pressure FW heaters are designed. The main feed-water pumps take suction from the FW booster pumps and provide flow to the high-pressure FW heaters. Two parallel and independent strings of three high-pressure FW heaters are located in the turbine building.

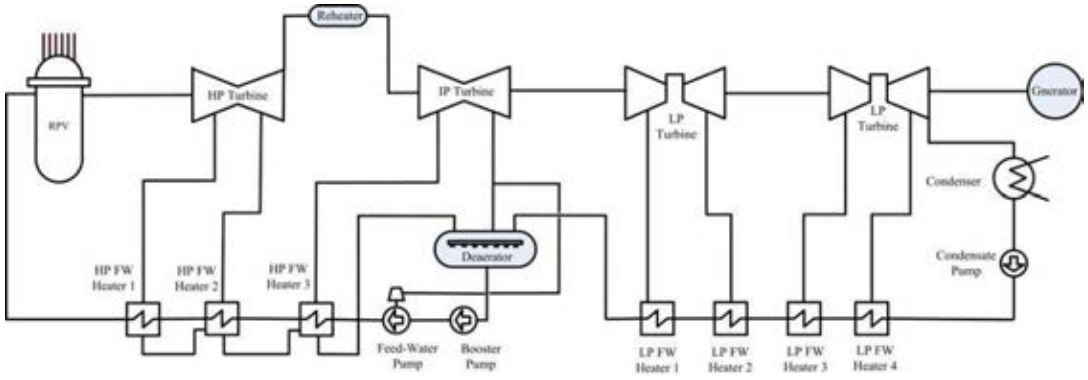

FIG. 2.11. Scheme of the SCWR-M thermodynamic cycle.

2.2.2. Conceptual core design

Figure 2.12 shows schematically the geometrical arrangement of the proposed mixed core [2-28]. There are totally 284 fuel assemblies in the core. The basic idea is to divide the core into two parts with different neutron spectra. In the outer zone with 164 fuel assemblies, the neutron energy spectrum is similar to that of a thermal reactor. The inner zone with 120 fuel assemblies has fast neutron spectrum. The average linear power generation rate is 18 kW/m in the thermal and fast zones. The active height is 4.5 m for the thermal zone and 2.0 m for the fast zone. The average power density is 90.26 MW/m^3 including blanket fuel and the equivalent core diameter is 3.4 m.

In the thermal zone, the co-current flow mode is applied to the fuel assembly. The cold water entering the pressure vessel is directed to the upper dome and into both the moderator channels and the cooling channels of the thermal zone. In the thermal zone, 25% of the mass flow rate passes through the moderator channels. It exits the thermal zone in the lower plenum, from where it enters the fast zone of the reactor core (the inner zone in Fig. 2.12b). The water temperature at the inlet of the pressure vessel is 280°C and at the exit of the pressure vessel is 510°C. It is assumed that the water through the thermal zone is heated up to 385-400°C. Table 2.5 summarizes some main parameters of the proposed mixed core.

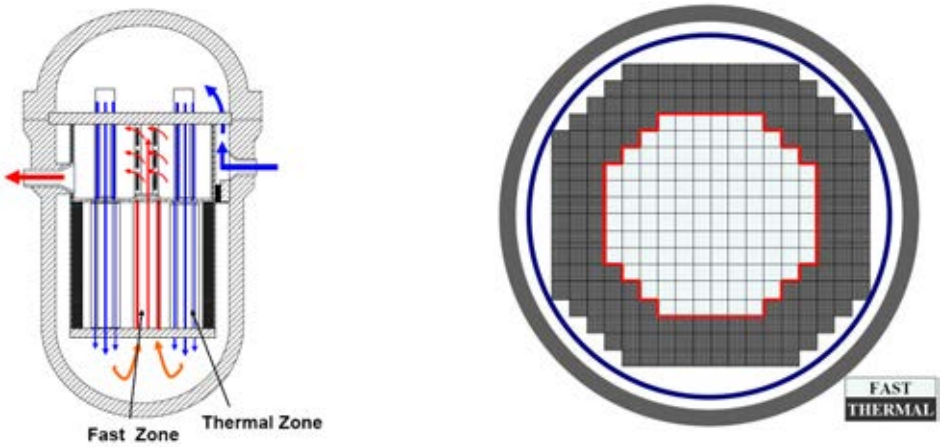

(a) Flow paths in the core (b) Fuel assembly arrangement in the core

FIG. 2.12. Scheme of the SCWR-M core [2-28].

TABLE 2.5. MAIN PARAMETERS FOR THE PROPOSED SCWR-M [2-28]

Design parameter	Thermal zone	Fast zone	Whole core
Pressure (MPa)	25.0	<25.0	<25.0
Thermal power (MW)	2400.0	1400.0	3800.0
Electrical power (MW)	—	—	1650.0
Core height (m)	4.5	2.0	—
Equivalent diameter (m)	3.4	2.14	3.4
Number of fuel assemblies (-)	164	120	284
Fuel rod diameter (mm)	8.0	8.0	—
Pitch to diameter ratio (-)	1.20	1.20	—
Average power density (MW/m^3)	100.89	75.74	90.26
Flow rate (kg/s)	1927.0	1927.0	1927.0

2.2.3. Conceptual fuel assembly design

The selection of the fuel assembly design is derived from an optimization work, which is performed by Yang et al. [2-29]. For the thermal zone, the basic idea of the multi-layer concept is axially to divide the

active length into several layers with different enrichment, schematically illustrated in Fig. 2.13a. For the fast zone, in order to achieve negative void reactivity coefficients, the seed core is designed to be short to increase neutron leakage as schematically shown in Fig. 2.13b. Axial blankets with depleted uranium are also introduced to increase the conversion ratio and to reduce the void reactivity coefficient. The seed and blanket materials are axially divided into 11 layers [2-29]. The detailed design parameters of the fuel assembly are indicated in Table 2.6.

TABLE 2.6. MAIN PARAMETERS FOR THE PROPOSED FUEL ASSEMBLY [2-29]

Design parameter	Thermal FA	Fast FA
Number of fuel rods (-)	180	324
Fuel rod diameter (mm)	8.0	8.0
Pitch to diameter ratio (-)	1.20	1.20
Fuel (-)	UO_2	MOX
Enrichment (%)	5.0; 6.0; 7.0	24.0
Conversion ratio (-)	0.60	0.99

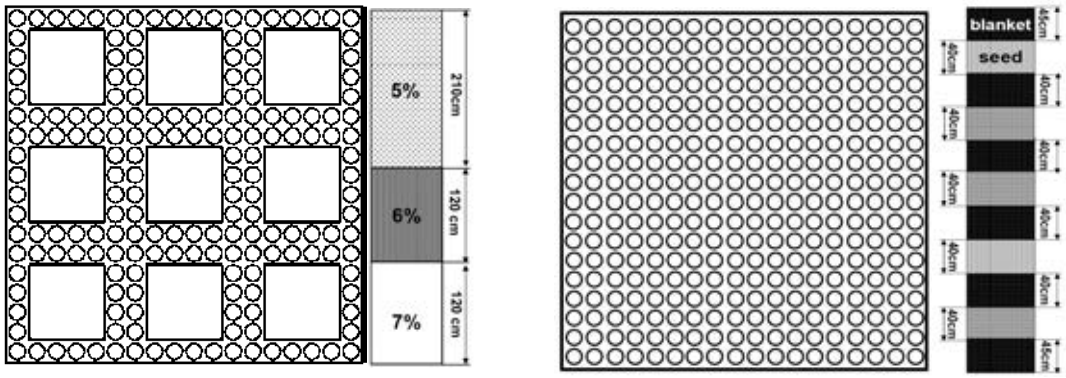

(a) Fuel assembly in the thermal zone (b) Fuel assembly in the fast zone

FIG. 2.13. Reference fuel assembly structures in the thermal and fast zones (a) and (b) show the cross sections of the assemblies (left) and the distribution of the enrichment (a, right) and the seed blanket arrangement (b, right) over the core height [2-29].

2.2.4. Safety system design

Safety systems design is generally derived from the advanced water reactors, especially the passive concept from the ESBWR and AP 1000. Considering SCWR-M character, a preliminary engineered safety features scheme of SCWR-M is proposed as shown in Fig. 2.14.

The functions for each component are as followed:

Accumulator for safety injection;
Automatic Depressurization System for pressure depressurization;
Isolation Condenser System (ICS) for decay heat removal;
Safety/Relief Valves for overpressure protection;
Standby Liquid Control System for backup shutdown;
Containment Spray system and Suppression Pool Spray System for spray cooling;
Suppression Pool Cooling System and ICS Cooling System for heat sink cooling;

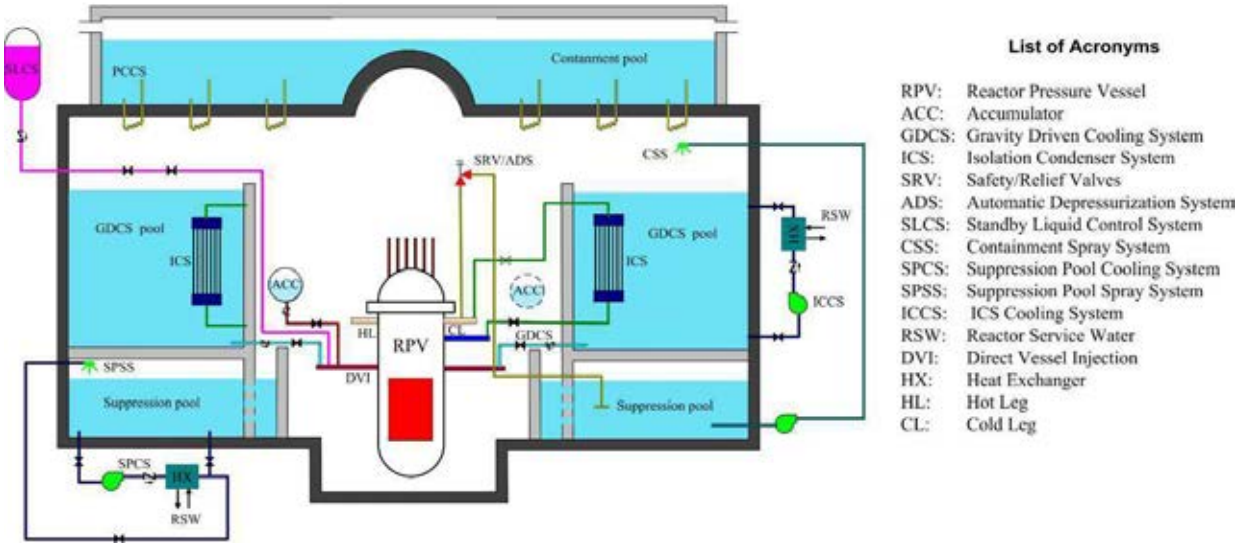

FIG. 2.14. Scheme of the SCWR-M safety system.

2.3. EURATOM SCWR CONCEPT

The High Performance Light Water Reactor (HPLWR) is the European concept of a Super-Critical Water cooled Reactor (SCWR). It is a pressure-vessel type reactor with a core exit temperature of at least 500°C at a supercritical system pressure of around 25 MPa. Most work has been performed for a core with a thermal neutron spectrum. This reactor concept has been promoted and assessed by a consortium of European partners, supported by the European Commission, during a period of time from 2006 to 2010 [2-30]. The design objectives included a net electric power of 1000 MW, net plant efficiency of around 44% and to evaluate the potential for cost reduction due to reducing the size of components or omitting them.

2.3.1. Thermodynamic cycle

With plant efficiency of about 44%, the HPLWR is considered to represent an economic advantage compared to the current LWRs. As supercritical water is a single-phase fluid, the reactor pressure vessel (RPV) is simpler than in a boiling water reactor (BWR) without the need for steam-water separators above the core and the possibility for the control rods to be inserted through the top of the vessel as in a PWR. But like a BWR (and in a supercritical fossil fired power plant), a direct cycle is possible with steam exiting the core at 500°C being fed directly to the high pressure (HP) steam turbine. This saves all costs related to a separated primary and secondary loop and the use of steam generators.

The once-through cycle is sketched in Fig. 2.15, and shows the actual steam cycle concept for the balance of the plant [2-31]. After expansion in the HP turbine, the steam at 4.25 MPa and 260°C is reheated to 441°C by part of the steam extracted, and supplied, without the need of steam separators, to the intermediate pressure (IP) and low pressure (LP) turbines.

Considering the river water at 15°C, the steam is assumed to condense at 5 kPa and 33°C. After the condenser, four condensate pumps and three preheaters (PH5 to PH7 in Fig. 2.15) which use the steam extractions from the LP turbine heat the feedwater up to 135°C. A feedwater tank at 0.55 MPa is also

used as a preheater using steam extracted at the exit of the IP turbine. Three high-pressure feedwater pumps provide the full mass flow rate of 1179 kg/s and produce a pressure of 25 MPa at the reactor inlet. A fourth pump is kept on hot standby. Another four preheaters (PH1 to PH4 in Fig. 2.15) are finally used to attain the feedwater temperature of 280°C. A net efficiency of 43.5% is predicted for this steam cycle.

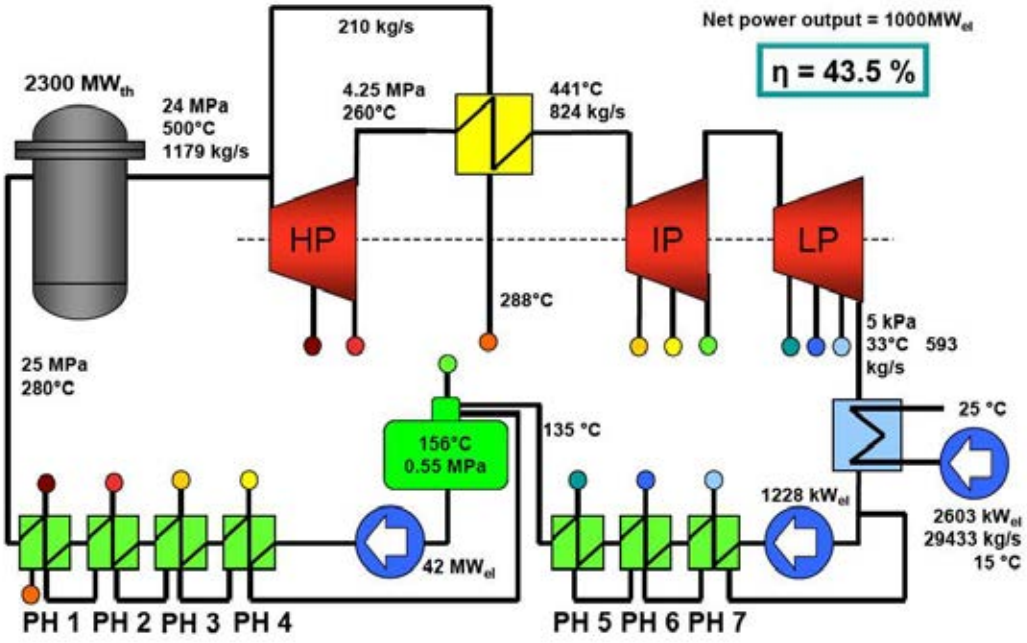

FIG. 2.15. HPLWR steam cycle concept [2-31].

Considering a load range from 500 MW to 1000 MW net electric power, the turbine control valve shall be able to keep a constant reactor inlet pressure of the feedwater at 25 MPa. Feedwater mass flow is controlled with the feedwater pumps, while the temperature of the superheated steam is kept constant at 500°C by the control rods of the core. A control valve for the extracted steam is keeping the temperature of the reheated steam constant at 441°C. A first turbine design concept [2-32] has demonstrated that the half speed rotor design of saturated steam turbines used for conventional light water reactors can be replaced by a full speed turbine rotor (50 Hz) showing significant cost savings for the balance of plant.

2.3.2. Conceptual core design

The HPLWR concept differs from current light water reactors not only by the higher pressure and core outlet temperature, but also by a higher enthalpy rise in the core. The enthalpy difference of 1936 kJ/kg between steam and feedwater is about 8 times higher than in a PWR. This implies that with an overall hot channel factor of 2 between the peak and the average coolant heat-up, this enthalpy rise would result in peak coolant temperatures of 1200°C, which is far beyond the tolerable values for strength and corrosion resistance of any available cladding material.

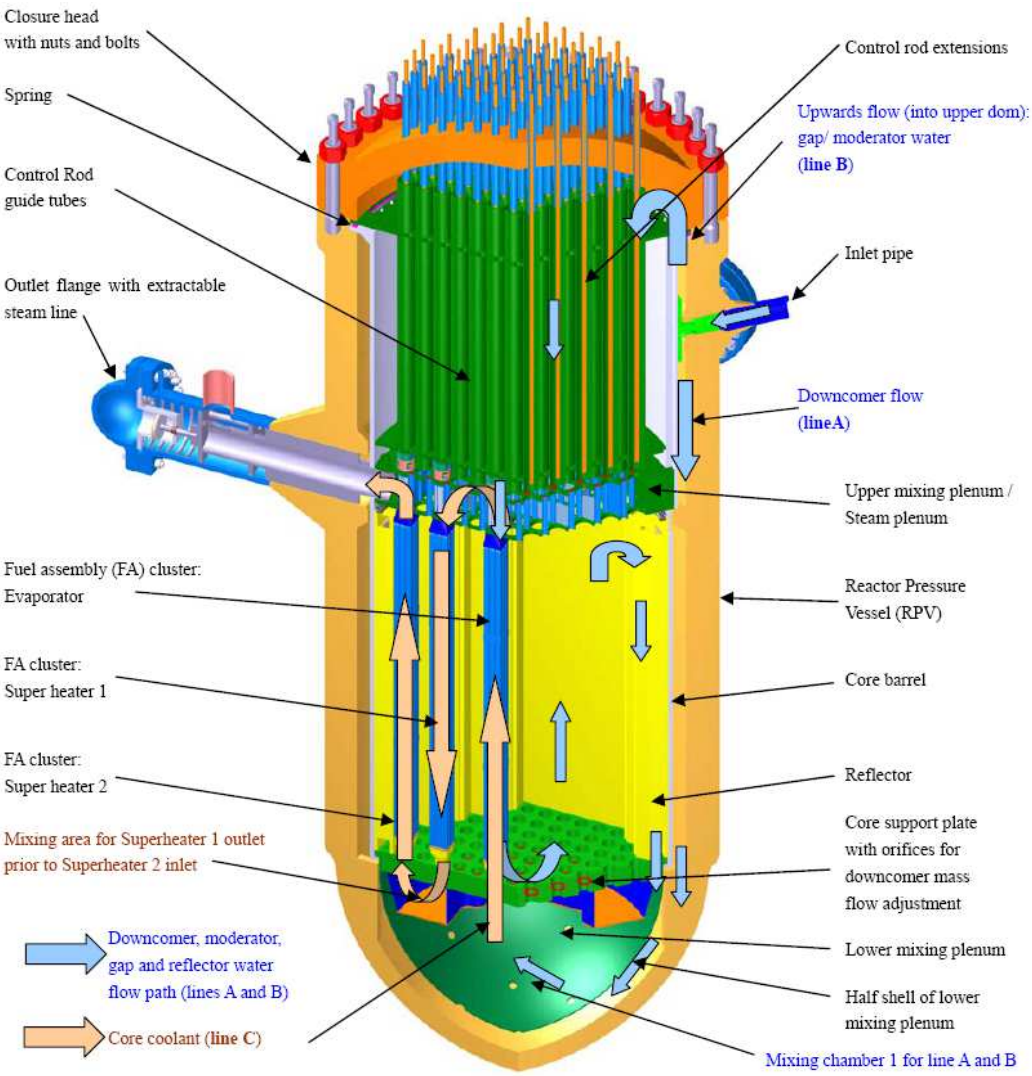

FIG. 2.16. HPLWR pressure vessel and internals [2-42].

To overcome this issue, three heat-up steps with intensive coolant mixing between them to eliminate hot streaks are proposed in the HPLWR [2-33]. The three pass core design is based on the assembly design concept [2-34] with its 40 fuel pins each, arranged in 3x3 clusters (see 2.3.3).

As shown in Fig. 2.16, the feedwater enters the 52 evaporator assembly clusters in the center of the core from the core bottom, through which it is heated up beyond the pseudo-critical temperature. After mixing in an upper mixing chamber above the core, the coolant is directed into another 52 assembly clusters with a downward flow, which build the first superheater. Coolant mixing then occurs again in an annular mixing chamber underneath the core. Final heat up to the expected core outlet temperature takes place in a second superheater formed by 52 clusters at the core periphery.

Assuming that each heat up step has the same hot channel factor of 2, the power ratio of these 3 core regions should be 4:2:1 to reach the same peak coolant temperature each. This means that the core power distribution is not uniform, but highest in the core centre and lowest at the core periphery. The proposed core layout is trying to reach this power ratio by placing the second superheater at the core periphery

where the neutron leakage is reducing the neutron flux anyway. Considering a reference peak cladding temperature of 630°C, which remains extremely challenging for stainless steels, the peak coolant temperature should not exceed 600°C, including all uncertainties and allowances for operation.

The coolant is also used as moderator water to enable the thermal neutron spectrum. A flow path of moderator water [2-33] has been designed to provide a stable flow structure through the entire load range with a constant core inlet pressure. Half the feedwater entering the RPV is split to flow upwards to cool the RPV dome, then downwards through and between the control rod guide tubes, entering the gaps between the assembly boxes and through the moderator boxes inside the assemblies. It is used afterwards to cool the radial reflector with a downward flow. All moderator water is then mixed with the remaining downcomer water in the inner part of the lower mixing chamber. A specific spherical shell provided with orifices underneath the core guarantees a mixing plenum, where mixing jets of the downcomer water are formed inside the mixing plenum.

The heat exchange between the moderator water flowing downwards and the rising coolant yields a mixed coolant temperature of 310°C at the evaporator inlet. The coolant temperature rises from 310°C to 390°C in the evaporator section. The passage through the first superheater with downward flow increases the coolant temperature up to 433°C. After the third mixing in the outer part of the lower mixing chamber without any addition of fresh coolant, the coolant finally reaches 500°C in the second superheater. The coolant leaves the reactor at 500°C through the outer part of the upper mixing chamber. This three pass core arrangement is sketched in Fig. 2.17. The arrangement of clusters is sketched in Fig. 2.18 in a cross-section of the whole core. A circle indicates the common head or foot piece of this cluster.

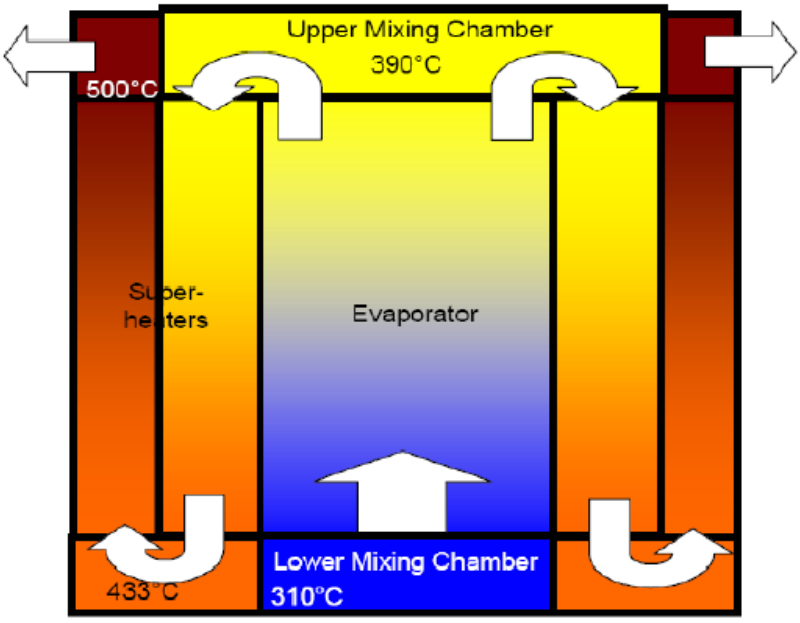

FIG. 2.17. HPLWR three-pass core.

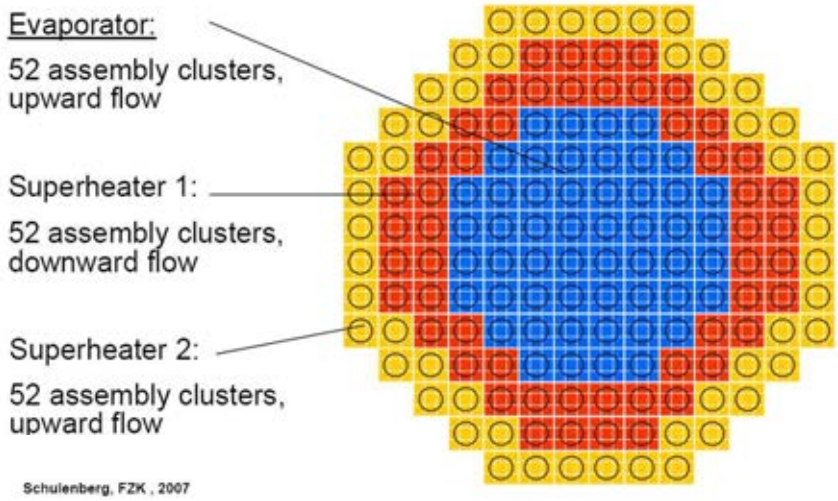

FIG. 2.18. HPLWR core cross-section.

2.3.3. Conceptual fuel assembly design

It is based originally on an assembly cluster design [2-34] consisting of 9 smaller assemblies with 40 fuel rods each, surrounded by an assembly box and provided with an additional moderator box in the centre (Fig. 2.19). The fuel rods have an outer diameter of 8 mm and a pitch to diameter ratio of 1.18. Spiral wires of 1.34-mm diameter wrapped around them with an axial pitch of 200 mm serve as a spacer with excellent mixing performance in both flow directions. Additional moderator water is provided in the 9 mm gaps between the assembly boxes as well as inside the moderator box. A honeycomb structure [2-36] with thermal insulation is suggested to minimize the thermal conductance and the mass of structural material, while keeping a high stiffness against the pressure difference and to avoid pseudo boiling of the moderator water. Three groups of 52 of these assembly clusters are taken for the evaporator, the first and the second superheater each. Control rods are assumed to run inside the moderator boxes. Neutronic analyses [2-37], [2-38], [2-39] indicate that the highest power density is located in the evaporator while the lowest power in the second superheater, achieving an average power density of 60 MW/m^3. Since density wave oscillations might take place in the evaporator assemblies, like in a boiling water reactor, the use of inlet orifices for each assembly to keep sufficient margin from stability limits is suggested as a solution [2-40].

Assembly Design Data:

Fuel pin diameter	8mm
p/d	1.18
wire wrap diameter	1.34mm
fuel pins per assembly	40
active length	4200mm
assembly box size	67.5mm
assembly box length	4851mm
water box	26.9mm
box material	SS 347

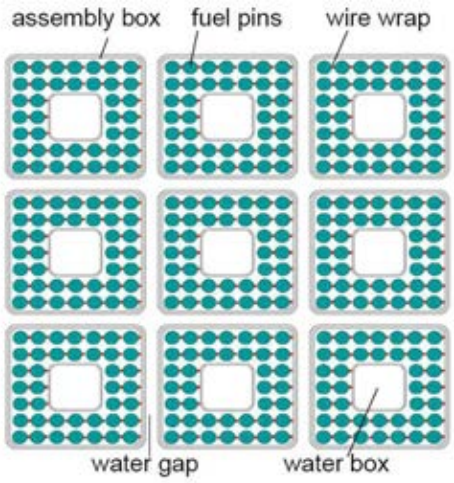

FIG. 2.19. Cross-section fuel assembly cluster.

The head piece of the fuel assembly cluster consists of four elements: a head piece plate, a transition nozzle, a window element and a bushing (see Fig. 2.20). The nine assembly boxes together with the transition nozzle and the window element are welded to the head piece plate. The moderator boxes are welded on the top of the window element. In this way the coolant will be accelerated once through the transition nozzle into the window element and then will flow horizontally into the steam plenum. The bushing, screwed on top of the window element, enables the handling of the cluster for maintenance and replacement. The metal-C-rings avoid leakage between the moderator water and the hot coolant.

The foot piece consists of a bottom plate and a diffuser. The bottom plate of the cluster foot piece supports the fuel rods of the nine assemblies. The central fuel assembly box of the cluster is instead bolted to the foot piece. The remaining eight assembly boxes are welded in the head piece and hang freely to minimize thermal deflection of the cluster. A sealing is used to minimize the leakage between the assembly boxes and the bottom plate.

Outlet nozzles at the lower end of the moderator boxes control the variation of the moderator mass flow rate at different control rod positions. The moderator water is injected through these nozzles into the diffuser. After mixing in the diffuser, the coolant flows upwards through multiple holes in the bottom plate.

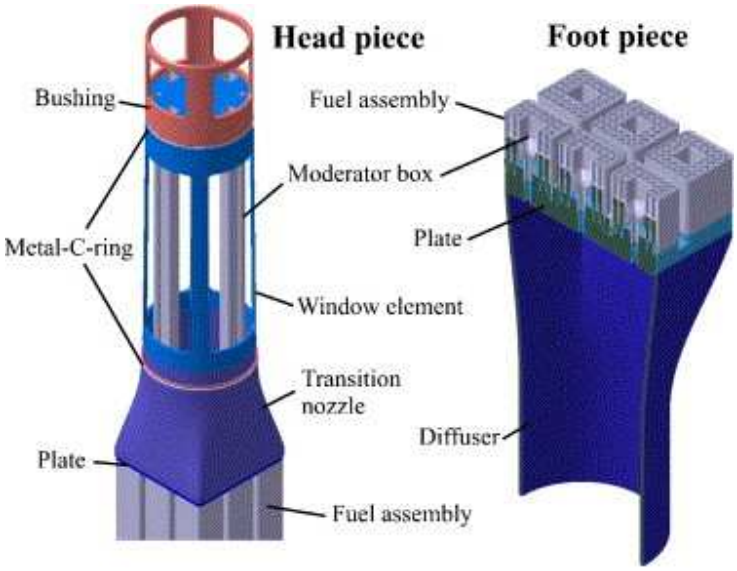

FIG. 2.20. Fuel assembly cluster head piece and foot piece [2-34].

2.3.4. Safety system design

The HPLWR plant concept is often referred as an evolution of the current boiling water reactor (BWR) facility. However, in terms of safety it differs fundamentally. In case of BWR´s it is one of the main safety characteristics that the core is always covered with water after scram in all non LOCA cases and decay heat can be removed by evaporation. In a HPLWR a continuous coolant mass flow rate through the reactor is required since the once through steam cycle provides no closed coolant loop inside the reactor. Alternative solutions include the use of redundant feedwater pumps or the depressurization of the pressure vessel such that the residual heat is removed by the discharged medium flow. These functions must also be provided inside the containment in the unlikely case of a severe accident. Many safety systems of the latest BWR safety and containment concepts can indeed be applied to the HPLWR, too.

A first design proposal for such containment is shown in Fig. 2.21. Each of the four feedwater and steam lines are equipped with two containment isolation valves, inside and outside of the containment, that close automatically in case of a feedwater or steam line break. The reactor is shutdown (scram) while the depressurization valves open releasing the steam through 8 spargers into 4 upper pools. The residual heat is removed by the 4 redundant, active low pressure coolant injection pumps in the basement of the containment. In case of a steam line break inside the containment, the increase in pressure due to the steam release is controlled by a large pressure suppression pool in the lower half of the containment equipped with 16 open pressure suppression tubes. A proposal exists for an additional passive safety system [2-41] which consists of steam injectors, which supply feedwater at high pressure from coolers, situated in the upper pools and driven by the steam produced in the core. An overflow line to the spargers is able to start the steam injectors within the first 10 seconds. However, this innovative safety system design still needs to be demonstrated. Long-term passive residual heat removal from the containment is designed to be supplied by containment condensers to the spent fuel pool above the containment.

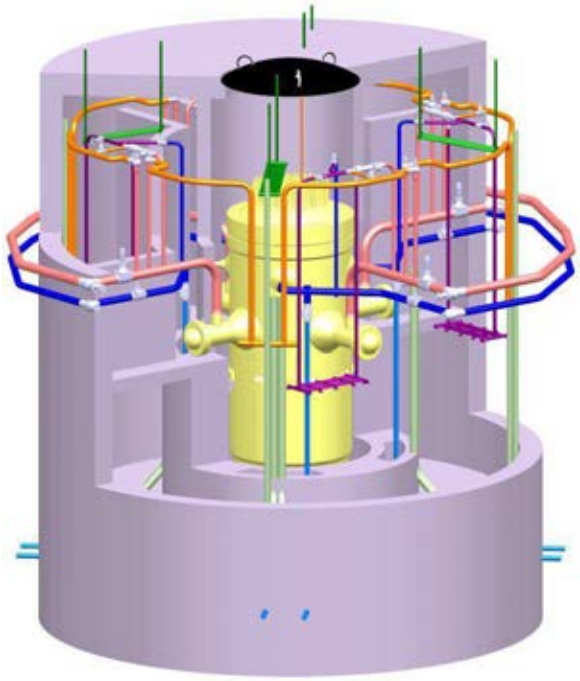

FIG. 2.21. HPLWR containment design concept [2-41].

2.4. SCWR CONCEPTS IN JAPAN

Two SCWR concepts are being developed in Japan, one corresponding to the thermal spectrum reactor and the other to the fast spectrum reactor. Yamada et al. [2-43] described the thermal-spectrum reactor concept referred to as the Japan SCWR (or JSCWR). This concept was developed under the financial support of the Ministry of Economy, Trade and Industry (METI) [2-44]. The basic philosophy of the JSCWR development is to utilize proven light water reactor and supercritical fossil-fired power plant technologies as much as possible to minimize the R&D cost, time and risks. Therefore, the JSCWR is designed as a thermal neutron spectrum reactor using light water as moderator and reactor coolant. The JSCWR plant consists of a pressure-vessel type, once-through reactor and a direct Rankine cycle system. Reactor coolant fed through inlet nozzles is heated up in the core and flows through outlet nozzles with no recirculation in the vessel. Other options to the JSCWR core design are being investigated at the University of Tokyo. The electric output of the JSCWR is assumed to range from 600 MWe to 1700 MWe class to fulfill user's requirements as much as possible. In this section, the reference value is selected to 1725 MWe, which corresponds to a reactor thermal output of 4039 MWth.

Nakatsuka et al. [2-45] described the core design for the fast-spectrum reactor, which is based on a similar plant system compared to that of the thermal-spectrum reactor. The fast-spectrum reactor, however, would produce higher power rating than the thermal-spectrum one of the same reactor pressure-vessel size. Since the fast-spectrum reactor does not require the moderator, its unit capital cost would be lower than the thermal-spectrum reactor.

2.4.1. Thermodynamic cycle

One of the most attractive advantages of the JSCWR over conventional LWRs is its high thermal efficiency, which is estimated about 43% without reheating, and no or little need for R&D for the turbine

and entire BOP because supercritical pressure fossil-fired power plant systems can be applied with minor design changes. The core outlet coolant, which is customarily called 'steam' although there is no distinction between steam and water above the supercritical pressure, is directly delivered to the turbine system, and the feedwater comes back directly from the feedwater pumps. The balance of plant (BOP) consists of three-stage turbines, condensers, and condensate and feedwater system, and electricity is generated by a generator driven by the turbines, which is a well-matured technology and needs essentially no additional R&D.

The turbine system of the JSCWR consists of one dual-exhaust high-pressure (HP) section, one dual-exhaust intermediate-pressure (IP) section and three dual-exhaust low-pressure (LP) sections (that is, a six flow, tandem compound system). The cycle uses a moisture separator to reduce the wetness fraction of steam to prevent damages of the LP turbine blades.

The turbine system could be simplified by adopting a combined high-pressure and intermediate-pressure turbine, which is under development in the fossil-fired power industry, if the steam flow rate is low enough. The adoption of the combined turbine as well as full-speed turbine system might reduce the length of total turbine system and hence reduces the volume of turbine building. Figure 2.22 shows the BOP system of the JSCWR and its heat balance.

The steam cycle of the JSCWR employs an eight-stage re-generative system consisting of four-stage low-pressure feedwater heaters, one-stage deaerator, and three-stage high-pressure feedwater heaters as shown in Fig. 2.22. Steam bled from the HP, IP and LP turbines is conveyed to high-pressure and low-pressure feedwater heaters (HP/LP-FWHs).

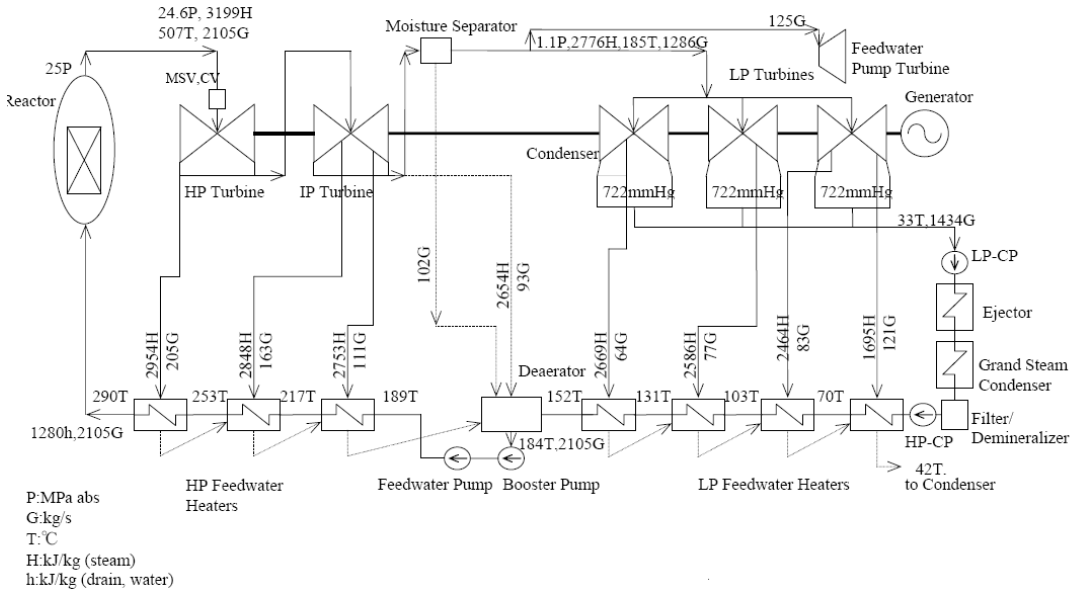

FIG. 2.22. Balance of plant system of JSCWR.

The condensate collected in the condensers is pumped by low-pressure condensate pumps (LP-CPs) to an air ejector, a grand steam condenser and a set of demineralizer and filters. Being pumped up further by high-pressure condensate pumps (HP-CPs), the condensate passes through the low-pressure feedwater heaters including a deaerator. The feedwater from the deaerator is pumped up to supercritical pressure by booster and reactor feedwater pumps (RFPs) and passes through the high-pressure feedwater heaters. The feedwater heaters heat the feedwater to a temperature of 290ºC at the rated conditions.

The volumetric capacity of the turbines as well as the feedwater heaters used in the JSCWR is much smaller than those used in current LWR plants because of the small volumetric flow rate per electricity production resulted from high enthalpy/pressure of supercritical coolant.

The main auxiliary systems in the turbine island consists of the turbine building closed cooling water system (TCW), and the turbine building seawater system (TSW). In addition, there are many other auxiliary systems. Basically the same technology used in BWR plants can be applicable to the JSCWR.

2.4.2. Conceptual core designs

2.4.2.1. Thermal-spectrum core

The reactor core is operated at 25 MPa. The feedwater temperature is 290℃, and the average core outlet coolant temperature is 510℃. Because the operating pressure is higher than the critical pressure of water (22.1 MPa), no phase change occurs in the core and the coolant changes continuously from a low-temperature high-density fluid at the inlet of the core to a high-temperature low-density fluid at the outlet. The coolant flow rate, 2105 kg/s, is significantly lower than current fleet of reactors, since the enthalpy rise in the core is higher, than that of current LWRs.

The structure of the JSCWR RPV is similar to that of PWR. The inner diameter is about 4.8 m; the total inside height is 16.5 m. The flow in the RPV is depicted in Fig. 2.23. The coolant is provided through cold legs (inlet nozzles) and flows out through hot legs (outlet nozzles). Most of the coolant flows downward through the annulus region between the RPV wall and the shroud (downcomer), and flows into the lower plenum. A part of coolant is directed to the upper dome to remove heat from the shroud head and flows into the bypass line. The coolant from the downcomer mixes with the coolant from the bypass line in the lower plenum and flows upward through the core. The inner surface of RPV wall is cooled by the inlet coolant as in PWRs to keep the temperature low enough to use the same materials used for PWRs.

Control rods are used for primary reactivity control. The control rod drives are mounted on the bottom of the RPV. Cruciform control rods are vertically inserted into and withdrawn from the core by the control rod drives. To ensure adequate shut down margin and to minimize the local peaking during the entire operation cycle, gadolinium (Gd, a burnable poison) is incorporated in the fuel.

The standard fuel cycle for the JSCWR is the same as that of LWRs in Japan. The JSCWR has a potential to fully utilize uranium and plutonium resources as fuel due to the flexible neutron spectrum. The aqueous-reprocessing technology is applicable to the JSCWR fuel.

The reactor core consists of 372 fuel assemblies. Each fuel assembly stays in the core for three cycles. The cross sectional view of the core is shown in Fig. 2.24 together with its loading pattern.

The U^{235} enrichment for the equilibrium core exceeds 7% to achieve the similar discharge burnup as current LWR fuels. This high enrichment is mainly due to relatively high neutron captures of the structural materials especially fuel cladding and channel boxes.

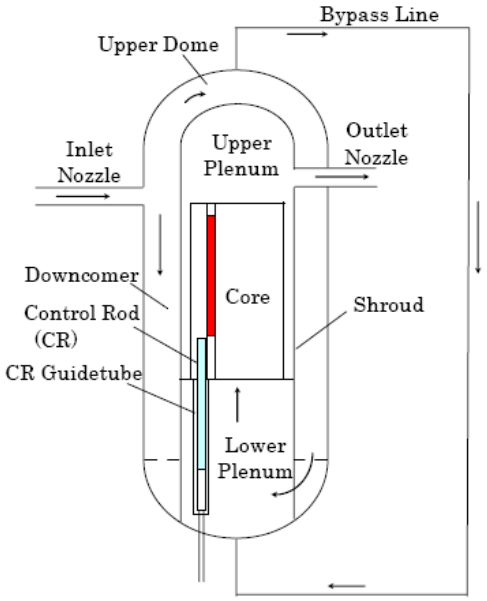

FIG. 2.23. Configuration of JSCWR pressure vessel and coolant flow.

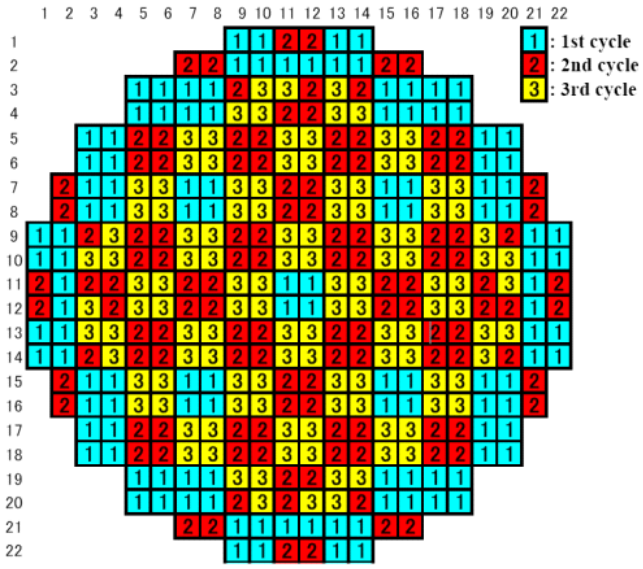

FIG. 2.24. Cross sectional view of the JSCWR core and its loading pattern.

2.4.2.2. Fast-spectrum core

The conceptual core design of the Japan SCWR with the fast spectrum is referred to as the 'super fast reactor'. It is shown in Fig. 2.25 and consists of seed and blanket fuel assemblies [2-46]. Figure 2.26 shows cross section of the seed assembly and the blanket assembly and the core. The coolant flow scheme in the reactor vessel is also shown in Fig. 2.25. A part of the feedwater flows to the top dome and then

downward through the blanket assemblies. It mixes with the flow coming from the downcomer at the lower plenum. The mixed coolant flows upward through the seed assembly. Based on the fuel rod and fuel assembly designs, a 700 MWe core was designed with 3-D neutronic thermal-hydraulic coupled calculations and subchannel analyses.

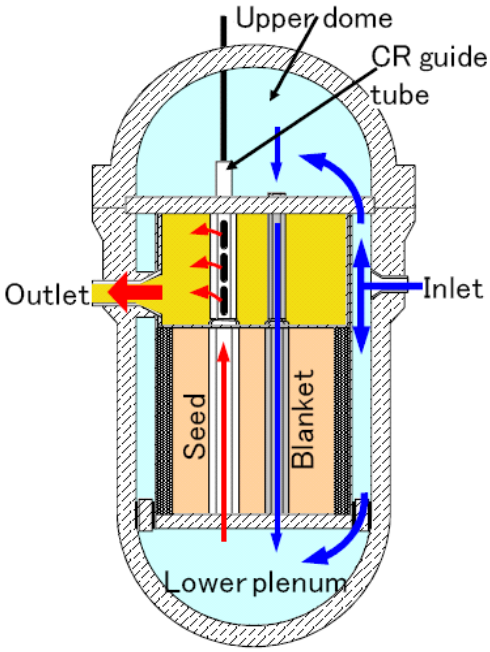

FIG. 2.25. Configuration of fast-spectrum SCWR pressure vessel and coolant flow.

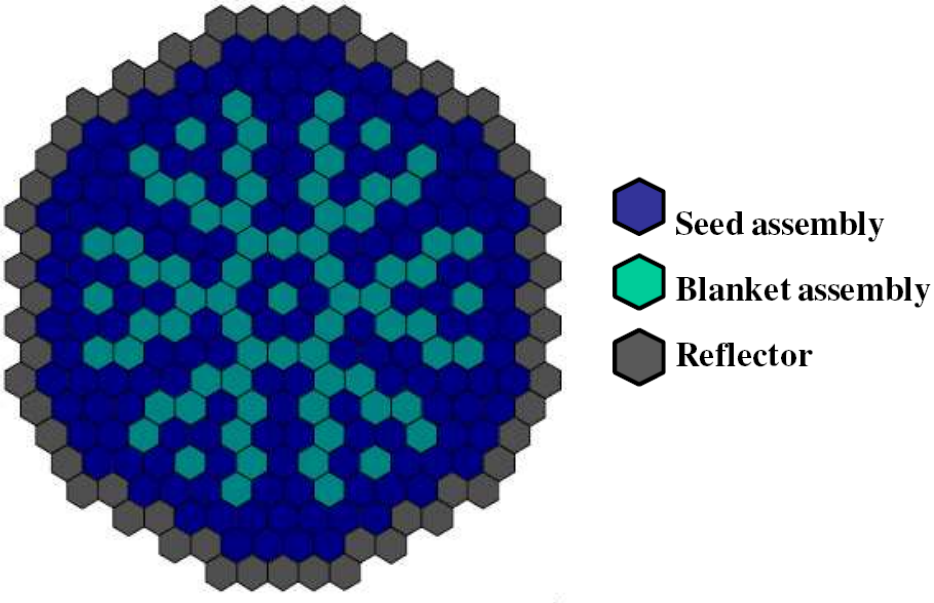

FIG. 2.26. Cross sectional view of the fast-spectrum JSCWR core.

2.4.3. Conceptual fuel assembly designs

2.4.3.1. Thermal-spectrum core

The JSCWR fuel assembly consists of 192 fuel rods and a square water (moderator) rod in the centre [2-47]. The square channel box (137-mm x 137-mm with area equivalent to 8x8 fuel rods) isolates the coolant flow and prevents the cross flow between fuel assemblies. The fuel rods contain UO_2 pellets like LWR fuels in the modified stainless-steel cladding and are arranged in 16x16 square lattices. The active fuel length is 4.2 m, which is a little longer than typical LWR fuel lengths, to reduce the linear heat generation rate. The total fuel length is about 5.8 m. The channel box, water rod and fuel rods are made of stainless steel.

The vertical cross sectional view of the fuel assembly is shown in Fig. 2.27 to illustrate the coolant flow path. A part of coolant flows through the 'outchannel' that is the area outside of channel box, and through the water rod subsequently. Then it is mixed with another part of flow that comes from core bottom directly. Finally this mixture flows through the channels between the fuel rods and cools the fuel rods.

The axial enrichment zoning and the Gd rods distribution are based on BWR fuel design technology (refer to Fig. 2.28). High enrichment fuel is inserted in the bottom zone to avoid the top peak power distribution. A natural uranium blanket is introduced at the top of the fuel rod. The 'heat transfer control area' (refer to Fig. 2.28), at locations between 70-cm and 90-cm from the bottom, has slightly lower enrichment than neighbour zones. It has been introduced to achieve the bottom-peak axial-power distribution as well as to avoid the peak position between 50-cm and 100-cm from the bottom of the core. The number of Gd rods is reduced from 20 to 16 in a zone under the heat transfer control area. Gd concentration in these rods is 12 wt%. Figure 2.29 shows the Gd rod position and an enrichment distribution to achieve the target local power distribution for bundle exposures from 0 to 35 GWd/t.

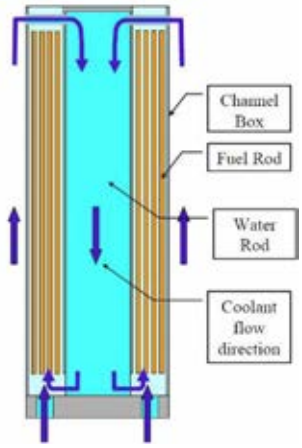

FIG. 2.27. Vertical cross sectional view of a fuel assembly.

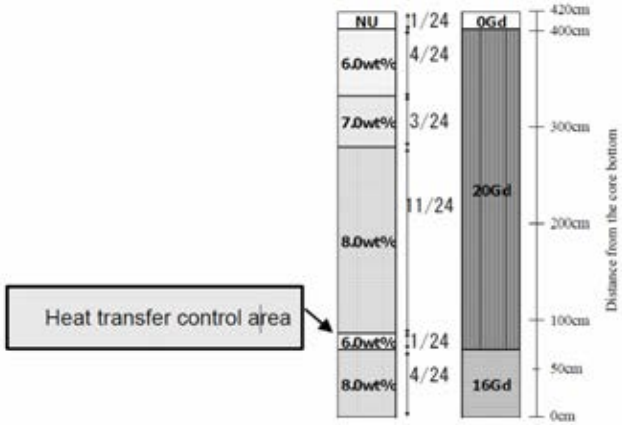

FIG. 2.28. Axial enrichment zoning

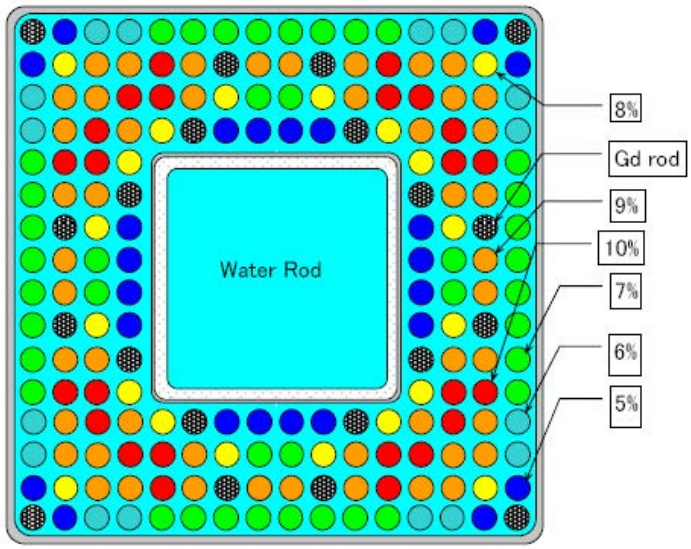

FIG. 2.29. Horizontal cross sectional view of JSCWR fuel assembly.

2.4.3.2. Fast-spectrum core

The core of the super fast reactor consists of seed and blanket fuel assemblies [2-45]. Figure 2.30 shows the cross section of the seed assembly and the blanket assembly. In the fuel rod and core designs, MOX fuel and stainless steel cladding are used for seed fuel rods, and depleted UO_2 and stainless steel cladding are used for blanket fuel rods. The fuel rod parameters are determined to satisfy thermal, fluid dynamic, and mechanical criteria and also to achieve high power density and high average outlet temperature. In the blanket assembly, the fuel rod region is surrounded by a solid moderator (ZrH layer) so that fast neutrons coming from the seed fuel slow down in the ZrH layer and are absorbed by the blanket fuel without causing fast fissions. It enables the super fast reactor to have a negative void reactivity without adopting flat core shape or additional devices.

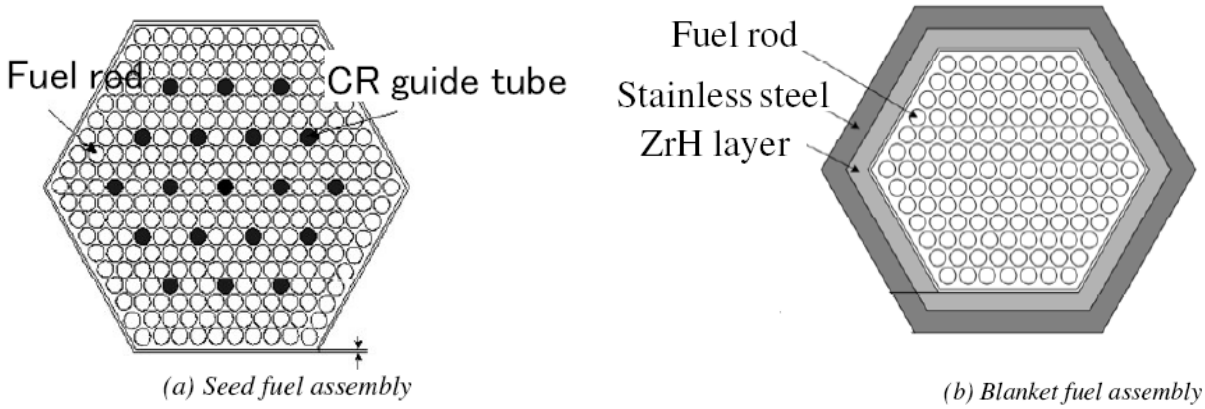

FIG. 2.30. Cross sectional view of the Japan fast-spectrum fuel assemblies.

2.4.4. Safety system design

The JSCWR safety philosophy is based on that of advanced LWRs, which reflects experiences and lessons learned of the past and current LWRs. The design philosophy for safety and reliability are as follows:

- Maximum utilization of the matured, proven technologies that have been accumulated in the successful commercial operation of LWRs as well as supercritical pressure fossil-fired power plants;
- Safety system development based on inherent feature of water cooled reactor and well developed LWR safety technologies. The inherent feature includes negative void (density) and Doppler coefficients. The well-developed LWR safety technologies mainly include reactivity control systems and emergency core cooling systems (ECCS).

Safety systems of the JSCWR are schematically described in Fig. 2.31, and mainly consist of high-pressure auxiliary feedwater systems (AFS), automatic depressurization systems (ADS), and LPCIs that also work as RHR [2-48]. Reactor scram, AFS and LPCI are actuated by low core flow rate signals instead of low water level signals, which is commonly used in current BWRs.

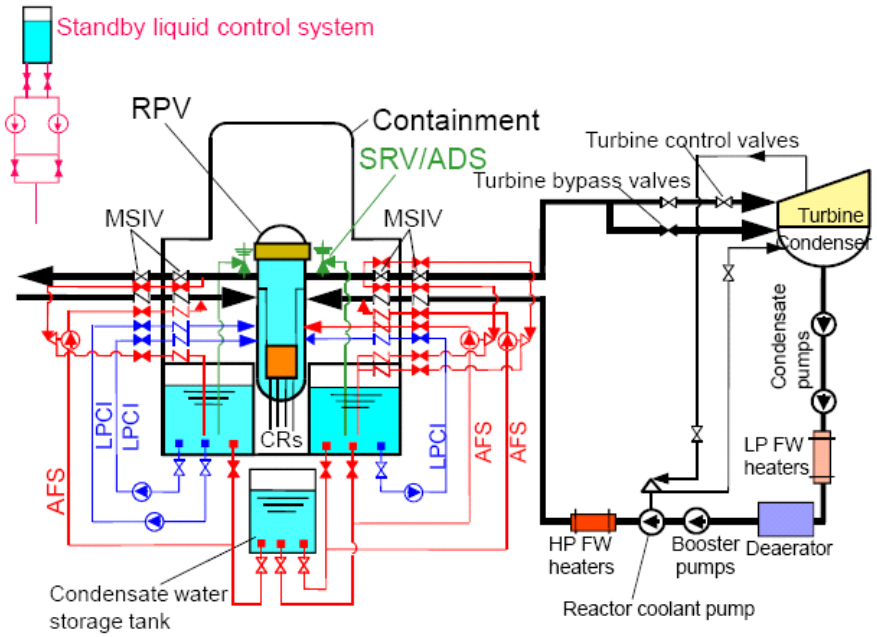

FIG. 2.31. Safety system design of JSCWR.

2.5. SCWR CONCEPT IN KOREA

One of the major difficulties in the design of an SCWR is the additional neutron moderation in order to compensate the low coolant density in the later stage of coolant heat-up. The water rod concept was introduced as a simple method to provide additional moderation, however it may result in an inevitable complexity in the design of the reactor upper part. A solid moderator concept was introduced in the Korean SCWR to avoid this difficulty. A conceptual design of a 1400 MWe SCWR core with a cruciform type of U/ZrH_2 solid moderator has been studied [2-49]. The design features include a solid moderator design, an axial zoning of the burnable poison and fuel rod, a flow rate control by adjusting the orifice design, and a control rod design for an excess reactivity control. The maximum power peaking is 2.48 and

the maximum coolant temperature is 577°C. Reactivity coefficients such as the moderator temperature coefficient and fuel temperature coefficient are negative for the whole burn-up period. At a cold zero power condition, the minimum shutdown margin is 1.16%Δρ at the beginning of a cycle, which satisfies the required shutdown margin limit. The concept described here should not be considered as a complete one, but a preliminary idea. It is solely based on information frozen at the time, and is subject to further improvement.

2.5.1. Thermodynamic cycle

Thermal efficiencies of various thermodynamic cycle design options were evaluated [2-50] and the results are summarized in Table 2.7. For the purpose of a direct comparison with the APR1400, the core thermal power was set as 4000 MW(th). Among various options, the direct cycle showed the best thermal performance of 43.1%.

TABLE 2.7. EVALUATION OF THERMAL EFFICIENCY FOR THERMAL CYCLE DESIGN OPTIONS

	Option 1. Reference Cycle (APR1400)	Option 2. High Sat. Steam	Option 3. High Sup. Steam	Option 4. Supercritical secondary	Option 5. VHP turbine	Option 6. Direct Cycle
Core Power (MW(th))	4000	4000	4000	4000	4000	4000
Net electric power (MW(e))	1455.1	1546.4	1613.5	1635.4	1677.8	1723.1
Pump power (MW)	28.24	72.86	72.87	100.14	69	99.13
Cycle efficiency (%)	36.38	38.66	40.34	40.88	41.95	43.10

A heat balance calculation was performed for a system with 3180.4 MW(th). The resultant heat balance is shown in Fig. 2.32. The basic BOP concept here is a two-stage reheating and an eight-stage regenerative system. The steam cycle is equipped with one moisture separator and two reheaters as in the ABWR. High-pressure, intermediate-pressure and low-pressure turbines are used, as in the supercritical pressure fossil-fired power plant. A deaerator is not adopted here because of a concern regarding radioactivity release during the deaeration process. For the heat balance calculation, the important design parameters of the BOP components for thermal efficiencies, such as the turbine isentropic efficiency and pump efficiency, were tuned so that the heat balance results were matched with the ABWR value. The calculated thermal efficiency is 44.02 %, which is similar to 44% of the SCLWR-H.

2.5.2. Conceptual core design

The KAERI's conceptual core contains 193 fuel assemblies with a four-batch fuel loading strategy. The target burn-up is 45 GWd/tHM with a 44% thermal efficiency. The linear heat generation rate is 144.2 W/cm. The core design parameters are summarized in Table 2.8.

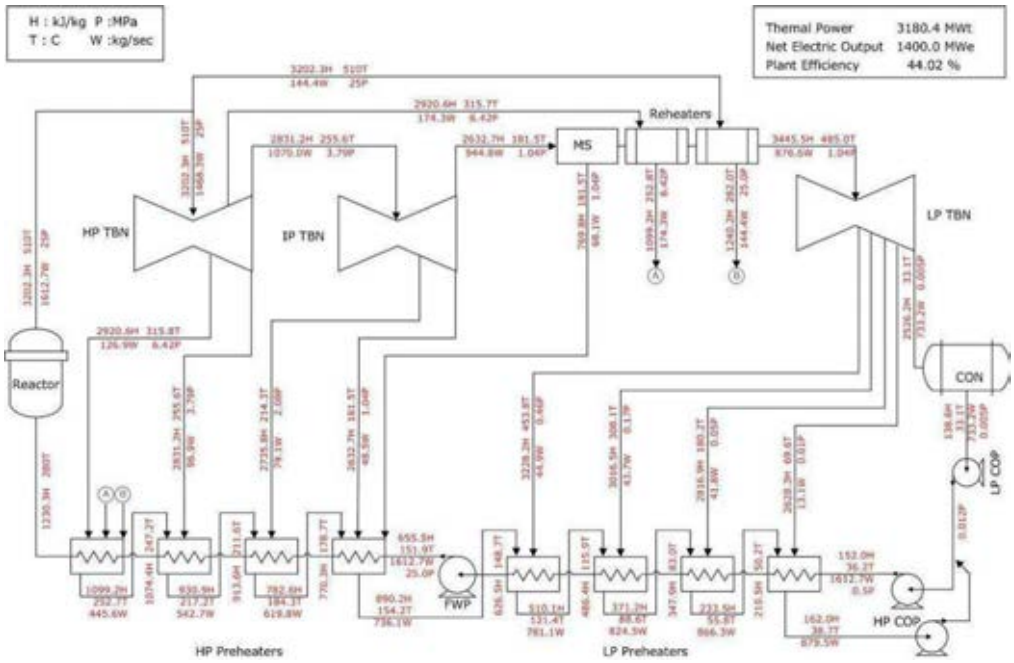

FIG. 2.32. Typical BOP layout and heat balance data for a direct cycle.

TABLE 2.8. CORE DESIGN PARAMETERS

Design Parameters	Values
Thermal/electric power (MW)	3182/1400
Number of assembly	193
Avg. discharge burnup (GWd/tHM)	45
Avg. linear heat generation rate (W/cm)	144.2
Active core height (cm)	381
Inlet/outlet temperature (℃)	280/510
Max. cladding temperature (℃)	620

Figure 2.33(a) shows a four-batch fuel loading scheme for the equilibrium fuel cycle of the conceptual SCWR core. Fresh fuel assemblies are loaded at the inner region of the core according to a low leakage loading pattern. The coolant flow rate at each orifice is adjusted to reduce the maximum coolant temperature at the core outlet. The SCWR operates with a boron free condition, since it adopts a direct cycle without steam generators, steam separators, and steam dryers. Control rods are solely responsible for an excess reactivity control during a reactor operation period without soluble boron. Generally, the control rod driving mechanism is located at the top of the core in a SCWR system like in a conventional PWR and inserted from the top during a core operating period, which can cause the axial power shape to

become distorted and shifted to the bottom of the core combined with a coolant density variation. There are six types of control banks to control the excessive reactivity and the power distribution. A neutron absorber material of 100-cm long is introduced for the axial power shape control only. All control banks are assumed to move individually without any systematic overlap mechanism. The assembly-wise relative power distribution of the equilibrium core is shown in Fig. 2.33(b). During the burn-up, the peak assembly-wise relative power occurs in the inner region of the core where the coolant flow rate is the highest and CR banks are not inserted at the BOC. The peak assembly-wise power at the MOC and the EOC occur at the fresh fuel assembly where the CR banks are almost withdrawn. However, the maximum relative assembly-wise power is nearly the same as that of a conventional PWR.

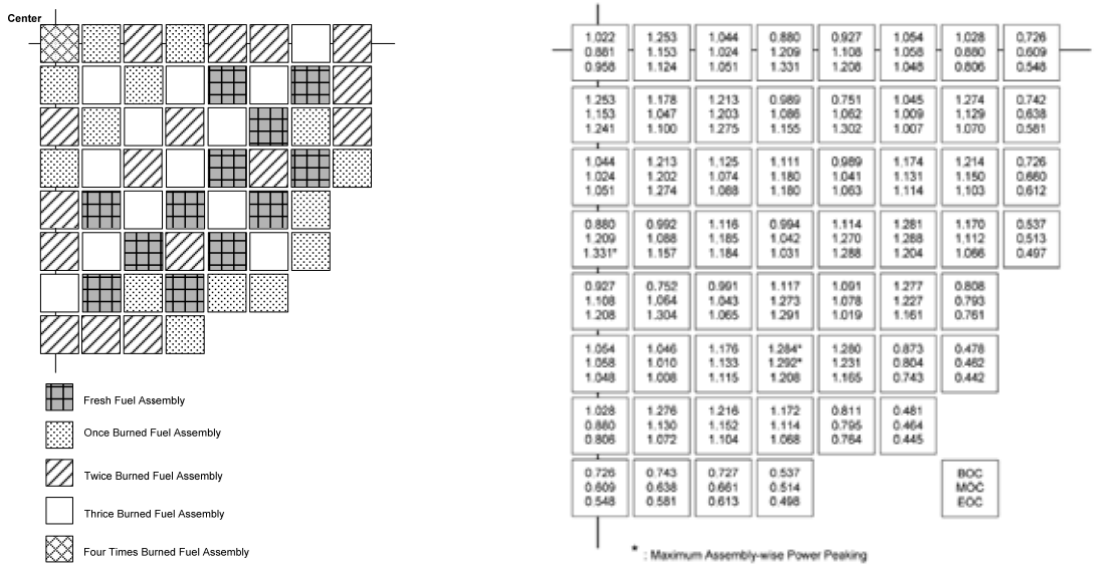

a) Fuel Loading Pattern b) Assembly-Wise Power Distribution

FIG. 2.33. Core design concept.

The axial power shapes of the conceptual SCWR core at the BOC, MOC, and EOC are shown in Fig. 2.34. The axial power peak appears near the bottom of the core at the BOC and moves to the top of the core at the EOC due to the control banks withdrawal. The maximum axial power peaking factor is less than 1.45 at the EOC, which is almost the same as that of a conventional PWR.

2.5.3. Conceptual fuel assembly design

The fuel assembly has 21x21 fuel rods array with a pitch of 25.25 cm and the gap between the fuel assemblies is 1.1 cm. Sixteen fuel pins in the fuel assembly are additionally replaced by 16 single pins of solid moderator in order to increase the neutron moderation. The fuel assembly is composed of 300 fuel rods, 25 cruciform-type solid moderator pins and 16 single pins of the solid moderator. The power peaking factor limit, corresponding to the maximum linear heat generation rate of 39 kW/m, is 2.7. Gadolinia, Gd_2O_3, is used as a burnable poison. The fuel assembly is shown in Fig. 2.35.

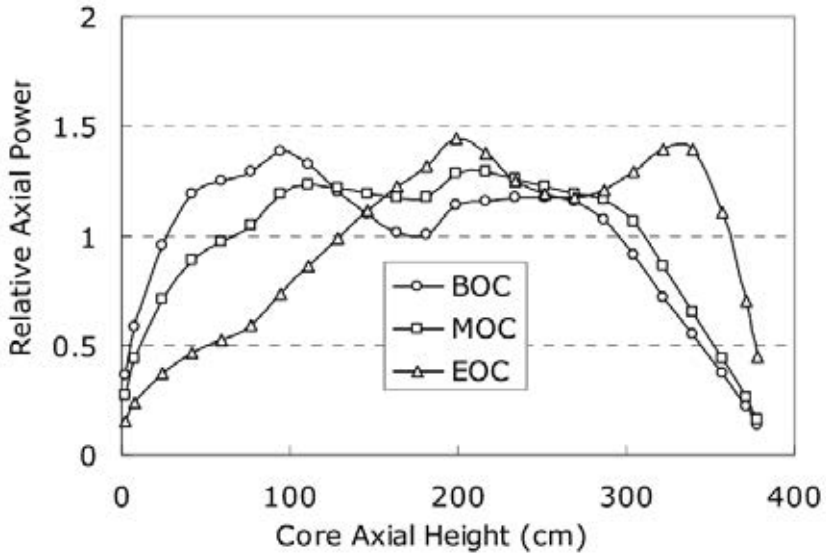

FIG. 2.34. Axial power distributions of conceptual SCWR core.

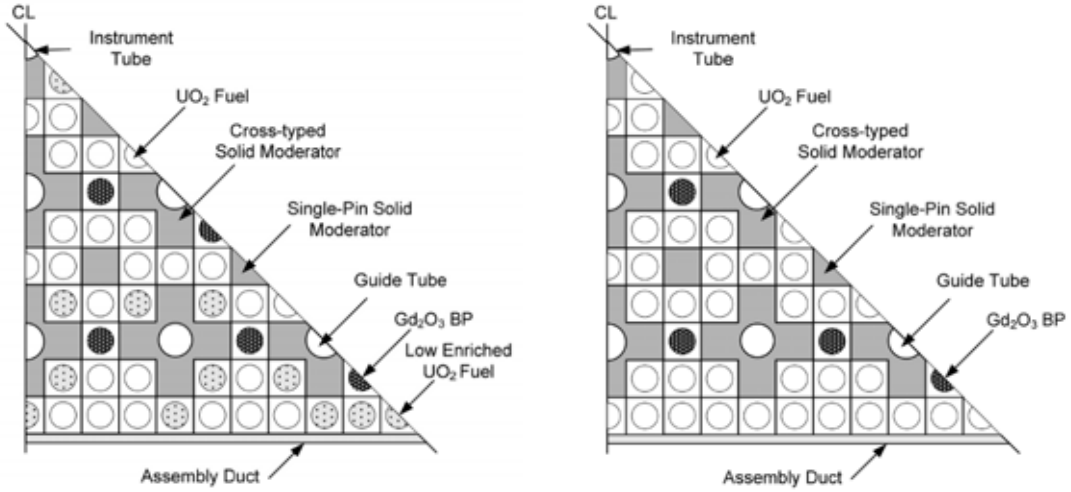

(a) Assembly Design A (b) Assembly Design B

FIG. 2.35. Fuel assembly design with solid moderators of cruciform and single pin.

One of the criteria for a successful core design with a ZrH_2 solid moderator concept is an acceptable axial power shape during operation. The control of the axial power shape of the core is difficult because of a dramatic coolant density variation along the axial direction and the control rod insertion from the top of the core where the reactivity is smaller due to a lower coolant density than at the bottom of the core. To control the axial power shape, the fuel assembly is divided into three axial zones having a different enrichment from each other as shown in Fig. 2.36. The core height is 381 cm.

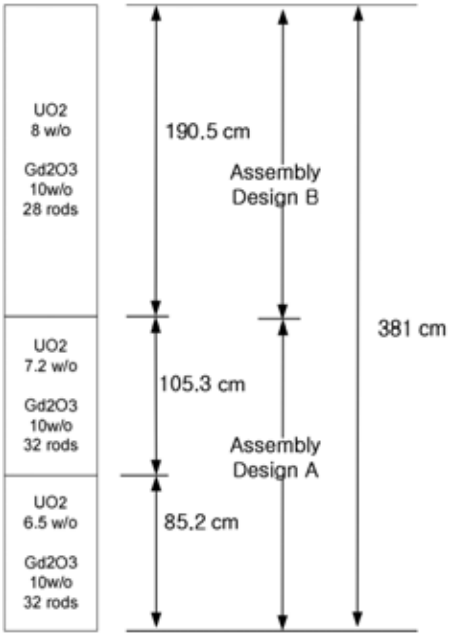

FIG. 2.36. Axial zoning of fuel and burnable poison rod.

2.5.4. Safety system design

Due to the limitation of resources, the safety system design was not covered in the Korean SCWR research program during 2007-2009.

2.6. SCWR CONCEPT IN RUSSIA[2]

An increase in the efficiency of NPPs with light-water reactors through 'nuclear' steam superheating was one of the problems solved in the field of nuclear power industry. The commissioning of the Beloyarsk NPP, Units 1&2 with the channel-type reactor in the sixties of the 20th century showed the potential of realization of this idea and the necessity to solve a series of problems in technology and materials science. The NPP operation experience, elaboration and operational experience of steam superheating channels are extremely important in choosing the ways of design development of Generation IV reactors with supercritical pressure coolant water.

The first technical proposal on a supercritical water cooled reactor of vessel type made in Russia in 1986 was the design of a two-circuit reactor plant (RP). The concept of the two-circuit RP of integrated type VVER-SCP-I with electric power of 500 MW was proposed in 1990. The design activities on these projects were performed at OKB GIDROPRESS and the analyses were carried out at the RRC Kurchatov Institute. The State Science Center of the Russian Federation Institute of Physics and Power Engineering (SSC RF IPPE) has been performing the computational studies of a single-circuit RP VVER-SCP [2-51], [2-52] since 2001. In 2006 OKB GIDROPRESS launched the design effort and computational analyses to corroborate the design of a single loop RP [2-53].

The purpose of a RP VVER-SCP is the electric power generation by the power unit with a concurrent rise in the conversion factor and a reduction in the natural uranium consumption for effective application of light-water power reactors in the closed nuclear fuel cycle [2-54]. The simplification of the schematic

[2] This section is based on paper: M.P. Nikitenko, P.L. Kirillov, A.E. Chetverikov, V.M. Makhin, A.P. Glebov, A.N. Churkin, "Russian Concept of a Single-Circuit RP with Vessel Type Supercritical Water-Cooled Reactor"

diagram of NPP due to a transfer to a single-loop RP is supposed to reduce the capital costs for its construction and to make the construction period shorter. The specified advantages and significant operation experience for NPPs with 'nuclear' steam superheating are the positive factors in support of the development of the given trend in Russia. Moreover, the experience gained in the thermal power industry that has been using the boiler-turbine plants with supercritical water is of great use.

Thus, the VVER-SCP design is being developed starting with available experience gained in the creation of a RP with 'nuclear' steam superheating and boiler-turbine supercritical water plants in thermal power industry.

2.6.1. Thermodynamic cycle

SSC RF IPPE has carried out a calculation of the RP thermal pattern with electric power 1600 MW oriented at the application of the two available turbines K-800-240-5 (LMZ). The thermal pattern of the plant with turbine K-800-240-5 provides an eight-stage system of feedwater heating that consists of mixing heaters: four low-pressure heaters (LPH), deaerator, three high-pressure heaters (HPH). The low-pressure heaters, LPH1 and LPH2, are vertical, of mixing type, and are made as per the scheme with transfer pumps. The main condensate goes to LPH1, and then is pumped into LPH2. From LPH2, condensate is supplied through heaters, LPH3 and LPH4, into the deaerator. Three HPHs are connected in series on the feedwater side and are designed for feedwater in the amount of 105% of the maximum steam supplied to the turbine. The thermal pattern of the reactor plant with VVER-SCP-1600 is given in Fig. 2.37.

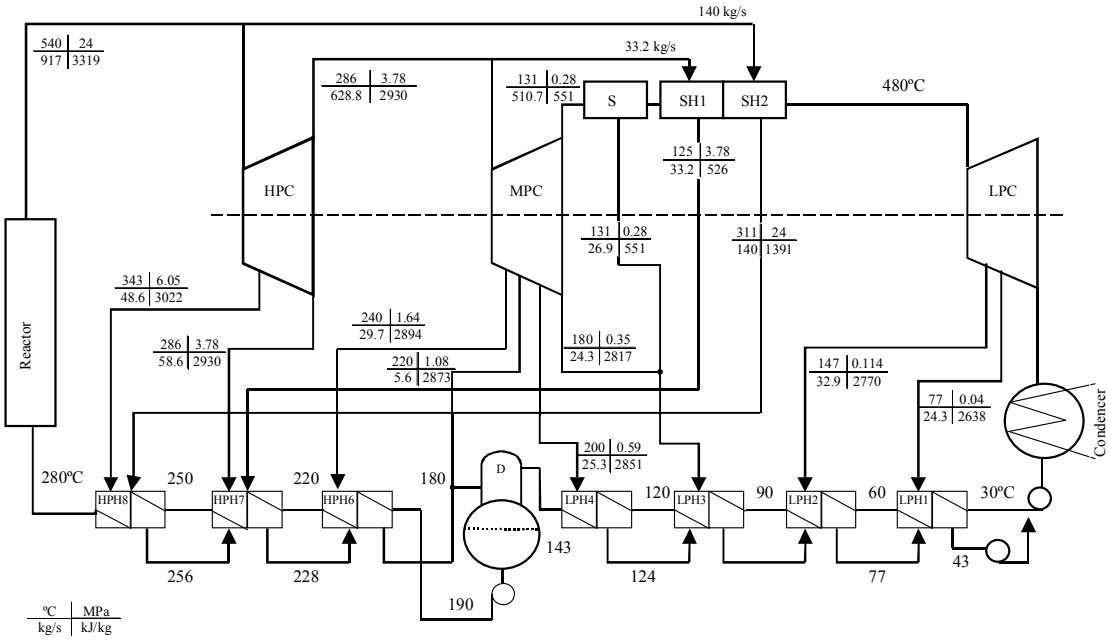

FIG. 2.37. Thermal pattern of reactor plant with VVER-SCP-1600 MW(el.) (one turbine is shown).

2.6.2. Conceptual core design

So far OKB GIDROPRESS has developed at the conceptual level the reactor design (Fig. 2.38), reactor internals and several versions of hexahedral jacketed FAs for a core with a single-pass and double-pass coolant flow diagram. The RP design for a power unit of 1700 MW(el.) is considered. The main characteristics of the reactor are given in Table 2.9.

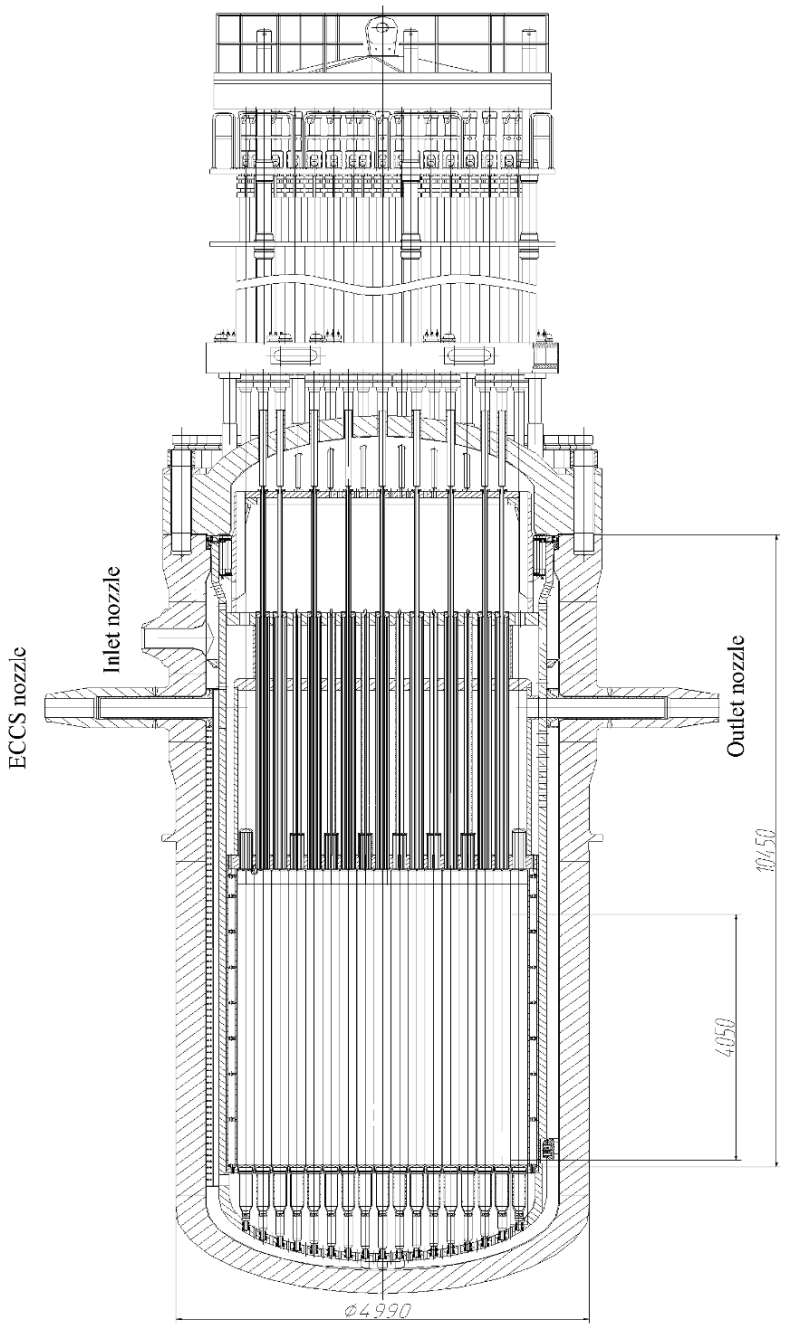

FIG. 2.38. Conceptual VVER-SCP reactor.

TABLE 2.9. DESIGN PARAMETERS AND PERFORMANCE OF VVER-SCP REACTOR

Parameter	Value [a]
Nominal thermal power of the reactor, MW	3830
Coolant flowrate through the reactor under the nominal conditions, kg/s	1890
Coolant pressure at the reactor outlet, absolute, MPa	24.5
Coolant temperature at the reactor inlet, nominal, °C	290
Coolant temperature at the reactor outlet, nominal, °C	540
Design temperature of the reactor vessel, °C	350
Design pressure of the reactor vessel, MPa	27
Design temperature of the reactor internals, °C	600
The assigned service life of the reactor, years	60
Overall dimensions of the reactor vessel, m:	
- height	21.1
- maximum diameter	5.32
Quantity of the FAs in the core, pcs.	241
FA-to-FA pitch (nominal), mm	207
Average specific heat rate of the core, kW/l	
- single-pass	107
- double-pass	115
Fuel height in the cold state, m:	
- single-pass	4.05
- double-pass	3.76
Conversion factor	0.9 – 1
Fuel burn-up, MWD/kg U	40 – 60
Limiting damaging dose in the cladding, dpa	50
Time of FA operation in the reactor, years	4 – 5
Time between refuellings, months	12

[a] Parameter values can be specified in the course of further designing.

The main requirements for the core are as follows:

- Fuel conversion factor is close to one (the requirement is met when 'tight' fuel grids are applied where the fast-resonance neutron spectrum is realized);
- Inherent safety of the reactor in accidents with core uncovering;
- Maximum permissible temperature of fuel rod cladding and FA structural components under normal operation judging by the tentative estimations shall not exceed 730ºC (the temperature was chosen on the basis of the operational experience of structural materials in the BN-type reactors and in the reactors at the Beloyarsk NPP, Unit 1, 2);
- Limiting damaging dose in the fuel rod cladding shall not exceed 50 dpa;
- Minimization of coolant leaks (bypass) from the inlet chamber into the outlet one (the 'hot' and 'cold' coolant mixing can result in thermal stresses and local pressure changes with appearing of the thermo-acoustic effect).

The specified requirements are taken into account when elaborating the two versions of the reactor that differ in core coolant flow diagram:

- single-pass flow diagram (Fig. 2.39),
- double-pass flow diagram (Fig. 2.40).

The core of both reactor concepts consists of jacketed hexahedral FA (Fig. 2.41). The FAs are designed with guide tubes for control rods of the rod cluster control assemblies (RCCA). The arrangement of RCCAs in the core is shown in Fig. 2.42. Figures 2.43 and 2.44 show an example of the calculated relative distributions of FA power across the core for two reactor versions.

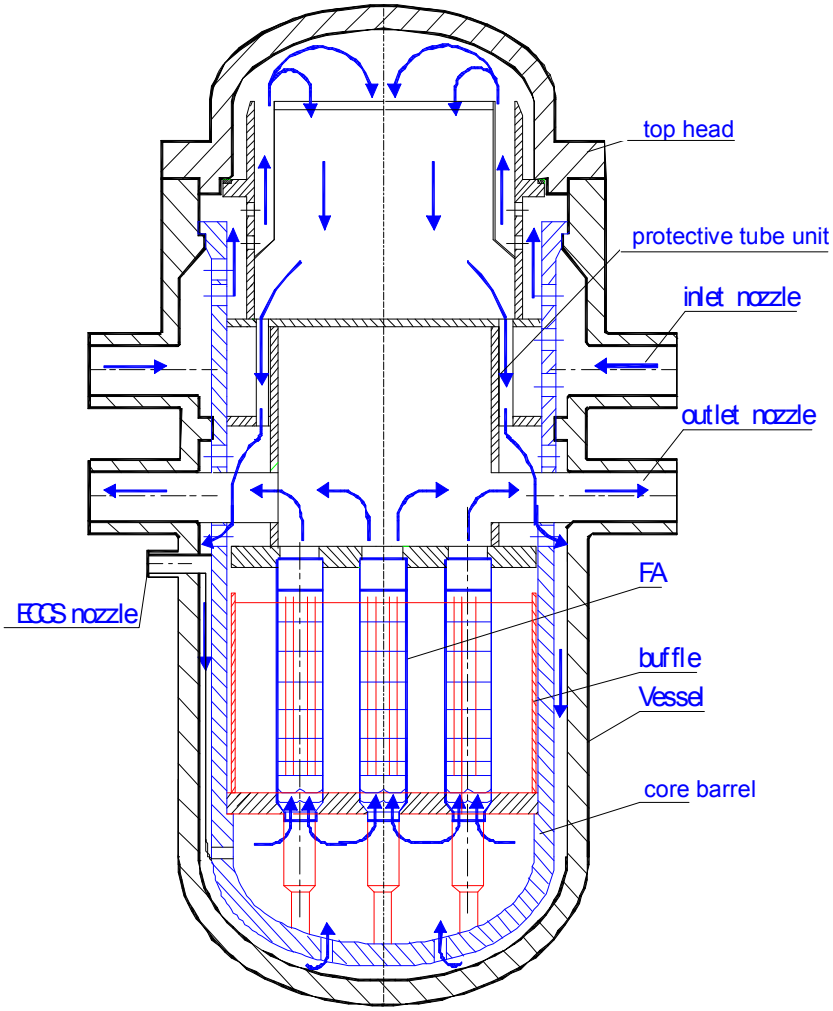

FIG. 2.39. Direction of coolant flow in VVER-SCP core with a single-pass flow diagram.

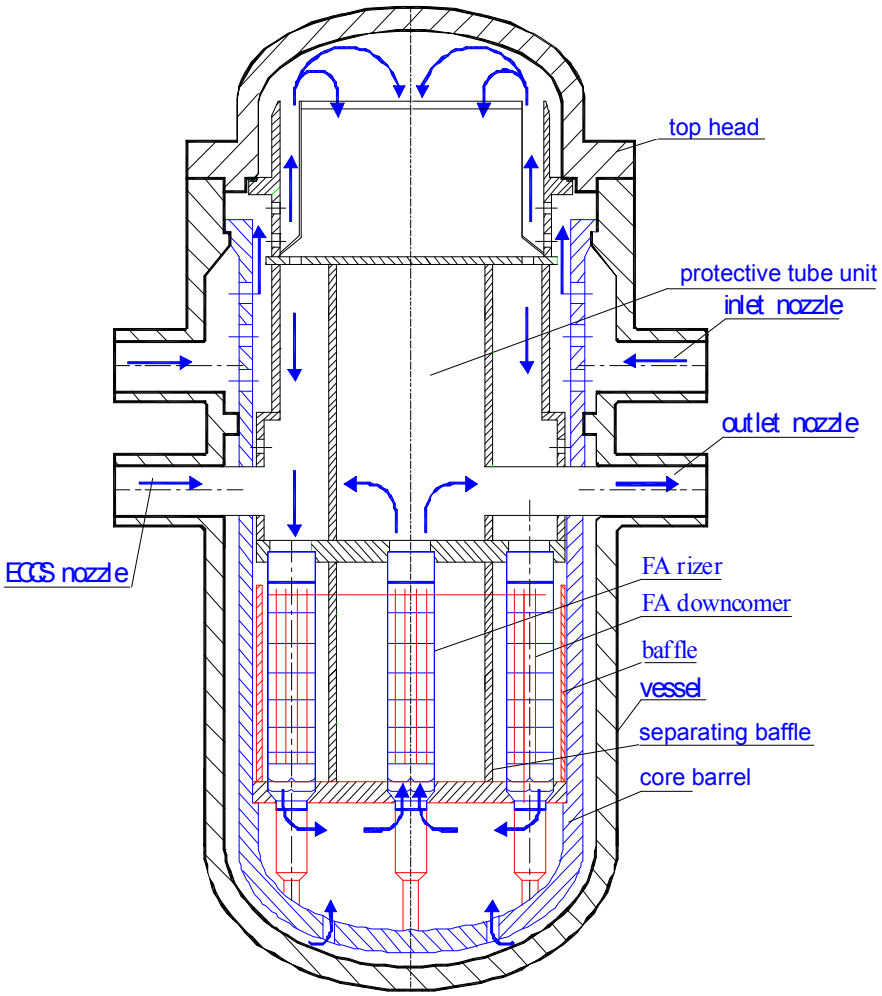

FIG. 2.40. Direction of coolant flow in VVER-SCP core with a double-pass flow diagram.

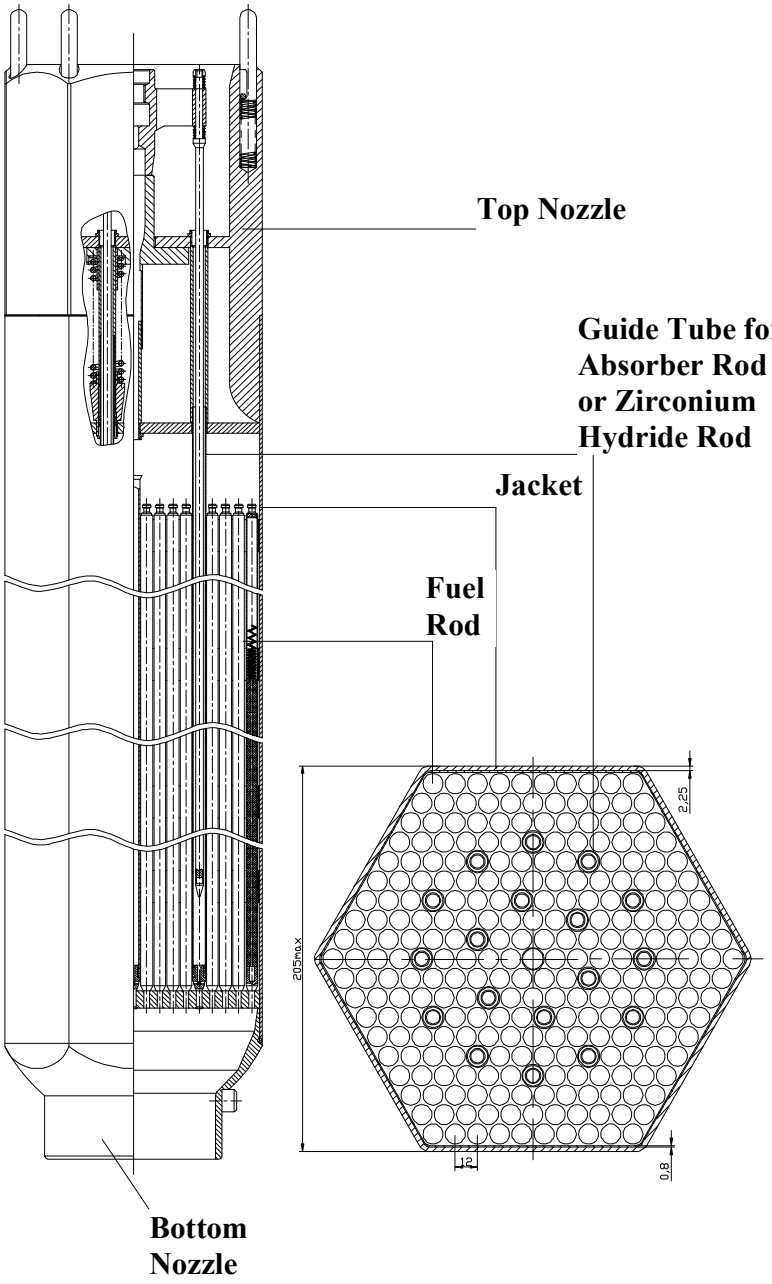

FIG. 2.41. Design of a jacketed FA.

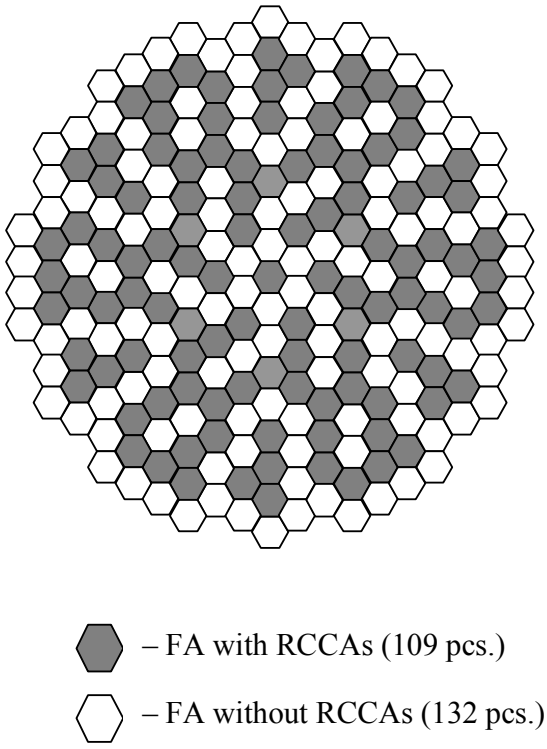

FIG. 2.42. Fuel assembly layout in the VVER-SCP core.

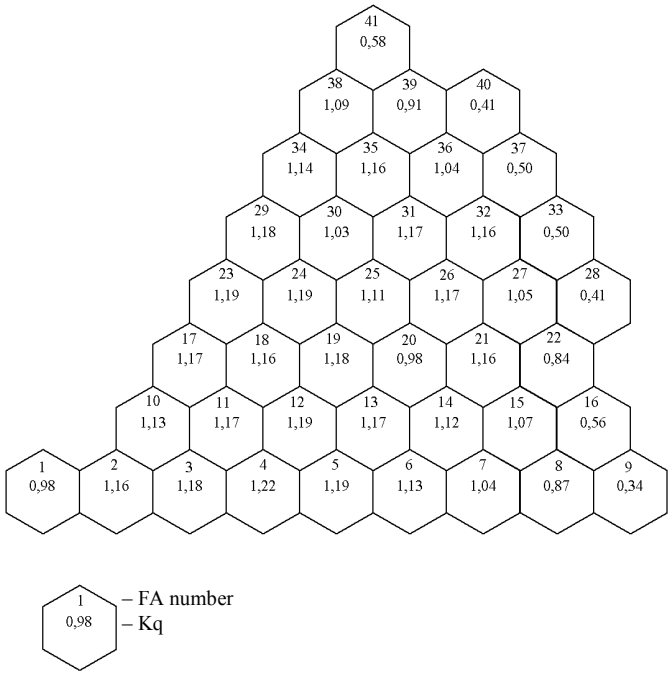

FIG. 2.43. FAs relative power distribution in core at BOC for single-pass flow diagram.

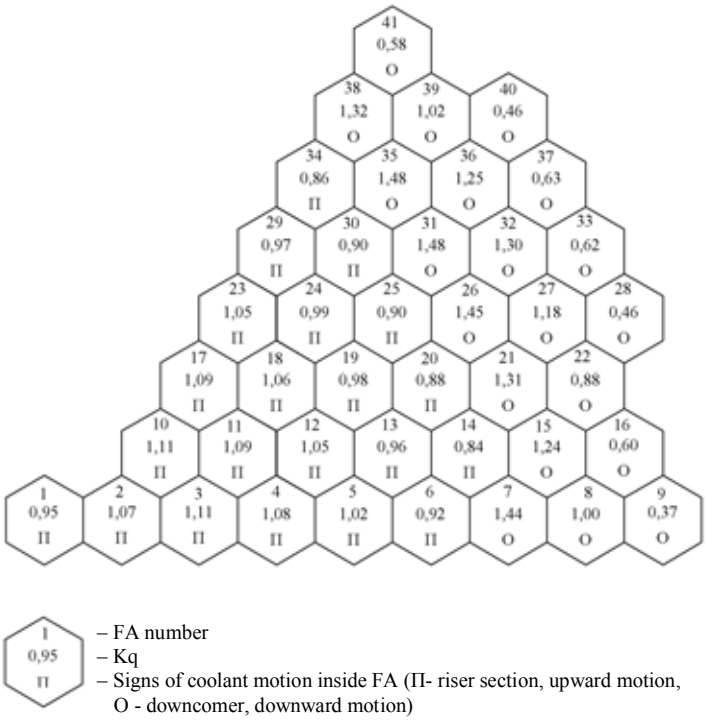

FIG. 2.44. FAs relative power distribution in core at BOC for double-pass flow diagram.

The usage of the single-pass flow diagram with once-through upward coolant flow in the reactor core results in a design simplification and improves the plant safety under the conditions with natural coolant circulation. However, there are two key problems that need to be solved [2-55]:

- Strong axial power peaking (this problem can be solved by profiling fuel enrichment and/or arrangement of elements with moderator in the upper part of the core);
- Special engineering solutions are required for provision of negative void reactivity effect at EOC.

To avoid the positive void reactivity effect in the core with coolant single-pass flow a version with a sandwich-type core is considered (Fig. 2.45). MOX-fuel layers 0.9-m high are separated by layers that consist of depleted uranium and zirconium hydride.

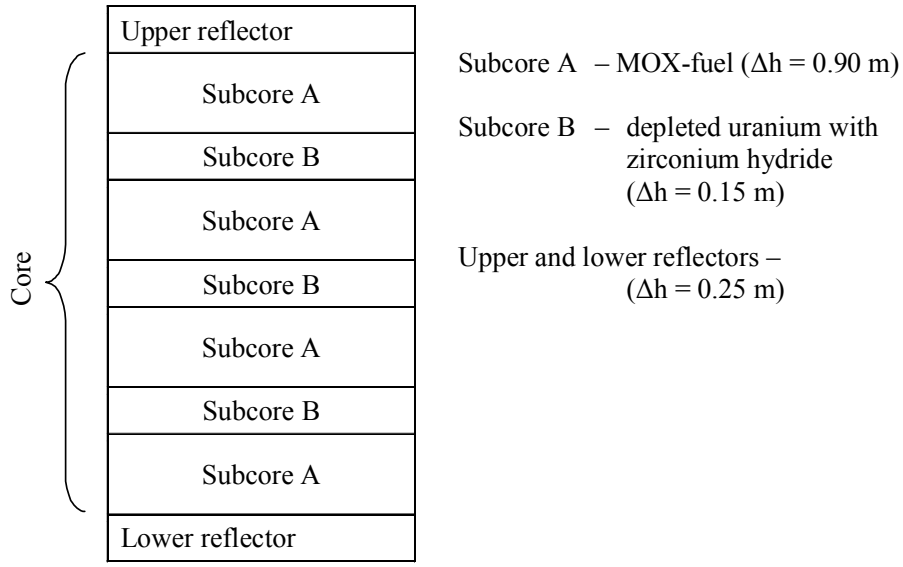

FIG. 2.45. Diagram of a sandwich-type core (axial breakdown into layers of the core).

In the double-pass flow diagram the coolant moves downwards along the peripheral circular part and moves upwards in the central part. The application of the double-pass flow diagram ensures [2-56]:

- negative void reactivity effect within the entire fuel cycle without special technical solutions;
- improvement of the conditions of fuel rods cooling due to an increase in coolant flow velocity;
- reduction in temperature differentials along the core height;
- shift of the point with coolant pseudo-critical temperature into the core lower part, in which relatively small heat fluxes take place (deposits of impurities on fuel rods claddings and the conditions of deteriorated heat transfer are expected in the pseudo-critical temperature field);
- coolant mixing in the lower chamber, which decreases the unevenness of coolant heating at the outlet of the FA central part.

However, the effectiveness of coolant natural circulation and large pressure loss over the core remain concerns for this configuration.

Two versions of the core with a double-pass flow diagram are studied now: with a separating core baffle (Fig. 2.40) and without one, in the latter case its functions are to be performed by FA jackets.

2.6.3. Conceptual fuel assembly design

The FA for VVER-SCP consists of fuel rods, a jacket tube, guide tubes for the RCCA absorber rods to move inside them, elements to create the neutron spectrum using zirconium hydride, spacer elements and structural components. A specific feature of the FA is a tight fuel grid. The distance between the fuel rods is 1.3 mm. Several versions of fuel rod spacing are being developed. The analogues for the considered FA are the jacket-free TVS-2M of VVER-1000 reactor; the jacketed FA for BN fast reactor and the jacketed FA of Unit 5 at the Novovoronezh NPP. The analogues of solutions for the fuel rod spacing are:

- the cellular design of TVS-2M spacing grids;
- fuel rods for the FA of BN fast reactors using wire spacing spirals.

One of the versions of the jacketed FA under development (for single-pass flow diagram) is given in Fig. 2.41. Main parameters of VVER-SCP FA are given in Table 2.10.

TABLE 2.10. MAIN PARAMETERS OF FA

Parameter	Value [a]
FA width across flats, mm	205
Quantity of fuel rods in FA, pcs.	252
Fuel rod diameter and cladding thickness, mm	10.7×0.55
Fuel pellet diameter, mm	9.4
Pitch of triangular grid, mm	12
Quantity of guide tubes for the RCCA absorber rods, pcs.	18
Central tube, pcs.	1
Guide and central tubes diameter and thickness, mm	12×0.55
Jacket thickness, mm	2.25

[a] Parameter values can be specified in the course of further designing.

2.6.4. Safety system design

The basic diagram of a single-circuit RP within the containment is shown in Fig.46. Only one out of three coolant circulation loops is shown in the figure, one channel from each safety system is also shown performing the following functions[3]: containment isolation (MSIV); passive residual heat removal from the core (PHRS); emergency core cooling system and reactor makeup (PCFS accumulators and tanks, ECCS pumps); prevention of pressure increase in the containment (PPDS, spray system); heat removal from the containment (CECS). Figure 2.47 shows one channel from the pressure decrease system under emergency conditions (BRU), and one channel from the pressure limitation system in the reactor (PORV).

Reactor trip is actuated by the reactor trip system by insertion RCCA absorber rods, their location in the core is shown in Fig. 2.42.

[3] Systems performing safety functions are listed in the round brackets.

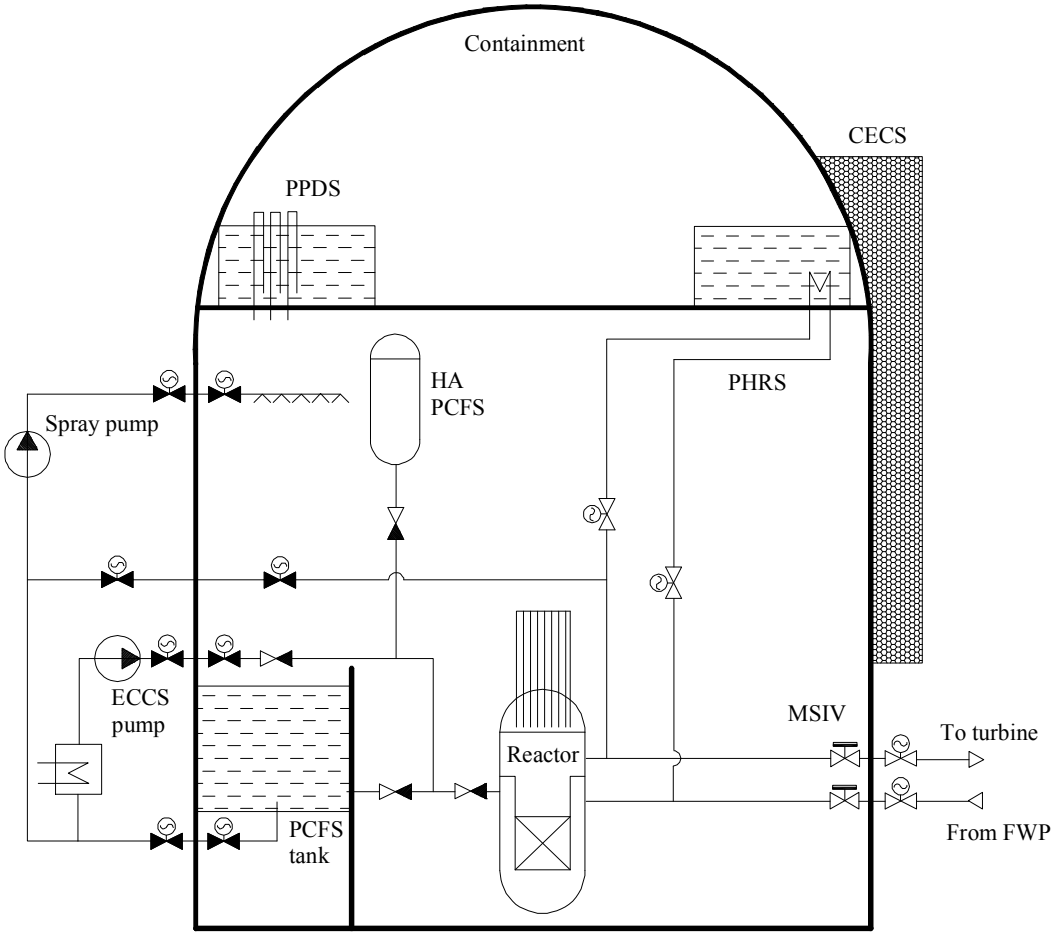

FIG. 2.46. VVER-SCP safety systems.

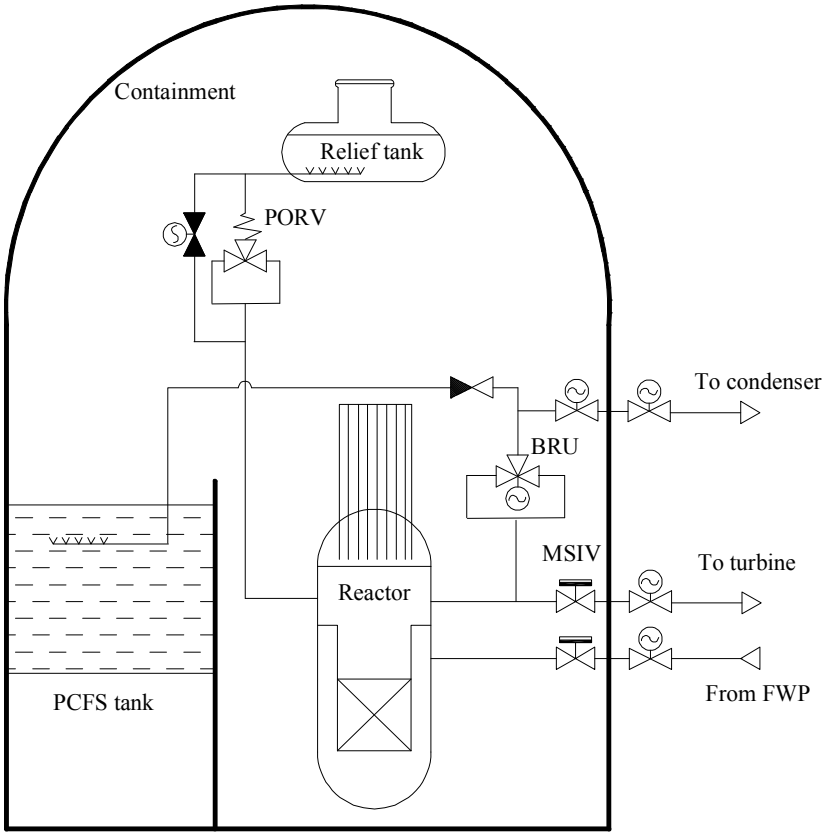

FIG. 2.47. Safety systems for pressure decrease under emergency conditions and pressure restriction in the reactor.

LIST OF SYMBOLS FOR SECTION 2

Δh	height (thickness) of the transverse core layer, m
D_{rod}	Rod diameter, mm
Kq	FA relative power
T_{in}	Inlet temperature, ºC
T_{max}	Maximum temperature, ºC
T_{out}	Outlet temperature, ºC

REFERENCES FOR SECTION 2

[2-1] IDAHO NATIONAL LABORATORY, The U.S. Reference Design - Supercritical-Water-Cooled Reactor Pressure Vessel, Addendum A2-1 of Generation IV Nuclear Energy Systems Ten-Year Program Plan – Fiscal Year 2007, Idaho National Laboratory Report, Volume I, September 2007 (2007).

[2-2] YETISIR, M., DIAMOND, W., LEUNG, L.K.H., MARTIN, D., DUFFEY, R., "Conceptual Mechanical Design for A Pressure-Tube Type Supercritical Water-Cooled Reactor", Proc. 5th Int. Sym. SCWR (ISSCWR-5), Vancouver, British Columbia, Canada, March 13–16 2011 (2011).

[2-3] DUFFEY, R.B., et al., "Nuclear Energy for Oil Sands Production: Providing Security of Energy and Hydrogen Supply at Economic Cost", Proc. IAEA-CN-/108/5P, IAEA International Conference, Vienna, June 2003 (2003).

[2-4] BRADY, D., et al., "Canada's NSERC/NRCan/AECL Generation IV Energy Technologies Program", Proc. 30th Annual Conference of the Canadian Nuclear Society, Calgary, Alberta, Canada, May 31–June 03 2009 (2009).

[2-5] PIORO, I.L., DUFFEY, R.B., Heat Transfer and Hydraulic Resistance at Supercritical Pressures in Power Engineering Applications, ASME Press, ISBN 0-7918-0252-3, New York, NY, USA (2007).

[2-6] HENDRICKS, R.C., et al., Survey of Heat Transfer to Near-Critical Fluids, Report No. NASA TN-D-5886, Lewis Research Center (Report No. E-5084), NASA, Cleveland, OH, USA, 116 pages, 1970a (1970).

[2-7] HENDRICKS, R.C., et al., Survey of Heat Transfer to Near-Critical Fluids, Advances in Cryogenic Engineering, Cryogenic Engineering Conference, Plenum Press, USA, Vol. 15, pp. 197-237, 1970b (1970).

[2-8] PIORO, I.L., et al., "Supercritical Water-Cooled Nuclear Reactors: Thermodynamic-Cycles Options", Proc. 6th International Conference on Heat Transfer, Fluid Mechanics and Thermodynamics (HEFAT-2008), Pretoria, South Africa, Paper #PI1, June 30–July 02 2008 (2008).

[2-9] DUFFEY, R.B., PIORO, I., ZHOU, X., ZIRN, U., KURAN, S., KHARTABIL, H., NAIDIN, M., "Supercritical Water-Cooled Nuclear Reactors (SCWRs): Current and Future Concepts – Steam Cycle Options", Proc. 16th International Conference on Nuclear Engineering (ICONE16), Orlando, Florida, USA, May 11–15 2008 (2008).

[2-10] BUSHBY, S.J., et al., "Conceptual designs for Advanced, High-temperature CANDU Reactors", Proc. 8th International Conference on Nuclear Engineering (ICONE-8), Paper #8470, Baltimore, Maryland, USA (2000).

[2-11] MCDONALD, M.H., HYLAND, B., HAMILTON, H., LEUNG, L.K.H., ONDER, N., PENCER, J., XU, R., "Pre-Conceptual Fuel Design Concepts For the Canadian Super Critical Water-Cooled Reactor", Proc. 5th Int. Sym. SCWR (ISSCWR-5), Vancouver, British Columbia, Canada, March 13–16, 2011 (2011).

[2-12] VENKATAPATHI, S., MEHMI, A., WONG, H., "Pressure Tube-to-End Fitting Roll-Expanded Joints in a CANDU PHWR", Proc. CNS International Conference on Expanded and Rolled Joint Technology, Toronto, Ontario, Canada (1993).

[2-13] CHOW, C.K., KHARTABIL, H., "Conceptual Fuel Channel Designs for CANDU – SCWR", Proc. 3rd International Symposium on SCWR – Design and Technology, Shanghai, China, March 12–15, 2007 (2007).

[2-14] SHAN, J., JIANG, Y., LEUNG, L., "Subchannel and Radiation Heat Transfer Analysis of 54 Element CANDU-SCWR Bundle", Proc. 5th Int. Sym. SCWR (ISSCWR-5), Vancouver, British Columbia, Canada, March 13–16, 2011 (2011).

[2-15] GUZONAS, D., TREMAINE, P., JAY-GERIN, J.-P., "Chemistry Control Challenges in A Supercritical Water-Cooled Reactor", Proc. International Conference on Water Chemistry of

Nuclear Reactor Systems, Berlin, Germany, September 15–18, 2008, (also VGB PowerTech e.V. TB 430-08, Paper L15-1) (2008).
[2-16] HOPWOOD, J.M., FEHRENBACH, P., DUFFEY, R., KURAN, S., IVANCO, M., DYCK, G.R., CHAN, P.S.W., TYAGI, A.K., MANCUSO, C., "CANDU Reactors with Thorium Fuel Cycles", Proc. Pacific Basin Nuclear Conf., Sydney, Australia, October 15, 2006 (2006) 42.
[2-17] DYCK, G.R., BOCZAR, P.G., "Fuel Cycle Flexibility in the ACR", Proc. Pacific Basin Nuclear Conference and Technology Exhibition, Honolulu, Hawaii, USA, March 21, 2004 (2004).
[2-18] BOCZAR, P.G., DYCK, G.R., CHAN, P.S.W., BUSS, D.B., "Thorium Fuel Utilization: Options and Trends", IAEA-TECDOC-1319, IAEA, Vienna (2002) 10.
[2-19] HYLAND, B., DYCK, G.R., EDWARDS, G.W.R., MAGILL, M., "Homogeneous Thorium Fuel Cycles in CANDU Reactors", Proc. Global 2009, Paris, France, September 6–11, 2009 (2009).
[2-20] MAGILL, M., PENCER, J., PRATT, R., YOUNG, W., EDWARDS, G.W.R., HYLAND, B., "Thorium Fuel Cycles in the CANDU Supercritical Water Reactor", Proc. 5th Int. Sym. SCWR (ISSCWR-5), Vancouver, British Columbia, Canada, March 13–16, 2011 (2011).
[2-21] PENCER, J., HYLAND, B., "Physics Aspects of the Pressure Tube Type SCWR Preconceptual Design", Proc. Int. Conf. Future of HWRs (HWR-Future), Ottawa, Ontario, Canada, October 2–5, 2011 (2011).
[2-22] OVANES, M., CHAN, P.S.W., HOPWOOD, J.M., "Thorium and Other Fuel Cycle Flexibility of ACR 1000", Proc. Global 2009 Conference, Paris, France, September 6-11, 2009 (2009).
[2-23] GUZONAS, D.A., WILLS, J., DO, T., MICHEL, J., "Corrosion of Candidate Materials for use in a Supercritical Water CANDU® Reactor", Proc. 13th International Conference on Environmental Degradation of Materials in Nuclear Power Systems (2007) 1250–1261.
[2-24] LI, C.Y., SHAN, J.Q., LEUNG, L.K.H., Subchannel Analysis of CANDU-SCWR Fuel, Progress in Nuclear Energy, Vol. 51 (2009) 799–804.
[2-25] SHAN, J.Q., LEUNG, L.K.H., "Optimisation of CANFLEX-SCWR Bundle through Subchannel Analysis", Proc. 30th Annual Conference of the Canadian Nuclear Society, Calgary, Alberta, Canada, May 31–June 3, 2009 (2009).
[2-26] KHARTABIL, H.F., "A Flashing-Driven Moderator Cooling System for CANDU Reactors: Experimental and Computational Results", IAEA Technical Committee Meeting on Experimental Tests and Qualification of Analytical Methods to Address Thermohydraulic Phenomena in Advanced Water Cooled Reactors, PSI, Switzerland (1998).
[2-27] CHENG, X., LIU, X.J., YANG, Y.H., A Mixed Core for Supercritical Water-cooled Reactors, Nuclear Engineering and Technology, 40(2) (2007) 117–126.
[2-28] LIU, X.J., YANG, T., CHENG, X., "Core and Sub-channel Analysis of SCWR with Mixed Spectrum Core", Proc. ICAPP'10, San Diego, CA, USA, Paper 10032, June 13–17, 2010 (2010).
[2-29] YANG, T., LIU, X.J., CHENG, X., "Optimization for Fast Multilayer Fuel Assemblies of Mixed Supercritical Water-cooled Reactors", Proc. 8th International Topical Meeting on Nuclear Thermal-Hydraulics, Operation and Safety (NUTHOS-8), Shanghai, China, October 10–14, 2010 (2010).
[2-30] SCHULENBERG, T., STARFLINGER, J., MARSAULT, P., BITTERMANN, D., MARACZY, C., LAURIEN, E., LYCKLAMA, J.A., ANGLART, H., ANDREANI, M., RUZICKOVA, M., HEIKINHEIMO, L., "European Supercritical Water Cooled Reactor", FISA 2009, Prague, Czech Republic, June 22–24, 2009 (2009).
[2-31] BRANDAUER, M., SCHLAGENHAUFER, M., SCHULENBERG, T., "Steam Cycle Optimization for the HPLWR", Proc. 4th International Symposium on Supercritical Water-Cooled Reactors, Heidelberg, Germany, Paper No. 36, March 8–11, 2009 (2009).
[2-32] HERBELL, H., WECHSUNG, M., SCHULENBERG, T., "A Turbine Design Concept for the High Performance Light Water Reactor", Proc. 4th International Symposium on Supercritical Water-Cooled Reactors, Heidelberg, Germany, Paper No. 76, March 8–11, 2009 (2009).
[2-33] SCHULENBERG, T., STARFLINGER, J., HEINECKE, J., Three Pass Core Design Proposal for a High Performance Light Water Reactor, Progress in Nuclear Energy, 50 (2008) 526–531.

[2-34] HOFMEISTER, J., WAATA, C., STARFLINGER, J., SCHULENBERG, T., LAURIEN, E., Fuel Assembly Design Study for a Reactor with Supercritical Water, Nuclear Engineering and Design, 237 (2007) 1513–1521.
[2-35] KOEHLY, C., SCHULENBERG, T., STARFLINGER, J., "HPLWR Reactor Design Concept", Proc. 4th International Symposium on Supercritical Water-Cooled Reactors, Heidelberg, Germany, Paper No. 37, March 8–11, 2009 (2009).
[2-36] HERBELL, H., HIMMEL, S., SCHULENBERG, T., "Mechanical Analysis of an Innovative Assembly Box with Honeycomb Structures Designed for a High Performance Light Water Reactor", Proc. IYNC 2008, Interlaken, Switzerland, Paper No. 132, September 20–26, 2008 (2008).
[2-37] MONTI, L., SCHULENBERG, T., "Coupled ERANOS/TRACE System for HPLWR 3 Pass Core Analyses", Proc. International Conference on Mathematics, Computational Methods & Reactor Physics (M&C 2009), Saratoga Springs, New York, May 3–7, 2009 (2009).
[2-38] MARÁCZY, C., HEGYI, G., HORDÓSY, G., TEMESVÁRI, E., HEGEDÖS, C., MOLNÁR, A., "High Performance Light Water Reactor Core Design Studies", Proc. 16th Pacific Basin Nuclear Conference (16PBNC), Aomori, Japan, Paper P16, p. 1221, October 13–18, 2008 (2008).
[2-39] BERNNAT, W., CONTI, A., "2D and 3D Assembly Burnup Analysis for HPLWR", Proc. 4th International Symposium on Supercritical Water-Cooled Reactors, Heidelberg, Germany, Paper No. 40, March 8–11, 2009 (2009).
[2-40] ORTEGA GOMEZ, T., CLASS, A., LAHEY, R.T. JR., SCHULENBERG, T., Stability Analysis of a Uniformly Heated Channel with Supercritical Water, Nuclear Engineering and Design, 238 (2008) 1930-1939.
[2-41] DE MARSAC, B., SCHULENBERG, T., SCHLAGENHAUFER, M., "Residual Heat Removal System of the HPLWR", Proc. International Students Workshop on High Performance Light Water Reactors, Karlsruhe, Germany, March 31–April 3, 2008 (2008).
[2-42] KOEHLY, C., SCHULENBERG T., STARFLINGER J., "Design Concept of the HPLWR Moderator Flow Path", Proc. 2009 International Conference on Advanced Power Plant (ICAPP'09), Tokyo, Japan, May 10–14, 2009 (2009).
[2-43] YAMADA, K., SAKURAI, S., ASANUMA, Y., HAMAZAKI, R., ISHIWATARI, Y., KITOH, K., "Overview of the Japanese SCWR Concept Developed under the GIF Collaboration", Proc. 5th International Symposium on Supercritical Water-Cooled Reactors (ISSCWR-5), Vancouver, British Columbia, Canada, March 13–16, 2011 (2011).
[2-44] ISHIWATARI, Y., OKA, Y., YAMADA, K., "Japanese R&D Projects on Pressure-Vessel Type SCWR," Proc. of 4th International Symposium on Supercritical Water-Cooled Reactors, Heidelberg, Germany, March 8–11, 2009 (2009).
[2-45] NAKATSUKA, T., OKA, Y., ISHIWATARI, Y., IKEJIRI, S., OKUMURA, K., NAGASAKI, S., TEZUKA, K., MORI, H., EZATO, K., AKASAKA, N., NAKAZONO, Y., SASAKI, K., TERAI, T., MUROYA, Y., YAMAKAWA, M., "Current Status of Research and Development of Supercritical Water-Cooled Fast Reactor (Super Fast Reactor) in Japan", Proc. IAEA Technical Meeting on Heat Transfer, Thermal-Hydraulics and System Design for Super-Critical Water-Cooled Reactors, Pisa, Italy, July 5–8, 2010 (2010).
[2-46] JU, H., et al., "Core Design and Fuel Rod Analyses of a Super Fast Reactor with High Power Density", Proc. 2009 International Conference on Advanced Power Plant (ICAPP'09), Shinjuku, Tokyo, Japan, Paper 9264, May 10–14, 2009 (2009).
[2-47] SAKURAI, S., et al., "Japanese SCWR Fuel and Core Design Study", Proc. 5th International Symposium on Supercritical Water-Cooled Reactors, Vancouver, Canada, March 13–17, 2011 (2011).
[2-48] ISHIWATARI, Y., et al., "Safety Analysis of JSCWR", Proc. 5th International Symposium on Supercritical Water-Cooled Reactors, Vancouver, Canada, March 13–17, 2011 (2011).
[2-49] BAE, K. M., JOO, H.K., BAE, Y.Y., "Conceptual Design of a 1400 MWe Supercritical Water Cooled Reactor Core with a Cruciform Type U/Zr Solid Moderator", Proc. 2007 International

Conference on Advanced Power Plant (ICAPP'07), Nice, France, Paper 7502, May 13–18, 2007 (2007).
[2-50] BAE, Y.Y., KANG, H.O., "Thermohydraulic Study of Supercritical Pressure Water-Cooled Reactor Options", Proc. 2003 International Conference on Advanced Power Plant (ICAPP'03), Córdoba, Spain, Paper 3223, May 4–7, 2003 (2003).
[2-51] KIRILLOV, P.L., Changing-Over to Supercritical Parameters – Way of Advancement of NPP with VVER, Heat-Power Engineering, No. 12 (2001) 6–10.
[2-52] DOLGOV, V.V., VVER Units with Supercritical Coolant Parameters, Atomic Energy, 92 (4), (2002) 277–280.
[2-53] DRAGUNOV YU, G., RYZHOV, S.B., NIKITENKO, M.P., et al., Water- Cooled Reactors with Supercritical Parameters – Advanced Reactors of the 4th Generation, Scientific Transactions, MIFI-2007, Moscow, Russia, Volume 8 (2007) 34–35.
[2-54] RYZHOV, S.B., MOKHOV, V.A., PODSHIBYAKIN, A.K., et al., "About New VVER Reactor Plant Designs at Current Stage of Development of Atomic Energy", Proc. 6th International Scientific and Technical Conference, Podolsk, Russia, Volume 1 (2009) 7–36.
[2-55] BARANOV YU, D., KIRILOV, P.L., POPLAVSKY, V.M., SHARAPOV, V.N., Nuclear Reactors with Supercritical Pressure Water, Atomic Energy, 96 (5) (2004) 374–380.
[2-56] GLEBOV, A.P., KLUSHIN, A.V., Reactor with Quick-Resonance Spectrum of Neutrons, Which is Cooled by Supercritical Pressure Water in Case of Two-Way Pattern of Coolant Flow, Atomic Energy, 100(5) (2006) 349–355.

3. HEAT TRANSFER CHARACTERISTICS OF SUPERCRITICAL WATER

The fuel-design criterion for the SCWR is based on the cladding temperature limit because phase change is not present in the core for normal operation. The lack of qualified experimental data on heat transfer for supercritical water flow in rod bundles has been identified as a significant challenge to the SCWR design. This is due to the possibility of drastic deterioration of heat transfer occurring in the vicinity of the critical point. Fundamental understanding of thermalhydraulics characteristics has relied on experimental information obtained with tubes, annuli, and bundle sub-assemblies.

Information on the supercritical pressure (referred simply to as 'supercritical' hereafter) heat-transfer characteristics for water is of prime interest. Several heat-transfer databases for supercritical water flow have been assembled. Most supercritical heat-transfer correlations were developed using subsets of these databases. Improved correlations have been derived using the combined database and provide better prediction accuracy and more appropriate parametric trends than existing correlations.

Supercritical heat transfer data for surrogate fluids have been applied as supplemental information to the water data. Testing with surrogate fluids is usually more flexible due to the relatively less severe conditions than with water. Most studies employed carbon dioxide and Freon as the surrogate fluids to examine separate effects on heat transfer characteristics. Direct applications of surrogate fluid heat-transfer data in SCWR design and safety analyses require the development of fluid-to-fluid modelling parameters to relate the surrogate-fluid heat-transfer coefficients to water-equivalent values.

3.1. HEAT TRANSFER IN SUPERCRITICAL PRESSURE WATER

Experimental data for water obtained with tubes and bundles under supercritical pressure conditions are required for the development and validation of heat-transfer correlations. Several literature surveys (e.g., [3-1]) were performed and identified many sets of supercritical heat-transfer data with water flow in support of boiler applications. Correlations were developed using these data.

3.1.1. Heat transfer data obtained using tubes

Tube data can help to provide a fundamental understanding of supercritical heat transfer phenomena. Such data were used in developing most supercritical pressure heat-transfer correlations, which have been implemented into subchannel codes in support of the SCWR fuel design. Previous reviews of published information concluded that available information on SCW flow in tubes is limited [3-1]. In particular, most experimental data were obtained with large diameter tubes (some with ribbed tubes), whereas in SCWR applications the subchannel equivalent diameters are quite small. Justification and validation are required to extend the application of correlations, based on these data, to the SCWR design and safety analyses.

3.1.1.1. AECL database

A database on supercritical heat transfer in water has been established at AECL [3-2]. Table 3.1 lists the expanded water database. These databases are applicable for:

- Assessing various heat transfer correlations and identifying suitable correlations for the required operating range of SCWRs;
- Developing prediction methods (in the form of either correlations or a look-up table) for supercritical heat transfer;
- Identifying experimental needs to fill in missing ranges in available data; and
- Developing and validating fluid-to-fluid modeling techniques for heat transfer in the near critical and supercritical pressure regimes.

TABLE 3.1. SCHT WATER DATA SETS CONSIDERED ACCESSIBLE IN THE AECL DATABASE

Reference	Pressure (MPa)	Temp. (°C) or Enthalpy ($kJ \cdot kg^{-1}$)	Heat Flux ($kW \cdot m^{-2}$)	Mass Flux ($kg \cdot m^{-2} \cdot s^{-1}$)	Tube ID (mm) / Orientation	Data Format
Ackerman [3-4]	*22.75 to 41.3*	*T_b: 76 to 350*	*126 to 1735*	*135 to 2170*	*9.4 to 24.4*	*Graph*
Alekseev et al. [3-5]	*24.5*	*T_{in}: 100 to350*	*100 to 900*	*380 to 820*	*10.4 / vert.*	*Graph*
Alferov et al. [3-6]	*26.5*	*---*	*480*	*447*	*20 / vert.*	*Graph*
Bazargan et al. [3-7]	*23 to 27*	*T_w: 405 to 670*	*up to 310*	*330 to 1200*	*6.3 / hor.*	*Graph*
Belyakov et al. [3-8]	*24.5*	*H_b: 1004 to 1800*	*232 to 1395*	*300 to 700*	*20 / vert. and hor.*	*Graph*
Harrison et al. [3-9]	*24.5*	*T_b: 50 to 350*	*1300, 2300*	*940, 1560*	*1.64, 3.1 / vert. and hor.*	*Graph*
Herkenrath et al. [3-10]	*14 to25*	*$T_{b(min)}$: 345 to 370 $T_{b(max)}$: 374 to 437*	*60 to 1400*	*720 to 3620*	*10 to 20 / vert.*	*Graph, Tables*
Goldmann [3-11]	*34.5*	*T_{in}: 204 to 760 T_b:204 to 537*	*315 to 9464*	*2034 to 5424*	*1.27 to 1.9*	*Graph*
Glushchenko et al. [3-12]	*22.6 to 29.4*	*H_b: 85 to 2400*	*up to 3000*	*500 to 3000*	*3, 4, 6, 8 / vert.*	*Graph*
Ishigai et al. [3-13]	-	-	-	-	-	*Graph*
Kamenetskii [3-14]	*23.5 to 24.5*	*H_b: 100 to 2300*	*up to 1200*	*50 to 1700*	*21 to 22*	*Graph*
Kamenetskii [3-15]	*24.5*	*H_b: 100 to 2200*	*up to 1300*	*300 to 1700*	*21.1 to 21.9 / vert. and hor.*	*Graph*
Kirillov et al. [3-16]	*23 to 25*	*T_{in}: 320 to 380*	*up to 1400*	*200 to 2000*	*10 / vert.*	*Tables*
Kondratev [3-17]	*23 to 30*	*T_b: 105 to 560*	*116 to 1163*	-	*10.47*	*Graph*
Krasyakova et al. [3-18]	*24.5*	*H_b: 400 to1900*	*100 to 1400*	*90 to 2000*	*20 / upward and downward*	*Graph*
Lee and Haller [3-19]	*24.1*	*T_b: 260 to 383*	*252 to 1577*	*542 to 2440*	*38*	*Graph*
Malkina et al. [3-20]	*24.5 to 31.4*	*T_b: 20 to 383*	-	*Velocity: 7 to 10 m/s*	*2 to 3*	*Graph*
Ornatsky et al. [3-21]	*22.6 to 29.4*	*H_{in}: 420 to1400*	*up to 3000*	*450 to 3000*	*3 / vert.*	*Graph*
Ornatsky et al. [3-22]	*22.6 to 29.4*	*H_{in}: 800 to 1500*	*up to 3000*	*500 to 3000*	*3 / vert.*	*Graph*
Razumoviskiy [3-23]	*23.5*	*T_{in}: 20 to 380*	*up to 515*	*250 to 500*	*6.28 to 9.5 / vert.*	*Graph, Tables*
Schmidt [3-24]	*17 to 30*	*T_b: 200 to 700*	*290 to 820*	*700 to 1700*	*5 / vert. and hor.*	*Graph*
Seo et al. [3-25]	*23 to 24.5*	*H_b: 1500 to 2500*	*210 to 933*	*430 to 1260*	*7.5 to 8 / vert.*	*Graph*
Shitsman [3-26]	*23 to 25*	*T_b: 280 to 580*	*280 to 1100*	*300 to 1500*	*8 / vert.*	*Graph, Tables*
Shitsman [3-27]	*10 to 35*	*T_b: 100 to 250*	*270 to 700*	*400*	*3, 8, 16 / vert.*	*Graph*
Treshchev and Sukhov [3-28]	*23 to 25*	*t_{in}: 300*	*815*	*750*	*---*	*Table*
Vikhrev et al. [3-29]	*24.5*	*H_b: 230 to 2750*	*230 to 1250*	*500 to 1900*	*7.85 / vert.*	*Graph*
Yamagata et al. [3-30]	*22.6 to 29.4*	*T_b: 230 to 540*	*1200 to 930*	*310 to 1830*	*7.5, 10 / vert. (upward and downward) and hor.*	*Graph*

The ranges of parameters covered in the database are: tube diameters from 1.27 to 38 mm, pressures from 10.0 to 41.3 MPa, mass fluxes from 50 to 5424 $kg \cdot m^{-2} \cdot s^{-1}$, and heat fluxes from 60 to 9464 $kW \cdot m^{-2}$. Ranges of fluid temperatures and enthalpy appear to be similar to those of the previous database. Figure 3.1 illustrates the range of reduced pressure and reduced temperature covered in these data sets. Several data sets cover a wide range of conditions.

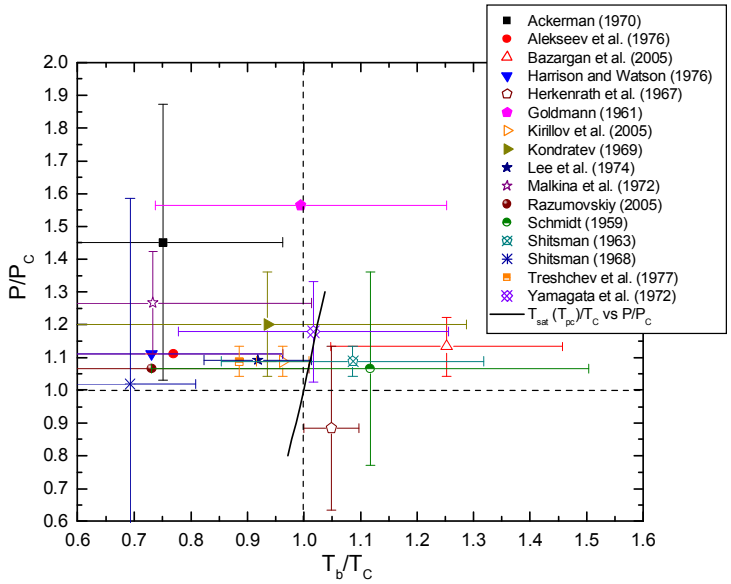

FIG. 3.1. Range of selected AECL supercritical heat-transfer databases for water.

3.1.1.2. SJTU database

An extensive literature survey has been performed at the Shanghai Jiao Tong University (SJTU) to establish a valid database for heat transfer investigations with fluids at supercritical pressures in vertical upward flow in vertical tubes and other channels. Up to now, a total of 14150 data points for upward flow have been collected, checked, analysed, categorized and put into a data bank. The water database consists of 8624 data points. Table 3.2 lists the data source, flow conditions, and test-section geometry. Some duplication of data can be seen compared with the AECL database.

TABLE 3.2. PARAMETERS OF WATER TEST DATA IN THE SJTU DATABASE [3-31]

	Fluid	Pressure (MPa)	Mass Flux ($kg \cdot m^{-2} \cdot s^{-1}$)	Heat Flux ($kW \cdot m^{-2}$)	Geometry
Shitsman [3-26]	water	23.3	430	233~291	ID=8.0 mm, L=1.5 m
Dickson	water	31.03	664~3607	309~3474	ID=7.62 mm
Swenson et al. [3-70]	water	22.75~31.0	2149	789~1741	ID=9.42 mm, L=1.83 m
Vikhrev et al. [3-29]	water	27.3	1400	697~1161	ID=20.0 mm, L=6.0 m
Miropolski et al. [3-37]	water	24.5	600	520	ID=16.0 mm
Ackerman [3-4]	water	22.7~31.0	407~1220	157~1261	ID=9.42 mm, L=1.8 m
Yamagata et al. [3-30]	water	24.5	1200	233~930	ID=7.5 mm, L=1.5 m
Alekseev et al. [3-5]	water	24.5	380	270~580	ID=10.4 mm, L=0.5 m
Griem [3-139]	water	25.0	500~2500	300~600	ID=14.0 mm
Hu	water	23~30	600~1200	200~500	ID=26.0 mm, L=2.0 m
Xu [3-33]	water	23~30	600~1200	200~600	ID=12.0 mm, L=1.2 m
Zhu	water	23~30	600	200~300	ID=26.0 mm, L=1.0 m

Parametric distributions of the data collected for heat transfer to water at supercritical pressures in vertical upward flow are summarized in Fig. 3.2. These data cover the current typical parametric range of SCWR for some main thermohydraulic parameters. However, for certain combined conditions, existing data distribution is still not satisfactory for SCWR applications, especially for certain transient and accident conditions. For example, at the typical SCWR pressure of 25 MPa, the range of heat fluxes covered in the database remains inadequate for transient or postulated accident analyses. In addition, only few data exhibit the trend of heat transfer deterioration at large ratios of heat flux to mass flux (i.e., q/G).

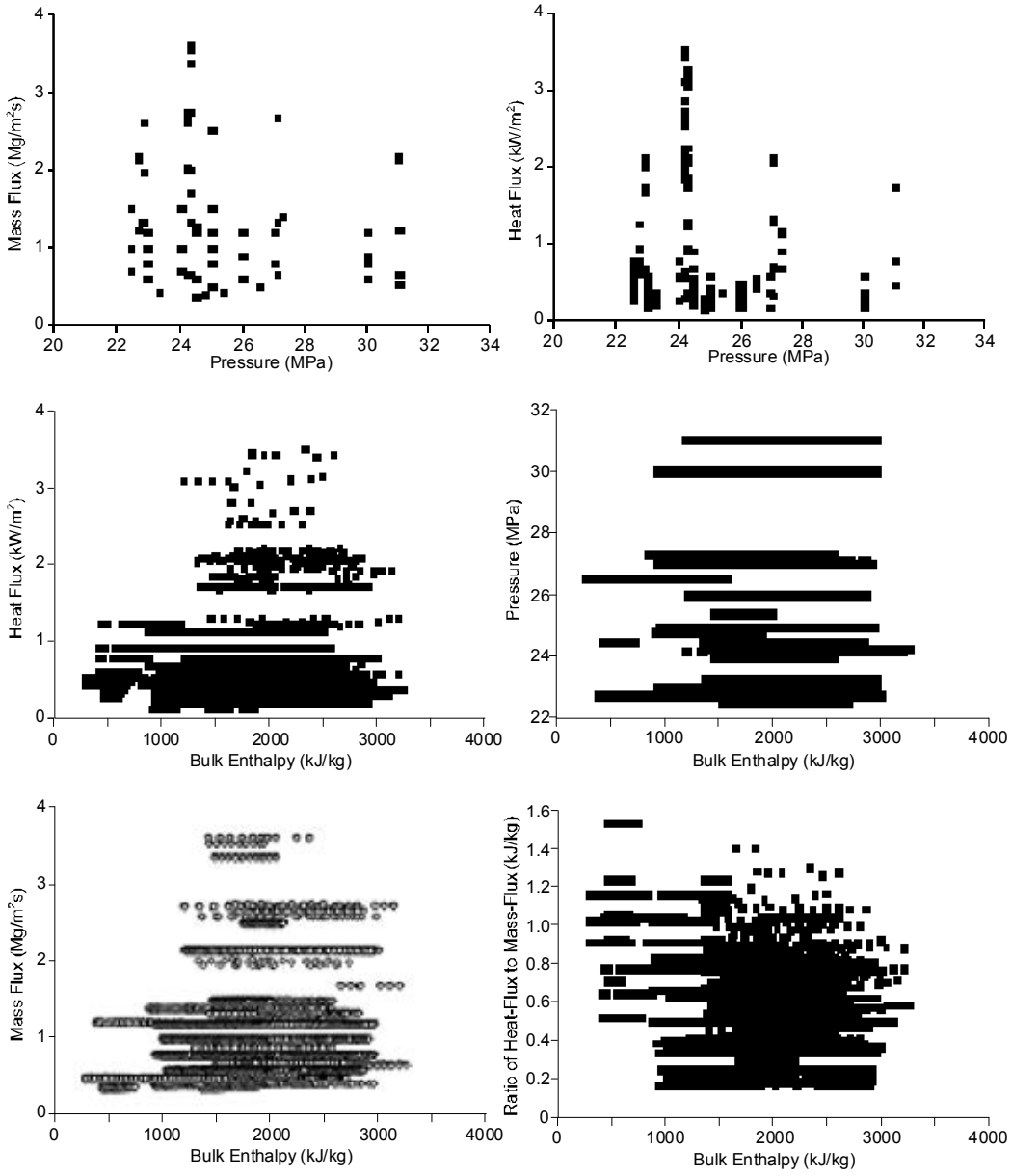

FIG. 3.2. Parametric distributions of the SJTU water database.

The distribution of data is considered to be 'non-homogeneous'; this may lead to imbalance in information synthesis and data correlation. For example, few data were obtained at pressures higher than 27 MPa and all of these data correspond to low mass fluxes and low heat fluxes only. These conditions should perhaps be focused on in future experiments.

3.1.1.3. Institute of Physics and Power Engineering (IPPE) database

The review of experimental research to supercritical water heat transfer in vertical and horizontal tubes is given in [3-34] (also in [3-35] and [3-36]). Most of the research work was carried out in Russia in the period 1950 to 1980 to justify the thermal hydraulic calculation methods for the supercritical pressure boilers of fossil fuel power plant. Characteristics of investigations on supercritical water heat transfer performed by Russian scientists presented in the open literature for vertical tubes under heated conditions are shown in Table 3.3. Most publications present experimental data in charts giving the wall temperature, T_w, along the heated length or as a function of bulk enthalpy.

TABLE 3.3. PARAMETERS OF RUSSIAN EXPERIMENTS ON SUPERCRITICAL WATER IN HEATED VERTICAL TUBES PERFORMED BETWEEN 1950 AND 1990

Authors	Test section parameters	Experimental parameter				Remarks
		P, MPa	T_b, °C	G, $kg \cdot m^{-2} \cdot s^{-1}$	q, $MW \cdot m^{-2}$	
Miropolsky, Shitsman [3-37], [3-38]	Tube, experimental stainless steel "ЭЯ1Т", D_{in} = 7.8 mm, δ = 0.6 mm, L_{heat} = 160 mm; upward flow	0.4-27.4	25-420 ΔT_b=9-215	170-3000	0.116-2.33	Processed in coordinates: $Nu_f/(Re_f)^{0.8}$, $(Pr_{min})^{0.8}$, where $Nu_f = 0.023(Re_f)^{0.8}(Pr_{min})^{0.8}$. Figure of $h = f(\Delta T_b)$ for 4 regimes.
Armand et al. [3-39]	Tube, experimental stainless steel 'ЭЯ1Т', D_{in} = 6.0 mm, δ = 0.25 mm, L_{heat} = 250 mm Tube, nickel, D_{in} = 8.0 mm, δ = 0.25 mm, L_{heat} = 350 mm; upward flow	22.3, 23.5, 24.8, 25.5 24.8, 26.3	300-420	450-658	0.174-0.255 0.186-0.348 0.186-0.348	132 experiments for D_{in} = 6.0 mm and 50 experiments for D_{in} = 8.0 mm. Figures of heat transfer coefficients $h = f(T_b)$ for 6 regimes Processed in coordinates: $Nu_f/(Pr_{min})^{0.8}$, Re (log)
Doroschuk et al. [3-40]	Tube, silver, D_{in} = 3.0 mm, δ = 0.5 mm, L_{heat} = 246 mm; downward flow	24.3	100-250	velocity 4-10 m/s	3.0-3.95	Summary table for 25 experiments, including plots of T_w along L_{heat}, ΔT_b, h in Ref. (1 $kCal \cdot m^{-2} \cdot h^{-1} \cdot K^{-1}$)
Aladiev et al. [3-41]	Tube, stainless steel 1X18H9T (0.01% carbon, 18% chromium, 9% nickel, ~1% titanium), D_{in} = 12.0 mm, δ = 1.5 mm, L_{heat} = 500 mm; upward flow	4.9, 9.8, 14.7, 19.6, 24.5, 28.9	ΔT_{min} = 35 173-526	velocity 0.023-0.046 m/s	0.12-0.39 kW/m^2	Summary table 103 experiments, including values of h and Re_f.

Authors	Test section parameters	Experimental parameter				Remarks
		P, MPa	T_b, °C	G, $kg \cdot m^{-2} \cdot s^{-1}$	q, $MW \cdot m^{-2}$	
Shitsman [3-42]	Tube, stainless steel 1X18H9T (0.01% carbon, 18% chromium, 9% nickel, ~1% titanium), D_{in} = 8.0 mm, δ = 2 mm, L_{heat} = 1500 mm; upward flow	22.6, 23.5, 24.5	200-445	300-1500	up to 1.16	373 experiments, 4000 points. Figures $T_w = f(L_{heat})$, tabular data for some regimes
Smolin and Poliakov [3-43]	Tube, stainless steel 1X18H9T (0.01% carbon, 18% chromium, 9% nickel, ~1% titanium), D_{in} = 10.0 mm, δ = 2 mm, L_{heat} = 2600 mm; D_{in} = 8.0 mm, δ = 1 mm, L_{heat} = 2600 mm; upward flow	25.4, 27.4, 30.4	250-440	1500-3000	0.7-1.75	Processing: $Nu_f/(Pr_{min})^{0.8}$, Re (log)
Vikhrev and Barulin [3-44]	Tube, stainless steel 1X18H9T (0.01% carbon, 18% chromium, 9% nickel, ~1% titanium), D_{in} = 7.85 mm, δ = 2 mm, L_{heat} = 1515 mm; upward flow	24.5	H_b =315-2350 kJ/kg	485-510	0.565-0.630	Figures $T_w = f(H_b)$ for 8 regimes.
Krasiakova et al. [3-45]	Tube, stainless steel 12ХМФ (0.12% carbon, ~1% chromium, ~1% molybdenum, ~1% vanadium), D_{in} = 20.0 mm, δ = 4 mm, L_{heat} = 2200 mm; upward flow, horizontal flow	15.0, 18.8, 23.0	200-400 H_b =964-2472 kJ/kg	300-2000	0.23-0.70	Figures $T_w = f(L_{heat})$ at given H_b (6 regimes); Figures $T_w = f(H_b)$ – 21 regimes.
Shitsman [3-46]	Tube, stainless steel 1X18H9T (0.01% carbon, 18% chromium, 9% nickel, ~1% titanium), D_{in} = 20.0 mm, δ = 2 mm, L_{heat} = 1600 mm; upward flow, downward flow; D_{in} = 12.0 mm, δ = 2 mm, L_{heat}/D = 400 upward flow	10-35	60-440	325-600	до 0.5	Figures $L_{heat}/D = f(T_w)$ – 30 regimes
Tarasova and Leontiev [3-47]	Tube, stainless steel, D_{in} = 8.03 and 3.43 mm; L_{heat}/D = 50; upward flow	22.6-26.5	H_b =40-80 kJ/kg	2000 - 5000	0.58-1.32	Figures $\Delta P = f(H_b)$

Authors	Test section parameters	Experimental parameter				Remarks
		P, MPa	T_b, °C	G, $kg \cdot m^{-2} \cdot s^{-1}$	q, $MW \cdot m^{-2}$	
Alferov et al. [3-48]	Tube, stainless steel 1X18H10T (0.01% carbon, 18% chromium, 10% nickel, ~1% titanium), D_{in} = 14 and 20 mm, L_{heat}/D = 100, 185 mm; upward flow	14.7-29.4	20-400	250-1000	0.18-0.7	Figures $T_w = f(L_{heat}/D)$
Kondratiev [3-49]	Tube, stainless steel 1X18H9T (0.01% carbon, 18% chromium, 9% nickel, ~1% titanium), D_{in} = 10.47 mm; L_{heat} = 521 mm; downward flow	22.5, 24.5, 29.4	310-420		0.12-1.16	Figures heat transfer coefficient h and pressure drop coefficient ξ as function of T_b
Ornatsky et al. [3-50]	Tube, stainless steel, D_{in} = 3.0 mm, L_{heat} = 750 mm; upward flow, downward flow	22.6, 25.5, 29.4	20-400	500-3000 800-3000	Up to 3.0	Figures $T_w = f(L_{heat}/D)$
Beliakov et al. [3-51]	Tube, stainless steel 1X1MΦ (0.01% carbon, 1% chromium, ~1% molybdenum, ~1% vanadium), D_{in} = 20.0 mm, L_{heat} = 6500 -7500 mm, upward flow; L_{heat} = 4000 mm, horizontal flow	24.5	100-390 H_b =412-3350 kJ/kg	300-3000	0.232-1.239	Figures $T_w = f(L_{heat}/D)$ Figures $T_w = f(H_b)$ and $h = f(H_b)$
Barulin et al. [3-52]	Tube, stainless steel, D_{in} = 3.0; 8.0; 20.0 mm, $L_{heat}/D < 300$ upward flow, downward flow, horizontal flow	22.5, 26.5	50-500	480-5000	0.2-6.5	Experimental data are not available, there is only short abstract
Gluschenko et al. [3-53]	Tube, stainless steel, D_{in} = 3.0; 4.0; 8.0 mm, L_{heat} = 750-1000 mm; upward flow; D_{in} = 3.0 mm, downward flow; annular channel δ = 0.3; 0.7; 1 mm	22.6, 25.5, 29.4 23.5, 25.5, 29.4	H_b = 85-2400 kJ/kg	500-3000 650-7000	Up to 0.3 ≤ 5.4	Figures $T_w = f(H_b)$.
Alferov et al. [3-54], [3-55]	Tube, stainless steel, D_{in} = 20.0; 14.0 mm; L_{heat}/D = 185; upward flow, downward flow	26.5	80-250 H_b = 375-1125 kJ/kg	447	0.48	Figures $h/h_{forced} = f(L_{heat}/D)$; $T_w = f(H_b)$ $h_{min}/h_{forced} = h_{forced}/h_{natural}$, where h_{forced} and $h_{natural}$ – heat transfer coefficient in forced and natural convection

Authors	Test section parameters	Experimental parameter				Remarks
		P, MPa	T_b, °C	G, $kg \cdot m^{-2} \cdot s^{-1}$	q, $MW \cdot m^{-2}$	
Chakrygin et al. [3-56]	Tube, stainless steel 1X18H10T (0.01% carbon, 18% chromium, 10% nickel, ~1% titanium), D_{in} = 16.0 mm, δ = 3 mm, L_{heat} = 5010 mm; upward flow	17.7, 23.5	220 H_b = 838-1886 kJ/kg	300-1300 from 0.1-0.035 kg/s	Heat supply from 0.005 to 0.63 MW	Figures $\Delta p = f(H_b)$ and $\Delta p = f(G)$, $Q = f(H_b)$
Kamenetsky [3-57]	Tube, stainless steel, D_{in} =21.0; 22.0 mm, δ = 5 mm, L_{heat} = 3000 mm; non-uniform heating	23.5, 24.5	H_b = 100-2300 kJ/kg	50-1700	up to 1.2	Figures $h_{n.u.heat}/h_{u.heat} = f(G)$; $Nu/(Pr_{min})^{0.8} = f(Re)$; $T_w = f(H_b)$.
Alexeev et al. [3-58]	Tube, stainless steel X18H10T (0.01% carbon, 18% chromium, 10% nickel, ~1% titanium), D_{in} = 10.4 mm, L_{heat} = 500 - 750 mm; upward flow	24.5	100-375	380, 490, 650, 820	0.1-0.9	Figures $T_w = f(L_{heat})$ for 29 regimes; Figures $T_w = f(T_b)$, where T_b – mean bulk temperature of the flow
Treschev and Sukhov [3-59], [3-60]	Tube, stainless steel, D_{in} = 6.0 mm, L_{heat} = 1000, 750, 500 mm; upward flow	23, 25	300	750	0.81	Research in bifucartive heat load; tabular data for 22 regimes.
Krasiakova et al. [3-61]	Tube, stainless steel 12X1MФ (0.12% carbon, 1% chromium, ~1% molybdenum, ~1% vanadium), D_{in} = 20.0 mm, L_{heat} = 3500 mm; downward flow	24.5	98-360	90-2000	0.1-1.4	Figures $t_w = f(L_{heat})$; $T_w = f(H_b)$ and $h = f(H_b)$, comparison with h for upward flow in vertical tube and with h in horizontal tube
Smirnov and Krasnov [3-62] Smirnov and Michurov [3-63]	Tube, stainless steel D_{in} = 4.08 mm, D_{out} = 8.15 mm; L = 1089 mm; upward flow	25, 28, 30	T_w = 250 - 700	500-1200	0.25-1	Figures $h = f(\tau)$, where τ - reduced coefficient of transient heat transfer
Kamenetsky [3-64]	Tube, stainless steel, D_{in} = 21.1, 21.9 mm; L_{heat} = 3000 mm; upward flow, horizontal flow	24.5	H_b = 100-2200 kJ/kg	300-1700	up to 1.3	Figures $T_w = f(H_b)$ for horizontal tube. Turbulizing insertion – spiral steel band thickness δ = 0.8 mm, wideness 21 mm, s/d = 12-15
Smolin and Soloviev [3-65]	Tube, experimental stainless steel 'ЭИ-847', D_{in} = 10.4 mm, L_{heat} /d = 580; upward flow	22.6, 23.6, 24.6, 26.5, 29.4	80-320	400-4800	up to 1.6	Figures $T_w = f(L_{heat})$; tabular data for regimes with normal and deteriorated heat transfer
Razumovskiy et al. [3-66]	Annuli and round tube, stainless steel, D_{eq} = 3 mm, L_{heat} = 440 mm	23.5	220-350	1000-2600	0.25-2.5	220 experiments on pressure drop in short channels Figures $\xi = f(H_b)$

Authors	Test section parameters	Experimental parameter				Remarks
		P, MPa	T_b, °C	G, $kg \cdot m^{-2} \cdot s^{-1}$	q, $MW \cdot m^{-2}$	
Selivanov and Smirnov [3-67]	Tube, stainless steel 12X18H10T (0.12% carbon, 18% chromium, 10% nickel, ~1% titanium), D_{in} = 10.06 mm; δ = 1.98 mm, L_{heat} = 1000 mm; upward flow	24.5	50-450	200-10000	0.13-0.38 $q/\rho w < 0.2$ kJ/kg	Figures $T_w = f(L_{heat})$ for 15 regimes
Razumovsky et al. [3-68]	Tube, stainless steel, D_{in} = 6.28 mm; L_{heat} = 1440 mm; upward flow	23.5	H_b = 1400, 1600, 1800 kJ/kg	2190	0.66-3.4	Figures $\xi = f(H_b)$ and $T_w = f(H_b)$; reduced heat transfer coefficient $h = h_{exp}/h_{const} = f(H_b)$

Many studies present data in an implicit form as a result of the processing, for example, in such coordinates as: $Nu_f/(Re_f)^{0.8}$, $(Pr_{min})^{0.8}$ or Re (log), where $Nu_f = 0.023(Re_f)^{0.8}(Pr_{min})^{0.8}$ [3-37], [3-39], [3-57]. Such presentation does not allow the data on supercritical water flowing in tubes of different diameter to be generalized.

Experimental data sets (28 in all) in Table 3.3 cover regime parameters in the following ranges: P = 0.4-29.4 MPa, T_b = 20-500°C, H_b = 400-3350 $kJ \cdot kg^{-1}$, G = 170-10000 $kg \cdot m^{-2} \cdot s^{-1}$, q =0.13-3.4 $MW \cdot m^{-2}$. A number of empirical correlations give a rather satisfactory description of experimental data in case of the normal heat transfer regime (e.g., Bishop et al. [3-69], Swenson et al. [3-70], Petukhov and Kirillov [3-71], Krasnoschekov and Protopopov (for water and CO_2) [3-72], and Jackson and Hall [3-73]). However, it should be noted that during the period from 1950 to 1990 the thermophysical properties of water were calculated using old standards based on a reference book by Vargaftik [3-74], a reference book by Vukalovich [3-75] and other sources. International formulation IF-1997 [3-76] for thermophysical properties of water and steam was accepted in January 1999. Kurganov [3-77] has shown that the calculations based on the above stated formuli by IF-1997 standard may cause over estimation of heat transfer coefficients by up to 40-80% over wide ranges of enthalpy.

3.1.1.4. Data obtained at the University of Manchester

During the 1960s and 1970s, the Nuclear Engineering Research Group at Manchester carried out a number of experimental investigations on heat transfer to fluids at supercritical pressures. Two large-scale test facilities were constructed, one for experiments with carbon dioxide and another for experiments with water. Two other smaller scale facilities for experiments with water were also constructed.

Figure 3.3 shows the test facility for the carbon dioxide experimentals. Figure 3.4 shows the test section of 19-mm ID used for experiments with upward and downward flow on the carbon dioxide facility and Figure 3.5 shows further test sections of 8-mm and 5-mm IDs. Table 3.4 shows the range of conditions covered in the carbon dioxide experiments. A detailed description of the test facility and the experiments performed with upward and downward vertical flow using the three test sections can be found in [3-78]. The data obtained are presented in that report in graphical form, which has been digitized.

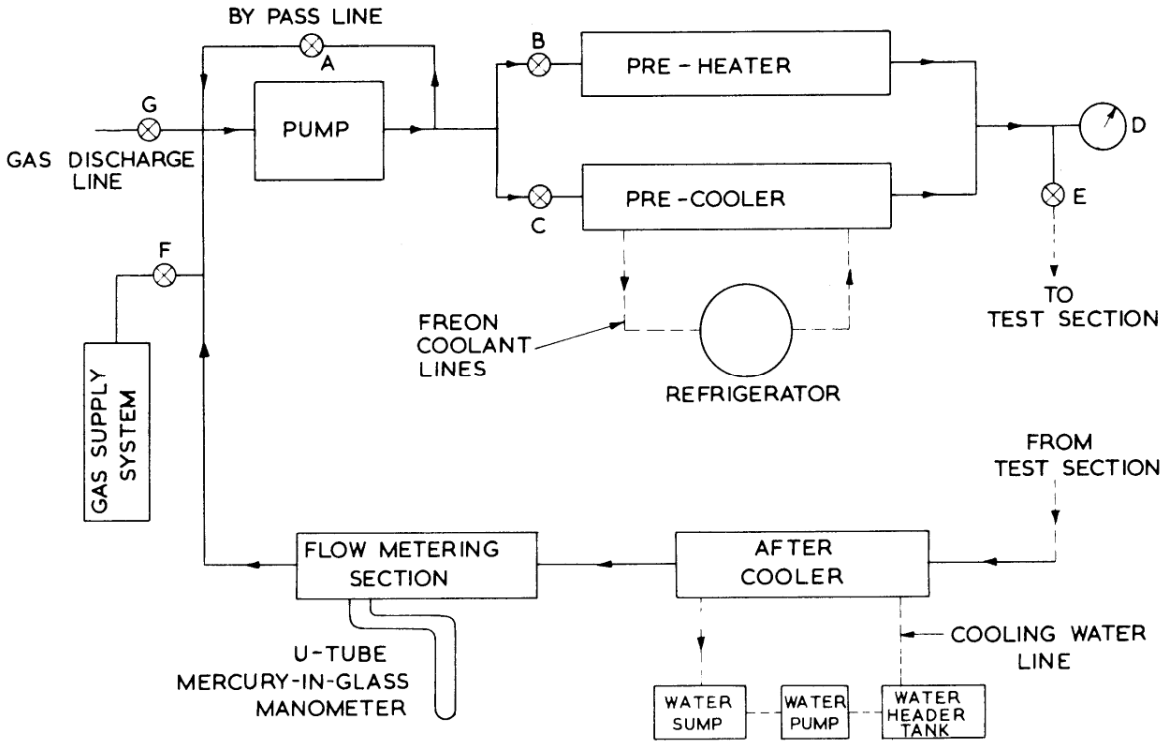

FIG. 3.3. Supercritical pressure carbon dioxide flow test facility.

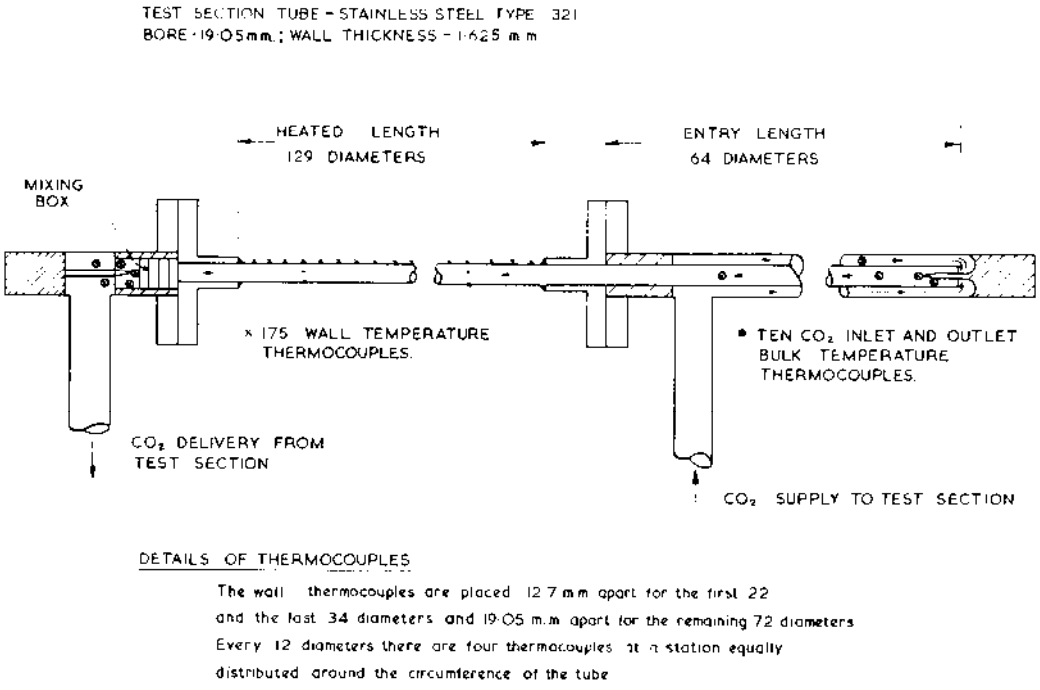

FIG. 3.4. The 19-mm diameter -test section for experiments with carbon dioxide.

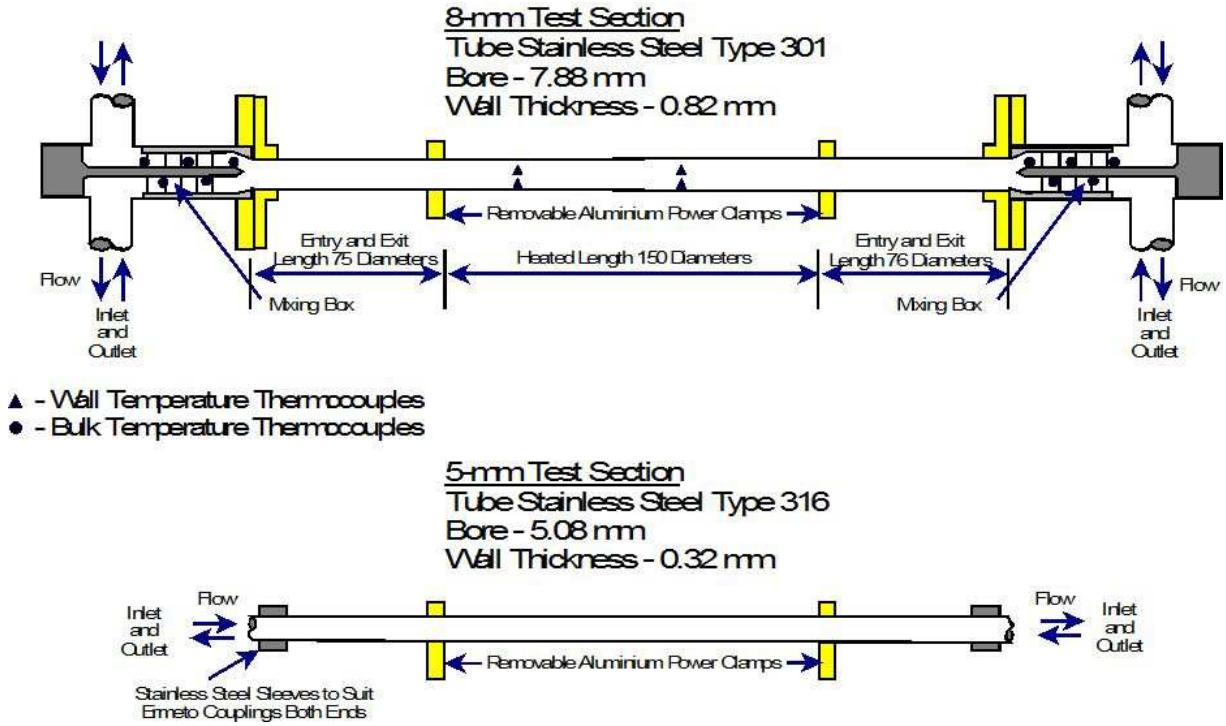

FIG. 3.5. The 8-mm and 5-mm-bore test sections for experiments with carbon dioxide.

TABLE 3.4. SUMMARY OF EXPERIMENTAL CONDITIONS WITH CARBON DIOXIDE AT A PRESSURE OF 7.584 MPA

Tube Inside Diameter (mm)	Flow Direction	Fluid Inlet Temperature (°C)	Mass Flux ($kg/m^2.s$)	Heat Flux (kW/m^2)
19 [3-80]	Upflow and Downflow	0 – 31.5	102 – 564	0.73 – 56.7
8 [3-81]	Upflow and Downflow	8 – 28	179 – 1990	4.3 – 302
5 [3-82]	Upflow and Downflow	5.5 – 30	295 – 3280	9.9 – 45.5

Figure 3.6 shows the large-scale test facility used for experiments with water at supercritical pressure. A special feature of this was that the circulation of water round the circuit for both upward and downward flow through the vertical test section was achieved by means of natural circulation. Table 3.5 shows the range of conditions covered in experiments using a tube of 25.4 mm ID. A detailed description of the test facility and the experiments performed using the above-mentioned test section has been produced [3-79]. The data obtained are presented in graphical form, which has been digitized.

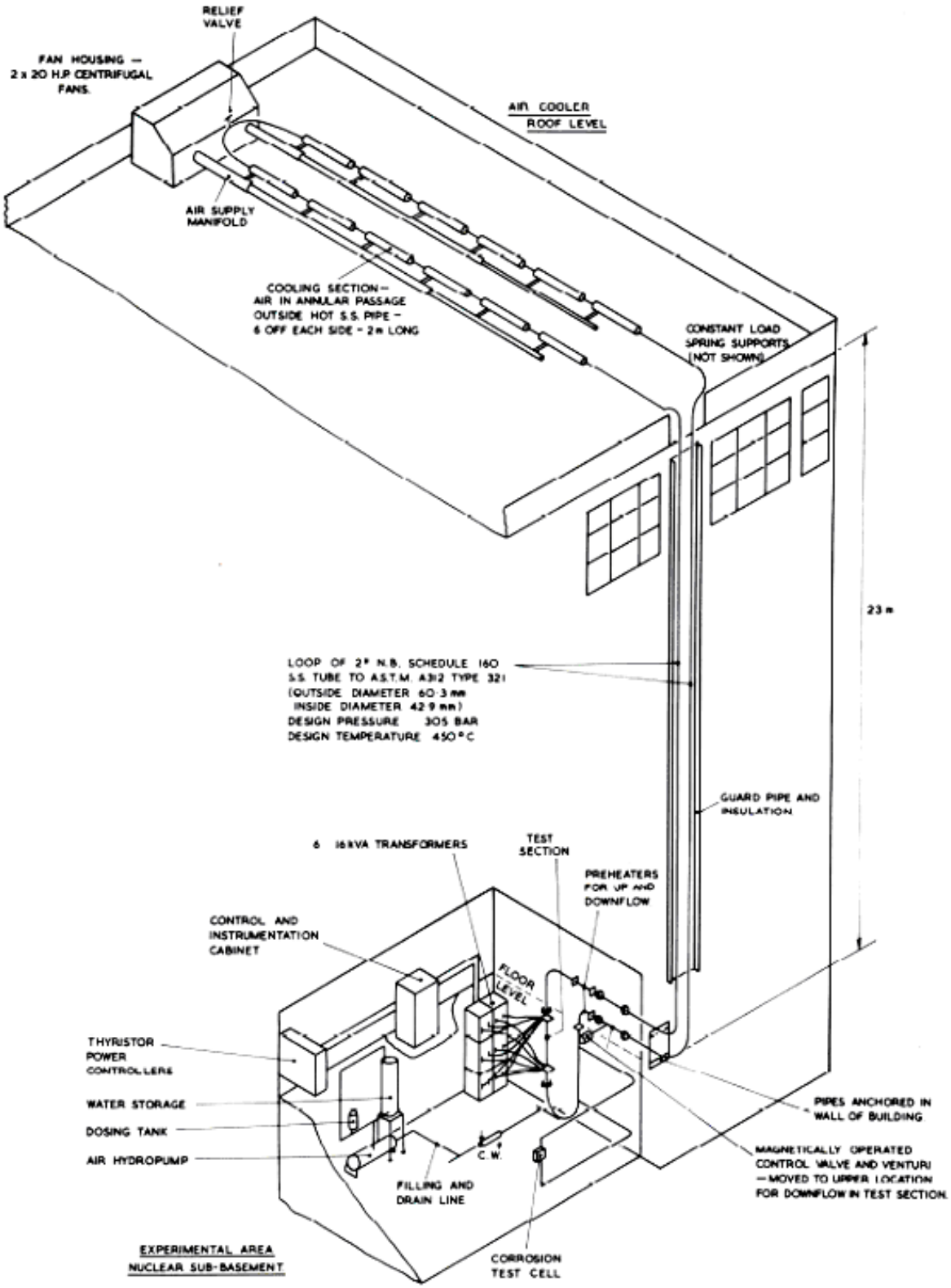

FIG. 3.6. Supercritical pressure water test facility.

TABLE 3.5. SUMMARY OF CONDITIONS FOR THE EXPERIMENTS WITH WATER AT A PRESSURE OF 25 MPA IN A 25.4 MM ID TUBE [3-83]

Flow Direction	Fluid Inlet Temp. (°C)	Mass Flux (kg/m^2.s)	Heat Flux (kW/m^2)
Upflow and Downflow	150 – 320	132 – 1062	170 - 450

3.1.1.5. NTUU KPI experimental studies

The following experiments with supercritical pressure water were performed at the National Technical University of Ukraine, Kiev Polytechnic Institute：

- experiments on deteriorated heat transfer in inlet region of vertical tubes of small diameters to supercritical pressure water flowing upward and downward with significant influence of buoyancy;
- experiments on pressure drop and heat transfer in smooth channels; and
- experiments on heat transfer to supercritical water in a gaseous state, in vertical annuli, 3- and 7-rod bundle simulators.

3.1.2. Annuli data

3.1.2.1. Xi'an Jiaotong University experiment

An experiment was performed at Xi'an Jiaotong University (XJTU) using an annulas test section to obtain supercritical heat-transfer data for water for validation of supercritical heat-transfer correlation [3-86]. Both the inner and outer tubes of the test section were made of stainless-steel tubes. The inner tube has an outer diameter of 8 mm and a wall thickness of 1.5 mm. It was heated with electric current over a heated length of 2 m. The outer tube has an outer diameter of 16 mm and a wall thickness of 2 mm. Ceramic cylindrical spacers were installed at several axial locations to maintain the spacing between the inner and outer tubes. Thermocouples were installed inside the test section to measure the inner-wall temperature. Figure 3.7 illustrates schematically the annulus test section design at XJTU for supercritical pressure heat-transfer tests.

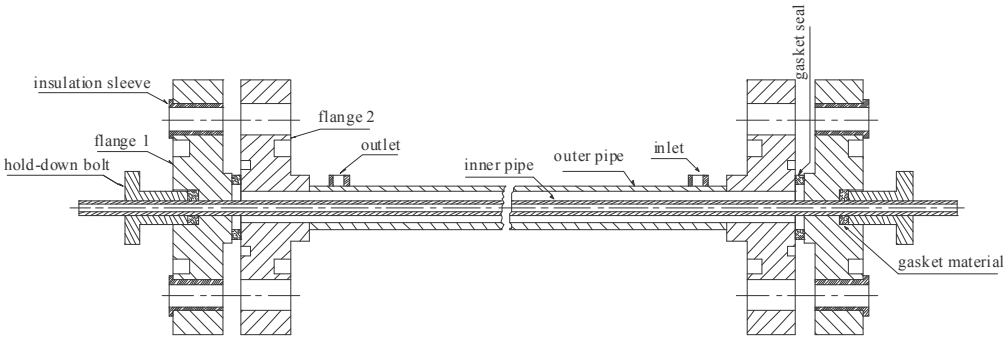

FIG. 3.7. Schematic diagram of the XJTU annular test section geometry.

The test section was installed vertically in the loop and tested with an upward flow of water. Inlet and outlet fluid-temperatures, outlet pressure, and pressure drop over the test section were measured. Several fixed thermocouples were installed to measure wall temperature along the heated length (see Fig. 3.8). Wall temperature measurements have been obtained over a range of mass fluxes and heat fluxes at an outlet pressure of 25 MPa. Figure 3.9 illustrates variation of wall-temperature with local enthalpy and heat flux. The wall temperature increases with increasing fluid enthalpy and increasing heat flux. The temperature increase becomes more gradual at the pseudo-critical enthalpy.

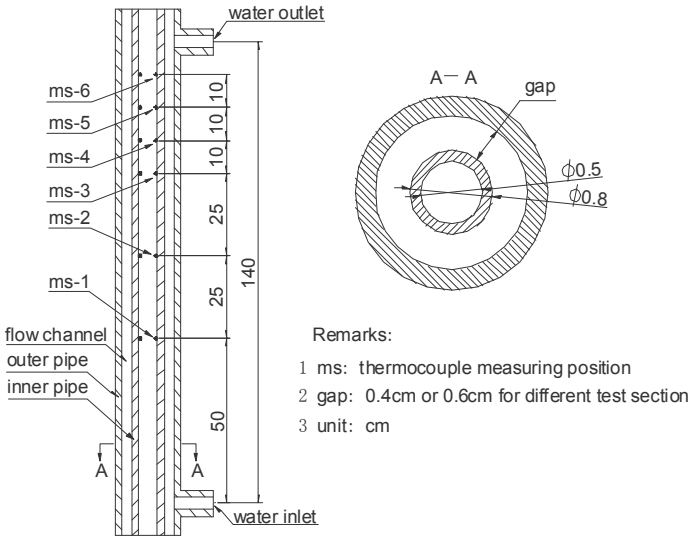

FIG. 3.8. Thermocouple arrangement in the XJTU annular test section.

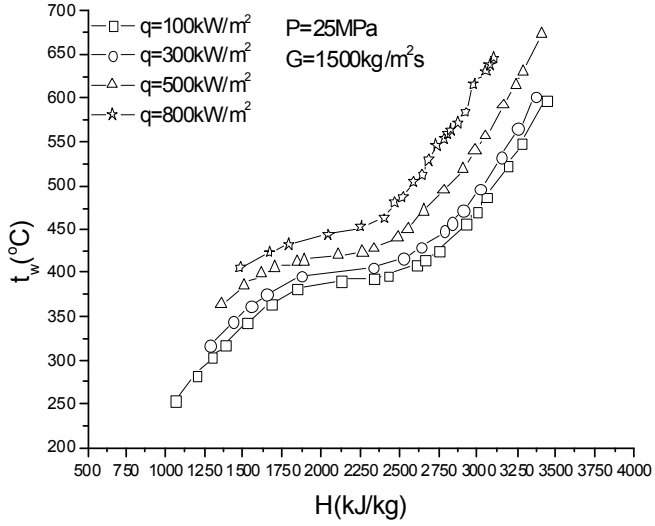

FIG. 3.9. Wall temperature measurements obtained with vertical upflow of supercritical water inside an annulus.

3.1.2.2. University of Wisconsin experiments

Supercritical water heat-transfer experiments were performed at the University of Wisconsin using two internally heated annulus test sections. The heated rod for both annulus test sections was 3.3-m long with an outer diameter of 10.7 mm. Its heated length was 1.01 m. Sixteen thermocouples were evenly spaced along inner cladding over the heated length. The outer shroud of one test section was circular (i.e., another tube) with an inside diameter of 4.29 cm, while that of the other test section was of square cross

section 28.8x28.8 mm^2. Six spacers were installed along the heated length to centre the heated rod inside the shroud. Figure 3.10 illustrates the spacer designs for the two test sections. Test conditions covered mass fluxes from 200 to 2000 $kg \cdot m^{-2} \cdot s^{-1}$, heat fluxes up to 1.5 $MW \cdot m^{-2}$, and bulk inlet temperatures between 300°C and 400°C. All experiments were conducted at 25 MPa and with upward flow.

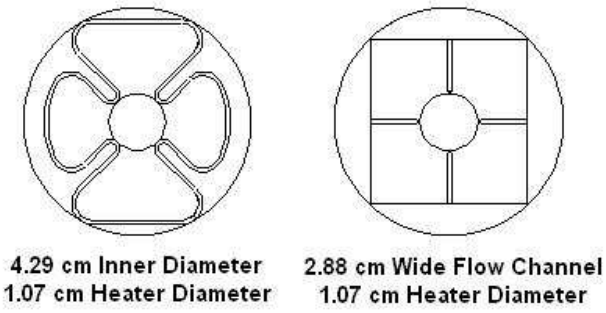

FIG. 3.10. Circular and square annular geometries in the University of Wisconsin experiments.

3.2. SUPERCRITICAL HEAT TRANSFER WITH SURROGATE FLUIDS

Heat-transfer experiments with supercritical pressure water flow are challenging to design, difficult to perform, and expensive due to the high pressures and temperature and the high level of heating power required. Surrogate fluids (such as carbon dioxide and refrigerants) have been used instead. Such fluids have previously been utilized in studies of critical heat flux and film-boiling heat transfer at subcritical pressure conditions. Using surrogate fluids reduces costs, simplifies test-section design, reduces operation risk, and increases the testing flexibility. These benefits stem from the fact that supercritical conditions for surrogate fluids are less severe than those for water. Table 3.6 summarizes the critical properties of water, carbon dioxide and refrigerant R-134a.

TABLE 3.6. CRITICAL PARAMETERS FOR WATER, CARBON DIOXIDE AND REFRIGERANT R-134A

Parameter	Unit	Water	CO_2	R-134a
Critical pressure, P_c	MPa	22.1	7.38	4.06
Critical temperature, T_c	K (ºC)	647.3 (374.1)	304.2 (31.0)	374.2 (101.0)
Critical density, ρ_c	$kg \cdot m^{-3}$	315	468	512

Heat-transfer experiments using surrogate fluids have considerably expanded the database and produced data at equivalent conditions that could lead to test-section damage in corresponding water tests. However, experimental data obtained with surrogate fluids are not directly applicable to applications involving water. Transformation of thermal hydraulics parameters for surrogate fluid experiments is needed to establish equivalent values for water applications. Fluid-to-fluid modeling procedures have been established for critical heat flux and film-boiling heat transfer at subcritical conditions, and found to be appropriate. Attempts have been made to extend this approach to supercritical water conditions (see Section 3.3).

3.2.1. Carbon dioxide flow

3.2.1.1. AECL database

Table 3.7 lists the AECL carbon dioxide database, which covers the following range of parameters: tube diameters from 0.5 to 22.8 mm, pressures from 7.3 to 12 MPa, mass fluxes from 78 to 7520 $kg \cdot m^{-2} \cdot s^{-1}$, and heat fluxes from 0.8 to 1540 $kW \cdot m^{-2}$. The range of fluid temperature (or enthalpy) is difficult to specify due to differences in referencing. Figure 3.11 illustrates the range of reduced pressure and reduced temperature covered in the AECL carbon-dioxide datasets. Nearly all data were collected at supercritical pressures.

TABLE 3.7. SCHT CARBON-DIOXIDE DATA SETS CONSIDERED ACCESSIBLE

Reference	Pressure (MPa)	Temp. (°C) or Enthalpy ($kJ \cdot kg^{-1}$)	Heat Flux ($kW \cdot m^{-2}$)	Mass Flux ($kg \cdot m^{-2} \cdot s^{-1}$)	Tube ID (mm) / Orientation	Data Format
Adebiyi and Hall [3-87]	7.6	T_{in}: 10 to 31 T_w: up to 100	5 to 40	78 to 390	22.14 / hor.	Graph
Ankudinov and Kurganov [3-88]	Up to 7.7	H_{in}: Up to 552	Up to1540	2100 to 3200	8.0	Graph
Bae [3-89]	7.3 to 10	T_{in}: 5	Up to 150	400 to 1200	4.4 to 9.0	Graph
Bourke et al. [3-90]	7.4 to 10.3	T_b: 15 to 35 T_w: 20 to 300	Up to 350	311 to 1702	22.8	Graph, Table
Bringer and Smith [3-91]	8.27	T_b: 21 to 49	31.5 to 315.25	---	4.5	Table
Huai et al. [3-92]	7.4 to 8.5	T_{in}: 22 to 53	0.8 to 9.0	113.7 to 418.6	1.31	Graph
Fewster [3-93]	Up to 7.58	20 to 80	Up to 455	---	5 to 19	Graph
Kim et al. [3-94]	Up to 8.0	T_{in}: 15, 25, 32	3 to 180	209 to 1230	7.8	Graph
Kim et al. [3-95]	7.75 to 8.85	T_{in}: 5 to 35	Up to 150	400 to 1200	4.4	Graph
Kim et al. [3-96]	7.75 to 8.12	T_{in}: 0 to 37	Up to 150	400 to 1200	Annular tube ID=10, rod OD=8	Graph
Kim et al. [3-97]	8.12	-	30 to 50	400 to 1200	4.4 and 9	Graph
Koppel [3-98]	7.8	$T_{b(min)}$: 26.1 to 40.9 $T_{b(max)}$: 38.2 to 41.1	224 to 820	890 to 3140	4.93	Table
Krasnoschekov and Protopopov [3-99]	7.85, 9.81	$T_{b(min)}$: 29.6 to 30.8 $T_{b(max)}$: 39 to 44.5	430-2520	1135-7520	4.1	Table
Kurganov and Ankudinov [3-100]	Up to 7.7	H_{in}: 520 to 580	390	3200	---	Graph
Kurganov [3-101]	Up to 9.0	500 to 800	Up to 1056	Up to 2400	22.7	Graph
Liao and Zha [3-102]	7.4 to 12	20 to 110 T_b-T_w: 2 to 30	10 to 200	218 to 4075	0.5 to 2.16 / vert. And hor.	Graph
Petukhov et al. [3-103]	8.8	$T_{b(min)}$: 27 to 59.5 $T_{b(max)}$: 30 to 62	32 to 126	870	6	Table
Pioro and Khartabil [3-104]	7.6 to 8.8	T_{in}: 20 to 40	Up to 616	900 to 3200	8	Tables
Shiralkar and Griffith [3-105]	7.58 to 7.92	-	Up to 211	1560 to 2170	3.175 to 6.35	Graph
Shiralkar and Griffith [3-106]	7.58 to 7.92	-	Up to 211	1560 to 2170	3.175 to 6.35	Graph
Tanaka et al. [3-107]	7.86	$T_{b(min)}$: 27.9 to 29.2 $T_{b(max)}$: 36.5 to 37.2	14.2-51.8	495 to 990	10	Table
Tanaka et al. [3-108]	Up to 8.0	T_{in}: Up to 35 T_w: up to 500	Up to 640	Up to 1930	6	Graph
Yang and Khartabil [3-109]	Up to 8.37	---	55.4 to 291.3	Up to 1196	8	Graph

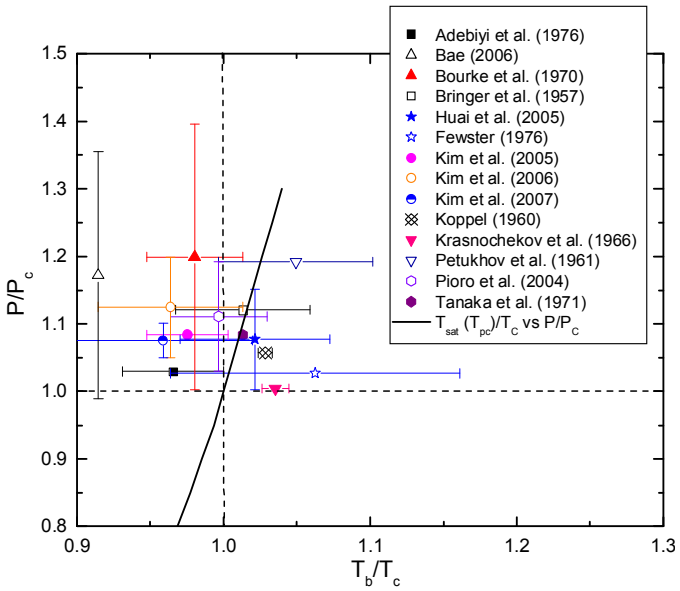

FIG. 3.11. Range of selected AECL supercritical heat-transfer database for carbon dioxide flow.

The similarity in heat transfer behaviour at supercritical pressure between water and carbon dioxide flow has been assessed using carbon dioxide data obtained at AECL by Pioro and Khartabil [3-104] and water data obtained by Dickinson and Welch [3-85] and Kirillov et al. [3-16]. Figure 3.12 shows the variation of normalized Nusselt numbers with the normalized bulk-fluid enthalpy for water and carbon dioxide flows. The experimental Nusselt number, Nu_{exp}, is normalized with respect to the predicted Dittus-Boelter Nusselt number value, Nu_{DB}, which is given by

$$Nu_{DB} = 0.023\, Re_f^{0.8}\, Pr^{0.4} \tag{3-1}$$

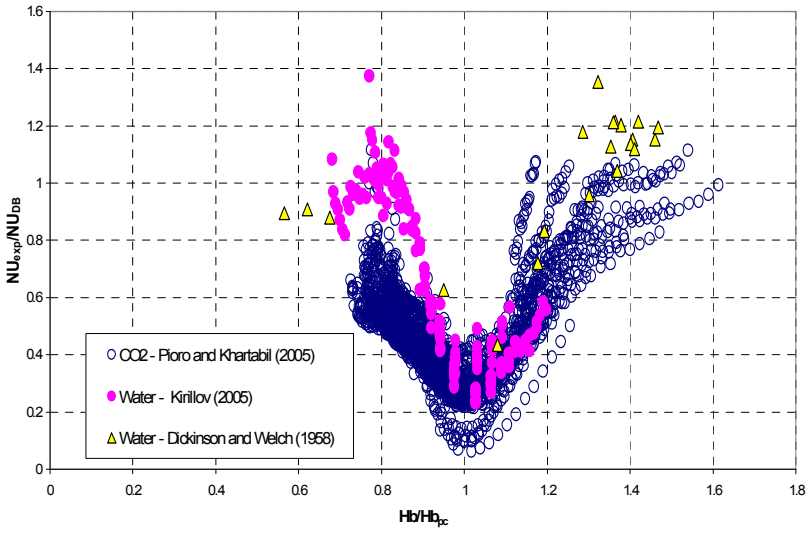

FIG. 3.12. Relationship between dimensionless Nusselt number dimensionless bulk coolant enthalpy.

The bulk-fluid enthalpy, H_b, is normalized with respect to the enthalpy at the pseudo-critical temperature, H_{pc}, where the specific heat reaches a maximum. The normalized Nusselt numbers follow similar trends for water and carbon dioxide flows. Table 3.8 lists the range of flow conditions covered in these three datasets.

TABLE 3.8. DATA RANGE FOR THE ASSESSMENT OF SUPERCRITICAL HEAT TRANSFER SIMILARITY BETWEEN WATER AND CARBON DIOXIDE

Fluid	Water	Water	Carbon Dioxide
Authors	Kirillov et al. [3-16]	Dickinson and Welch [3-85]	Pioro and Khartabil [3-104]
No. of data	156	21	2464
L, mm	4000	1600	2208
D, mm	10.0	7.62	8.06
T_b/T_c	0.92 - 1.03	0.84 - 1.16	0.97 - 1.31
P/P_c	1.09	1.09	1.026 - 1.2
$Re_f \cdot 10^{-3}$	180 - 520	259~930	106 - 1210
Pr	0.89 - 10.35	0.8 - 7.23	0.90 - 34.50

3.2.1.2. SJTU database

SJTU collected 4881 data points for supercritical heat transfer in tubes with upward flow of carbon dioxide. Table 3.9 lists the data sources, flow conditions, and test-section geometry. Some duplication of data has been observed compared with the AECL database.

TABLE 3.9. PARAMETERS OF CO_2 TEST DATA [3-31]

	Fluid	Pressure (MPa)	Mass Flux ($kg \cdot m^{-2} \cdot s^{-1}$)	Heat Flux ($kW \cdot m^{-2}$)	Geometry
Shiralkar and Griffith [3-105]	CO_2	7.58/7.93	678~2712	95~296	ID=3.17 and 6.35 mm, L=0.21 m
Bourke et al. [3-90]	CO_2	7.44/10.32	1234	8.5~270	ID=22.8 mm, L=4.56 m
Tanaka	CO_2	7.84	1179~2358	488~640	ID=6.0 mm, L=1.0 m
Ikryannikov	CO_2	9.12	269	14~95	ID=29.0 mm, L=0.58 m
Petukhov et al. [3-103]	CO_2	7.7/8.9	3250	389~1053	ID=8.0 mm, L=1.67 m
Jiang	CO_2	8.6/9.5	579~2690	10.8~549	ID=0.95 and 0.27 mm, L=0.055 and 0.09 m
Kim	CO_2	7.75/8.85	400~1200	10~150	ID=4.4 mm, L=2 m
Kim	CO_2	8.0	419~628	35~110	ID=7.8 mm, L=1.2 m
Bae	CO_2	7.25/8.85	400~1000	30~110	ID=4.4 mm, L=2.0 m

3.2.1.3. KAERI database

A series of supercritical heat transfer tests have been carried out using carbon dioxide at KAERI (Korea Atomic Energy Research Institute) as a part of the Korean National Nuclear Research and Development program [3-110], [3-111], [3-97], [3-112], [3-113], [3-114], [3-115]. The purpose of the experiments was

to provide preliminary supercritical heat transfer data for use in the Korean SCWR core conceptual design that uses a solid moderator (referred to as the SCWR-SM).

The shape of the flow channels tested included four different tubes having inner diameters of 4.4, 4.57, 6.32, and 9.0 mm and two annular channels. One of the annular channels consists of a tube with inner diameter of 10 mm and a concentric rod with outer diameter of 8 mm. The other annular channel consists of a tube with inner diameter of 12.5 mm and an eccentric rod with outer diameter of 9.5 mm (eccentricity of 0.33). Figure 3.13 shows the tube test section and the locations of the measuring points. The test section was basically a circular Inconel-625 tube with an inner diameter of 6.32 mm, which was heated uniformly by a direct current power supply. The vertically aligned test section was 3 m long. Forty one adhesive, K-type thermocouples were attached at 50 mm intervals onto the outer surface of the tube to measure the wall temperature distribution. At both the upstream and downstream of the test section flange, mixing chambers were provided. The test section was electrically insulated using Teflon in the flange at both ends of the test section. The direct current busbar was connected to the test section with a sufficient clearance from the first thermocouple from the inlet in order to provide a fully developed turbulent flow at the location of the first thermocouple. The lengths of the heated section are summarized in Table 3.10. The voltage between the clamped terminals controlled the heat flux.

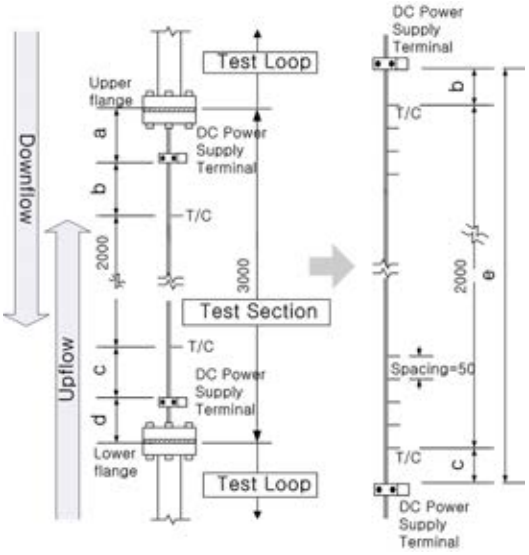

FIG. 3.13. KAERI tube test section.

TABLE 3.10. DIMENSIONS OF THE KAERI TUBE TEST SECTIONS

Axial dimensions (see FIG. 3.13)	Upward flow				Downward flow			
	Ø4.4 mm	Ø4.57 mm	Ø6.32 mm	Ø9.0 mm	Ø4.4 mm	Ø4.57 mm	Ø6.32 mm	Ø9.0 mm
a, mm	250	250	150	150	500	200	200	
b, mm	50	50	150	150	200	500	500	
c, mm	50	200	500	500	50	150	150	
d, mm	650	500	200	200	250	150	150	
e, mm	2100	2250	2650	2650	2250	2650	2650	
Thickness, mm	0.9	0.89	1.60	0.93	0.89	1.60	0.93	

Two types of annular test sections were tested. Figure 3.14(a) shows a sketch of the concentric annular test section which was internally heated by a heater rod [3-116]. An annular channel was created between an unheated outer housing tube with an inner diameter of 10.0 mm and the heated rod with an outer diameter of 8.0 mm. The heated length of the test section was 1800 mm. The inner rod with an Inconel 600 sheath was heated by passing an alternating current through the internal heater element and held coaxially with the outer tube by spacers placed axially at 200 mm intervals. Twelve thermocouples were installed on the surface of the heater rod to measure surface temperatures of up to 650ºC. The first and the last thermocouples were installed 50 mm from the lower and upper ends of the heater rod to avoid interference from the unheated sections of the heater rod. Six thermocouples in the lower part of the heater rod were equally spaced 100 mm apart and each thermocouple was circumferentially separated by 60º. The other six thermocouples in the upper section of the heater rod were equally spaced 200 mm apart and each thermocouple was also circumferentially separated by 60º. The thermocouple diameter was 0.5 mm. The thermocouples were installed on the surface of the heater rod in small grooves. Since the sizes of the thermocouples and grooves were small, it is considered that the installed thermocouples did not influence the flow and temperature fields. The test section maintained a uniform wall heat flux along its heated length and was insulated to minimize heat loss to the environment. The bulk fluid temperature along the channel was calculated from a heat balance using the measured inlet temperature.

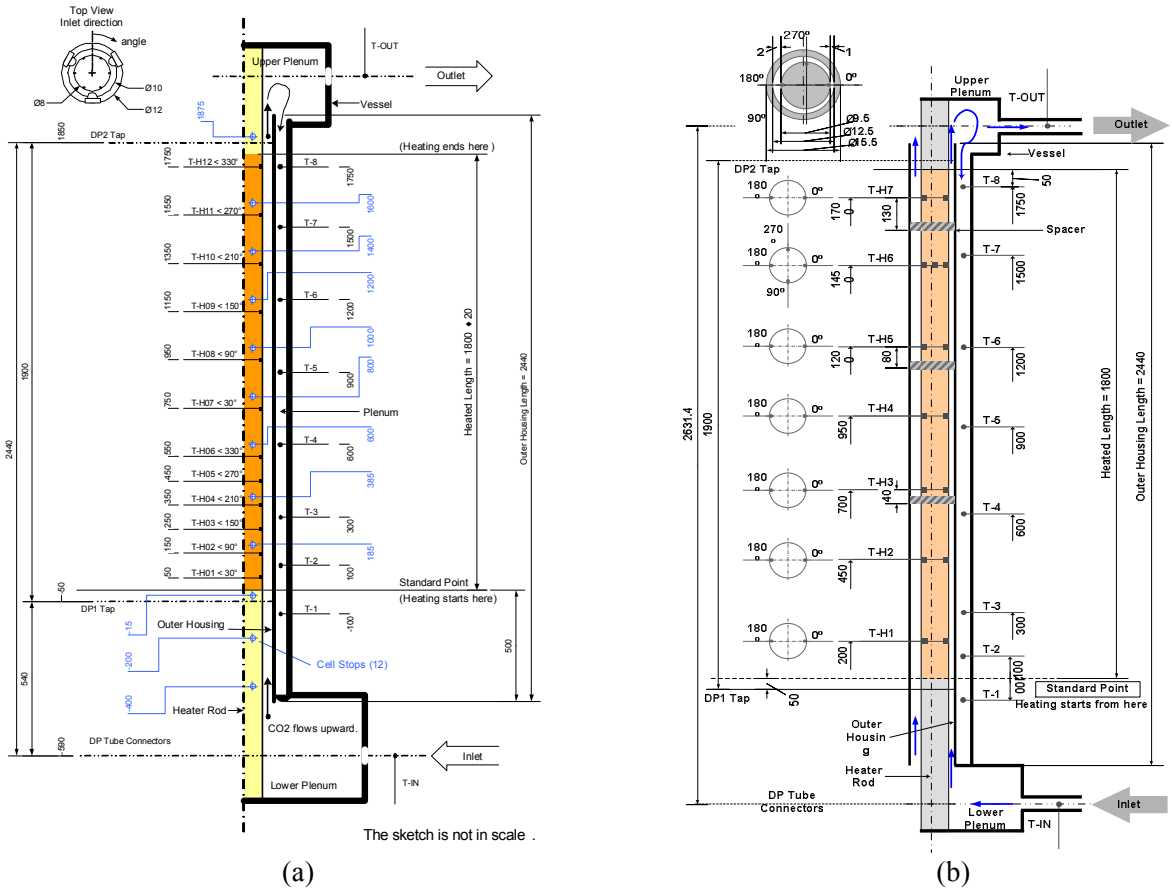

FIG. 3.14. Annular test sections: (a) concentric, (b) eccentric.

The channel of the eccentric annulus test section was constructed by placing a 9.5 mm outer diameter heater rod in a 12.5 mm inner diameter tube, as shown in Fig. 3.14(b) [3-116]. The narrowest gap was 1.0 mm and the widest gap was 2.0 mm. The eccentricity defined as $e = 1/(R_o - R_i)$ was 0.33. The tube was

surrounded by an outer housing. Stagnant CO_2 occupied the space between the enclosure tube and the outer housing. CO_2 of pre-determined temperature and pressure was heated as it flowed upward through the annular channel. The flange-to-flange length was 2,631 mm and the heated length was 1,800 mm. The heater rod was a tube type sheath made of NCF600 filled with Boron Nitride. The heater rod was heated indirectly by a Nickel-Chrome heating coil made of NCHW1 embedded in the Boron Nitride core, which acted as an insulator between the sheath and the heating coil. Sixteen (16) thermocouples were inserted into grooves machined on the outer surface of the sheath. The tips (3 mm) were TIG welded and 100 mm from the tips was welded by silver brazing. The locations of the thermocouples are shown in Fig. 3.14(b). At the upper and lower ends, mixing plenums were provided for the supply of homogeneous CO_2 into the annular channel. Three spacers of height 30 mm were installed upstream of the third, fifth, and seventh rows of the thermocouples with distances 40, 80, and 130 mm each. The thickness of the spacer was 0.4 mm. The centerline of the spacer was aligned with the centerline of the heater rod and the position was secured by a wire of 1 mm diameter inserted along the widest gap of the channel.

Table 3.11 summarizes the geometries and flow directions of the tests performed using the KAERI SPHINX test facility. The test began with the upward flow tests with the geometries summarized in Table 3.11 and the downward flow tests were followed with the selected geometries. Downward flow tests were not performed for the 4.4 mm tube, the 6.32 mm tube with wire-type spacer, and the eccentric annular channel.

TABLE 3.1. SUMMARY OF FLOW DIRECTION COVERED IN KAERI TEST

			Upward flow	Downward flow
Tube	4.4 mm		●	
	4.57 mm		●	●
	6.32 mm	Plain	●	●
		Wire-inserted	●	
	9.0 mm		●	●
Annular Channel	Concentric annular channel 8 x 10 mm		●	●
	Eccentric annular channel 9.5 x 12.5 mm, eccentricity = 0.33		●	

Effect of Mass Flux. Figure 3.15 shows variations of wall temperatures with enthalpy for mass fluxes from 285 to 1200 $kg \cdot m^{-2} \cdot s^{-1}$ at the pressure of 8.12 MPa and heat flux of 50 $kW \cdot m^{-2}$. As the mass flux increases, the wall temperature decreases and the heat transfer coefficient increases. This is a consistent result, where the heat transfer is proportional to the power of the Reynolds number or the mass flux. For mass fluxes higher than 600 $kg \cdot m^{-2} \cdot s^{-1}$, the wall temperature does not show any irregular behavior and increases in a manner which is almost parallel to the bulk temperature distribution. At the mass flux of 500 $kg \cdot m^{-2} \cdot s^{-1}$, the wall temperature displays a mild temperature peak. The peak gradually reduces spreading the heat transfer deterioration over a wide range of enthalpy at low mass fluxes. The scatter in the heat-transfer coefficients at the mass flux of 1200 $kg \cdot m^{-2} \cdot s^{-1}$ is attributed to the small difference between the wall and bulk temperatures (which is comparable to the measurement uncertainty).

Effect of Pressure. The pressure effect was investigated by comparing the test results for two different pressures, 7.75 and 8.12 MPa, which correspond to 105% and 110% of the critical pressure of CO_2, whereas other conditions were unaltered. The tube inner diameter is 6.32 mm. In Fig. 3.16, the solid symbols are for 8.12 MPa, and the open symbols are for 7.75 MPa. A comparison of wall temperature was made for three different heat fluxes of 30, 50 and 70 $kW \cdot m^{-2}$. The wall temperature increases (and the corresponding heat-transfer rate decreases) with increasing pressure. The effect of pressure on wall

temperature is more significant at the pseudo-critical enthalpy but diminishes at enthalpies beyond the pseudo-critical point. Similarly, the effect is stronger at low heat flux than at high heat flux. Over the current test range of pressure, the characteristics of heat transfer deterioration appear to be similar. At heat fluxes of 50 and 70 $kW \cdot m^{-2}$, the wall temperature becomes higher and the peak is shifted towards the pseudo-critical point due to the increase in the inlet bulk enthalpy. However, the overall wall-temperature distributions remain the same for the two pressures. Obviously, the effect of pressure is strong at the critical point, especially in the vicinity of the critical temperature due to the steep variation of the physical properties there. The pressure effect on wall temperature is less pronounced than that on specific heat, according to experimental evidence of Kang and Chang [3-147].

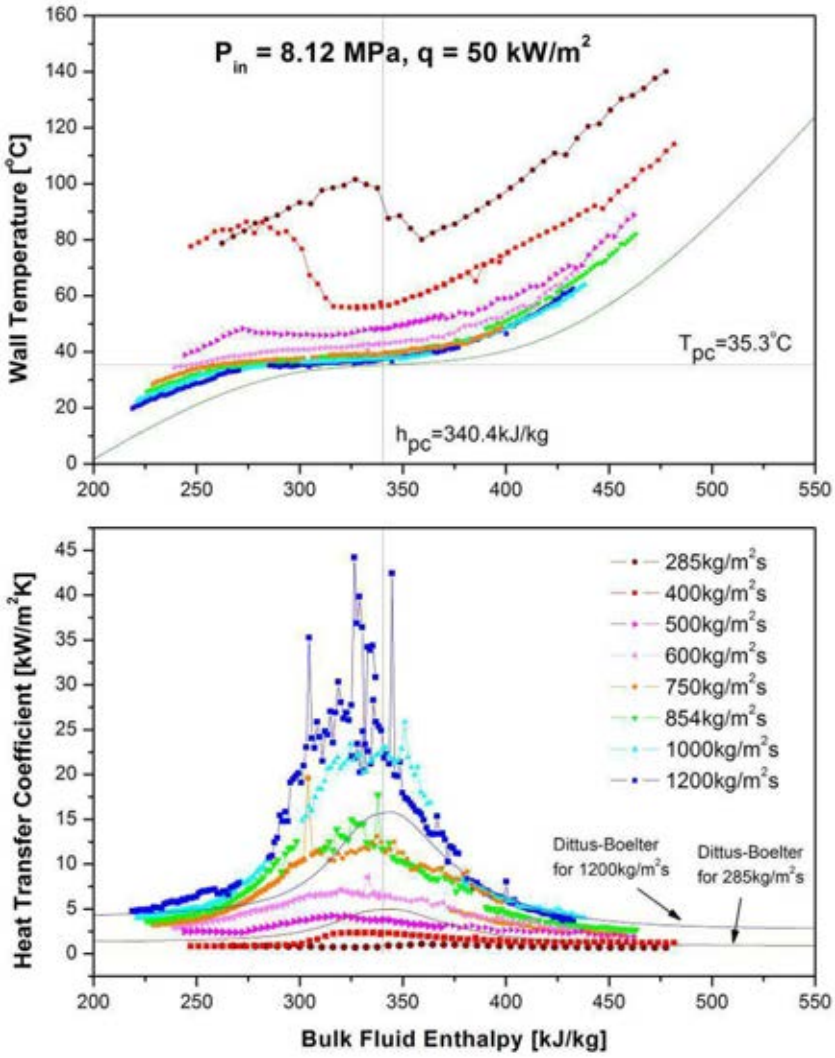

FIG. 3.15. Effect of Mass Flux on Wall Temperature and Heat Transfer Coefficient at q=50 $kW \cdot m^{-2}$, D_{in}=6.32 mm.

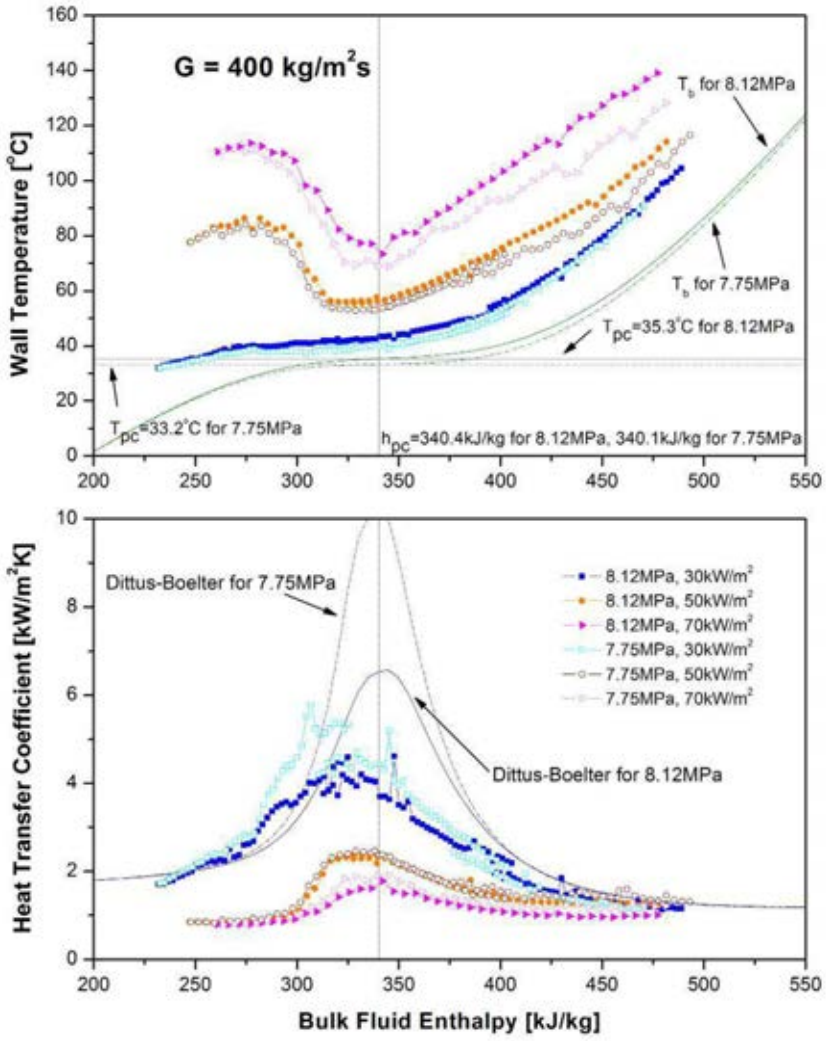

FIG. 3.16. Effect of inlet pressure on wall temperature and heat transfer coefficient at G= 400 kg·m^{-2}·s^{-1}, D_{in}=6.32 mm.

Effect of Heat Flux. Figure 3.17 shows the variations of wall temperature and corresponding heat-transfer coefficient with enthalpy for heat fluxes varying from 29.3 to 67.9 kW·m^{-2} at the pressure of 8.12 MPa and mass flux of 400 kg·m^{-2}·s^{-1}. The horizontal and vertical lines in the wall-temperature plot represent the pseudo-critical temperature and pseudo-critical enthalpy, respectively. The solid curve without a symbol in the heat-transfer-coefficient plot represents the prediction using the Dittus–Boelter heat transfer correlation for heating.

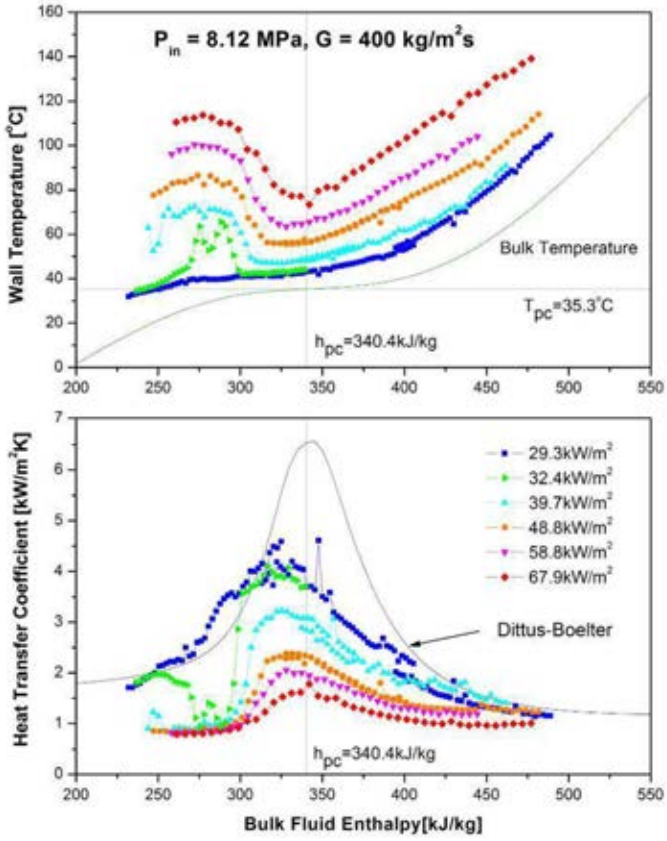

FIG. 3.17. Effect of heat flux on wall temperature and heat transfer coefficient at G=400 kg·m^{-2}·s^{-1}, D_{in}=6.32 mm.

As the heat flux increases, the heat transfer coefficient decreases, except at the region with heat transfer deterioration. In the deterioration regime, sometimes the heat transfer coefficient is larger at high heat flux than lowheat flux, although such a reversed situation had only been observed at the region of wall temperature peaks or plateau. When the heat flux is increased to 32.4 kW·m^{-2}, multiple localized temperature peaks are observed. As the heat flux is further increased to 39.7 kW·m^{-2}, the peaks become gradual and eventually flatten. At the heat flux of 48.8 kW·m^{-2}, the plateau reaches the position of the first thermocouple. As the heat flux increases, the maximum of peak or the plateau shifts in the direction of the test section inlet. The heat transfer coefficient converged to the prediction of the Dittus–Boelter correlation for bulk enthalpies outside of the vicinity of the pseudo-critical temperature.

3.2.2. Other surrogate fluids

3.2.2.1. AECL database

Table 3.12 lists the expanded database for other surrogate fluids. The overall ranges of parameters covered in the database remain the same as those in the previous database. Figure 3.18 illustrates the ranges of reduced pressure and reduced temperature covered in the expanded database for other fluids. The ranges are wide for the data set of Brassington et al. [3-118], but relatively narrow for other data sets.

TABLE 3.2. SUPERCRITICAL HEAT TRANSFER DATA OF SURROGATE FLUIDS

Reference	Fluid	Pressure (MPa)	Temp. (°C) or Enthalpy ($kJ \cdot kg^{-1}$)	Heat Flux ($kW \cdot m^{-2}$)	Mass Flux ($kg \cdot m^{-2} \cdot s^{-1}$)	Tube ID (mm) / Orientation	Data Format
Brassington and Cairns [3-118]	Helium	0.22 to 1.4	T_{in}: 4.4 to 15 K	Up to 2.5	$Re = 4x10^4$ to 10^6	18 / Up and Down	Table
Chun et al.[3-119]	R-134a	Up to 4.3 (transient)	Up to 150	Power: 720 kW DC	Up to 1500	5x5 bundle Rod OD=9.5, Pitch=12.85	Graph
Dimitrov et al. [3-120]	Nitrogen	4.0	T_{in}: 101 to 125 K	9 to 21	12 to 26	20 to 22	Graph
Kalbaliev [3-121]	Toluene	4.3 to 12.5	T_{in}: 16 to 272; T_w: 64 to 593	10 to 6000	40 to 3200	2 to 6.3	Graph
Kataoka [3-122]	R-22	Up to 5.5	---	10 to 190	200 to 2000	4.4, 13	Graph
Kulieva et al. [3-123]	n-Heptane	Up to 5.0	T_w: up to 318	3000 to 3100	Up to 2000	2.09	Graph
Mayinger et al. [3-20]	R-12	4.28 to 4.5	T_{wi}: up to 250	8.6 to 56.7	347 to 1255	12.5 to 24.3	Graph
Yamashita et al. [3-30]	HCFC22	5.5	H_b: 215 to 360	10 to 170	400 to 2000	4.4	Graph

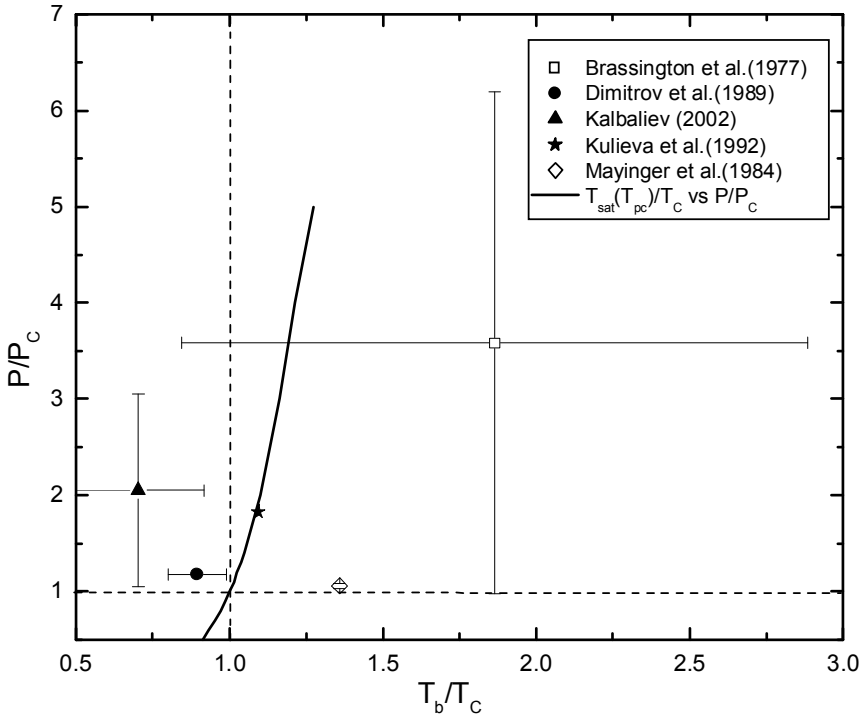

FIG. 3.18. Range of selected AECL supercritical heat-transfer data for other fluids.

3.2.2.2. SJTU Freon-22 database

SJTU collected 645 data points on supercritical heat transfer in tubes with upward flow of Freon-22. Table 3.13 lists the data source, flow conditions, and test-section geometry.

TABLE 3.13. PARAMETERS OF FREON-22 TEST DATA [3-31]

	Fluid	Pressure (MPa)	Mass Flux ($kg \cdot m^{-2} \cdot s^{-1}$)	Heat Flux ($kW \cdot m^{-2}$)	Geometry
Mori	R-22	5.5	700	20~60	ID=4.4 mm, L=2.0 m
Kitou	R-22	5.5	400, 1000	10~70	Annular tube D_{hy}=2.0 mm,L=1.8 m

3.2.2.3. Russian helium database of natural convection from a vertical tube

Experiments were performed with supercritical helium in an 1100-mm high metal cryostat of 100-mm inside diameter, designed for high pressures [3-124]. An experimental assembly with a test section was placed in the lower part of the cryostat. The 30×30 mm^2 working plate was made of very pure copper (not less than 99.993 Cu) with a high thermal conductivity in the region of helium temperatures. Heat transfer was studied with natural convection of helium near the vertically placed working plate at pressures of 0.233 – 0.456 MPa (P/P_c = 1.03 – 2.01). At set values of pressure, P, and heat load, q, on the heated surface in the range of 100 – 5000 $W \cdot m^{-2}$ helium temperature inside the space of cryostat T_∞ varied from 4.2 – 4.6 K to 6 – 10 K. The Rayleigh numbers varied from 10^{10} to 10^{14}. A considerable discrepancy between the experimental data on the average heat transfer coefficients and the values calculated by the equation for carbon dioxide and water at supercritical pressures has been observed. A modified criterion equation was found to correlate with an accuracy of ±20% the results of the authors, as well as those of Klipping and Kutzner [3-125] for natural convection of supercritical helium on a horizontal cylinder in the range of the Rayleigh numbers from 10^7 to 10^{14}.

$$Nu = 0.135\,\mathrm{Ra}_f^{1/3}\left(\frac{c_{p,a}}{c_{p,b}}\right)^n\left(\frac{\rho_w}{\rho_b}\right)^{0.15} \tag{3-2}$$

where $n = 0.5$ for $T_b \le T_{pc}$, and $n = 1$ for $T_b > T_{pc}$. The empirical correlation is corroborated by the results of numerical modeling of the heat transfer process for turbulent natural convection of the fluid with strongly varying properties.

Heat-transfer experiments were performed with natural convection of supercritical helium in narrow slot channels, under both steady-state heat supply to heat transfer surface and at step-wise thermal power increase beginning with zero level [3-126]. A thin strip (~ 1 μm) of nickel Grade NO, obtained by sputtering on a glass substrate 0.5-mm thick was both the heating element and simultaneously the resistance thermometer. The nickel strip was 6-mm wide and 40-mm long. The test section has special contact areas for current to go through the sputtered layer of nickel at about 4Ω resistance. The test section was fastened in helium vessel of the cryostat in such a way that it was possible to change the orientation of the heat transfer surface relative to the direction of gravity forces. One side of the glass substrate was thermally insulated from helium with a fibre glass plate 5-mm thick and the other one with the sputtered layer of nickel and contact areas was directly washed by helium of the working space of the cryostat. In the experiments with limited volume of helium, fastening a plexiglass cover to the glass substrate created a slot above the nickel strip. The cover and the heating surface made a rectangular channel filled up with helium. The helium in the cryostat communicated with the helium in the slot channel only in the edge cross-sections of the latter. The channel was 10-mm wide, its length corresponded to the length of the nickel strip (l = 40 mm), and the size of the channel slot gap, d, in different experiments was 1.0, 0.5, and 0.3 mm. All the tests were performed at the pressure of 0.25 MPa

($P/P_c = 1.10$) in the working space of the cryostat. Conditions of natural convection were studied in supercritical helium on vertical heat transferring surface and on horizontal heat transfer surface turned upwards, under the conditions of large and limited volume of fluid with helium temperatures from 4.7 to 10 K. The heat-flux density on the heated surface at steady-state heating and step-wise power increase varied from 2000 to 9000 $W \cdot m^{-2}$. The experimental data obtained under steady-state conditions in a large volume of supercritical helium were fitted using the form of Equation (3-2). In the calculations the surface height for vertical heated surface and the ratio of the heated area to the surface perimeter for horizontal-up surface were used as the characteristic lengths. The deviation of the data for the nickel surface from Equation (3-2) with the constant of 0.085 instead of 0.135 does not exceed ±30% within the Rayleigh number range from 10^8 to 10^{13}. Moreover, this equation was found to correlate the data on natural convection heat transfer in vertical channels with the ratio of l/d ranged from 40 to 133 in this study. In the case of narrow horizontal channels it is convenient to use a gap width, d, as the characteristic length. Therefore, the correlation for gaps with face-up heated surfaces was obtained as follows

$$\mathrm{Nu} = 3.3\left(\frac{l}{d}\right)^{-0.75} \mathrm{Ra}_f^{1/3}\left(\frac{c_{p,a}}{c_{p,b}}\right)^{n}\left(\frac{\rho_w}{\rho_b}\right)^{0.15} \tag{3-3}$$

where the value of n is the same as in Equation (3-2). This correlation predicts the data for horizontal channels within ±20% in the range of the Rayleigh numbers from 10^5 to $2 \cdot 10^8$.

3.3. FLUID-TO-FLUID SCALING OF SUPERCRITICAL HEAT TRANSFER

3.3.1. Introduction

Fluid-to-fluid modelling is a technique used to model thermalhydraulic phenomena in a working fluid (usually water) using a surrogate fluid (such as a member of the Freon family). The two main reasons for using modelling fluids are the reduction of costs and convenience in performing more extensive tests because of less severe test conditions. Fluid-to-fluid modelling of CHF has been applied successfully in many heat transfer laboratories using Freons as modelling fluids to simulate the occurrence of CHF in water (e.g., Groeneveld et al. [3-127], [3-128]). Reliable CHF predictions for water can be made based on CHF measurements in Freons at considerably lower pressures, temperatures and powers, and have resulted in cost savings of around 80% compared to equivalent experiments in water [3-129]. Fluid-to-fluid modelling techniques for film boiling are not as well established as for CHF. They have been studied by several researchers (e.g., Groeneveld et al. [3-129], Hammouda [3-130], El Nakla [3-131]).

Successful fluid-to-fluid modelling or scaling of supercritical heat transfer requires the use of appropriate similarity relationships. For supercritical heat transfer, the following dimensionless groups are relevant:

(i) P/P_c *and* T/T_c: For the subcritical region, the saturation lines of CO_2, water and R-134a nearly coincide on a P/P_c vs. T/T_c (absolute temperatures) diagram, as can be seen in Fig. 3.19. For supercritical conditions, it is hypothesized that the dependence of the pseudocritical temperature T_{pc} on pressure might be similar to the dependence of the saturation temperature on pressure, because the enthalpy gradient, dh/dT, reaches a maximum at these temperatures. A remarkable degree of similarity in the supercritical behaviour of these three fluids was evident on Fig. 3.19. On a P/P_c vs. T/T_c plot, the pseudocritical temperature lines for all three fluids coincide and the pseudocritical line appears to be an extension of the saturation line.

(ii) Reynolds number, Prandtl number and Nusselt number: At supercritical conditions that are well beyond the critical or pseudo critical points, single-phase heat transfer characteristics prevail and

conventional Nu = f (Re, Pr) relationships are considered to be applicable for calculating heat transfer. The mode of heat transfer at these conditions is described as 'normal' [3-1]. Thus, the product $Re \cdot Pr^{0.5}$ can be used as a first approximation to determine equivalent mass flux conditions, especially when the Prandtl number is not far from unity. For near-pseudocritical conditions, where the fluid properties change drastically with temperature, heat transfer displays anomalous behaviour, as shown in Fig. 3.12. Because this behaviour appears to be similar for both CO_2 and water, when normalizing Nu by Nu_{DB} (see Fig. 3.12), it is suggested that this methodology can be used for preliminary fluid-to-fluid modelling. We therefore scale test conditions for all three fluids by maintaining the same value of $Re \cdot Pr^{0.5}$. We also assume that some kind of limited similarity might apply equally to heat transfer under conditions of deteriorated heat transfer, which, compared to the normal heat transfer mode, is characterized by lower values of the heat transfer coefficient (again see Fig. 3.12) and locally higher values of wall temperature at high heat fluxes and low mass fluxes. Various authors (e.g., Jackson and Hall [3-132]) have described the mechanisms responsible for this deterioration in heat transfer. Additional confirmation that the fractional decrease in heat transfer (or the ratio Nu_{exp} /Nu_{DB}) is the same in all three fluids of interest (i.e., water, carbon dioxide and refrigerants) is required for a wider range of fluids, and reduced pressure, P/P_c, and Reynolds number which are of interest.

(iii)

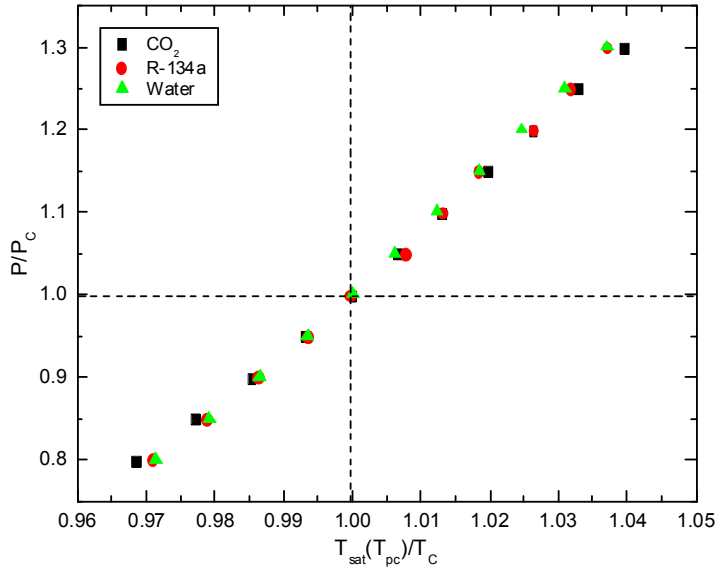

FIG. 3.19. Relationship between reduced pressure and reduced temperature for water, CO_2 and R-134a at saturation and pseudo-critical conditions.

(iv) Dimensionless Heat flux: Jackson and Hall [3-132] examined the governing equations for supercritical heat transfer and suggested that the heat flux parameter $qD/(k_bT_b)$ should be the same in the prototype and modelling fluid (D is the tube inside diameter, k_b is the thermal conductivity and T_b is the absolute bulk coolant temperature). Yang and Khartabil [3-109] found that the heat flux parameter $q/G H_b$, when included in a Nu = f(Re, Pr, T_b/T_c, P/P_c) type of correlation, provided an improved description of deteriorated heat transfer for the AECL supercritical CO_2 data and the supercritical water data of Yamagata et al. [3-30]. We should therefore explore the usefulness of both these heat flux parameters for supercritical fluid-to-fluid modelling.

(v) Geometry: For non-circular passages, *Re* and *Nu* are defined using an equivalent diameter. However, the idea of using an equivalent diameter to try to relate heat transfer behaviour in passages of differing cross-sectional shape does not have any really rigorous basis and should be regarded as an

approximate approach which might work up to a point under certain conditions. In previous CHF and film boiling modelling studies (e.g., Groeneveld et al. [3-129]), it was found that the accuracy of fluid-to-fluid modelling could be adversely affected if the geometries differed significantly. To remove this uncertainty, it is recommended that supercritical fluid-to-fluid modelling experiments should be based on identical test section geometries.

3.3.2. SJTU approach

Cheng et al. [3-133] described some important requirements on scaling methods for heat transfer of supercritical fluids. They derived a set of dimensionless parameters starting from the governing equations (continuity, momentum, energy, surface heat transfer), based on phenomenological analysis and the distortion approach of Ahmad [3-134]. A set of fluid-to-fluid scaling parameters were proposed and were validated against available test data for various fluids using existing heat transfer correlations.

Scaling of tube diameter. For simplicity, identical tube diameter is used for both the model fluid and prototype fluid, i.e.,

$$(D)_M = (D)_P \tag{3-4}$$

Scaling of pressure and bulk temperature. The aim in scaling pressure and bulk temperature is to achieve similar non-uniformity of fluid properties for both fluids. In fluid-to-fluid scaling of heat transfer at sub-critical pressure conditions, pressure is often scaled either using the critical pressure or using density ratios. At sub-critical conditions, there are two characteristic density values at a fixed pressure, the densities of saturated liquid phase and the vapour phase. However, supercritical fluids do not undergo phase change. Examination of using various density values as characteristic values shows that the approach using density ratio is not satisfactory for supercritical conditions. Therefore, the proposed model scales pressure by taking the critical pressure into consideration, so that

$$\left(\frac{P}{P_C}\right)_M = \left(\frac{P}{P_C}\right)_P \tag{3-5}$$

In the literature, different options are proposed for scaling bulk temperature. Two most widely applied approaches are normalising with the critical temperature and the pseudo-critical temperature, respectively,

$$\left(\frac{T}{T_C}\right)_M = \left(\frac{T}{T_C}\right)_P \tag{3-6}$$

$$\left(\frac{T}{T_{PC}}\right)_M = \left(\frac{T}{T_{PC}}\right)_P \tag{3-7}$$

Units of all the temperatures are in Kelvin.

The validity of the scaling approaches suggested above is assessed by the variation of properties with dimensionless temperature. Figure 3.20 shows the dependence of dimensionless heat capacity versus dimensionless temperatures at a normalized pressure of 1.13 for three different fluids, i.e., water, CO_2 and Freon R-134a. Over a wide range of temperature, all three fluids show very similar behaviour with respect to the variation of specific heat. Large deviations occur between the curve for CO_2 and the other curves, where the relative specific heat is presented as a function of relative temperature based on the critical value (T_C). The agreement is significantly improved if the relative temperature based on the pseudo-critical value (T_{PC}) is applied.

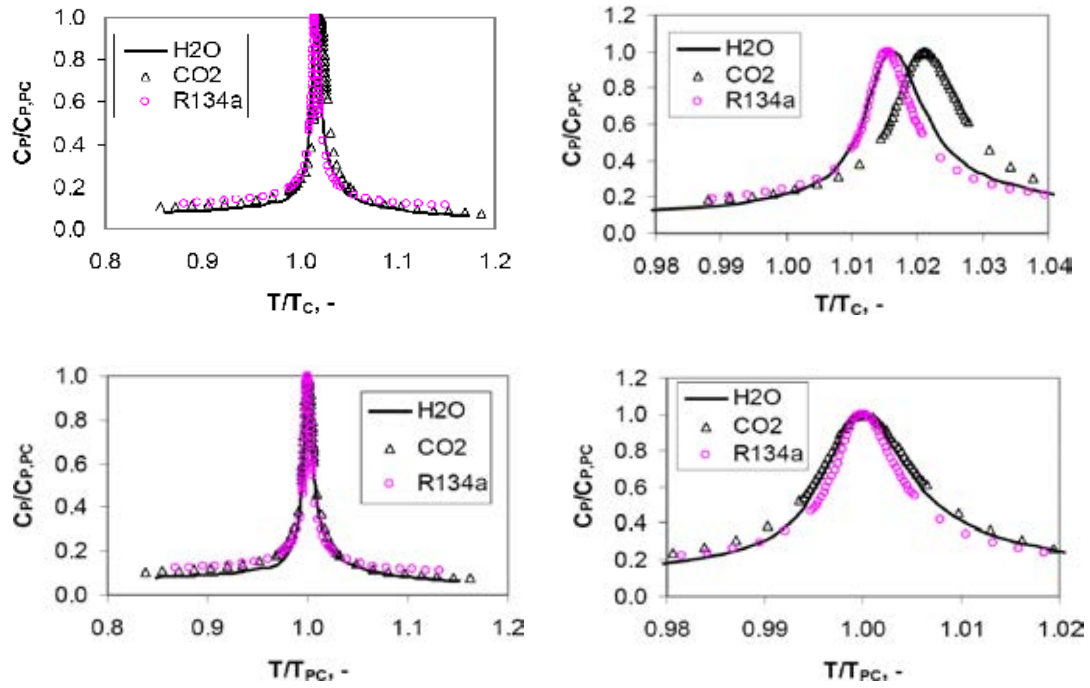

FIG. 3.20. Relationships between dimensionless heat capacity and dimensionless temperatures at normalized pressure of 1.13 for three different fluids.

Cheng et al. [3-133] proposed another dimensionless temperature, which is based on the ratio of temperature difference and expressed as below:

$$\theta = \frac{T - T_{PC}}{T_{PC} - T_C} \tag{3-8}$$

The parameter θ has negative values, when the fluid temperature is below the pseudo-critical value, whereas it gives positive values, if the fluid temperature exceeds the pseudo-critical value. Therefore, this parameter can be characterized as 'pseudo steam quality'.

Figure 3.21 shows the relative specific heat and the relative density versus pseudo steam quality in the region close to the pseudo-critical value. Compared with Fig. 3.20, better agreement is achieved with the new dimensionless temperature for both relative specific heat and relative density. Thus, the following temperature scaling is recommended:

$$\left(\frac{T - T_{PC}}{T_{PC} - T_C}\right)_M = \left(\frac{T - T_{PC}}{T_{PC} - T_C}\right)_P \tag{3-9}$$

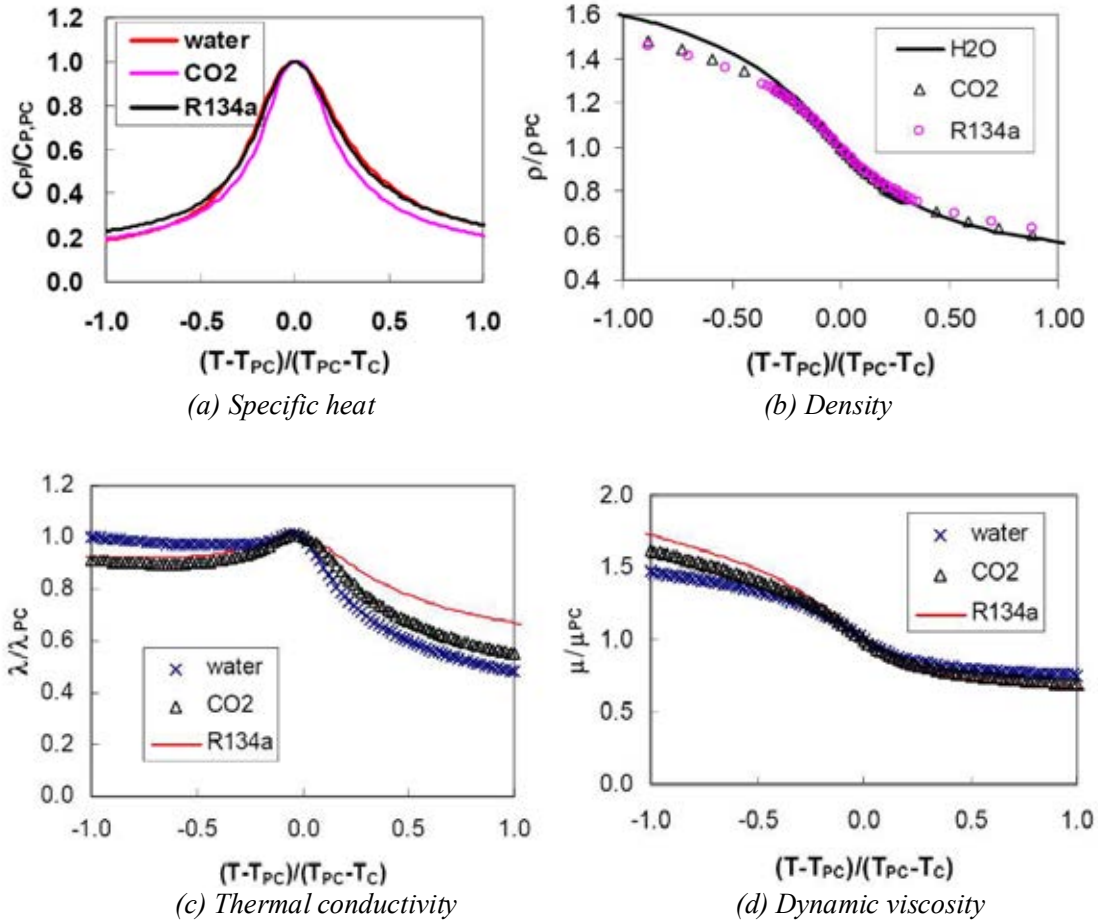

FIG. 3.21. Relationship between dimensionless fluid properties and pseudo steam quality at normalized pressure of 1.13 for three different fluids.

Scaling of heat flux. The purpose of heat flux scaling is to achieve similarity in the effect of heat flux on heat transfer. The Acceleration number contains a heat-flux term and can be rearranged as follows:

$$\frac{q\,L_o}{\lambda_o(T_{pc}-T_c)}=\frac{q\,L_o}{\lambda_o(T_w-T_b)}\frac{T_w-T_b}{T_{pc}-T_c}=Nu(\theta_w-\theta_b) \tag{3-10}$$

This parameter contains two terms, i.e., Nusselt number and the dimensionless temperature difference between the heated wall and the bulk fluid. The effect of heat flux on the effectiveness of heat transfer is mainly due to the strong property variation, which is present across the flow channel cross section, especially in the area close to the heated wall [3-135]. The temperature variation over the cross-section plays a key role in the effectiveness of heat transfer. Therefore, the following scaling of heat flux is proposed:

$$\left(\frac{q\,L_o}{k_b(T_{pc}-T_c)}\right)_M=\left(\frac{q\,L_o}{k_b(T_{pc}-T_c)}\right)_P \tag{3-11}$$

Scaling of mass flux. There are three dimensionless parameters remaining available for mass flux scaling.

Referring to the distortion approach of Ahmad [3-134], these three remaining dimensionless numbers are combined into one single dimensionless parameter:

$$\pi_C = Re^{n1}\ Pr^{n2}\ Fr^{n3} \tag{3-12}$$

Heat transfer to supercritical fluids can be considered separately in two regions. In the first region with low heat flux or bulk temperature far away from the pseudo-critical point, heat transfer can be well-described by conventional correlations, such as the Dittus-Boelter equation. This region is characterized as the 'normal' heat transfer region. In the region of high heat fluxes and bulk-fluid temperatures close to the pseudo-critical value, heat transfer behaviour deviates from that described by conventional correlations. Here, this region is called 'heat flux affected region'. In the present fluid-to-fluid model, the similarity of heat transfer in the heat flux affected region is achieved with Equation (3-11). The aim of mass flux scaling is to achieve similarity of heat transfer in the normal heat transfer region. Assuming that in the normal heat transfer region, heat transfer coefficient can be expressed by the following equation:

$$Nu = c\ \mathrm{Re}^m\ \mathrm{Pr}^n \tag{3-13}$$

The mass flux scaling is thus selected to give

$$\left(\mathrm{Re}^m\ \mathrm{Pr}^n\right)_\mathrm{M} = \left(\mathrm{Re}^m\ \mathrm{Pr}^n\right)_\mathrm{P} \tag{3-14}$$

Assuming a conventional Dittus-Boelter form of correlation for the normal heat transfer region:

$$Nu = c\ \mathrm{Re}^{0.8}\ \mathrm{Pr}^{1/3} \tag{3-15}$$

The mass flux modelling parameter becomes

$$\left(\mathrm{Re}^{0.8}\ \mathrm{Pr}^{1/3}\right)_\mathrm{M} = \left(\mathrm{Re}^{0.8}\ \mathrm{Pr}^{1/3}\right)_\mathrm{P} \tag{3-16}$$

Scaling of heat transfer coefficient. Equality of Nusselt number is required to scale the heat transfer coefficient, i.e.,

$$(\mathrm{Nu})_\mathrm{M} = (\mathrm{Nu})_\mathrm{P} \tag{3-17}$$

In summary, the complete set of scaling factors is expressed as:

$$\mathrm{f_D} = \frac{D_M}{D_P} = 1.0 \tag{3-18}$$

$$\mathrm{f_P} = \frac{P_M}{P_P} = \frac{P_{C,M}}{P_{C,P}} \tag{3-19}$$

$$f_\theta = \frac{\theta_{b,M}}{\theta_{b,P}} = 1.0 \tag{3-20}$$

$$f_G = \frac{G_M}{G_P} = \frac{Pr_{b,P}^{5/12}}{Pr_{b,M}^{5/12}} = \frac{\mu_{b,M}}{\mu_{b,P}} \tag{3-21}$$

$$f_q = \frac{q_M}{q_P} = \frac{k_{b,M}(T_{pc} - T_c)_M}{k_{b,P}(T_{pc} - T_c)_P} \tag{3-22}$$

$$f_\alpha = \frac{h_M}{h_P} = \frac{k_{b,M}}{k_{b,P}} \tag{3-23}$$

The fluid-to-fluid scaling parameters (Equations (3-18)-(3-23)) have been validated against two sets of experimental data (i.e., transforming test data from one fluid to the equivalent conditions for the other fluid). One data set was obtained with water and the other one with carbon dioxide. Table 3.14 lists the range of test parameters covered in these datasets.

TABLE 3.14. SELECTED VALIDATION DATA SETS FOR FLUID-TO-FLUID MODELLING PARAMETERS

ID-No.	Authors	Ranges of test parameters					
		Fluid	Diameter mm	Pressure MPa	Mass flux $kg \cdot m^{-2} \cdot s^{-1}$	Heat flux $MW \cdot m^{-2}$	Data points
1	Herkenrath [3-10]	H_2O	10.0, 20.0	22.5- 25.0	700 – 3500	0.30-2.0	4599
2	Kim [3-136]	CO_2	4.4	7.75 - 8.85	400 – 1200	0.01-0.15	2662

With the equivalent parameters in the modelling fluid, new values of heat transfer coefficient were calculated using selected heat transfer correlations. Two heat transfer correlations were applied: the water-data-based correlation of Bishop [3-135] and the correlation of Krasnoshchekov [3-99] based on both water and carbon dioxide data. The calculated heat transfer coefficient was compared with the equivalent experimental heat transfer coefficient. The deviation between test results and correlation for each test point is defined as:

$$e_i = 2\frac{(h_C - h_M)_i}{(h_C + h_M)_i} \tag{3-24}$$

Two statistic parameters, i.e., the average value and the standard deviation, of the deviation parameter are defined as below, to evaluate the accuracy of the scaling method:

$$\bar{e} = \frac{1}{N}\sum_{i=1}^{N} e_i \tag{3-25}$$

$$\sigma = \left(\frac{1}{N-1}\sum_{i=1}^{N}(\bar{e} - e_i)^2\right)^{1/2} \tag{3-26}$$

Table 3.15 summarizes the results. The test data transformed from carbon dioxide to water conditions, on average, agree well with both correlations. For 2661 test data points, the average value of the deviation is about 1%. The correlation of Krasnoshchekov [3-99] over-predicts the carbon-dioxide data transformed from water data of Herkenrath [3-10].

TABLE 3.15. COMPARISON OF VARIOUS CORRELATIONS WITH DIFFERENT TEST DATA

ID-No.	Data Source	Correlations					
		Bishop [3-135]			Krasnoshchekov [3-99]		
		N	$\bar{e}$	σ	N	$\bar{e}$	σ
1	Herkenrath [3-10]	---	---	---	4599	0.2838	0.3117
2	Kim [3-136]	2661	-0.0039	0.3813	2661	0.0099	0.3822

3.4. HEAT-TRANSFER CORRELATIONS ASSESSMENT

Up to now, most of the correlation equations published in the literature for heat transfer to water under supercritical pressure conditions have been based on experimental results rather than the result of computational studies using turbulence models. Only a few have been developed for flow channels other than circular tubes. Test conditions and parametric ranges for applications vary considerably. Most correlations have the form of the Dittus-Boelter equation with various modifications [3-32]. On the basis of dimensional analysis, and considering specific features of supercritical heat transfer, the most commonly used dimensionless parameters in the correlation equations are Nu, Re, Pr, Gr and non-dimensional fluid property ratios.

Wang et al. [3-137] assessed four correlations for supercritical heat-transfer coefficient against the AECL database for supercritical water heat transfer in tubes. The Dittus-Boelter correlation for forced convection heat transfer in uniformly heated tubes with negligible influence of buoyancy was considered as the reference (most correlations have been derived based on that form). It is expressed as

$$Nu_b = 0.023\,\mathrm{Re}_b^{\,0.8}\,\mathrm{Pr}_b^{\,0.4} \tag{3-27}$$

where

$$Nu_b = \frac{hD}{k_b} \tag{3-28}$$

$$\mathrm{Re}_b = \frac{GD}{\mu_b} \tag{3-29}$$

$$Pr_b = \frac{c_{p,b}\mu_b}{k_b} \tag{3-30}$$

The Krasnoshchekov correlation [3-99] was derived with a relatively large database for water and carbon dioxide flows

$$Nu = Nu_0\left(\frac{\rho_w}{\rho_b}\right)^{0.3}\left(\frac{c_{p,a}}{c_{p,b}}\right)^{n} \tag{3-31}$$

where

$$Nu_0 = \frac{(\xi/8)\,\mathrm{Re}_b\,\overline{\mathrm{Pr}}}{12.7\sqrt{(\xi/8)\left(\overline{\mathrm{Pr}}^{2/3}-1\right)}+1.07} \tag{3-32}$$

$$\xi = \frac{1}{\left(1.82\log_{10}\mathrm{Re}_b - 1.64\right)^2} \tag{3-33}$$

$$c_{p,a} = \frac{H_w - H_b}{T_w - T_b} \tag{3-34}$$

The exponent 'n' is:

n =0.4 for $T_w / T_{pc} \leq 1$ or $T_b / T_{pc} \geq 1.2$

$n = n_1 = 0.22 + 0.18\,(T_w / T_{pc})$ for $1 \leq (T_w / T_{pc}) \leq 2.5$

$n = n_1 + (5 \cdot n_1 - 2)\,(1 - (T_b / T_{pc}))$ for $1 \leq (T_b / T_{pc}) \leq 1.2$

where T_b, T_{pc} and T_w are in K.

The modified Krasnoschekov Protopopov correlation [3-138] (used by Jackson [3-140]) has also been widely employed in various supercritical heat-transfer assessment studies

$$Nu = 0.0183\,Re_b^{0.82}\,Pr_b^{0.5}\left(\frac{\rho_w}{\rho_b}\right)^{0.3}\left(\frac{c_{p,a}}{c_{p,b}}\right)^n \tag{3-35}$$

where the exponent 'n' is:

n =0.4 for $T_b < T_w < T_{pc}$ and $1.2\,T_{pc} < T_b < T_w$

$n = 0.4 + 0.2\,(T_w / T_{pc}-1)$ for $T_b < T_{pc} < T_w$

$n = 0.4 + 0.2\,(T_w / T_{pc}-1)(1-5(T_b / T_{pc}-1))$ for $T_{pc} < T_b < 1.2\,T_{pc}$ and $T_b < T_w$

where T_b, T_{pc} and T_w are in K.

The Yang correlation [3-109] was derived mainly with the heat-transfer data for upflow of carbon dioxide. It has been validated against heat transfer data of Kirillov [3-16] for water flow in tubes. The correlation consists of two components (one for the normal heat transfer regime and the other for the deteriorated heat transfer regime). The correlation for the normal heat transfer regime is expressed as

$$Nu = 0.41179\left(\frac{P}{P_c}\right)^{-0.43274}\left(\frac{T_b}{T_{pc}}\right)^{1.84087}\left(\frac{10000\cdot q}{GH_b}\right)^{0.13205}\left(Nu_0\right)^{1.10223}\left(\frac{\mu_b}{\mu_w}\right)^{-0.92839}\left(\frac{k_b}{k_w}\right)^{0.16801}\left(\frac{c_{p,a}}{c_{p,b}}\right)^{0.72487} \tag{3-36}$$

where the reference Nusselt number, Nu_o, is expressed as

$$Nu_0 = \frac{(\xi/2)\,Re_b\,Pr_b}{12.7(\xi/2)^{1/2}\left(Pr_b^{2/3}-1\right)+1.07} \tag{3-37}$$

and

$$\xi = \frac{1}{\left(3.64 \log_{10} Re_b - 3.28\right)^2} \tag{3-38}$$

The correlation for the deteriorated heat-transfer regime is expressed as

$$Nu = 1.7065\left(\frac{P}{P_c}\right)^{-0.53838}\left(\frac{T_b}{T_{pc}}\right)^{2.46823}\left(\frac{10000 \cdot q}{GH_b}\right)^{-0.32562}\left(Nu_0\right)^{0.94871}\left(\frac{\mu_b}{\mu_w}\right)^{0.50388}\left(\frac{k_b}{k_w}\right)^{-0.54941}\left(\frac{c_{p,a}}{c_{p,b}}\right)^{0.57156} \tag{3-39}$$

The criterion for transition between normal and deteriorated heat-transfer regimes for vertically upward flow is based on the recommendation of Yamagata et al. [3-30], and is defined as

$$k_w = \frac{q}{G^{1.2}} \tag{3-40}$$

Among the four correlations, the modified Krasnoschekov-Protopopov correlation [3-138] provides the best prediction accuracy for the vertical upflow database with over 65% of all data predicted within the ±30% error range (see Fig. 3.22). Both the Dittus-Boelter and the Krasnoshchekov-type correlations give smaller number of data within the same error range. The accuracy of the Yang correlation is comparable to that of the Jackson correlation, and is better than that of the other two correlations. All these correlations underpredict the wall temperature in the deteriorated heat-transfer region. For such conditions additional non-dimensional groups are needed to account for effects such as fluid, thermal expansion, compressibility and buoyancy.

Figure 3.23 illustrates the percentage of all vertical downflow data predicted within various error ranges. The Jackson correlation again provides the best prediction accuracy. Over 85% of all data have been predicted within the ±30% error range. The Yang correlation performs poorly against the vertical downflow data. Both the Dittus-Boelter and the Krasnoshchekov correlations provide similar prediction accuracy to the Jackson correlation. A notable difference, as compared with upflow, is that deterioration heat transfer region is not observed with downflow.

Kuang et al. [3-31] assessed a number of correlations against the SJTU database. Figure 3.24 illustrates the comparison of correlation predictions against the Swenson data for supercritical water heat transfer in a vertical tube [3-143]. The data exhibit normal heat-transfer behaviour, i.e., without the heat-transfer deterioration. All the assessed correlations give peak values of heat-transfer coefficient in the region near to the pseudo-critical point. However, some deviations in the bulk enthalpy and magnitude were observed for the peak heat-transfer coefficient. At regions far from the pseudo-critical point, all the correlations provide similar predictions in heat-transfer coefficient.

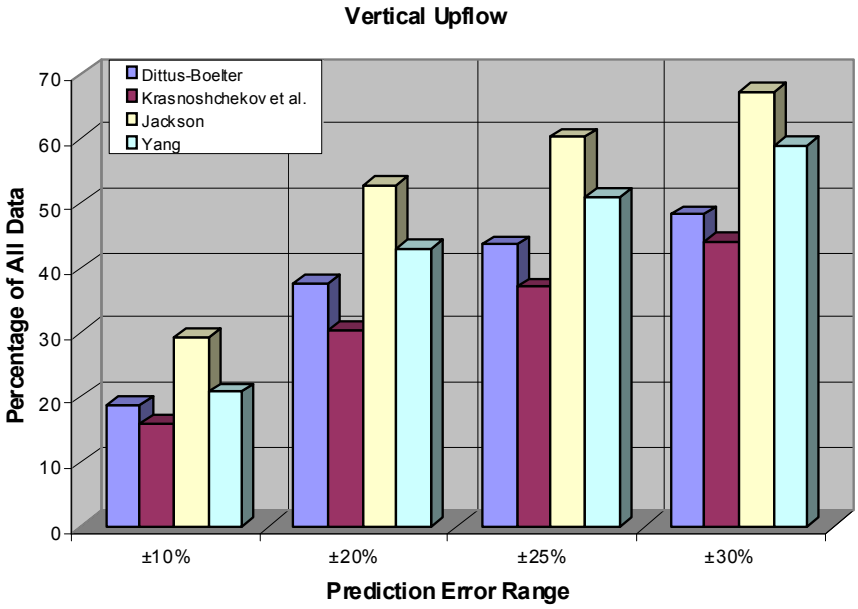

FIG. 3.22. Percentage of all vertical upflow data predicted within error ranges.

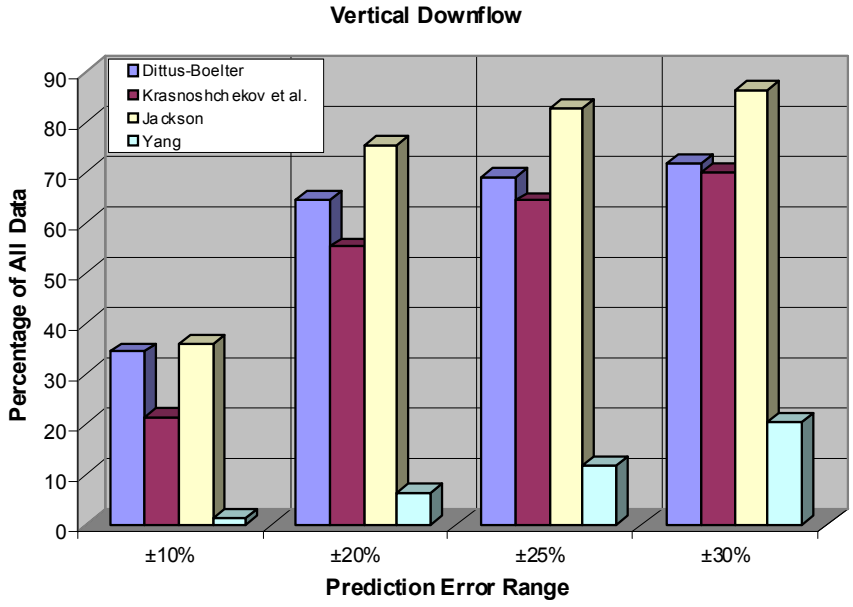

FIG. 3.23. Percentage of all vertical downflow data predicted within error ranges.

Figure 3.25 illustrates the assessment results of the Xu correlation [3-33] and the Jackson correlation [3-84] against the SJTU water data for vertical tubes [3-31]. The Xu correlation [3-33] predicts the experimental Nusselt numbers of the SJTU water database with better accuracy than the Jackson correlation [3-84].

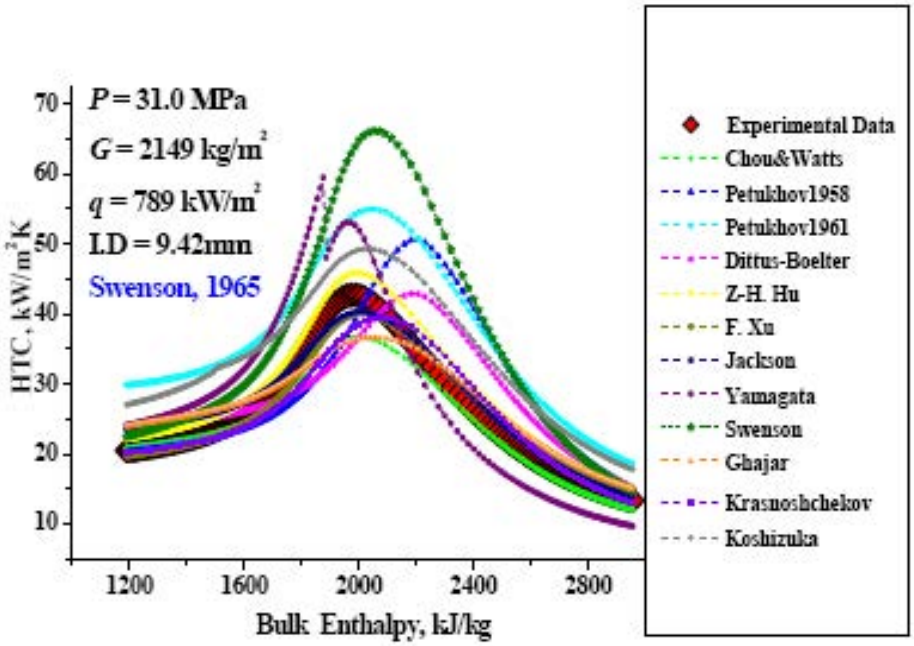

FIG. 3.24. Comparison of various heat transfer correlations.

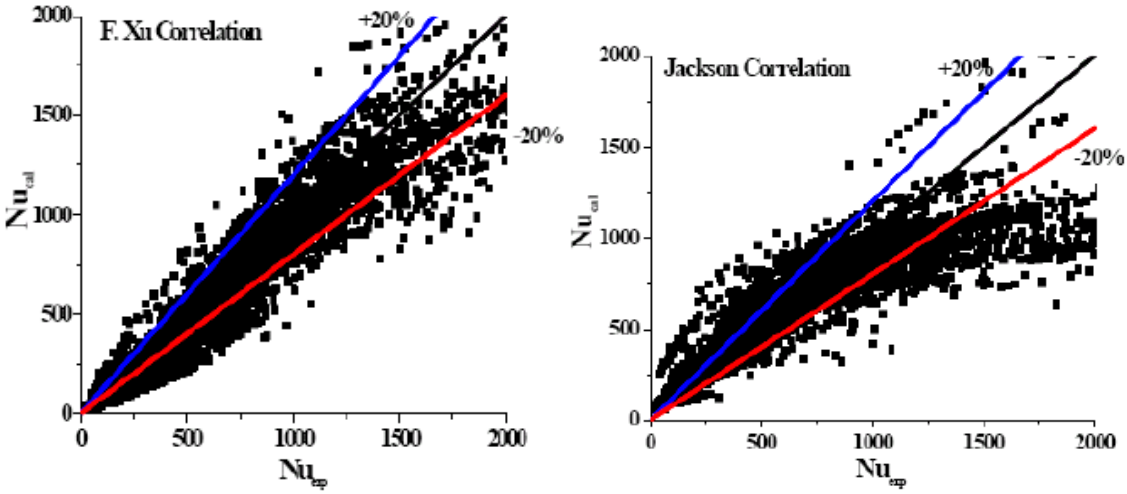

FIG. 3.25. Comparison of correlations with water test data [3-32].

3.5. SEPARATE EFFECTS ON SUPERCRITICAL HEAT TRANSFER

SCWR design and safety analyses must take into account separate effects on supercritical heat transfer. Such effects represent the heat-transfer changes as a consequence of departures from the reference geometry, which has been used in experiments to obtain the experimental data for correlation development. As illustrated in several literature surveys (e.g., Pioro and Duffey [3-1]), most experimental data were obtained using with tubular test sections. Hence the correlations are only strictly applicable for tubes (and need to be extended for use in subchannel applications). Experimental data for rod bundles are scarce and hence only a limited number of correlations have been proposed. These are strictly only applicable for the specific geometry, power profiles, and flow conditions, which were used in the experiments. From the point of view of design, the following separate effects are of main interest:

- Diameter (change in flow area);
- Geometry (tubes, annuli, and bundles);
- Axial power profile (uniform and non-uniform with various shapes);
- Radial power profile in bundles (uniform and non-uniform with various shapes);
- Circumferential power profile in fuel rods (uniform and non-uniform with various shapes);
- Spacing devices (wrap-around wires, spacer grids, and spacers);
- Gap size (small and large);
- Flow direction (upward and downward);
- Transient (postulated accident scenarios).

Experimental data covering these separate effects are very limited. Only some selected effects are discussed in following sections since no experimental data are available for the others.

3.5.1. Effect of diameter

Subchannel sizes in a SCWR fuel bundle are optimized to minimize the flow and enthalpy mal-distributions and enhance heat transfer leading to cladding temperature reduction. Change in subchannel size affects the subchannel flow area, thus impacting on the heat-transfer characteristics. Most heat-transfer correlations implicitly take account of the flow area change through the mass flux and diameter (which together determine Reynolds number). The applicability of these terms in accounting for the flow-area change has been examined with heat-transfer data obtained in tubes of various diameters.

Kuang et al. [3-31] compared wall-temperature measurements obtained with two tubes of 12-mm and 26-mm diameter. Figure 3.26 shows the effect of tube diameter on wall temperature and heat transfer. For the same flow and heat flux conditions, there appears to be no effect of tube diameter on wall temperature at bulk-fluid enthalpies lower than the pseudo-critical enthalpy. The wall temperature becomes lower for the small-diameter tube with increasing bulk-fluid enthalpy beyond the pseudo-critical point. Heat-transfer coefficients are higher for the small-diameter tube at high bulk-fluid enthalpies but the difference diminishes with decreasing enthalpy.

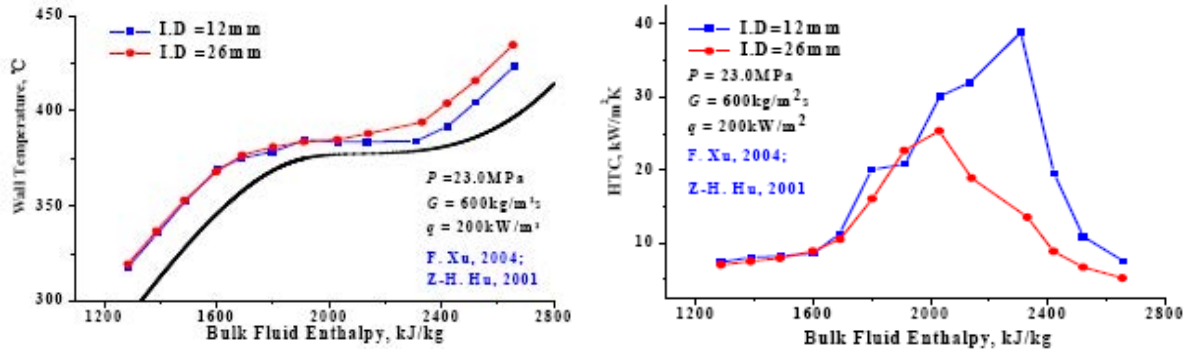

(a) Wall temperature *(b) Heat transfer coefficient*

FIG. 3.26. Effect of tube diameter on heat transfer [3-31].

Bae et al. [3-114] compared heat-transfer coefficients obtained with tubes of 4.4 mm, 6.32 mm and 9.0 mm for heat fluxes of 30, 50 and 60 kW·m^{-2} at a pressure of 8.12 MPa and a mass flux of 400 kg·m^{-2}·s^{-1}. The results are shown in Fig. 3.27. At a heat flux of 30 kW·m^{-2}, a deteriorated heat transfer region is observed only in the tube of 9.0 mm while normal heat transfer occurred in tubes of 4.4 mm and 6.0 mm. As the heat flux increases to 50 kW·m^{-2}, heat transfer deterioration is observed in all three tubes. However, the recovery is slightly better in the smaller tube. It seems as though there is less likelihood of heat transfer deterioration in smaller tubes. With further increase of heat flux to 60 kW·m^{-2}, the heat transfer coefficients in the tube of 9.0 mm diameter are larger than those in the tubes of 4.4 and 6.0 mm diameter until the bulk enthalpy reaches ~310 kJ·kg^{-1}. At constant mass flux, the heat transfer rate is roughly proportional to $d^{-0.2}$, according to the Dittus–Boelter type correlation. This relationship appears to be valid at low heat fluxes in Fig. 3.27, but changes with increasing heat flux. This observation is consistent with the report by Kim et al. [3-146], who reported an effect of tube diameter by examining differences between test results for a tube with inner diameter of 4.4 mm and those for an annular channel having an equivalent heated diameter (based on heated perimeter). The addition of an extra term or some other special treatments may be required to incorporate this effect into currently available heat transfer correlations.

Figure 3.28 illustrates variations of Nusselt number ratio (with values for an 8-mm tube as reference) with enthalpy and tube diameter for vertical upflow. In general, the Nusselt number increases with increasing tube diameter. The deteriorated heat-transfer region appears to be less pronounced in small diameter tubes than large diameter tubes.

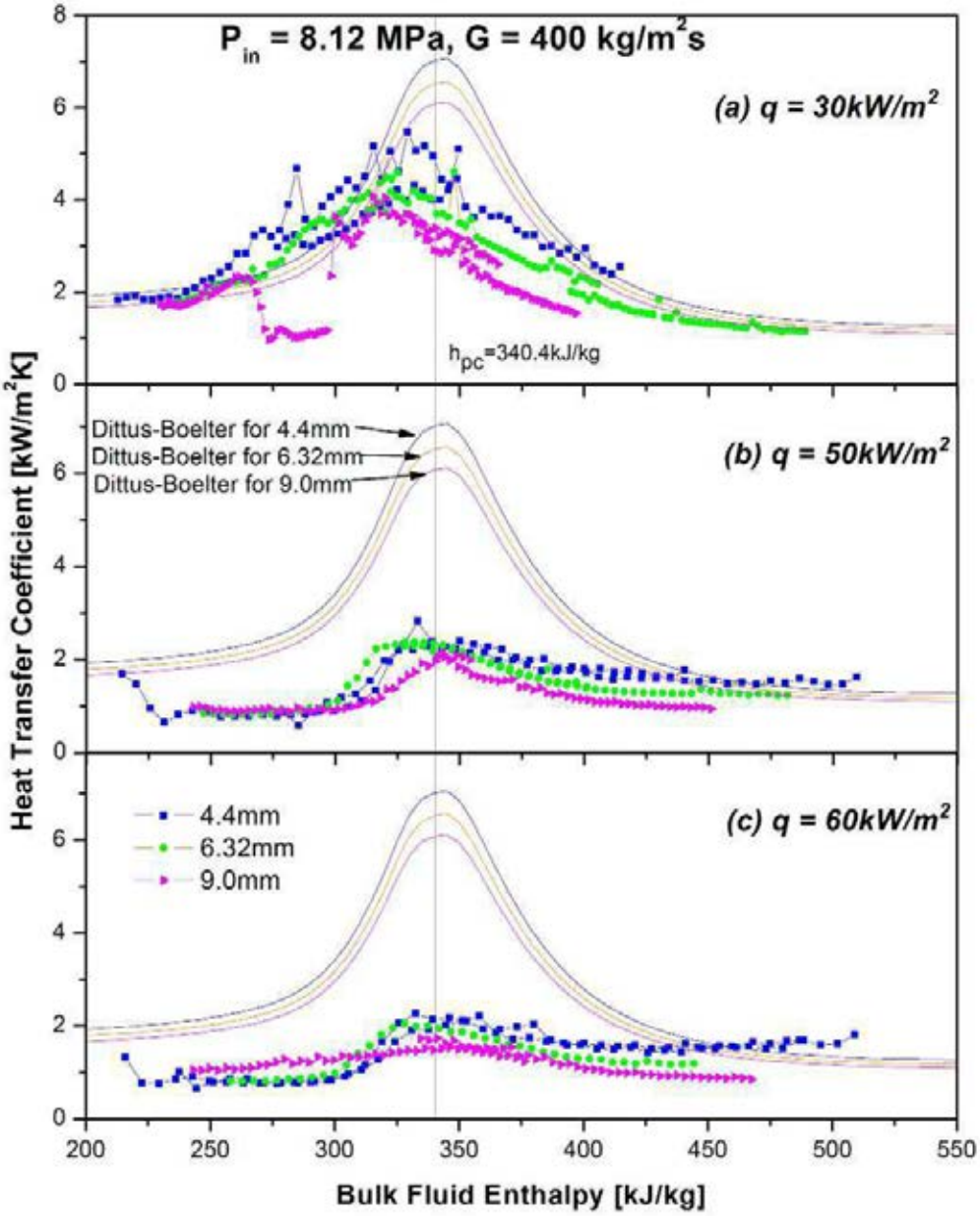

FIG. 3.27. Effect of tube diameter on the heat transfer coefficient: (a) q=30 kW·m^{-2}, (b) q=50 kW·m^{-2}, (c) q=60 kW·m^{-2}.

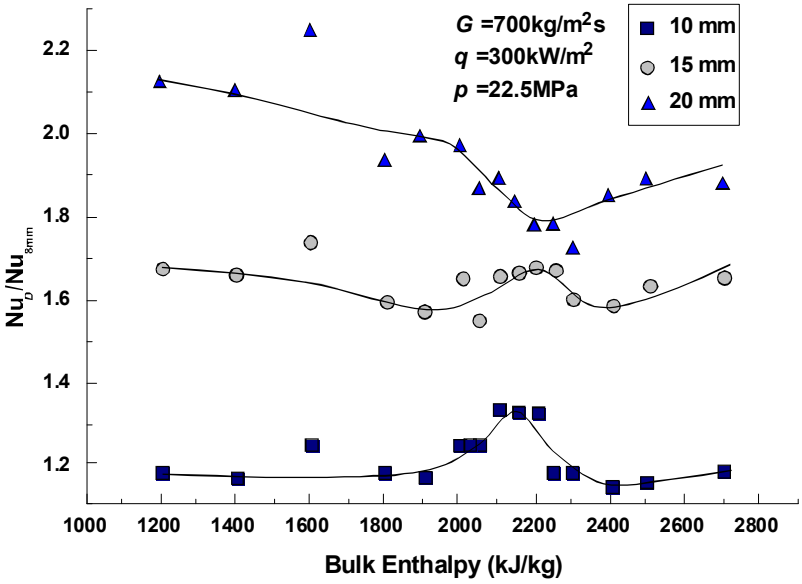

FIG. 3.28. Effect of diameter on Nusselt number in tubes.

3.5.2. Effect of spacing devices

Spacing devices are essential to maintain the subchannel flow area and gap size and to reduce fuel pin vibration in bundles. Various types of spacing devices have been used in nuclear reactor cores; grid spacers in light-water reactors, wire-wrapped spacers in gas-cooled reactors, and appendage-type spacers in pressurized heavy-water reactors. The spacer type for SCWR fuel bundles has not yet been finalized, but wire-wrapped spacers are proposed because of the similarity between gas-cooled reactors and SCWRs.

Bae et al. [3-149] examined the effect of wrapped wire on supercritical heat transfer to carbon dioxide in a tube. Figure 3.29 compares the wall-temperature distributions and corresponding heat-transfer coefficients obtained with a plain 6.32-mm ID tube (red circular symbols) and with the same tube having a 1.3 mm wire-type turbulence generator inside (blue rectangular symbols) at the condition P=7.75 MPa, G=400 $kg \cdot m^{-2} \cdot s^{-1}$, and q=30 $kW \cdot m^{-2}$. The solid and the dotted lines in the lower box represent the heat transfer coefficients calculated using the correlations suggested by Bae and Kim [3-145] and the Dittus–Boelter correlation. The Bae and Kim correlation predicted the experimental data very well, even in the region of heat-transfer deterioration. The heat transfer enhancement by the helical wire appeared to be considerable over most of the enthalpy range covered (the heat-transfer coefficients are almost double or even larger in the vicinity of the pseudo-critical temperature region) except for the low and high-enthalpy region (i.e., H < 250 $kJ \cdot kg^{-1}$ and H > 400 $kJ \cdot kg^{-1}$), where the heat transfer coefficients for both the plain and the wired tubes seem to approach predictions of the Dittus–Boelter equation and the Bae-Kim correlation. In the region where the bulk enthalpies are greater than 400 $kJ \cdot kg^{-1}$, both the wall and the bulk temperatures are much higher than the pseudo-critical temperature, and the property variations across the channel no longer involve drastic changes. Consequently, the fluid properties are relatively uniform, and the heat transfer coefficient is accurately predicted even by the simple Dittus-Boelter equation. Similar characteristics prevailed in the region close to the entrance where the enthalpy is less than 250 $kJ \cdot kg^{-1}$, and both the wall and the bulk temperatures are well below the pseudo-critical temperature; and the property variation across the flow is relatively small. Heat transfer enhancement in

the wired test section remains effective in the region of the high bulk enthalpy, as can be seen by the step-wise temperature decrease.

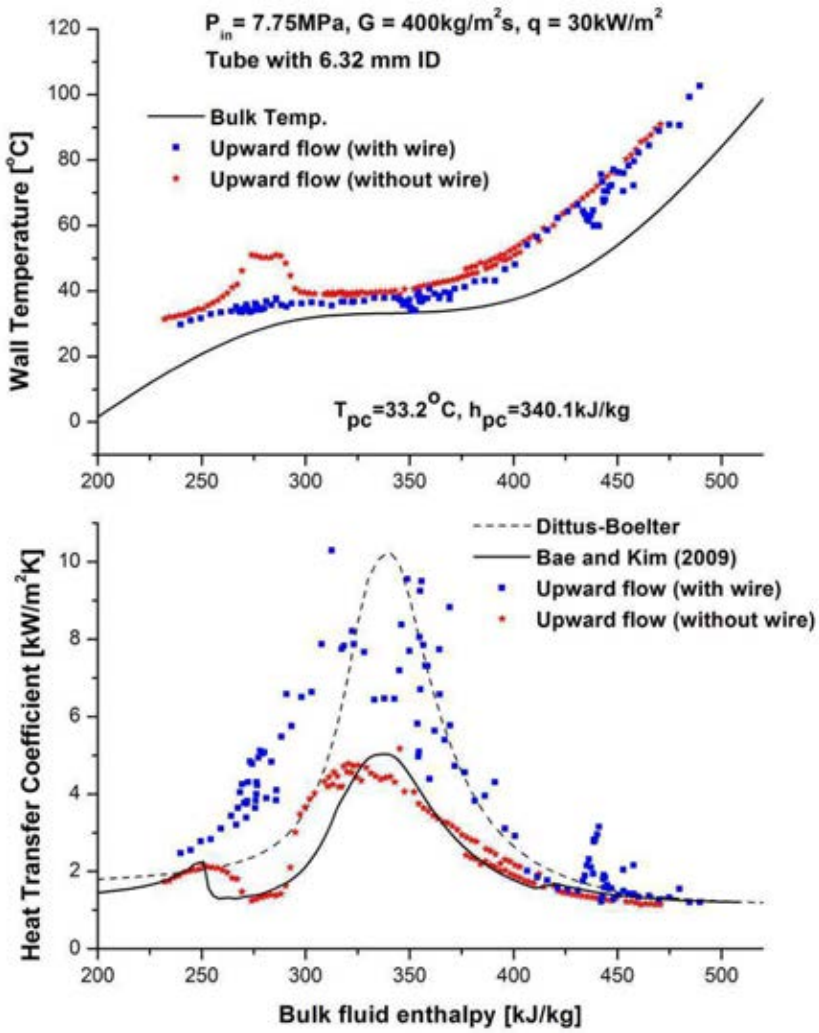

FIG. 3.29. Comparison of test results for a tube with a helical wire insert and for a plain tube; P=7.75 MPa, G=400 kg·m^{-2}·s^{-1}, q=30 kW·m^{-2}, D_{in}=6.32 mm.

Figure 3.30 shows a similar comparison at the condition P=7.75 MPa and G=400 kg·m^{-2}·s^{-1}, but with q= 50 kW·m^{-2}, where deterioration of heat transfer occurred in both the wired and plain tubes. Again, the solid and the dotted lines in the lower box represent the heat transfer coefficients predicted using the Dittus–Boelter equation and the Bae-Kim correlation [3-145]. The Bae and Kim correlation predicted the experimental behaviour fairly well except for the region near the pseudocritical temperature. The heat transfer coefficient in the wired tube increased considerably even in the region of deterioration. This could be due to an addition to the turbulence generated by the helical wire.

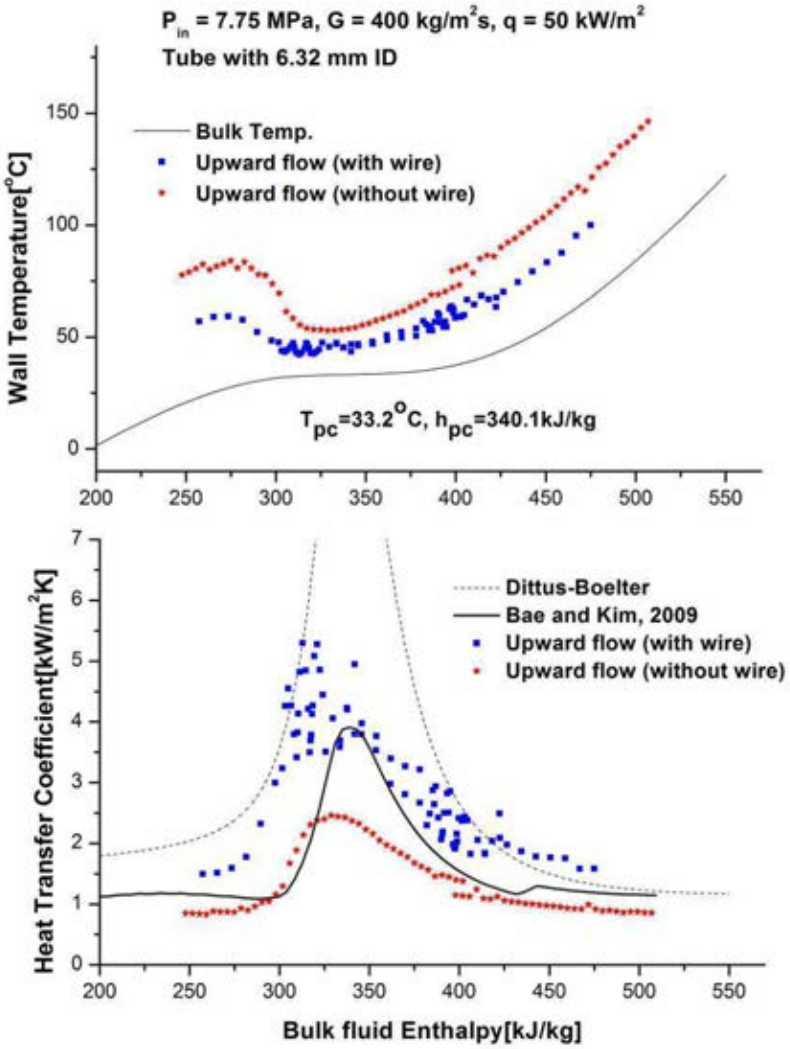

FIG. 3.30. Comparison between test results for a tube with a helical wire insert and for a plain tube; P=7.75 MPa, G=400 kg·m^{-2}·s^{-1}, q=50 kW·m^{-2}, D_{in}=6.32 mm.

Details of the comparison between the heat transfer coefficients for the wired and the plain tubes are shown in Table 3.16. Enhancement of heat transfer coefficient by the inserted wire is most obvious near the pseudo-critical temperature, and reaches a maximum of 3.64 times the value for the plain tube at the specific enthalpy of 300 kJ·kg^{-1}. Except for the region around the pseudo-critical temperature, the enhancement ratios range from 1.6 to 2.3. The largest enhancement due to the wire occurs well upstream of the pseudo-critical temperature region. Evidently, the helical wire suppresses heat transfer deterioration to some extent, but it is not eliminated completely. When the heat flux is sufficiently high, heat-transfer deterioration is still observed.

TABLE 3.16. COMPARISON OF HEAT-TRANSFER COEFFICIENTS BETWEEN WIRED AND PLAIN TUBES: P=7.75 MPA, G=400 KG·M^{-2}·S^{-1}, Q=50 KW·M^{-2}, D_{IN}=6.32 MM

H_b (kJ·kg^{-1})	h (kW·m^{-2}·K^{-1})		(A)/(B)
	Wired tube (A)	Plain tube (B)	
270	1.56	0.83	1.89
280	1.74	0.77	2.26
290	2.36	0.82	2.86
300	3.14	0.86	3.64
310	3.73	1.13	3.30
320	5.16	2.64	1.96
330	4.03	2.54	1.59
340	3.98	2.29	1.74
350	3.86	2.04	1.89
360	3.48	2.17	1.60
370	3.27	1.65	1.98
380	3.07	1.62	1.89
390	2.57	1.44	1.79
400	2.41	1.21	1.99
410	2.04	1.11	1.83
420	2.22	1.02	2.18

Other spacer types have been installed in annuli and bundle subassemblies used in heat-transfer experiments. Figure 3.31 illustrates the spacer design for the annulus test section of a recent supercritical heat-transfer test at Xi'an Jiaotong University [3-151]. The ceramic spacer was not attached to the heated surface minimizing the stagnation flow effect that could potentially lead to high surface temperature. Figure 3.32 shows the observed surface temperature distribution along the test section. The temperature increases with axial distance, but drops rapidly at the spacer location. This illustrates the heat-transfer enhancement effect of the spacer. There is no measurement upstream of the first spacer.

FIG. 3.31. Spacer design in the XJTU supercritical heat transfer test section.

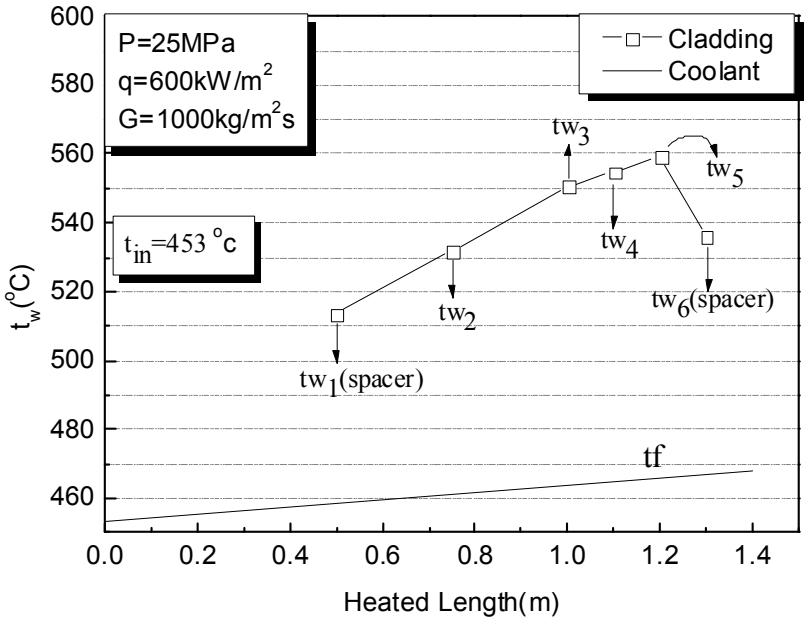

FIG. 3.32. Wall temperature distribution in the spacer-equipped annulus test section.

3.5.3. Effect of channel geometry

Most heat-transfer data have been obtained using tubular test sections. Little information is available on heat transfer for non-circular cross-sectional shapes (such as triangular, square, or rectangular) [3-94]. Some data have been obtained using annuli and bundle subassemblies. However, these test sections were equipped with spacer devices making it difficult to isolate the geometry effect. Figure 3.33 compares wall-temperature measurements and corresponding heat-transfer coefficients for a tube, an annulus test section, and a 3-rod bundle subassembly [3-150]. These experiments were performed with Refrigerant-22 at a pressure of 5.5 MPa with a mass flux of 400 $kg \cdot m^{-2} \cdot s^{-1}$, and a heat flux of 20 $kW \cdot m^{-2}$. It appears that the effect of geometry is strong at subcritical bulk enthalpy as it approaches the pseudo-critical value. Heat transfer deterioration is mainly observed in measurements using the tubular test section but not so much in those of annular cross section. A small surface-temperature rise was observed for the bundle. Unlike in the tubular test section, the surface temperature decreases as the enthalpy increases. Beyond the heat-transfer deterioration region, there is no noticeable effect of geometry on either surface temperature or heat-transfer coefficient.

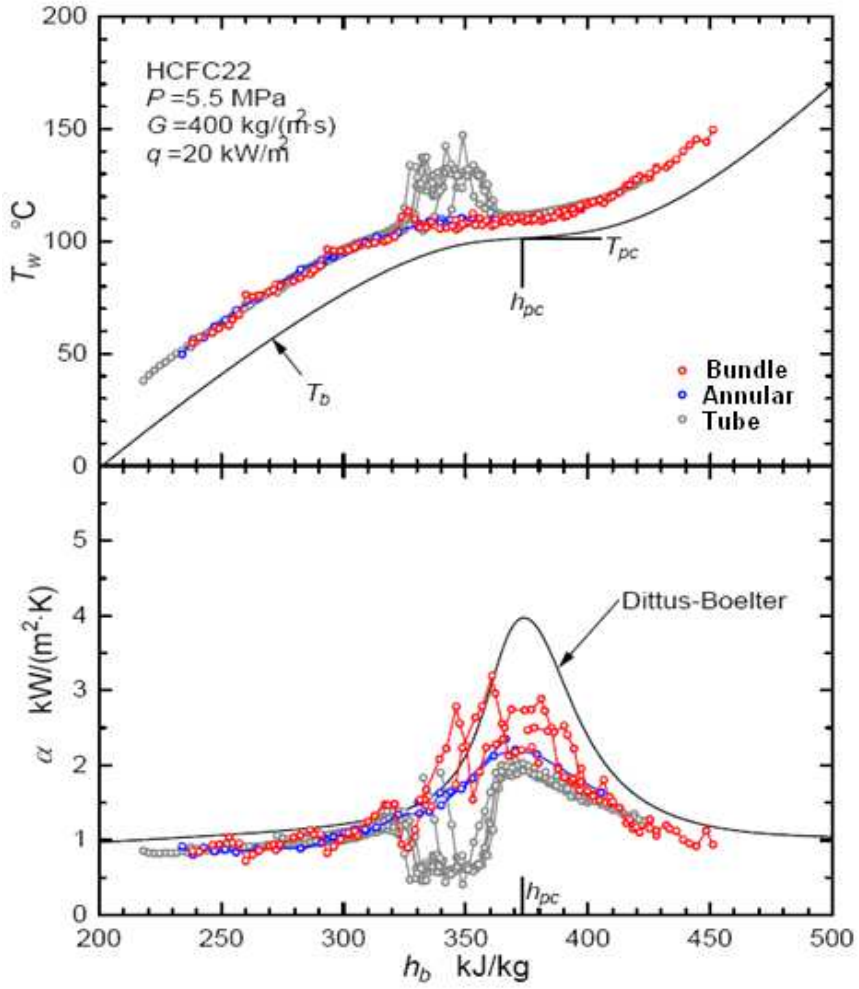

FIG. 3.33. Effect of test-section geometry on supercritical heat transfer.

3.5.4. Effect of flow direction

The flow direction of the supercritical pressure coolant in current SCWR design concepts can be upward, downward, or both upward and downward (in a multi-path core). While most experimental data have been obtained with upward flow in tubes, quite a number of experiments have been performed to examine the heat-transfer characteristics with downward flow. Kim and Bae [3-113] obtained wall-temperature measurements with upward and downward flows of carbon dioxide in 4.4-mm and 6.32-mm tubes. Figure 3.34 compares wall-temperature measurements with upward and downward flows in a 4.4-mm tube. Wall-temperature measurements are consistently lower for downward flow than upward flow, but the difference diminishes with increasing bulk-fluid enthalpy. One noticeable difference is the absence of a deteriorated heat-transfer conditions with downward flow in the low enthalpy region.

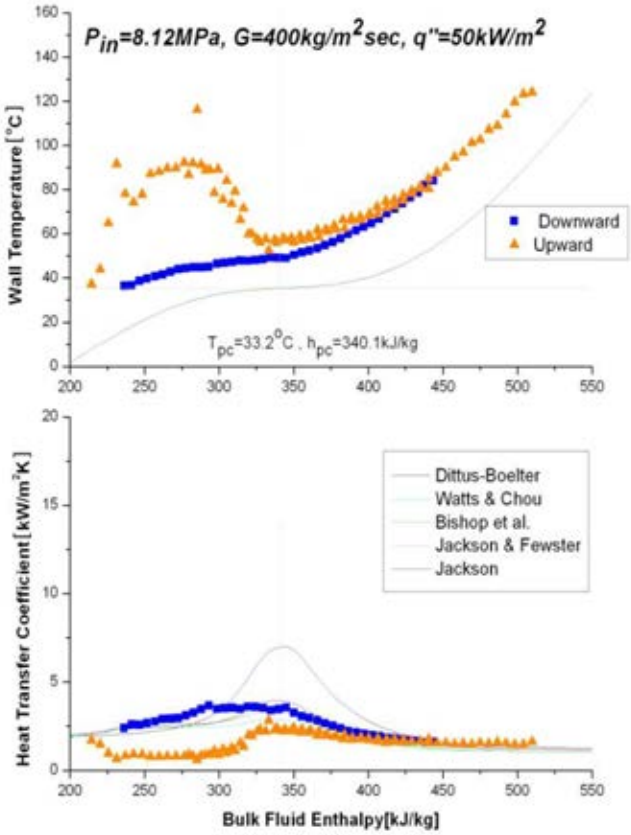

FIG. 3.34. Effect of flow direction on supercritical heat transfer in tubes.

Similar trends have been observed in wall-temperature measurements with upward and downward flows of Refrigerant through a 3-rod bundle. Figure 3.35 compares wall-temperature measurements for upward and downward flows at a pressure of 5.5 MPa, a mass flux of 400 $kg \cdot m^{-2} \cdot s^{-1}$, and a heat flux of 30 $kW \cdot m^{-2}$. Wall-temperature measurements are higher for upward flow than for downward flow in the deteriorated heat-transfer region. Beyond this region, the wall-temperature measurements are similar for both upward and downward flows.

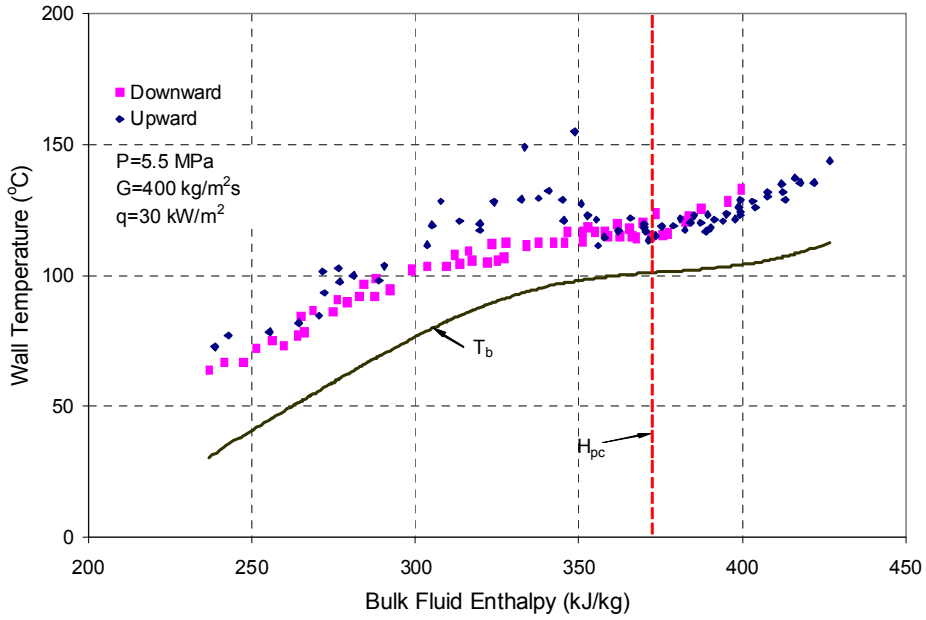

FIG. 3.35. Effect of flow direction on supercritical heat transfer in a 3-rod bundle.

3.6. APPLICATIONS OF HEAT-TRANSFER CORRELATIONS

Supercritical pressure heat transfer information from analytical and experimental studies has been used for preliminary core design and fuel design calculations as well as safety analyses. Supercritical pressure heat transfer correlations have been recommended on the basis of assessments against experimental data. These correlations were implemented into safety analysis codes for preliminary safety analyses and subchannel codes for fuel design support. Due to the lack of bundle data, validation of these correlations under such conditions is not possible at the moment and hence any recommendations have to be considered as tentative.

Heat-transfer correlations have been implemented into a subchannel code to optimize the CANDU fuel design for the SCWR. Surface temperature and coolant temperature distributions in subchannels of the 37-element and CANFLEX® bundle were assessed using a subchannel code. Based on the fuel-cladding temperature criteria of 850°C for the same set of heat transfer, friction factor, and subchannel-mixing correlations, the maximum predicted wall temperature and coolant temperature are systematically higher for the 37-element bundle than for the CANFLEX bundle. Figure 3.36 illustrates the predicted surface temperature and coolant temperature distributions in the 37-element and CANFLEX bundles. The maximum surface temperature is 850ºC in the 37-element bundle and is 804ºC in the CANFLEX bundle, while the maximum coolant temperature is 762ºC in the 37-element bundle and is 693ºC in the CANFLEX bundle. In addition to temperatures being lower, the distributions of temperature are more uniform for the CANFLEX bundle than the 37-element bundle. The gravity effect on the temperature distributions is also stronger in the 37-element bundle than the CANFLEX bundle. High temperatures have been predicted for elements at the top of the 37-element bundle and the bottom region of the CANFLEX bundle.

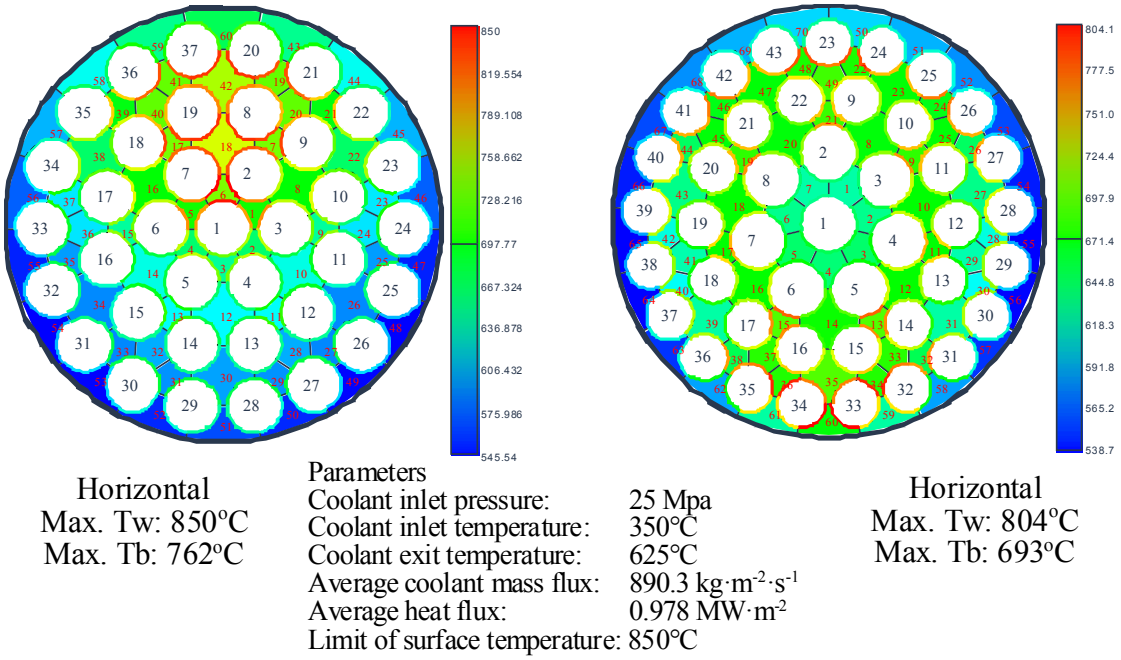

FIG. 3.36. Cladding and coolant temperature distributions in subchannels of 37-element and CANFLEX bundles.

Surface and coolant temperatures are lower and the distributions are more uniform for the CANFLEX bundle. Further optimization of the fuel to reduce surface temperature (hence increasing the operating margin) has been explored. This was focused on varying the pitch-circle diameter and fuel enrichment of each element ring. In addition, the impact of channel orientation (from the current horizontal configuration to the vertical upflow configuration) has been examined to study the gravity effect on temperature distributions.

Based on subchannel calculations at a constant set of flow conditions and a fuel-cladding temperature criteria of 850°C, the cladding and coolant temperatures have been reduced considerably for the optimized CANFLEX bundle with graded enrichment ranging from 2.5 to 6% in various element rings. Figure 3.37 shows that the coolant temperature distribution for the optimized CANFLEX fuel in the vertical channel is more uniform than that for the reference CANFLEX fuel in the horizontal channel. The maximum surface temperature has been reduced to 727°C and the maximum coolant temperature decreased to 637°C for the optimized fuel. Limiting subchannels were observed at the outer ring near the pressure tube for the reference CANFLEX fuel in the horizontal channel. For the optimized fuel in the vertical channel they have been predicted between the intermediate and inner rings. This study has shown that further optimization of the CANDU fuel is feasible to reduce the cladding temperature and improve the operating margin or power.

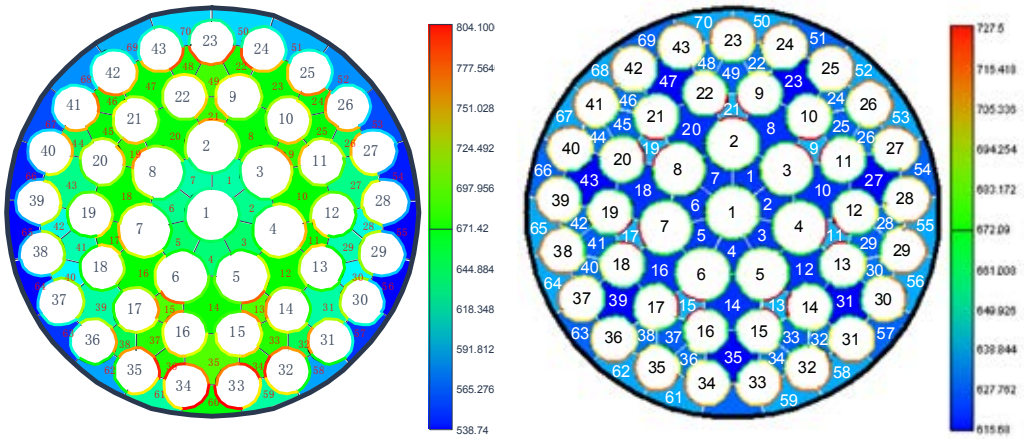

Horizontal

Max. Tw: 804°C

Max. Tb: 693°C

Parameters	Values
Coolant inlet pressure	25 MPa
Coolant inlet temperature	350°C
Coolant exit temperature	625°C
Average coolant mass flux	890.3 $kg \cdot m^{-2} \cdot s^{-1}$
Average heat flux	0.978 $MW \cdot m^{-2}$
Limit of cladding surface temperature	850°C

Vertical

Max. Tw: 727°C

Max. Tb: 637°C

FIG. 3.37. Cladding and coolant temperature distributions in subchannels of reference (uniform enrichment) and optimized (graded uranium) CANFLEX bundles.

LIST OF SYMBOLS FOR SECTION 3

$c_{p,a}$	Average heat capacity, $kJ \cdot kg^{-1} \cdot K^{-1}$
$c_{p,b}$	Heat capacity, $kJ \cdot kg^{-1} \cdot K^{-1}$
D	Diameter, meter
D_{in}	Inside diameter, meter
D_{out}	Outside diameter, meter
D_{eq}	Equivalent diameter, meter
d	Wire diameter, mm
e	Eccentricity
$\bar{e}$	Average deviation
e_i	Deviation between test results and correlation at test point 'i'
Fr	Froude number
G	Mass flux, $kg \cdot m^{-2} \cdot s^{-1}$
H_b	Bulk-fluid enthalpy, $kJ \cdot kg^{-1}$
H_{in}	Inlet-fluid enthalpy, $kJ \cdot kg^{-1}$
H_{pc}	Pseudo-critical enthalpy, $kJ \cdot kg^{-1}$
h	Heat-transfer coefficient, $kW \cdot m^{-2} \cdot K^{-1}$
h_{forced}	Forced convection heat-transfer coefficient, $kW \cdot m^{-2} \cdot K^{-1}$
h_{min}	Minimum convection heat-transfer coefficient, $kW \cdot m^{-2} \cdot K^{-1}$
$h_{natural}$	Natural convection heat-transfer coefficient, $kW \cdot m^{-2} \cdot K^{-1}$
$h_{n.u.heat}$	Heat-transfer coefficient for non-uniform heating, $kW \cdot m^{-2} \cdot K^{-1}$
$h_{u.heat}$	Heat-transfer coefficient for uniform heating, $kW \cdot m^{-2} \cdot K^{-1}$
k_b	Bulk-fluid thermal conductivity, $kW \cdot m^{-1} \cdot K^{-1}$
k_w	Wall-fluid thermal conductivity, $kW \cdot m^{-1} \cdot K^{-1}$
L	Length, meter
L_{heat}	Heath length, meter
l	Narrow gap size, meter
N	Number of data points
Nu_b	Bulk-fluid Nusselt number
Nu_{DB}	Nusselt number based on the Dittus-Boelter equation
Nu_{exp}	Experimental Nusselt number
Nu_f	Nusselt number
P	Pressure, kPa (or MPa)
P_c	Critical pressure, kPa
Pr	Prandtl number
Pr_b	Bulk-fluid Prandtl number

Pr_{min}	Minimum Prandtl number
q	Heat flux, $kW \cdot m^{-2}$
Ra_f	Rayleigh number
Re_b	Bulk-fluid Reynolds number
Re_f	Reynolds number
R_i	Inner-tube radius, meter
R_o	Outer-tube radius, meter
s	Wire spacing, mm
T_b	Bulk-fluid temperature, °C
$T_{b(min)}$	Minimum bulk-fluid temperature, °C
$T_{b(max)}$	Maximum bulk-fluid temperature, °C
T_c	Critical temperature, °C
T_{in}	Inlet-fluid temperature, °C
T_{pc}	Pseudo-critical temperature, °C
T_{sat}	Saturation temperature, °C
T_w	Wall temperature, °C
w	Mass flow rate, $kg \cdot s^{-1}$
δ	Gap size, mm
μ	Viscosity, $kg \cdot m^{-1} \cdot s^{-1}$
μ_b	Bulk-fluid viscosity, $kg \cdot m^{-1} \cdot s^{-1}$
μ_w	Wall-fluid viscosity, $kg \cdot m^{-1} \cdot s^{-1}$
ξ	Friction factor
ρ	Local density, $kg \cdot m^{-3}$
ρ_{avg}	Average density, $kg \cdot m^{-3}$
ρ_b	Bulk-fluid density, $kg \cdot m^{-3}$
ρ_c	Critical density, $kg \cdot m^{-3}$
ρ_w	Wall-fluid density, $kg \cdot m^{-3}$
σ	Standard deviation
τ	Transient heat-transfer coefficient, $kW \cdot m^{-2} \cdot K^{-1}$
θ	Ratio of temperature difference

REFERENCES FOR SECTION 3

[3-1] PIORO, I.L., DUFFEY, R.B., Experimental Heat Transfer to Supercritical Water Flowing inside Channels (Survey), Nucl. Eng. Des., 235 (22) (2005) 2407–2420.

[3-2] GROENEVELD, D.C., TAVOULARIS, S., GUDLA, P.R.S.S., YANG, S.K., LEUNG, L.K.H., Analytical and Experimental Program of Supercritical Heat Transfer Research at the University of Ottawa, Nucl. Eng. Techn., 40 (2) (2008) 107–116.

[3-3] LEUNG, L.K.H., GROENEVELD, D.C., GUDLA, P.R.S.S., TAVOULARIS, S., "An Expanded Database on Supercritical Heat Transfer for Water, Carbon Dioxide and Other Fluids", Proc. 7th International Topical Meeting on Nuclear Reactor Thermal Hydraulics, Operation and Safety (NUTHOS-7), Seoul, Korea, October 5-9, paper 262 (2008).

[3-4] ACKERMAN, J.W., Pseudo boiling Heat Transfer to Supercritical Pressure Water in Smooth and Ribbed Tubes, J. Heat Transfer, Trans. ASME, 92 (3), pp. 490-498 (Paper No. 69-WA/HT-2, 1-8) (1970).

[3-5] ALEKSEEV, G.V., SILIN, V.A., SMIRNOV, A.M., SUBBOTIN, V.I., Study of the Thermal Conditions on the Wall of A Pipe During The Removal of Heat by Water at A Supercritical Pressure, High Temp., 14 (4) (1976) 683–687.

[3-6] ALFEROV, N.S., BALUNOV, B.F., RYBIN, R.A., Calculating Heat Transfer with Mixed Convection, Therm. Eng., 22 (6) (1975) 96–100.

[3-7] BAZARGAN, M., et al., Effect of Buoyancy on Heat Transfer in Supercritical Water Flow in A Horizontal Round Tube, J. Heat Transfer, 127 (2005) 897–902.

[3-8] BELYAKOV, I.I., KRASYAKOVA, L.YU., ZHUKOVSKII, A.V., FEFELOVA, N.D., et al., Heat Transfer in Vertical Risers and Horizontal Tubes at Supercritical Pressure, Therm. Eng., 18 (11) (1971) 55–59.

[3-9] HARRISON, G.S., et al., An Experimental Investigation of Forced Convection to Supercritical Pressure Water in Heated Small Bore Tubes, Fluid Flow, Heat and Fluid Flow (1976) 97–103, 1976.

[3-10] HERKENRATH, H., MÖRK-MÖRKENSTEIN, P., JUNG, U., WECKERMANN, F.J., Warmeübergang an Wasser bei Erzwungener Strömung im Druckbereich von 140 bis 250 Bar, EUR-3658d (1967).

[3-11] GOLDMANN, K., "Heat Transfer to Supercritical Water at 5000 Psi Flowing at High Mass Flow Rates Through Round Tubes", International Developments in Heat Transfer: Papers presented at International heat transfer conference, Part III, January 8-12, ASME, University of Colorado, Boulder, CO, USA, Paper 66 (1961) 561–568.

[3-12] GLUSHCHENKO, L.F., KALACHEV, S.I., GANDZYUK, O.F., Determining the Conditions of Existence of Deteriorated Heat Transfer at Supercritical Pressures of the Medium, Therm. Eng., 19 (2) (1972) 107–111.

[3-13] ISHIGAI, S., KADGI, M., NAKAMOTO, M., "Heat Transfer and Friction for Water Flow in Tubes at Supercritical Pressures", Teplomassoobmen (Heat-Mass-Transfer)—V, Proc. 5th All-Union Conference on Heat Mass Transfer, Minsk, Belarus, May, 1(1) (1976) 261–269 (in Russian).

[3-14] KAMENETSKII, B.YA., Heat-Transfer Characteristics of A Non-Uniformly Circumferentially Heated Pipe, High Temp., 13 (3) (1975) 613–616.

[3-15] KAMENETSKII, B.YA., The Effectiveness of Turbulence Promoters in Tubes with Nonuniformity Heated Perimeters Under Conditions of Impaired Heat Transfer, Therm. Eng., 27 (4) (1980) 222–223.

[3-16] KIRILLOV, P.L., POMET'KO, R.S., SMIRNOV, A.M., GRABEZHNAIA, V.A., Investigation of Heat Transfer to Water at Supercritical Pressures in Tubes and Rod Bundles, IPPE Report FEI-3051, Obninsk (2005).

[3-17] KONDRAT'EV, N.S., Heat Transfer and Hydraulic Resistance with Supercritical Water Flowing in Tubes, Therm. Eng., 16 (8) (1969) 73–77.

[3-18] KRASYAKOVA, L.YU., BELYAKOV, I.I., FEFELOVA, N.D., Heat Transfer with A Downward Flow of Water at Supercritical Pressure, Therm. Eng., 24 (1) (1977) 9–14.
[3-19] LEE, R.A., HALLER, K.H., "Supercritical Water Heat Transfer Developments and Applications", Proc. 5th International Heat Transfer Conference, Tokyo, Japan, September 3–7, 4, pp. 335–339, Paper B7.7 (1974).
[3-20] MAYINGER, F., et al., Heat Transfer in the Supercritical Region with Vertical Upflow, Wärme- und Stoffübertragung, 18 (1984) 207–214.
[3-21] ORNATSKY, A.P., GLUSHCHENKO, L.P., SIOMIN, E.T., et al., "The Research of Temperature Conditions of Small Diameter Parallel Tubes Cooled by Water Under Supercritical Pressures", Proc. 4th International Heat Transfer Conference, Paris, Versailles, France, 6, Paper B8.11 (1970).
[3-22] ORNATSKIY, A.P., GLUSHCHENKO, L.F., KALACHEV, S.I., Heat Transfer with Rising and Falling Flows of water in Tubes of Small Diameter at Supercritical Pressures, Therm. Eng., 18 (5) (1971) 137–141.
[3-23] RAZUMOVSKIY, V.G., Experimental Study on Heat Transfer to Supercritical Water Flowing in Small Diameter Vertical Tubes at Low Mass Fluxes, National Technology University of Ukraine 'KPI', Kyiv, Ukraine (2005).
[3-24] SCHMIDT, K.R., Wärmetechnische Untersuchungen an hochbelasteten Kesselheizflachen, Mitt. Ver. Grosskesselbesitzer, **63** (1959) 391.
[3-25] SEO, W.K., ANDERSON, M.H., CORRADINI, M.L., OH, B.D., KIM, M.H., "Studies of Supercritical Heat Transfer and Flow Phenomena", Proc. 11th Topical Meeting on Nuclear Reactor Thermal-Hydraulics (NURETH-11), Avignon, France, October 2-6, 2005 (2005).
[3-26] SHITSMAN, M.E., Impairment of the Heat Transmission at Supercritical Pressures, High Temp., 1 (2) (1963) 237–244.
[3-27] SHITSMAN, M.E., Temperature Conditions in Tubes at Supercritical Pressures, Teploenergetika, 15 (5) (1968) 57–61.
[3-28] TRESHCHEV, G.G., SUKHOV, V.A., Stability of Flow in Heated Channels in the Supercritical Region of Parameters of State, Therm. Eng., 24 (5) (1977) 68–71.
[3-29] VIKHREV, YU.V., BARULIN, YU.D., KON'KOV, A.S., A Study of Heat Transfer in Vertical Tubes at Supercritical Pressures, Therm. Eng., 14 (9) (1967) 116–119.
[3-30] YAMAGATA, K., NISHIKAWA, K., HASEGAWA, S., FUJII, T., YOSHIDA, S., Forced Convective Heat Transfer to Supercritical Water Flowing in Tubes, International Journal of Heat and Mass Transfer, 15 (12) (1972) 2575–2593.
[3-31] KUANG, B., ZHANG, Y.Q., CHENG, X., "A New, Wide-Ranged Heat Transfer Correlation of Water at Supercritical Pressures in Vertical Upward Ducts", Proc. 7th International Topical Meeting on Nuclear Reactor Thermal Hydraulics, Operation and Safety (NUTHOS-7), Seoul, Korea, October 5-9, Paper 189 (2008).
[3-32] CHENG, X., SCHULENBERG, T., Heat Transfer at Supercritical Pressures—Literature Review and Application to an HPLWR, Wissenschaftliche Berichte (Tech. Report) FZKA 6609, Forschungszentrum Karlsruhe, Mai (2001).
[3-33] XU, F., "Study on Flow and Heat Transfer Characteristics of Water in Tubes at Supercritical Pressures", Master Degree Thesis, Xi'an, China (2004). (in Chinese)
[3-34] PIORO, I.L., DUFFEY R.B., Heat Transfer and Hydraulic Resistance at Supercritical Pressures in Power-Engineering Applications, New York, ASME Press (2007).
[3-35] KONDRATIEV, A.P. Heat Transfer and Pressure Drop in Supercritical Water Flow in Tubes, Thermal Engineering, **4** (1969) 49.
[3-36] BARULIN, YU.D., et al., "Heat Transfer in Turbulent Flow in Vertical and Horizontal Tubes of Supercritical Water", Inzhenerno-fisichesky zhurnal (1975) 929 (In Russian).
[3-37] MIROPOLSKY, Z.L., SHITSMAN, L.E., Heat Transfer to Water and Steam at Variable Heat Capacity (in Near Critical Area), Journal of Technical Physics, 27 (1957) 2359.

[3-38] MIROPOLSKY, Z.L., SHITSMAN, L.E., Investigation of Heat Transfer to Water and Steam at Pressures up to 280 Ata, Collection: Investigations of Heat Transfer to Steam and Water Boiling at High Pressures, M., Atomizdat (1958) 54 (In Russian).
[3-39] ARMAND, A.A., et al., Investigation of Heat Transfer from Wall to Steam near Critical State, Collection: Heat Transfer under High Thermal Loads and Other Special Conditions, Editors: A.A. Armand and M. Gosenergoizdat (1959) 41 (In Russian).
[3-40] DOROSCHUK, V.E., et al., Heat Transfer to Water at High Pressure, Collection: Heat Transfer under High Thermal Power and other Special Conditions, M., GEI (1959) 30 (In Russian).
[3-41] ALADIEV, I.T., et al., Convective Heat Transfer under High Pressure, Collection: Heat transfer and Thermal Modeling, M., Issued by Academy of Science USSR (1959) 158 (In Russian).
[3-42] SHITSMAN, M.E., Deteriorated Heat Transfer at Supercritical Pressures, High Temperatures, 1 (1963) 237.
[3-43] SMOLIN, V.N., POLIAKOV, V.K., "Experimental Research of Heat Transfer to Water in Tubes under Supercritical Pressure", Proc. CKTI Heat Transfer in Condensation and Boiling, p. 130 (1965) (In Russian).
[3-44] VIKHREV, YU.V., BARULIN, YU.D., Investigation of Heat Transfer in Vertical Tubes under Supercritical Pressure, Thermal Engineering, 9 (1967) 80.
[3-45] KRASIAKOVA, L.YU., et al., "Temperature Regime in Vertical and Horizontal Heated Tubes under Supercritical Pressure", Proc. CKTI Inner Boiler Processes under Supercritical Pressure of Steam (1968) 105 (In Russian).
[3-46] SHITSMAN, M.E., Specific Features of Temperature Regime in Tubes under Supercritical Pressure, Thermal Engineering 5 (1968) 57.
[3-47] TARASOVA, N.V., LEONTIEV, A.I., Hydraulic Resistance in Water Flow Though The Tube under Supercritical Pressure, High Temperature, 6 (1968) 755.
[3-48] ALFEROV, N.S., et al., Heat Transfer in Turbulent Flow of Water under Conditions of Essential Influence of Natural Convection, Thermal Engineering, 12 (1969) 66.
[3-49] KONDRATIEV, A.P., Heat Transfer and Pressure Drop in Supercritical Water Flow in Tubes, Thermal Engineering, 4 (1969) 49.
[3-50] ORNATSKY, A.P., et al., Heat Transfer in Upward Flow and Downward Flow of Water in Tubes of Small Diameter under Supercritical Pressure, Thermal Engineering, 5 (1971) 91.
[3-51] BELIAKOV, I.I., et al., Heat Transfer in Vertical Upward Flow and in Horizontal Flow at Supercritical Pressure, Thermal Engineering, 11 (1971) 39.
[3-52] BARULIN, YU.D., et al., Heat Transfer in Turbulent Flow in Vertical and Horizontal Tubes of Supercritical Water, Inzhenerno-fisichesky zhurnal (1975) 929 (In Russian).
[3-53] GLUSCHENKO, L.F., et al., Definition of Conditions for Existence of Deteriorated Heat Transfer Regimes under Supercritical Pressure, Thermal Engineering, 2 (1972) 69.
[3-54] ALFEROV, N.S., et al., "To the Problem of Deteriorated Heat Transfer in the Area of Supercritical Pressures", Proc. IVth All-Union Meeting on Heat and Mass Transfer, Minsk, 2 (1972) 37 (In Russian).
[3-55] ALFEROV, N.S., et al., To Calculation of Heat Transfer in Mixed Convection, Thermal Engineering, 4 (1975) 71.
[3-56] CHAKRYGIN, V.G., et al., Experimental Definition of Boundaries of Aperiodical Instability under High and Supercritical Pressures, Thermal Engineering, 1 (1974) 12.
[3-57] KAMENETSKY, B.YA., Specific Features of Heat Transfer in Tubes with Non-Uniform Heating of Perimeter, High Temperature, 13 (1975) 671 (In Russian).
[3-58] ALEXEEV, G.V., et al., Investigation of Temperature Regimes of Tube Wall during Heat Removal by Supercritical Water, High Temperatures, 14 (1976) 769 (In Russian).
[3-59] TRESCHEV, G.G., SUKHOV, V.A., "On Change in Boundaries of Stable Flow of Postcritical Water in Heated Channel in Case of Shifting of Heat Removal Area", Proc. IVth All-Union Meeting on Heat and Mass Transfer, Minsk, 2 (1972) 16 (In Russian).
[3-60] TRESCHEV, G.G., SUKHOV, V.A., Flow Stability in Heated Channels in Postcritical State Parameters, Thermal Engineering, 5 (1977) 79.

[3-61] KRASIAKOVA, L.YU., et al., Heat Transfer in Downward Flow of Postcritical Water, Thermal Engineering, 4 (1977) 8.
[3-62] SMIRNOV, O.K., KRASNOV, S.N., Investigation of Transient Heat Transfer under Supercritical Pressure, Thermal Engineering, 4 (1978) 86.
[3-63] SMIRNOV, O.K., MICHUROV, YU.P., Investigation of Heat Transfer Research теплоотдачи to Water with околокритическими in Parameters in a Pipe with a Changing Roughness, Moscow Power Institute, 466, pp. 64-69, 1980 (in Russian).
[3-64] KAMENETSKY, B.YA., Effectiveness of Turbulizers in Tubes with Non-Uniform Heating of Perimeters in Regimes of Deteriorated Heat Transfer, Thermal Engineering, 4, pp. 57-58, 1980.
[3-65] SMOLIN, V.N., SOLOVIEV, S.L., Perspective Direction of Development of Water-Cooled Reactors in Century – The Use of Supercritical Parameters of the Coolant, Problems of Atomic Science and Technology, Series: NPP safety, 6, p. 100, 2006 (In Russian).
[3-66] RAZUMOVSKY, V.G., et al., Pressure Drop and Heat Transfer in Smooth Channels in Turbulent Flow of Supercritical Water, Thermal Engineering, 2, p. 69, 1984.
[3-67] SELIVANOV, V.M., SMIRNOV, A.M., "Experimental Researches of Heat Transfer in Tube under Supercritical Pressure of Water", Preprint IPPE1602, Obninsk, 1984 (In Russian).
[3-68] RAZUMOVSKY, V.G., et al., Heat Transfer and Local Hydraulic Characteristic of Smooth-Bore Channels in Turbulent Flow of Supercritical Water, Two-Phase Flows, Heat Transfer and Hydrodynamics, Nauka, Leningrad, 1987 (In Russian).
[3-69] BISHOP, A.A., SANDBERG, R.O., TONG, L.S., Forced Convection Heat Transfer to Water at Near-Critical Temperatures and Supercritical Pressures, Westinghouse Electric Corp., Pittsburgh, USA, Report WCAP-2056, Part IV, November.
[3-70] SWENSON, H.S., et al.,Heat Transfer to Supercritical Water in Smooth-Bore Tubes, Journal of Heat Transfer, Transactions of ASME, 87 (4) (1965) 477.
[3-71] PETUKHOV, B.S., KIRILLOV, P.L., To the Problem of Heat Transfer in Turbulent Flow of Liquid in Tubes, Thermal Engineering, 4 (1958) 63.
[3-72] KRASNOSCHIEKOV, E.A., PROTOPOPOV, V.S., To the Problem of Heat Transfer in Flow of CO_2 and Water at Supercritical Parameters, Thermal Engineering, 10 (1960) 94.
[3-73] HALL, W., JACKSON, J., "Heat Transfer near the Critical Point", Proc. 6th Int. Heat Transfer Conf, Toronto, Canada, 6 (1978) 377.
[3-74] Thermophysical Properties of Substances, Hand-book VTI, Issued by Vargaftik N.B., Gosenergoizdat, Moscow (1956) (In Russian).
[3-75] VUKALOVICH, M.P., et al., Tables of Thermophysical Properties of Water and Water Steam, Izd-vo Standartov, Moscow (1969) (In Russian).
[3-76] ALEXANDROV, A.A., GRIGORIEV, B.A., Tables of Thermophysical Properties of Water and Water Steam, Issued by MPEI (2003) (In Russian).
[3-77] KURGANOV, V.A., et al., "Problems and Results of Generalized Description of Heat Transfer to Supercritical Coolants", Proc. International Meeting on Water and Steam of Supercritical Parameters in Nuclear Power Engineering: Problem and Solutions, Moscow, NIKIET (2008) (In Russian).
[3-78] JACKSON, J.D., Heat Transfer Studies at Manchester with Carbon Dioxide at Supercritical and Near-Critical Pressures, Report produced for AECL in connection with the database on SCWR Heat Transfer being established by IAEA, Ref. JDJ/IAEA/CRP/Report No. 1, October (2009).
[3-79] JACKSON, J.D., Supercritical Pressure Water Heat Transfer Study at Manchester, Report produced for AECL in connection with the database on SCWR Heat Transfer being established by IAEA, Ref. JDJ/IAEA/CRP/Report No. 2, October (2009).
[3-80] EVANS LUTTERODT, K.O.J., "Forced Convection Heat Transfer to Carbon Dioxide at Near-Critical Pressure Conditions", Ph.D. Thesis, University of Manchester (1968).
[3-81] WEINBERG, R.S., "Experimental and Theoretical Study of Buoyancy Effects in Forced Convection Heat Transfer to Carbon Dioxide at Supercritical Pressure", Ph.D. Thesis, University of Manchester (1972).

[3-82] FEWSTER, J., "Mixed Forced and Free convective Heat Transfer to Supercritical Pressure Fluids Flowing in Vertical Pipes", Ph.D. Thesis, University of Manchester (1976).
[3-83] WATTS, M.J., "Heat Transfer to Supercritical Pressure Water – Mixed Convection with Upflow and Downflow in A Vertical Tube", Ph.D. Thesis, University of Manchester (1980).
[3-84] JACKSON, J.D., COTTON, M.A., AXCELL, B.P., Studies of Mixed Convection in Vertical Tubes, Int. J. Heat Fluid Flow, 10 (1989) 2.
[3-85] DICKINSON, N.L., WELCH, C.P., Heat Transfer to Supercritical Water, Trans. ASME, 80 (1958) 746.
[3-86] WU, G., BI, Q., ZHU, X., YANG, Z., WANG, H., "Experimental Investigation on Heat Transfer of Supercritical Pressure Water in Annular Flow Geometry", Proc. 5th Int. Sym. SCWR (ISSCWR-5), Vancouver, British Columbia, Canada, March 13–16, 2011 (2011).
[3-87] ADEBIYI, G.A., HALL, W.B., Experimental Investigation of Heat Transfer to Supercritical Pressure CO_2 in A Horizontal Pipe, Int. J of Heat Transfer, 19 (1976) 715–720.
[3-88] ANKUDINOV, V.B., KURGANOV, V.A., Intensification of Deteriorated Heat Transfer in Heated Tubes at Supercritical Pressures, High Temp., 19 (6) (1981) 870–874.
[3-89] BAE, Y.Y., Private communication (2006).
[3-90] BOURKE, P.J., PULLING, D.J., GILL, L.E., DENTON, W.H, Forced Convective Heat Transfer to Turbulent CO_2 in the Supercritical Region, Int. J of Heat Transfer, 13 (1970) 1339–1348.
[3-91] BRINGER, R.P., SMITH, J.M., Heat Transfer in the Critical Region, AIChE, 3(1) (1957) 49.
[3-92] HUAI, X.L., KOYAMA, S., ZHAO, T.S., An Experimental Study of Flow and Heat Transfer of Supercritical Carbon Dioxide in Multi-Port Channels Under Cooling Conditions, Chem. Engg. Sci., 60 (2005) 3337–3345.
[3-93] FEWSTER, J., "Mixed Forced and Free Convective Heat Transfer to Supercritical Pressure Fluids Flowing in Vertical Pipes", Ph.D. Thesis, University of Manchester (1976).
[3-94] KIM, J.K., JEON, H.K., YOO, J.L., LEE, J.S., "Experimental Study on Heat Transfer Characteristics of Turbulent Supercritical Flow in Vertical Circular/Non-Circular Tubes", Proc. 11th Topical Meeting on Nuclear Reactor Thermal-Hydraulics (NURETH-11), Avignon, France, October 2–6, 2005 (2005).
[3-95] KIM, H., SONG, J.H., BAE, Y.Y., KIM, Y.H., "Assessment of Heat Transfer Correlations on Supercritical Pressure Flows For an Upward Flow of CO_2 in A Circular Tube", Proc. 5th Korea-Japan Symposium on Nuclear Thermal Hydraulics and Safety (NTHAS-5), Jeju, Korea, November 26–29, 2006 (2006).
[3-96] KIM, Y.H., KIM, H., KANG, D.J., SONG, J.H., BAE, Y.Y., "Heat Transfer Experiments For an Upward Flow of Supercritical Pressure CO_2 in A Narrow Annulus", Proc. 3rd Int. Symposium on SCWR-Design and Technology, March 12–15, Shanghai, China (2007).
[3-97] KIM, H., KIM, H.Y., SONG, J.H., BAE, Y.Y., Heat Transfer to Supercritical Pressure Carbon Dioxide Flowing Upward Through Tubes and A Narrow Annulus Passage, Progress in Nuclear Energy, **50** (2008) 518–525.
[3-98] KOPPEL, L.B., "Heat Transfer and Thermodynamics in the Critical Region", Ph.D. Thesis, North-Western University, Illinois, USA (1960).
[3-99] KRASNOSHCHEKOV, E.A., PROTOPOPOV, V.S., Experimental Study of Heat Exchange in Carbon Dioxide in the Supercritical Range at High Temperature Drops, Teplofizika Vysokikh Temperatur, 4(3), May (1966) 389–398.
[3-100] KURGANOV, V.A., ANKUDINOV, V.B., Calculation of Normal and Deteriorated Heat Transfer in Tubes with Turbulent Flow of Liquids in The Near-Critical and Vapour Region of State, Thermal Engg., 32 (6) (1985) 332–336.
[3-101] KURGANOV, V.A., Predicting Normal and Deteriorated Heat Transfer with Mixed Convection Heat Carrier at Supercritical Pressure in Vertical Tubes, Teploenergetika, 38 (1), (1991) 63–68.
[3-102] LIAO, S.M., ZHAO, T.S., An Experimental Investigation of Convection Heat Transfer to Supercritical Carbon Dioxide in Miniature Tubes, J. of Heat and Mass Transfer, 45 (2002) 5025–5034.

[3-103] PETUKHOV, B.S., KRASNOSCHEKOV, E.A., PROTOPOPOV, V.S., An Investigation of Heat Transfer to Fluids Flowing in Pipes Under Supercritical Conditions, International Developments in Heat Transfer: Papers presented at the 1961 International Heat Transfer Conference, ASME, University of Colorado, Boulder, Colorado, USA, January 8–12, Part III, Paper 67 (1961) 569–578.

[3-104] PIORO, I.L., KHARTABIL, H.F., "Experimental Study on Heat Transfer to Supercritical Carbon Dioxide Flowing Upward in A Vertical Tube", Proc. 13th Int. Conf. on Nuc. Engg. (ICONE-13), Paper-50118, Beijing, China, May 16-20, 2005.

[3-105] SHIRALKAR, B.S., GRIFFITH, P., Deterioration in Heat Transfer to Fluids at Supercritical Pressures and High Heat Fluxes, J. Heat Transfer, Trans. ASME, 91 (1) (1969) 27–36.

[3-106] SHIRALKAR, B.S., GRIFFITH, P., The Effect of Swirl, Inlet Conditions, Flow Direction, and Tube Diameter on The Heat Transfer to Fluids at Supercritical Pressure, J. Heat Transfer, Trans. ASME, 92 (3) (1970) 465–474.

[3-107] TANAKA, H., NISHIWAKI, N., HIRATA, M., "Turbulent Heat Transfer to Supercritical Carbon Dioxide", Proc. Japan Soc. Mech. Engrs Semi-Int Symp., Tokyo, Heat Mass Transfer, 2 (1967) 127.

[3-108] TANAKA, H., NISHIWAKI, N., HIRATA, M., TSUGE, A., Forced Convection Heat Transfer to Fluid Near Critical Point Flowing in Circular Tube, Int. J. Heat Mass Transfer, 14 (6) (1971) 739–750.

[3-109] YANG, S.K., KHARTABIL, H.F., Normal and Deteriorated Heat Transfer Correlations for Supercritical Fluids, Transactions, ANS meeting, Washington, USA, 95, November (2005) 635–637.

[3-110] KIM, H.Y., KIM, H., SONG, J.H., CHO, B.H., BAE, Y.Y., Heat Transfer Test in a Vertical Tube Using CO_2 at Supercritical Pressures, Journal of Nuclear Science and Technology, **44** (3) (2007) 1–9.

[3-111] KIM, H.Y., KIM, H., KANG, D.J., SONG, J.H., BAE, Y.Y., Experimental Investigations on Heat Transfer to CO_2 Flowing Upward in a Narrow Annulus at Supercritical Pressures, Nuclear Engineering and Technology, **40** (2) (2008) 155–162.

[3-112] KIM, H., BAE, Y.Y., KIM, H.Y., SONG, J.H., CHO, B.H., Experimental Investigations on Heat Transfer Characteristics in Upward Flow of Supercritical Carbon Dioxide, Nuclear Technology, **164** (2008) 119–129.

[3-113] KIM, H.Y., BAE, Y.Y, „Experimental Study on Heat Transfer to Supercritical CO_2 in a Circular Tube", Proc. 16th Pacific Basin Nuclear Conference, Aomori, Japan, Oct. 13-18, 2008 (2008).

[3-114] BAE, Y.Y., KIM, H.Y., Convective Heat Transfer to CO_2 at a Supercritical Pressure Flowing Vertically Upward in Tubes and an Annular Channel, Exp. Therm. Fluid Sci. **33** (2) (2009) 329–339.

[3-115] BAE, Y.Y., KIM, H.Y., KANG, D.J., Forced and Mixed Convection Heat Transfer to Supercritical CO_2 Vertically Flowing in a Uniformly-Heated Circular Tube, Exp. Therm. Fluid Sci. (2010).

[3-116] BAE, Y.Y., KIM, H.Y., "Heat Transfer at Supercritical Pressure in an Eccentric Annulus Channel", Proc. 6th Japan-Korea Symposium on Nuclear Thermal Hydraulics and Safety (NTHAS6), Okinawa, Japan, November 24–27, 2008 (2008).

[3-117] LEMMON, E.W., MCLINDEN, M.D., HUBER, M.L., Reference Fluid Thermodynamics and Transport Properties, NIST Standard Reference Database 23, Version 7.1, Beta version (2006).

[3-118] BRASSINGTON, D.J., CAIRNS, D.N.H., Measurements of Forced Convective Heat Transfer to Supercritical Helium, Int. J. Heat Mass Transfer, 20 (1977) 207–214.

[3-119] CHUN, S.Y., HONG, S.D., SHIN, C.H., Heat Transfer Characteristics of 5x5 Heater Bundle Cooled with Refrigerant HFC-134a Near The Critical Pressures, PaRTSEE-5, Auckland, New Zealand, April 28–29, 2005 (2005).

[3-120] DIMITROV, D., ZAHARIEV, A., KOVACHEV, V., Forced Convective Heat Transfer to Supercritical Nitrogen in A Vertical Tube, Int. J. Heat and Fluid Flow, 10 (3) (1989) 278–280.

[3-121] KALBALIEV, R.F., Experimental Investigation of Changes in the Wall Temperature in Different Regimes of Motion of Supercritical Pressure Liquids, J. of Engg. Phy. and Thermophysics, 75 (5) (2002) 1037–1042.
[3-122] KATAOKA, K., "Development Project of Supercritical Water Cooled Power Reactor", Information exchange meeting between US institutes and JP team (2002).
[3-123] KULIEVA, I.G., ARABOVA, I.T., MAMEDOV, F.KH., ISAEV, G.I., Improved Heat Transfer at Supercritical Pressures of Organic Heat Transfer Agents, Translated from Inzhenerno-Fizicheskii Zhurnal, 62 (3) (1992) 356–359.
[3-124] DEEV, V.I., KONDRATENKO, A.K., PETROVICHEV, V.I., et al., "Natural Convection Heat Transfer from A Vertical Plate to Supercritical Helium", Proc. 6th International Heat Transfer Conference, Toronto, Canada, 2 (1978) 205–209.
[3-125] KLIPPING G., KUTZNER K., Heat Transfer from Metal to Supercritical Helium, Liquid Helium Technology, Bulletin IIF/IIR, Annexe 1966-5 (1966) 97–107.
[3-126] DEEV, V.I., KHARITONOV, V.S., SAVIN, A.N., KUTSENKO, K.V., "Transient Subcritical and Supercritical Helium Heat Transfer in an Open Bath and Gaps", Proc. 14th International Cryogenic Engineering Conference and International Cryogenic Materials Conference (ICEC-14, ICMC), Kiev, (also Cryogenics, 32 (1992) 237–240) (1992).
[3-127] GROENEVELD, D.C., KIAMEH, B.P., CHENG, S.C., "Prediction of Critical Heat Flux (CHF) for Non-Aqueous Fluids in Forced Convective Boiling", Proc. 8th Int. Heat Transfer Conference, 5 (1986).
[3-128] GROENEVELD, D.C., BLUMENROEHR, D., CHENG, S.C., "CHF Fluid-to-Fluid Modelling Studies in Three Laboratories using Different Modelling Fluids", Proc. 5th Int. Topical Meeting on Nuclear Thermal Hydraulics, Salt Lake City, Utah, USA, Sept. (1992).
[3-129] GROENEVELD, D.C., DOERFFER, S.D., TAIN, R.M., HAMMOUDA, N., CHENG, S.C., "Fluid-to-Fluid Modelling of the Critical Heat Flux and Post-Dryout Heat Transfer", Proc. 4th World Congress on Experimental Heat Transfer, Fluid Mechanics and Thermodynamics, Brussels, June 2–6, 1997 (1997).
[3-130] HAMMOUDA, N., "Subcooled Film Boiling in Non-Aqueous Fluid", Ph.D. thesis, University of Ottawa (1996).
[3-131] EL NAKLA, M., "Experimental and Analytical Study of Inverted Annular Flow Film Boiling Heat Transfer in a Vertical Tube using R-134a", Ph.D. thesis, University of Ottawa (2007).
[3-132] JACKSON, J.D., HALL, W.B., Forced Convection Heat Transfer to Fluids at Supercritical Pressure, Turbulent Forced Convection in Channels and Bundles, Editors: S. Kakac and D.B. Spalding, Hemisphere Corp., New York, USA, 2 (1978).
[3-133] CHENG, X., LIU, X.J., GU, H.Y., "Scaling of Heat Transfer of Supercritical Fluids", Shanghai Jiaotong University Report submitted to the Coordinated Research Program on Heat Transfer Behavior and Thermohydraulics Code Testing for SCWR (2010).
[3-134] AHMAD S.Y., Fluid to Fluid Modeling of CHF: A Compensated Distortion Model, Int. J. Heat Mass Transfer, **16** (1973) 641–662.
[3-135] BISHOP, A.A., SANDBERG, L.O., TONG, L.S., Forced Convection Heat Transfer to Water at Near Critical Temperatures and Supercritical Pressures, WCAP-2056-P, Part-III-B, February (1964).
[3-136] KIM, H.Y., BAE, Y.Y., "Heat Transfer Test in a Tube Using CO_2 at Supercritical Pressures", Proc. GLOBAL 2005, Paper 103, Tsukuba, Japan, Oct 9–13, 2005 (2005).
[3-137] WANG, S., YUAN, L., LEUNG, L., "Assessment of Supercritical Heat-Transfer Correlations against AECL Database for Tubes", Proc. 2nd Canada-China Joint Workshop on Supercritical Water-cooled Reactors, Toronto, Canada, April 25–28, 2010 (2010).
[3-138] JACKSON, J.D., "Consideration of the Heat Transfer Properties of Supercritical Pressure Water in Connection With the Cooling of Advanced Nuclear Reactors", Proc. 13th Pacific Basin Nuclear Conference, Shenzhen City, China, October 21–25, 2002 (2002).
[3-139] GRIEM, H., Untersuchungen zur Thermohydraulik innenberippter Verdampferrohre, Dissertation an der Technischen Universität München, Februar (1995).

[3-140] JACKSON, J.D., Heat Transfer to Supercritical Pressure Fluids, Part 1 – Summary of Design Recommendation and Equations, HTFS design report No.34, AERE-R8157, September (1975).
[3-141] JACKSON, J.D., "Semi-Empirical Model of Turbulent Convective Heat Transfer to Fluids at Supercritical Pressure", Proc. 16th International Conference on Nuclear Engineering, (ICONE16), Orlando, Florida, USA, Paper No. 48914, May 11–15, 2008 (2008).
[3-142] KOSHIZUKA, S., TAKANO, N., OKA, Y., Numerical Analysis of Deterioration Phenomena in Heat Transfer to Supercritical Water, Int. J. Heat Mass Transfer, 38(16) (1995) 3077–3084.
[3-143] SWENSON, H.S., CARVER, J.R., KAKARALA, C.R., Heat Transfer to Supercritical Water in Smooth-Bore Tube, Journal of Heat Transfer (1965) 477–484.
[3-144] CHENG, X., YANG, Y.H., "Prediction Methods for Supercritical Water Heat Transfer in Circular Tubes", Shanghai Jiaotong University Report submitted to the IAEA Coordinated Research Program (CRP) on Heat Transfer Behavior and Thermohydraulics Code Testing for SCWR (2010).
[3-145] BAE, Y.Y., KIM, H.Y., KANG, D.J., Forced and Mixed Convection Heat Transfer to Supercritical CO_2 Vertically Flowing in A Uniformly-Heated Circular Tube, Experimental Thermal and Fluid Science, 34 (2010) 1295–1308.
[3-146] KIM, H.Y., KIM, H., KANG, D.J., SONG, J.H., BAE, Y.Y., Experimental Investigations on Heat Transfer to CO_2 Flowing Upward in A Narrow Annulus at Supercritical Pressures, Nucl. Eng. Tech., 40 (2) (2008) 155–162.
[3-147] KANG, K.H., CHANG, S.H., Experimental Study on the Heat Transfer Characteristics during the Pressure Transients under Supercritical Pressures, Int. J. Heat Mass Transfer, 52 (2009) 4946–4955.
[3-148] KURGANOV,V.A., KAPTIL'NYI, A.G., Velocity and Enthalpy Fields and Eddy Diffusivities in A Heated Supercritical Fluid Flow, Experimental Thermal and Fluid Science, 5(4) (1992) 465–478.
[3-149] BAE, Y.Y., KIM, H.Y., YOO, T.H., Effect of a Helical Wire on Mixed Convection Heat Transfer to Carbon Dioxide in A Vertical Circular Tube at Supercritical Pressures, International Journal of Heat and Fluid Flow (2010).
[3-150] MORI, H., YOSHIDA, S., MOROOKA, S., KOMITA, H., "Heat Transfer Study under Supercritical Pressure Conditions for Single Rod Test Section", Proc. Int. Congress on Advances in Nuclear Power Plants (ICAPP-05), Seoul, Korea, May 15–19, Paper No. 5404 (2005).
[3-151] WU, G., BI, Q., YANG, Z., LI, M., "Experimental Investigation on Heat Transfer of Supercritical Pressure Water in Annular Channel", Proc. 2nd Canada-China Joint Workshop on SCWR, Toronto, Canada, April 25–29, 2010 (2010).

4. PRESSURE LOSS CHARACTERISTICS OF SUPERCRITICAL WATER

Pressure losses in the heat-transport system have a direct impact on the pump capacity and the power output, affecting the capital and operating costs. In addition, these losses affect the local flow conditions along the fuel assembly impacting the heat-transfer characteristics. Depending on the design, the pressure loss components consist of frictional loss, form losses (such as valves and elbows), head loss due to gravity, and loss due to acceleration. A significant portion of the overall pressure loss occurs in the core region (particularly over the bundle assembly). Therefore, it is important to evaluate the core pressure loss accurately.

The overall pressure loss in the heat-transport system is complex and can be expressed as

$$\Delta P = \sum \left(\frac{f}{2D} \frac{L}{\rho_{avg}} G^2 \right)_i + \Delta \left(\frac{G^2}{\rho} \right) \pm \rho_{avg} g L \sin\theta + \sum \left(K \frac{G^2}{2\rho} \right)_i + \ldots \tag{4-1}$$

where f is the friction factor over the pipe section, L is the length of the pipe section, D is the pipe diameter, G is the local mass flux in $kg \cdot m^{-2} \cdot s^{-1}$, g is the gravitational constant (=9.806 $m \cdot s^{-2}$), K is the local form-loss coefficient (for valves, elbow, bend, sudden contraction, sudden expansion, etc.), θ is the pipe inclination angle to the horizontal plane, and ρ and ρ_{avg} are the local and average densities in $kg \cdot m^{-3}$. The sign for the gravitational term changes with '+' referring to the upward flow and '–' to the downward flow. Outside of the core region, the bulk-fluid temperature does not vary considerably over various sections. Therefore, applying the average fluid properties over each section in the calculation is appropriate.

The pressure drop over a bundle assembly consists of several components: skin friction, spacing devices, acceleration, and gravity. In general, the pressure drop due to skin friction is the largest component. The pressure drop due to acceleration can be significant due to the large change in density, particularly over the pseudo-critical point. Therefore, it must be considered separately at conditions of interest.

The pressure loss over the fuel assembly can be likewise expressed as

$$\Delta P_{fuel} = \frac{f_{fuel}}{2D_{hy}} \frac{L_{fuel}}{\rho_{avg}} G_{fuel}^2 + \Delta \left(\frac{G_{fuel}^2}{\rho} \right) \pm \rho_{avg} g L_{fuel} \sin\theta + \sum \left(K_{sp} \frac{G_{fuel}^2}{2\rho} \right) \tag{4-2}$$

where f_{fuel} is the friction factor of the fuel assembly, L_{fuel} is the fuel-assembly length, D_{hy} is the hydraulic diameter of the fuel, G_{fuel} is the local cross-sectional average mass flux within the fuel assemblies in $kg \cdot m^{-2} \cdot s^{-1}$, and K_{sp} is the local form loss-coefficient for the spacing devices (e.g., grids, appendages, etc.). With heating along the fuel, the enthalpy and coolant temperature increase leading to changes in fluid properties. In addition, the sharp change in fluid properties at the pseudo-critical point makes it difficult to apply average fluid properties over the fuel assembly in the calculation.

This study proposes separating the pressure loss calculation over the fuel assembly into two regions based on the pseudo-critical enthalpy (or temperature). This is an analogy to the current reactor safety analyses with the departure from nucleate boiling or dryout as the transition point. Separating the fuel assembly into two regions would minimize the effect of rapid fluid-property change at the pseudo-critical point.

Pressure-drop relationships were compiled and described in an IAEA technical document for advanced water-cooled reactors [4-1]. These relationships cover both the single-phase and two-phase flows. The single-phase pressure-drop models are likely applicable to supercritical flow, while the two-phase pressure-drop models are relevant for start-up, shut-down, and pressure-transient analyses.

4.1. FRICTIONAL PRESSURE DROP

An extensive review of water and carbon dioxide experiments and correlations for friction factor is available [4-2]. However, applying some of these correlations is difficult as information is incomplete or difficult to determine (i.e., wall conditions). An abundance of experimental work exists for heat transfer using supercritical fluids and pressure loss data were obtained over the test section as part of the experiments [4-3]. Pressure loss measurements were reported without key parameters (such as surface roughness and wall conditions) making it difficult to apply the information. The assumption of a smooth tube may not be justifiable as the corrosive behaviour of supercritical fluids often leads to a rapid change in surface conditions.

A number of friction factor correlations were proposed for tube flows [4-2]. The most common correlations are the Blasius and Colebrook and White (C-W) equations [4-4]. The Blasius friction factor equation is based on the assumption of fully developed turbulent flow in a smooth tube:

$$f_{Blasius} = \frac{0.316}{\mathrm{Re}_b^{1/4}} \tag{4-3}$$

It is applicable for bulk Reynolds numbers (Re_b) up to 10^5. The C-W friction factor equation is applicable for turbulent flow and takes into account the surface roughness [4-5]:

$$\frac{1}{f_{C-W}^{1/2}} = -2\log\left(\frac{\varepsilon/D}{3.7} + \frac{2.51}{Re_b\sqrt{f_{C-W}}}\right) \tag{4-4}$$

The C-W factor formula is implicit, so the solution must be determined iteratively.

Applying the friction factor correlations to piping calculations with unheated surfaces and little changes in fluid properties (or temperature), it is considered to be appropriate. However, it is not justifiable for pressure-loss calculations over the fuel assembly. Surface heating (or cooling) affects the near-wall fluid conditions changing the hydraulic behaviours as compared to adiabatic flow. The impact of surface heating (or cooling) effect has been examined with pressure-loss data reported in open literature for several fluids. These pressure-loss data, in both heating and cooling modes, were applied in assessing several correlations. For clarification, heating mode refers to heat being added to the bulk fluid ($T_w > T_b$), while cooling mode refers to heat removal from the bulk fluid ($T_w < T_b$).

4.1.1. Heating mode pressure losses

Data for three fluids were found in literature: water, carbon dioxide, and Refrigerant-22) – all above critical pressures (see Table 4.1). All experiments in the heating mode had vertically oriented test sections with vertical flow.

TABLE 4.1. CRITICAL PRESSURES AND TEMPERATURES FOR SELECTED FLUIDS

Fluid	Critical Pressure (MPa)	Critical Temperature (°C)
Water	22.1	374
CO_2	7.38	30.98
R-22	4.99	96.13

Pressure-loss data with water flow in tubes were obtained mainly from two sources: Razumovskiy et al. [4-6] and Ishigai et al. [4-7]. These data were reported in graphical form [4-2]. Frictional pressure losses were reported with the pressure losses due to gravity subtracted from measured overall channel pressure-

loss values. Relevant parameters for each experiment are listed in Table 4.2. Razumovskiy et al. [4-6] used several tube lengths and tested differing values of heat flux, while holding constant inlet bulk enthalpy at 1800 kJ/kg, while Ishigai et al. [4-7] varied inlet bulk enthalpy and heat flux.

TABLE 4.2. PARAMETERS OF TEST SECTIONS AND BOUNDARY CONDITIONS FOR WATER EXPERIMENTS [4-2]

	Diameter (mm)	Length (mm)	Pressure (MPa)	Mass Flux ($kg \cdot m^{-2} \cdot s^{-1}$)	Heat Flux ($kW \cdot m^{-2}$)
Razumovskiy et al. [4-6]	6.28	239, 358, 477	23.5	2190	0 - 1750
Ishigai et al. [4-7]	3.92	625	25.3	1000	290.8, 825.7, 1372.3

Carbon dioxide data is from the Supercritical Pressure Heat Transfer Investigation for NeXt Generation (SPHINX) facility, which exists at the Korea Atomic Energy Research Institute (KAERI) [4-8]. Experimental conditions covered various system pressures, mass fluxes, and heat fluxes (Table 4.3), but the inlet temperature was maintained at 27°C for all cases. The frictional pressure drop was reported in the work; however, no surface roughness data was reported. Based on the schematic from the paper, it is somewhat unclear which length is appropriate to use for calculation of the pressure drop. The length used was 300 mm (Table 4.3) based upon the schematic layout.

TABLE 4.3. TEST SECTION GEOMETRIES AND CONDITIONS FOR HEATED CO_2 AND R-22 FLOW STUDIES

	Fluid	Diameter (mm)	Length (mm)	Pressure (MPa)	Mass Flux ($kg \cdot m^{-2} \cdot s^{-1}$)	Heat Flux ($kW \cdot m^{-2}$)
Kim et al. [4-8]	CO_2	4.4	300	7.75, 8.12, 8.85	400 - 1200	0 - 150
Yamashita et al. [4-9]	R-22	4.4	200	5.5	700	0-60

Yamashita et al. [4-9] reported pressure losses with R-22 flow at various powers in a 4.4-mm tube at constant pressure and mass flux. Frictional pressure drop data were reported but the value of surface roughness was not provided.

Both the values calculated with the Blasius and C-W equations agree reasonably close with pressure-loss data for water and R-22 flow (see Figs 4.1 and 4.2) although the calculated pressure losses are higher than the measurements. This is considered to be attributed to the possible uncertainty in the test-section length in the CO_2 test. After removing the CO_2 data in the comparison, both the values calculated with the Blasius and C-W equations overpredict the measurements only slightly (see Fig. 4.3). This means a possible reduction in pressure loss with the channel in heating mode. Additional experimental data for CO_2 flow may be needed to confirm the observed trends with water and R-22 flows. Corrections to the friction factor equations were suggested to account for the heated-wall effect [4-2].

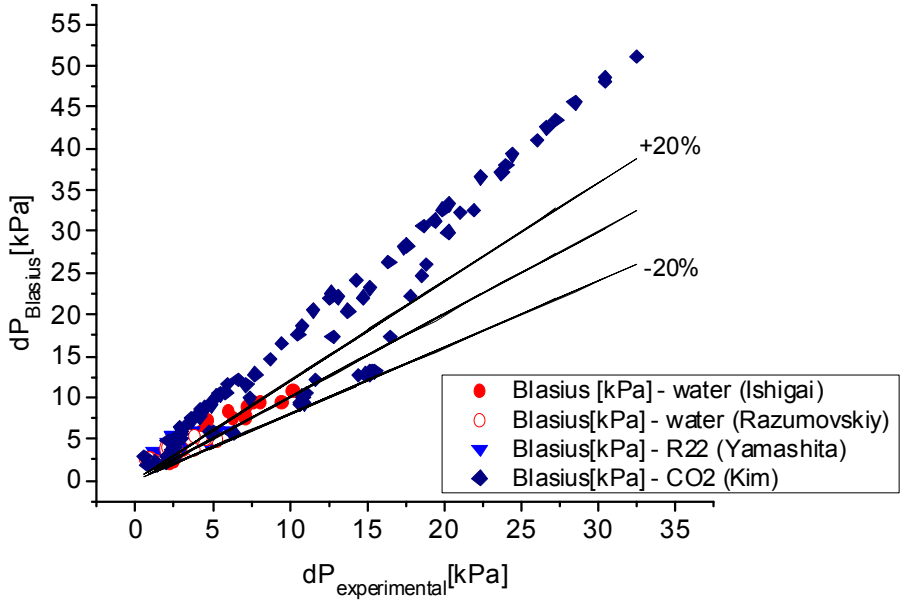

FIG. 4.1. Comparison of pressure losses in heating mode against the blasius equation for water, R-22 and CO_2 flows.

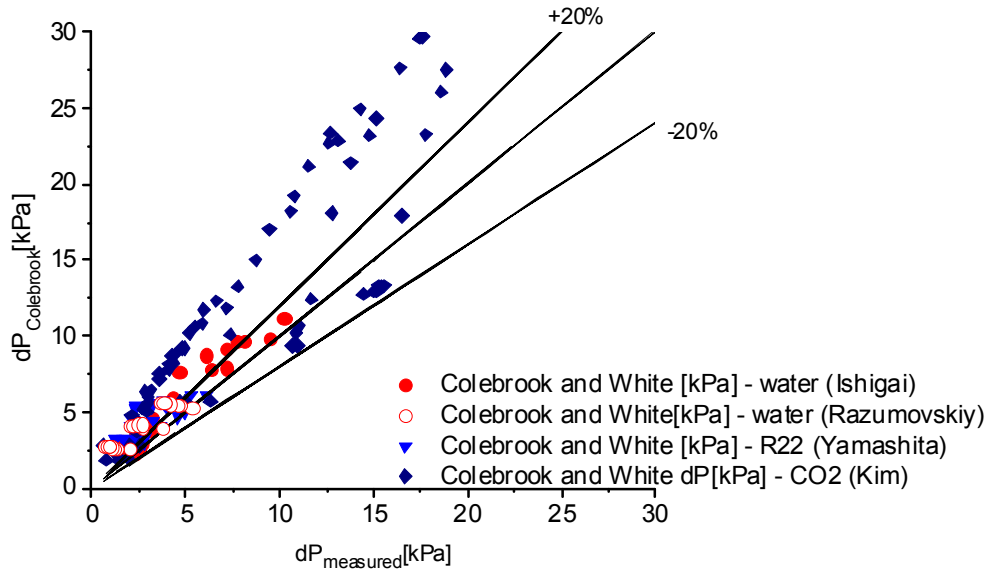

FIG. 4.2. Comparison of pressure losses in heating mode against the C-W equation for water, R-22 and CO_2 flows.

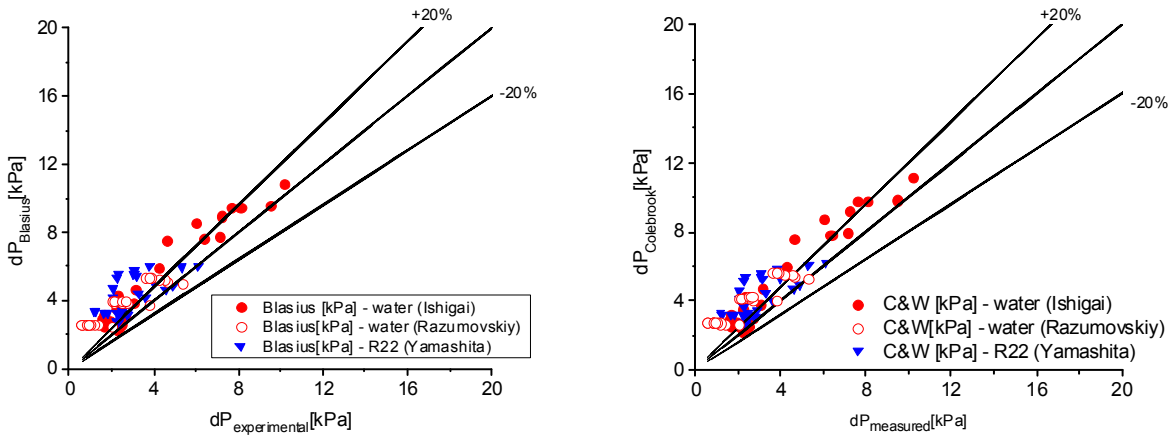

FIG. 4.3. Comparisons of pressure loss in heating mode against the Blasius and C-W equations for water and R-22 flows.

4.1.2. Cooling mode pressure losses

Pressure-loss data were reported from three experiments with CO_2 flowing in a cooling mode. One of these experiments was performed with a horizontal tube [4-10], while the others with horizontal multiple-parallel channels (consisting of twenty-five extruded aluminum channels) [4-11]. Pettersen et al. [4-11] reported the range of experimental parameters and the surface roughness of the inner tubes as 1×10^{-6} metres.

TABLE 4.4. PARAMETERS OF INTEREST FOR CO_2 EXPERIMENTS WITH COOLING MODE HEAT TRANSFER

	Diameter (mm)	Length (mm)	Pressure (MPa)	Mass Flux ($kg\cdot m^{-2}\cdot s^{-1}$)
Pettersen et al. [4-11]	0.79 (25 channels)	503	8.1 - 10.1	600 - 1200
Dang et al. [4-10]	1, 2 (single tube)	500	8 - 10	200 - 1200
Kruizenga [4-12]	1.9 (nine channels)	500	7.4 - 10.2	326 - 973

Dang et al. [4-10] performed experiments with several tubes of different diameter but with the same length. Due to the high uncertainty associated with the low pressure losses in large diameter tubes, Dang et al. [4-10] reported pressure-loss measurements of the two small-diameter tubes only. The surface roughness of these tubes was not reported.

Kruizenga [4-12] performed experiments with a nine semi-circular parallel channel, which was prototypic of a diffusion bonded plate heat exchanger. These experiments covered ranges of pressure, mass flux, heat flux, and inlet conditions. The surface roughness was reported as 7.4×10^{-6} metres.

Figure 4.4 compares the Blasius equation against the cooling pressure loss data. There is a vast under

prediction of the pressure loss, especially in Kruizenga's data [4-12], which is likely due to the rough surface. Petterson's data [4-11] were within 20% with the Blasius equation; this seems reasonable considering the low surface roughness reported within the flow channels.

Figure 4.5 shows an improvement in frictional pressure loss prediction using the C&W correlation, with the appropriate surface roughness. Data reported from Dang et al. [4-10] are still underpredicted and this may be due to the fact that surface roughness values were not reported for their tubes. The C&W correlation clearly illustrates the importance of surface roughness ($\varepsilon=1\times10^{-6}$ metres for Pettersen et al. [4-11], $\varepsilon=7.4\times10^{-6}$ metres for Kruizenga [4-12], but none given for Dang et al. [4-10]). When the surface roughness is given, calculated values of pressure drop closely match the experimental values.

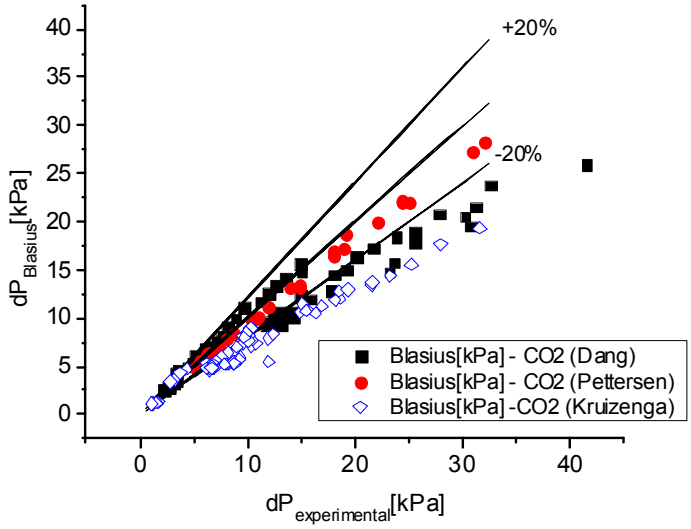

FIG. 4.4. Comparison of pressure loss in cooling mode against the Blasius equation.

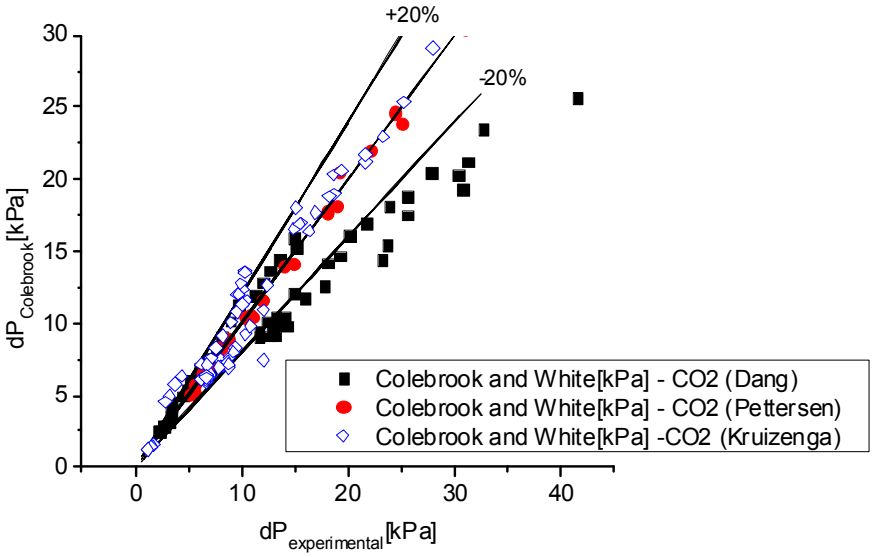

FIG. 4.5. Comparison of pressure loss in cooling mode against the C-W equation.

4.2. LOCAL PRESSURE LOSS

Local pressure losses due to piping components (such as valves, elbows, bends, etc.) and fuel assembly appendages (such as spacer grids) are calculated with

$$\Delta P_{form} = K \frac{G^2}{2\rho} \tag{4-5}$$

The loss coefficient, K, is established with experimental data. Little information is reported in available literature on loss coefficients for various piping components in supercritical flow.

Spacing devices in fuel assemblies of various SCWR concepts have not been established or finalized. Wire-wrapped and grid spacers are being considered. Experimental pressure-loss data are required to establish the loss coefficient for a specific grid-spacer design. On the other hand, the equivalent friction factor approach is often applied for the wire-wrapped spacer (i.e., the loss coefficient for the wire-wrapped spacer is distributed over the length of the assembly as an equivalent friction factor). Experimental data for the relevant bundle geometry and spacer configuration are required to establish the equivalent friction factor.

LIST OF SYMBOLS FOR SECTION 4

D	Pipe diameter, meter
D_{hy}	Hydraulic diameter of the fuel assembly, meter
$dP_{Blasius}$	Pressure loss based on the Blasius equation, kPa
$dP_{Colebrook}$	Pressure loss based on the Colebrook-White equation, kPa
$dP_{experimental}$	Experimental pressure loss, kPa
$dP_{measured}$	Measured pressure loss, kPa
f	Friction factor
$f_{Blasius}$	Friction factor based on Blasius equation
f_{C-W}	Friction factor based on Colebrook-White equation
f_{fuel}	Friction factor of the fuel assembly
G	Local mass flux, $kg \cdot m^{-2} \cdot s^{-1}$,
G_{fuel}	Local mass flux in the fuel assembly, $kg \cdot m^{-2} \cdot s^{-1}$,
g	Gravitational constant (=9.806 $m \cdot s^{-2}$)
K	Local form-loss coefficient
K_{sp}	Spacer-loss coefficient
L	Channel length, meter
L_{fuel}	Fuel assembly length, meter
Re_b	Bulk-fluid Reynolds number (defined as $G \cdot D/\mu$)
T_b	Bulk-fluid temperature, °C
T_w	Wall temperature, °C
ΔP	Pressure loss (or drop), Pa
ΔP_{form}	Form loss, Pa
ΔP_{fuel}	Pressure loss over the fuel assembly, Pa
ε	Surface roughness, meter
μ	Viscosity, $kg \cdot m^{-1} \cdot s^{-1}$
ρ	Local density, $kg \cdot m^{-3}$
ρ_{avg}	Average density, $kg \cdot m^{-3}$
θ	Channel inclination angle to the horizontal plane, radian

REFERENCES FOR SECTION 4

[4-1] INTERNATIONAL ATOMIC ENERGY AGENCY, Thermohydraulic Relationships for Advanced Water-Cooled Reactors, IAEA-TECDOC-1203, April (2001).

[4-2] PIORO, I., DUFFEY, R., DUMOUCHEL, T., Hydraulic Resistance of Fluids Flowing in Channels at Supercritical Pressures (Survey), Nuclear Engineering and Design, 231 (2) (2004) 187–197.

[4-3] PIORO, I.L., DUFFEY, R.B., Experimental Heat Transfer to Supercritical Water Flowing inside Channels (Survey), Nuclear Engineering and Design, 235 (22) (2005) 2407–2420.

[4-4] CHENG, L., RIBATSKI, G., THOME, J.R., Analysis of Supercritical CO_2 Cooling in Macro- and Micro-Channels, International Journal of Refrigeration, 31 (8) (2008) 1301–1316.

[4-5] COLEBROOK, C.F., Turbulent Flow in Pipes, with Particular Reference to Transition Region between Smooth and Rough Pipe Laws, Institution of Civil Engineers of London -- Journal, 12 (4) (1939) 393–422.

[4-6] RAZUMOVSKIY, V.G., ORNATSKIY, A.P., MAEVSKIY, E.M., Hydraulic Resistance and Heat Transfer of Smooth Channels with Turbulent Flow of Water of Supercritical Pressure, Thermal Engineering (Теплоэнергетика, стр. 69–72), 31 (2) (1984) 109–113.

[4-7] ISHIGAI, S., KADGI, M., NAKAMOTO, M., Heat Transfer and Friction for Water Flow in Tubes at Supercritical Pressures, Teplomassoobmen (Heat-Mass-Transfer)-V, Proc. Vth All-Union Conf. on Heat Mass Transfer, Minsk, Belarus, May, 1 (1) (1976) 261–269 (In Russian).

[4-8] KIM, H.Y., KIM, H., SONG, J.H., CHO, B.H., BAE, Y.Y., Heat Transfer Test in A Vertical Tube Using CO_2 at Supercritical Pressures, Journal of Nuclear Science and Technology, 44 (3) (2007) 285–293.

[4-9] YAMASHITA, T., MORI, H., YOSHIDA, S., OHNO, M., Heat Transfer and Pressure Drop of A Supercritical Pressure Fluid Flowing in A Tube of Small Diameter, Memoirs of the Faculty of Engineering, Kyushu University, 63 (4) (2003) 227–244.

[4-10] DANG, C., HIHARA, E., In-Tube Cooling Heat Transfer of Supercritical Carbon Dioxide. Part 1. Experimental Measurement, International Journal of Refrigeration, 27 (7) (2004) 736–747.

[4-11] PETTERSEN, J., RIEBERER, R., MUNKEJORD, S., Heat Transfer and Pressure Drop for Flow of Supercritical and Subcritical CO_2 in Microchannel Tubes, European Research Office of the U.S. Army, Final Report, Contract N-68171-99-M-5674. SINTEF Energy Research, Feb. (2000).

[4-12] KRUIZENGA, A., ANDERSON, M., FATIMA, R., CORRADINI, M., TOWNE, A., RANJAN, D., Heat Transfer of Supercritical Carbon Dioxide in Printed Circuit Heat Exchanger Geometries, Journal of Thermal Science and Engineering Applications, 3 (3), August 10, 2011 (2011).

5. EXPERIMENTAL PLANS FOR OBTAINING HEAT TRANSFER DATA IN SUPPORT OF CORRELATION VALIDATION AND IMPROVEMENT

Design and safety analyses of Supercritical Water Cooled Reactors (SCWRs) require experimental data on supercritical heat transfer in relevant bundle geometry. The majority of the current supercritical heat transfer databases, however, were obtained with tubes and annuli (see Section 3). While the tube-data-based prediction methods are applied in subchannel calculations, subchannel-code predictions must be validated against experimental data for bundles of relevant geometry. As illustrated in Section 3, the heat-transfer characteristics are considerably different between tubes and bundles.

Current reference supercritical heat transfer correlations were based on tube data. Despite of the relatively large database, the range of covered flow conditions remains inadequate for the design and safety analyses of SCWR. Additional data are required at postulated accident conditions where insufficient or no data are available. A number of separate effects must be accounted for in design and safety analyses. Predictions of these separate effects require applicable correlations that are based on relevant experimental data.

Extending prediction methods developed with tube or small bundle subassembly data is necessary in the conceptual design phase due to the high cost and long preparation time in testing large assemblies or full-scale bundles at relevant conditions. This approach is justifiable but the associated high prediction uncertainty could have an impact on the reactor design, power output, and safety margin. Therefore, additional experiments using complex bundle geometries are necessary for generating relevant experimental data to minimize the uncertainty and validate the prediction methods and analytical toolsets.

5.1. SUPERCRITICAL HEAT TRANSFER TEST FACILITIES

Experimental facilities are required for tests with simple test sections and complex bundle geometries. A summary of these facilities is provided in following sections for establishment of future experimental needs.

5.1.1. Water test facilities

Experimental data with high-pressure high-temperature water flow are the most crucial for correlation development and validation. Information on six supercritical existing water heat-transfer test facilities has been compiled and described below. Other facilities under design or construction have not been included.

5.1.1.1. China Institute of Atomic Energy

The supercritical water loop at China Institute of Atomic Energy (CIAE) is shown in Fig. 5.1 [5-1]. De-ionized water is supplied using a three-head piston pump with a maximum pressure of 45 MPa and a flow rate of 2.4 $m^3 \cdot h^{-1}$. It passes through a dumping tank and a preheater, and flows upward in the test section. The water is cooled with heat exchangers and directed back to the pump. The flow rate of the test section is controlled using valves in the bypass and main paths. The inlet temperature of the water is controlled with the power to preheater. A DC power supply with capacity of 7,000A×65V is applied to heat the test section. An AC power supply is connected to the preheater. The following loop parameters are measured: the outlet pressure using a pressure transducer (DCY-1151), the flow rate using a turbine flow-meter (LWGY-6), the inlet and outlet water temperatures of the test section using NiCr-NiSi thermocouples and the voltage and current across the test section. All measurements are recorded using a data acquisition system.

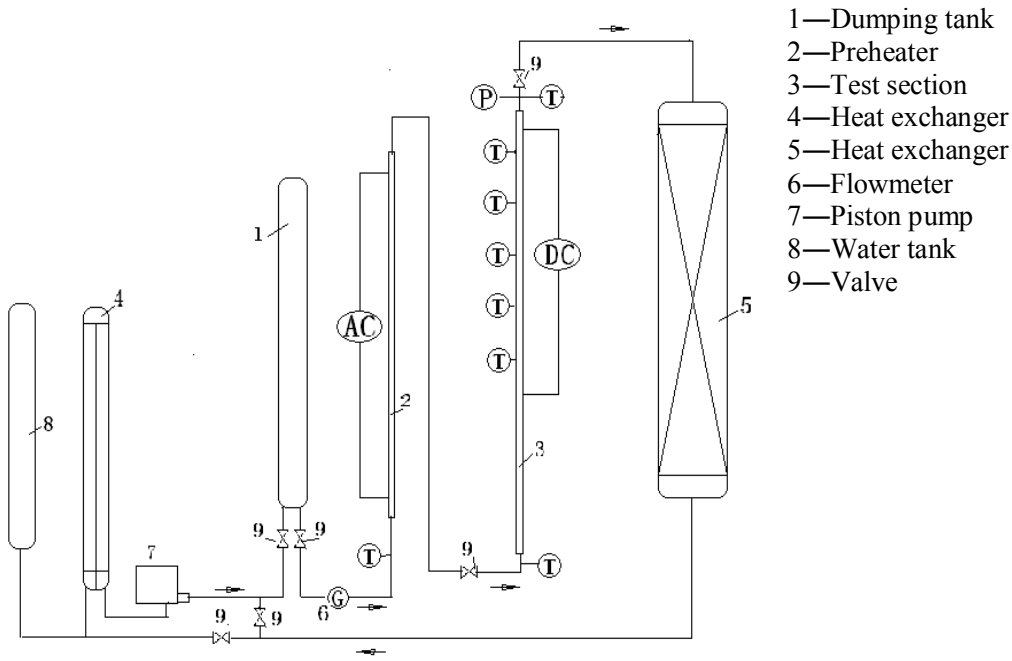

FIG. 5.1. Schematic diagram of the CIAE test loop.

5.1.1.2. AREVA in Germany

A high-pressure test facility was constructed in 1975 at Siemens in Erlangen, Germany [5-2]. It is referred to as the BENSON test loop and can be operated over a wide range of supercritical water flow conditions. Design conditions of the BENSON test loop are:

- System pressure: 330 bar;
- Temperature: 600°C;
- Mass flow rate: 28 $kg \cdot s^{-1}$;
- Heating capacity: 2000 kW.

The schematic diagram of the BENSON loop is shown in Fig. 5.2. The test facility is made of austenitic stainless steel and is thermally insulated. Demineralized and deaerated water or boiler feedwater, to which chemicals have been added to obtain the required water chemistry, is provided in a feedwater tank. The water is injected into the test loop using a piston pump. To minimize flow oscillations caused by the pump's six pistons, a damping vessel is installed in the pump discharge line. Prior to entering the test section, the water is heated with a pre-heater to the defined flow conditions at the inlet. A spray-type condenser is installed at the exit of the test section to cool the fluid. The fluid then passes to a circulation pump, which circulates part of the flow for cooling the spray condenser. Condenser cooling water is taken from the main flow immediately downstream of the pump as well as from the main cooler, which is supplied on its secondary side with water from a wet cooling tower. System pressure is controlled using a large thermal pressurizer and a throttling valve (pressure reducing valve) downstream of the test object. Various locations of the test loop are instrumented to measure pressure, temperature, and flow rate.

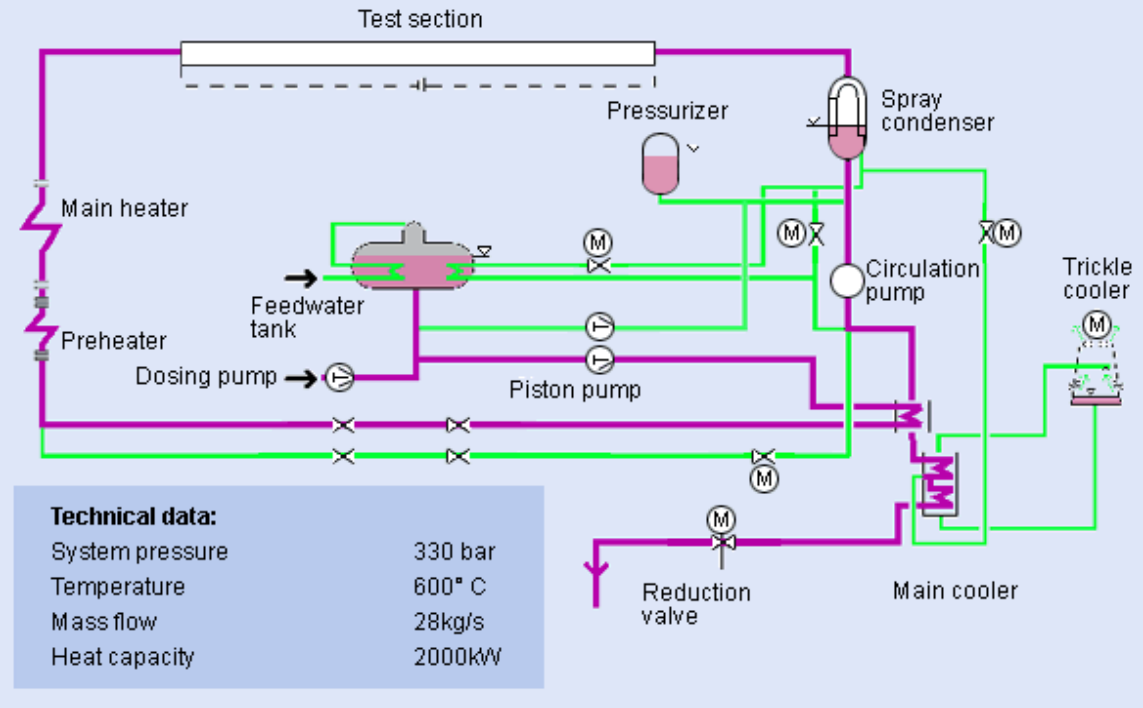

FIG. 5.2. Schematic diagram of the BENSON test loop.

5.1.1.3. Institute of Physics and Power Engineering in Russia

The supercritical pressure test facility (SKD-1, see Fig. 5.3) at the Institute of Physics and Power Engineering (IPPE) is constructed for thermophysical investigations of prototypical water cooled reactor fuel assemblies. It was designed for a wide range of test conditions at pressures up to 28 MPa covering steady state and transient conditions. The maximum power applied to the test section is 0.6 MW.

All components in the test facility are made of stainless steel. The one-loop scheme of the test facility with one circulating pump provides a coolant flow rate up to 3.0 $m^3 \cdot h^{-1}$; it has two positions for mounting test sections with separate coolant supply. The mixing steam-cooler-condenser permits temperatures at the test section outlet up to 500°C. Distilled, ion exchange treated, water is used as coolant.

Four alternating current controllers of industrial frequency provide an independent power supply through four channels. Two of these controllers can be connected over a test section or over a test section and a preheater section installed to increase the water temperature at the test section inlet up to 450°C. Heating of the test section is carried out using autotransformers (Model AOMKT-250 type) via step-down transformers (Model OSU-100 type) with natural air cooling. The controllers can be connected to the test sections in parallel or in series. Heat extracted from the high-pressure loop is removed in heat exchangers with circulating water subjected to magnetic treatment. Thermal expansion of the high-pressure loop is compensated with a nitrogen gas pressurizer. The pressure in the high-pressure loop is produced using a supply pump.

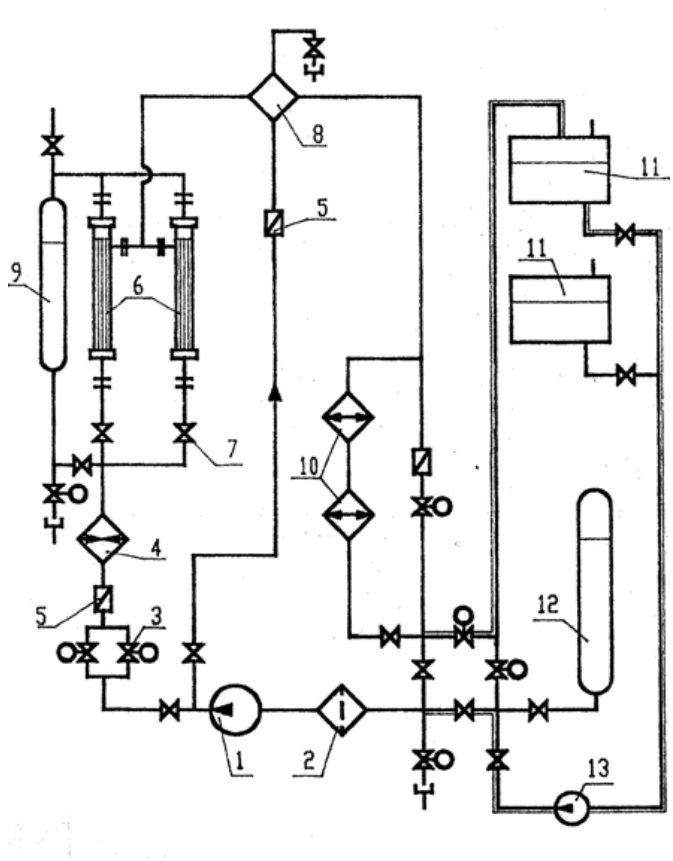

FIG. 5.3. The principal scheme of the test facility SKD-1 at IPPE.

A programmable measuring system is used for acquisition, recording and instantaneous processing of experimental data. An error analysis of the system equipment including amplifiers, a block of commutators, a L1250 card and a personal computer provides an estimated total error on the order of ±0.3%.

The high pressure test facility (SVD-2, see Fig. 5.4) at IPPE was designed to research heat transfer, hydrodynamics, critical heat flux, post critical heat transfer and deteriorated heat transfer regimes at subcritical and supercritical pressures. Models of multi-channels fuel assemblies of water cooled reactors and other heat exchange units with powers up to 10 MW and maximum pressure of 26 MPa can be studied under steady state and dynamic conditions. The test facility consists of three loops. The high-pressure circuit (Circuit 1) consists of two loops: a high-pressure loop (HPL) and a medium pressure loop (MPL), which can operate together or separately. The intermediate circuit (Circuit 2) removes heat from the high-pressure loop to the recirculating water circuit.

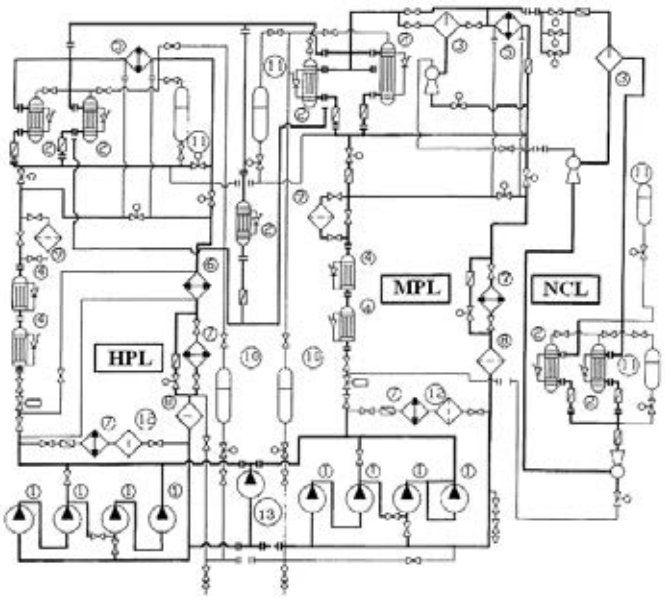

1 - Pumps H-149 (10 t/h)
2 - Test section
3 - Separator
4 - Electrical heater
5 - Condenser
6 - Heat exchanger (regenerative)
7 - Cooler
8 - Mechanical filter
9 - Special filter
10 - Compensator for HP, MP loop
11 - Compensator for natural circulation loop
12 - Ionic filter
13 - Pump H-1459 (to 10 - 100 t/h)
HPL - High-pressure loop
MPL - Medial-pressure loop
NCL - Natural convection loop

FIG. 5.4. The principal scheme of the SCP test facility SVD-2 at IPPE.

The medium pressure loop (MPL) is hydraulically similar to the high-pressure loop. Combining the operation of the high- and medium-pressure loops through one test section at a coolant pressure of 20 MPa, the maximum coolant flow rate through the test section is 70 $m^3 \cdot h^{-1}$.

The maximum coolant flow rate of the hydraulic circuit (loop) in the high pressure loop (HPL) can be varied from 10 to 35 $m^3 \cdot h^{-1}$ (with a corresponding pressure drop range from 6.0 to 1.0 MPa) at the pressure of 26 MPa using sequential-parallel cut-in of four circulating pumps. The steam-cooler-condenser installed immediate downstream of the test section can accommodate outlet coolant temperatures up to 505°C.

After being manufactured, assembled and equipped with sensing devices, the test sections are installed vertically in a special box (horizontal installation is also possible), where they are connected to the high-pressure loop, electric power supply and the data acquisition and processing system.

Four electric power supplies of direct current with a rapid thyristor control provide power of the test sections; the power suppies can be connected in series as well as parallel providing two supply channels with a voltage of 225V, and current 25000A in each parallel circuit. This allows a wide range of operation in the test facility. The length of a test section can be more than 10 m allowing for prototypical bundle tests.

Electrical heaters with a power rating of 1.8 MW provide power for water heating, steam-water mixture generating and superheated steam production at temperatures up to 450°C. The thyristor converters are controlled by means of a special-purpose device that provides the control of the output power of a test section both under steady-state and transient conditions, power change according to the respective test specification, full or partial power drop in case of alarm signals received from the control subsystem.

The test facilities (SKD-1 and SVD-2) are equipped with the discharging system based on balance chamber to compensate one-way effect of coolant pressure on thin-walled elements of the test section. Both test facilities are equipped with a computer-based system for data acquisition and processing.

Temperatures are measured with L-Type thermocouples (KTMC XK (Chromel-Copel) or thermocouple wires XK (Chromel-Copel) insulated with a high-temperature fiber). Pressure measurements are obtained using Sapfir-22 or Metran-22 series transducers. Signals of measuring transducers are delivered through the amplifiers with an analog to digital convertor, which performs signal normalization and interference suppression to the high-speed measuring multi-channel programmable unit by L-card (512 channels) at a rate of 100 thousand measurements per second. Measurements are stored in the computer (the basic measurement error is ±0.15%). Results from the on-line data processing are displayed on the monitor. The control subsystem provides an effective protection against damages to loop components and test sections in the event the control parameters are out of range.

5.1.1.4. Shanghai Jiao Tong University in China

A Supercritical WAter MUlti-Purpose test loop (SWAMUP) has been constructed at Shanghai Jiao Tong University (SJTU). The SWAMUP system serves as an experimental facility for thermal hydraulic tests in supercritical water. The design parameters for the test loop are as follows:

- Design pressure: 30.0 MPa;
- Fluid: water;
- Test section outlet temperature: 550^{o}C;
- Mass flow: 1.4 kg·s^{-1};
- Heat capacity: 1.2 MW.

The SWAMUP is a closed-loop system as shown schematically in Fig. 5.5. The test loop mainly consists of a water supply system, circulating pump, pre-heater, heat exchangers, accumulator and test section. The material used for the main test loop is stainless steel (Cr18Ni9).

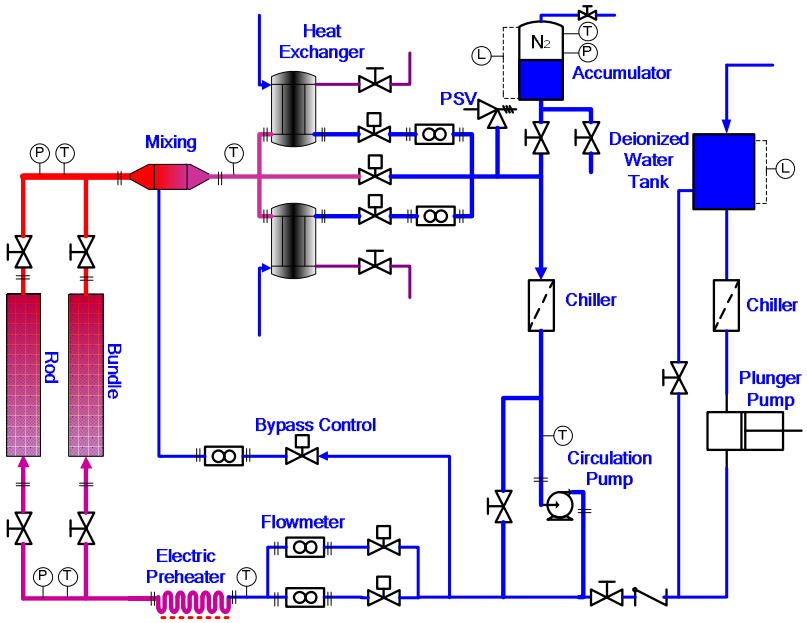

FIG. 5.5. Schematic diagram of the SWAMUP test facility at SJTU.

In the water supply system, de-ionized and de-aerated water is produced and provided in a water tank, from which water is injected into the test loop using a piston pump. Water in the test loop is circulated using a centrifugal pump (SAMJIN IND.CO., LTD., Korea). The maximum flow rate is 1.4 kg·s^{-1} with a

total pump head of 0.8 MPa. Operating temperature and pressure is 350°C and 35.0 MPa, respectively.

The mass flow rate through the test section is measured using two venturi-type flowmeters and regulated by adjusting control valves in both the main and the bypass loops. An electric pre-heater is located upstream of the test section to control the inlet temperature. The pre-heater is made of bended stainless steel tubes (Cr17Ni12Mo2) of ϕ32x4.5 and 3.0 meters in length. It is directly heated using an AC power supply. The advantage of this direct heating method is to allow a precise control of the heat added to the fluid. The capacity of the AC power supply is 0.3 MW. Figure 5.6 shows schematically the configuration of the pre-heater.

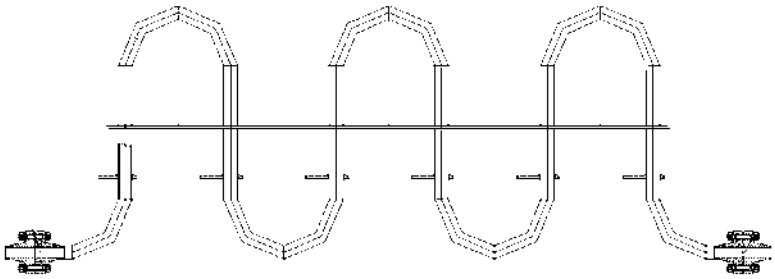

FIG. 5.6. Pre-heater configuration.

Various types of test sections, such as circular tubes, annuli and rod bundles, can be installed into the test facility. A DC power source with low voltage and high current (90V, 10000A) is used to heat the test section with direct or indirect electric heating method.

High temperature water existing within the test section and low temperature water through the bypass loop are mixed in a mixer, which is shown in Fig. 5.7, and cooled down to 380°C or less.

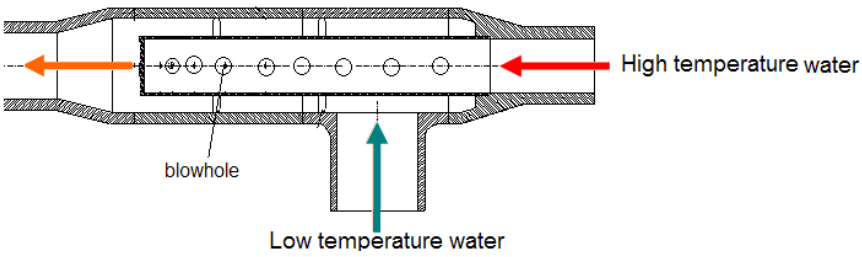

FIG. 5.7. Mixer configuration.

The main heat sinks of the test loop are two U-tube heat exchangers with 0.6 MW and 0.4 MW cooling capacity, respectively. Supercritical water flows through the tube side and cooling water through the shell side. An auxiliary chiller system is designed to feed city water into the heat exchangers. An accumulator with a volume of 0.6 m^3 filled with gaseous nitrogen is installed downstream of the heat exchangers and has the function of controlling the main loop pressure. A pressure relieving device (PSV) is installed to prevent an over-pressurization of the main loop. Main measurement items are pressure, temperature, flow rate, differential pressure and electric power. These measurements are stored in the 'LabView™' data acquisition system.

5.1.1.5. University of Wisconsin – Madison in the United States of America

A supercritical water loop was built at the University of Wisconsin - Madison to study heat transfer phenomena at various conditions and geometries details of the loop operation and design can be found in references [5-4], [5-5]. The loop is approximately 2-m wide by 3-m tall with 4.29-cm inner-diameter Iconel-625 piping. It has been built to be capable of operating up to 600ºC and 25 MPa. Figure 5.8 illustrates the schematic diagram of the supercritical heat-transfer test facility. A pump capable of operating at supercritical conditions circulates the supercritical water in the range of 200-2000 kg/m^{2}s past the heater. Inlet temperature is controlled using copper cooling coils of various contact areas, through which cooling water is pumped to remove heat. The facility has the ability to utilize an optical test section to allow laser based measurements of the boundary layer along the simulated electrically heated nuclear fuel pin. The facility also has the capability to conduct bundle tests with a maxium power of 400kW.

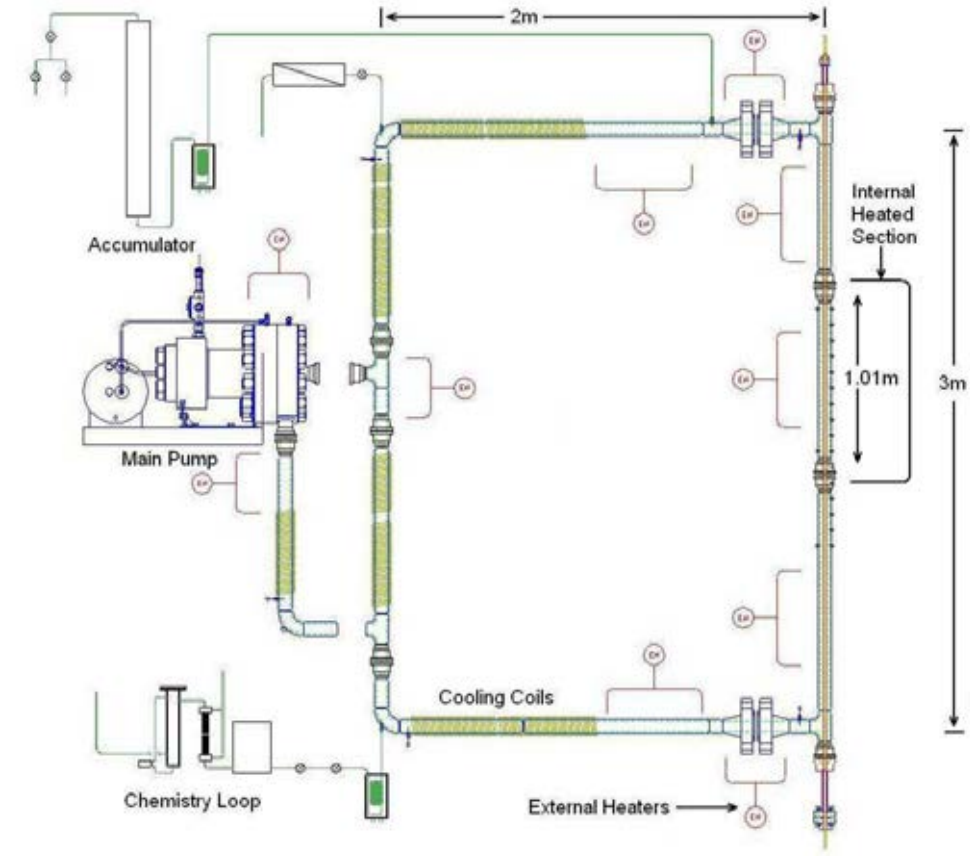

FIG. 5.8. SCW heat transfer facility at the University of Wisconsin-Madison.

5.1.1.6. Xi'an Jiaotong University in China

The high-pressure steam-water test loop in Xi'an Jiaotong University (XJTU) is shown schematically in Fig. 5.9 [5-6]. Distilled and de-ionized feed water from the water tank are driven through a filter with a high pressure plunger-type pump capable of operating at up to 40 MPa. The feed water is pre-heated in a heat exchanger and a main pre-heater before flowing into the test section. The pre-heater and the test

section are electrically heated by alternating current power supply with maximum heating capacities of 1.0 MW and 0.5 MW, respectively. The test section inlet bulk-fluid temperature and heat flux is adjusted by controlling the alternating current power supply. The feed water flowing from the test section is cooled with a regenerative heat exchanger and a condenser, and then flowed back to the water tank. The pressure and the mass flux in the test section are controlled by adjusting the main valve and bypass valve, respectively.

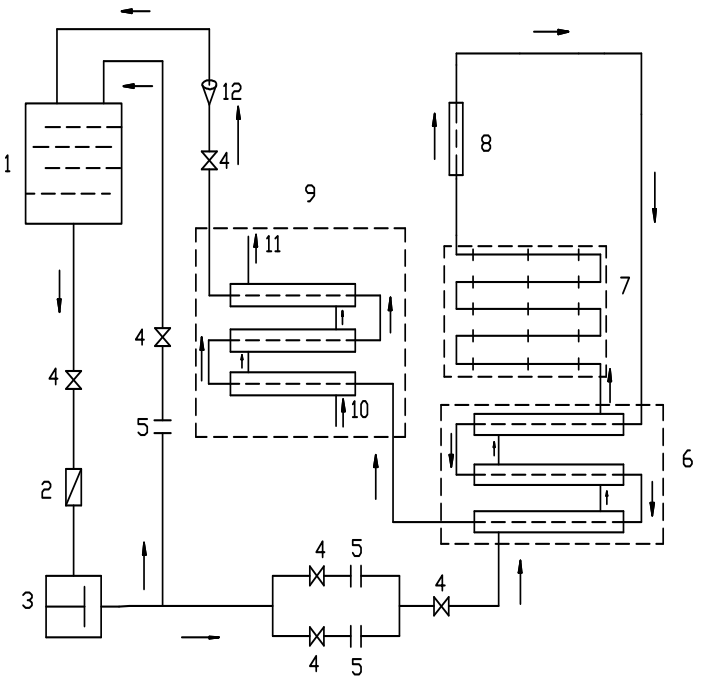

1: Water tank
2: Filter
3: Water pump
4: Valve
5: Orifice
6: Heat exchanger
7: Preheater
8: Test section
9: Condenser
10: Cooling water inlet
11: Cooling water outlet
12: Rotor flow meter

FIG. 5.9. Schematic diagram of the XJTU test loop.

5.1.2. Surrogate fluid test facilities

Performing supercritical heat-transfer experiments with surrogate fluids is more cost effective than with water. This is attributed to the reduction in operating pressure and power to achieve water-equivalent conditions. Information on three supercritical heat-transfer test facilities (two with CO_2 flow and one with refrigerant flow) are compiled and described below. Other facilities under design or construction are not included.

5.1.2.1. Institute of Physics and Power Engineering in Russia

The thermophysical Freon test facility (STF) [5-3] at IPPE is dedicated for investigation of heat transfer at supercritical pressures using Freon-12 as coolant (Fig. 5.10). The STF facility is a circulating loop consisting of the following components: two circulating pumps, preheater, test sections (or test channels), heat exchangers, recuperator, deaerator, and level indicator. Two Freon tanks are mounted at this test facility. Pipes of the circulating loop of the STF facility have an inside diameter of 50 mm and are made of stainless steel. This test facility has been designed for operating pressure of 5.0 MPa.

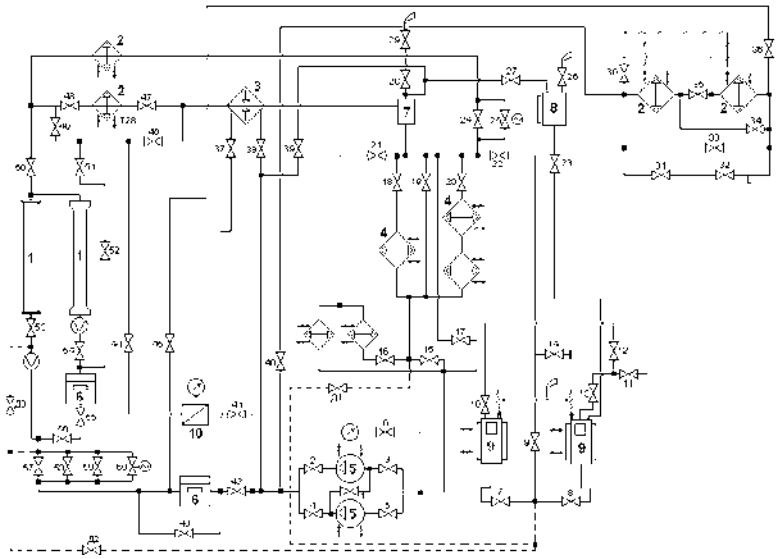

1 – Test sections (test channels)
2 – Heat exchangers
3 – Recuperator
4 – Refrigerators
5 – Pumps
6 – Preheaters
7 – Deaerator
8 – Tank-indicator
9 – Freon tanks
10 – Filter

FIG. 5.10. The principle scheme of the STF-1 test facility.

The circulating pumps can operate in parallel, in series or independently from each other. The capacity of each pump is 20 $m^3 \cdot h^{-1}$ with a pressure head of 1.0 MPa. These pumps also provide a sufficiently high head (0.8 MPa) at flow rates up to 30 $m^3 \cdot h^{-1}$.

The preheater is manufactured with an electrically heated tube. Its electrical power is 160 kW. Heat exchangers are also used to increase the coolant temperature at the inlet by supplying hot water into these exchangers through the second loop. The coolant temperature can also be lowered by supplying cooling water into these exchangers.

Two different test channels are presented in the STF principal scheme, one of them is generally under preparation for experiments, whereas the second one is being used for tests. In the case of using the higher power model (left channel), experiments are carried out using the heat exchangers.

Freon tanks are placed below the level of test loop and test channel, providing the coolant discharge from them into the preliminary stage. These tanks are also used as steam pressurizers in the course of experiments. Electrical heaters are mounted inside these tanks to preheat coolant. The tanks are provided with the exterior annular chambers where hot or cold water can be supplied.

The electric heater is primarily used to keep the pressure in the circulating loop at a given level, whereas feed of hot or cold water to the annular chamber provides fast filling of the loop with coolant or its discharge. The volume of each tank is 0.25 m^3. The electrical power supply of the test channel is provided using a direct current generator of capacity of 540 kW (equivalent to 8 MW for water).

In the course of an experiment on thermohydraulic processes, the following operating parameters are measured: coolant temperatures at inlet and outlet of the channel, flow temperatures, outlet pressure, pressure drop over the channel, coolant flow rate, wall temperatures along the test section, and voltage and current in the channel. To enhance reliability and reduce uncertainty obtained in the course of measuring these parameters, two independent gauges are applied.

Coolant temperatures at the inlet and outlet of the fuel-assembly simulator are measured using two chromel-copper type thermocouples located at each position. In this case, each thermocouple is

differentially connected to the similar thermocouple by means of a stabilized temperature cold junction, and all thermocouples are subjected to individual calibration.

When required, coolant temperatures at various axial distances and radial locations of the channel are measured using similar thermocouples. Wall temperatures along the simulator are measured using chromel-alumel or chromel-copper type thermocouples. These temperature measurements are evaluated on the basis of standard calibration characteristics (unless otherwise specified).

The pressure at the channel outlet is measured using standard manometers (visual control) and transducers of 'Sapfir-22DI' type. The pressure drop over the fuel assembly model is measured using similar pressure drop transducers of 'Sapfir-22DD' type with a nominal range from 0.003 to 0.001 MPa. All pressure gauges are subjected to individual calibration to achieve measurement uncertainty of less than 0.5-1.5%.

The coolant flow rate through the fuel assembly model is measured using an orifice combined with pressure drop transducers of 'Sapfir-22DD' type; this flow meter is preliminary calibrated against water by the volume–time method using the test facility certified by Gosstandard Service of Russian Federation with a flow rate measurement uncertainty of 0.11%. Approximate relationships for the flow rate have the relative uncertainty of 0.4%.

The data acquisition system is equipped with 256 measuring channels. This system includes a control crate of L-card type, high-speed commutators and an analogous-digital transducer with accuracy class of 0.05. Converted signals enter for processing using personal computer.

The data acquisition system potentially provides recording of signals with speed up to 300 kHz (during experiments the recording speed is 2-3 kHz). Average values of measured parameters, such as pressure, pressure drop, flow rate in the measuring channel, are obtained over 50 cycles. The conversion of voltage signals to physical values is performed accounting for available calibration characteristics of gauges and tables of thermophysical properties for Freon-12. The limiting admissible temperature of Freon-12 is 400°C at the critical pressure of 4.1 MPa and critical temperature of 112°C.

5.1.2.2. Korea Atomic Energy Research Institute

A supercritical heat-transfer test facility, SPHINX, has been constructed at Korea Atomic Energy Research Institute (KAERI) as a part of the Korean National Nuclear Research and Development program [5-7]. Figure 5.11 shows a schematic diagram of the test facility. The design pressure and temperature of the main loop are 12.0 MPa and 80°C, respectively. The test loop is initially charged with CO_2 by an air-driven reciprocating compressor. The CO_2 is pumped by a gear pump installed at the bottom of the test section and passed through an electric heater, which heats the fluid to a pre-set fluid temperature at the test section inlet. The CO_2 leaving the test section enters the heat exchanger and is cooled down to a pre-set temperature. The heat exchanger is cooled by chilled water, and its temperature is controlled by a cooler. A gear type pump is adopted to minimize the flow fluctuation. An accumulator filled with gaseous nitrogen, which is located at the discharge of the pumps, also reduces any fluctuation in flow. The pre-heater and the power supply unit control the inlet and outlet temperatures of the fluid, respectively. The mass flow rate is regulated by adjusting the bypass valve and/or the pump speed. A Coriolis type flow meter, manual flow control and isolation valves, pressure transmitters, and thermocouples are installed in the test facility. The inner diameter of the main loop is about 20 mm. The main loop is insulated to minimize any heat loss to the atmosphere. The flanges for the tube and annular channel test section are separately prepared. The loop is designed to accommodate the upward flow and downward flow tests without re-installation of the test section.

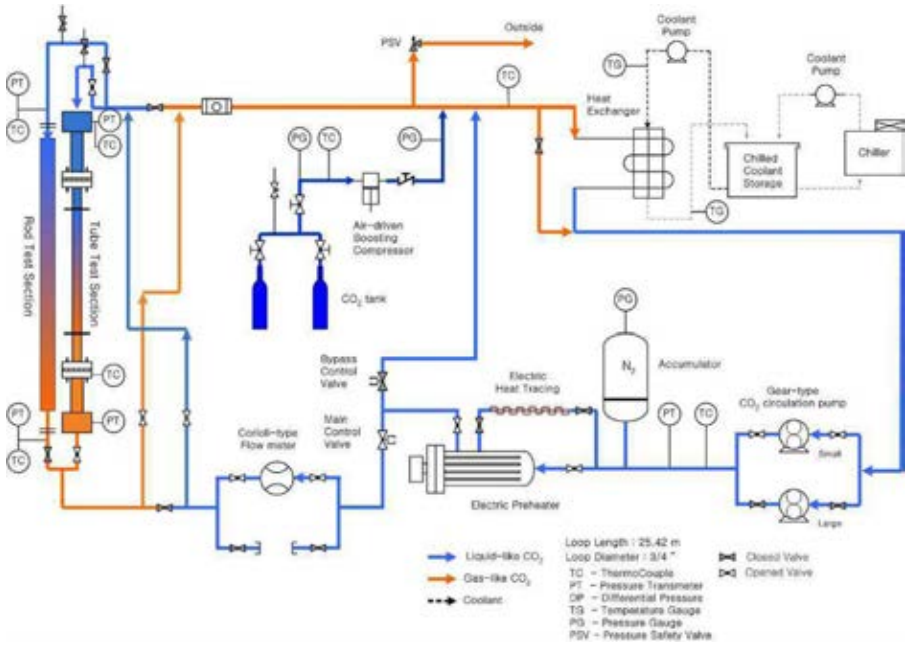

FIG. 5.11. Schematic diagram of SPHINX test facility.

5.1.2.3. Shanghai Jiao Tong University in China

A Freon test facility has been constructed for modeling experiments at Shanghai Jiao Tong University (SJTU). Figure 5.12 shows schematically the test facility SMOFTH (Supercritical MOdel Fluids Thermal-Hydraulics). The main design parameters are:

- Fluid: Freon 134a
- Pressure: 6.0 MPa
- Temperature: 200°C
- Flow rate: 10 $t \cdot h^{-1}$
- Heating power: 300 kW

5.1.2.4. University of Ottawa in Canada

A carbon-dioxide test facility has been constructed for supercritical heat-transfer experiments at the University of Ottawa [5-8]. Figure 5.13 shows the schematic diagram of the test facility. Although this facility is used mainly for carbon-dioxide tests in the current scope, it is capable to handle other fluids having lower critical pressure and temperature than carbon dioxide. Figure 5.14 illustrates the 3-dimensional view of the test section set up. The loop is constructed for quick change over to different test sections (such as tubes of different sizes and bundle subassembly). All test sections are installed at various locations of the loop. Valves are used to direct the flow through the relevant test section in the experiment.

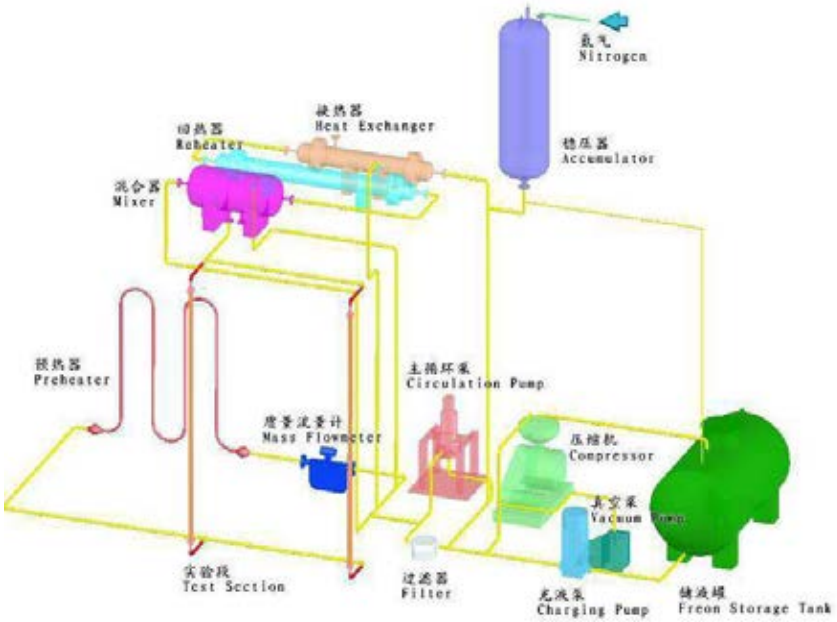

FIG. 5.12. Schematic diagram of the SMOFTH test facility.

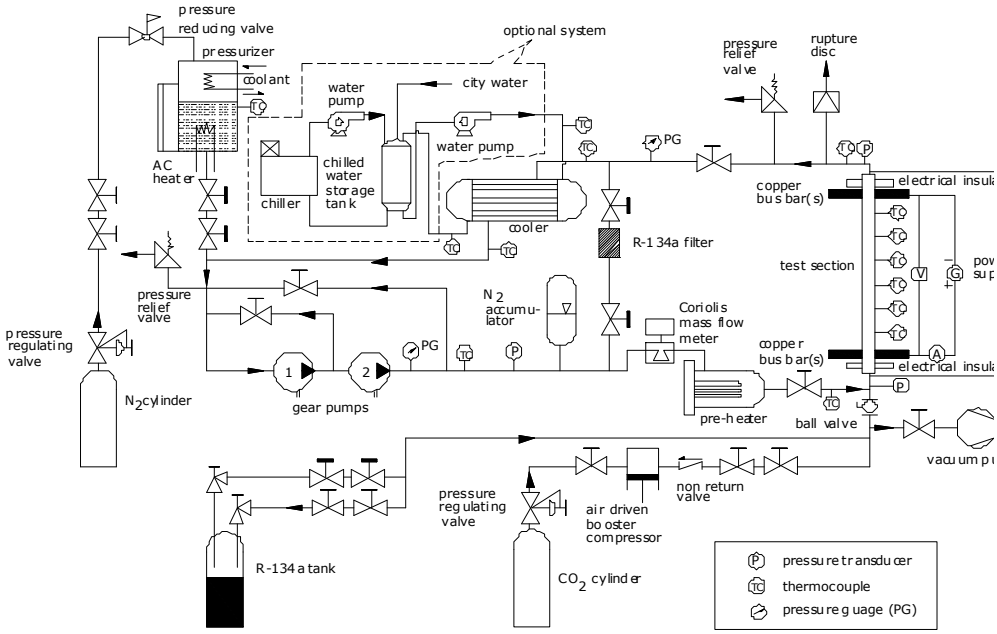

FIG. 5.13. Schematic diagram of the carbon-dioxide test facility at University of Ottawa.

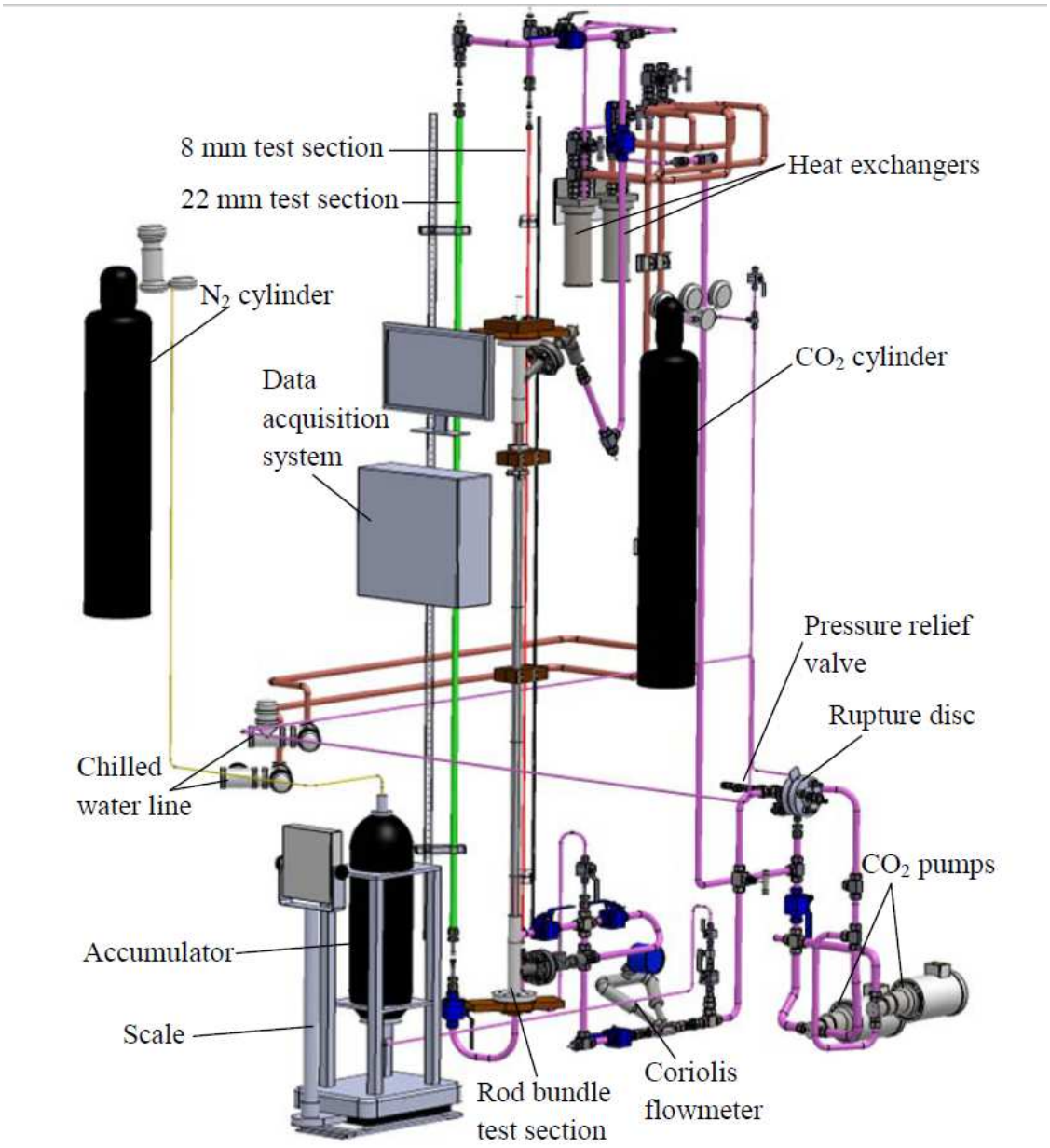

FIG. 5.14. 3-Dimensional view of the carbon-dioxide test facility at University of Ottawa.

The loop is designed for a maximum pressure of 15 MPa and a nominal operating pressure of 10 MPa. It is filled with CO_2 from cylinders with an internal pressure of 13 MPa through a regulating valve. CO_2 flow is driven by a gear pump (Cole-Palmer, Model GLH23.JVS; E.M2N1CH15). A second pump is available for operation in parallel with the first one to increase the flow rate; additional pumps can be installed for further increasing the flow rate. A gear pump design is adopted to keep flow fluctuations as low as possible.

A bladder accumulator is used to maintain the loop pressure at the desired value during its operation. The inner side of the bladder is connected to a pressurized nitrogen cylinder, whereas its outer side is connected to the CO_2 in the loop downstream of the pump. The accumulator is mounted on a scale so that the weight of liquid or liquid-like CO_2 in it can be monitored.

The flow rate in the loop is regulated by adjusting the pump speed using a single inverter (Cole-Parmer, Model 3PH Nema 4VFD7.5HP). A pressure relief device and a rupture disc are installed to prevent over-pressurization of the loop. The test sections are heated electrically by passing direct current through their walls; power is provided by a DC power supply rated at a maximum voltage of 60V and a maximum current of 2833A.

The CO_2 leaving the test section is cooled by passing through two single helical tube heat exchangers (Sentry Equipment Corp., Model FXF-6223U) connected in series. The secondary side of one heat exchanger is connected to the central chilled water supply. The other heat exchanger uses Dowtherm J synthetic organic heat transfer fluid (Dow Chemical Co.), which has a relatively low viscosity at low temperatures (e.g., 1.8×10^{-3} kg·m^{-1}·s^{-1} at -20°C and is much lower than that of glycol or other commonly used low temperature liquids). This facilitates lowering further the test section inlet temperature, if required. The Dowtherm J fluid is stored in a tank in a walk-in freezer and pumped to the CO_2 loop using a low-temperature pump (Dynapump Corp., Model JSB-2HP-1S, rated at 75 l/min). The same fluid is recirculated by a separate pump (Dynapump Corp., Model JSB-2HP-1S, rated at 38 l/min) to two radiators (Heat Innovations, Inc., 2-Row, 36x36) inside the freezer to maintain its temperature at a low level. Both pumps are located outside the walk-in freezer. All coolant supply lines are thermally insulated to keep heat losses to the surroundings as low as possible.

The CO_2 temperatures at the inlet and at the outlet of each test section are measured by platinum, ultra-precise, long-stem RTDs (Omega Engineering, Inc., Model P-M-1/10-8-5-1/2-G-15). The pressure in the loop is measured using a pressure transducer (Omega Engineering, Inc., Model PX01C1-3KA5T), which is installed near the inlets of the three test sections. A Coriolis-type flow meter (Micro Motion, Model CFM050M320N0A2E2ZZ) is also installed near the inlets of the test sections to measure the mass flow rate.

All signals from the sensors, the flowmeter and the scale are monitored, recorded and processed using a dedicated data acquisition and processing system (National Instruments) along with the 'Labview 2009' software interface. This system consists of a 1.73 GHz quad-core embedded controller (NI PXIE-8133) installed in a PXIE 1065 chassis that can hold up to 18 modules. Currently, there are three 32-channel thermocouple modules (NI PXI 4353) used for temperature measurement, three high-precision temperature and voltage modules (NI PXI 4351) used for temperature measurement with RTDs and one high-accuracy multifunction M-Series data acquisition (DAQ) module (NI PXI 6289) used for voltage measurement (flowmeter, pressure transducer and scale).

5.2. ON-GOING AND PLANNED SUPERCRITICAL HEAT TRANSFER EXPERIMENTS

A number of experiments are on-going or being planned for various test facilities. The majority of these experiments focus on simple test sections, such as tubes and annuli, to expand the current database and provide validation data for recent developed prediction methods. Some of these experiments have been established as commissioning tests for newly constructed facilities. A few bundle-assembly experiments have been scheduled to provide essential data for quantifying the bundle effect and validating subchannel codes and computational fluid dynamic tools.

5.2.1. Water flow

A supercritical heat transfer test is being planned at Xi'an Jiaotong University (XJTU) using a 4-rod bundle. The test aims to provide supercritical heat-transfer data for development of the supercritical heat-transfer correlation and validation of subchannel codes. Figure 5.15 illustrates the configuration of the 4-rod bundle test section. Both the inner and outer tubes of the test section are made of stainless-steel tubes. Inner tubes have an outer diameter of 8 mm and a wall thickness of 2 mm. The heated length is 0.6 m. The outer tube has an inner diameter of 30 mm and a wall thickness of 4 mm. A ceramic insulator

is inserted between the inner tubes and outer tube forming a square flow channel. Wrapped around wires are installed as the spacing device between inner tubes and between inner tubes and ceramic insulator. Sliding thermocouples are installed inside the inner tubes to measure the inner-wall temperature. The test will cover the following range of flow conditions:

Pressure: 23, 25 and 28 MPa
Mass velocity: 400, 700, 1000 $kg \cdot m^{-2} \cdot s^{-1}$
Heat fluxes: 200 - 1000 $kW \cdot m^{-2}$
Inlet fluid temperature: 200~300 ^{o}C

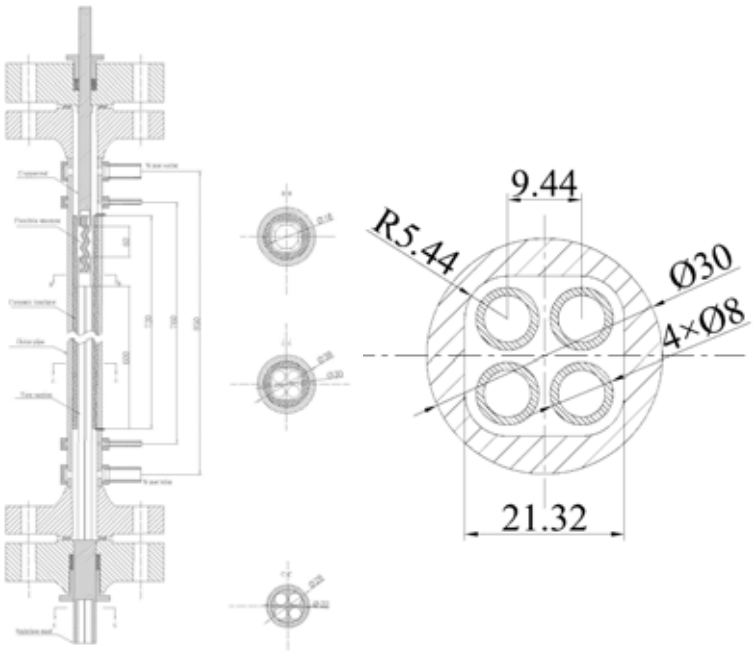

FIG. 5.15. Schematic diagram of the supercritical water 4-rod bundle test section.

5.2.2. Surrogate fluid flow

The SPHINX carbon-dioxide loop at KAERI was used to obtain a large amount of supercritical heat transfer data. No new experiments, however, are planned in the future. Two new test facilities have been constructed: one with carbon dioxide as coolant and the other with Refrigerant-134a. Both test facilities are being commissioned with tubular test sections and will be applied for bundle subassembly experiments.

An 8-mm tubular test section has been constructed for commissioning the newly constructed CO_2 test facility at the University of Ottawa [5-8]. Figure 5.16 shows the test section design, which consists of a circular tube made of Inconel-625 with an ID of 8.0 mm, a wall thickness of 1.0 mm and a length of 3.05 m. This tube is connected to the loop using electrically insulating connectors and to the power supply using two clamped electric terminals (which can be adjusted for the heated-length requirement). The nominal heated length of the tube was 1.87 metres. An unheated section of at least 1 meter (i.e., 125 diameters) has been introduced upstream of the heated section for flow development. Eleven T-type thermocouples (Omega Engineering, Inc., Model SA1XL-T-SRTC) were installed along the test section at a distance of 254 mm from each other. Table 5.1 lists proposed test conditions for commissioning of

the CO_2 Loop at University of Ottawa.

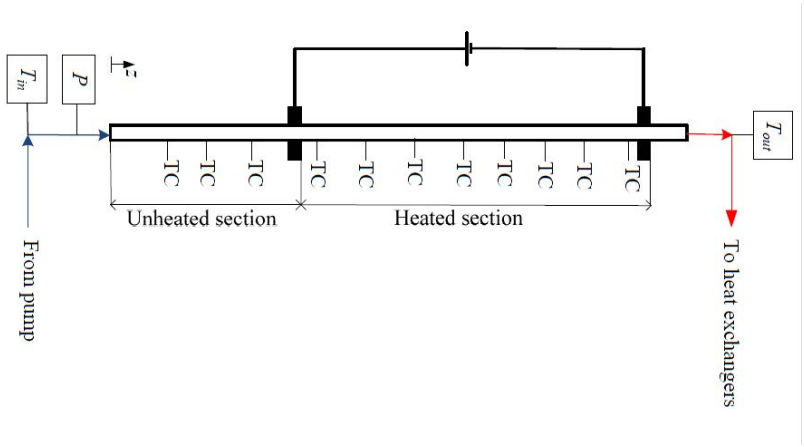

FIG. 5.16. Schematic diagram of the 8-mm tube for commissioning the CO_2 loop at University of Ottawa.

TABLE 5.1. PROPOSED CONDITIONS FOR THE COMMISSIONING TEST OF THE CO_2 LOOP AT UNIVERSITY OF OTTAWA

Parameter	Range for CO2 tests	Equivalent range in water
Inlet pressure (MPa)	6.60, 7.36, 8.36, 8.80	19.8, 22.1, 25.1, 26.4
Inlet temperature (°C)	5 – 30	320 – 350
Outlet temperature (°C)	20 – 60	350 – 435
Mass flux ($kg \cdot m^{-2} \cdot s^{-1}$)	800, 1000, 1500	594, 1188, 1782
Heat flux ($kW \cdot m^{-2}$)	20 – 500	150 – 3800

An experiment is being planned to measure wall temperatures of a 3-rod bundle in supercritical carbon-dioxide flow. Figure 5.17 shows the test section comprising a pressure tube with an inner diameter of 25.4 mm and a bundle arrangement of three directly heated rods. Three unheated rod segments are installed along the pressure-tube wall to minimize the flow bypass to the outer subchannels. Figure 5.18 presents the cross-section geometries at the endplate, spacer, and bundle sections.

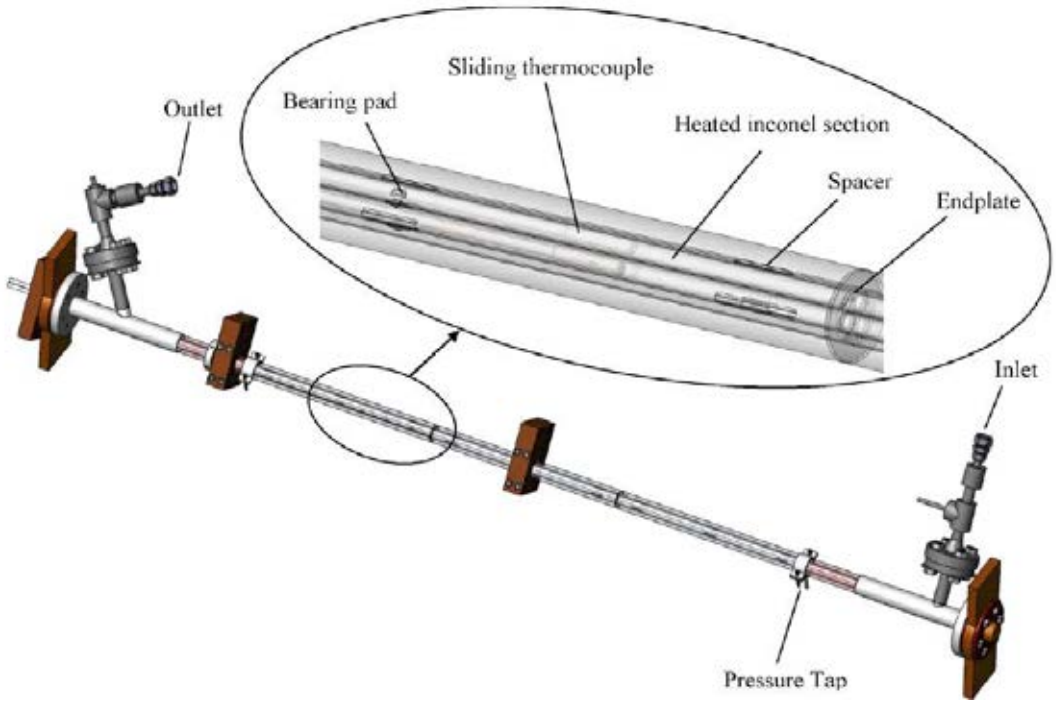

FIG. 5.17. Layout of the 3-rod bundle to be tested in the CO_2 loop at University of Ottawa.

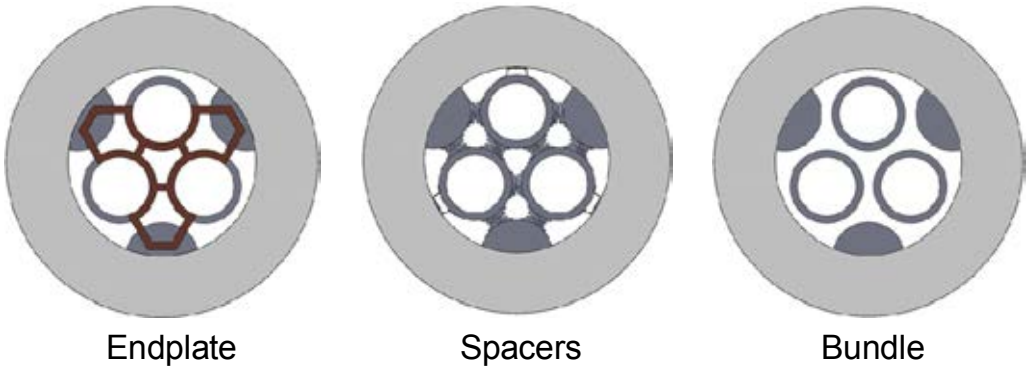

FIG. 5.18. 3-rod bundle geometry for the carbon-dioxide test at University of Ottawa.

The rod bundle has five sections, each 500-mm long, connected in series and separated from the neighbouring sections by endplates. Pads are positioned between the rods and on the rod sides that face the pressure tube at regular intervals to ensure that the gaps remain as uniform as possible. The first and last sections of the rod bundle are made of copper, whereas the three sections in the middle are made of Inconel, so that only these three sections are subject to significant direct heating. The rod diameter is 10.0 mm and the pitch to diameter ratio is 1.14. The hydraulic diameter of the rod bundle is 6.7 mm and the flow area is 177 mm^2.

The ends of the three rods are fastened on copper plates, which are connected to the power supply. The inner surface of the pressure tube is electrically insulated. Each of the three rods in the last heated section of the rod bundle contains a sliding thermocouple assembly. This assembly consists of a carriage rod, near the upstream end of which two insulated K-type thermocouples are mounted across from each other. A loaded spring pushes each thermocouple against the heated surface to ensure good thermal contact. Each thermocouple may be rotated within the rod over 360° and traversed along the rod over a distance of 378 mm.

Heat transfer and pressure drop measurements in the rod bundle will be conducted over the same ranges of conditions as those listed in Table 5.1. The axial and azimuthal variations of wall temperature in the three rods of the last heated section will be measured and used to calculate the heat transfer coefficient. These results will be compared to available measurements in tubes and predictions of empirical correlations. Of particular interest will be to determine whether deteriorated heat transfer occurs in flow under supercritical pressures in rod bundles, and, if so, the conditions under which it does.
Available test facilities for supercritical heat transfer experiments using water or surrogate fluids as coolant have been described. Most of these facilities have relatively small capacity and hence are applicable for experiments with simple test sections and small bundle subassemblies. A new water test facility and two surrogate-fluid test facilities have recently been constructed. These facilities are equipped with advanced instrumentation minimizing the measurement uncertainty.

Experiments have been planned using simple test sections (mainly tubes for loop commissioning) and small bundle assemblies. These data are essential for establishing the bundle effect on supercritical heat transfer and for validating the subchannel code and computational fluid dynamic tools.

The planned experiments cover simple bundle subassemblies (either 3 rods or 4 rods only). Experimental data may not be applicable to complex bundle effect in large assemblies. In addition, all rods in the bundles are uniformly heated. Therefore, experimental data on separate effects, such as axial and radial power profiles, will still be required.

REFERENCES FOR SECTION 5

[5-1] CHEN, Y., YANG, C., ZHAO, M., DU, K., ZHANG, S., "Progress on The Research of Thermal-Hydraulics for SCWR in CIAE", Proc. 2nd Canada-China Joint Workshop on Supercritical Water-Cooled Reactors (CCSC-2010), Toronto, Ontario, Canada, April 25–28, 2010 (2010).

[5-2] SCHMIDT, H., KÖHLER, W., KASTNER, W., High-Pressure Test Facility -25 Years of Operation, Framatome ANP GmbH Report, March (2001).

[5-3] KIRILLOV, P.L., "Experimental and Numerical Researches of Supercritical Water Heat transfer in Rod Bundles", Institute for Physics and Power Engineering Report submitted to IAEA (Research Contract No. 15221) (2011).

[5-4] LICHT, J., ANDERSON, M., CORRADINI, M., Heat Transfer and Fluid Flow Characteristics in Supercritical Pressure Water, Journal of Heat Transfer, 131 (Compendex) (2009) 1–14.

[5-5] LICHT, J., ANDERSON, M., CORRADINI, M., Heat Transfer to Water at Supercritical Pressures in A Circular and Square Annular Flow Geometry, International Journal of Heat and Fluid Flow, 29 (Compendex) (2008) 156–166.

[5-6] WU , G., BI, Q., YANG , Z., LI, M., "Experimental Investigation on Heat Transfer of Supercritical Pressure Water in Annular Channel", Proc. 2nd Canada-China Joint Workshop on Supercritical Water-Cooled Reactors (CCSC-2010), Toronto, Ontario, Canada, April 25–28, 2010 (2010).

[5-7] KIM, H.Y., KIM, H., SONG, J.H., CHO, B.H., BAE, Y.Y., Heat Transfer Test in A Vertical Tube Using CO_2 at Supercritical Pressures, Journal of Nuclear Science and Technology, **44** (3) (2007) 1–9.

[5-8] JEDDI, L., JIANG, K., TAVOULARIS, S., GROENEVELD, D.C., "Preliminary Tests at the University of Ottawa Supercritical CO_2 Heat Transfer Facility", Proc. 5th Int. Sym. SCWR (ISSCWR-5), Vancouver, British Columbia, Canada, March 13–16, 2011 (2011).

6. DEVELOPMENT OF NEW CORRELATIONS FOR HEAT TRANSFER TO SUPERCRITICAL PRESSURE FLUIDS

6.1. INTRODUCTION

6.1.1. Purpose

As part of this IAEA coordinated research project, new approaches and equations have been developed for determining heat transfer to fluids at supercritical pressure. The introductory material which follows sets the scene for this activity and also provides those who are new to the field with a picture of early developments, some general background, a picture of the state of the art and research priorities.

6.1.2. Early work on heat transfer to fluids at supercritical pressure

Research on heat transfer to fluids at supercritical pressure dates back to the late 1950's when advances in the design of thermal power plant aimed at improving thermal efficiency led to the development of once-through steam generators operating at supercritical pressure (see Miropolsky and Shitsman [6-1], Dickinson and Welch [6-2], Shitsman [6-3], Schmidt [6-4] and Petukhov et al. [6-5]). At that time, supercritical pressure water was also being actively considered as a coolant for advanced nuclear reactors (Goldman [6-6,6-7]), hydrogen and oxygen were being studied in connection with rocket propulsion systems (Powell [6-8], Hsu and Smith [6-9] and Hendricks et al. [6-10]) and supercritical pressure helium was becoming of interest in connection with the cooling large electromagnets. Supercritical pressure carbon dioxide was mainly being used as a convenient working fluid for fundamental experimental studies (Bringer and Smith [6-11]).

As early as 1953, severe, localized impairment of heat transfer to supercritical pressure water flowing upwards through an electrically heated vertical tube was reported by Shitsman [6-3] (also see Shitsman [6-12]). By the mid 1960s a widespread interest had developed in heat transfer to fluids at supercritical pressure. A detailed review of work up to that time was published in 1968 by Hall, Jackson and Watson [6-13]. In that paper, a comparison was presented of heat transfer coefficients calculated using the correlation equations for forced convection heat transfer to supercritical pressure water which were available then. The coefficients were presented as a function of wall temperature for water at 254 bar at a specified bulk temperature of 360^{o}C. Agreement in terms of the values obtained proved to be poor and it was concluded that:-

(a) The available equations were inadequate as a means of describing heat transfer in the critical region;
(b) There existed sets of data for apparently similar conditions which exhibited radically different behaviour;
(c) The effect of buoyancy on flow and heat transfer did not appear to have received sufficient attention.

On the basis of these conclusions it was recommended that: a series of carefully planned experiments should be undertaken with due attention being paid to the additional mechanisms that might affect the heat transfer process; that more research should be done on heat transfer under buoyancy-influenced conditions; that turbulence measurements should be made in fluids at supercritical pressure; that systematic experiments aimed at resolving questions concerning thermal development under conditions forced convection heat transfer should be performed and; finally, that selected experiments should be repeated using a variety of fluids.

The above-mentioned review, coincided with one by published Petukhov [6-14], which described work on heat transfer to supercritical pressure fluids in the USSR. This was followed soon afterwards, by a

review produced in the USA by Hendricks et al [6-15].

6.1.3. Buoyancy-induced deterioration of heat transfer with fluids at supercritical pressure

Although as early as 1963 striking localized deterioration of heat transfer with upward flow of water in a heated vertical tube had been observed by Shitsman, it was not until three years later that this was shown by experiments with upward and downward flow under otherwise identical conditions to be due to the influence of non-uniformity of density in the fluid and the action gravity and thought of in terms of the concept of buoyancy. This mode of heat transfer is often referred to as 'combined free and forced convection' or 'mixed convection'. Soon afterwards (1969) Hall and Jackson [6-16] demonstrated by means of a simple physically-based semi-empirical model that the impairment of heat transfer with upward flow was a consequence of greatly reduced production of turbulence, an effect which is sometimes described as partial laminarization of a turbulent flow.

6.1.4. Some ideas for correlating, screening and categorizing experimental data

A useful outcome of the modeling study of Hall and Jackson [6-16] was the identification of a parameter $Gr_b / \mathrm{Re}_b^{2.7}$ which combines Grashof number and Reynolds number in a manner designed to characterize the strength of the buoyancy influence. An attempt was made using it to correlate the data of Fewster [6-17] for carbon dioxide at supercritical pressure obtained using three tubes of different diameter. This proved to be successful for conditions of fully-developed heat transfer with downward flow but not for upward flow (see Jackson and Hall [6-18]).

Another outcome was the development of criteria for determining the conditions under which buoyancy effects can be neglected and the mode of heat transfer is forced convection rather than mixed convection (again see Jackson and Hall [6-18]). For conditions where the wall temperature did not exceed the pseudo-critical value, the criterion for the buoyancy effect to be less than 5% was found to be $\overline{G}r_b /(\mathrm{Re}_b^{2.7}\,\mathrm{Pr}_b^{0.5}) < 10^{-5}$. The corresponding one for conditions where the wall temperature exceeded the pseudo-critical value was $\overline{G}r_b / \mathrm{Re}_b^{2.7} < 10^{-5}$.

6.1.5. Forced convection heat transfer with non-uniform fluid properties

For fully developed, variable property forced convection heat transfer with fluid at a specified pressure above the critical value, the appropriate dimensionless parameters for correlating experimental data are Reynolds number $\mathrm{u_b D / v_b}$, Prandtl number $\mu_b c_{p_b} / k_b$ and thermal loading parameter $\mathrm{q_w D/(k_b T_b)}$ (see Jackson and Hall [6-19]). Thus a functional relationship of the following form is applicable

$$\left(\frac{\mathrm{q_w D}}{\mathrm{k_b}\left(\mathrm{T_w - T_o}\right)}\right) = \psi\left[\left(\frac{\mathrm{u_b D}}{\mathrm{v_b}}\right),\left(\frac{\mu_b \mathrm{c_{p_b}}}{\mathrm{k_b}}\right),\left(\frac{\mathrm{q_w D}}{\mathrm{k_b T_b}}\right)\right] \tag{6.1}$$

The thermal loading parameter $\left(\mathrm{q_w D / k_b T_b}\right)$ affects the magnitude of the temperature variation within the fluid and, therefore, the extent of the non-uniformity of fluid properties. However, in the various approaches which were adopted to correlate experimental data for variable property forced convection that parameter was not employed directly to account for fluid property non-uniformity. Instead, 'variable property effects' were accounted for by adding carefully chosen ratios of certain properties evaluated at the wall and bulk temperatures to well-established correlation equations for constant property forced convection.

6.1.6. An evaluation of equations for forced convection heat transfer to supercritical pressure fluids

An evaluation of equations for forced convection heat transfer to fluids at supercritical pressure was reported in 1975 by Jackson et al [6-19] (see Jackson and Hall [6-20]). Sixteen equations were used to calculate heat transfer coefficients for approximately 2000 different experimental conditions. About 75% of the data points were for water and the remainder were for carbon dioxide. It should be noted that all the data used had been carefully screened using the criteria quoted earlier to exclude any for which the influence of buoyancy might have been significant. The discrepancies between calculated and experimental values were evaluated and tabulated (see Jackson and Hall [6-20]). The approach of Krasnoschekov and Protopopov [6-21] proved to be the most effective. A slightly modified form of it in which the constant properties forced convection equation of Petukhov and Kirillov [6-22] was replaced by a simpler Dittus-Boelter type expression with a coefficient of 0.0183 and a Reynolds number index of 0.82 was also tried and found to be equally good. If the more widely used combination of values, 0.023 and 0.8, (see Kays [6-23]), had been used instead, as in the version presented below, the results obtained would have been virtually the same

$$Nu_b = 0.023 \mathrm{Re}_b^{0.8} \ \mathrm{Pr}_b^{0.4} \left(\frac{\rho_w}{\rho_b} \right)^{0.3} \left(\frac{\bar{c}_p}{c_{p_b}} \right)^{n_2} \tag{6.2}$$

The value of the index n_2 in the specific heat ratio term depends on the values of T_w and T_b in relation to the pseudo-critical value T_{pc} and is determined using the following set of three simple equations specified by Krasnoschekov and Protopopov.

$$\begin{aligned} &n2 = 0.4 \text{ for } Tb < Tw < Tpc \text{ and for } 1.2\ Tpc < Tb < Tw \\ &n2 = 0.4 + 0.2\ ((Tw/Tpc) - 1) \text{ for } Tb < Tpc < Tw \\ &n2 = 0.4 + 0.2\ ((Tw/Tpc) - 1)\ (1 - 5\ ((Tb/Tpc) - 1)) \\ &\text{for } Tpc < Tb < 1.2\ Tpc \text{ and } Tb < Tw \end{aligned} \tag{6.3}$$

The index n_2 was approximately 0.4 for many of the conditions covered in the evaluation exercise.

The equations proposed earlier (1965) by Bishop et al [6-24] and Swenson et al [6-25] performed reasonably well in the evaluation. They are shown below as Equations 6.4 and 6.5 respectively.

$$Nu_b = 0.00459\, \mathrm{Re}^{0.923}\, \overline{\mathrm{Pr}}_w^{0.613} \left(\frac{\rho_w}{\rho_b} \right)^{0.231} \tag{6.4}$$

$$Nu_b = 0.0067\, \mathrm{Re}_b^{0.9}\, \overline{\mathrm{Pr}}_b^{0.66} \left(\frac{\rho_w}{\rho_b} \right)^{0.43} \tag{6.5}$$

However, a better compromise in terms of all round performance was obtained using the following simplified version of Equation 6.2 where a constant value of 0.4 is used for n_2, and $\overline{\mathrm{Pr}}_b = \mu_o \bar{c}_p / k_b$ (see Jackson and Hall [6-20]).

$$Nu_b = 0.023\ \mathrm{Re}_b^{0.8}\ \overline{\mathrm{Pr}}_b^{0.4} \left(\frac{\rho_w}{\rho_b} \right)^{0.3} \tag{6.6}$$

It is of interest to note the similarity between this equation and those of Bishop et al and Swenson et al, but also to notice that the values of the coefficient 0.023 and Reynolds number index 0.8 in Equation 6.6 are very different from those in Equations 6.4 and 6.5. The latter were established by fitting the equations to the experimental data available at that time for upward flow in heated vertical tubes. Some of those data were certainly influenced by buoyancy (no means of screening the data for buoyancy influence had been developed in 1965 at the time that the Bishop et al and Swenson et al correlation equations were proposed).

6.1.7. Conditions for achieving similarity with fluids at supercritical pressure

Soon after the phenomenon of buoyancy-induced laminarization of a turbulent flow had been identified as a mechanism for the severe deterioration of heat transfer sometimes found with upward flow fluids at supercritical pressure in heated tubes (impaired mixed convection) a further mechanism for deterioration was identified. This was also due to the temperature dependence of density and an associated effect of this on turbulence. However, it did not depend on gravity because it occurred with both upward and downward flow under otherwise identical conditions. This is why it is sometimes referred to as 'impaired forced convection'.

The details of this second mechanism are best discussed after first considering the requirements for similarity in the case of heat transfer to fluids with highly temperature dependent fluid properties. These can be established by representing the governing equations, initial conditions and boundary conditions for flow in a heated tube in non-dimensional form (see Jackson and Hall [6-20]). This enables the following statements to be made concerning similarity between two geometrically similar thermal systems A and B in the form of vertical heated tubes of different diameter with wall heat fluxes and inlet velocities which are different:-

If the same fluid is involved in each case, and the reduced pressure p_o/p_c at inlet and the reduced temperature T_o/T_c at inlet are the same for each system, and, furthermore, if the following conditions are satisfied, $(u_o D/\nu_o)_A = (u_o D/\nu_o)_B$ (equal Reynolds numbers) and, $(q_w D/(k_o T_o))_A = (q_w D/(k_o T_o))_B$ (equal thermal loading parameters), and the characteristic dimensions of the systems are small enough that no significant influence on the flow field of buoyancy is experienced but large enough that effects of compressibility and viscous dissipation are negligible, then complete similarity can be achieved.

This rather limited possibility of achieving complete similarity was discussed in a note by Hall and Jackson [6-26]. There they argued that where the above requirements in terms of Reynolds number and thermal loading parameter are met, measurements of wall temperature from experiments using tubes of different diameter should coincide if plotted on a base of bulk temperature or bulk enthalpy.

This was demonstrated experimentally by Harrison and Watson in 1976 [6-27] see Figure 6.1, using water at supercritical pressure in tubes of relatively small diameter (1.64 mm and 3.10 mm) where the absence of any significant buoyancy influence was checked by performing experiments with upward and downward under otherwise identical conditions.

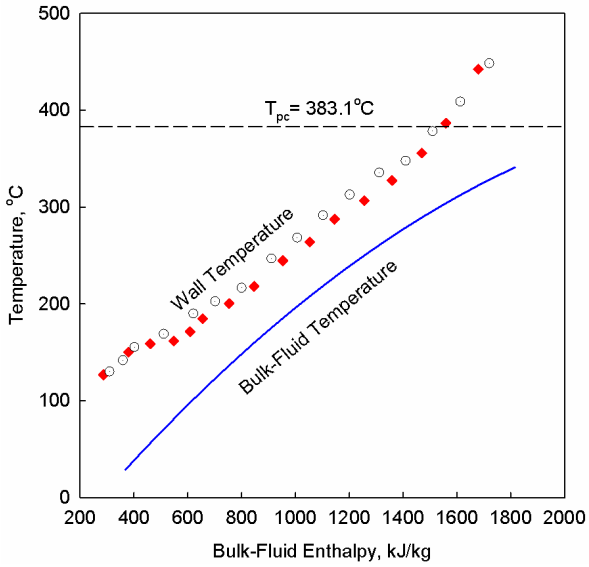

FIG. 6.1. Measured wall temperatures for 'similar' conditions.

6.1.8. The further mechanism for heat transfer deterioration – acceleration-induced laminarization

Where wall temperature distributions are compared on the basis described in the preceding section and found to differ, this points to the presence of a significant influence of buoyancy or thermal expansion/compressibility being present. Figure 6.2, from Hall and Jackson [6-26], shows three sets of results from separate investigations where the Reynolds number, $u_o d/v_o$, and thermal loading parameter, $q_w D/k_o T_o$, are very similar in each case. Two are influenced by buoyancy (because the temperature distributions for upward and downward flow under otherwise identical conditions are very different) and one is not (because the results for upward and downward flow were more or less the same). The sharp wall temperature peaks present for upward flow in the buoyancy influenced case are indicative of strong localized buoyancy-induced deterioration of heat transfer which we could refer to as 'impaired mixed convection'. The wall temperature distribution in the non-buoyancy-influenced case, which also rises to peak value and then falls, is also indicative of strong deterioration of heat transfer ('impaired forced convection'). The mechanism which has been proposed to explain this phenomenon is based on the idea that the density falls along the tube. This can be due to increase of temperature and also reduction of pressure. The associated acceleration of the flow leads to reduced turbulence and impairment of heat transfer. Thus, in order to correlate data for 'impaired forced convection' additional dimensionless groups need to be employed which involve the thermal expansion coefficient and compressibility.

Note, the contrast between the wall temperature distribution for impaired forced convection, which is in the form of a broad peak (data of Shiralkar and Griffith [6-28, 6-29]), and the sharp localized buoyancy-induced wall temperature peaks which are present for upward flow data in the other two cases, (taken from Hall and Jackson [6-16] and Bourke et al [6-30]). Note also that, downstream of those peaks the effectiveness of heat transfer is much better than for impaired forced convection, as is also the case in the corresponding downward flow experiments. The distinction between buoyancy-induced deterioration of heat transfer and acceleration-induced deterioration of heat transfer (impaired forced convention) which the above ideas illustrate so clearly, is of considerable importance.

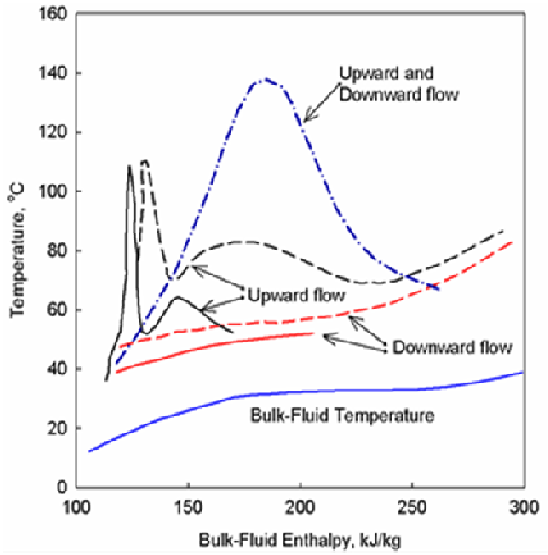

FIG. 6.2. Experimental results compared on a forced convection basis (Hall and Jackson [6-26]); all lines above the bulk temperature are wall temperatures.

6.1.9. Summary of the background material, ideas and effects discussed in this introductory material

In this introductory section a number of important matters have been covered which are of direct relevance to the task of developing improved correlation equations for heat transfer to supercritical pressure fluids:-

(a) The effect of buoyancy in causing strong localized deterioration of heat transfer is highlighted;
(b) A physically-based model of the phenomenon of buoyancy-induced laminarization which explains localized deterioration of heat transfer is outlined;
(c) An attempt to correlate data on buoyancy-influenced heat transfer to carbon dioxide at supercritical pressure using a local dimensionless parameters provided by the model is described;
(d) Criteria based on the model are presented for determining the conditions under which the effect of buoyancy influence is small enough to be neglected;
(e) Some questions are raised concerning the limitations of early empirical equations for forced convection heat transfer to supercritical pressure water;
(f) The requirements for strict similarity in the case of heat transfer to fluids at supercritical pressure are stated;
(g) The idea of limited similarity is used to illustrate the phenomenon of impaired forced convection heat transfer;
(h) The need to develop extended equations which account for and describe the effects of buoyancy and bulk flow acceleration on heat transfer to fluids at supercritical pressure is highlighted.

The remainder of this section is devoted to work which has been carried in the course of the IAEA CRP to develop equations which are able to describe heat transfer behaviour with fluids at supercritical pressure more reliably taking.

6.2. DEVELOPMENT OF A TRANS-CRITICAL LOOK-UP TABLE AND ASSESSMENT OF CORRELATION EQUATIONS BY ATOMIC ENERGY OF CANADA LTD. (AECL), THE UNIVERSITY OF OTTAWA (U OF O) AND THE UNIVERSITY OF ONTARIO INSTITUTE OF TECHNOLOGY (UOIT)

6.2.1. Trans-critical heat transfer database

Zahlan, Groeneveld and Tavoularis [6-31] have reported work on the development of a heat transfer look-up table for use in the case of upward flow of water in tubes at supercritical pressure near the critical point. The intention was to construct a table that would cover all conditions for which reliable correlation equations are not available. To this end, a large databank has been compiled at the University of Ottawa. This originally contained 36,030 data points. After screening this databank a final version containing more than 24,000 screened data points was produced. The method of screening the data, which involved removing, (i) duplicates (runs and points between different datasets and within a dataset), (ii) data that did not satisfy a simple heat balance, and (iii), obvious outliers, is described in Zahlan et al [6-32]. It was not designed to eliminate data on the basis of buoyancy influence being significant.

The databank was the result of the combination of four different databases. Table 6.1 shows a summary of the SCHT water databases from different sources which were used. Some of these data were extracted from graphs using data digitization software (as were some of the data included in the original U of O database). Frequently, more than one set of SCHT data covers similar flow conditions.

TABLE 6.1 SCHT WATER DATA COMPILATION

Database source	Number of references	Number of data points after screening	Form of original data
UO	28	6024	Tables and graphs
SJTU	11	7168	Tables and graphs
Stuttgart U	15	2936	Tables and graphs
UOIT	20	8125	Tables and graphs
Combined databank for all four databases			
Number of data before screening	36030	Number of data after screening	24253

At an earlier stage, the SCHT data were classified into three distinctive supercritical sub-regions: (i) a high density state (liquid-like) region ($T_w < T_{pc}$ and $T_b < T_{pc}$), (ii) a near-critical or near-pseudo-critical region ($T_{pc} < T_w$ and $T_b < T_{pc}$), and (iii) a low density (gas-like) region ($T_{pc} < T_w$ and $T_{pc} < T_b$). This classification was intended to take into consideration the distinct heat transfer modes associated with the sub-regions. However, that approach did not account for the fact that the thermophysical properties change very significantly within a particular range of temperatures near the pseudo-critical value. Therefore, it was decided to redefine the boundaries of the near-critical/pseudo-critical region by introducing a narrow range of temperatures $T_{pc} - \Delta T < T < T_{pc} - \Delta T$, within which the thermophysical properties change significantly. It was found that this range was described fairly well for different pressures by the empirical relationship $\Delta T/T_{pc} = 3.1\times10^{-3}(P/P_c)$, where the numerical values of all temperatures are in degrees K. Each SCW data point was classified as being in one of these three re-defined sub-regions: (i) a high density state (liquid-like) region (T_w, $T_b < T_{pc} - \Delta T$), (ii) a near-critical or near-pseudo-critical region ($T_{pc} - \Delta T < T_w$ and $T_b < T_{pc} + \Delta T$), and (iii) low density state (gas-like) region ($T_{pc} + \Delta T < T_w$, T_b).

6.2.2. Approach adopted to developing the trans-critical look-up table

The development of the look-up table first required the construction of a skeleton table to provide the initial estimates of the heat transfer coefficient (*HTC*) values at discrete values of the independent parameters, pressure (*P*), mass flux (*G*), coolant enthalpy (H_b) and heat flux or wall temperature. A skeleton table which present *HTC* as a function of *p, G, D,* H_b, ΔT_w was developed at U of O. Values from the table were used for evaluating the gradients of HTC with respect to *p*, *G* and H_b. The table included default values based on predictions from successful heat transfer correlation equations for conditions at which no experimental data were available. The skeleton table was not smooth and exhibited an irregular variation (devoid of any physical basis) with the three parameters *p, G* and H_b. These fluctuations are attributed to data scatter, systematic differences between different data sets, and possible effects of secondary parameters such as heated length, surface conditions and flow stability. Sharp variations in heat transfer coefficient are also likely be observed at boundaries between regions where experimental data are available and regions where correlations, or other approaches have had to be employed, and also at the lower pressure limit where the changeover is necessary to using subcritical prediction methods for film boiling, CHF or single phase heat transfer.

6.2.3. An assessment of empirical heat transfer calculation methods

An assessment of available heat transfer correlation equations was carried out. This covered more empirical equations than earlier evaluation exercises and compared them against a much larger database than had been available hitherto. Twelve SCHT correlation equations and four single-phase equations were evaluated. The details of the correlations can be found in Zahlan, Groeneveld, Tavoularis, Mokry and Pioro [6-32].

The overall average error (e_A) and the root mean square (rms) error (e_S) were calculated for all the correlation equations. The distributions of e_A and e_s for the equations which performed best were presented by Zahlan et al [6-31] with respect to Re_b, Pr_b, and P/p_c in the form of plots for the three SCHT regions for the combined U of O database. Table 6.2 compares the average and rms errors in the three supercritical regions (i) close to the critical or pseudo-critical point, (ii) the high-density or liquid-like state and (iii) the low-density or gas-like state, for the sixteen equations assessed. It can be seen that the Mokry et al equation [6-33], which dates from 2009, has the least rms error in each of the three SCHT regions.

An error analysis and an examination of parametric trends were performed for the most promising correlations. Table 6.3 shows five of the equations which performed well (the Swenson et al and Bishop et al equations, which also performed quite well, can be found earlier in this section, see Equations 6.4 and 6.5 in Section 6.1.3). Table 6.4 shows the results for error bands of +10% (e10), +20% (e20), +30% (e30), and +50% (e50) calculated using the equations which performed best. The Mokry et al equation is again seen to be the most successful one in terms of describing the data overall. For a recent review of correlation equations for heat transfer to fluids at supercritical pressures see Pioro and Mokry (2011) [6-34].

TABLE 6.2. OVERALL AVERAGE AND RMS ERRORS IN THE THREE SUPERCRITICAL SUB-REGIONS

Correlation	**Liquid-like region**		**Gas-like region**		**Close to CP or PC point**	
	e_A, %	e_S, %	e_A, %	e_S, %	e_A, %	e_S, %
Bishop et al. (1965) [6-24]	5	28	5	20	23	31
Swenson et al. (1965) [6-25]	1	31	-16	21	4	23
Krasnochekov (1967) [6-21]	18	40	-30	32	24	65
Watts and Chou (1982) [6-35], Normal heat transfer	6	30	-6	21	11	28
Watts and Chou (1982) [6-35], Deteriorated	2	26	9	24	17	30
Griem (1996) [6-36]	2	28	11	28	9	35
Jackson et al (1975) [6-19]	15	36	15	32	30	49
Mokry et al. (2009) [6-33]	-5	26	-9	18	-1	17
Kuang et al. (2008) [6-37]	-6	27	10	24	-3	26
Cheng et al. (2009) [6-38]	4	30	2	28	21	85
Gupta et al. (2010) [6-39]	-26	33	-12	20	-1	
Koshizuka and Oka (2000) [6-40]	26	47	27	54	39	
Hadaller and Banerjee (1969) [6-41]	34	53	14	24	-	-
Sieder and Tate (1936) [6-42]	46	65	97	132	-	-
Dittus-Boelter (1930) [6-43]	24	44	90	127	-	18
Gnielinski (1976) [6-44]	10	36	99	139	-	83

TABLE 6.3. DETAILS OF SOME OF THE EQUATIONS WHICH PERFORMED WELL IN THE EVALUATION STUDY

Reference	**Equations**
Watts and Chou (1982) [6-35]	$Nu_b = 0.021\mathrm{Re}_b^{0.8}\,\mathrm{Pr}_b^{0.55}(\frac{\rho_w}{\rho_b})^{0.35} f(Bo_b)$ in which $\mathrm{Bo_b} = \overline{\mathrm{Gr}}_\mathrm{b}/(\mathrm{Re}_\mathrm{b}^{2.7}\,\mathrm{Pr}^{0.5})$, where $\overline{\mathrm{Gr}}_\mathrm{b} = \mathrm{gD}^3(\rho_\mathrm{b} - \overline{\rho})/(\rho_\mathrm{b}\mathrm{v}_\mathrm{b}^2)$ $f(Bo_b) = [1 - 3000Bo_b]^{0.295}$ $if\ Bo_b \le 10^{-4}, or\ f(Bo_b) = (7000Bo_b)^{0.279}\ if\ Bo_b > 10^{-4}$
Kuang et al (2008) [6-37]	$Nu_b = 0.023\mathrm{Re}_b^{0.759}\mathrm{Pr}^{0.833}\overset{*}{F}(Gr)^{0.014}(\overset{+}{q_w})^{-0.021}$ in which $F = (k_w/k_b)^{0.832}(\mu_w/\mu_b)^{0.832}(\rho_w/\rho_b)^{0.31}$
Mokry et al (2009) [6-33]	$Nu_b = 0.0061\ \mathrm{Re}_b^{0.904}\overline{\mathrm{Pr}}_b^{0.684}(\rho_w/\rho_b)^{0.564}$
Gupta et al (2010) [6-39]	$Nu_b = 0.0033\mathrm{Re}_w^{0.941}\mathrm{Pr}_{avg,w}^{0.764}(\rho_w/\rho_b)^{0.156}(\mu_w/\mu_b)^{0.398}$
Bishop et al (1965) [6-24]	$Nu_b = 0.0069\mathrm{Re}_b^{0.9}\overline{\mathrm{Pr}}_b^{0.66}(\rho_w/\rho_b)^{0.43}(1 + 2.4D/L)$

TABLE 6.4. ERROR BANDS FOR THE MOST SUCCESSFUL EQUATIONS IN THE THREE SCHT REGIONS

Error band for 15283 data points	**Percentage of data predicted by a correlation, %**		
	Mokry et al. (2008)	Gupta et al. (2010)	Swenson et al. (1965)
Near CP region			
e_{10}	46	50	44
e_{20}	79	78	71
e_{30}	92	91	86
e_{50}	99	98	95
Error band for 4386 data points	Mokry et al. (2008)	Watts & Chou (1982), DHT	Kuang et al. (2008)
High density state region (liquid-like region)			
e_{10}	41	28	33
e_{20}	64	57	59
e_{30}	79	79	79
e_{50}	94	95	94
Error band for 4584 data points	Mokry et al. (2008)	Gupta et al. (2010)	Bishop et al. (1965)
Low density state region (gas-like region)			
e_{10}	47	35	45
e_{20}	79	71	75
e_{30}	92	88	89
e_{50}	99	98	97

6.2.4. Conclusions

The extended and screened databank for supercritical pressure water compiled by U of O for use in the development of a trans-critical pressure LUT has been used in the assessment of the performance of available empirical equations for describing heat transfer to water at supercritical pressure with upward flow. It should be noted, however, that the databank was not screened to eliminate buoyancy-influenced results. The equation which proved to be the most successful overall in describing the data was that of Mokry et al 2009 [6-33].

6.3. AN APPROACH BY SHANGHAI JIAO TONG UNIVERSITY (SJTU) TO THE CORRELATION OF DATA AND THE CALCULATION OF HEAT TRANSFER TO SUPERCRITICAL PRESSURE FLUIDS USING A NEW CORRELATION EQUATION

6.3.1. Introduction

An approach developed by Cheng, Yang and Huang 2009 [6-45] to establish a new correlation equation for calculating heat transfer to supercritical fluids is presented in this sub-section. Emphasis was put on the simplicity of the equation and explicit connection with physical phenomena. Based on a phenomenological assessment of heat transfer behaviour a new structure of heat transfer correlation is proposed, which involves one single dimensionless number and excludes the direct dependence of heat transfer coefficient on tube wall temperature.

Most empirical correlations equations take the general form of a modified Dittus-Boelter equation, $Nu_b = C \cdot \mathrm{Re}_b^n \mathrm{Pr}_b^n F$. The correction factor F takes into account effects resulting from property non-

uniformity due to the variation of temperature between the tube wall and the bulk fluid values. In several of the correlation equations which have been proposed, the correction factor involved the density ratio, and specific heat ratio, ρ_w/ρ_b and $\bar{c}_p/c_{p_b}$, (where $\bar{c}_p = (h_w - h_b)/(T_w - T_b)$).

6.3.2. The new heat transfer correlation

The following criteria were used in deciding the structure of the correction factor F:-

1) The correlation should be based on dimensionless numbers, so that it can be applied to various fluids;
2) It should contain as few parameters as possible;
3) It should cover both normal and deteriorated heat transfer (DHT) conditions; and
4) It should not contain the tube wall temperature or parameters depending on it.

Based on phenomenological analysis and assessment using the test data of Herkenrath et al. (1967) [6-45], the following structure was proposed,

$$Nu = 0.023\,\mathrm{Re}_b^{0.8}\,\mathrm{Pr}_b^{1/3}\,F\,,$$

in which F = min(F_1, F_2), where $F_1 = 0.85 + 0.776\left(\pi_A \cdot 10^3\right)^{2.4}$

and $F_2 = 0.48\left(\pi_{A,PC} \times 10^3\right)^{-1.55} + 1.21 \times \left(1 - \pi_A/\pi_{A,PC}\right)$

(6-7)

The acceleration number π_A is defined as $\beta q_w/(c_p G)$.

A selected dataset from of the experimental results of Herkenrath et al. was used to establish the equations. That experimental study was chosen because of the large number of test data points and the well documented experimental procedure. The parameter range of the test data was: Inside diameter of the tube, 10mm, 20mm; pressure: 22.5, 23.5, 24.0, 25.0 MPa, mass flux: 700, 1000, 1500, 2250, 3500 kg/m^{2}s; heat flux: 0.3 – 2.0 MW/m^2; bulk temperature: 300^{o}C – 450^{o}C; number of data points used: 2152 (compared with 4599 measured).

6.3.3. Assessment of the new equation

Figure 6.3 shows plots of the ratio of the measured and calculated Nusselt numbers versus, (a) Reynolds number, (b) Prandtl number and (c) Acceleration number. For nearly all the data points the ratio varies between 0.5 and 1.5. There was no systematic deviation associated with the various parameters. However, a particularly large scatter was found for conditions of large acceleration number. For all the 2152 data points the average value of the ratio was 0.995, and the standard deviation was 19.5%.

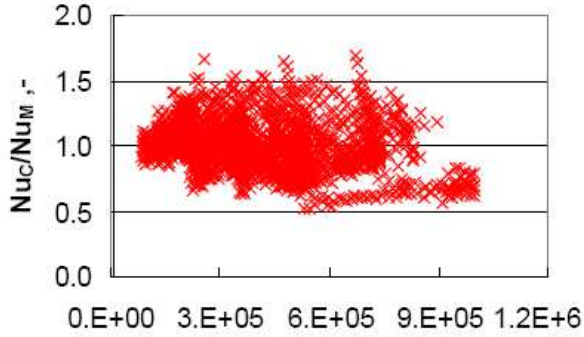

(a) Reynolds number

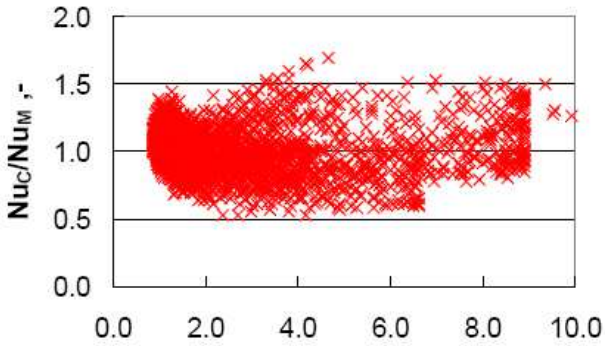

(b) Prandtl number

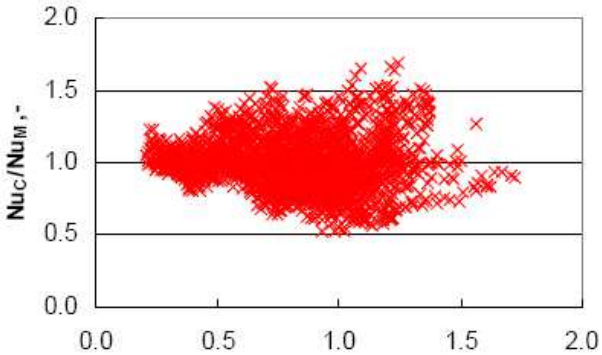

(c) Acceleration number

FIG. 6.3. Ratio of calculated to measured Nusselt number versus Reynolds, Prandtl and Acceleration numbers.

Figure 6.4 presents the distribution density function and the accumulated probability of the ratio. The ratio is symmetrically distributed with the average value being about 1. For about 70% of the data points the deviation between the measured and the calculated Nusselt numbers falls into an error band of 20%. It should be pointed out that if all the 4599 data points obtained by Herkenrath et al were used for the comparison, an average value and a standard deviation of 1.068 and 40.9%, respectively, was obtained. For more than 10% of the data points the correlation gave an over-prediction of more than 60%. This indicates the importance of carrying out a thorough evaluation of test data points.

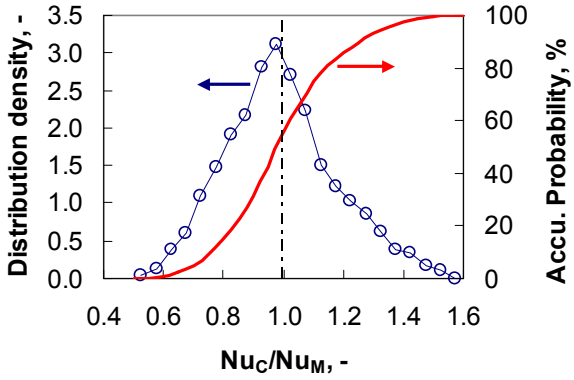

FIG. 6.4. Distribution density function and the accumulated probability of the ratio of the calculated to measured Nusselt number.

Table 6.5 summarizes the performance of the new correlation equation and several others. When compared with the Dittus-Boelter equation, all of them show a significant improvement. The SJTU approach gave the best results. Among the others, the approach of Griem [6-36] also did well.

TABLE 6.5. COMPARISON OF VARIOUS CORRELATIONS WITH TEST DATA

	Average value	Standard deviation
Dittus-Boelter (1930) [6-48]	1.566	0.666
Bishop (1964) [6-24]	1.268	0.273
Swenson (1965) [6-25]	0.932	0.285
Krasnoshchekov (1966) [6-21]	1.193	0.358
Griem (1995) [6-36]	1.036	0.209
Jackson et al (1975) [6-19]	1.222	0.321
Present correlation	0.995	0.195

6.3.4. Conclusions

As can be seen, in this assessment, the equation developed by SJTU provided the best description of the data. However, the equation of Griem [6-36] also performed well. The Dittus-Boelter equation (which was proposed many years ago for forced convection heat transfer to conventional fluids such as water at normal pressure) and not designed to account for non-uniformity of fluid properties could not be expected to describe the data. Also those of Jackson [6-19] and Krasnoshchekov [6-21], which were proposed for conditions of variable property forced convection heat transfer to supercritical pressure fluids in the absence of any buoyancy influence, could not be expected to provide a good description of the data used in this assessment which was undoubtedly in some cases influenced by buoyancy. Those of Bishop [6-24] and Swenson [6-25] which were developed using data which had not been screened for buoyancy, and were probably influenced to some extent by it, gave results somewhere between the SJTU results and the others.

6.4. ASSESSMENT BY THE KOREA ATOMIC ENERGY RESEARCH INSTITUTE (KAERI) OF FOUR MIXED CONVECTION HEAT TRANSFER CORRELATION EQUATIONS FOR SUPERCRITICAL PRESSURE FLUIDS

6.4.1. Correlation equations and test data

In the KAERI assessment of supercritical pressure correlation equations, attention is focused on forced and mixed convection heat transfer a mode of heat transfer for which only a limited number of equations are available. Correlation equations designed to apply for both normal and deteriorated heat transfer conditions are evaluated here against test data for carbon dioxide and water.

Correlation equations by Bae and Kim [6-46], Cheng et al [6-38], Jackson [6-47] and a recently proposed set of equations by Bae [6-48], were used in this assessment. They are referred to using the symbols BK, (Bae and Kim), CH (Cheng et al), JK (Jackson) and BA (Bae), respectively and are shown in Table 6.6. The new set of equations designated as Bae, was based on the test data obtained with upward flow in a tube with an inside diameter of 4.57 mm of carbon dioxide at a pressure of 7.75 MPa; those equations were designed to be as simple as possible.

In Figure 6.5 experimental Nusselt numbers Nu_b for mixed convection normalized using calculated corresponding forced convection values Nu_{b_o} are shown plotted against a buoyancy parameter, $\overline{Bo}_b = \overline{Gr}_b / \mathrm{Re}_b^{2.7}$ along with distributions of the normalized Nusselt number calculated using the BA equations.

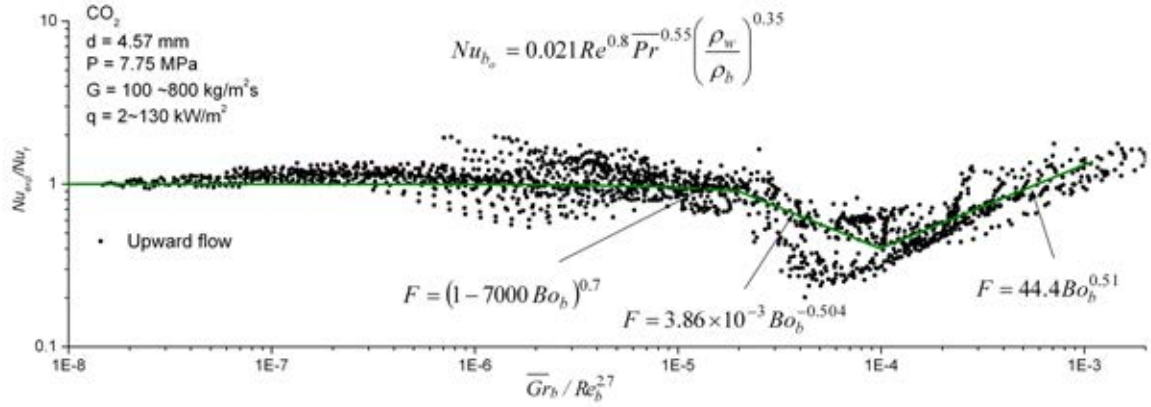

FIG. 6.5. Normalized experimental Nusselt number versus buoyancy parameter.

As can be seen, the experimental data exhibits highly irregular uncorrelated behaviour in the region of transition from forced to mixed convection, $10^{-7} < Bo_b < 10^{-4}$. The normalized Nusselt number did not increase monotonically to the forced convection condition with reduction of buoyancy parameter.

Data for water were also used to evaluate the selected correlation equations. These were obtained from three different sources; Yamagata et al [6-49], Shitsman [6-3], and Vikhrev et al [6-50]. The Yamagata data were for normal heat transfer and the other two sets of data were for deteriorated heat transfer. The ten experimental cases, A, B, C, D, E, F, G, H and J, selected for comparison with those calculated using the four mixed convection equations are summarized in Table 6.6.

TABLE 6.6. CORRELATION EQUATIONS USED IN THE EVALUATION

Correlations
$Nu_b / Nu_{b_o} = F(Bo_b)$ Bae and Kim [6-46]: slightly modified $F(Bo_b)=(1+1.0x10^8 Bo_b)^{-0.032}$ for $5.0x10^{-8}<Bo_b<7.0x10^{-7}$ $F(Bo_b)=0.00185xBo_b^{-0.43465}$ for $7.0x10^{-7}<Bo_b<1.0x10^{-6}$ $F(Bo_b)=0.75$ for $5.0x10^{-6}<Bo_b<1.0x10^{-5}$ $F(Bo_b)=0.0119xBo_b^{-0.36}$ for $1.0x10^{-5}<Bo_b<3.0x10^{-5}$ $F(Bo_b)=32.4xBo_b^{0.40}$ for $3.0x10^{-5}<Bo_b<1.0x10^{-4}$ $Nu_f = 0.0183\,Re_b^{0.82}\,Pr_b^{0.5}(\rho_w/\rho_b)^{0.3}(\bar{c}_p/c_{p_b})^{n_2}$, $Bo_b = \overline{Gr}_b/(Re_b^{2.7}\,\overline{Pr}_b^{0.5}), \overline{Gr}_b = \dfrac{\rho_b(\rho_b-\bar{\rho})gD^3}{\mu_b^2}$ The index n_2 can be found using Equation [6-3].
$\dfrac{Nu_b}{Nu_{b_o}} = \left[\left\|1 \pm 1875 Bo_b F_{VP_1}\left(\dfrac{Nu_b}{Nu_{b_o}}\right)^{-1.1}\right\|\right]^{0.46}$ Jackson [6-47] $Nu_{b_o} = 0.023\,Re_b^{0.8}\,Pr_b^{1/3}$, $F_{VP_2} = (\rho_w/\rho_b)^{0.3}(\bar{c}_p/c_{p_b})^{n_2}$ (see Equations [6-2] and [6-3]) $Bo_b = \dfrac{Gr_b}{Re_b^{2.625}\,Pr_b^{1/3}}, Gr_b = \dfrac{\rho_b(\rho_b-\rho_w)gD^3}{\mu_b^2}, F_{VP_1} = \left(\dfrac{\bar{\mu}}{\mu_b}\right)\left(\dfrac{\bar{\rho}}{\rho_b}\right)^{-0.5}$ The minus sign is for upward flow and the plus sign for downward flow.
$Nu = 0.023\,Re_b^{0.8}\,Pr_b^{1/3}\,F$ Cheng et al. [6-38] $F = \min(F_1, F_2)$, $F_1 = 0.85 + 0.77(\pi_A x10^3)^{2.4}$ $F_2 = \dfrac{0.48}{(\pi_{A,pc}x10^3)^{1.55}} + 1.21\left(1-\dfrac{\pi_A}{\pi_{A,pc}}\right)$, $\pi_A = \dfrac{\beta_b q_w}{G c_{p,b}}$
$Nu_b / Nu_{b_o} = F(Bo_b)$ Bae [6-49] $F=(1-7000Bo)^{0.7}$ for $Bo_b<2x10^{-5}$ $F=3.86x10^{-3}Bo_b^{-0.504}$ for $Bo_b<2x10^{-5}$ $F=44.4Bo_b^{0.51}$ for $Bo_b>1x10^{-4}$ $Nu_{b_o} = 0.021\,Re_b^{0.8}\,\overline{Pr}_b^{0.55}\left(\dfrac{\rho_w}{\rho_b}\right)^{0.35}$, $Bo_b = \overline{Gr}_b/Re_b^{2.7}, \overline{Gr}_b = \dfrac{\rho_b(\rho_b-\bar{\rho})gD^3}{\mu_b^2}$

6.4.2. Results of the evaluation

On Fig. 6.6, heat transfer coefficients calculated using the correlation equations shown in Table 6.6 are presented along with the experimental values for carbon dioxide. The CH correlation completely failed to describe the experimental data for CO_2 in most cases, (except Case E). It severely under or over-predicted observed behaviour near the pseudo-critical temperature. The BK and BA correlation equations were in general agreement with the trends of experimental data. This is not surprising because they were specifically designed to do this. However, noticeable deviations from the experimental values were evident in cases C, E and F. Those covered the region $10^{-7} < Bo_b < 4\times10^{-5}$. The JK generally over-predicted the experimental values regardless of whether the heat transfer was deteriorated or not.

On Fig. 6.7, the distribution of heat transfer coefficients determined using the selected correlation equations are compared with experimental data for water. For case G, the normal heat transfer, the BK, and BA equations performs well, while the JK and CH equations slightly under-predict the data. As the heat flux was increased keeping mass flux constant (case H), the performance of the JK and CH equations improves, especially in the high enthalpy region, whereas the BK and BA equations strongly under-predict the experimental results over the entire region.

In Case I, heat transfer deterioration, the BK and BA equations describe the experimental result quite closely; however, the agreement starts to deviate as soon as the wall temperature becomes higher than the pseudo-critical value. The CH equation provides a good description of these experimental results over the high enthalpy range, whereas it over-predicts them over the low enthalpy range. The JK equation over-predicts the results over the whole enthalpy range.

In Case J, the CH equation performs best. It also performs satisfactorily over the somewhat higher enthalpy range; however, it starts over-predicting in the enthalpy range greater than 800 kJ/kg. Neither the JK, BK or BA equations follow the tortuous heat transfer variation closely, showing monotonically increasing or decreasing trends.

TABLE 6.7. SELECTED EXPERIMENTAL CASES

Case	Fluid	Flow direction	d (mm)	G (kg/m^2s)	q_w (kW/m^2)	P(MPa)	Author(s)
A	CO_2	Upward	4.57	100	15	7.75	KAERI
B				200	38		
C				400	30		
D				400	50		
E				800	50		
F				800	120		
G	Water		7.5	1260	233	24.5	Yamagata et al.
H			10	1260	465	24.5	
I			12	375	348	24.5	Shitsman
J			20.4	495	570	26.5	Vikhrev et al.

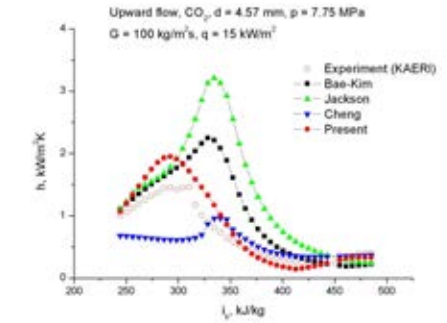

(a): case A

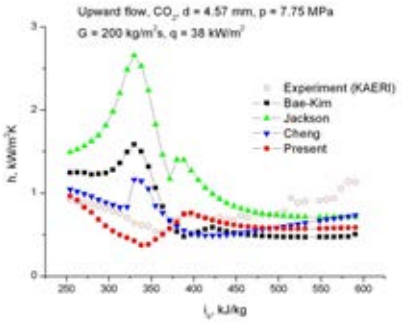

(b): case B

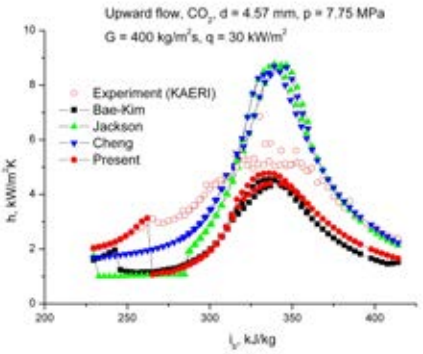

(c): case C

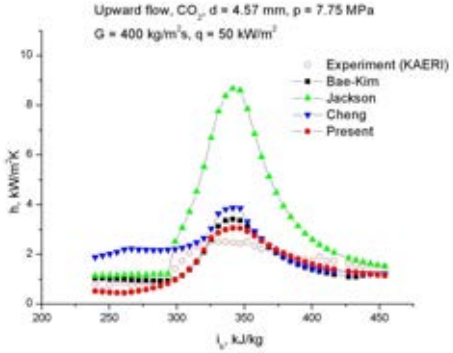

(d): case D

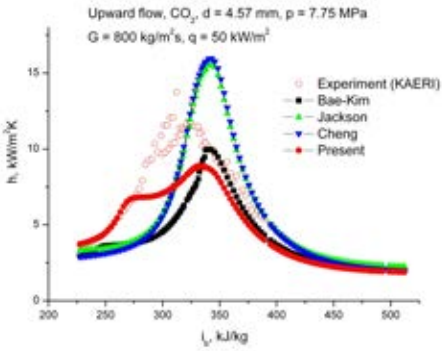

(e): case E

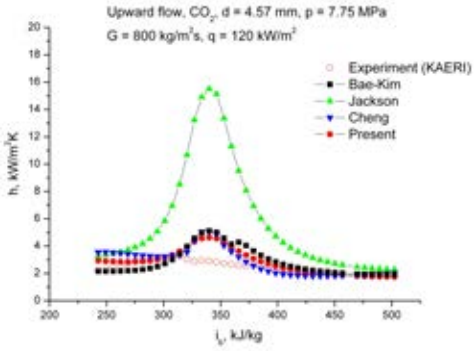

(f): case F

FIG. 6.6. Heat transfer coefficient versus bulk enthalpy for various combinations of mass and heat flux with upward flow of CO_2, D = 4.57 mm, p = 7.75 MPa.

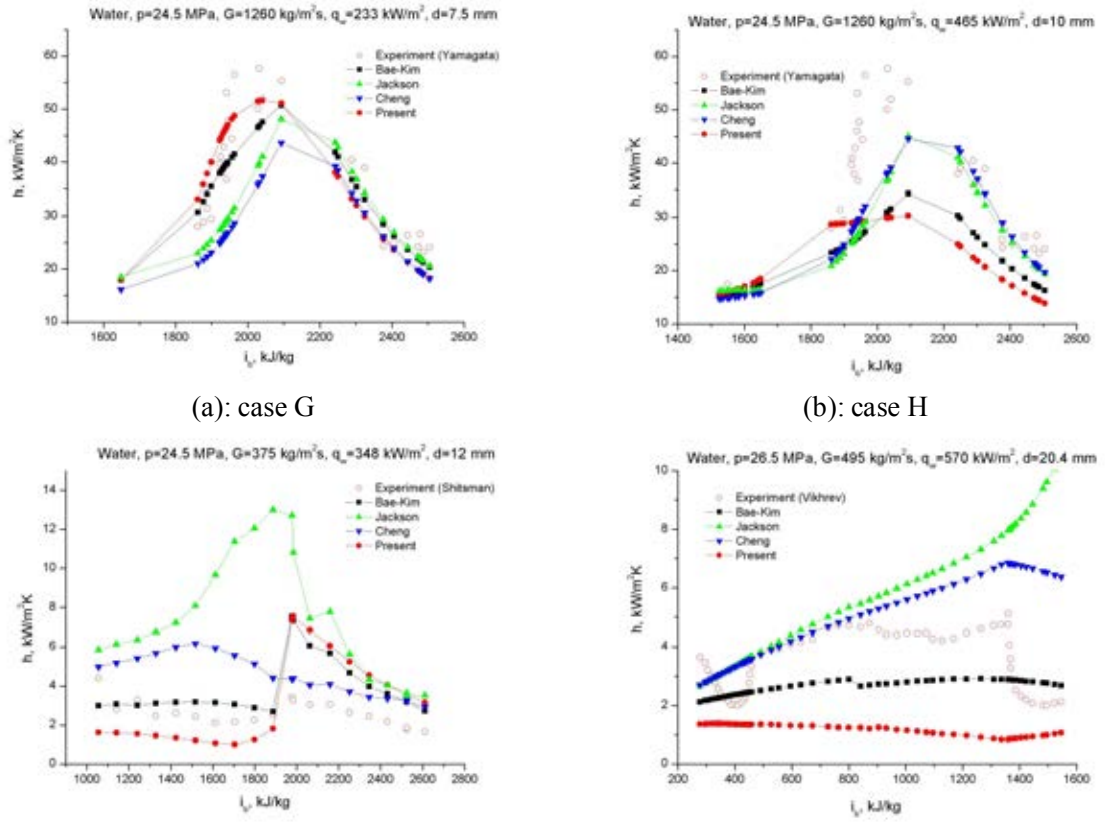

FIG. 6.7. Heat transfer coefficients versus bulk enthalpy for various combinations of mass and heat fluxes with upward flow of water.

6.4.3. Conclusions

Unfortunately, this assessment of the available mixed convections equations yielded results which do not enable clear conclusions to be drawn from the exercise other than that the KAERI equations do provide a general description of the trends exhibited by the KAERI data. It is clear that that further work needs to be done to develop equations which describe mixed convection heat transfer to fluids at supercritical pressure in a reliable manner.

6.5. DEVELOPMENT OF AN EXTENDED PHYSICALLY-BASED SEMI-EMPIRICAL MODEL OF HEAT TRANSFER TO FLUIDS AT SUPERCRITICAL PRESSURE IN VERTICAL TUBES ACCOUNTING FOR THE INFLUENCE OF BUOYANCY (MU/TU)

6.5.1. Introduction

The purpose of the remaining work to be described in the remainder of this section was to develop physically-based, semi-empirical models and equations designed to describe the effects of buoyancy and bulk flow acceleration on convective heat transfer to fluids at supercritical pressure. Models of this kind lead to simple algebraic equations which, hopefully, involve appropriate dimensionless parameters and variable property functions for correlating experimental data and should provide a framework for describing observed behaviour.

In this section, the influence of buoyancy on heat transfer is considered for the case of upward and

downward flow in heated vertical tubes. Buoyancy is a physical influence which is experienced in fluids as a result of the combined effect of non-uniformity of density and the action of gravity. The model of heat transfer presented here gives an equation which relates the ratio of Nusselt number for buoyancy-influenced conditions to that for buoyancy-free conditions to a buoyancy parameter and property functions which together characterize the strength of the influence of buoyancy. It leads to a description of variable property buoyancy-influenced heat transfer which covers the whole range of modes from forced convection right through the mixed convection region to what is, effectively, free convection.

6.5.2. Effects of buoyancy on turbulent heat transfer in vertical heated tubes

Even in the case of conventional fluids such as water at normal pressure the effect of buoyancy on turbulent heat transfer in vertical tubes is complicated and the trends are rather surprising, (see, Jackson et. al., [6-51]) and Jackson, [6-52]). For upward flow in a heated tube, impairment of heat transfer develops with onset of significant buoyancy influence. This occurs due to turbulence, production being reduced and turbulent diffusion of heat becoming impaired. The resulting deterioration of heat transfer occurs in spite of the fact that the mean motion of the buoyant fluid near the wall is aided by buoyancy and, as a consequence, the advection of heat is improved. The net impairment of heat transfer builds up with increase of buoyancy influence until a stage is reached where heat transfer effectiveness falls to about one half that expected for the same flow rate in the absence of any influence of buoyancy. Then, with further increase in buoyancy influence the heat transfer process recovers until, eventually, the effectiveness of heat transfer becomes enhanced in relation to that for forced convection. With downward flow in a heated tube, a systematic net improvement in heat transfer effectiveness occurs with increase of buoyancy influence, even through the mean motion in the near-wall region is opposed by buoyancy and the advection of heat there is reduced.

Thus, buoyancy-influenced heat transfer in vertical tubes with a conventional fluid such as water at normal pressure exhibits complex behaviour. Similar trends are also found with fluids at supercritical pressure. However, with such fluids, the non-uniformity fluid properties can be extremely strong and lead to rather striking additional effects. The empirical equations currently available for calculating convective heat transfer to fluids at supercritical pressure are not able to describe such effects. An extended semi-empirical model is presented here which is designed to account for buoyancy under the conditions of strong non-uniformity of fluid properties encountered in fluids at supercritical pressure.

6.5.3. An early semi-empirical model of turbulent buoyancy-influenced heat transfer in a vertical tube

A semi-empirical model of fully developed turbulent mixed convection heat transfer in vertical tubes aimed at describing buoyancy-influenced heat transfer, in a conventional fluid, such as water at atmospheric pressure was first proposed by Jackson [6-53]. In an early form (see Jackson and Hall [6-18]) the model related the ratio of Nusselt number for mixed convection, Nu_b, and that for forced convection Nu_{b_o} to a buoyancy parameter $Bo_b = Gr_b/(Re_b^m Pr_b^n)$, in which $Gr_b = gD^3(\rho_w - \rho_b)/\rho_b \nu_b^2$. The Reynolds number index m took the value 2.7 or a slightly lower one, 2.625, depending upon the empirical equation used to relate friction coefficient to Reynolds number in the analysis. The Prandtl number index n was assigned the value 0.4 based on empirical evidence of the effect of that parameter on turbulent heat transfer.

The model involved the assumption that the average density of the buoyant fluid in the boundary layer could be approximated $(\rho_b + \rho_w)/2$. It gave the following relationship between Nusselt number ratio

Nu_b / Nu_{b_o} and the buoyancy parameter Bo_b

$$\frac{Nu_b}{Nu_{b_o}} = \left[\left| 1 \pm C_B Bo_b \left(\frac{Nu_b}{Nu_{b_o}} \right)^{-1.1} \right| \right]^{0.46} \tag{6.8}$$

in which the coefficient C_B had an estimated value of 2300.

The negative sign in Equation 6.8 refers to the buoyancy-aided case (upward flow in a heated tube) and the positive sign to the buoyancy-opposed case (downward flow in a heated tube). The modulus signs within the outer brackets are there to avoid a problem which arises with upward flow as the influence of buoyancy becomes strong enough to cause the sign of the expression within the square brackets to become negative.

Later the above model was re-cast into an equivalent form with a buoyancy parameter $Bo_b^* = Gr_b^* / (\mathrm{Re}_b^m \, \mathrm{Pr}^n)$, in which $\mathrm{Gr}_b^* = g\beta_b D^4 q_w / (k_b \nu_b^2)$. The index m then took the value 3.5 or 3.425 and n the value 0.8, (see Jackson et al [6-51] and [6-52]). In this form the relationship between Nusselt number ratio and buoyancy parameter took the form

$$\frac{\mathrm{Nu_b}}{\mathrm{Nu}_{b_o}} = \left[\left| 1 \pm C_B Bo_b^* \left[\frac{\mathrm{Nu_b}}{\mathrm{Nu}_{b_o}} \right]^{-2.1} \right| \right]^{0.46} \tag{6.9}$$

In this re-cast version of the model the coefficient C_B has an estimated value of 10^5.

Figure 6.8 shows the variation of Nusselt number ratio with buoyancy parameter Bo_b^* given by the Equation 6.9 for upward and downward flow in a heated tubes.

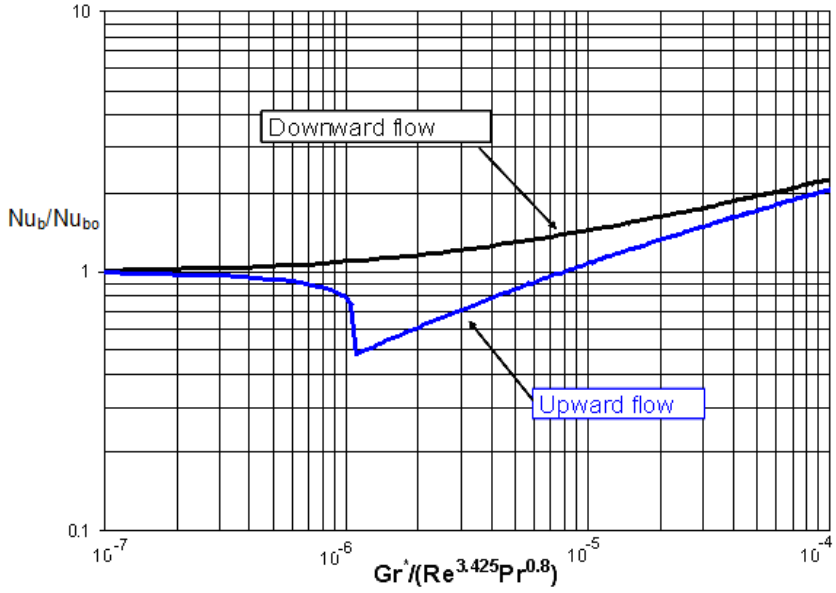

FIG. 6.8. Heat transfer behaviour for fully developed turbulent mixed convection with conventional fluid such as water at normal pressure.

With upward flow the Nusselt number for mixed convection falls to about 70% of that for forced convection when the buoyancy parameter reaches a value just over 10^{-6} (with the shear stress at the edge of the buoyant layer then being only about 50% of the wall value). At this stage Nu_b then falls suddenly to about 47% of the forced convection value, with the shear stress at the outer edge of the buoyant wall layer then becoming negative and the velocity profile in the core region being inverted. With further increase of buoyancy parameter, a progressive improvement in the effectiveness of heat transfer is predicted. With downward flow in a heated tube, systematic enhancement of heat transfer is predicted with increase of buoyancy influence.

Over the years the above model has been used with some success as a framework for correlating and describing data for fully developed mixed convection heat transfer to water at normal pressures in vertical tubes, Rouai [6-54] and Buyukalaca [6-55]. In the course of the present IAEA CRP, efforts have been made to extend the early semi-empirical model to account for the effects of the strong non-uniformity of fluid properties which can be present in fluids at supercritical pressure (see [6-56] and [6-57]). The latest version of the extended analysis is presented below.

6.5.4. Extension of the model of fully developed mixed convection in a vertical tube to account for strong non-uniformity of fluid properties

The effect of buoyancy on the distribution of shear stress across the thermal layer in a vertical heated tube can be determined by approximate analysis using the following simplified equation of motion in which the inertia terms are neglected.

$$0 = \pm\rho g(a-y) - (a-y)\frac{dp}{dx} + \frac{d[(a-y)\tau]}{\partial y} \tag{6.10}$$

The symbol x is used for the coordinate in the flow direction, y is the transverse coordinate (measured into the fluid from the wall), p is pressure, ρ is density and τ is the local total shear stress (molecular plus turbulent) at any distance y from the wall. The symbol, a (=D/2), is used for tube radius.

In this initial attempt to extend the earlier model of buoyancy-influenced heat transfer in vertical tubes to account for the strong dependence on temperature of the physical and transport properties of fluids at supercritical pressure it has been assumed that the temperature of the fluid varies linearly with *y* between the wall value T_w and the bulk value T_b across a buoyant thermal layer within a region of extent δ_T and is uniform at the value T_b across the region $y > \delta_T$. Thus, integrating Equation [6.10], with respect to y term by term across the entire flow and then across the wall layer only, re-organizing the two resulting equations and subtracting them to eliminate axial pressure gradient, the following expression is obtained for the reduction of shear stress across the buoyant wall-layer, after neglecting higher order terms.

$$\tau_w - \tau_{\delta_T} = \pm\delta_T(\rho_b - \rho_{av})g \tag{6.11}$$

where the positive sign applies for upward flow and the negative sign for downward flow. In the above equation

$$\rho_{av} = \frac{1}{\delta_T}\int_o^{\delta_T} \rho\, dy \tag{6.12}$$

It is assumed that thermal layer thickness δ_T can be related to boundary layer thickness δ by an approximate relationship $\delta_T = \delta / Pr_{av}^{n_1}$, which is based on observed heat transfer behaviour in turbulent pipe flow. Pr_{av} is an integrated average value of Prandtl number over the temperature range from T_b to T_w given by $Pr_{av} = \frac{1}{\delta_T}\int_o^{\delta_T} Pr\,dy$ and the index n_1 is assigned a value of about 0.4. Substituting for δ_T in Equation [6.11] using the above relationship we obtain

$$\tau_w - \tau_{\delta_T} = \pm\delta(\rho_b - \rho_{av})g\,Pr_{av}^{-n_1} \tag{6.13}$$

The following equation relates δ to δ^+, a boundary layer thickness expressed in terms of 'universal' parameters defined using integrated average values of density and viscosity and a near-wall value of total shear stress τ_{δ_T}.

$$\delta = \frac{\delta^+ \mu_{av}}{\tau_{\delta_T}^{1/2}\rho_{av}^{1/2}} \tag{6.14}$$

The integrated average value of viscosity is defined by $\mu_{av} = \frac{1}{\delta_T}\int_o^{\delta_T} \mu dy$.

Thus, on substituting for δ in Equation 6.13 using Equation 6.14 we obtain

$$\frac{\tau_{\delta_T}}{\tau_w} = 1 \pm \frac{\delta^+ \mu_{av}(\rho_b - \rho_{av})g\,Pr_{av}^{-n_1}}{\tau_w^{3/2}\rho_{av}^{1/2}}\left(\frac{\tau_{\delta_T}}{\tau_w}\right)^{-1/2} \tag{6.15}$$

Next, the wall shear stress τ_w in Equation 6.15 is related to ρ_b, u_b and friction factor $f_{b_o}\,(= \tau_w / \tfrac{1}{2}\rho_b u_b^2)$. Then the latter is expressed in terms of Reynolds number Re_b using an empirical equation of the form $f_{b_o} = K_1, Re_b^{-m_1}$. Hence the following expression is obtained for τ_{δ_T} / τ_w.

$$\frac{\tau_{\delta_T}}{\tau_w} = 1 \pm 2\sqrt{2}\delta^+ K_1^{-3/2}\frac{F_g}{Re_b^{m_3}\,Pr_b^n}\left(\frac{(\rho_b - \rho_{av})}{\rho_b}\right)\left(\frac{\mu_{av}}{\mu_b}\right)\left(\frac{\rho_{av}}{\rho_b}\right)^{-\frac{1}{2}}\left(\frac{Pr_{av}}{Pr_b}\right)^{-n_1}\left(\frac{\tau_{\delta_T}}{\tau_w}\right)^{-\frac{1}{2}} \tag{6.16}$$

In Equation 6.16, F_g is a dimensionless gravitational body force gD^3/ν_b^2 and the index m_3 is related to m_1 by the expression $3(1\text{-}m_1/2)$.

The Nusselt number for mixed convection, Nu_b, divided by that for variable property forced convection Nu_{b_o}, can be related to τ_{δ_T} / τ_w using the idea that the effect of buoyancy in modifying the near-wall distribution of shear stress enables a buoyancy-influenced flow to thought of as one which is not affected by buoyancy but is flowing at some different mean velocity (lower or higher than the actual one, depending on whether the flow direction is upward or downward). Thus, assuming that f_{b_o} is proportional to $Re_b^{-m_1}$ and that Nu_{b_o} is proportional to $Re_b^{m_2}$, we find that

$$\frac{Nu_b}{Nu_{b_o}} = \left(\frac{\tau_{\delta_T}}{\tau_w}\right)^{m_4} \tag{6.17}$$

in which $m_4=m_2/(2-m_1)$.

Thus, combing Equation 6.17 with Equation 6.16 to eliminate τ_{δ_T}/τ_w the following equation describing the effect of buoyancy on heat transfer in a heated vertical tube, as characterized by the ratio Nu_b/Nu_{b_o}, is obtained

$$\frac{Nu_b}{Nu_{b_o}} = \left[\left| 1 \mp C_B \frac{Gr_b}{Re_b^{m_5} Pr_b^{n_1}} \left(\frac{\mu_{av}}{\mu_b}\right)\left(\frac{\rho_{av}}{\rho_b}\right)^{-1/2} \left(\frac{Pr_{av}}{Pr_b}\right)^{n_1} \left(\frac{\rho_b - \rho_{av}}{\rho_b - \rho_w}\right)\left(\frac{Nu_b}{Nu_{b_o}}\right)^{-m_5} \right|\right]^{m_6} \tag{6.18}$$

in which $C_B = 2\sqrt{2}\delta^+ K_1^{-3/2}$, $Gr_b = gD^3(\rho_b - \rho_w)/(\rho_b \nu_b^2)$ and $m_5=1/(2m_4)$.

The –ve sign applies for upward flow and the +ve one for downward flow. The modulus signs ensure that for upward flow a real solution for Nu_b/Nu_{b_o} is always obtained.

It should be noted that in this initial attempt to develop a model of buoyancy-influenced turbulent heat transfer in vertical tubes taking account of strong dependence of fluid properties the assumption was made that the fluid temperature varied in a simple linear manner across the thermal layer. Thus the integrated average properties, ρ_{av}, μ_{av} and Pr_{av} defined earlier reduce to the mean values $\overline{\rho}$, $\overline{\mu}$ and $\overline{Pr}$ obtained by integrating ρ, μ and Pr with respect to temperature between the limits T_b and T_w. This observation serves to point to a major reason why the accuracy of the present version of the model might prove to be limited in terms of correlating and fitting experimental data (see later).

Equation 6.18 involves an empirical coefficient K_1 and the several empirical indices which need to be specified. Different combinations of the coefficient K_1 and the index m_1 have been used in the power law form of the empirical friction factor-Reynolds relationships which are commonly used for pipe flow, examples being $K_1=0.079$ in conjunction with $m_1=0.25$ and $K_1=0.046$ with $m_1=0.20$. In spite of the big differences between the values of K_1 and m_1 in these two particular cases, rather similar values of friction factor are obtained using them. Also, a variety of combinations of K_2 and m_2 are used in the Dittus-Boelter form of the empirical Nusselt number – Reynolds number relationship, a widely used combination being $K_2=0.023$ and $m_2=0.80$. It turns out that for values of the indices m_1 and m_2 in common use, very similar values of the index m_4 are obtained (about 0.46) and, therefore, also of the index m_5 (about 1.1). Hence if K_1 is assigned the value 0.079 and m_1 the value 0.25, and ρ_{av}, μ_{av} and Pr_{av} are replaced by $\overline{\rho}$, $\overline{\mu}$ and $\overline{Pr}$. Equation 6.18 becomes

$$\frac{Nu_b}{Nu_{b_o}} = \left[\left| 1 \mp C_B \frac{Gr_b}{Re_b^{2.625} Pr_b^{n_1}} \left(\frac{\overline{\mu}}{\mu_b}\right)\left(\frac{\overline{\rho}}{\rho_b}\right)^{-\frac{1}{2}} \left(\frac{\overline{Pr}}{Pr_b}\right)^{-n_1} \left(\frac{\rho_b - \overline{\rho}}{\rho_b - \rho_w}\right)\left(\frac{Nu_b}{Nu_{b_o}}\right)^{-1.1} \right|\right]^{0.46} \tag{6.19}$$

Notice that in Equation 6.19, the dimensionless groups Gr_b, Re_b and Pr_b combine together in the manner $Gr_b/(Re_b^{2.625} Pr_b^{n_1})$ to form a buoyancy parameter Bo_b which together with the various property ratio terms shown, characterizes the strength of buoyancy influence under conditions of variable property mixed convection.

The Nusselt number Nu_{b_o}, for developing, variable property forced convection in a tube, can be determined using an empirical equation of the form

$$Nu_{b_o} = K_2 F_{TD} Re_b^{m_2} Pr_b^{n_1} F_{VP_2} \tag{6.20}$$

in which F_{TD} is a thermal development function, which according to Petukhov and Polyakov [6-58], can take the form

$$F_{TD} = 1 + 2.35 Re_b^{-0.15} Pr_b^{-0.4} (x/D)^{-0.6} \exp[-0.39 Re_b^{-0.1} (x/D)] \tag{6.21}$$

Thus, F_{TD} can be determined at any location x/d along the tube knowing Re_b and Pr_b.

F_{VP_2} is an empirical correction factor to account for the effect of the non-uniformity of fluid properties on heat transfer under conditions of turbulent, variable property, forced convection. The approach proposed by Krasnoschekov and Protopopov [6-21] (quoted earlier in Section 6.1) takes the form $(\rho_w/\rho_b)^{0.3}(\bar{c}_p/c_{p_b})^{n_2}$ in which $\bar{c}_p$ is the mean value of specific heat integrated with respect to over the temperature range from T_b to T_w and n_2 is an index which depends on the values of T_w and T_b in relation to the pseudo-critical value T_{pc} and can be determined using Equation 6.3.

In order to determine Nu_{b_o} as a function of x/D using Equation 6.18 for the specified values of fluid temperature at inlet, mass flow rate and wall heat flux, it is necessary to perform an iterative calculation starting with an approximate value for wall temperature $T_{wo}^{(1)}$. This enables an improved value of wall temperature $T_{wo}^{(2)}$ to be determined. The procedure is repeated until convergence is achieved and values for T_{w_o}, F_{VP_2} and Nu_{b_o} are obtained.

Equation 6.19 can be written in the following condensed form

$$\frac{Nu_b}{Nu_{b_o}} = \left[\left|1 \mp C_B Bo_b F_{VP_1} F_{VP_3} F_{VP_4} \left(\frac{Nu_b}{Nu_{b_o}}\right)^{-1.1}\right|\right]^{0.46} \tag{6.22}$$

in which

$$Bo_b = \frac{Gr_b}{Re_b^{2.625} Pr_b^{n_1}} \quad F_{VP_1} = \left(\frac{\bar{\mu}}{\mu_b}\right)\left(\frac{\bar{\rho}}{\rho_b}\right)^{-1/2}, \quad F_{VP_3} = \left(\frac{\bar{Pr}}{Pr_b}\right)^{-n_1} \text{ and } \quad F_{VP_4} = \left(\frac{\rho_b - \bar{\rho}}{\rho_b - \rho_w}\right) \tag{6.23}$$

As can be seen, the relationship between Nu_b / Nu_{b_o}, and $C_B F_{VP_1} F_{VP_3} F_{VP_4} Bo_b$ is an implicit one so that if a value for $C_B F_{VP_1} F_{VP_3} F_{VP_4} Bo_b$ is specified an iterative approach must be used to determine Nu_b / Nu_{b_o}. However, if Equation 6.22 is re-arranged as follows

$$C_B Bo_b F_{VP_1} F_{VP_3} F_{VP_4} = \left(\frac{Nu_b}{Nu_{b_o}}\right)^{1.1} - \left(\frac{Nu_b}{Nu_{b_o}}\right)^{3..3} \tag{6.24}$$

The relationship between Nu_b / Nu_{b_o} and $C_B Bo_b F_{VP_1} F_{VP_3} F_{VP_4}$ can be readily established in a direct manner by specifying values for Nu_b / Nu_{b_o} and calculating values of $C_B F_{VP_1} F_{VP_3} F_{VP_4} Bo_b$.

Notice that the function $C_B Bo_b F_{VP_1} F_{VP_3} F_{VP_4}$ is zero when Nu_b / Nu_{b_o} =0 and it is also zero when Nu_b / Nu_{b_o} =1. As Nu_b / Nu_{b_o} varies between these limits $C_B Bo_b F_{VP_1} F_{VP_3} F_{VP_4}$ passes through a maximum. It can be shown using Equation 6.24 that the value of Nu_b / Nu_{b_o} at which this maximum occurs is 0.607 and that $C_B Bo_b F_{VP_1} F_{VP_3} F_{VP_4}$ is then 0.385.

Thus, the variation of $\mathrm{Nu_b / Nu_{b_o}}$ with $C_B Bo_b F_{VP_1} F_{VP_3} F_{VP4}$ given by Equation 6.23 can be represented by the three unique curves shown below on Fig. 6.9.

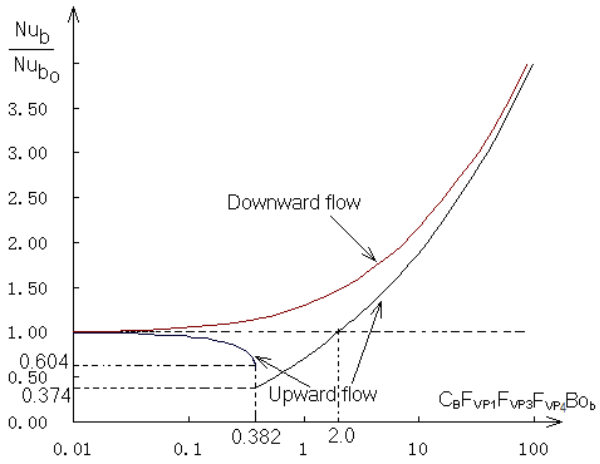

FIG. 6.9. Effect of buoyancy on heat transfer.

6.5.5. Criterion for negligible influence of buoyancy provided by the extended model

The model enables experimental data to be screened to assess whether or not it is buoyancy-influenced. As can be seen from Fig. 6.9, if $C_B Bo_b F_{VP_1} F_{VP_3} F_{VP_4}$ is very much less than unity the ratio $\mathrm{Nu_b / Nu_{b_o}}$ tends to unity and the effect of buoyancy is very small. Noting that for x/d>>1, $F_{TD} \rightarrow 1$ we see that, according to the model, if $C_B Bo_b F_{VP_1} F_{VP_3} F_{VP_4}$ is less than 4×10^{-2} the effect of buoyancy on heat transfer should be less than about 2%. As indicated earlier (under Equation 6-18), the coefficient $C_B = \sqrt[2]{2}\delta^+ K_1^{-\nu_2}$. If δ^+ is assigned the value 36 then C_B is about 5500. If C_B is assigned this value then the model gives the following criterion for the effect of buoyancy to be less than 2%

$$\mathrm{Bo_b} < 10^{-5}\left[(\bar{\mu}/\mu_b)(\bar{\rho}/\rho_b)^{-1/2}\right]^{-1}\left(\bar{\mathrm{Pr}}/\mathrm{Pr_b}\right)^{n_1}\left[(\rho_b - \bar{\rho})/(\rho_b - \rho_w)\right]^{-1} \qquad (6.25)$$

In the above criterion, $\bar{\mu}, \bar{\rho}$ and $\bar{\mathrm{Pr}}$ are evaluated by integrating over the temperature range T_b to T_w using the local experimental value of T_w and the corresponding value of T_b obtained from an energy balance. The mean values of density, viscosity and Prandtl number can be found by performing the integration specified earlier.

6.5.6. Correlation of experimental data using the extended model

The model identifies the variables which should be used to correlate experimental data on fully developed buoyancy-influenced heat transfer to supercritical pressure fluids in vertical tubes. As can be seen from

Equation 6.22, Nu_b / Nu_{b_o} should be plotted against the buoyancy function $F_B (= Bo_b F_{VP_1} F_{VP_3} F_{VP_4})$. The curves calculated using Equation 6.22 with the coefficient C_B assigned the estimated value of 5500 are presented in terms of these correlating parameters on Fig. 6.10.

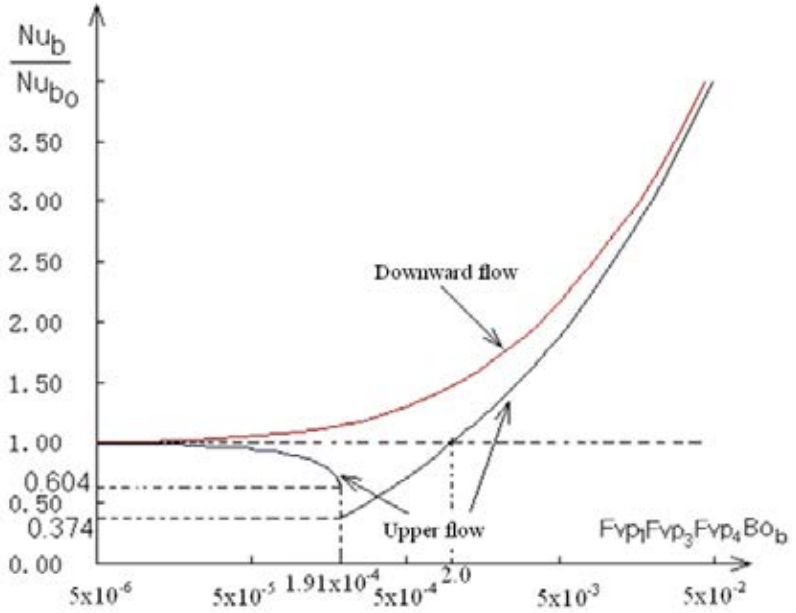

FIG. 6.10. Coordinates for correlations data and comparing it with the model curves.

Of course the value 5500 is simply an estimated one and can be adjusted if necessary with view to bringing the model predictions in line with experimental data. If C_B is increased above or reduced below the estimated value this simply shifts the three curves backwards or forwards in the direction of the abscissa. Thus, the model can be 'fitted' to 'correlated' experimental data on such a plot by adjusting C_B.

It should be noted that in the case of developing, buoyancy-influenced heat transfer, dimensionless axial distance x/d from the start of heating is a further variable on which heat transfer can actually depend. However, this has not been accounted for in the model because the inertia terms in the equation of motion were neglected.

6.5.7. The conditions for severe buoyancy-induced impairment of heat transfer

As can be seen from Equation 6.23, and also from Fig. 6.9, if the parameter $C_B Bo_b F_{VP_1} F_{VP_3} F_{VP_4}$ is about 0.3, severe impairment of heat transfer can be expected for upward flow, with Nu_b / Nu_{b_o} falling to about 0.5. Thus, the model provides a means of specifying the conditions under which very significant impairment of heat transfer might be expected. If C_B is assigned the estimated value of 5500, the criterion for this is

$$Bo_b \approx 1.5x10^{-4} \left[(\bar{\mu}/\mu_b)(\bar{\rho}/\rho_b)^{-1/2}\right]^{-1} (\bar{P}r/Pr_b)^{n_1} \left[(\rho_b - \bar{\rho})/(\rho_b - \rho_w)\right]^{-1} \quad (6.26)$$

The averaged properties μ_{av}, ρ_{av} and Pr_{av} are evaluated by integrating Pr over the range T_b to T_w, where the wall temperature T_{w_o} is estimated by solving the equation for Nu_{b_o} and then applying a factor 0.5 to

Nu_{b_o} to obtain an approximate value for Nu_b from which a value for T_w can be found.

6.5.8. The limiting condition of buoyancy-dominated heat transfer

In the case of upward flow, further increase of buoyancy influence beyond that needed to cause laminarization brings about a recovery of turbulence production and an improvement in the effectiveness of heat transfer. When the parameter $C_B Bo_b F_{VP_1} F_{VP_3} F_{VP_4}$ reaches the value 2 the ratio Nu_b / Nu_{b_o} has risen back up to unity. Then, the effectiveness of heat transfer is the same as for forced convection, but it should be noted that the flow is, in fact, strongly influenced by buoyancy and the velocity profile is inverted in the core region. With further increase of buoyancy influence beyond this point the heat transfer process becomes progressively enhanced. Eventually when the influence of buoyancy becomes very strong indeed the curve for upward flow approaches that for downward flow. Heat transfer effectiveness then no longer depends on the magnitude of the mass flow rate or the direction flow. When such a condition is achieved the model yields an expression for Nu_b of the form

$$Nu_b = C(Gr_b \, \mathrm{Pr}_b)^{0.3} \tag{6.27}$$

Note that there is a close similarity between the above equation and widely quoted empirical equations for turbulent free convection from heated vertical surfaces.

6.5.9. Using the extended model in the predictive mode

Next, we consider how the model might be used to calculate the distribution of wall temperature for buoyancy-influenced flow in a heated tube of specified diameter with specified wall heat flux and the fluid entering at specified values of pressure temperature and flow rate. Together, this information enables the axial distributions of bulk enthalpy h_b and bulk temperature T_b to be determined from an energy balance. Hence values of Re_b, Pr_b and Bo_b can then be found at any x/D.

Then, the axial distribution of Nusselt number Nu_{b_o} for variable property forced convection with negligible influence of buoyancy can be found using Equation 6.20. In that equation, the thermal entry development factor F_{TD} can be determined from Equation 6.21 for any axial location x/D, knowing Re_b and Pr_b. The determination of the variable property correction factor for forced convection F_{VP_2} involves knowing the wall temperature for forced convection T_{w_o} as well as T_b and thus an iterative computational procedure needs to be employed to solve Equation 6.20 to determine T_{w_o}, Nu_{b_o} and F_{VP_2}.

At this stage, Bo_b, F_{TD}, Nu_{b_o} and F_{VP_2} have all been determined and next, the unknown variable Nu_b in the model equation for variable property buoyancy-influenced flow and heat transfer, (Equation 6.22), should be expressed in terms of the unknown variable T_w by replacing it by $q_w D/(k_b(T_w - T_b))$. The property ratio terms F_{VP_1}, F_{VP_3} and F_{VP_4} are functions of the unknown variable T_w. Thus, with these changes, Equation 6.23 is, effectively, a non-linear algebraic equation from which local values of the unknown variable T_w can be determined at any specified axial location x/d using standard iterative computational procedures. The process can be conveniently initiated at x=0, where T_w has a value close to the fluid temperature at entry, and continued step by step along the tube using the converged value of T_w for the iterative process at each location as the initial value at the next one. Nu_b can be determined at each stage from $q_w D/(k_b(T_w - T_b))$ using the converged value of T_w.

6.5.10. Evaluation of the extended model and conclusions

Work has been in progress for some time at Tsinghua University, Beijing, to evaluate the model by using it to try to correlate and fit experimental data on heat transfer to carbon dioxide at supercritical pressure. This work has reported recently by Jackson et al [6-62]. Encouraging progress has been made which indicates that when the data are presented in terms of the correlating parameters suggested by the present version of the model the general behaviour is surprisingly consistent with expected behaviour. However, it has become apparent that the extent to which the data can be correlated and fitted by the model is likely to be greatly improved if the over-simplistic linear nature of the assumed distribution of temperature in the thermal layer is refined and a more realistic non-linear representation is adopted. Such an approach, which makes use of established empirical information describing the velocity boundary layer in terms of the universal parameters u^+ and y^+ and employs this to establish a much more realistic distribution of fluid temperature in the thermal layer, has recently been developed. This will be reported on shortly, (see [6-65]). This refinement should prove to be of key importance in enabling the averaged values ρ_{av}, μ_{av} and Pr_{av} in the modeling of the near wall-region to be properly described in the case of heat transfer to fluids at supercritical pressure under conditions where the physical and transport properties of very non-uniform.

6.6. FORCED CONVECTION HEAT TRANSFER TO FLUIDS AT SUPERCRITICAL PRESSURE FLOWING IN A HEATED TUBE WITH THERMALLY-INDUCED BULK FLOW ACCELERATION (MU/TU)

6.6.1. Impairment of forced convection heat transfer due to bulk flow acceleration

The ideas presented below represent a first stage in the direction of producing a model of impaired forced convection arising as a result of bulk flow acceleration. When fluid flows through a heated tube its bulk enthalpy increases, its temperature rises and its density falls. Since the mass flow rate is the same at all axial positions, the bulk velocity increases and, therefore, the fluid must accelerate. An applied pressure difference (over and above that required to overcome friction) is needed to cause the acceleration. In the boundary layer region of the flow the velocity of the fluid is lower than in the core region and so the pressure gradient applied there is greater than that needed to accelerate the fluid. Thus, the gradient of shear stress across the flow in the wall region has to undergo an adjustment to balance the excess pressure gradient. It follows that the shear stress falls more quickly with distance from the wall than it would in the absence of acceleration. Consequently, in the buffer layer region the shear stress will be lower than that for a steady fully developed flow at the same mass flow rate and less turbulence will be produced. Thus, the flow will take on some of the characteristics of a fully developed flow at a reduced value of flow rate. The viscous sub-layer will be thicker and the effectiveness of heat transfer will be reduced. The semi-empirical model is presented below has been developed to describe such behaviour.

The effect of thermally-induced bulk flow acceleration on the distribution of shear stress across the wall layer region can be determined using an approximate approach in which the following simplified form of the equation of motion for flow in a heated tube is used.

$$\rho(a-y)u\frac{\partial u}{\partial x} = -(a-y)\frac{dp}{dx} + \frac{\partial(a-y)\tau}{\partial y} \tag{6.28}$$

The radius of the tube is denoted by the symbol a, the axial coordinate by x, the transverse coordinate measured inwards from the wall by y, the local bulk (=D/2) value of density by ρ_b and the local shear stress by τ. It is assumed that the local axial velocity u varies with distance y from the wall across a thin layer of fluid of extent δ according to the linear relationship $u = u_b(x)y/\delta$ and remains uniform at the

value u_b in the core region. Thus, integrating with respect to y across the entire flow and then across the wall layer only, re-organizing the two equations and then subtracting them to eliminate $\frac{dp}{dx}$, the following expression for the reduction of shear stress, $\Delta\tau_\delta (= \tau_w - \tau_\delta)$ across the wall layer region, is obtained.

$$\Delta\tau_\delta = \frac{2\delta}{3}\rho_b u_b \frac{du_b}{dx} \tag{6.29}$$

If the foregoing analysis is performed taking account of non-uniformity of density across the wall layer due to the heating, the coefficient in Equation 6.29 is found to be greater than 2/3 and to increase as the ratio ρ_w / ρ_b decreases. However, the effect is relatively small with the coefficient 2/3 only increasing to an upper limit of 3/4 when ρ_w is very much less than ρ_b.

Noting next that the mass flow rate does not vary with x and assuming that the change of bulk density is mainly due to the increase of bulk temperature (but see the recent paper by Jackson [6-59] which also takes account the effect of decrease of pressure), it follows that

$$\frac{du_b}{dx} = u_b \beta_b \frac{dT_b}{dx} \tag{6.30}$$

in which β is the thermal expansion coefficient of the fluid $\left(= -\frac{1}{\rho}\left(\frac{\partial\rho}{\partial T}\right)_p\right)$.

Applying the steady flow energy equation to relate the axial gradient of bulk temperature to the heat flux and mass velocity we obtain

$$\frac{dT_b}{dx} = \frac{4q_w}{\rho_b u_b c_{p_b} D} \tag{6.31}$$

Combining Equations 6.29 to 6.31, the fractional reduction of shear stress across the wall layer, $\Delta\tau_\delta / \tau_w$, is given by

$$\frac{\Delta\tau_\delta}{\tau_w} = \frac{8 u_b \beta_b q_w \delta}{3 c_{p_b} \tau_w D} \tag{6.32}$$

Defining a dimensionless buffer layer thickness $\delta^+ = \delta\rho_{av}^{1/2}(\tau_w - \Delta\tau_\delta)^{1/2} / \mu_{av}$, according to the universal wall layer approach, using a reduced shear stress $(\tau_w - \Delta\tau_\delta)$ and integrated mean values of density and viscosity $\overline{\rho}$ and $\overline{\mu}$ (over the range T_b to T_w), Equation 6.32 becomes

$$\frac{\Delta\tau_\delta}{\tau_w} = \frac{8}{3}\delta^+ \frac{\beta_b q_w \mu_b u_b}{\tau_w^{\frac{3}{2}} \rho_b^{\frac{1}{2}} c_{p_b} D}\left(\frac{\tau_\delta}{\tau_w}\right)^{-\frac{1}{2}}\left(\frac{\overline{\mu}}{\mu_b}\right)\left(\frac{\overline{\rho}}{\rho_b}\right)^{-\frac{1}{2}} \tag{6.33}$$

Introducing the friction factor f_b $(= \tau_w / \frac{1}{2}\rho_b u_b^2)$ and relating this to Reynolds number Re_b using $f_b = K_1 Re_b^{-m_1}$, Equation 6.33 can be re-written as

$$\frac{\Delta\tau_\delta}{\tau_w} = \frac{16\sqrt{2}}{3K_1^{3/2}}\delta^+ \frac{Q_b}{Re_b^{m_s}\,Pr_b}\left(\frac{\tau_\delta}{\tau_w}\right)^{-\frac{1}{2}}\left(\frac{\bar{\mu}}{\mu_b}\right)\left(\frac{\bar{\rho}}{\rho_b}\right)^{-\frac{1}{2}} \tag{6.34}$$

in which Q_b is a dimensionless thermal expansion group $\beta_b q_w D/k_b$ and $m_3 = 2 - 3m_1/2$.

Using an empirical equation for forced convection heat transfer relationship of the form, $Nu_{b_o} = K_2 Re_b^{m_2} Pr_b^{n_1}$ in conjunction with the one shown above for friction factor, it can be argued, using similar ideas similar to those presented under Equation 6.16, that Nusselt number Nu_b for conditions of thermally-induced bulk flow acceleration in a heated tube divided by that in the absence of such an effect, Nu_{b_o}, is related to the ratio τ_δ/τ_w by

$$\frac{Nu_b}{Nu_{b_o}} = \left(\frac{\tau_\delta}{\tau_w}\right)^{m_4} \tag{6.35}$$

in which $m_4 = m_2/(2-m_1)$.

Noting that $\Delta\tau_\delta/\tau_w = 1 - \tau_\delta/\tau_w$ and combining Equations 6.34 and 6.35, the impairment of heat transfer due to thermally-induced bulk flow acceleration in terms of Nusselt number ratio Nu_b/Nu_{b_o} is described by the equation can then be determined from

$$\frac{Nu_b}{Nu_{b_o}} = \left[1 - C_A \frac{Q_b}{Re_b^{m_3} Pr_b}\left(\frac{\bar{\mu}}{\mu_b}\right)\left(\frac{\bar{\rho}}{\rho_b}\right)^{-\frac{1}{2}}\left(\frac{Nu_b}{Nu_{b_o}}\right)^{-m_5}\right]^{m_4} \tag{6.36}$$

in which $C_A = 16\sqrt{2}\delta^+/(3K_1^{3/2})$ and $m_5 = 1/(2m_4)$.

Notice that the thermal expansion group Q_b combines with Reynolds number Re_b and Prandtl number Pr_b to form an acceleration parameter $Q_b/(Re_b^{m_3} Pr_b)$ which when multiplied by the property ratio factor $(\bar{\mu}/\mu_b)(\bar{\rho}/\rho_b)^{-1/2}$ characterizes the effect of thermally-induced bulk flow acceleration on forced convection heat transfer.

If δ^* is assigned a value typical of the turbulent buffer layer thickness, say 36, and again the combination K_1=0.080 and m_1=0.25 is used and m_2 is assigned the 0.8, then the Reynolds number index m_3 in the acceleration parameter Ac_b takes the value 1.625 and the coefficient C_A has an estimated value of 12,000.

Thus, Equation 6.33 takes the following specific form

$$\left(\frac{Nu_b}{Nu_{b_o}}\right) = \left[1 - C_A F_{VP_1} Ac_b \left(\frac{Nu_b}{Nu_{b_o}}\right)^{-1.1}\right]^{0.46} \tag{6.37}$$

in which F_{VP_1} is a variable property function $\left(\frac{\bar{\mu}}{\mu_n}\right)\left(\frac{\bar{\rho}}{\rho_b}\right)^{-1/2}$ and $Ac_b = Q_b/Re_b^{1.625} Pr_b$.

Of course the value for C_A of 12,000 quoted above has been arrived at after making a number of simplifying assumptions and can only be regarded as an estimate which might need to be established more reliably later by comparing results obtained using the model with observed behaviour.

As can be seen, the relationship between Nu_b / Nu_{b_o}, and $C_A F_{VP_1} Ac_b$ is an implicit one so that if a value for $C_A F_{VP_1} Ac_b$ is specified an iterative approach must be used to determine Nu_b / Nu_{b_o}. However, if Equation 6.37 is re-arranged as follows

$$C_A F_{VP_1} Ac_b = \left(\frac{Nu_b}{Nu_{b_o}} \right)^{1.1} - \left(\frac{Nu_b}{Nu_{b_o}} \right)^{3..3} \tag{6.38}$$

then the relationship between Nu_b / Nu_{b_o} and $C_A F_{VP_1} Ac_b$ can be readily established in a direct manner by specifying values for Nu_b / Nu_{b_o} and calculating values of $C_A F_{VP_1} Ac_b$.

The variation of Nu_b / Nu_{b_o} with $C_A F_{VP_1} Ac_b$ is of the form shown below on Fig. 6.11. The full line is a physical solution showing the unique curve relating Nu_b / Nu_{b_o} to $C_A F_{VP_1} Ac_b$ and the chain-dotted curve is a non-physical solution.

Notice that the function $C_A F_{VP_1} Ac_b$ is zero when Nu_b / Nu_{b_o} = 0 and it is also zero when Nu_b / Nu_{b_o} =1. As Nu_b / Nu_{b_o} varies between these limits $C_A F_{VP_1} Ac_b$ passes through a maximum. It can be shown using Equation 6.37 that the value of Nu_b / Nu_{b_o} at which this maximum occurs is 0.607 and that $C_A F_{VP_1} Ac_b$ is then 0.385.

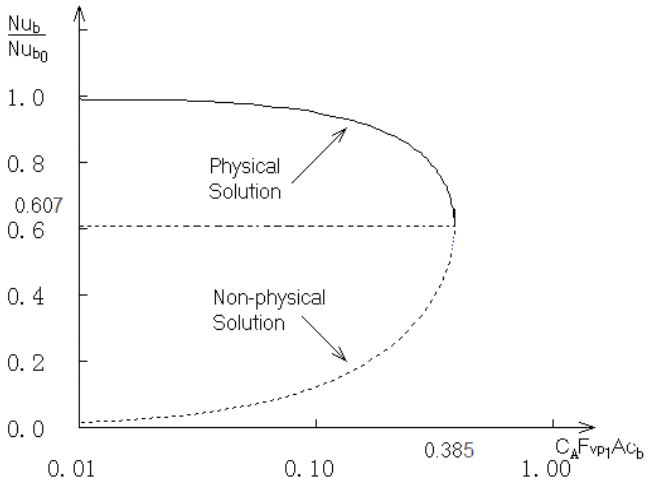

FIG. 6.11. Predicted effect of bulk flow acceleration on heat transfer.

6.6.2. Criterion for the effect of bulk flow acceleration on heat transfer to be small

If the acceleration parameter Ac_b is sufficiently small, Nu_b tends to the value Nu_{b_o} and heat transfer is not significantly affected by thermally-induced bulk flow acceleration. A criterion for this to be so can be readily determined by inspection of Equation 6.37. Provided that $C_A F_{VP_1} Ac_b$ is less than 0.04 the reduction in Nu_b due to bulk flow acceleration should be less than about 2%. Noting that the property ratio function F_{VP_1} is of order unity, a criterion for the effect of bulk flow acceleration on heat transfer to be less than about 2% based on the estimated value of C_A of 1.2×10^4 is

$$Ac_b < 5 \times 10^{-6} \tag{6.39}$$

in which $Ac_b = Q_b / (\mathrm{Re}_b^{1.625} \mathrm{Pr}_b)$

6.6.3. Laminarization of a turbulent flow due to thermally-induced bulk fluid acceleration

As can be seen from Fig. 6.11, with increase of Ac_b and, therefore, increase of $C_A F_{VP_1} Ac_b$, the ratio Nu_b / Nu_{b_o} is predicted to decrease systemically with $C_A F_{VP_1} Ac_b$, falling to about 0.6 when $C_A F_{VP_1} Ac_b$ reaches the value 0.385. This reduction in Nu_b / Nu_{b_o} occurs as a result of turbulence production being reduced. The acceleration parameter is then about 5×10^{-5}.

At some greater value of acceleration parameter the excess pressure force acting on the wall layer will be able to balance the shear force exerted on it by the wall and if this happens the core flow will not experience any shear stress and the velocity there will be uniform. Thus, the fluid will simply 'be taking a ride' on the wall layer. Under such conditions, the entire flow might become completely 'laminarized'. Simple theory for laminar slug flow in a uniformly heated tube predicts that for such conditions Nusselt number would take a constant value of 8. The ratio Nu_b / Nu_{b_o} would then vary in the manner indicated on right hand side of Fig. 6.12.

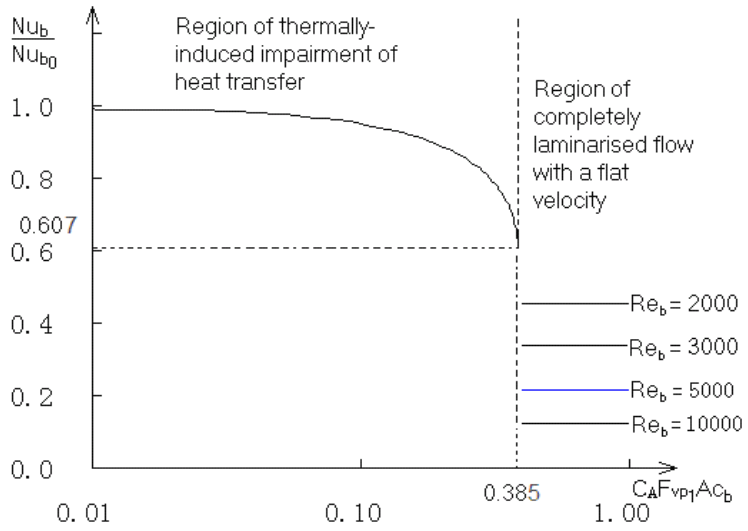

FIG. 6.12. Laminarization due to bulk flow acceleration.

6.6.4. Using the model to try to reproduce experimental behaviour

We consider next how Equation 6.37 can be used to determine the distribution of wall temperature along a heated tube taking account of thermally-induced bulk flow acceleration. In order to do this, the mass flow rate and the pressure and temperature of the fluid entering the tube must be specified and also the wall heat flux. Together, this information enables the distribution of bulk enthalpy h_b and bulk temperature T_b along the tube to be determined using the steady flow energy equation. Hence values of Re_b, Pr_b and Q_b can then be found at any specified axial location.

In Equation 6.36 the Nusselt number Nu_{b_o} for developing, variable property forced convection in the absence of any bulk flow acceleration can be found using Equation [6.20], see Section 6.1.3, earlier.

In Equation 6.36, the Nusselt number Nu_b for variable property forced convection with thermally-induced flow acceleration can be expressed in terms of q_w, T_b and T_w. With Nu_{b_o} being a specified parameter, obtained using Equation 6.20, Equation 6.36 is simply a non-linear algebraic equation which enables local values of the unknown variable T_w to be determined at any specified axial location along the tube. This can be done using standard iterative numerical procedures. The process can be initiated at x=0, where $T_w=T_b$, and continued step by step along the tube using the converged value of T_w after each step as the initial value at the next axial location.

It should be noted that although the model takes account of thermally-induced bulk flow acceleration as a result of the inclusion of the bulk inertia term in the simplified equation of motion (Equation 6.32), the detailed flow development is not modelled.

6.6.5. Refinement of the model using more realistic distributions of velocity and temperature in the near-wall region

The model of heat transfer with bulk flow acceleration presented here can also be refined by replacing the very simplistic linear representation of the near-wall distribution of velocity by one based the established 'universal' distribution u^+ versus y^+ referred to earlier in sub-section 6.5.10 and also accounting for non-uniformity of density across that region using a realistic distribution of temperature across that region. Such ideas are being actively developed and will also be reported soon in (see [6-65]).

6.6.6. Bulk flow acceleration due to axial pressure variation

Finally, mention has been made earlier, above Equation 6.30, that the model presented here is restricted to conditions where the bulk flow acceleration is thermally-induced, i.e., that it occurs mainly as a result of bulk temperature increase due to heating and the resulting thermal expansion of the fluid which arises as a consequence of that. In practice, density changes can also occur as a result of the pressure falling, i.e., due to the compressibility of the fluid (see Jackson [6-59] and [6-61]). This additional mechanism by which acceleration of the flow is partly produced could be of considerable importance in practice in causing the 'impaired forced convection' which has been referred to earlier in the discussion of the deteriorated heat transfer found by Shiralkar and Griffith [6-28] and [6-29] which is illustrated on Fig. 6.2, and also that reported by others (such as in Domin [6-64]).

6.6.7. A model which combines the influences of acceleration and buoyancy

The model of forced convection with thermally-induced bulk acceleration can be combined with that for buoyancy-influenced heat transfer in vertical tubes developed earlier in Section 6.5.3 to take account of both influences. The following equation, describes the combined effect on heat transfer. It involves both the parameters Ac_b and Bo_b.

$$\frac{Nu_b}{Nu_{b_o}} = \left[\left|1-(C_A Ac_b \pm C_B Bo_b F_{VP_3} F_{VP_4})F_{VP_1}\left(\frac{Nu_b}{Nu_{b_o}}\right)^{-1.1}\right|\right]^{0.46} \tag{6.40}$$

The acceleration parameter $Ac_b = Q_b/(\mathrm{Re}_b^{1.625}\,\mathrm{Pr}_b)$, where $\mathrm{Q_b} = \beta_b q_w D/k_b$. The buoyancy parameter $Bo_b = Gr_b/(\mathrm{Re}_b^{2.625}\,\mathrm{Pr}_b^{n_1})$, where $\mathrm{Gr_b} = gD^3(\rho_b - \rho_w)/(\rho_b \nu_b^2)$.

$\mathrm{F_{VP_1}} = (\mu_{av}/\mu_b)(\overline{\rho}/\rho_b)^{-1/2}$ and $\mathrm{F_{VP_3}} = (\overline{\mathrm{Pr}}/\mathrm{Pr_b})^{-n_1}$, where n_1 has a prescribed value of about 0.4 and $\mathrm{F_{VP_4}} = (\rho_w - \overline{\rho})/(\rho_w - \rho_b)$. The + sign in the ± applies for upward flow in a heated vertical tube and the – sign applies for downward flow.

Equation 6.40 can be re-written in the following condensed form

$$\frac{\mathrm{Nu_b}}{\mathrm{Nu_{b_o}}} = \left[\left|1-\mathrm{C_B F_{A/B}}\left(\frac{\mathrm{Nu_b}}{\mathrm{Nu_{b_o}}}\right)^{-1.1}\right|\right]^{0.46} \tag{6.41}$$

in which $F_{A/B} = ((C_A/C_B)Ac_b \pm Bo_b F_{VP_3} F_{VP_4})F_{VP_1}$

The acceleration coefficient C_A has an estimated value of 10,000 for an assumed value of δ^+ of 30. The buoyancy coefficient C_B has an estimated value of 4600 (again based of δ^+=30). However, it should be noted that the ratio C_A/C_B takes a fixed value of 2.5.

The fully developed model indicates that, in order to correlate experimental data for conditions of fully developed flow, $\mathrm{Nu_{b_{exp}}}/\mathrm{Nu_{b_o}}$ should be plotted against $F_{A/B}$. However, to take account of the effects of fluid inertia and flow development an extended version of the model is needed.

6.6.8. Conclusions

The model of forced convection heat transfer to fluids at supercritical pressure flow in a heated tube with thermally-induced flow acceleration presented in this section needs to be refined to utilize improved descriptions of the velocity and temperature distributions in the near-wall regions and extended to include the effect of the pressure falling in the axial direction due to friction and compressibility following the approach cited earlier which was developed recently for a gaseous fluid having an idealized equation of state $p/\rho = R/T$. If this were to be done and combined with the model of buoyancy-influenced flow in the manner suggested here it would open up the possibility of understanding the particularly difficult problem of heat transfer to fluids at supercritical pressure with combined effects of buoyancy and acceleration and would represent an important step forward.

6.7. GENERAL DISCUSSION

The extended and screened U of O databank is a valuable resource which has already been put to good use in the development of a trans-critical look-up table and the assessment of the performance of correlation equations for heat transfer to supercritical pressure fluids. It needs to subjected to further screening using criteria provided by up to date versions of the physically-based, semi-empirical models discussed here for deciding whether or not the data are influenced significantly by buoyancy and also bulk flow acceleration. This would enable correlation equations for forced convection heat transfer to fluids at supercritical pressure under conditions where such influences are negligible to be properly evaluated. The

further extended databank compiled in the course of the present IAEA CRP also needs to be subjected to similar screening.

The approach to developing a new correlation equation of simple form, using a function of a single additional dimensionless parameter, covering both normal and deteriorated heat transfer conditions without involving wall temperature or parameters depending on it is a laudable one. Should it prove to have sufficiently wide-ranging validity, it is likely to be widely used. Thus, validation of this correlation equation against reliable data from experiments from a variety of sources covering a wide range of conditions is needed. In this connection, the result of the recent assessment of correlations equations against the extended U of O database, which included the SJTU correlation equation, is of particular interest.

The two sets of correlation equations for mixed convection developed by KAERI to describe CO_2 data from upward flow experiments obtained using one test section provided only a general description of the observed heat transfer behaviour throughout the mixed convection region because the data were not correlated satisfactorily by means of the parameters employed. Furthermore, the data appeared to exhibit some anomalous features. It would be of interest to know what the reasons for this were.

The attempt to develop physically-based, semi-empirical models to extend currently available correlations for forced convection heat transfer to fluids at supercritical pressure to account for the influences of buoyancy and bulk flow acceleration remains to be extended further as described and properly evaluated. The models presented here should provide an improved means screening experimental data to identify those which are not affected by such influences. This would be helpful in enabling correlation equations for forced convection to be assessed more reliably. The physically-based, semi-empirical models presented here do indicate the parameters which are appropriate for the purpose of correlating experimental data. However, further work remains to be done to demonstrate that the models do provide a reliable means of calculating heat transfer to fluids at supercritical pressure.

The work reported in this section represents a useful start on the problem of developing new and improved correlations for heat transfer to fluids at supercritical pressures and has exposed some important issues that remain to be addressed. It is clear, however, that more work needs to be done on assessing correlation equations if we are to reach a stage where thermal analysis for high pressure, water cooled nuclear reactors can be performed with the high degree of confidence needed in the case of such plant.

LIST OF SYMBOLS FOR SECTION 6

a	Radius of tube (=d/2), m
A	Decay constant defined under Equation 6.27
Ac_b	Acceleration parameter $(= Q_b /(Re_b^{1.625} Pr_b))$
c_p	Specific heat at constant pressure, kJ/kgK
Bo_b	Buoyancy parameter $(Gr_b /(Re_b^{2.625} Pr_b^{n_1}))$ or boundary parameter defined in Table 6.6
Bo_b^*	Buoyancy parameter $Gr_b /(Re_b^{3.425} Pr_b^{2n})$
$\bar{c}_p$	Integrated value of c_p over range T_b to T_w $(= (h_w-h_b)/(T_w-T_b))$
C_A	Acceleration coefficient in Equation 6.36
C_B	Buoyancy coefficient in Equation 6.8
D	Tube diameter, m
e	Error band (±10%, ±20%, ±30%, etc)
h	Enthalpy, kJ/kg
f_b	Friction factor $(\tau_w /(½\rho_b u_b^2))$
f_{b_o}	Friction coefficient for conditions of forced convection
F_{TD}	Thermal development function, see Equation 6.21
$F_{A/B}$	Combined acceleration/buoyancy function, defined below Equation 6.41
F_g	Dimensionless gravitational group, the Gallileo number, $(= gD^3/\nu_o^2)$
F_{VP_1}	Variable property function 1 $(= (\bar{\mu}/\mu_b)(\bar{\rho}/\rho_b)^{-1/2})$
F_{VP_2}	Variable property function 2 $(= (\rho_w/\rho_b)^{0.3}(\bar{c}_p/c_{p_b})^{n_2})$
F_{VP_3}	Variable property function 3 $(= (\bar{P}r/Pr_b)^{-n_1}$
F_{VP_4}	Variable property function 4 $(= ((\rho_b - \bar{\rho})/(\rho_b - \rho_w)))$
F_{TB}	Thermal development function, see Equation 6.21
F	Variable property correction factor, or, a function, defined in Equation 6.7, or a function of Bo_b defined in Table 6.6
g	Acceleration due to gravity, m/s^2
G	Mass velocity, kg/m^2s
$\overline{Gr}$	Grashof number defined using $\bar{\rho}$ $(= gD^3(\rho_b - \bar{\rho})/\nu_b^2)$
Gr	Grashof number based on wall to bulk temperature difference $(= g\beta_b(T_w - T_b)D^3/\nu_b^2)$
Gr_b	Grashof number based on density difference $(= gD^3(\rho_b - \rho_w)/(\rho_b\nu_b^2))$
Gr_b^*	Grashof number based on wall heat flux $(= g\beta_b q_w D^4/k_b\nu_b^2)$
k	Thermal conductivity, kW/mK
K_1	Coefficient defined below Equation 6.33
K_2	Coefficient in Equation 6.20
ℓ	Turbulent mixing length, m
L	Test section heated length
m_1	Index defined above Equation 6.16
m_2	Index defined in Equation 6.20
m_3	Index defined below Equation 6.16 $(=3(1-m_1/2))$
m_4	Index defined below Equation 6.17 $(=m_2/(2-m_1))$
m_5	Index defined below Equation 6.18 $(=1/(2m_4))$
n_1	Prandtl number index, under Equation 6.12
n_2	Index in Equation 6.2 (defined in terms of T_b, T_u and T_{pc} by Equation 6.3)
Nu_b	Nusselt number $(= q_w D/(k_b(T_w - T_b)))$

Nu_{b_o} Nusselt number for variable property forced convection $(= q_w D/(k(T_{w_o} - T_b)))$

$Nu_{b_{exp}}$ Experimental value of Nusselt number

Nu_f Nusselt number with properties evaluated at the film temperature

Nu_F Nusselt number for forced convection

p Pressure, MPa or bar

Pr Prandtl number $(= \mu c_p / k)$

Pr_{n_1} Integrated average value of Prandtl number $\left(= \frac{1}{\delta_T} \int_o^{\delta_T} Pr\, dy \right)$

Pr_f Bulk value of Prandtl number $(= \mu_b c_{p_b} / k_b)$

$\bar{P}r_b$ Prandtl number defined using $\bar{c}_p$ $(= \mu_b \bar{c}_{p_b} / k_b)$

q_w Wall heat flux, kW/m^2

Q_b Thermal expansion parameter $(= q_w \beta_b D / k_b)$

r Radial coordinate, m

rms root mean square

Re_b Reynolds number $(= \rho_b u_b D / \mu_b)$

T Temperature, ^oC or K

T_b Local bulk temperature, ^oC

T_w Local wall temperature, ^oC

$T_{w_{exp}}$ Experimental value of local wall temperature

T_{w_o} Local wall temperature for conditions of variable property forced convection

ΔT Specified temperature drop

u Local axial component of velocity, m/s

u_b Local bulk velocity, m/s

v local transverse component of velocity, m/s, or specific volume, m^3/kg

x Axial coordinate, m

y Transverse coordinate (measured inwards from wall), m

Greek symbols

α Heat transfer coefficient $(=q_w/(T_w-T_b))$, kW/m^2K

β Thermal expansion coefficient $(= -(1/\rho)(\partial\rho/\partial T)_p)$

μ Viscosity, kg/ms

μ_{av} Integrated average viscosity $\left(= \frac{1}{\delta_T} \int_o^{\delta_T} \mu\, dy \right)$

ν Kinematic viscosity, m^2/s

ρ Density, kg/m^3

ρ_{av} Integrated average density $\left(= \frac{1}{\delta_T} \int_o^{\delta_T} \rho\, dy \right)$

δ Turbulent buffer layer thickness, m

δ_T Thermal layer thickness, m

τ_{δ_T} Shear stress at edge of the thermal layer, N/m^2

τ_δ Shear stress at edge of turbulent buffer layer N/m^2

τ Shear stress, N/m^2

τ_w Wall shear stress, N/m^2

τ_t Local turbulent shear stress
ω Mass velocity, kg/m^2s
π_A Acceleration number in Equation 6.7 $(=\beta q_w/(c_p G)$
π_B Buoyancy number $(=Q_b F_s/(Re_b Pr_b))$

Subscripts
b Denotes properties evaluated at the local bulk temperature T_b
f Denotes properties evaluated at the film temperature $T_f (= (T_w + T_b)/2)$
w Denotes properties evaluated at the local wall temperature T_w
pc Denotes pseudo-critical temperature
c Denotes critical point values
av Denotes average value of fluid properties (integrated wrt distance y across the thermal layer)

Superscripts
- Bar over a property symbol denotes that it is integrated over the range between the wall and the bulk temperature, or bar over a velocity component denotes that it is a time mean value in turbulent flow
+ Denotes the thickness of buffer layer in the universal wall coordinate form, $\delta^+ = \rho_b \tau_w^{1/2} \delta / \mu_b$
1 Region 1
2 Region 2
′ Denotes fluctuating component of velocity component in turbulent flow
* Denotes normalized fluid property ratio made dimensionless using the value at the inlet fluid temperature T_o and pressure P_o
ψ Denotes function of a group of variables

REFERENCES FOR SECTION 6

[6-1] MIROPOLSKY, Z.L., SHITSMAN, M.E., Heat transfer to water and steam at variable specific heat (in near critical region), Soviet Physics, Vol. 2, No. 10 (1957) 2196–2208.

[6-2] DICKINSON, N.L., WELCH, C.P., Heat transfer to supercritical water, Trans. ASME, 80, 746. (1958).

[6-3] SHITSMAN, M.E., Impairment of the heat transmission at supercritical pressures, Teplofiz. Vysokikh Temperatur, Vol. 1, No. 2 (1963).

[6-4] SCHMIDT, K.R., Thermal investigations with heavily loaded boiler heating surfaces, Mitt. Verb. Gross, No. 63 (1959) 391.

[6-5] PETUKOV, B.S., KRASNOSCHEKOV, E.A., PROTOPOPOV, V.S., An investigation of heat transfer to fluids flowing in pipes under supercritical conditions, Proc. Int. Heat Transfer Conf., Boulder, U.S.A., 1961-2 (1961).

[6-6] GOLDMAN, K., Heat transfer to supercritical water and other fluids with temperature dependent properties, A.I. Chem. Eng. Chemical Engineering Progress Symposium Series, Nuclear Engineering, Part 1, Vol. 50, No. 11 (1954) 105.

[6-7] GOLDMAN, K., Heat transfer to supercritical pressure water at 5000 lb/in2 flowing at high mass flow rates through round tubes, Paper 66, Int. Heat Transfer Conf., Boulder, USA (1961).

[6-8] POWELL, W.B., Heat transfer to fluid in the region of the critical temperature, Jet Propulsion, No. 27 (1957).

[6-9] HSU, Y.Y., SMITH, J.M., The effect of density variation on heat transfer in the critical region, J. Heat Transfer, Vol. 83, No. 2, May (1961).

[6-10] HENDRICKS, R.C., GRAHAM, R. W. HSU, Y.Y., MEDEIROS, A., Correlation of Hydrogen Heat Transfer in Boiling and Supercritical Pressure States ARS Journal, Vol. 32, no. 2 February (1962) 244–252.

[6-11] BRINGER, R.P., SMITH, J.M., Heat transfer in the critical region, J. Am. Inst. Chem. Engrs., Vol. 3, No. 1 (1957).

[6-12] SHITSMAN, M.E., Natural convection effect on heat transfer to a turbulent water flow in intensively heated tubes at supercritical pressures, Proc. I. Mech. E., 1967-68, Vol. 182, Part 3I (HTFS 3915).

[6-13] HALL, W.B., JACKSON, J.D., WATSON, A., A review of forced convection heat transfer to fluids at supercritical pressures, Proc. I. Mech. E., Vol. 182, Part 3I, Bristol Symposium, HTFS 3907 (1968).

[6-14] PETUKHOV, B.S., Heat transfer in a single-phase medium under supercritical conditions, Teplofizika Vysokikh Temperatur, Vol. 6, No. 4, pp. 732-745, HTFS 5050, July-August (1968).

[6-15] HENDRICKS, R.C., SIMONEAU R. J., SMITH, R.V., Survey of heat transfer to near critical fluids, NASA Technical Memorandum NASA TM X-S 2612, 1969 also Adv. Cryogenic Engng. Vol. 15 (1970) 197–237, HTFS 12278.

[6-16] HALL, W.B., JACKSON, J.D., Laminarization of a turbulent pipe flow by buoyancy forces. Paper 69-HT55, ASME AIChE National Heat Transfer Conference, Minneapolis, Minnesota, USA (1969).

[6-17] FEWSTER, J., Mixed Forced and Free Convective Heat Transfer to Supercritical Pressure Fluids in Vertical Pipes. PhD Thesis, University of Manchester, UK (1975).

[6-18] JACKSON, J.D., HALL, W.B., Influences of buoyancy on heat transfer to fluids flowing in vertical tubes under turbulent conditions. Turbulent Forced Convection in Channels and Bundles (eds. S. Kakac, and D.B. Spalding, Hemisphere Publishing Corporation, USA) (1979) 613–640.

[6-19] JACKSON, J.D., HALL, W.B., FEWSTER, J., WATSON, A. AND WATTS, M.J., Review of heat transfer to supercritical pressure fluids', H.T.F.S. Design Report No. 34, A.E.R.E. Harwell, (1975).

[6-20] JACKSON, J.D., HALL, W.B., Forced convection heat transfer to fluids at supercritical pressure, Turbulent Forced Convection in Channels and Bundles (eds. S. Kakac and Spalding D.B., Hemisphere Publishing Corporation, USA), pp 563-611, 1979a (1979).

[6-21] KRASNOSHCHEKOV, E.A., PROTOPOPOV, V.S., Experimental study of heat exchange in carbon dioxide in the supercritical range at high temperature drops, Teplofizika Vysokikh Temperatur, 4(3) (1966).
[6-22] PETUKHOV, B.S., KIRRILLOV, V.V., Questions concerning heat transfer in turbulent flow of liquids in tubes, Tepleonergetika No. 4 (1958) 63–68.
[6-23] KAYS, W.M., Convective heat and mass transfer, published by McGraw Hill, New York, USA (1966).
[6-24] BISHOP, A.A., SANDBERG, R.O., TONG, K.S., Forced convection heat transfer to water at near-critical temperatures and supercritical pressures, *American Inst. Chem. Engrs*. – I. Chem. E. Symposium Series No. 2, (HTFS 7054) (London: Inst. Chem. Engrs.) (1965).
[6-25] SWENSON, H.S., CARVER, J.R., KAKARALA, C.R., Heat transfer to supercritical water in smooth-bore tubes, *A.S.M.E. Journal of Heat Transfer* (1965).
[6-26] HALL, W.B., JACKSON, J.D., Contribution to the discussion of paper no. 69-WA/HT-1 (Shiralkar B. and Griffith P.), the 90th A.S.M.E. Winter Annual Meeting, Los Angeles, USA (1969).
[6-27] HARRISON, G.S., WATSON, A., Similarity and the formation of correlations for forced convection to supercritical pressure fluids, Cryogenics, pp 147–151, March (1976).
[6-28] SHIRALKAR, B.S., GRIFFITH, P., Deterioration in heat transfer to fluids at supercritical pressure and high heat fluxes, *A.S.M.E., J. Heat Transfer*, Feb. (1969) 27–36.
[6-29] SHIRALKAR, B., GRIFFITH, P., The effect of swirl, inlet conditions, flow direction and tube diameter on the heat transfer to fluids at supercritical pressure, *Am. Soc. Mech. Engrs*. Paper No. 69-WA/HT-1, also *J. Heat Transfer*, Vol. 92 (1970) 465–474.
[6-30] BOURKE, P.J., PULLING, D.J., GILL, L.E., DENTON, W.H., Forced convective heat transfer to turbulent carbon dioxide in the supercritical region, *Int. J. Heat Mass Transfer*, Vol. **13**, pp 1339-1348 also AERE – R 5952 (1969).
[6-31] ZAHLAN, H., GROENEVELD, D.C., TAVOULARIS, S., Look-up table for trans-critical heat transfer, the 2nd Canada-China Joint Workshop on Supercritical Water-Cooled Reactors (CCSC-2010), Toronto, Canada, April 25–28 (2010) 18 pages.
[6-32] ZAHLAN, H., GROENEVELD, D.C., TAVOULARIS, S., MOKRY, S., PIORO, I., Assessment of supercritical heat transfer prediction methods, the 5th Int. Sym. SCWR (ISSCWR-5), Vancouver, British Columbia, Canada, March 13–16 (2011) 20 pages.
[6-33] MOKRY, S., GOSPODINOV, YE., PIORO, I., Kirillov, P., Supercritical water heat-transfer correlation for vertical bare tubes, Proceedings of the 17th International Conference on Nuclear Engineering ICONE-17, Brussels, Belgium, July 12-16, Paper # 76010 (2009) 8 pages.
[6-34] PIORO, I., MOKRY, S., Heat transfer to fluids at supercritical pressures, Section in Heat Transfer – Theoretical Analysis, Experimental Investigations and Industrial Systems, Edited by A. Belmiloudi INTECH, Rijeka, Croatia (2011) 481–504.
[6-35] WATTS, M.J., CHOU, C.T., Mixed convection heat transfer to supercritical pressure water, Proc. 7th International Heat Transfer Conference, Munich, Paper MC16, Vol. 3 (1982) 495–500.
[6-36] GRIEM, H., Untersuchungen zur Thermohydraulik innenberippter Verdampferrohre Dissertation an der Technischen Universität München, Februar (1995).
[6-37] KUANG, B., ZHANG, Y., CHENG, X., A new, wide-ranged heat transfer correlation of water at supercritical pressures in vertical upward ducts, NUTHOS-7, Seoul, Korea (2008).
[6-38] CHENG, X. YANG, Y.H., HUANG, S.F., A simple heat transfer correlation for SC fluid flow in circular tubes, NURETH-13, Kanazawa City, Ishikawa Prefecture, Japan, September 27–October 2, 2009 (2009).
[6-39] GUPTA, S., MOKRY, S., FARAH, A., KING, K., PEIMAN, W., PIORO, I., Developing a heat-transfer correlation for supercritical-water flow in bare vertical tubes and its application, UOIT unpublished report (2010).
[6-40] KOSHIZUKA, S., OKA, YO., Computational analysis of deterioration phenomena and thermal-hydraulic design of SCR, Proceedings of the 1st International Symposium on Supercritical Water-Cooled Reactor Design and Technology (SCR-2000), Paper No. 302 (2000).

[6-41] HADALLER, G., BANERJEE, S., Heat transfer to superheated steam in round tubes, AECL Report (1969).
[6-42] SEIDER, N.M., TATE, G.E., Heat transfer and pressure drop of liquids in tubes, Ind. Eng. Chem. 28 (12) (1936) 1429–1435.
[6-43] DITTUS, F.W., BOELTER, L.M.K., Heat transfer in automobile radiators of the tubular type, University of California, Berkeley, Publications on Engineering 2 (13) (1930) 443–461.
[6-44] GNIELINSKI, V., New equation for heat and mass transfer in turbulent pipe and channel flow, Intern. Chem. Eng., Vol. 16, No. 2 (1976) 359–366.
[6-45] HERKENRATH, H., MÖRK-MÖRKENSTEIN, P., JUNG, U., WECKERMANN, F.J., Warmeubergung an Wasser bei Erzwungener Stromung in Druckbereich von 140 bis 250 Bar, EUR-3658d (1967).
[6-46] BAE, Y. Y., KIM, H. Y., Convective heat transfer to CO2 at a supercritical pressure flowing vertically upward in tubes and an annular channel, Exp. Therm. Fluid Sci. Vol. 33, No. 2 (2009) 329–339.
[6-47] JACKSON, J.D., A semi-empirical model of turbulent convective heat transfer to fluids at supercritical pressure, Paper No. 48914, Proceedings of the 16th International Conference on Nuclear Engineering, ICONE16, Orlando, Florida, USA, May (2008).
[6-48] BAE, Y.Y., Mixed Convection Heat Transfer to Carbon Dioxide Flowing Upward and Downward in a Vertical Tube and an Annular Channel, Proc. of 1st Meeting of International Specialists on Supercritical Pressure Heat Transfer and Fluid Dynamics, University of Pisa, Pisa, Italy, July 5-8 2010 (2010).
[6-49] YAMAGATA, K., NISHIKAWA, K., HASEGAWA, S., FUJII, T. AND YOSHIDA, S., Forced convective heat transfer to supercritical water flowing in tubes, Int. J. Mass Transfer, Vol. 15 (1972) 2575–2593.
[6-50] VIKHREV, V., BARULIN, D., KONKOV, A. S., A study of heat transfer in vertical tubes at supercritical pressures, Thermal Engineering, Vol.14, No. 9 (1967) 116–119.
[6-51] JACKSON, J.D., COTTON, M.A., AXCELL, B.P., Studies of mixed convection in vertical tubes, International Journal of Heat and Fluid Flow, Vol. 10, No. 1 (1989) 2–15.
[6-52] JACKSON, J.D., Studies of buoyancy-influenced turbulent flow and heat transfer in vertical passages, Invited Keynote Lecture KN24, Proceedings of the 13th International Heat Transfer Conference, Sydney, Australia, August (2006).
[6-53] JACKSON, J.D., Mixed forced and free convection - the influence of buoyancy on turbulent forced flow in vertical pipes, Proceedings of the Euromech Meeting on Boundary Layers and Turbulence in Internal Flows, University of Salford, UK (1976).
[6-54] ROUAI, N. M., Influence of Buoyancy and Flow Transients on Turbulent Convective Heat Transfer in a Tube, PhD Thesis, University of Manchester, UK (1987).
[6-55] BÜYÜKALACA, O., On Transient Turbulent Convective Heat Transfer, Ph.D. thesis, University of Manchester (1993).
[6-56] JACKSON, J.D., Progress in developing and improved empirical heat transfer equation for use in connection with advanced nuclear reactors cooled by water at supercritical pressure, Proceedings of the 17th International Conference on Nuclear Engineering, ICONE17-76022, Brussels, Belgium, July 12-19, 2009 (2009).
[6-57] JACKSON, J.D., A model of developing mixed convection heat transfer in vertical tubes to fluids at supercritical pressure, Paper No. P104, Proceedings of the 5th Int. Sym. SCWR (ISSCWR-5), Vancouver, British Columbia, Canada, March 13-16, 2011 (2011).
[6-58] PETUKHOV, B.S. and POLYAKOV, A.F., Heat Transfer in Turbulent Mixed Convection, Ed. Launder, B.E., Hemisphere, Bristol, Pennsylvania (1988).
[6-59] JACKSON, J.D., Mechanisms for impairment of heat transfer in strongly-heated turbulent flow of air through a tube, Proceeding of the 12th UK National Heat Transfer Conference, Leeds, UK, 30 August–1 September 2011 (2011).
[6-60] JACKSON, J.D., ANDERSON, M., CHENG, X., ZAHLAN, H., BAE, Y.Y., YAMADA, K. , Review of progress on the development of new empirical correlation equations under the

framework of the IAEA Coordinated Research Programme on Heat Transfer in SCWR'S, Paper No. 12268, Proceedings of ICAPP '12, Chicago, USA, June 24–28, 2012 (2012).
[6-61] JACKSON, J.D., Heat transfer deterioration in tubes caused by bulk flow acceleration due to thermal and frictional influences, Paper No. 12425, Proceedings of ICAPP '12, Chicago, USA, June 24–28, 2012 (2012).
[6-62] JACKSON, J.D., JIANG, P.X., LIU, B., On the correlation of buoyancy-influenced turbulent convective heat transfer to fluids at supercritical pressure, Paper No. 12429, Proceedings of ICAPP '12, Chicago, USA, June 24–28, 2012 (2012).
[6-63] JACKSON, J.D., Fluid flow and convective heat transfer to fluids at supercritical pressure, Paper No. NED-NURETH14-28, Journal of Nuclear Engineering Design (2012).
[6-64] DOMIN, G., Heat transfer to water in pipes in the critical/supercritical region, (in German), *B.W.K.*, Vol. 15, No. 11 (1963).
[6-65] JACKSON, J.D., Deterioration of heat transfer to fluids at supercritical pressure, Plenary lecture, 8th International Symposium Heat Transfer (ISHT-8), Beijing, China, October (2012).

7. CRITICAL FLOW DURING DEPRESSURIZATION FROM SUPERCRITICAL CONDITIONS

7.1. INTRODUCTION

When a fluid discharges from a high pressure and high temperature system, a 'choking' or critical condition occurs, and the flow rate no longer increases as the downstream pressure is further decreased. During a postulated loss of coolant accident (LOCA) of a pressurized water reactor (PWR) the break flow will be subject to this condition. An accurate estimation of the critical flow rate is important for the evaluation of the reactor safety, because this flow rate controls the loss of coolant inventory and energy from the system, and thus has a significant effect on the accident consequence. A depressurization event or LOCA is particularly of a concern for the supercritical water (SCW) reactor safety due to the lower coolant inventory compared to a typical PWR for the same power output. This lower coolant inventory would result in a faster transient response of the reactor dominated by the discharge flow rate. Critical flow is coupled with drastic depressurization and vaporization, and the flow rate is heavily dominated by the vapor content or quality of the vapor, which is closely related with the onset of vaporization and the interfacial interaction between phases. This presents a major challenge for the estimation of the flow rate due to the lack of the knowledge on those processes, especially under the conditions of interest for the SCWR.

High pressure depressurization leading to critical flow has been investigated extensively, in both experimental and theoretical ways. These studies have mostly been conducted with sub-critical pressure or ideal gases well above the vapor dome, as presented in the comprehensive reviews by Levy et al. [7-1], Saha [7-2], Anderson [7-3], Ardron et al. [7-4] and Fauske [7-5], but little work has been done near or above the thermodynamic critical point. To the authors' knowledge, the - available experimental data for supercritical water are those obtained by Lee and Swinnerton at a maximum temperature of 402 ^{o}C [7-6] and Chen with a maximum temperature of 474 ^{o}C [7-7]. Experiments have also been performed with other supercritical fluids such as CO_2, which can be considered a suitable surrogate fluid to water, by Fredenhagen [7-8] and Mignot et al. [7-9]. These surrogate fluids offer a close approximation to the physics that occur during the SCW depressurization thus the study can be used as a qualitative indication of the water flow and the test tool of physical models.

Based on the limited data of supercritical fluids, the critical flows at conditions above the pseudo-critical point seem to be fairly stable and consistent with the subcritical homogeneous equilibrium model (HEM) predictions. Further, in this regime the flows tend to be lower than those in the two-phase region. Thus the major difficulty in the prediction of the depressurization flow rate remains in the region where two phases co-exist i.e., within the two-phase portion of the vapor dome. In this region, the flow rate is strongly affected by the nozzle geometry and tends to be unstable. Various models for this region have been developed with different assumptions, e.g. the HEM [7-10] and Moody mode [7-11], and the Henry-Fauske non-equilibrium model [7-12], and are currently used in subcritical pressure reactor safety design [7-13]. It appears that some of these models could be reasonably extended to above the thermodynamic pseudo-critical point. The more stable and smaller flow observed in conditions above the pseudo-critical point suggests that even though SCWR designs have a smaller coolant inventory, the safety implications of a LOCA and the subsequent depressurization from supercritical conditions may not be as severe as expected and the limiting accident scenario may be driven by the critical flow within the subcritical pressure region.

The following section will cover a brief review of critical flow followed by a short summary of existing critical flow experiments and modeling conducted at conditions above the pseudo-critical point at the University of Wisconsin, China Institute of Atomic Energy and the JRC as part of the CRP. In addition, the status of a series of experiments being planned in Canada and China are mentioned.

7.2. REVIEW OF CRITICAL FLOW MODELS AND PREVIOUS WORKS

Critical flow is defined as the maximum flow that can pass through an opening for a given thermodynamic condition. Under this definition, numerous different configurations are possible: orifices or long tubes, single-phase flow or two-phase flow, rough or smooth tubes, sharp or round entrances, etc. All of these configurations affect the flow in their own manner and thus have to be characterized upon the specific application, in this case, a LOCA of a SCWR.

The current understanding of critical flow for a single-phase gas is fairly well-developed and analytical solutions can be found in several gas dynamic text books [7-3]. However the presence of a second phase adds such a significant complexity, that an analytical solution, even with simplifying assumptions, is difficult to achieve. This has led to a large amount of work focused on obtaining two-phase critical flow models and correlations. A summary of the different models and correlations used in nuclear analysis is presented in this section

Imagine a vessel filled with a compressible fluid at stagnation pressure (P_0) and stagnation temperature (T_0) connected to the ambient surroundings at a certain pressure (P_{amb}). If P_0 and P_{amb} are equal, no flow will occur. Decreasing P_{amb} leads to an increase in the flow rate until a maximum value is achieved, this maximum flow rate is called the critical flow rate or, the flow is considered as 'choked flow'. If P_{amb} decreases further, the pattern of the exit jet may vary, however, neither the mass flow rate nor property profile upstream of the exit will change.

7.2.1. Single-phase critical flow

Single-phase critical flow is well understood. It is instructive to understand the process of reaching a maximum mass flow rate for a given geometry and thermodynamic condition. Assuming ideal gas behaviour and isentropic conditions (frictionless and adiabatic), the critical mass flow rate can be expressed by:

$$\dot{m} = \frac{A \cdot P_0}{R \cdot T_0} \sqrt{2 \cdot C_p \cdot T_0 \cdot \left[\left(\frac{P_c}{P_0} \right)^{\left(\frac{2}{\gamma} \right)} - \left(\frac{P_c}{P_0} \right)^{\left(\frac{\gamma+1}{\gamma} \right)} \right]} \tag{7-1}$$

with a critical pressure ratio defined by

$$\frac{P_c}{P_0} = \left[\frac{2}{\gamma + 1} \right]^{\left[\frac{\gamma}{\gamma - 1} \right]} \tag{7-2}$$

and C_p:

$$C_p = \frac{\gamma \cdot R}{\gamma - 1} \tag{7-3}$$

Physically, the critical flow is reached when the flow is moving at a velocity equal to the sound speed at this location. At this point, the downstream pressure information is unable to propagate upstream. Recall that the critical flow is defined as the maximum flow rate for any downstream pressure. Gas dynamics predicts that for an isentropic depressurization the critical flow will occur at the minimum area, usually the throat of a converging-diverging nozzle or the end of a long tube.

Significant work has also been conducted to relax some assumptions and add friction or heat (Fanno flow or Rayleigh flow, respectively). While this increases the complexity of the analysis, it is still well understood and discussed in several texts. In both cases, if we consider straight pipe geometry with a constant diameter, the flow is expected to reach the condition of Mach number equal to unity for the gas. However, for short tubes, as it will be discussed further, the vena contracta that forms at the entrance of the tube creates a geometrical condition similar to a converging-diverging nozzle such that the minimum area is located at the vena contracta rather than the tube exit. The critical flow is therefore dictated by the conditions at the entrance of the tube. The combination of these effects creates various possibilities for the flow with the possible presence of shock waves inside the tube that may form as a function of the applied boundary conditions.

7.2.2. Two-phase critical flow

In single phase flow the critical flow velocity is identical to the fluid sound speed at 'choking' (M = 1). In general it turns out that the identity between the critical flow velocity and the fluid sound speed is not valid for a multiphase flow. This occurs because the concept of a single phase fluid sound speed for a mixture of phases loses meaning unless some simplifying assumptions about the phase relationships are made. There may actually be more than one sound speed existing; i.e. one for each phase and one for the mixture depending on the flow pattern and geometry or quality of the mixture. Figure 7.1 shows the theoretical values of the speed of sound in a homogenous steam-water mixture.

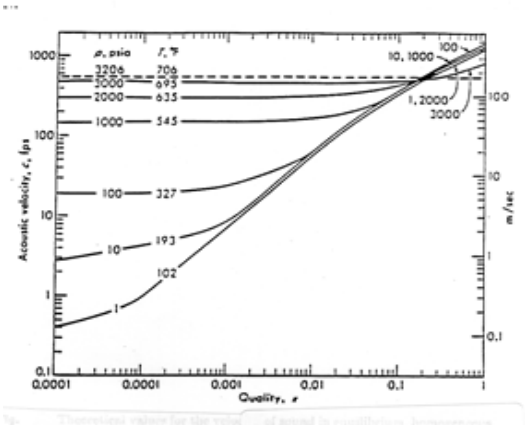

FIG. 7.1. Theoretical values for the speed of sound in an Equilibrium, Homogenous Steam-Water mixture.

Major complexity for analysis of two-phase critical flow comes from the non-homogeneous and non-equilibrium between phases. It is related to various factors, e.g. the pressure, quality, geometry, etc. Significant work has also been conducted to relax some assumptions, leading to equilibrium models with variable relative velocities and non-equilibrium models with variable degree of thermal non-equilibrium.

7.2.3. Equilibrium model

The simplest approach to model two-phase flow is to assume pressure and temperature equilibrium between the phases. These assumptions are usually satisfied for tube geometries with a large L/D (>40) since there is enough time for both phases to equilibrate their pressure and temperature. This does not imply, however, that the two phases flow at the same velocity, which leads to different models where one phase moves faster than the other or 'slips' past the other phase. The slip ratio is defined as the ratio of the phase velocities, however the exact form of this ratio is dependent on the model that is used. This will be discussed below. The simplest model is to assume that the phases move at the same velocity. This

assumption is called an 'equilibrium flow' condition and leads to a slip ratio of unity. This is the assumption used in the Homogenous equilibrium model (HEM). Numerous studies [7-7], [7-14]-[7-16] comparing critical flow data and HEM simulations show that the HEM model typically under-predicts the critical flow rate.

The HEM critical flow model has particular limitations when the density ratio is large (e.g., for water at low pressures) when the relative velocity is important and quality is low (when the non-equilibrium effect is important). As the stagnation pressure and quality increases the HEM prediction improves. Also as the L/D increases the HEM model prediction improves, due to more time for attainment of equilibrium (however as the pipe length increases it is necessary to include pipe friction). The stagnation conditions must also be homogeneous (dispersed or well-mixed) for the HEM model to successfully estimate the outlet flow. If the initial stagnation condition is better represented by stratified phases rather than co-dispersed phases, the HEM model does not give a reliable estimate until flashing occurs. This is due to the flushing inducing mixing which disperses the phases. Typically, for highly stratified conditions or short tube conditions, non-equilibrium should be considered and the HEM model is not valid (however it is typically used as an initial estimate of the flow).

To correct the difference between experimental data and the HEM prediction, several separated flow models, with various empirical slip ratios, were developed Fauske [7-17], [7-18] and Moody [7-11], [7-19]. Fauske considers that at the 'choked' location, the pressure gradient reaches a maximum and the momentum flow rate is maximized, leading to the following model for the critical slip ratio:

$$K = \left[\frac{v_g}{v_l} \right]^{1/2} \tag{7-4}$$

Moody, takes a slightly different approach and characterizes the critical flow by maximizing the kinetic energy of the flow, leading to the expression:

$$K = \left[\frac{v_g}{v_l} \right]^{1/3} \tag{7-5}$$

Both models are in good agreement with past experimental data from Ishii [7-20], Fauske [7-12] and Faletti. However, the Moody model seems to under-predict the critical flow for high quality conditions (0.5~1) whereas it over-predicts the flow for low quality (0.01~0.5). This over prediction is more conservative and has been used in analysis codes such as RELAP or RETRAN [7-21] for nuclear reactor safety analysis since, as pointed by Ardron and Furness [7-4], [7-22] it gives an upper bound for the depressurization rate with a reasonable margin.

7.2.4. Non-equilibrium models

Non-equilibrium models relax the assumption of constant temperature, pressure and velocity of phases. These models attempt to express the flashing effect, the growth of the vapor phase, the nucleation of the bubbles, and the metastable nature induced by the vaporization process, for example. In general, these non-equilibrium models are very specific to particular cases and difficult to apply to general critical flow configurations. However, they lead to factors that can be used to correct results from simple models. Saha [7-2] gives a good overview of the different non-equilibrium models, distinguishing the lumped model developed by Fauske et al. [7-12] and the distributed models. In the lumped model, a new parameter is

introduced to keep the quality below the equilibrium quality, as experimental results show the HEM over predicts the quality at the critical location. This parameter was correlated to experimental data.

For example, in the Henry-Fauske model [7-12], which is used in RELAP3/MOD3.3 as an option, a non-equilibrium parameter, N, is introduced, simply taking a constant (0.14). This value was derived from limited experimental data, but was found not suitable for extended conditions, e.g. the Marviken full scale test [7-23]. The non-equilibrium tends to increase as the pressure decreasing, and in low quality or low sub-cooling region it is more significant. Furthermore, the non-equilibrium is related to the geometry, and it is more important in a short nozzle or orifice.

The distributed model attempts to consider the creation of vapor locally based on bubble nucleation theory and goes into much more complex physics. The different physical behaviours are as follows:

- Flow patterns;
- Flashing at vena contracta location;
- Nucleation delay;
- Rate of bubble nucleation.

7.2.5. Geometrical effects on critical flow

Consider the effect of diameter and length of the nozzle, Fauske [7-12] studied this effect for short pipes and concluded that, for orifice and very short pipes, Bernoulli's equation with a contraction coefficient could be used. It is expressed as follows:
For an orifice:

$$G = 0.61 \cdot \sqrt{2 \cdot \rho \cdot (P_0 - P_b)} \tag{7-6}$$

For a short pipe (L/D < 3) the back pressure is replaced by the pressure that results in choking. For 3<L/D< 12, the same equation can be used, though it usually leads to an underestimation of the critical mass flux.

For larger L/D, Fauske observed that the critical mass flux decreased very slowly and the critical stagnation pressure ratio asymptotically approaches a constant. This leads to a conclusion that there is little effect of L/D on the critical mass flux. This conclusion holds only under conditions of saturation and may not be true in general.

In Saha's review [7-2], the majority of experiments exhibited the expected result, that the critical mass flux decreases with the diameter (however there were a few studies that did not show a clear decrease as the diameter was reduced – due to the instability of the flow and the subtle effects of several parameters). Experiments where the diameter was held constant and the length was varied were also consistent with expected results of a decrease in mass flux as the length of the tube was increased, however the combined effect of changing both parameters, L and D independently, were not sufficiently studied to give a definitive relationship of the mass flux as a function of L/D.

Other important parameters are the effects of the entrance geometry of the test section and the roughness of the pipe. As pointed out by Fauske [7-12], it can be expected that the mass flux of a sharp entrance pipe should be lower than a round entrance pipe for a given stagnation condition and L/D ratio. However, he also suggested that this effect will decrease as L/D increases. This conclusion should be used with caution as it comes from data of saturated water, and may not be applicable to supercritical fluids, which are more compressible. The roughness factor acts on the critical mass flux directly through the estimate of the friction factor used to characterize the pressure drop along the pipe. This could become an important

effect if the friction pressure drop is of the same magnitude as the momentum pressure drop.

Finally, another parameter that would affect the critical flow is heat addition. Most two-phase critical flow experiments have been conducted under adiabatic and steady state conditions to avoid the additional complications of this parameter. In fact, most of the two-phase critical flow models consider isentropic evolution and the assumed energy transfer only occurs between the phases, which may not be the case in a real situation.

7.3. PREVIOUS DATA ON SUPERCRITICAL FLUID DEPRESSURIZATION

Very few experiments have been found in the literature concerning supercritical fluid depressurization. Only two additional studies outside the scope of the CRP were found. One is performed with water at conditions just slightly above the vapor dome and one is performed with CO_2. The most relevant one is the work done by the Electric power research institute (EPRI) and can be found in reference [7-6], [7-24]. EPRI's study was motivated by the lack of data in high pressure sub-cooled water conditions encountered while studying anticipated transient without scram (ATWS). In certain types of ATWS, the peak pressure reached was higher than the critical pressure. The goal of this experiment was to generate a database and to compare the data with RETRAN calculations [7-23]. The second are a series of experiments conducted at the University of Hamburg-Harburg using CO_2 and mixtures of CO2 and H_2O or N_2 [7-25]. The goal of this work focused on the evolution of the fluid phase change within the vessel by observing the evolution of the void fraction and the phase separation during the blow-down. The goal of this work was to study conditions for safety analysis of a chemical plant.

7.3.1. Electrical Power Research Institute (EPRI) experiment

EPRI's study was motivated by the lack of data in high pressure sub-cooled water conditions encountered while studying anticipated transient without scram (ATWS). In certain types of ATWS, the peak pressure reached higher values than the critical pressure. The goal of this experiment was to generate a database and to compare the data with RETRAN calculations [7-24].

The experiment was conducted at steady state conditions. The water was brought to supercritical conditions by pumping through a heated pipe. The pressure ranged from 34 bars to 310 bars and the temperature ranged from 200 ºC to 400 ºC. However, of most interest in this report are conditions where the temperature and pressure are higher than the pseudo critical point. The mass flow rate was recorded using a flow meter inserted within the rig. The EPRI experiment used four different nozzles involving sharp edge and round edge nozzles and orifices, as well as a baffled nozzle. The minimum pipe diameter ranged from 1.7 mm to 2.54 mm with a maximum *L/D* ratio of 3. The details of the geometry and the stagnation conditions of the different runs can be found in references [7-6], [7-24]. Due to large enthalpy rise of SCF the power required to reach these operating conditions was considerable (up to 900 kW). Moreover, if one considers the different nozzles used to measure the critical mass flow and compare them to the amount of power input into the rig, it does not seem encouraging to build a steady state experimental system with a larger diameter pipe, which is desirable since it would be instructive to capture the effect of pipe diameter on the critical flow. The wider the range of diameter is, the better it is to obtain a complete study and analysis of this parameter. Figure 7.2 shows the stagnation conditions of the different runs in a TS diagram. It can be noticed that the temperature is well below the reactor outlet temperature of 500ºC expected in the SCW GEN IV design. However, this still gives a good complement to Fauske's [7-12] study for short nozzle and does extend the data above the vapor dome.

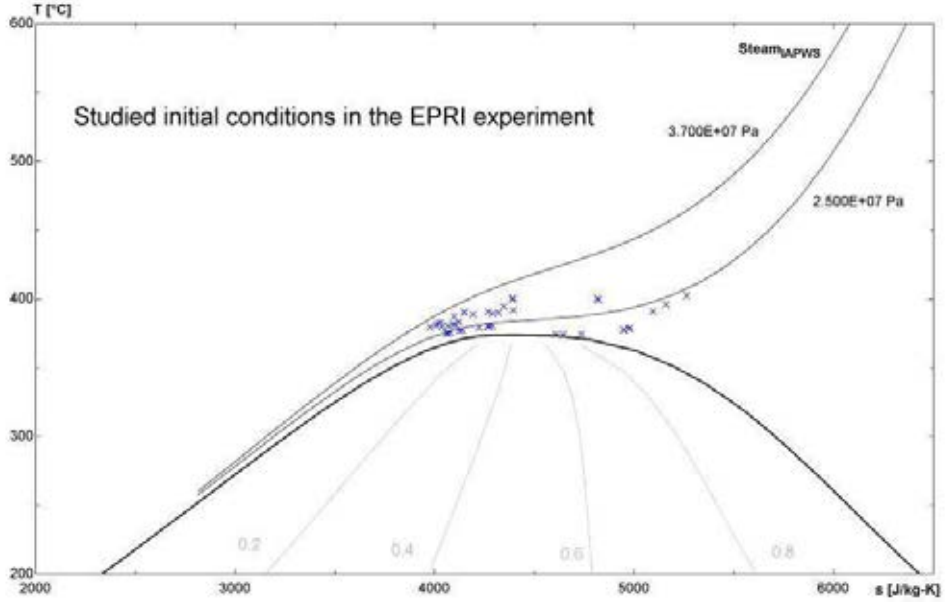

FIG. 7.2. Initial conditions of the EPRI experiments.

The results from the EPRI work were compared to the RETRAN predictions and the Bernoulli equation. RETRAN is a program for transient thermal-hydraulic analysis of complex fluid flow systems used in the nuclear field. The different analytical models implemented in this program are computed in the form of fitted parametric functions to avoid computational expense. In a similar manner, the water properties are implemented under fitted function form based on the ASME 1967 steam table.

It was shown that the HEM model did not correlate well at low pressures and low sub- cooling conditions and was found to predict mass fluxes 70% lower. However, the Extended Henry and Fauske model and the Modified Bernoulli model worked well in the range of pressures studied. As expected, the HEM model is not suitable for sub-cooled and saturated liquid conditions but may be suitable for conditions above the vapor dome.

7.3.2. University of Hamburg-Harburg experiments

Another experiment related to supercritical fluid blow-down was conducted at the University of Hamburg-Harburg using CO_2 and mixtures of CO_2 and H_2O or N_2 [7-25]. The goal of this work focused on the evolution of the fluid within the vessel itself by observing the evolution of the void fraction and the phase separation during the blow-down for chemical plant safety purposes. The experimental setup consisted of a 0.05 m^3 vertical vessel connected to a ball valve by a pipe whose area ranged between 7 mm^2 and 34 mm^2. The vessel was set on a scale to follow the evolution of the mass during the depressurization process. The mass flow rate was evaluated directly from this measurement. The pressure and temperature were measured, as well as the density, which was measured using a radioactive Cs^{137} gamma densitometer diagnostic. This technique allows determination of the evolution of the void fraction as the pressure drops inside the vessel, and the fluid enters two-phase condition. The data presented principally concerns the evolution in pressure and temperature with time, and the development of a model proposed to estimate the mass flow rate. The comparison is based on a ratio of the measured mass flow rate with respect to the estimated HEM mass flow rate prediction. For the HEM calculation, the void fraction and the pressure measured during the depressurization inside the vessel have been used. Two interesting conclusions have been drawn. First, the HEM simulation is in good agreement with the

experimental data for small pipe (7 mm^2). When the outlet area increased to 17 mm^2 and 34 mm^2, the normalized mass flow rate fell from 1 to 0.91 and 0.78, respectively. Second, the CO_2 saturated with water shows a less stable normalized critical mass flow rate than pure CO_2. This effect is amplified by the area of the outlet. Indeed, the smaller the area is, the more unstable the critical flow would be; this is characterized by wide oscillations that may lead to a flow interruption, as shown in Fig. 7.3.

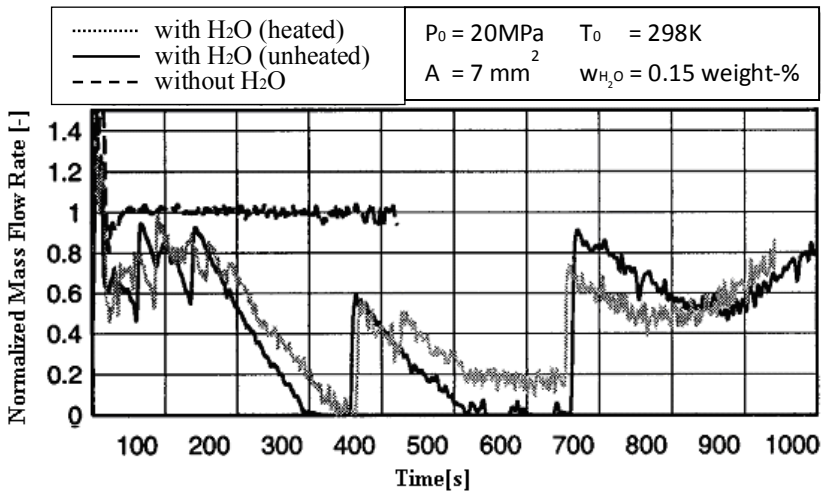

FIG. 7.3. Recording of the normalized mass versus time for sub-cooled CO_2-H_2O system [7-25].

Figure 7.3 shows the evolution of the normalized mass flow rate with time during a depressurization process. After a sudden drop in pressure, the second phase appears in the vessel. As time goes by, the void fraction increases inside the vessel and instabilities occur when water is presented with CO_2. These are not predicted by the HEM calculation, which explains why the normalized mass flow rate drops to zero with time. Fredenhagen [7-8] pointed out that, depending on the initial stagnation entropy, and assuming that the depressurization is isentropic until the fluid enters the two-phase dome, the formation of hydrate would occur. It results in the creation of instabilities within the critical flow itself and these hydrates can explain why obstruction of the flow can occur for small cross section area. This however, would not be of concern in a pure SCW system. As shown by Fig. 7.3, the flow is unstable for T=298 K. For T=313K, if all other parameters are kept the same, the mass flow rate are much more smoothly, as shown in Fig. 7.4.

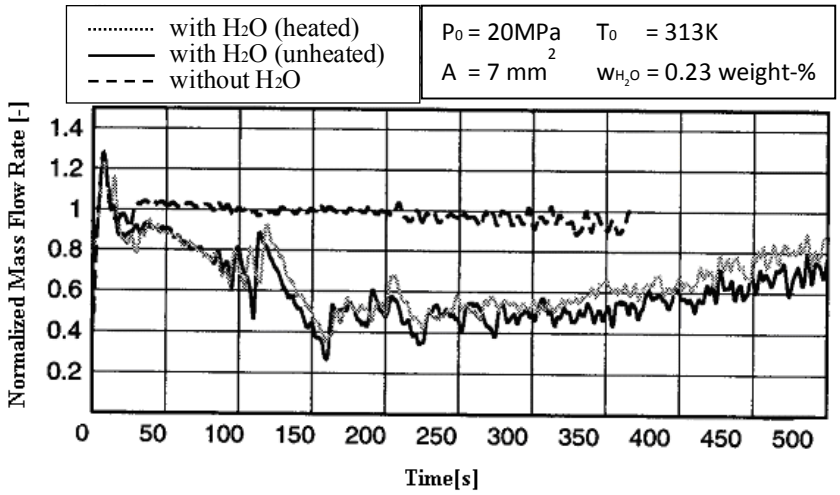

FIG. 7.4. Recording of the normalized mass versus time for supercritical CO_2-H_2O system [7-25].

7.3.3. China Institute of Atomic Energy experiments

As a part of the IAEA CRP, the China Institute of Atomic Energy (CIAE) conducted experiments measuring the depressurization of supercritical water in an apparatus similar to that used in the EPRI study, but with temperatures more consistent with the SCWR conditions. In this test SCW was ejected from two different nozzles both with a diameter of 1.41 mm and length of 4.35 mm but one with a rounded-edge and one with a sharp-edge entrance geometry. The test conditions covered the ranges of inlet pressures of 22.1 MPa – 29.1 MPa and inlet temperature of 38 ^{o}C – 474 ^{o}C. More than 200 data points were obtained at steady-state, the parametric trends were investigated, and the characteristics of the phenomena are summarized below.

In the region of near and beyond pseudo-critical temperature the thermal equilibrium was dominant, and the flow rate was found to be represented by a modified HEM.

$$G = \left[\frac{2(h_0 - x h_g - (1-x) h_l)}{\frac{C}{\rho^2} + (\frac{1-x}{\rho_l} + \frac{x}{\rho_g})^2} \right]^{1/2} \tag{7-7}$$

Below the pseudo-critical region the results were scattered as a result of a hysteresis effect in the onset of vaporization, exhibiting a bifurcation behaviour. This effect was found to be more significant in the nozzle with a sharp-edge, especially at higher pressures. For the temperatures well below the pseudo-critical point (low quality) the flow was represented reasonably well by the Bernoulli equation.

$$G = C_D \sqrt{2\rho_l (p_0 - p_b)}, \tag{7-8}$$

7.3.3.1. Experimental facility and procedure

The scheme of two nozzles is shown in Fig. 7.5. They have the same diameter of 1.41 mm and length of 4.35 mm but different inlet edges: (a) nozzle A with rounded-edge of 1 mm radius, and (b) nozzle B with sharp-edge. The experiment was conducted at the supercritical water loop in CIAE. As shown in Fig. 7.6, the de-ionized water was supplied by a three-head piston pump with a maximum pressure of 45 MPa and flow rate of 2.4 m^3/hr. It passed through a dumping tank and a pre-heater, and flowed upward through the nozzle. The discharge was condensed in a condenser, cooled further by heat exchangers, and then flowed back to the pump. The flow rate through the nozzle or the inlet pressure was controlled by a valve in bypass. The pre-heater was heated by a DC supply with a capacity of 75V × 15000A. With this system the data could be obtained at stable inlet pressure and temperature conditions.

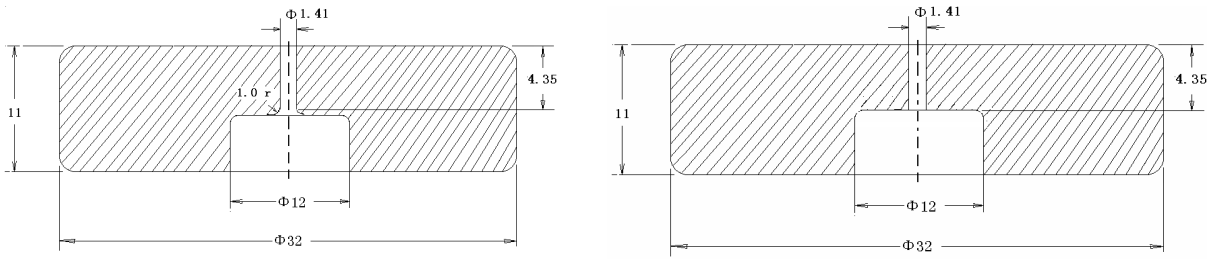

(a) Nozzle A with rounded-edge **(b)Nozzle B with sharp-edge**

FIG. 7.5. Scheme of two nozzles used in test.

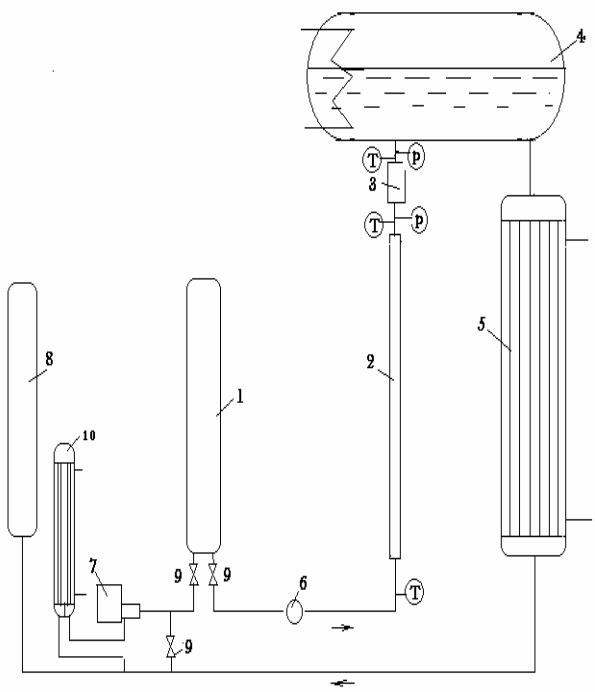

1—dumping tank;
2—preheater;
3—nozzle test section;
4—condenser;
5—heat exchanger;
6—flowmeter;
7—piston pump;
8—water tank;
9—valve;
10—heat exchanger

FIG. 7.6. Scheme of supercritical water test.

Major measurements included the flow rate with a turbine flow-meter at the upstream of the pre-heater,

the pressures with pressure transducers at the upstream and downstream of the nozzle, the inlet and outlet water temperatures with Ni-Cr/Ni-Si thermocouples and the voltage and current across the pre-heater. All the readings were recorded by a data acquisition system.

During a run, the pressure was kept unchanged, and the power of the pre-heater was stabilized. After a stable condition (i.e., the inlet pressure and temperature) was established, the data were recorded. Then the power of the pre-heater was adjusted for a next run at a varied temperature or/and pressure. The heat balance errors of the majority of runs were within 2%.

7.3.4. Experimental results and analysis

More than 200 experimental data points were obtained, covering the ranges of inlet pressures of 22.1 MPa – 26.8 MPa and temperatures of 38 ^{o}C – 474 ^{o}C in nozzle A, and the inlet pressures of 22.1 MPa – 29.1 MPa and temperatures of 263 ^{o}C – 454 ^{o}C in nozzle B.

7.3.4.1. Experimental results

Figure 7.7 shows the experimental results displaying GM versus DTPC, where GM is the measured mass flux, DT_{PC} the temperature difference $T_{PC} - T_0$, T_0 is the inlet bulk temperature, and T_{PC} is the pseudo-critical temperature, evaluated by the following expressions in ^{o}C.

$T_{PC} = 3.0\ p + 307.6$ for 22.1 MPa < p < 24.15 MPa,
$T_{PC} = 3.77\ p + 289.0$ for 24.15 MPa < p < 31.0 MPa.

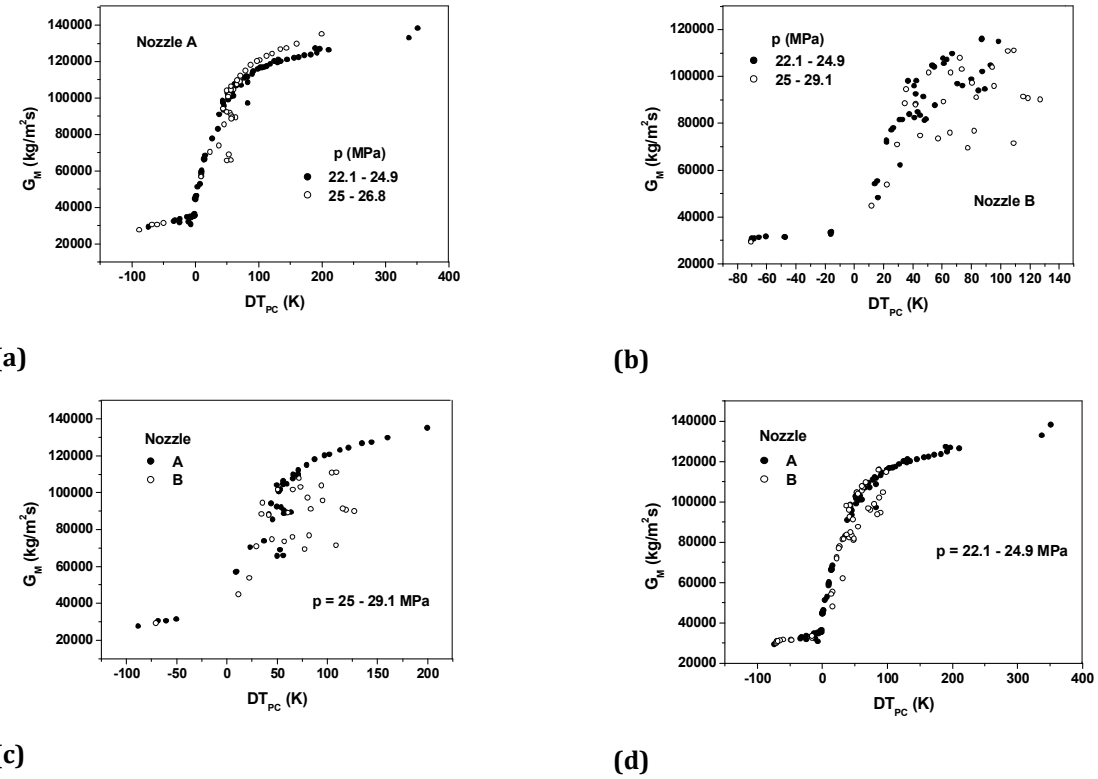

FIG. 7.7. Variation of measured mass flux with DT_{PC}.

As can be seen, the mass flux increases as DT_{PC} increases (or as inlet temperature decreases). The trend is

moderate in the negative DT_{PC} region (beyond pseudo-critical point), while it varies sharply when the temperature decreases below the T_{PC} (i.e., $DT_{PC} > 0$ K). It becomes moderate again for large DT_{PC}. This trend is understandable, because in both sides of the pseudo-critical point the specific volume of water varies substantially, associated with significant difference in the flow characteristics. This behaviour is similar with that observed at subcritical pressure as the pseudo-critical temperature refers to the saturation temperature [7-26].

It is also noticed that in the beyond pseudo-critical region ($DT_{PC} < 0$ K) the data trend is smooth, and the results of the two nozzles don't show too much differences. While in the region of $DT_{PC} > 0$ (> 30 K in particular) the results appear scattered. This behaviour is related to the experimental procedure. The test was started from a low temperature, and was proceeded by increasing the temperature run by run toward the pseudo-critical point, in this period the flow rate decreased smoothly. Then the test was repeated by decreasing the temperature run by run, in this period lower flow rates could be obtained and compared to those in the first period for the same p_0 and T_0. This behaviour appears more severe at high pressure, especially in nozzle B, but it is not so obvious in nozzle A with $p_0 < 25$ MPa.

In the near or beyond pseudo-critical region the results of the two nozzles are very similar. This is understandable, because in this region the overall flow resistance increases substantially, and the difference in the local resistance due to the inlet shape has a negligible effect. In the region of $DT_{PC} > 0$, however, the effect of inlet shape is more complicated and related to the vaporization, which will be discussed in the next section.

7.3.4.2. Analysis

Onset of vaporization:
Assuming that the pressure at a cross-section is uniform, the local pressure at the inlet of throat, p_t, is calculated by use of the Bernoulli equation:

$$p_t = p_0 - DP_t - \frac{G^2}{2\rho_t} \tag{7-9}$$

where DP_t is the pressure drop due to the local resistance of the inlet of throat, p_0 and p_b are the stagnation (inlet) and back pressures, respectively, p_{cr} is the pressure at critical flow area, as shown in Fig. 7.8.

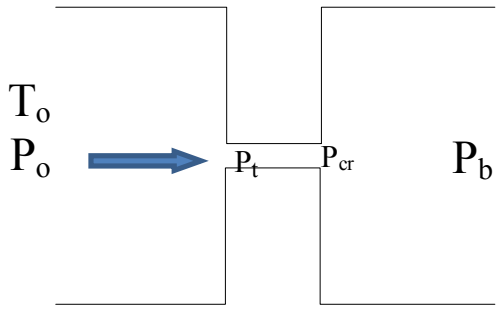

FIG. 7.8. Variation of pressure along the nozzle.

Actually, the velocity and pressure in the throat are not uniform and the onset of vaporization would firstly occur at the minimum pressure. Figure 7.9 shows the pressure distributions calculated by CFD in liquid-phase flow for two nozzles. A minimum pressure exists near the inlet of the throat, and the non-uniformity of the pressure in nozzle B is much more distinctive than nozzle A.

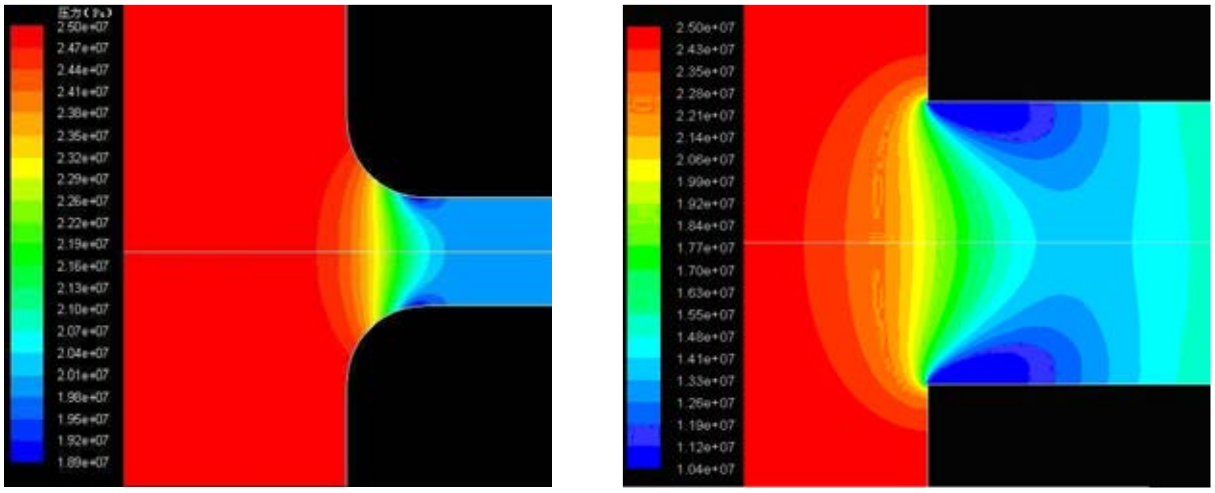

(a)Nozzle A **(b) Nozzle B**

FIG. 7.9. Pressure distribution in two nozzles with water flow (p_0 = 25 MPa, G = 97500 kg/m^{2}s).

It has been recognized that the drastic sub-cooled depressurization is a non-equilibrium process, and the first nucleation would occur at p_n, a pressure considerably lower than the local saturation pressure, p_s. A model on the pressure difference, p_s - p_n, which was called pressure undershoot, was proposed by Alamgir and Lienhard [7-27], [7-28] as:

$$P_s - P_n = 0.252 \frac{\sigma^{3/2} T_r^{13.73} (1+14\sum'^{0.8})^{0.5}}{\sqrt{kT_c(1-\frac{v_f}{v_g})}} \qquad (7\text{-}10)$$

where Σ' is the depressurization rate in Matm/s, σ is the surface tension, k is the Boltzman's constant, T_r is the reduced temperature,T/T_c and ν is the specific volume.

In the present experiment, the inlet pressure and the depressurization rate are much higher and out of the range of this model. Due to the lack of an appropriate method, this model is used for a rough estimation. As DT_{PC} decreases, the mass flux and depressurization rate decrease, leading to a decrease in the superheat. For p = 25 MPa and DT_{PC} = 60 K, for instance, p_s - p_n is around 6 MPa, corresponding to a superheat of 50 K, and 20 K for DT_{PC} = 30K.

In addition, on a hot surface the superheat for the first bubble formation is also related with the surface imperfection, dissolved gas or suspended particle in the liquid.

Hysteresis and bifurcation behaviour

For the inlet temperature below the pseudo-critical point by a certain value the minimum pressure at the inlet of throat is generally below the critical pressure and the vaporization would occur there. As discussed above, the onset of vaporization is related with various factors, including the local pressure, the depressurization rate and the surface condition. It is commonly accepted that the superheat for the onset of first nucleation could be quite large, but after the nucleus is activated the superheat for sustaining the vaporization could be small, characterizing a hysteresis effect.

Furthermore, the vaporization is accompanied by an increase in the local resistance, and hence by a decrease in the p_t, tending to enhance the vaporization further and to sustain the vaporization at reduced temperature. This hysteresis is illustrated in Fig. 7.10 by showing the variation of the quality, x_t, at the inlet of throat on increasing and then decreasing inlet temperature.

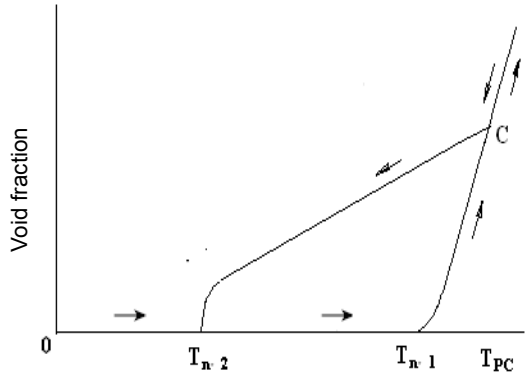

FIG. 7.10. Illustration of the hysteresis effect for the vaporization at the inlet of the throat.

Figure 7.11 exemplifies the variations of the minimum pressure, $p_{min,}$ with mass flux for two nozzles and the pressure at the critical flow area, p_{cr}, for p_0 = 25 MPa. The p_{min} is calculated by CFD in a flow of liquid water, and the p_{cr} is calculated by HEM. The p_{min} decreases rapidly as G increases. In nozzle B it is lower than nozzle A, especially at high mass flux. After the mass flux exceeds a certain value the p_{min} is lower than p_{cr}.

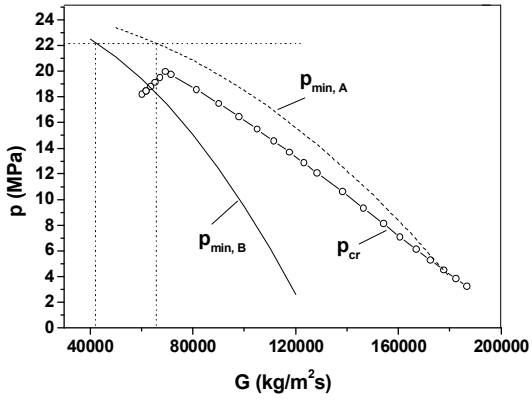

FIG. 7.11. Variation of p_{min} with G for the two nozzles without vaporization at the inlet (p_0 = 25 MPa).

Since the critical flow rate is sensitive to the vapor content, the hysteresis in the vaporization would made a complicated effect on the flow rate. Figure 7.12 illustrates the variation of mass flux with the inlet

temperature, which is calculated by HEM. On increasing the temperature the vaporization at the inlet of throat is not accounted, and the mass flux is simply calculated by HEM (i.e., it takes the maximum by Eq. (7.10) at successive decrease of pressure, as will be described later). While on decreasing the temperature from near-critical temperature, when $p_{min} < p_{cr}$ the mass flux is evaluated by Eq. (7.10) at $p = p_{min}$. The calculation results exhibit a bifurcation behaviour. It should be noted that the p_{min} is based on liquid-phase flow. It would be decreased when the vaporization occurs at the inlet, and the calculated mass flux would be even lower.

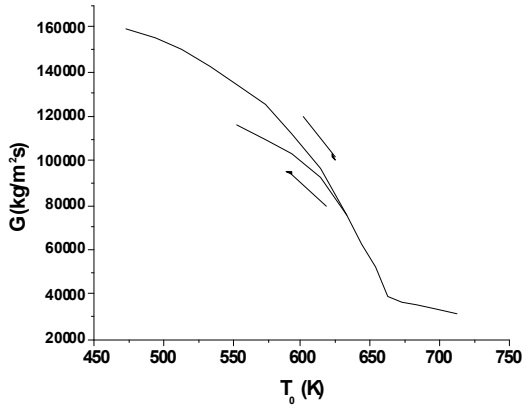

FIG. 7.12. Illustration of the bifurcation behaviour for critical mass flux (p_0 = 25 MPa).

Therefore the bifurcation behaviour in the mass flux is the result of hysteresis effect in the vaporization and the substantial decrease in the p_{min}. This explains more severely scattered results in nozzle B, especially at high pressure. For a same inlet temperature, higher pressure corresponds to a larger DT_{PC} and a higher mass flux, and thus a lower p_{min}. For p_0 = 25 and 29 MPa with T_0 = 350 ^oC, for instance, the critical mass flux is 109000 and 132000 kg/m^{2}s by HEM, and the p_{min} is around 6.5 MPa and 2 MPa, respectively, by CFD for liquid water flow.

It is also noticed in Fig. 7.11 that the pressure of p_{min} = 22.1 MPa corresponds to the mass flux of about 65000 kg/m^{2}s and 44000 kg/m^{2}s for nozzle A and B, respectively. This suggests that at a mass flux lower than these values the minimum pressure at the inlet of throat exceeds the critical pressure, so the phase transition does not occur. These mass fluxes correspond to the DT_{PC} less than 10 K. Therefore the data does not exhibit scattered feature essentially in the near-critical region.

Critical flow prediction

In the previous experiments, it has been concluded that the thermal non-equilibrium decreases as the pressure increases, and at supercritical pressure the thermal equilibrium is dominant [7-7], [7-26]. This statement is reasonable, because higher pressure corresponds to higher thermal conductivity and density of vapor and smaller bubble or droplet, associated with more efficient interfacial heat exchange. Same finding has been recorded in similar experiments in supercritical water [7-24] and CO_2 [7-29].

Based on the isentropic assumption with thermal equilibrium and equal velocity of two phases, a homogeneous equilibrium model (HEM) was proposed by Starkman et al. [7-10], as follows,

$$G = \frac{\left[2(h_0 - (1-x)h_l - xh_g)\right]^{1/2}}{(1-x)/\rho_l + x/\rho_g}, \tag{7-11}$$

where h is the enthalpy, ρ is the density, x is the equilibrium quality at the critical flow area, and the subscripts g and l refer to vapor and liquid, respectively, and 0 refers to the stagnation condition. The quality is evaluated by

$$x = \frac{s_0 - s_l}{s_g - s_l}$$

where s_0 is the specific entropy at the inlet, and s_l and s_g are the specific entropies for the liquid and vapor, respectively.

In the present study, based on the continuity and energy equations, considering the local resistance, the HEM is modified as

$$G = \left[\frac{2(h_0 - xh_g - (1-x)h_l)}{\frac{C}{\rho^2} + (\frac{1-x}{\rho_l} + \frac{x}{\rho_g})^2} \right]^{1/2} \tag{7-12}$$

The critical condition is defined by

$$\left.\frac{dG}{dP}\right|_p = 0.$$

The mass flux is predicted by Eq. (7.12) as the pressure decreases successively until a maximum is attained and it is taken as the critical mass flux.

Non-critical flow prediction

At certain sub-cooling the liquid is not vaporized before leaving the throat, and the flow would not be choked. The mass flux is calculated by use of the Bernoulli equation as:

$$G = C_D \sqrt{2\rho_l (p_0 - p_b)}, \tag{7-13}$$

where $p_{b,}$ is the back pressure, ρ_l is the water density, and C_D is the discharge coefficient.

Estimation of mass flux

The inlet effect of nozzle is mainly caused by the phase transition, and is related with the inlet shape and the pressure. It is ignored in the homogeneous equilibrium model and Bernoulli equation. This would be true in the region of near or beyond the pseudo-critical point. In Fig. 7.13 the experimental results of DT_{pc} < 30 K are compared with the calculations by the modified homogeneous model (M-HEM) with C = 0.2 for nozzle A and C = 0.6 for nozzle B. The differences are mostly within 15%. For G_c < 60000 kg/m^{2}s (or

DT_{PC} < 10 K), the agreements are better.

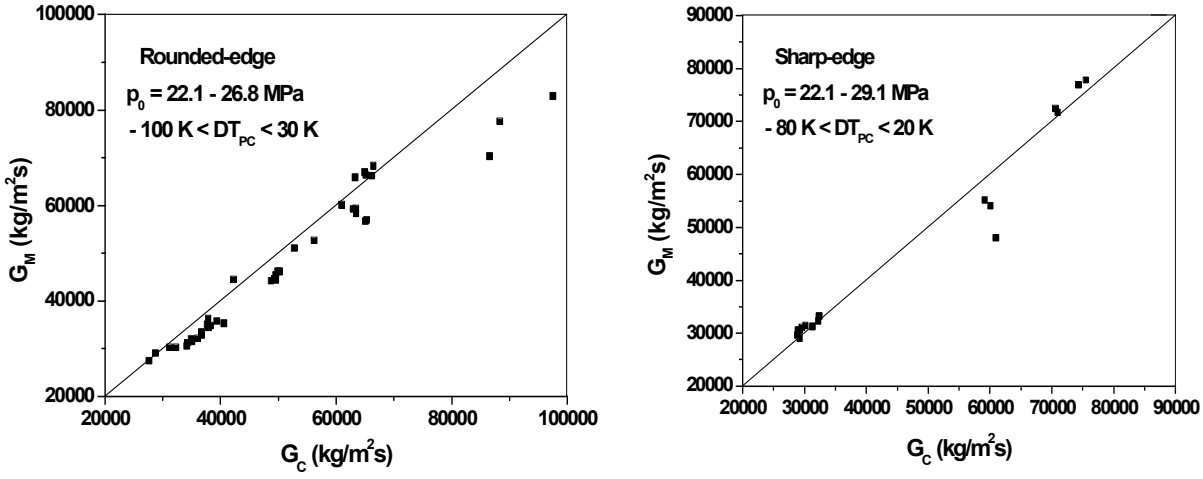

(a) Nozzle A (b) Nozzle B

FIG. 7.13. Comparison of experimental data with calculations of the M-HEM for near and beyond supercritical region.

Figure 7.14 shows the comparison of the experimental results for nozzle A and p < 25 MPa, with the calculations by the modified HEM at p = 24 MPa (with C = 0.2) and the Bernoulli equation (with C_D = 0.61). In this region the experimental data are not so scattered. The results are represented by:

$$G = \text{Min}\,(G_{M\text{-}HEM}, G_{Bernoulli}) \tag{7-14}$$

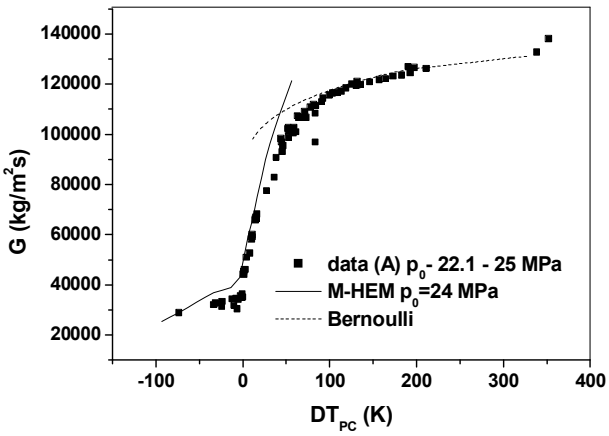

FIG. 7.14. Comparison of the experimental results of nozzle A with calculation of the M-HEM and Bernoulli equation (p_0 < 25 MPa).

Due to uncertainty in the onset of vaporization, the mass flux in the region below the pseudo-critical point cannot be estimated accurately for higher pressure, especially in the nozzle with sharp-edge. In Fig. 7.15 the experimental results of nozzle B with p > 25 MPa are compared with the calculations by the modified HEM (with C = 0.6) and Bernoulli equation. The calculations give the upper envelope of the scattered data. This result suggests that, from the reactor safety point of view, the HEM gives a conservative

estimation for the break discharge flow rate.

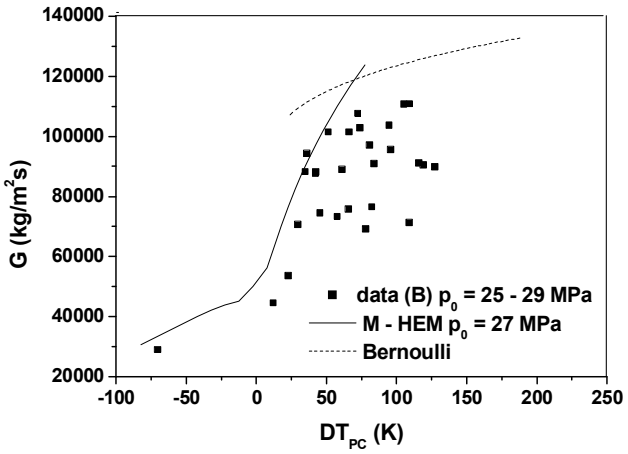

FIG. 7.15. Comparison of the experimental results of nozzle B with calculations of the M-HEM and Bernoulli equation for $p_0 > 25$ MPa.

7.3.4.3. Summary remarks based on CIAE work

Based on the experiments and the analysis of the above data from CIAE with critical flow of supercritical water through nozzles with rounded-edge and sharp-edge, the following conclusions were drawn：

- Flow rate decreases as the inlet temperature increases, and it varies drastically in the near pseudo-critical region.
- In the below pseudo-critical region the results of mass flux exhibit a scattered feature as a result of the hysteresis in the onset of vaporization, characterizing a bifurcation behaviour. The inlet shape of nozzle has a substantial effect, especially at higher pressure.
- In the region of near or beyond pseudo-critical point, the thermal-equilibrium is dominant, and the critical flow rate can be estimated reasonably by the modified homogeneous equilibrium model.
- At the inlet temperature well below the pseudo-critical point, the choking condition does not take place.

7.3.5. University of Wisconsin experiments

Due to the lack of data and understanding of supercritical fluid depressurization, the University of Wisconsin developed a test program to study critical flow in supercritical fluids in 2006. This work became a part of the IAEA CRP on supercritical fluids in 2008. The idea was to construct a very simple experimental system where depressurization from a large vessel with a clean opening could be studied. Due to the large amount of energy needed to conduct a steady state experiment with water, a surrogate fluid was used instead (CO_2). The tests were also conducted in a transient process similar to what would occur if there was a large break in a reactor system. In this study both short nozzles similar to the EPRI and CIAE studies in addition to long tubes (where the flow was found to be much more stable) were used. A detailed report of the experimental system and the results can be found in reference [7-9].

This work identified three regions of interest during depressurization from supercritical conditions (Fig. 7.16). For initial entropy less than the critical entropy a second phase was assumed to appear through vaporization (REGION III). Under conditions where the initial entropy is higher than the critical entropy the depressurization would result in condensation corresponding to the REGION II. Finally, if the initial entropy was significantly above the critical entropy (very high temperature and high pressure) the flow remains in a single phase and was classified as REGION I. For the most part the data found during this study was consistent with that of the previous work and the work conducted at CIAE, however it added significant insights into the phenomena by optically studying the discharge and adding significant data on the effects of the L/D ratio.

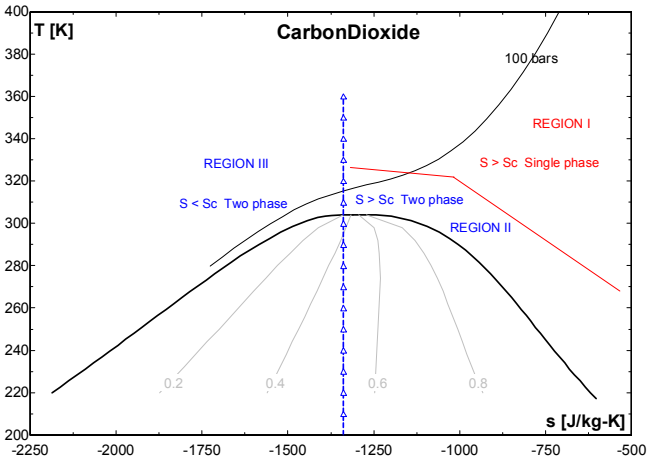

FIG. 7.16. Map of behaviours plotted in a T-S diagram.

Detailed discussion of experiments

Figure 7.17 shows a scheme of the facility constructed at the University of Wisconsin. It consisted of a 0.125 m^3 cylindrical vessel that was fitted with different size nozzles at one end. The different length to diameter ratios (*L/D*) of the nozzles ranged between 4 and 16 to allow the scaling of the effects of the size of a pipe break to be studied. The experiments were designed to generate depressurizations as 'clean' as possible, so they could be compared to CFD simulations. In this regard the nozzles were carefully machined with a known sharp entrance and were sealed internally using a sliding rod in order to avoid any interaction with the exiting jet during release and the beginning of the depressurization. The inside pressure, temperature and the mass of CO_2 were measured as a function of time with a strain gage pressure transducer, two bulk volume E-type thermocouples and a high accuracy dynamic scale respectively. Additional measurements of the vessel wall temperatures and jet temperature were also conducted. Figure 7.17 shows the different measurement locations of the diagnostics. An optical shadowgraph system was also utilized perpendicularly to the exit of the nozzle to record the jet expansion and the presence of shock structure in the jet.

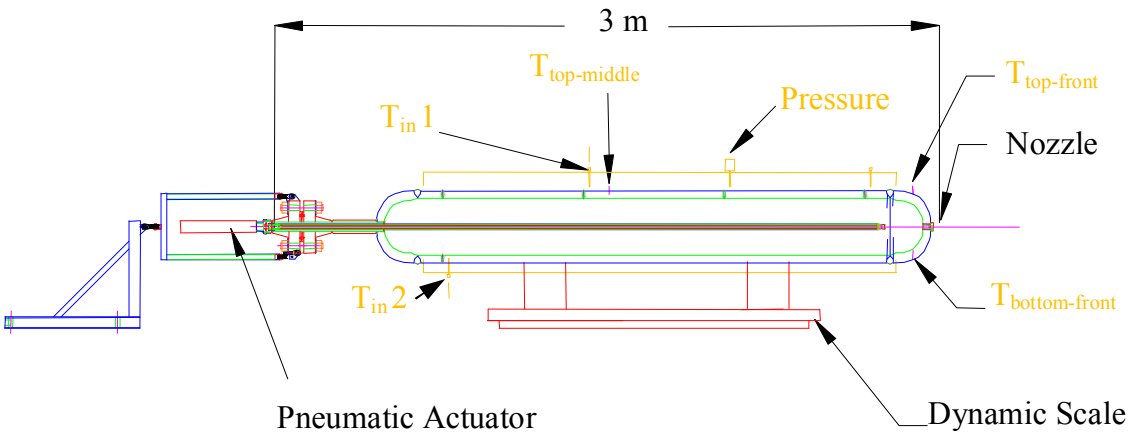

FIG. 7.17. Scheme of the experimental set-up.

In this study, 22 experimental depressurization tests were conducted by releasing supercritical CO_2 through a short straight nozzle, under transient conditions into the atmosphere (Table 7.1). The initial pressures ranged from 1340 psi (92 bars) to 3500 psi (241 bars) and the initial temperatures ranged from 96 °F (35 °C) to 500 °F (260 °C). The three straight 4.7 cm (1.85") long nozzles with sharp edge entrances had a length to diameter ratio (*L/D*) of 3.7, 7.3, and 14.6 corresponding to diameters of 12.7 mm (0.5"), 6.35mm (0.25") and 3.175 mm (0.125") respectively. Thermodynamic conditions of the fluid, vessel and exiting jet were monitored along with the mass flow rate throughout the depressurization time. In addition, visual observations associated with high speed shadowgraph and video recordings were completed for each test to document the physical behaviour of the exiting jet of S-CO_2.For temperatures higher than 140 °C, only a single flow was observed, whereas, for lower temperatures, a second liquid phase or even a third solid phase appeared, as the jet temperature approached the triple point of the fluid. The initial mass flux was compared among the three nozzles and it was found to be highest for the smallest diameter. This reproducible, unexpected phenomenon seemed to be more prevalent at lower temperatures near the critical point. This is of particular interest since it was expected that the mass flux should scale as *L/D*. Further tests with increased lengths are needed to confirm this result and determine the true scaling with the *L/D* ratio.

Thermocouple probe measurements of the high speed exiting jet were limited due to shock formation around the tip of the thermocouple. It was however concluded that the exiting jet had a minimum temperature as low as -78.51°C corresponding to the sublimation line at atmospheric pressure of the fluid.

Large vertical temperature gradients measured with thermocouples on the vessel and associated visual observation of the exiting jet indicate that under certain conditions a denser fluid may have been present in the lower portion of the vessel (fluid stratification in the vessel due to decrease in temperature during the course of depressurization). During particular experiments a stratification of the exiting fluid was observed where it appeared as if the lower portion of the jet was fluid of a higher density, perhaps corresponding to the entrained liquid CO_2 exiting from the nozzle. The entire database and parameters of the experiment are archived on the IAEA/NEA data bank under the auspicious of the CRP and only a summary of the key points is presented below.

TABLE 7.1. SUMMARY OF KEY DATA AND OBSERVATIONS OF THE EXPERIMENTS

run#	Initial Pressure [Psig]	Initial Temperature [°F]	Nozzle Diameter ["]	L/D L=1.835	Initial Mass Flow Rate [kg.s^{-1}]	Depressurization Time [s]	Minimum Stagnation Temperature [°F]	Minimum nozzle Temperature [°F]	Minimum Vessel Wall Temperature [°F]	Observations
3	1339	93.6	0.125	14.7	0.401	1250	12.8	7.5	-9	Two-phase Jet + Stratification
1	1400	146.1	0.125	14.7	0.206	650	74.3	54.7	108	Two-phase Jet
2	1399	140.5	0.125	14.7	0.264	650	67.1	34.8	102	Two-phase Jet
9	1420	360.7	0.125	14.7	0.262	400	279.9	261.4	338	Single Phase Jet
22	2788	497.7	0.125	14.7	0.292	520	390.2	NA**	419	Single Phase Jet
11	2823	289.4	0.125	14.7	0.429	620	189.6	161.7	257	Single Phase Jet
12	2840	140.5	0.125	14.7	0.692	1100	42.0	19.3	77	Two-Phase Jet
18	3498	162.7	0.125	14.7	0.784	750	61.0	31.0	104	Two-Phase jet
4	1339	93.4	0.250	7.3	1.331	450	-37.5	-9.1	-13	Two-phase Jet + Stratification+Triple point[3]
5	1391	142.9	0.250	7.3	0.973	150	13.2	3.6	113	Two-phase Jet[1]
6	1420	371.1	0.250	7.3	0.506	150	238.7	209.8	338	Single Phase Jet
17	2794	502.5	0.250	7.3	0.983	150	325.3	292.0	428	Single Phase Jet
16	2830	280.4	0.250	7.3	1.358	160	103.9	82.3	266	Single Phase Jet
13	2840	139.8	0.250	7.3	2.345	300	-2.2	1.7	23	Two-phase Jet + stratification[2]
21	3497	158.2	0.250	7.3	2.384	250	10.6	NA	59	Two-phase Jet
8	1340	92.7	0.500	3.7	4.419	110	-56.6	-25.6	30	Two-phase Jet + Stratification+Triple Point
7	1387	141.3	0.500	3.7	3.490	50	-4.5	-28.6	108	Two-phase Jet
10	1418	370.2	0.500	3.7	2.331	30	216.2	179.1	338	Single Phase Jet
20	2790	506.8	0.500	3.7	1.792	45	295.6	237.4	446	Single Phase Jet
15	2830	283.6	0.500	3.7	5.347	40	55.9	43.8	266	Single Phase Jet
14	2839	139.1	0.500	3.7	6.887	100	-38.9	-27.1	63	Two-phase Jet + stratification + Triple point?
19	3505	161.4	0.500	3.7	7.480	100	-27.1	-13.6	77	Two-phase Jet + stratification +Triple point

[1] A two-phase vapor is observed in the expanding jet and expected in the vessel
[2] A liquid phase appears in the vessel leading to a stratification of the flow (liquid at the bottom and gas on top)
[3] Low temperature leads to solidification of carbon dioxide around triple point thermodynamic conditions
* Colors indicate nozzle of different diameters
** Not applicable because of erroneous measurement

7.3.5.1. Mass measurement results

For each of the test conditions the mass flux was plotted as a function of the scaled time defined previously. Typical plots are presented in Fig. 7.18. Based on this figure, we notice that the scaling time collapses the different nozzles fairly well. At low temperature (a) we observe a difference in behaviours between the 3.175 mm (1/8") diameter nozzle and the other two after an initial time. Under these conditions a second phase is expected, which can explain the divergence. At high temperature (b), where the isentropic assumption seems verified, the scaling works even better. These plots enable us to readily compare any difference in the physical behaviour of the nozzle for a given condition.

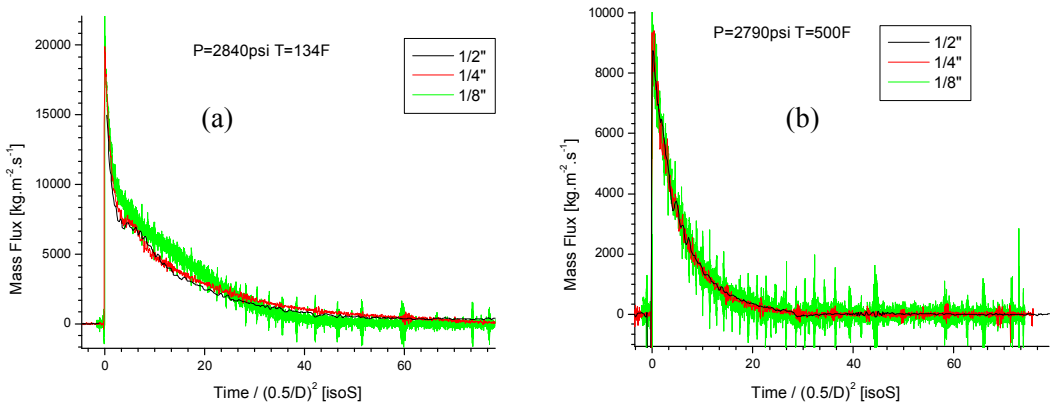

FIG. 7.18. Mass flux as a function of time (scaled) at low (a) and high (b) temperature.

Also the initial mass flux has been compared for each group of pressures. Results are presented in Figs 7.19, 7.20 and 7.21. The relative error in the critical mass flux increases with temperature as the mass flow rate decreases with temperature and thus the differential mass measurement uncertainty increases.

An interesting result mentioned previously is that the mass flux was found to decrease with an increase of diameter. As *L/D* increases the critical mass flux increases, which is contradictory to intuition and Fauske [7-30]. Fauske observed that as *L/D* increases the critical mass flux decreases, especially for short *L/D*. We should note that these results were generated from saturated water blow-down data, using a sharp edge nozzle of similar diameter but various lengths. Our observation is more valid for low temperature than high temperature as we can see on Figs 7.19 and 7.20. As the temperature increases, there appears to be less difference in the mass flux from the different nozzles. It behaves more like a single phase gas flow. It also suggests that the change in behaviour is due to the presence of a second phase in the process that would appear in the low temperature cases.

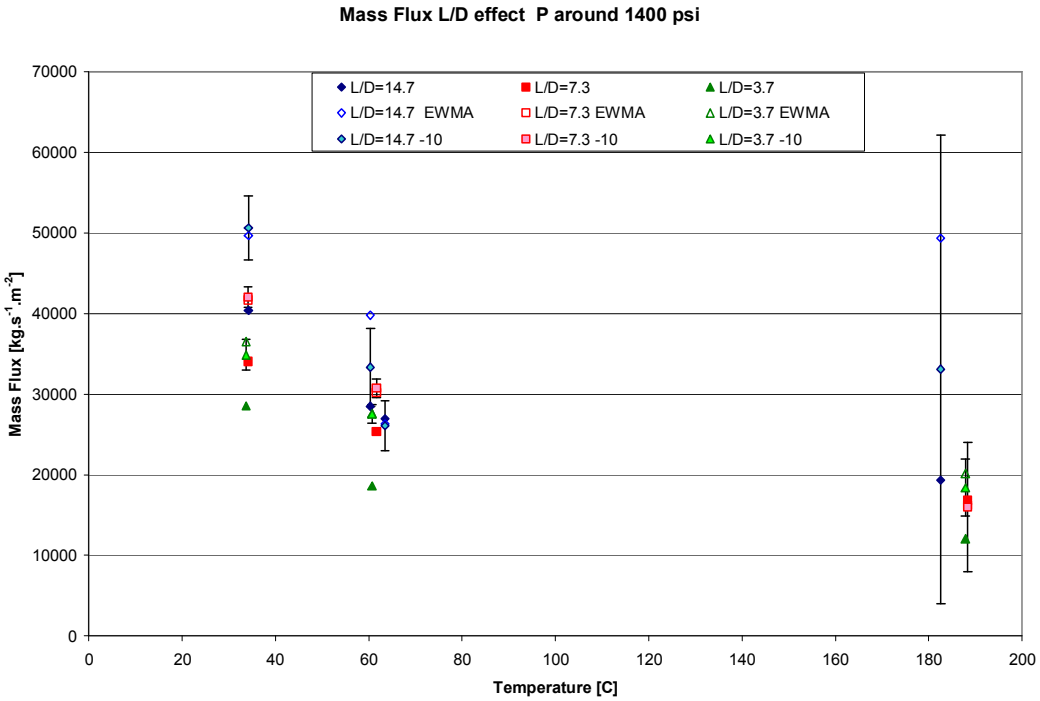

FIG. 7.19. Comparison of initial mass flux for the low pressure conditions.

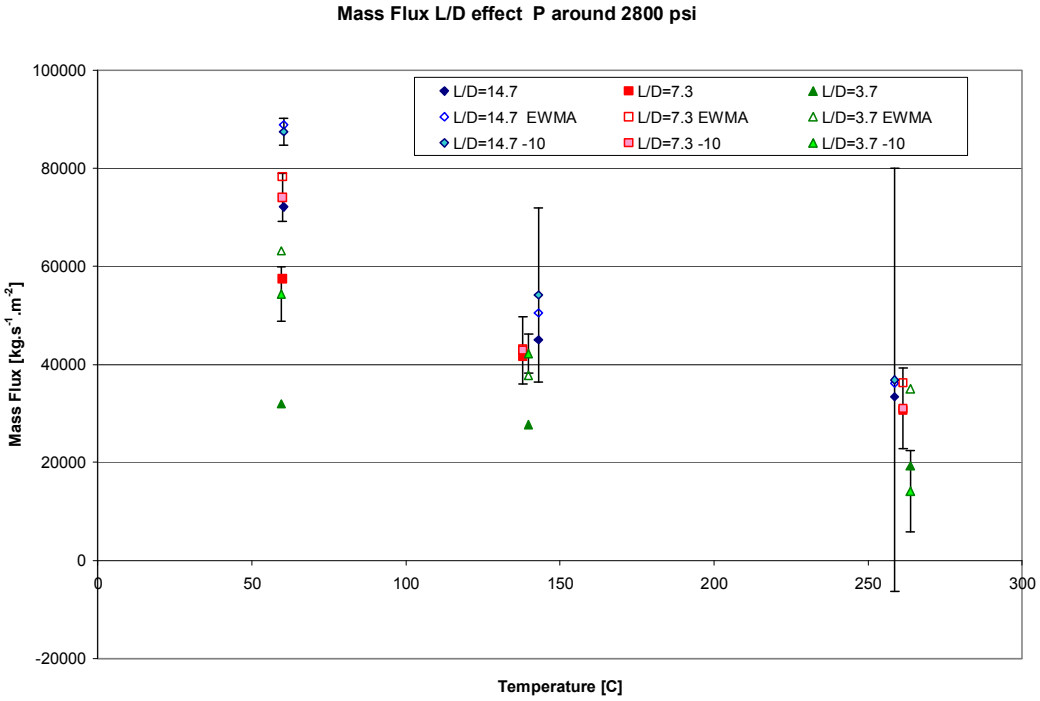

FIG. 7.20. Comparison of initial mass flux for the medium pressure conditions.

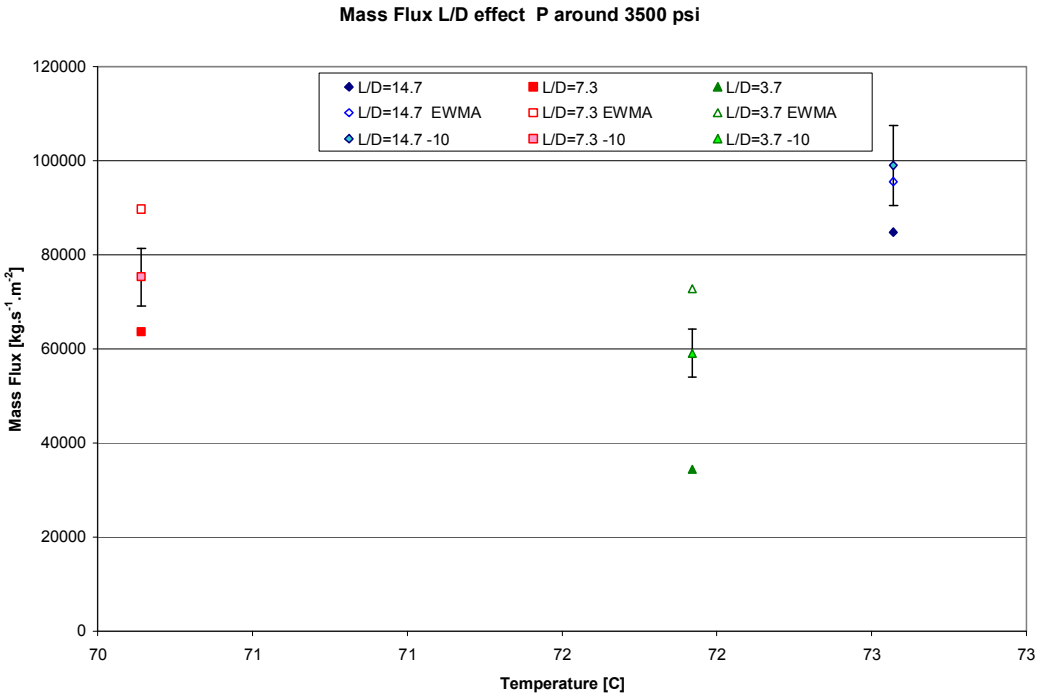

FIG. 7.21. Comparison of initial mass flux for the high pressure conditions.

7.3.5.2. Scaling of mass, pressure, and temperature

The experimental mass, pressure and temperature have been plotted as a function of the scaled time for all test conditions. Figure 7.22 reports the low temperature results and Fig. 7.23 reports the repeatability of the experiment. It can be noticed that the scaling captures the initial trend well in both cases. For the low temperature case, as time progresses, a divergence among the pressures and temperatures of the different nozzles appear, which can be explained by different physical effects and processes occurring during the blow-down such as heat inertia of the vessel, stratification, liquefaction or non-equilibrium condition, for example. These phenomena will be discussed in more details in the section below.

Finally the experiment shows a good reproducibility, the two independent data sets for the 3.175 mm (1/8") nozzle overlap remarkably except for a small bump around the non-dimensional time of 5, which has not to be explained yet. The difference in pressure and temperature between the two tests at a given scaled time appears to be quite constant.

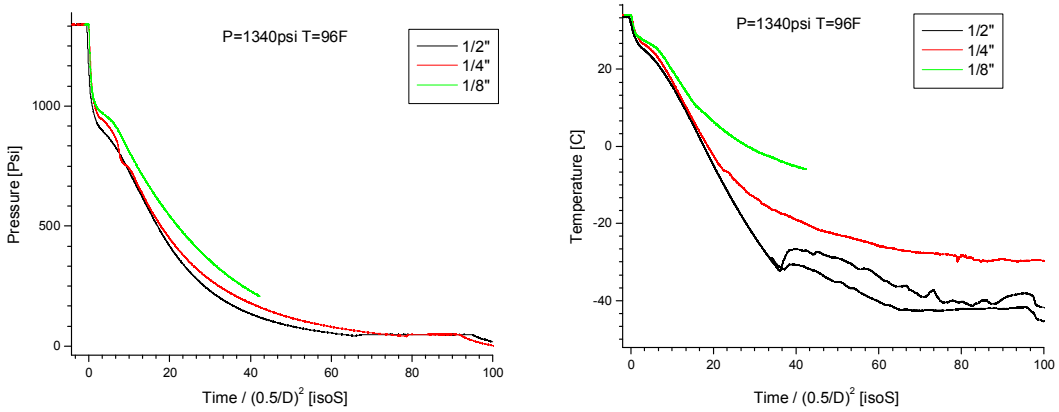

FIG. 7.22. Comparison of Pressure and temperature vs. scaled time.

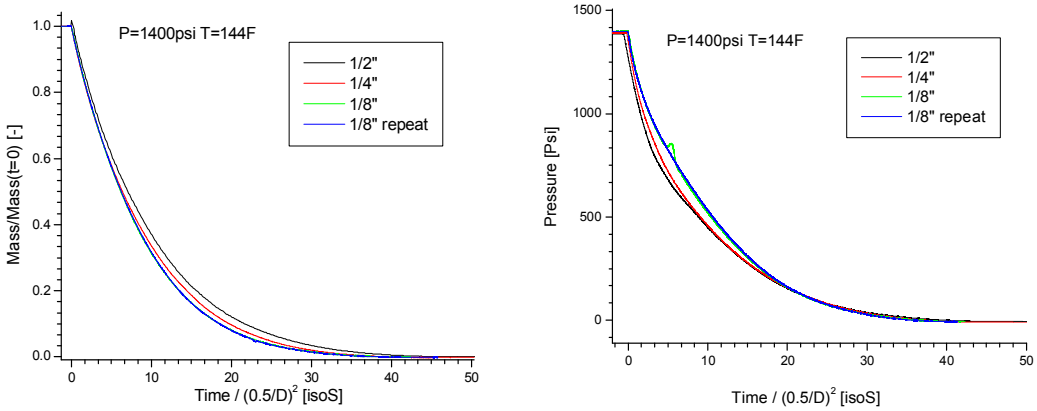

FIG. 7.23. Comparison of non-dimensionalized mass and pressure vs. scaled time.

7.3.5.3. Optical observation

Visual information on the depressurization event was collected using several techniques including shadowgraph with a fast frame camera. Two different cases have been observed for the exiting jet. They can be distinguished by either the presence or absence of two phases in the exiting jet. The dense phase in the jet scatters the light such that it appears white during the observation. The dense phase is expected to be initially liquid as the temperature and pressure starts from a point higher than the critical point. As the vessel depressurizes, the internal vessel temperature drops as low as -50 °C. If this occurs, a third solid phase can appear in the vessel. In the expanding jet the nature of the particles is not clear and future work should be done to characterize it.

Figure 7.24 shows a sketch of the exiting jet in the environment for a low temperature case. At the beginning of the blow-down (A), a strong shock structure appears at the nozzle exit location (barrel shock associated with a normal shock) surrounded by a white envelop composed of condensed particles. The shock structure is hardly visible initially due to the high scattering of the particles in the jet. The presence of a second phase is usually associated with the high density, low temperature initial stagnation conditions.

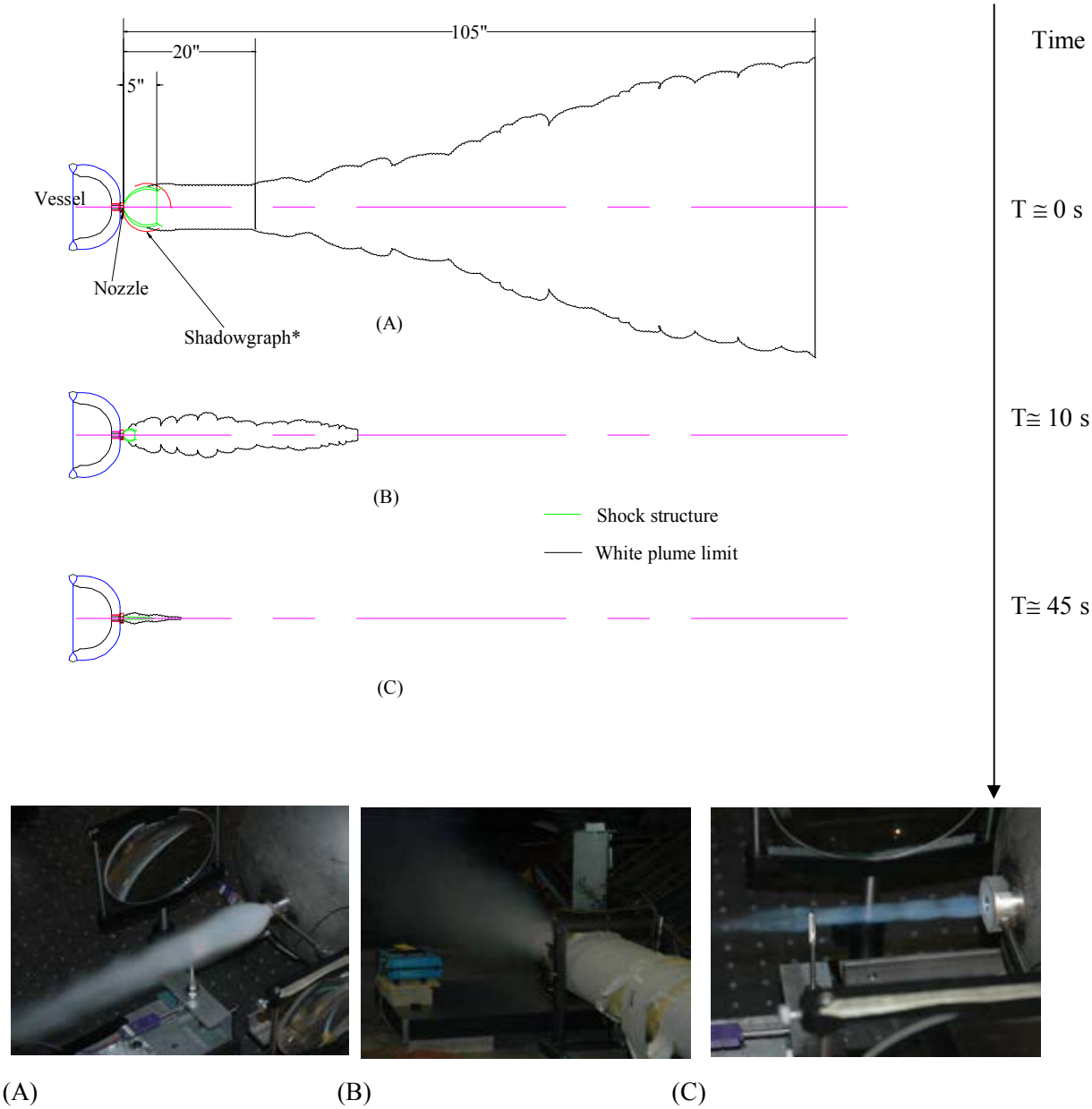

FIG. 7.24. Scheme of the exiting jet during a blow-down[*].*

[*] Distance is given in inches for ½" inner diameter nozzle at an initial pressure of 1340 psi and temperature of 96 °F and are just order of magnitude.

Following this rapid expansion of the jet in the atmosphere, the jet does not vary much within the next 40 diameters along downstream. The magnitude of the jet diameter is a function of the nozzle diameter and the internal pressure but the jet structures are similar. After approximately 40 diameters along downstream, the entrained air and the turbulence seems to take place (see Fig. 7.24 (A)) and lead to a wide white plume that can reach a few feet in diameter and expands along a distance of about 10 feet (approximate distance estimated from the 12.7 mm (½") ID nozzle). As the pressure inside the vessel drops with time, the shock structure as well as the white plume reduces rapidly in size (Fig. 7.24 (B)). Finally, only the shock structure of the exiting jet remains (Fig. 7.24 (C)) visible with the shadowgraph (i.e. density gradient Fig. 7.24 (C)).

For the high temperature cases no condensed particles were observed and the shock structure forming at the exit of the nozzle was observed clearly with the shadowgraph diagnostic as shown in Figs 7.25–7.27.

For the intermediate temperature case, the shock structure can be observed for small nozzles and tends to disappear within the condensed phase for the larger nozzles. Figure 7.28(c), Fig. 7.27, and Fig. 7.29 (c) show an example of the interaction of the jet with the traversing thermocouple used to measure the jet temperature. The structure does not seem to change as long as the thermocouple does not stand between the exit of the nozzle and shock plane of the 'Mach Disc'. It is expected that the minimum temperature occurs in front of the Mach Disc. However, measuring the temperature inside the jet with a thermocouple leads to erroneous measurement since a bow shock forms in front of the thermocouple, thus altering the flow. Also the measurement seems to be limited to around -80°C, which is approximately the sublimation temperature (-78.5°C) at atmospheric pressure for CO_2.

The series of pictures presented from Fig. 7.25 to Fig. 7.27 enable us to compare the expansion of the jet with the change in nozzle diameter. The 12.7 mm (½") nozzle caused some difficulty at high pressure to capture the entire expansion due to the limited size (about 5" in diameter) of the collimating lens that was used in the shadowgraph system. It is interesting that the shear and the turbulence on the outside of the jet tend to enlarge their diameter.

It is also interesting to notice that in the case presented in Fig. 7.25 no condensed phase seems to be present for the small nozzle (d). A condensed phase appears and becomes denser as the diameter increases (Fig. 7.26 (c) and (b)). The visual observation is consistent with the trend in the temperature plots, i.e., the minimum nozzle temperature decreases as the nozzle diameter increases. Therefore this condition appears to be a transition for the nozzle considered.

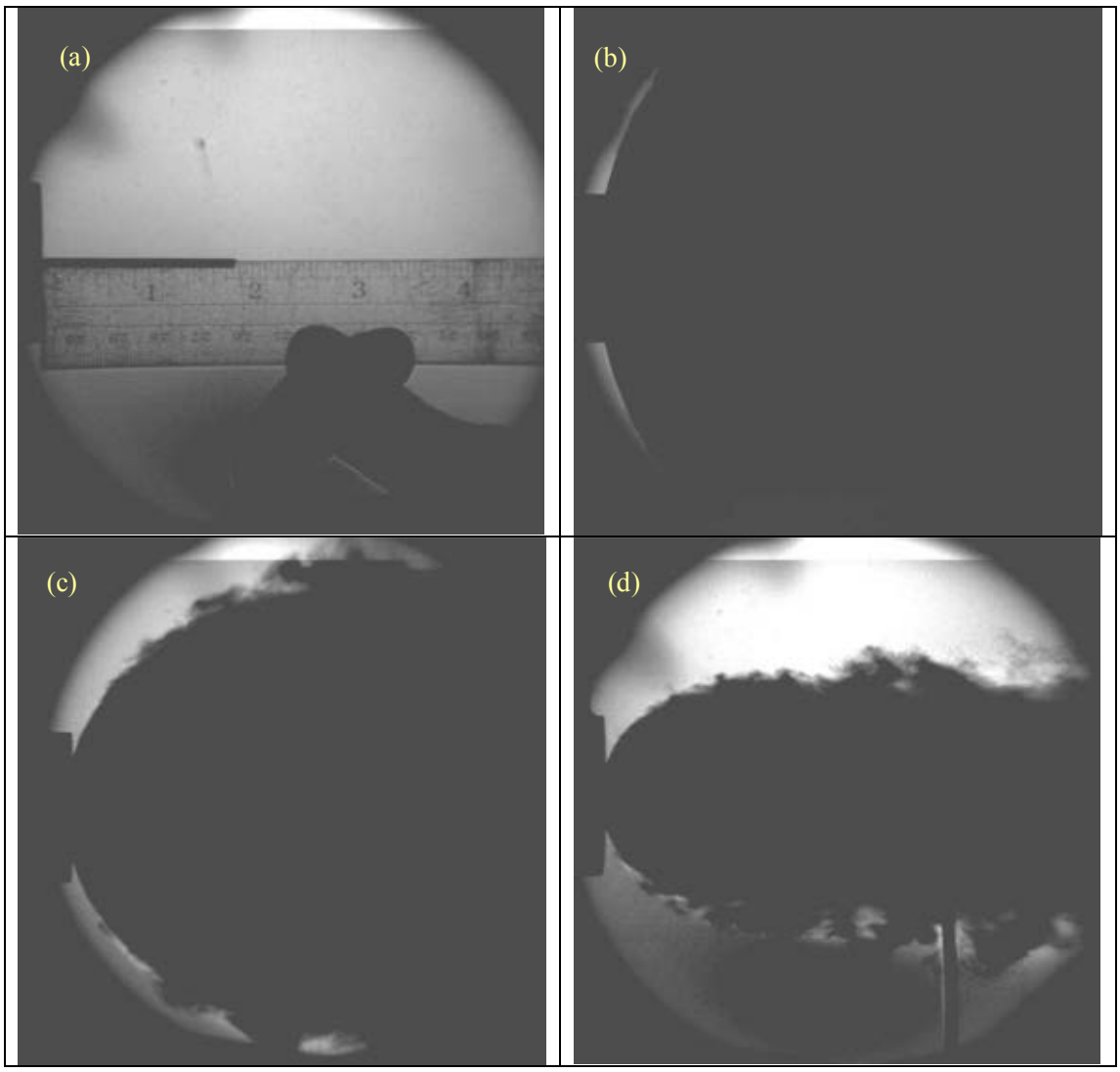

FIG. 7.25. Shadowgraph of the exiting jet - P= 3500psi - T=144 F (a) scale - (b)1/2" nozzle - (c) 1/4" nozzle – (d) 1/8" nozzle.

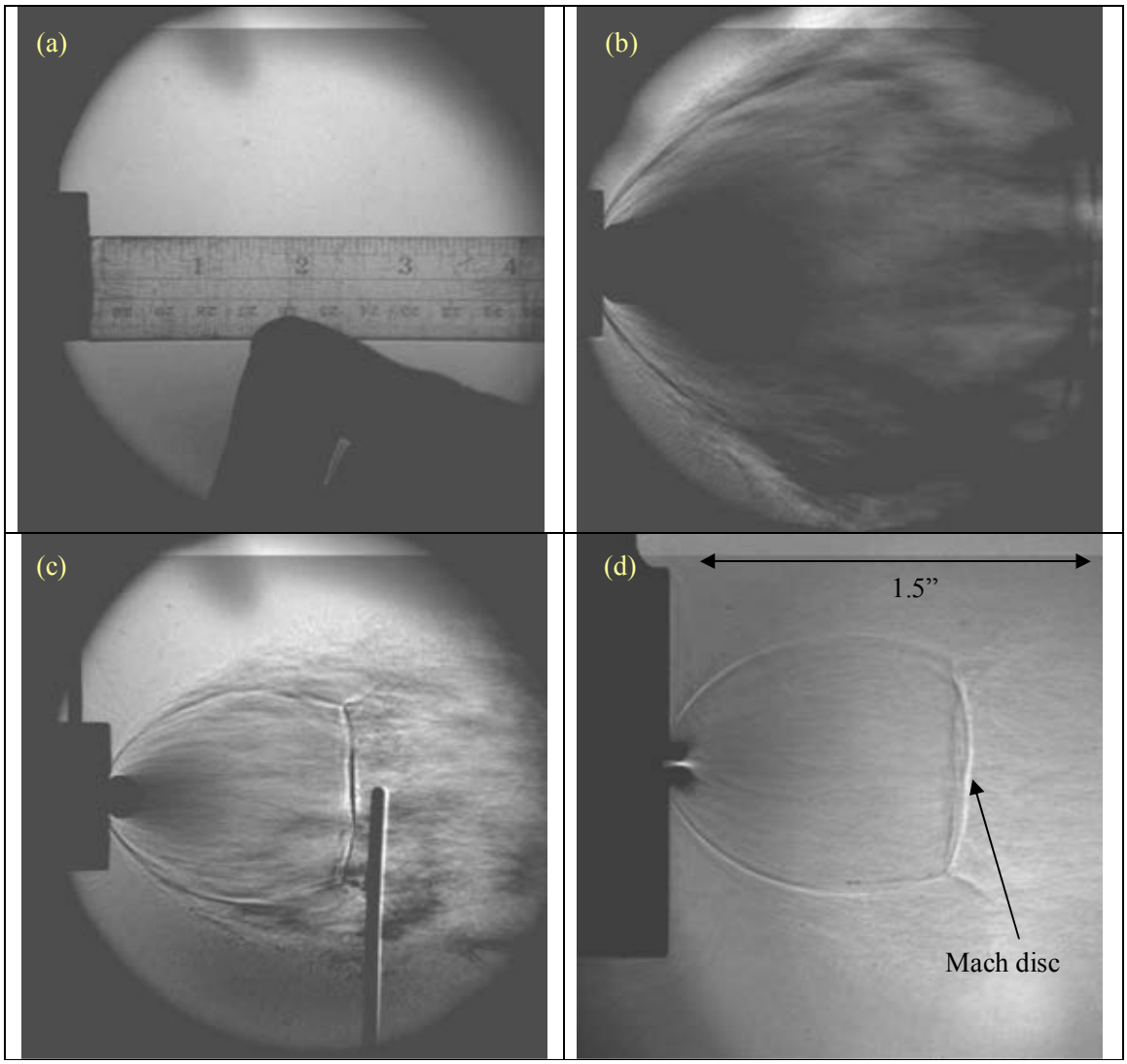

FIG. 7.26. Shadowgraph of the exiting jet - P=2830psi - T=287F (a) scale - (b)1/2” nozzle - (c) 1/4” nozzle – (d) 1/8” nozzle[*].*

[*] The scale is different than other pictures as we reduced the field of view

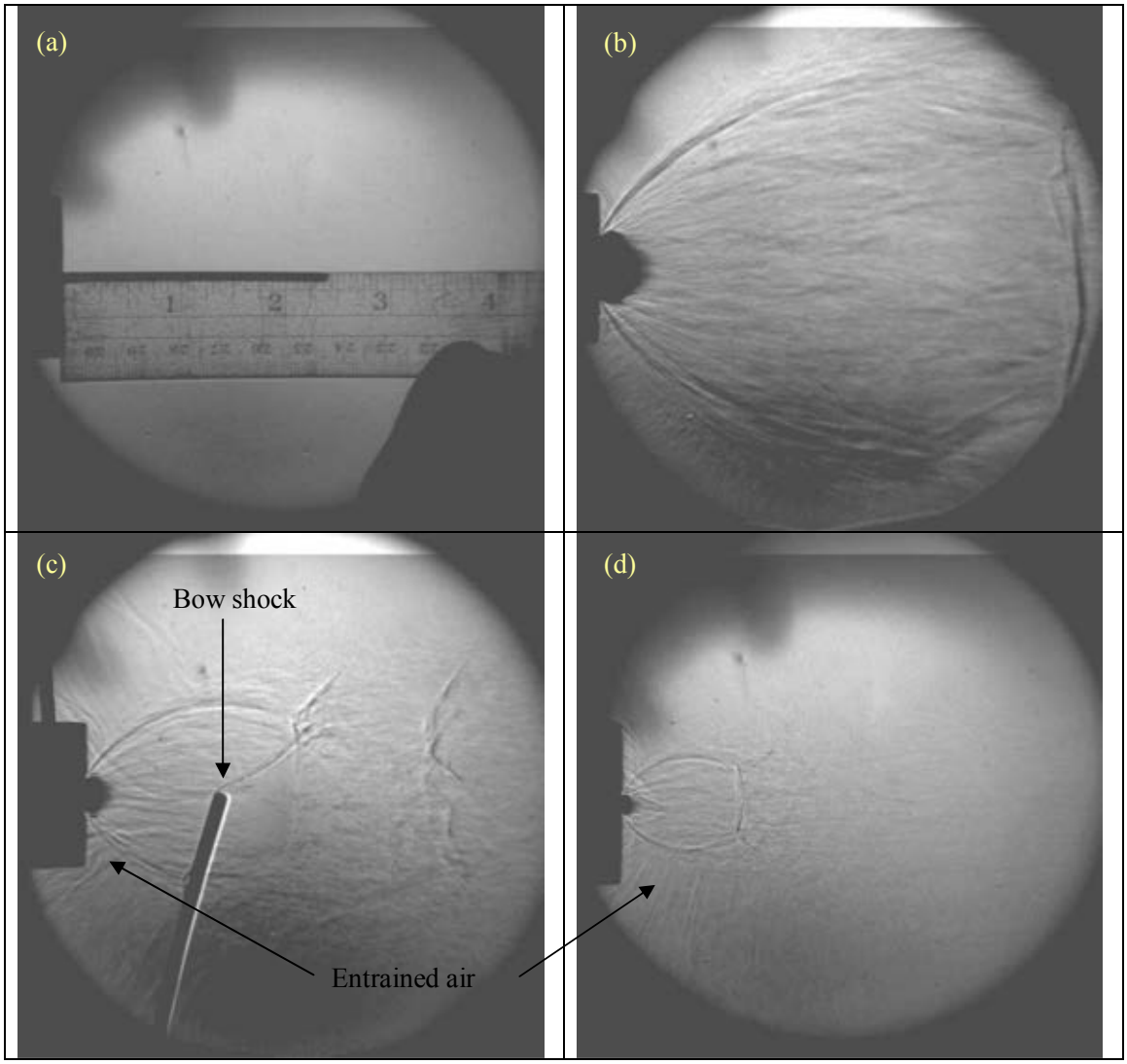

FIG. 7.27. Shadowgraph of the exiting jet - P=2790psi – T=500F (a) scale - (b)1/2" nozzle - (c) 1/4" nozzle – (d) 1/8" nozzle.

The condition presented in Fig. 7.27 shows the expansion of a pure CO_2 gas phase. It can be used to estimate the change in diameter and the location of the Mach Disc with nozzle diameter change for a given condition. Also, evident in shadow graphs of images (c) and (d) is that surrounding gas from outside of the vessel is entrained into the exiting gas due to the reduced pressure resulting from the high velocity exiting CO_2.

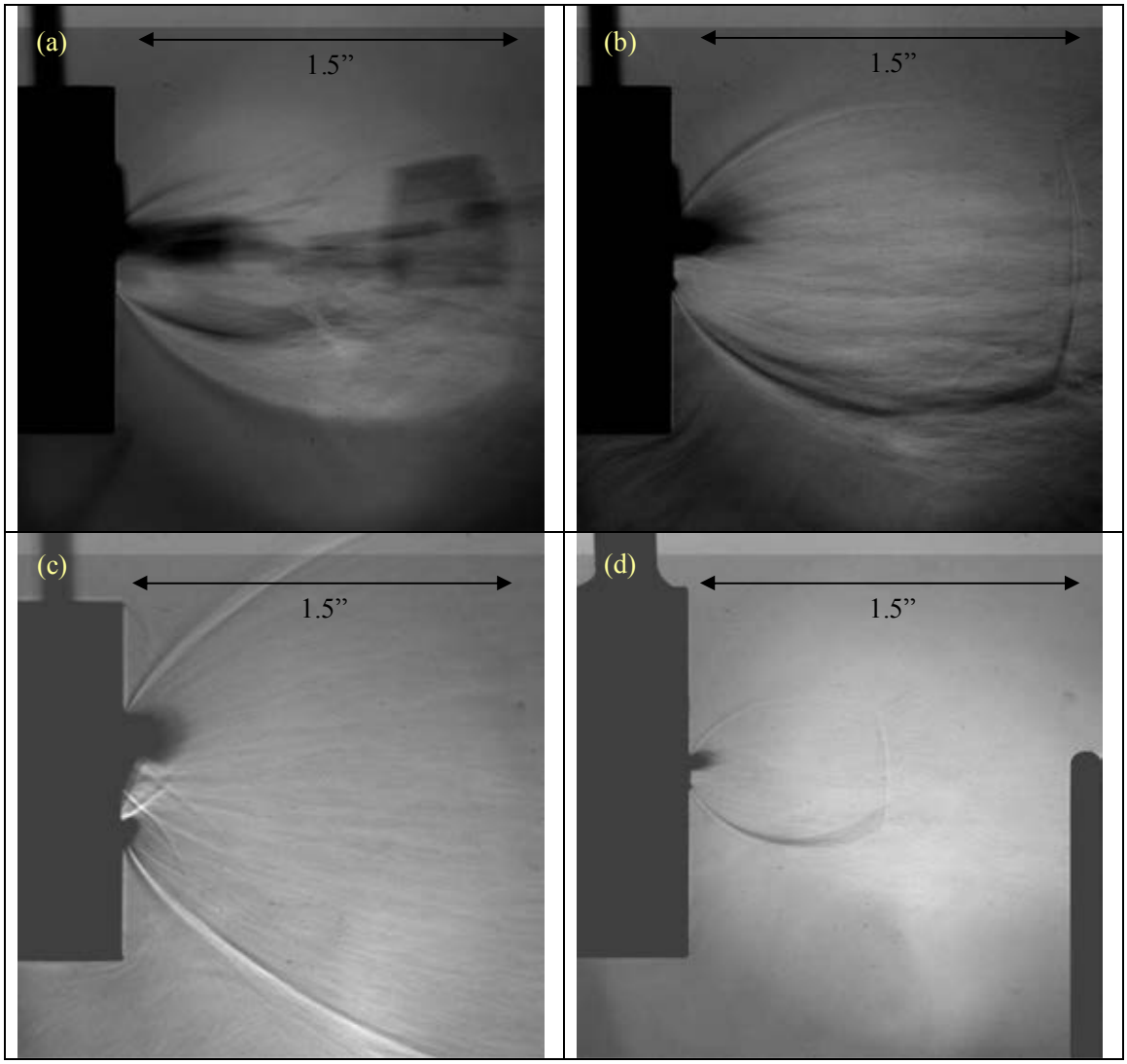

FIG. 7.28. Shadowgraph of the exiting jet - P=1420 psi-T=387F (a) 1/4” nozzle at t ≅ 0 - (b) 1/4” nozzle at t≅ 0 .016ms - (c) 1/2” nozzle –zoom in (d) 1/8” nozzle.

Similarly to the previous series, Fig. 7.28 shows a single phase expansion. Figure 7.28(c) which shows a magnified view of the 12.7 mm (½”) diameter nozzle allows visualization of the contraction line structure close to the exit of the nozzle.

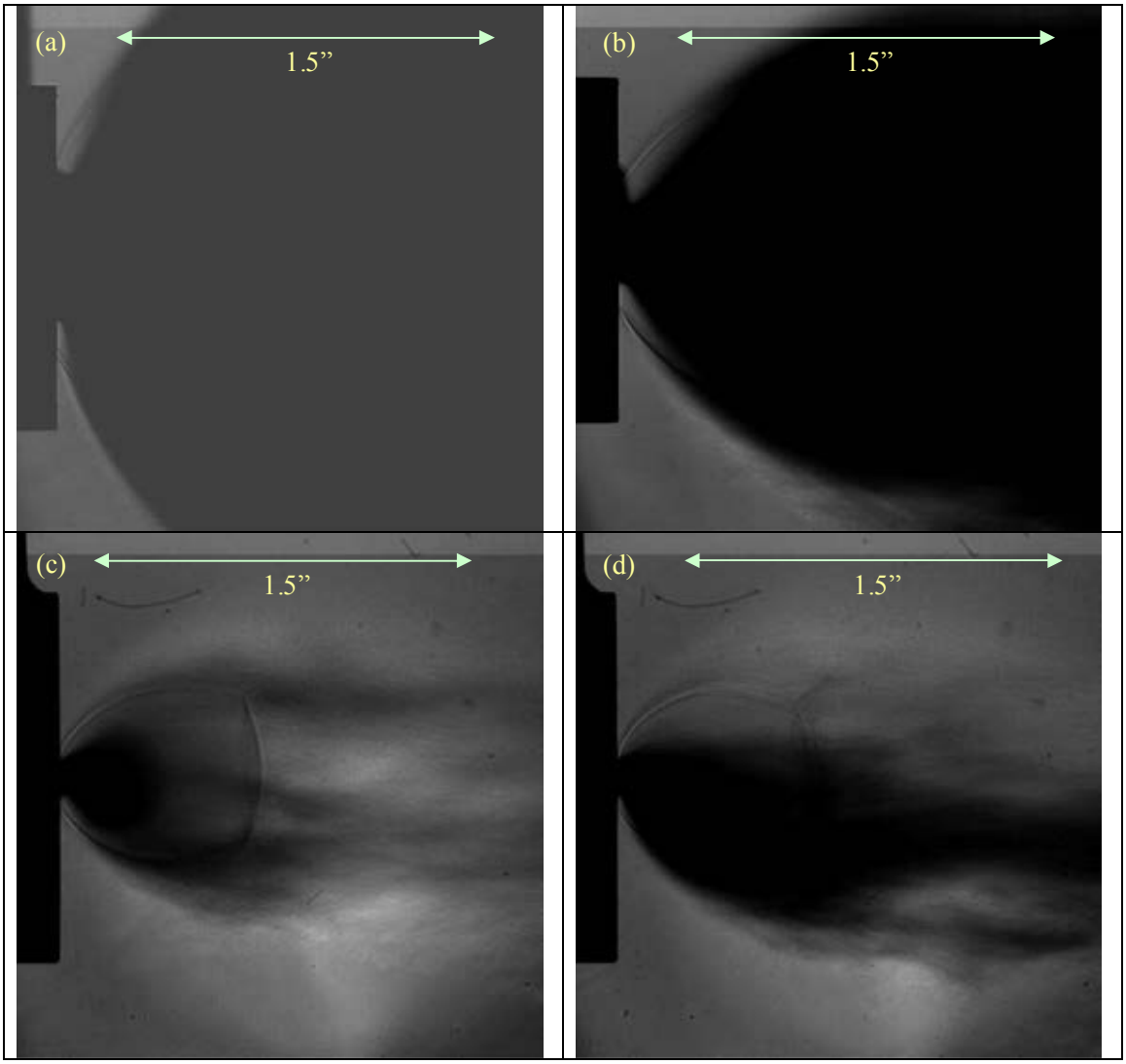

FIG. 7.29. Shadowgraph of the exiting jet – P=1400psi-T=144F (a) 1/2” nozzle - (b) 1/4” nozzle - (c) 1/8” nozzle – (d) 1/8” nozzle-repeat.

An interesting observation of the conditions presented in Fig. 7.29 is that the condensed phase seems to appear at the bottom of the jet only ((c) and (d)), which would suggest some possible stratification inside the vessel or at least along the nozzle. This is also supported by visual observation shown in Fig. 7.31. Due to this result, it may be of interest to study orientation of break, since this may drastically affect the mass flow from the vessel as the supercritical fluid passes through the critical point.

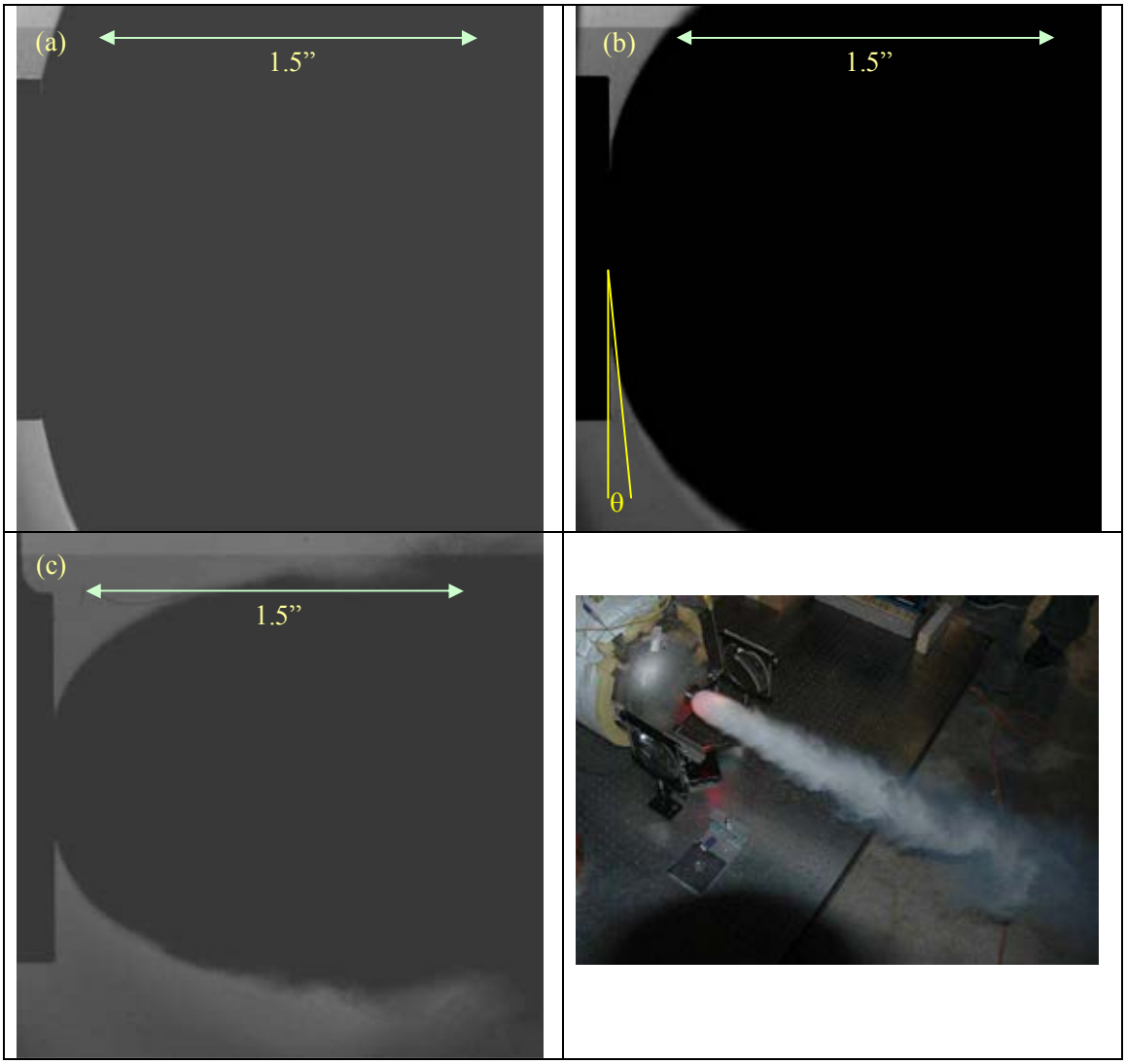

FIG. 7.30. Shadowgraph of the exiting jet - P= 1340psi-T=96F (a) 1/2” nozzle - (b) 1/4” nozzle - (c) 1/8” nozzle – (d) exiting jet in surrounding.

Little information is associated with the conditions presented in Fig. 7.30. It would mostly concern the steep expansion of the jet along the nozzle wall. Figure 7.31 shows a picture of the exiting jet and supports the conclusion that there is a denser phase that flows from the lower part of the nozzle, which suggests the idea of stratification. The red lighting appearing in the picture is due to a laser sheet passed through the jet in order to clearly observe the presence of particles inside the jet.

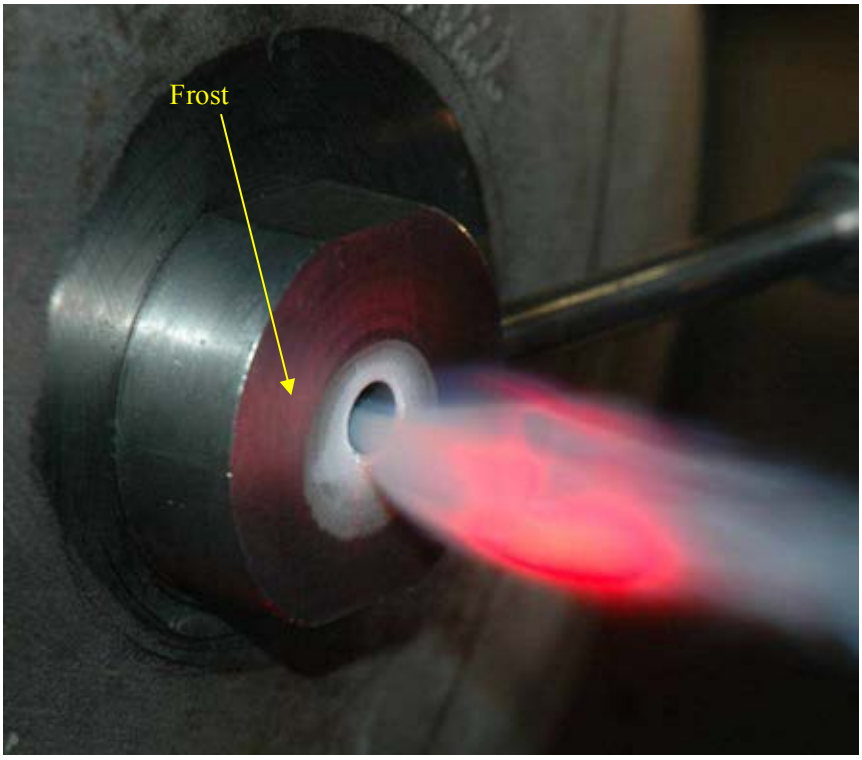

FIG. 7.31. Exiting jet cut transversally with a laser sheet - P=2840psi T=144F.

As the vessel cooled down during the depressurization, frost was observed at the bottom part of the outer wall up to 3" below the centerline of the vessel. Also local frost was observed around the nozzle due to a local internal cooling from the jet. The formation of the frost is also asymmetric further from the nozzle on the bottom.

In addition to the data shown on small *L/D* ratios (less than 15) a series of experiments were also conducted with large *L/D* ratios ranged from 40 to 170. Table 7.2 gives a description of these tests. Figure 7.32 shows a summary of the critical mass flow rates for the different cases. In cases where the *L/D* is larger than 40 there appears to be little effect of the *L/D* ratio and all three of the regions seemed to behave similarly above the critical point and result in predicted flow consistent with an HEM approach. Figure 7.33 shows a comparison of the data with several models, isentropic and with friction.

TABLE 7.2. SPECIFICATION OF THE TUBE OUTLET USED FOR THE UW-MADISON DEPRESSURIZATION EXPERIMENTS
(All tube lengths were 336.5mm)

Material	Tube Inside Surface Roughness (μm)	Tube Diameter (mm)	Tube Entrance Geometry
Stainless steel	1.5	7	Sharp edge
Stainless steel	4.3	3.175	Sharp edge
Stainless steel	3.8	2	Sharp edge
Stainless steel	3.8	2	Round edge
Quartz	0.007	2	Round edge

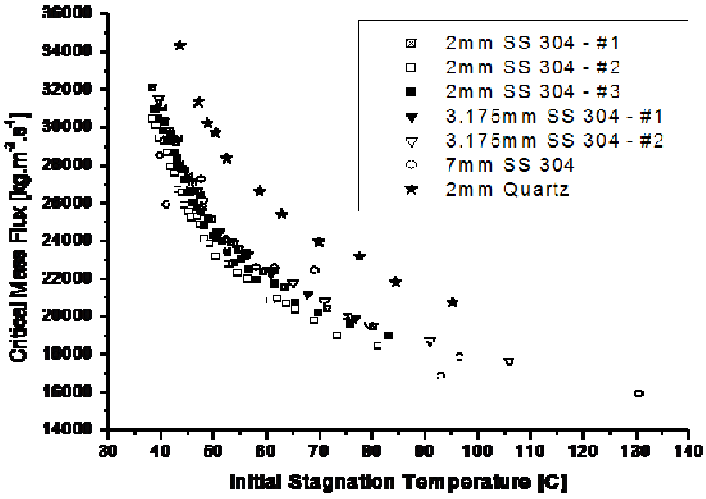

FIG. 7.32. Test data showing data at large L/D for various entrances (smooth and sharp), different surface roughness and different diameters.

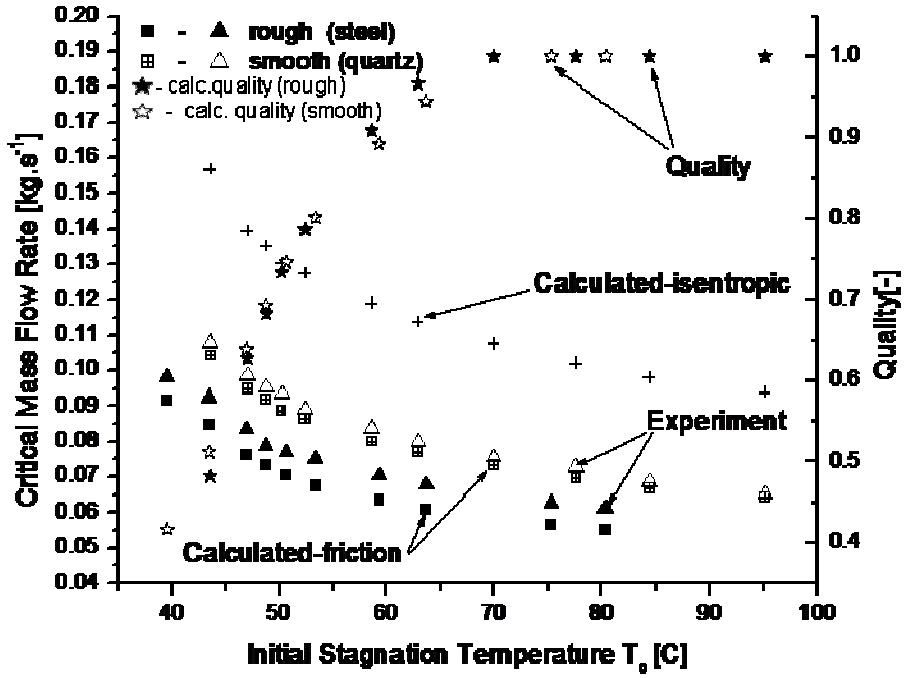

FIG. 7.33. Comparison of experimental and model. Estimated critical mass flow rate as a function of the stagnation temperature T_0 for a stagnation pressure P_0 of 10.1 MPa. Quartz 2 mm ID smooth entrance and steel 2 mm ID sharp entrance.

From Fig. 7.32 it can be seen for the large L/D that the scaling on the diameter seems to be as expected and as seen in past literature. Figure 7.33 shows the experimental results compared to a typical HEM simulation. The right axis of the plot indicates the quality of the gas as a function of the initial stagnation temperature (stars). This has a similar structure with the compressibility diagram showing how the quality of the fluid changes with respect to the initial stagnation temperature. The first series of points, plotted using the left side scale, are calculations using a simple isentropic approximation. This shows a significant over prediction of the critical mass flow rate for all of the experimental data. The second series of calculations uses an HEM model with friction added and compared to the large *L/D* nozzle for both rough and smooth tubes. As can be seen, the smooth tube agrees very well and essentially lies on the calculation. The case for high friction is slightly off (although the correct trend is observed). The slight discrepancy is thought to be due to the error in estimation of the friction on the rough tube. This plot indicates that for the large *L/D* tubes, the HEM model gives a good prediction of the critical mass flow rate.

From Fig. 7.33, we can also observe that at initial stagnation temperatures lower than 45 ºC, vaporization is expected, leading to low exit quality (< 0.5). For initial stagnation temperatures between 45 ºC and 62 ºC, condensation is expected, leading to higher exit quality. Finally, for temperatures higher than 62 ºC, a single-phase flow exists along the entire tube. Even though these various behaviours are very different from each another, the HEM calculation captures the trend of the critical flow as a function of stagnation temperature correctly, within less than few percent of error. The large *L/D* values imply that the phases have enough time to reach thermodynamic and velocity equilibrium, which are the assumptions imbedded within the HEM.

7.3.5.4. Summary of key findings

Based on the initial stagnation conditions of the S-CO_2, three different regions of possible different flows were defined, which can occur during a depressurization process from above the vapor dome. REGION I, for the single phase critical flow, and, REGION II and III would eventually develop into two phase critical flow through condensation or vaporization process, respectively. Since so many prospective scenarios can occur, each parameter has to be studied independently and a short summary based on the different conditions is presented here.

The analysis of the results shows that the behaviour for a long tube is fairly predictable with a simple homogeneous equilibrium model. However, the transient results obtained for the short nozzles are far more complicated. This observation is consistent with that observed in the CAIE studies even under steady state.

SCF - Critical Flow is Predictable for Long Tubes
As a general observation, for a given pressure, the critical flow increases with a decrease in the temperature. In fact, along a constant pressure line, the density of the fluid increases quickly at the approach of the pseudo-critical point (45 ºC for a stagnation pressure of 10.1 MPa). For long tubes of $L/D > 40$, the appearance of a second phase does not create any limitation on the critical flow. This was shown in Fig. 7.32 along with how the roughness and the entrance geometry of the tube affect the mass flow. To observe the roughness effect, the critical flow data between the 2 mm steel tube and the 2 mm quartz tube were compared. Their relative roughness differed by about three orders of magnitude. The rougher inner wall of the steel induces more friction leading to higher pressure drop and a lower mass flow rate for similar initial stagnation conditions. The mass flow rate of the steel tube differs by about 15% from the quartz tube data.

In agreement with data by CIAE and others, the sharp edge entrance tube shows a lower critical mass flow rate compared to a smooth entrance tube [7-16]. In fact, a sharp edge entrance induces a contraction of the flow (or vena contracta) reducing the effective area through which the fluid flows. This area reduction leads to an acceleration of the flow, and, an additional and irreversible pressure drop is produced. This may have been one of the reasons for the unstable and hysteresis effect seen in the CIAE data presented above. After the fluid passes the location of the vena contracta, the actual velocity of the fluid decreases, and a partial recovery of the pressure occurs. Figure 7.34 shows a schematic of the vena contracta effect and how it affects the minimum area of the flow. In the case of a round edge entrance, the flow lines follow the geometry and the minimum area is effectively the tube area. This has been shown by CFD calculations by several investigators, including the authors.

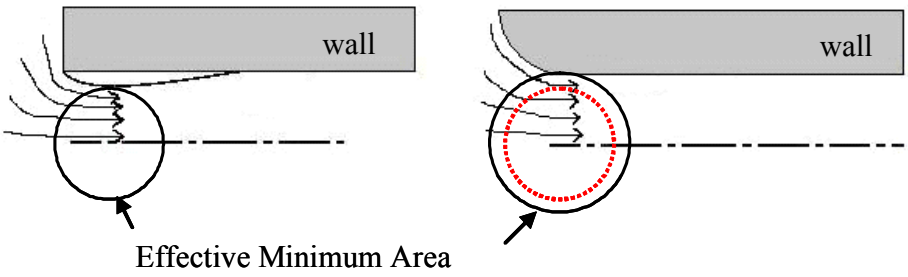

FIG. 7.34. Schematic of vena contracta effect at the entrance of the tube.

In the case of the large *L/D* experiments, the critical plane is expected to be at the exit of the tube so that, even the entrance geometry affects the flow, and its impact is limited to the additional pressure drop, about 7% in our case. However, the vena contracta would have a dominant effect for short tube since in that case, the choke plane is expected to be located around this contraction region. In fact, the acceleration becomes so large that sonic conditions can occur at the entrance of the pipe.

The last important qualitative observation from the large *L/D* experiments is related to the low apparent effect of the diameter. In other words, a change in diameter does not seem to significantly affect the critical mass flux. As the tube diameter varied from 2 mm to 7 mm, the *L/D* ratio changed by a factor of 3.5, however the mass flux remained the same within the experimental uncertainties (this was very reproducible). This is also consistent with the results obtained by Fauske [7-12] with saturated water. He observed that, for *L/D* of 12 or higher, the mass flux tended to an asymptotic value only dependent of the initial stagnation conditions. Since the *L/D* ratio is directly related to the friction term in the momentum equation, this means that the critical flow process for large *L/D* is not primarily governed by the friction but by the acceleration pressure drop. As long as the frictional pressure drop is small compared to the acceleration pressure drop the mass flux will vary slowly in regard to change of *L/D*.

Comparison with a Homogeneous Equilibrium Model

Figure 7.33 shows a comparison between the experimental critical mass flow rate and the corresponding values obtained with a 1-D HEM calculation. The calculated exit quality is also presented. The model shows a remarkably good prediction of the critical flow at every condition in the three previously defined regions. The implementation of the HEM with friction for a straight smooth pipe with a round edge entrance shows a good agreement with the quartz tube data with an error less than 5%. In the quartz series, two-phase flow occurs for stagnation temperatures below about 62 ºC. These results also agree with the data and analysis from CIAE.

Under these conditions, the HEM enthalpy and density definitions lead to a lower bounding of our experimental data, which was expected. This is due to the fact that the thermodynamic equilibrium and the no slip assumption result in an over-prediction of the momentum pressure drop. This results in an over-prediction of the actual flow rate. It corresponds to the prediction that the model would give of the mass flow rate for *L/D* of 0. The calculations assuming a HEM with friction and the calculation assuming an isentropic HEM bounded the experimental data.

Short Tubes L/D < 15

Sub-cooled or perfect gas

During a depressurization, the super-critical fluid can reach thermodynamic conditions such that one can consider it either a sub-cooled liquid or a gas, before a second phase appears. To understand the behaviour of the super-critical fluid critical flow for short tubes, it is important to remember how, in the limiting cases of sub-cooled and perfect gas, the critical flow evolves as a function of *L/D*. Table 7.3 shows how the compressibility of the supercritical fluid varies over the range of the initial conditions studied.

TABLE 7.3. COMPRESSIBILITY VALUE FOR TEST STAGNATION CONDITIONS

Stagnation Pressure (MPa)	Stagnation Temperature (ºC)	Compressibility *Z* (-)
9.2	34	0.23
9.6	61.6	0.59
9.8	186.3	0.91
19.6	60	0.43
19.5	140.2	0.74
19.2	261.3	0.94
24.1	71.5	0.52
10.3[4]	313.2	0.06

For comparison, the last row of the table presents the compressibility of saturated water at pressure conditions studied by Fauske [7-12]. Notice that the value of 0.06 is much lower than the lowest expected value of 0.23 for an initial condition above the vapor dome. So, a behaviour similar to incompressible flow, as presented by Fauske in his study of short tubes [7-12], cannot be expected.

Previous analysis has shown that for a perfect gas depressurizing through a converging-diverging section coupled with a tube of length *L* and diameter *D,* the flow is choked at the contraction location for *L/D* up to a specific value that is only dependent upon the area ratio at the contraction. The critical mass flux is then expected to be constant up to this value (*L/D* of 25 for a contraction ratio of 0.84). On the other hand, Fauske observed that for saturated water the critical mass flux decreases rapidly with *L/D* up to 12. For higher *L/D*, equilibrium conditions were expected and, the critical flow, dominated by the acceleration pressure drop, was only slightly affected by the change in *L/D*. An example of the evolution of the critical mass flux with *L/D*, for saturated water, is presented in Fig. 7.35. Depending on the initial condition, either one of these two scenarios has to be considered.

Another element that must be considered is the location of the choke plane. It has previously been stated that the choke plane was located at the exit of the long tubes. Referring once again to 1-D gas dynamics, this should not be expected for short tubes as the *L/D* ratios are small enough that multiple chokes configuration could occur. This argument is also supported by CFD analysis results from both UW and CIAE that shows numerous shock reflections along the tube under perfect gas condition.

[4] Value obtained for saturated water

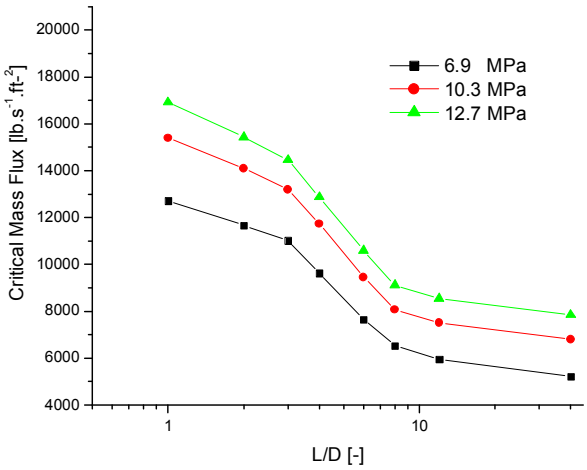

FIG. 7.35. Critical mass flux as a function of L/D for saturated water [7-14].

Based on the above discussion the experimental results can be divided into three cases: the perfect gas case scenario, corresponding to tests with initial temperatures higher than 140 ºC in the case of S-CO^2 or highly superheated in the case of SCW; the sub-cooled case scenario, which corresponds to the tests with initial entropy lower than the critical entropy: and finally, the condensation case scenario, which is characterized by the presence of two phases and an initial entropy higher than the critical entropy (only one test at 9.6 MPa and 61 ºC was done at these conditions with the S-CO_2 depressurization facility). The results are shown from Fig. 7.36 to Fig. 7.40.

Perfect gas case scenario

Based on the S-CO_2 data there were three test conditions corresponding to the criterion of high temperature. These are presented in Fig. 7.36. For the low pressure case, a constant mass flux is observed for *L/D* up to 14.7, confirming the behaviour predicted by 1-D gas dynamics. For the high pressure case the trend is more subtle and it appears that the mass flux stays constant for *L/D* only up to 7.3. The mass flux, for these cases, decreases by about 10 % from *L/D* of 3.7 to *L/D* of 14.7.

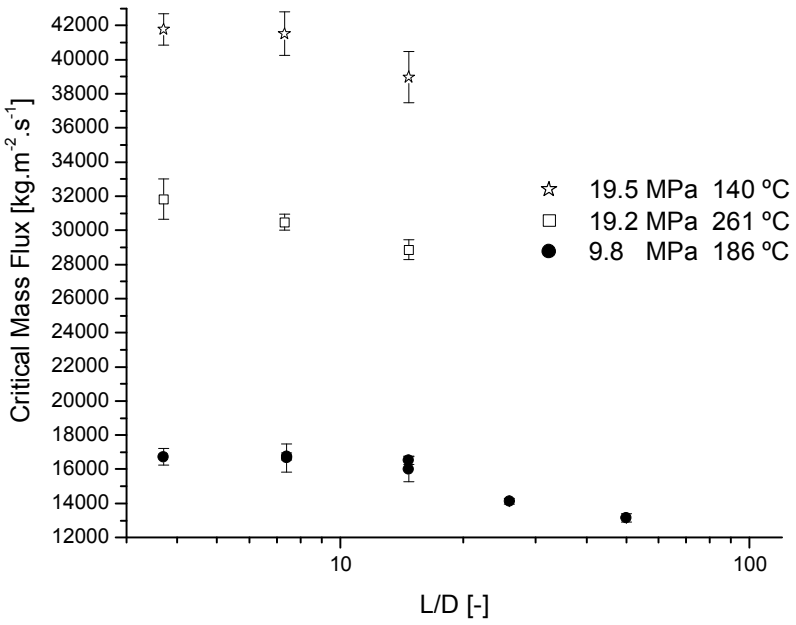

FIG. 7.36. Mass flux versus L/D for perfect gas case scenario.

The results suggest that the choke plane is actually located at the vena contracta since increasing the length does not affect the critical mass flux. Also, the pressure, the temperature, and the mass scaled waveforms lay on each other for the 12.7 mm diameter tubes with *L/D* ranging from 3.7 to 14.7. For this perfect gas scenario CFD results gave a qualitative insight on the actual physics occurring at the vena contracta location. First, the choking location could be compared with a strong initial normal shock (*M* >2) occurring in the tube. Second, the formation of oblique shocks clearly confirms the multidimensional effects induced by the vena contracta. Finally the exiting flow could be supersonic. All these observations showed that the critical flow was completely governed by the conditions encountered at the entrance of the tube, i.e., formation of the vena contracta.

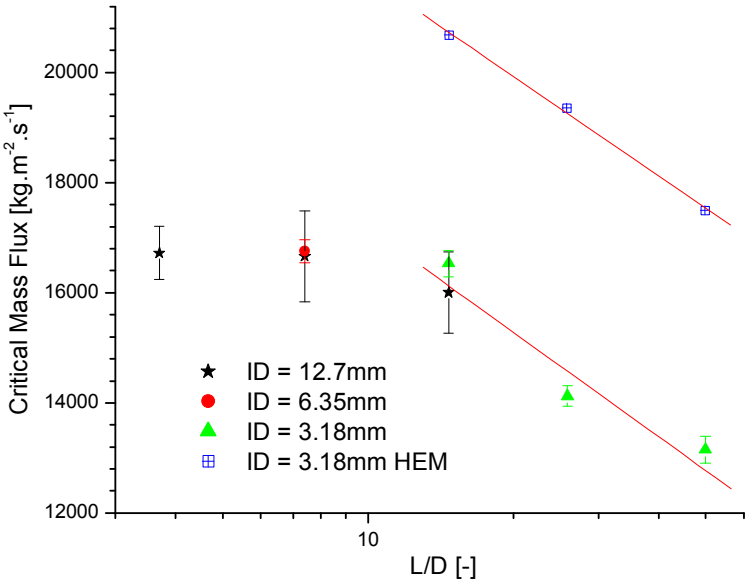

FIG. 7.37. Comparison between measured and calculated critical mass flux – Region II.

Figure 7.37 presents a comparison between the measured critical mass flux and the calculated critical mass flux, using a 1-D model with friction. The decreasing slopes are similar for the measured and the calculated mass flux. This implies that the model captures the right physics with some limitations. One is that the calculated mass flux is based on the stagnation conditions at t=0 whereas the measurement corresponds to an average over the first 2 s. The second is that the model does not account for the initial pressure drop due to the contraction. A final remark is that the model and the data can only be compared when the choke plane is not located at the vena contracta (L/D >14.7).

Sub-cooled case scenario

There are also three S-CO_2 tests corresponding to the criterion of the sub-cooled case. The results are shown in Fig. 7.39. The behaviour for these 'sub-cooled' tests is remarkably similar to the perfect gas case scenario. The results show an initial plateau of the mass flux for low L/D then a decreasing of mass flux for larger L/D. The limit seems to reside at an L/D of 7.3 for the high pressure cases and an L/D of 14.7 for the lower pressure case. Similarly to the perfect gas scenario, these results suggest that the critical mass flux is controlled by a phenomena occurring at the vena contracta location for low L/D values only. For this sub-cooled scenario, a second phase appears which might affect the critical flow if it occurs around the location of the contraction. This phase appearance is only driven by the stagnation conditions and the pressure drop associated with the vena contracta. If we consider the definition of the sound speed within the HEM assumptions, the flow would encounter a discontinuity of the sound speed at the phase transition location since the sound speed is lower for two-phase flow than sub-cooled single phase flow. It forces the two-phase mixture to flow under supersonic conditions.

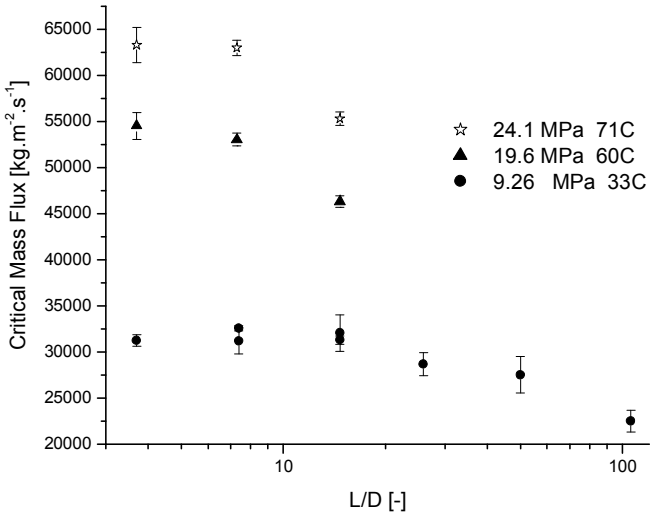

FIG. 7.38. Mass flux versus L/D for sub-cooled case scenario.

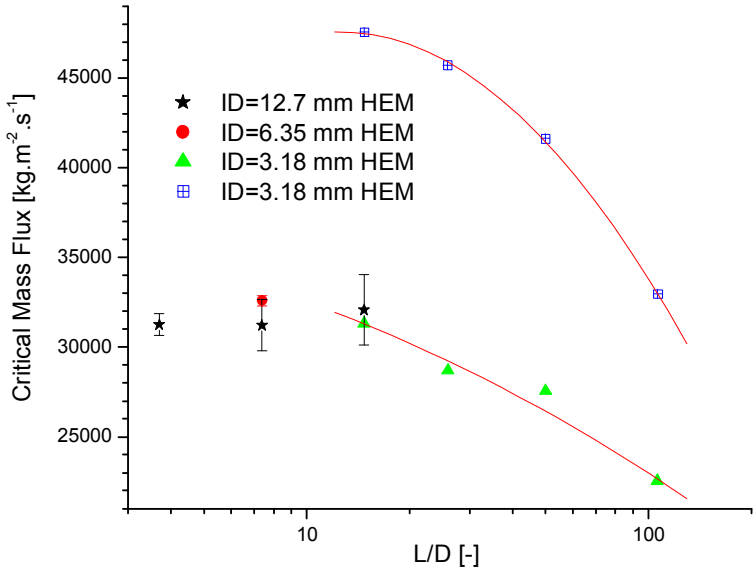

FIG. 7.39. Comparison between measured and calculated critical mass flux – Region III.

The comparison between the measured and the calculated mass flux, using the HEM 1-D model with friction, is presented in Fig. 7.40. It shows the effect of the discontinuity in sound speed as the fluid goes from sub-cooled to two-phase at the entrance of the two-phase dome. The model gives a maximum value of the critical mass flux corresponding to the conditions at the vapor line (x=0). For shorter tube the evolution of the fluid is closer to an isentropic flow such that the conditions at the vapor line do not change much for a given set of initial stagnation conditions. This leads to the plateau observed in the calculated mass flux. (No vena contracta effect is included in this model)

In summary, the pressure drop induced by the vena contracta at the entrance of the tube leads to the appearance of the second phase that creates a drop in the sound speed leading to a supersonic two-phase

flow. Therefore, the flow is choked under the influence of the stagnation conditions only. As *L/D* increases, the entrance pressure drop becomes smaller and the second phase appears further down the tube, under the effects of the friction, which explains the *L/D* influence of the critical mass flux for higher *L/D*. This discontinuity in the sound speed is also observed in the calculation even no contraction was considered.

These behaviours differ from Fauske's conclusion for saturated water. However, it can be explained by a much higher compressibility of the fluid. Also, the decrease of the mass flux with *L/D* is much less pronounced (15%) than that of saturated water (50%).

Condensation case scenario

Finally, there was one S-CO_2 test corresponding to the condensation case scenario. Figure 7.40 shows a behaviour similar to the two previous case scenarios: a plateau with constant mass flux for *L/D* up to 14.7 then a decrease of the mass flux with *L/D*. For this scenario, the physical process is identical to that of the sub-cooled case scenario. However, the HEM model is more suitable for higher quality flows such that the discontinuity of the sound speed across the condensation line is less pronounced. The higher compressibility (0.6) also suggests that, even though two-phase flow occurs, shock structures might still be present within the tube.

It can be noticed that the mass flux follows an exponential decay with *L/D*, which is a trend similar to what the HEM predicted as shown in Fig. 7.40. The difference in slope can be attributed to the actual estimation of the pressure drop along the tube and the estimation of the friction coefficient. Recall that the calculation was done using the initial stagnation condition whereas the experimental results represent an initial average over time. This explained why the HEM seemed to over predict the mass flux with a larger distortion for low *L/D*. Higher mass flow rates lead to faster change within the stagnation thermodynamic properties, which leads to larger error. Calculation with the HEM, using the stagnation conditions corresponding to the state of the fluid at the end of the averaging time, would lead to under prediction of the critical mass flux.

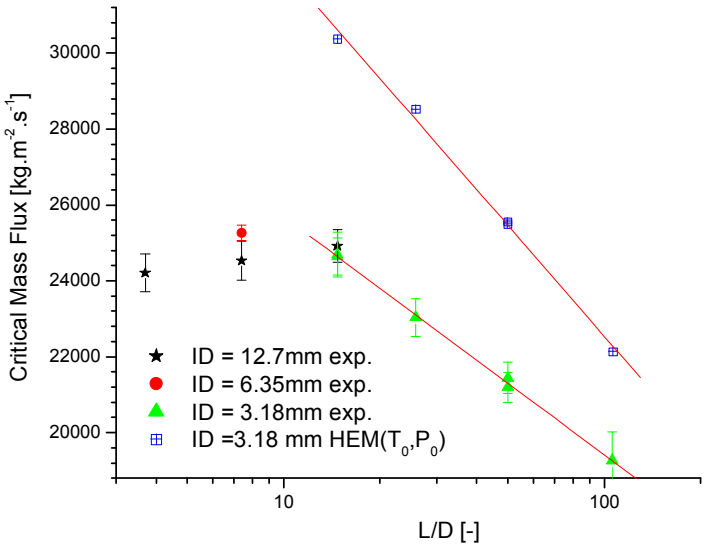

FIG. 7.40. Comparison between measured and calculated critical mass flux – Region II.

7.3.5.5. Summary remarks based on UW work

Based on the above discussion and data, it can be concluded that the limiting factor of the critical mass flux is located at the vena contracta for short tubes only. This contraction ratio depends on the compressibility of the fluid and the stagnation conditions. For sharp edge orifices, the minimum contraction varies from 0.61 for incompressible flow to 0.84 for compressible flow. This area contraction is the dominant factor that leads to the behaviours observed in terms of *L/D*. It depends upon the stagnation pressure as the plateau tends to disappear for high pressure (20 MPa).

The comparison between the measured mass flow rate and a calculated mass flow rate using the HEM without friction shows that the model over predicts the flow. The discrepancy between the model and the data has two different origins: the time averaging of the experimental mass flux and the input geometry. The time averaging leads to a mass flux lower than the one calculated at the initial conditions (at $t = 0$). Because of the vena contracta, the effective minimum area of the flow is in fact lower than the one used for the calculation, based on the tube dimension. The results in Table 7.4 show that the HEM predicts a critical mass flow rate about double of the measured data for the tests of Region III. For Region I and II the model is off by 40%.

In summary, the critical mass flux stays constant for *L/D* up to 14.7 for pressure around 9.5 MPa and for *L/D* up to 7.3 for pressure higher than 19.2 MPa. For higher values of *L/D* the critical mass flux decreases exponentially with respect to *L/D*. For short tubes, the flow area, used in the HEM calculation, has to be corrected to take into account the vena contracta effect; otherwise it may not predict the critical mass flux correctly for these conditions, but works well for larger *L/D* ratios.

TABLE 7.4. COMPARISON HEM CALCULATION WITH EXPERIMENTAL DATA FOR SHORT TUBE

P_0 (MPa)	T_0 (°C)	HEM critical flow ($kg.s^{-1}$)	Experiment critical flow ($kg.s^{-1}$)	Ratio EXP/HEM	Region
9.2	34.2	0.44	0.25	0.57	III
9.2	34.1	1.76	1.03	0.59	III
9.2	33.7	7.16	3.96	0.55	III
9.6	60.8	4.28	3.07	0.72	II
9.6	61.7	1.07	0.80	0.75	II
9.6	60.4	0.27	0.20	0.72	II
9.7	63.5	0.27	0.20	0.73	I
9.8	187.9	2.92	2.12	0.73	I
9.8	188.4	0.73	0.53	0.73	I
9.8	182.6	0.18	0.13	0.71	I
19.2	258.7	0.33	0.23	0.68	I
19.2	263.8	5.32	4.03	0.76	I
19.3	261.4	1.34	0.97	0.72	I
19.5	143.0	0.44	0.31	0.69	I
19.5	139.8	7.23	5.29	0.73	I
19.5	138.0	1.82	1.31	0.72	I
19.6	59.6	14.33	6.91	0.48	III
19.6	60.4	0.89	0.37	0.41	III
19.6	60.0	3.56	2.14	0.60	III
24.1	70.2	4.00	1.99	0.50	III
24.1	72.6	0.98	0.44	0.45	III
24.2	72.0	15.75	8.02	0.51	III

7.4. PLANNED EXPERIMENTS

In an effort to gather further data of the depressurization of SCF from above the vapor dome to add to the data presented above, Canada has established a research program to experimentally study critical flow phenomenon using water under supercritical conditions. A small supercritical water loop is being constructed at Ecole Polytechnique to carry out supercritical critical flow experiments. Detailed measurements of flow rate and pressure drop along two different nozzle designs will be obtained. Critical flow measurements will be compared against those recently obtained in other experimental studies and predictions of various models. If necessary, a revision of the model will be introduced to improve the prediction accuracy.

7.4.1. Experimental facility

The experimental set-up consists of a supercritical water sub-loop that is connected to an existing main steam-water loop of medium pressure. Test sections having different geometries will be installed at the outlet of the supercritical-water sub-loop. The existing steam-water loop serves as a low pressure-controlled reservoir in such a way that the discharge pressure can be changed independently from the flow pressure upstream, i.e., from the throat.

7.4.1.1. The medium pressure steam-water loop

The steam-water loop with a total installed thermal power of 550 kW has been extensively used to carry out Critical Heat Flux (CHF) experiments in test sections having different geometries [7-31], [7-33], two-phase pressure drop experiments in tubes with heat addition [7-34], [7-35], and steam-water choking flow experiments using steam-water mixtures under CHF or close to CHF flow conditions [7-32], [7-36]. A sonic velocity limit boundary, below which CHF occurrence is not possible, was established using the choking-flow data. The principal characteristics of the steam-water loop are: thermal power 2 kW - 550 kW; pressure 1 bar - 40 bar; water flow rate 0.05 kg/s - 5 kg/s and inlet sub cooling 0 ^{o}C - 100 ^{o}C. A currently existing medium pressure steam-water loop shown below in Fig. 7.41 will be modified for supercritical flow testing. Figure 7.41 shows the loop schematic, which consists of a steam drum, a direct contact condenser, two circulating pumps, a heat exchanger and two preheaters. To control the pressure of the system, the heater elements located in the steam drum are used to generate the necessary amount of steam required for operating the direct contact condenser at the desired pressure.

The use of the steam drum as a boiler, in conjunction with the condenser, permits loop operating in a pressurizer control mode (which does not necessitate the presence of a test section installed in the loop). The direct contact condenser maintains the system pressure within an error range of ±0.1 bars. In addition, the preheaters connected in series permit a very accurate control of the inlet sub-cooling (better than ±0.3^{o}C). The water flow rate is measured at the inlet side of the preheaters by using a bank of high temperature 'Flow Technology' turbine flow meters having accuracy better than ±1% of the full scale.

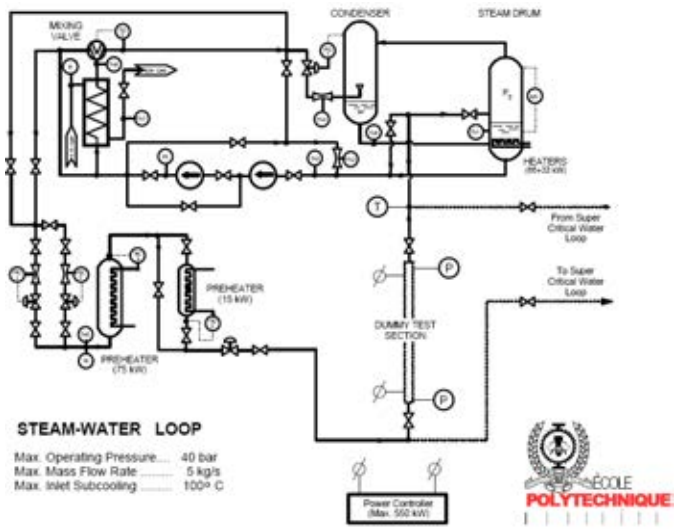

FIG. 7.41. Medium pressure steam-water thermal loop.

7.4.1.2. Modifications of the medium pressure steam-water thermal loop

As shown in Fig. 7.42, the supercritical water system mainly consists of a cooler, a water filter system, a high pressure volumetric pump, a pulsation dampener, a heater, a flow stabilization plenum, a test section and a flow discharge chamber. To determine the principal characteristics of the pump, the cooler and the heater elements, the following preliminary maximum experimental parameters have been established: pressure of 260 bar (abs), temperature of 625 °C and flow rate of 0.15 L/s.

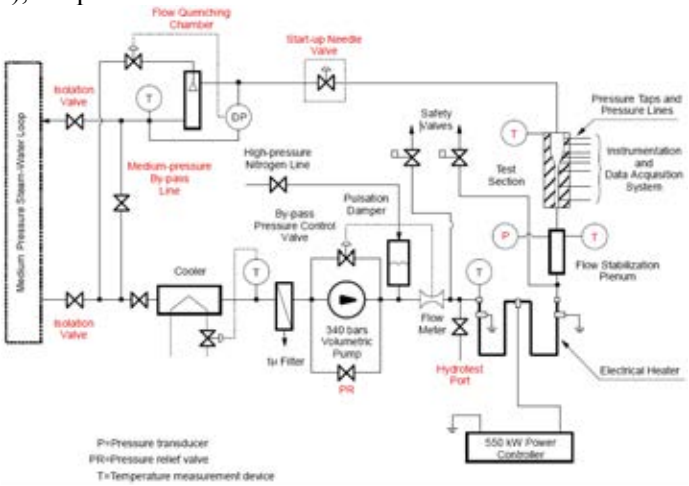

FIG. 7.42. Supercritical water sub-loop for critical flow experiments.

A high RPM six-plunger pump, designed to deliver 2.7 USGPM water at an inlet temperature lower than 70 °C, has been procured. In addition, a pulsation dampener system requiring a permanent high pressure nitrogen supply has been installed to reduce pulsations and hydraulic shocks. This system is more appropriate than the positive displacement pumps, which tend to create pulsations and hydraulic shocks due to the reciprocating nature of their stroking action with the potential of damaging the entire pumping

system. Furthermore, the positive displacement pump may introduce serious pressure and flow fluctuations that can compromise the quality of the experimental data. A needle-type bypass valve is initially used for maintaining the pressure constant during the experiments. This valve is controlled automatically by using an appropriate control unit. This pressure control system will be combined with a supplementary variable speed motor controller later to provide fine pressure adjustment. Taking into account that the high-pressure pump cannot operate at temperatures higher than 70 ^{o}C and that the normal operating temperature of the medium pressure thermal loop is much higher than this limit, a cooler at the inlet of the pump would be installed. To reach fluid temperatures higher than the critical value, a heater element is installed downstream of the flow meter station (upstream of the test-section inlet).

Due to relatively high heat fluxes applied to the heater element and a relatively low heat transfer associated with supercritical fluids [7-37], [7-38], a considerably non-uniform temperature distribution could occur at the outlet of the heater. To overcome this drawback, a flow stabilization plenum is installed between the heater outlet and the test section inlet.

The compressibility of the supercritical fluid contained in this vessel acts as a supplementary fluid damper and homogenizer before it enters into the test section. This dumper consists of a relatively high volume vessel manufactured from a double extra strong stainless steel pipe.

The flow from the test section is discharged in a specially manufactured outlet flow chamber, which is used to avoid a premature destruction of the piping line due to the erosion provoked by the jet that forms at the outlet of the test section and to reduce the effect of possible downstream flow perturbations that could propagate to the test section. Establishing the condition is crucial for accurately controlling the discharge pressure at the outlet of the test section. The pressure in this chamber is measured using an absolute pressure transducer.

7.4.1.3. Test sections

To characterize choking flow as a function of different flow conditions, eight test sections having different internal diameters (IDs) and discharge geometry are planned for the experiment. Figures 7.43 and 7.44 show preliminary designs of two test sections: one has a conical discharge and the other one has an abrupt discharge, respectively (similar test sections were used in previous two-phase choking flow experiments [7-36]). Test sections having inner diameters of 1, 2, 4 and 6 mm and a total length of 275 mm, are instrumented with 8 independent pressure taps and transducers. Three of these taps are located in the straight portion of the test section while the remaining taps are located in the discharge region (i.e., expansion region). This arrangement of pressure taps provides pressure losses of supercritical water flows in the straight channel and pressure profiles under choking flow conditions in the flow discharge region.

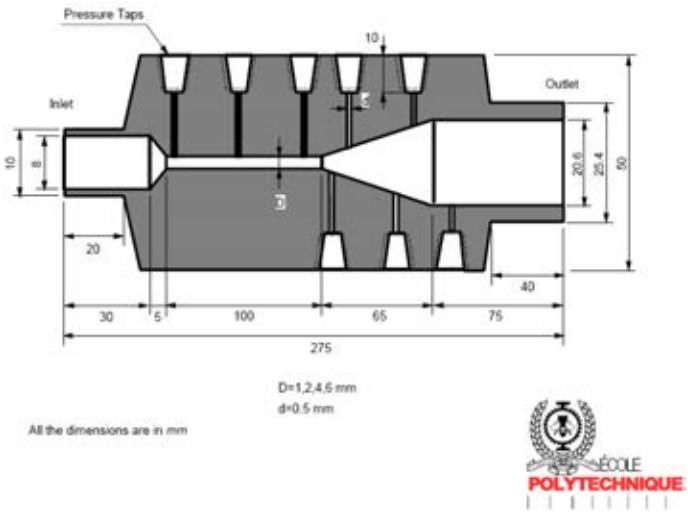

FIG. 7.43. Test section having conical discharge geometry.

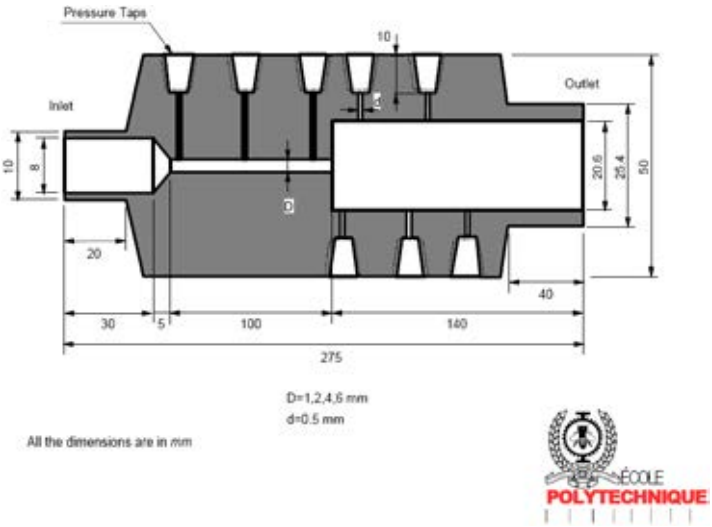

FIG. 7.44. Test section having abrupt discharge geometry.

7.4.1.4. Instrumentation

Pressure drops along the test section are measured using a series of high accurate independent absolute pressure transducers. An additional transducer is used to measure the flow pressure in the flow discharge chamber. The flow rate at the inlet of the heater element is measured using a turbine flow meter. To measure the flow temperature at the outlet of the heater element, RTDs (Resistance Temperature Devices) are used in the flow stabilization plenum. The thermal power applied to the heater elements are measured with a system already available in the steam-water loop. This measurement system uses 5000 A, Class 0.5, calibrated shunts and a highly accurate Hall Effect electric current measurement device (LEM 5000).

Responses of the instruments are simultaneously collected using a Data Acquisition System (DAS), capable of handling 1000 analog input channels with a 16 bits analog to digital conversion unit at a

maximum sampling rate of 1 ms per channel. The thermocouples are connected to the DAS unit through special galvanic isolation amplifiers. Furthermore, the DAS system also contains the filters required to avoid numerical alias problems.

7.5. SYSTEM CODE SIMULATIONS OF DEPRESSURIZATION FROM SUPERCRITICAL WATER CONDITIONS

The application of two-phase system codes in the supercritical region brings up several issues due to the single-phase nature of water above the critical pressure. This becomes particularly challenging when simulating depressurization transients from supercritical to subcritical water conditions. As part of the IAEA CRP the performance of three system codes, (RELAP5, CATHARE and APROS) able to perform such transients, were studied with regard to the computational benchmark known as supercritical Edward's pipe [7-39]. The results of the RELAP5 and CATHARE codes were taken from the work performed within the FP6 European project High Performance Light Water Reactor (HPLWR) Phase 2 [7-40] and are not discussed here due to space limitations. The results of APROS code are based on the work done within the CRP and are summarized below.

7.5.1. RELAP5 code

The REactor Leak Analysis Program (RELAP5) code [7-21] was developed for best-estimate transient simulation of light water reactor coolant systems during postulated accidents. The code was developed at Idaho National Engineering Laboratory (INL) for the Nuclear Regulatory Commission (NRC).

The code is based on a non-homogeneous and non-equilibrium model for the two-phase system that is solved by a fast partially implicit numerical scheme. The RELAP5 code is one-dimensional and solves six basic field equations for six independent variables: pressure, specific internal energies for liquid and vapour, void fraction and liquid and vapour velocities. The constitutive relations include models for defining flow-regimes and flow-regime-related models for inter-phase drag and shear, the coefficient of virtual mass, wall friction, wall heat transfer, and inter-phase heat and mass transfer.

A boiling curve is used in RELAP5 to govern the selection of the wall to fluid heat transfer correlations. The code boiling curve logic is based on the value of the heat slab surface temperature. These correlations are based on fully developed steady-state flow, while entrance effects are considered only for the calculation of the critical heat flux.

7.5.1.1. RELAP5 code modifications

In the framework of the Code Application and Maintenance Program (CAMP) of U.S. NRC, the code developers have modified the RELAP5 code to include the capability to simulate systems at supercritical conditions. The two main modifications included an increase in the number of discretization points in the steam tables and the implementation of the bilinear interpolation scheme at four corner points to compute derivatives of the Gibbs functions. This provides smoother values, in the vicinity of the critical point, for density and temperature derivatives with respect to pressure and internal energy and allows for a fast algorithm compared to calling REFPROP.

The code preserves the two-phase numerical structure also in the supercritical region where a pseudo void-fraction is defined. In this region, the pseudo void-fraction is equal to zero for temperatures below the supercritical value, and equal to unity for temperatures above. The plot of the void-fraction as implemented in RELAP5 is shown in the Fig. 7.45.

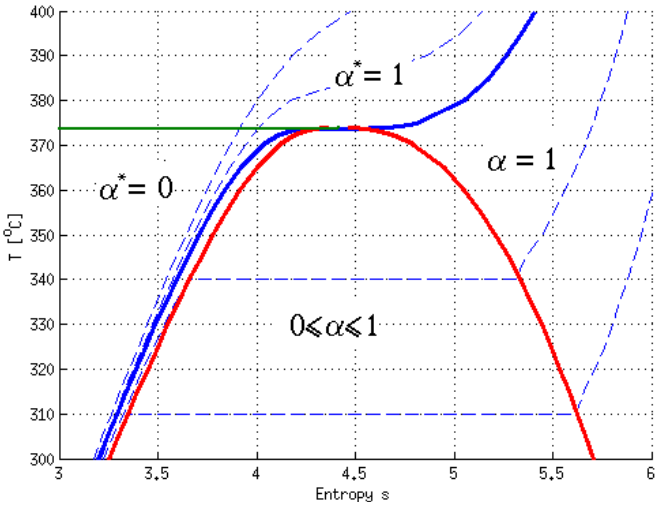

FIG. 7.45. The pseudo void-fraction in RELAP5.

Currently, the Dittus-Boelter correlation is the supercritical heat transfer correlation implemented in RELAP5. The physical properties for water used in RELAP5 are taken from the IAPWS-97 [7-14].

7.5.2. CATHARE code

The Code for Analysis of THermalhydraulics during an Accident of Reactor and safety Evaluation (CATHARE) is a system code for PWR safety analysis, accident management, definition of plant operating procedures and for research and development. It is also used to quantify conservative analysis margins and for licensing.

The code is based on a 2-fluid 6-equation model including non-condensable gas equations and additional equations for radio-chemical components transport. All two-phase flow patterns and all regimes of heat transfer with wall structures are modelled. Closure relationships concern mass, momentum, and energy exchanges between phases and between each phase and the wall. The numerical method is based on a first order finite volume - finite difference scheme with a staggered mesh and the donor cell principle. Time discretization is fully implicit for the 0-D and 1-D modules, and semi-implicit for the 3-D module. The 1-D 2-fluid model is established from the local instantaneous mass, momentum and energy equations. Up to four transport equations can be added when non condensable gases are present. These six equations are averaged for each phase (liquid and gas) over the cross section and over time. The time integration interval is considered to be larger than the largest turbulent time scale and the time scale of the two-phase intermittency.

The code allows the coolant circuits of any reactor to be represented by assembling modules. Sub-modules can be connected to these main modules to represent specific components or modelling features.

7.5.2.1. CATHARE code modifications

Implementation of IAPWS-97 water and steam tables

The CATHARE code was also modified to calculate the physical properties of the water using high order polynomials and their derivatives (Fig. 7.46) based on available IAPWS-97 industrial formulation. This avoids interpolation problems, especially in the vicinity of the critical point, where there are strong variations of the physical properties. Due to the fully implicit nature of the numerical scheme in CATHARE, high order splines ensure the continuity between regions where different polynomials are

used to approximate the physical properties.

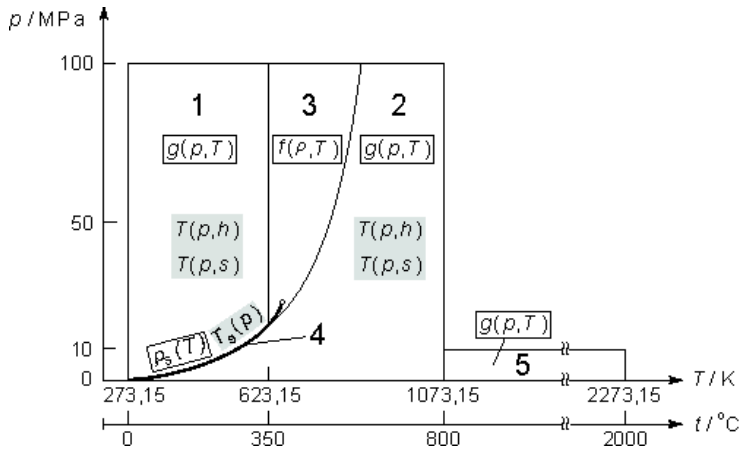

FIG. 7.46. Different regions used in CATHARE code for the physical properties of water and steam.

Implementation of the supercritical fluid model

Similarly to RELAP5, the CATHARE code preserves the two-phase numerical structure also in the supercritical region with the definition of a pseudo void-fraction [7-41]. However its value is determined differently, based on the value of bulk temperature with respect to pseudo-critical temperature. The void fraction is either zero (supercritical fluid behaves like 'pseudo-liquid') or one (supercritical fluid behaves like 'pseudo-vapour') (Fig. 7.47).

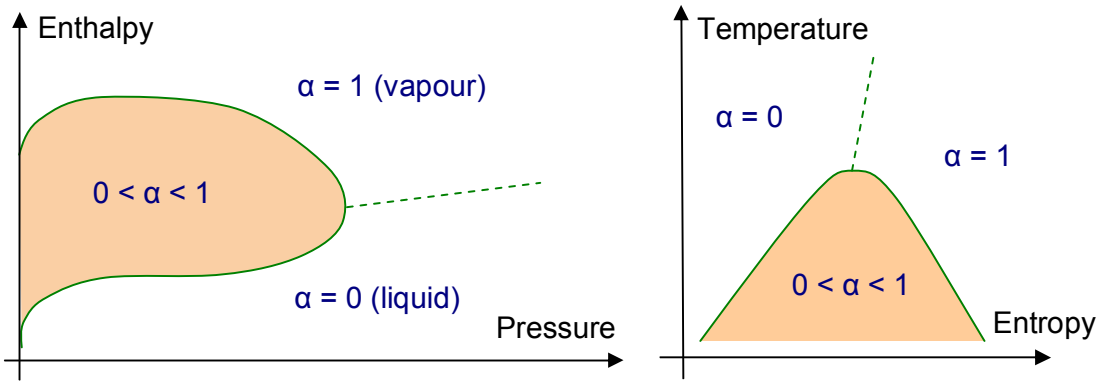

FIG. 7.47. Regions of liquid and vapour for CATHARE.

Implementation of specific supercritical correlations for heat transfer and pressure drop

Specific supercritical correlations for heat transfer and pressure drop in the supercritical water region are recommended [7-15] for HPLWR safety studies and some have been implemented in CATHARE. These include the Petrov and Popov correlation for pressure drop and the Jackson, Bishop, Dittus-Boelter and Swenson correlations for heat transfer. The use of a specific correlation is defined by the user in the input deck. Details on these can be found in other sections of this report.

7.5.3. APROS code

The Advanced PROcess Simulator (APROS) code is a multifunctional simulation environment for the dynamic simulation of nuclear and conventional power plant processes and for the simulation of industrial

process dynamics.

The separate two-fluid model (the 6-equation mode) of APROS is based on the two-fluid formalism developed by Ishii [7-20]. The field equations consist of conservation equations of mass, momentum and total energy, written separately for the liquid and the gas phase. In deriving the one-dimensional equation, constant pressure is assumed over the interface, and the diffusive terms are neglected.

In addition to the water and steam two-phase flow, the two-fluid model is able to simulate various non-condensable gases. The non-condensable gas can either be a part of the gas phase or it can be a dispersed component in the liquid phase. For the numeric solution, the field equations are discretized with respect to space and time, and the non-linear terms are linearized. A staggered scheme is applied for the spatial discretization. Under subcritical conditions, heat and mass transfer between the liquid and the gas phase must be calculated. The mass transfer calculation is based on requirement of zero energy balance over the interface, which is assumed to be in saturated state.

7.5.3.1. APROS code improvements and modifications

In APROS the thermophysical material properties of water are calculated making use of tables as a function of pressure and enthalpy. The values are based on IAPWS97 tables. One problem near the critical pressure point is that properties change very fast. All property values are extracted to correspond to the new pressures and enthalpies. At supercritical pressures, no phase change occurs but rather the properties of the fluid changes smoothly from those of a thick liquid-like fluid to those of a thin vapor-like fluid as its enthalpy increases, or vice versa when its enthalpy decreases. However, in the numeric solution of the two-phase flow equations, the mass contents of a control volume are always assigned to either the liquid phase or the gas phase, or divided between them. As long as the pressure stays above the critical point, it doesn't matter which numeric phase the mass is in, but if the pressure is allowed to decrease below the critical point, it is absolutely necessary, that the fluid is already in the correct numeric phase depending on its enthalpy, i.e. in the gas phase if the fluids enthalpy is above the critical enthalpy, and in the liquid phase otherwise. The approach taken to accomplish this in APROS, is to define a so-called pseudo-phase transition at supercritical pressures. This purely numeric phase transition transfers the mass from the numeric liquid phase to the numeric gas phase as the fluid's temperature passes a predefined line. A natural choice for the line at which the pseudo-phase transition occurs, is an extension of the saturation curve known as the pseudo-critical line. The pseudo-critical line is the line in enthalpy-pressure coordinate system where c_p has its maximum value. If enthalpy is below the pseudo saturation enthalpy the void fraction is zero and the enthalpy is above the line the void fraction is 1. The intention is that the fluid above the critical pressure is always the pseudo steam or pseudo liquid ($\alpha = 0$ or $\alpha = 1$). This kind of approach helps the treatment when the pressure decreases below the critical pressure or when it goes above the critical pressure. At the present time, the supercritical correlations available in APROS are the following:

- Wall friction: the correlation of Kirillov [7-37] suitable for flows in smooth circular tubes, was implemented. Unfortunately, a friction factor correlation suitable for flow in nuclear fuel bundles under supercritical pressures does not currently exist at least in the open literature;
- Heat transfer correlation : Dittus-Boelter [7-42], Bishop [7-43], Jackson and Hall [7-44], Watts and Chou [7-45].

The implemented heat transfer correlations have very limited parameter ranges of applicability – for example the Watts and Chou correlation is valid only for p = 25.0 MPa – which results inevitably in it being applied outside the conditions at which they were developed. This unfortunate fact burdens the user of the simulation tool with an additional problem of assessing the accuracy of the simulation results, which may not be impossible without additional experimental data. Also, all the correlations presented here are valid only for circular tubes. Correlations for nuclear fuel bundles or annuli are not available, at

least in the open literature.

7.5.4. The supercritical Edwards-O'Brien benchmark

7.5.4.1. Description of the facility

The Edwards-O'Brien experiments [7-39] consisted of a series of fluid depressurization tests performed in a straight pipe 4.096 m long with an inner diameter of 0.073 m (Fig. 7.48). A glass disk at one end of the pipe was designed to rupture with a single shot from a pellet gun to initiate the depressurization phase of the transient. The time for the disk to fully open was estimated to be about 1ms. Due to a small amount of glass observed around the circumference of the opening after the tests the break flow area was reduced by 13% from the pipe cross sectional area. The experiments were characterized by a first phase of the transient where a depressurization wave was travelling inside the pipe towards its closed-end on which it was reflected and later the blow-down phase controlled by the strong evaporation of the liquid (flashing). A series of fast-response temperature and pressure measuring instruments were located along the length of the pipe ('gauge-stations'), identified as GS-1 through GS-7 (Fig. 7.48).

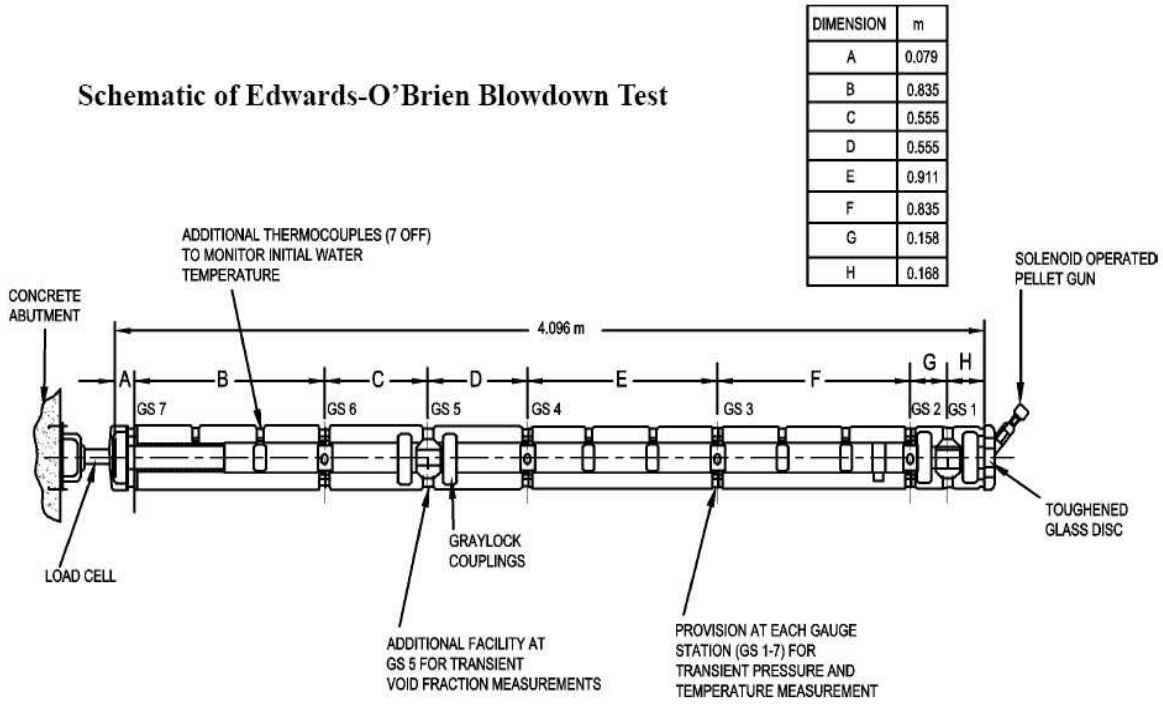

FIG. 7.48. Schematic of Edwards-O'Brien blow-down test section [7-12].

7.5.4.2. The RELAP 5 model for Edward's blow-down tests

The RELAP5 model is shown in Fig. 7.49. The pipe is modeled by means of 20 nodes of equal size. The center of node 8 corresponds to the measuring position GS-5, where experimental data is available. A break component is used to impose a time-dependent pressure boundary condition at the pipe-end. The rupture of the disc is supposed to occur in 1 millisecond.

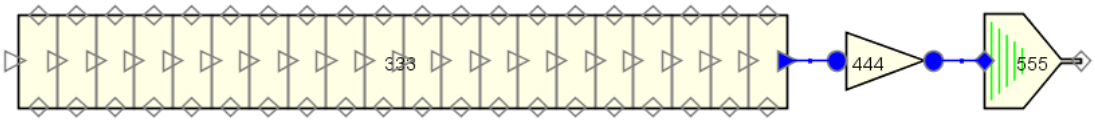

FIG. 7.49. RELAP5 nodalization for the Edward's pipe test.

The nodalization is the same as suggested in the RELAP5 manual for the Edwards' pipe test [7-40]. Calculations with a refined mesh have shown that with the selected nodalization mesh-independent results are obtained.

7.5.4.3. The CATHARE model for Edward's blow-down tests

Experience using CATHARE has shown that the critical flow prediction at the break is usually more accurate when calculated with 1D model of the flow nozzle instead of using a critical flow correlation function based on upstream parameters. Therefore a boundary condition was used to model the break that imposes either the external pressure or a sonic blockage (Fig. 7.50). However such a break model has some constraints in the nodalization of the pipe, since the last node element before the break should not exceed 1mm length, and the length ratio of two successive nodes should not exceed 1.2. Moreover the nodes were chosen so that each measuring station (GS-1 through GS-7) was located at the centre of their corresponding node. These conditions led to a model consisting of 50 non-uniform nodes.

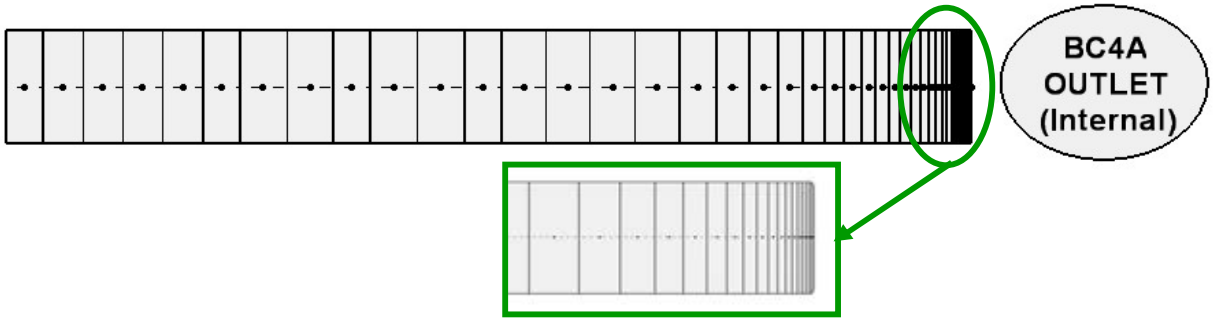

FIG. 7.50. The CATHARE meshing.

7.5.4.4. Description of the APROS model for Edward's blow-down tests

The initial conditions of the simulation cases are listed in Table 7.5. In Fig. 7.51, two separate thermal-hydraulic nodalizations of the pipe are presented. In nodalization #1, constant-length calculation cells are used, and in nodalization #2 the length of the calculation cells is carefully refined towards the open end of the pipe. Moody's critical flow limitation model [7-16] is applied in nodalization #1, whereas the refined nodalization #2 is able to predict the flow limitation intrinsically.

TABLE 7.5. INITIAL CONDITIONS OF THE SIMULATIONS CASE

Case	Standard	01	02	03
p_0	6.99 MPa	25.0 MPa	25.0 MPa	25.0 MPa
T_0	502 K	580 K	653 K	700 K

In case of Edward's pipe the mass flow was limited using the Moody's model [7-15]. However it is not known how well the model predicts the critical mass flow when the pressure is above the critical pressure. However at the outlet the pressure drops below the critical pressure very quickly so the overall error in the calculation even if the critical mass flow is not known well may be small. The case was also calculated without the special limitation at the outlet, however, a very dense nodalization was used in order to predict the pressure decrease near the outlet. The overall goal of this simulation was to see how well the basic equations were able to limit the flow rate. Once this is understood and new models are developed, improvements can be made to the calculations.

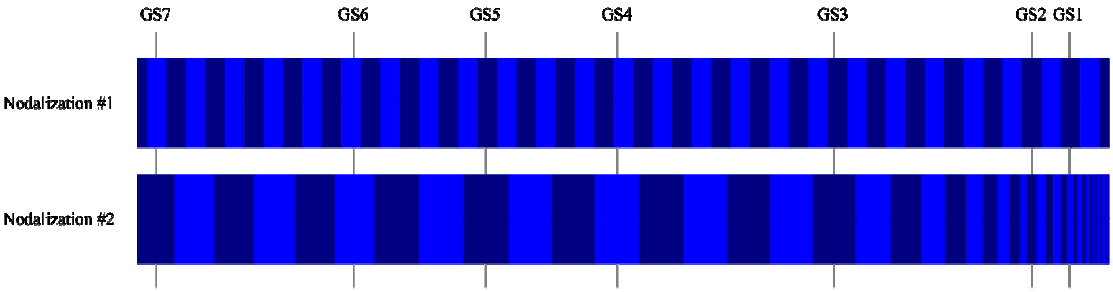

FIG. 7.51. Two different nodalizations used for the APROS simulation.

7.5.5. System code results

7.5.5.1. Results of the RELAP5 and CATHARE tests

RELAP5 and CATHARE results for the standard test show a good agreement (Fig. 7.52) in terms of both pressure and void fraction evolutions with respect to the experimental data. The void fraction is, however, much higher during depressurization in RELAP than in CATHARE but this is also observed in the first supercritical water test. Since no experimental data are available for the last three tests, only code-to-code comparison is possible. Both codes show similar pressure evolutions, while the void fraction in Test No. 1 is much higher for RELAP5 at the beginning of the depressurization but reach a similar value at the end of the transient (Fig. 7.53). Tests No. 2 and No. 3 show a much better agreement between the codes (Fig. 7.54). Since flashing has the highest impact on the evolution of the void fraction, some sensitivity studies on the flashing heat transfer correlation were performed in CATHARE and it was found that if this is multiplied by four there is a good fit with RELAP this suggests the need to better understand the heat transfer correlations. The results (Fig. 7.55) show that the discrepancies between CATHARE and RELAP5 are similar indicating that the differences are coming from the flashing heat transfer model of the two codes.

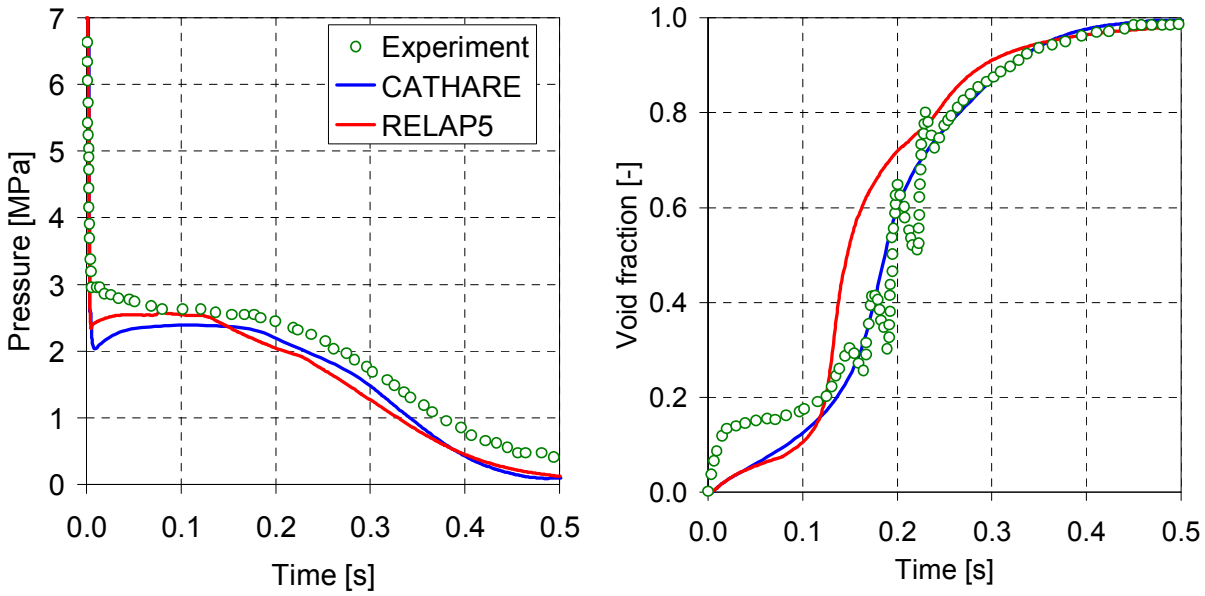

FIG. 7.52. Standard test case.

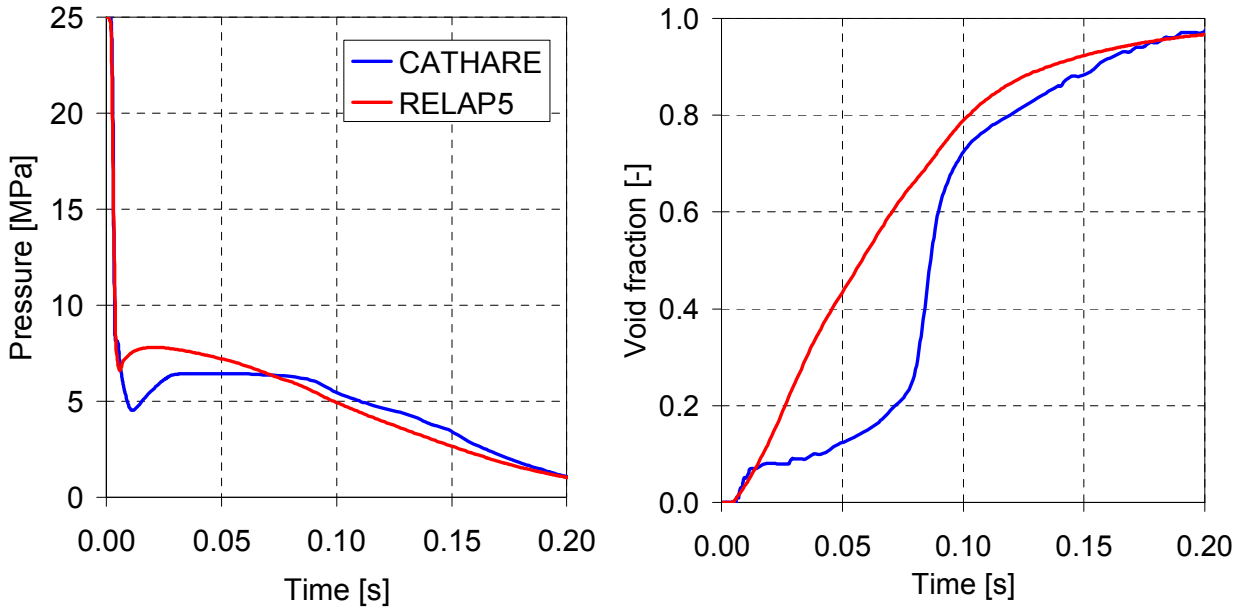

FIG. 7.1. Test No.1.

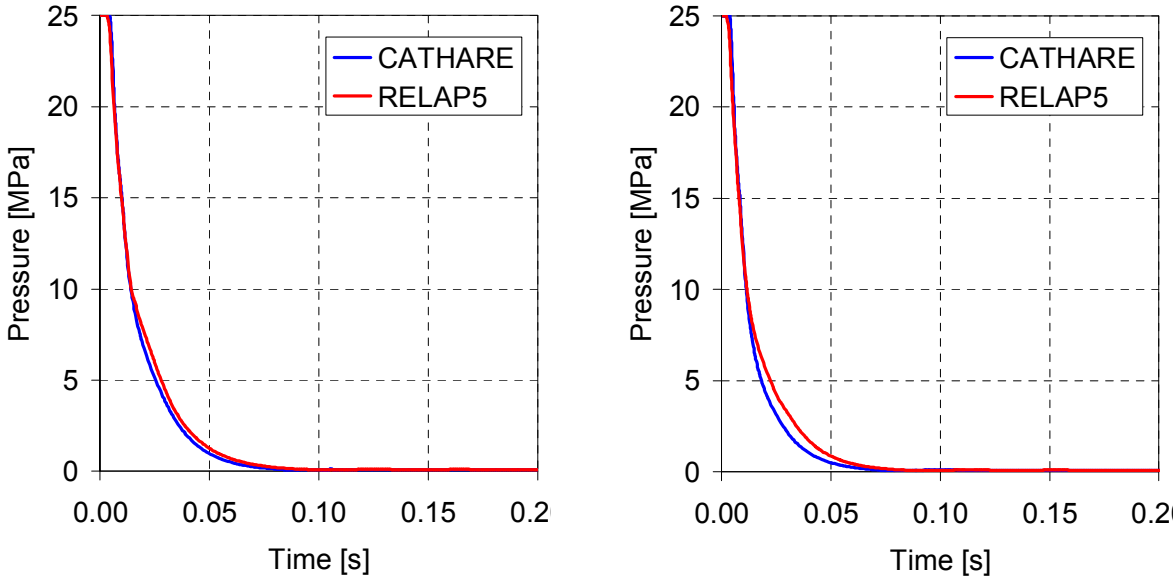

FIG. 7.54. Depressurization test No.2 and test No.3.

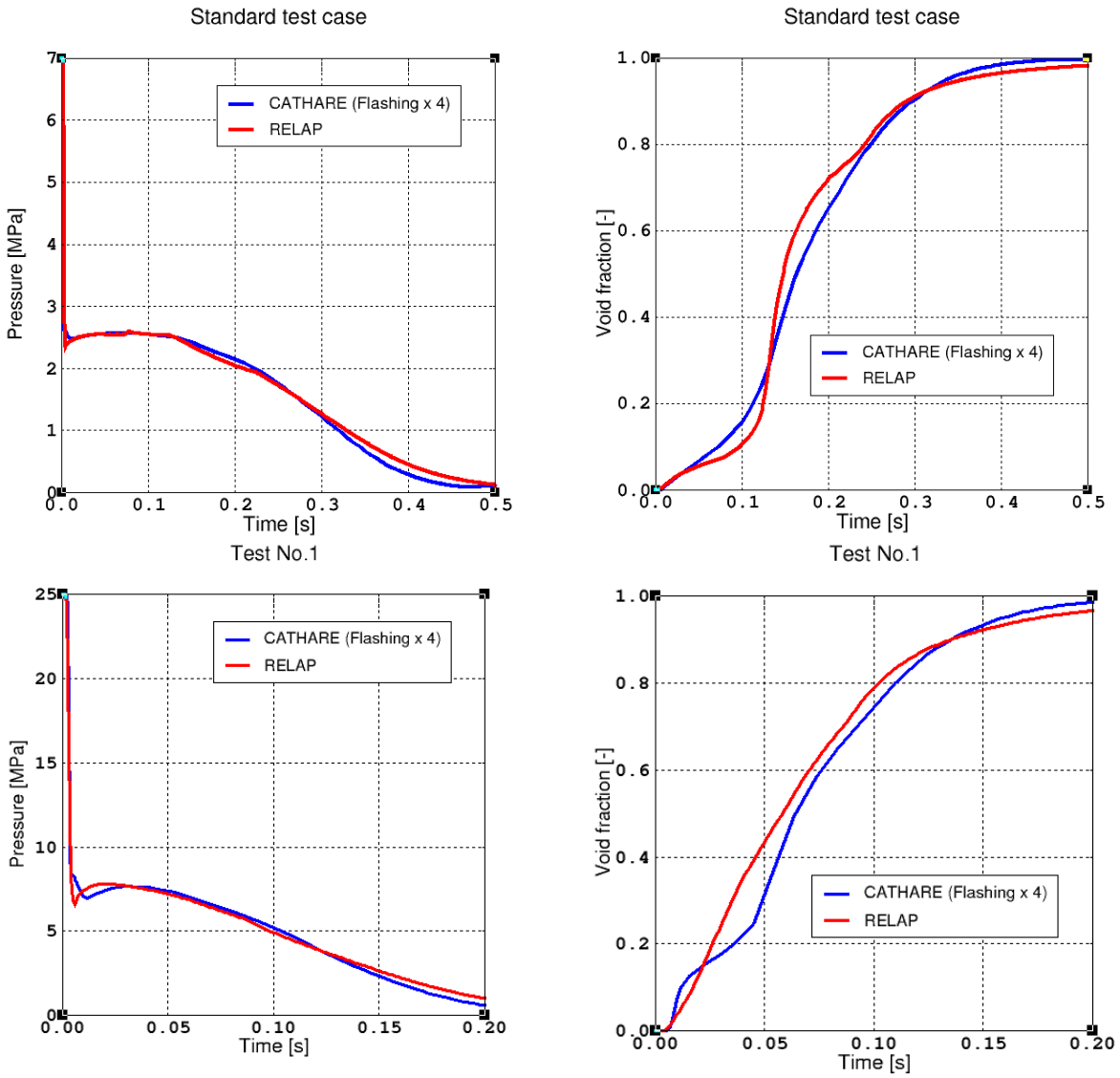

FIG. 7.55. Comparisons of CATHARE and RELAP5 results.

7.5.5.2. Results of the APROS tests

Three modified cases of the Edwards-O'Brien blow-down experiment were simulated with APROS 5.09. The modified cases mimic the experiment geometry conducted by Edwards and O'Brien in 1970, but the initial pressure is increased to 25.0 MPa, i.e. the hypothetical nominal operating pressure of a SCWR. These modified versions of the experiment have not been conducted in the experiment, and thus no actual data is available for validation of the results however it is instructive to look at the trends in the depressurization and look at a code to code comparison. The results, shown in Figure 7.56 through Fig. 7.58, are in good agreement with the calculations made using RELAP5 and CATHARE. Another observation was that the use of Moody's model for choked flow has a marginal effect, more evident at higher fluid temperatures. But it requires a less dense nodalization at the outlet point. Overall the

depressurization seems reasonable but the code has yet to be tested against the new data from CIAE and UW presented above.

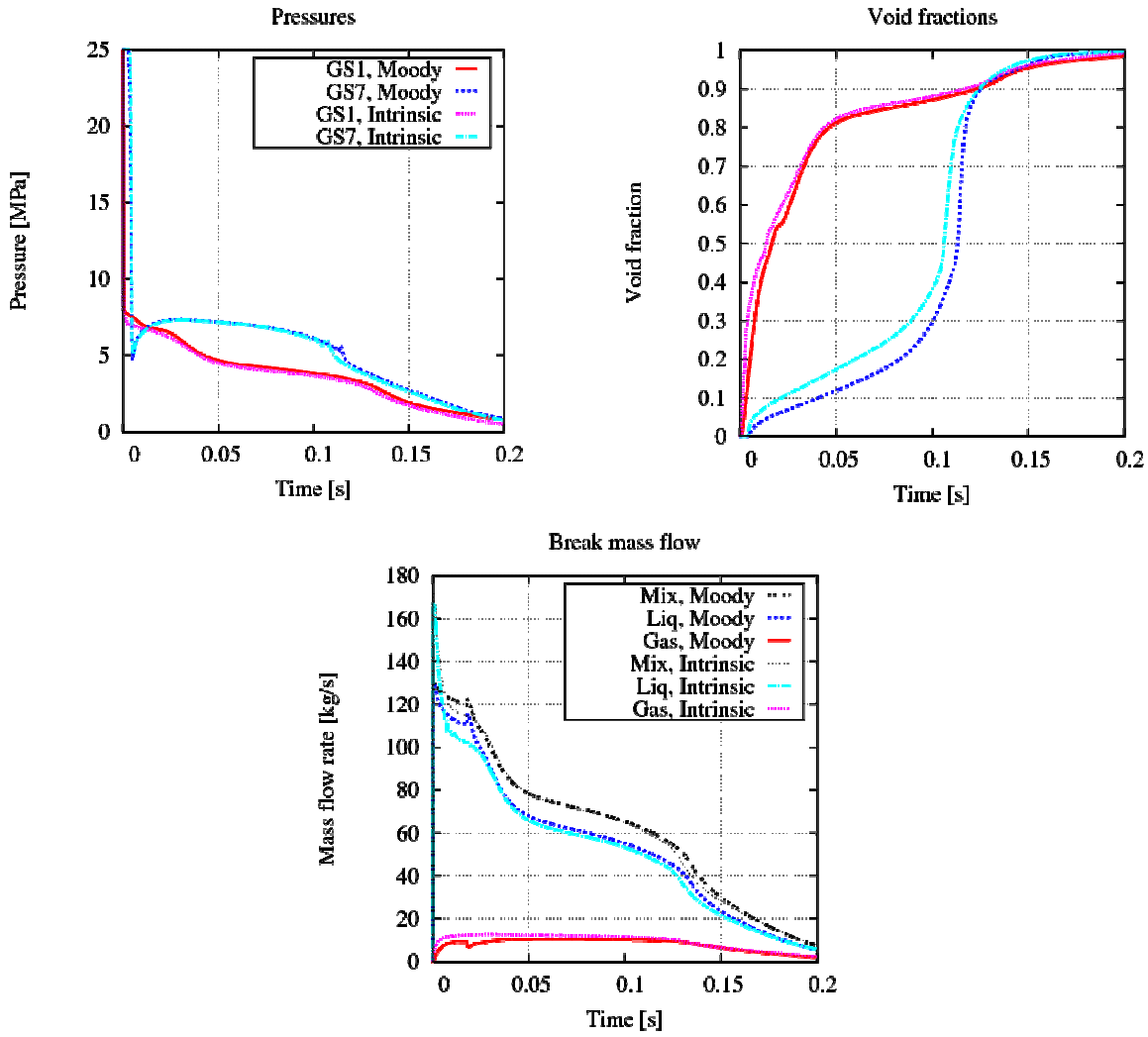

FIG. 7.56. Results of simulation case 01.

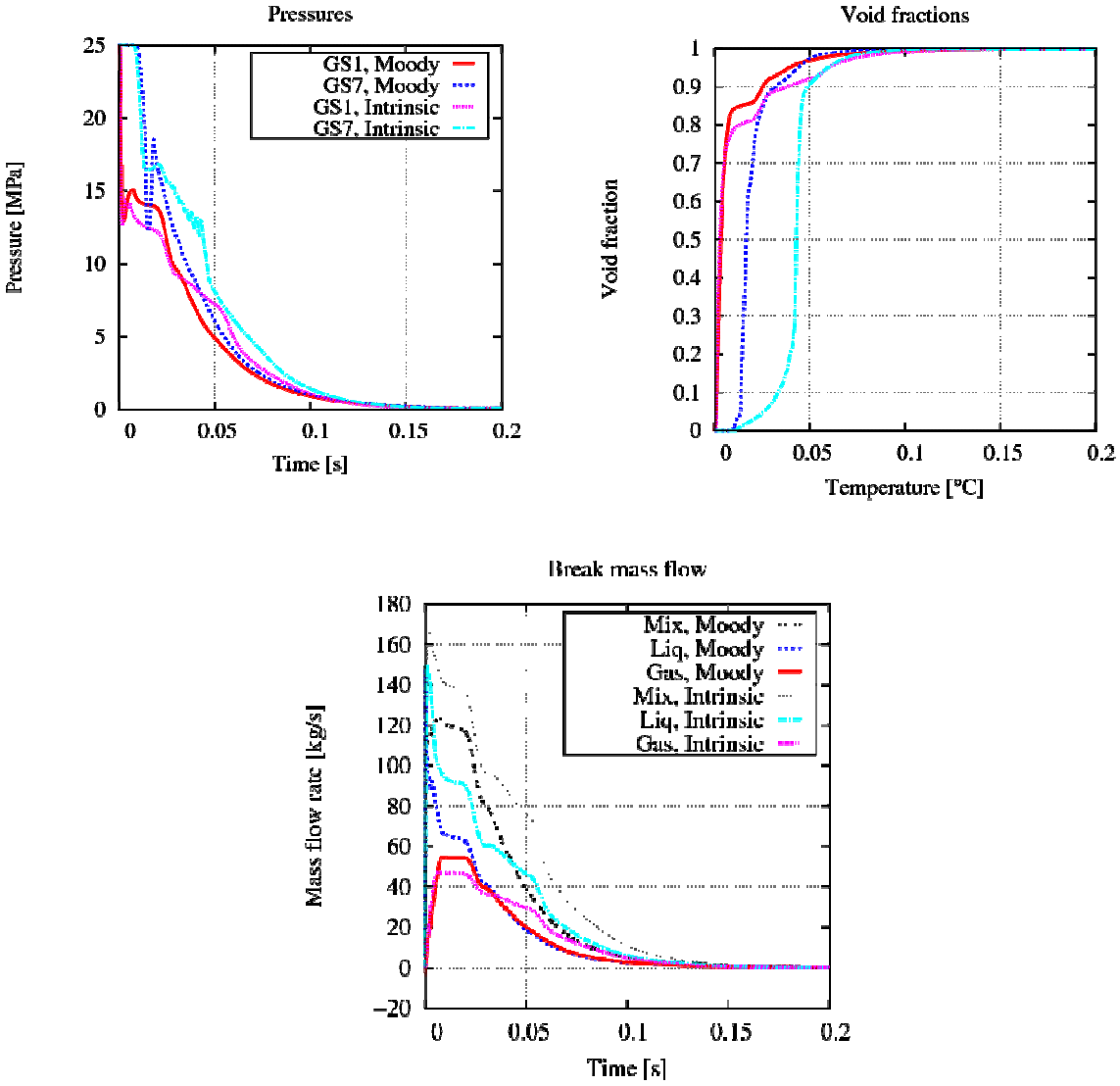

FIG. 7.57. Results of simulation case 02.

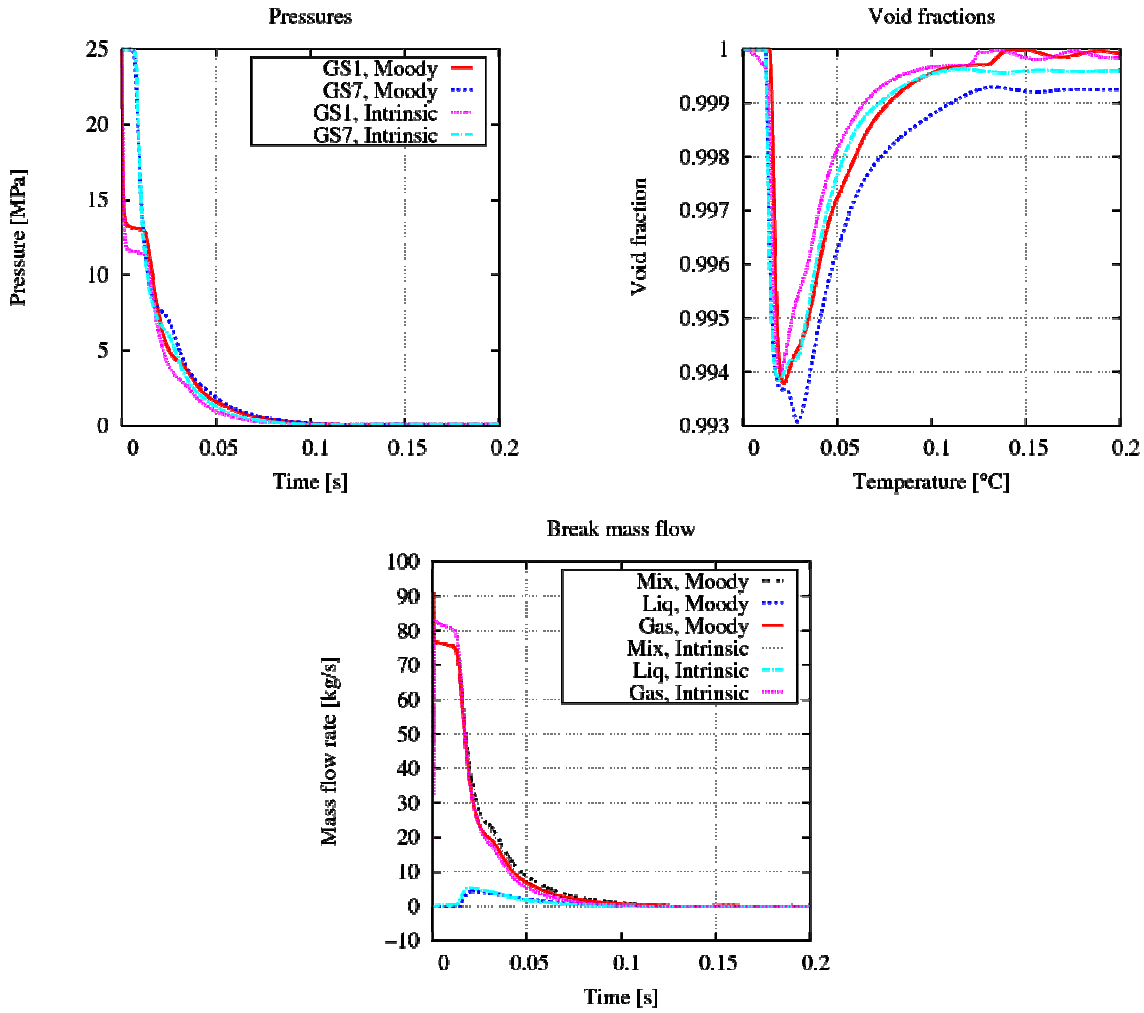

FIG. 7.58. Results of simulation case 03.

LIST OF SYMBOLS FOR SECTION 7

A	Discharge cross sectional area
C_D	Discharge coefficient
D	Tube diameter
DP_t	Pressure drop
DT_{PC}	Temperature difference $T_{PC} - T_0$
G	Mass flux
G_M	Measured mass flux
h	Enthalpy
K	Slip ratio
k	Boltzman's constant
L	Tube length
M	Mach number
P	Pressure
P_{amb}	Ambient pressure
P_b	Back pressure
P_{min}	Minimum pressure
P_n	Pressure at which first nucleation occurs
P_s	Local saturation pressure
P_t	Inlet throat pressure
P_0	Stagnation pressure
P_α	Critical plane pressure
R	Universal gas law constant
s_g	Specific entropy (gas)
s_l	Specific entropy (liquid)
s_0	Specific entropy at the inlet
T_r	Reduced temperature
T_0	Stagnation temperature
T_{PC}	Pseudo-critical temperature
t	Time
v_g	Momentum flow rate (gas)
v_l	Momentum flow rate (liquid)
w_g	Phase velocity (gas)
w_l	Phase velocity (liquid)
x	Equilibrium quality at the critical plane (pg 17)
γ	Specific heat ratio
v	Specific volume
ρ	Density
ρ_l	Density of water
Σ'	Depressurization rate
σ	Surface tension

REFERENCES FOR SECTION 7

[7-1] LEVY S, A.D., HEALZER, J., et al, Critical—flow data review and analysis (1982).

[7-2] SAHA, P.A., A review of two-phase steam-water critical flow models with emphasis on thermal non-equilibrium, 1978: BNL-NUREG-50907 (1978).

[7-3] ANDERSON, J., Modern Compressible Flow1990: McGraw-Hill publishing Co. (1990)

[7-4] ARDRON, K.H., FURNESS, R.A., Study of the critical flow models used in reactor blowdown analysis. Nuclear Engineering and Design, 1976. 39(2-3) (1976) 257–266.

[7-5] FAUSKE, H.K., Discharge of saturated water through tubes. Chemical Engineering Progress Symposium Series, 1965. 61(59) (1965) 210–216.

[7-6] LEE, D.H., SWINNERTON, D., Evaluation of critical flow for supercritical steam-water, Electr. Power Res. Inst., Palo Alto, CA, USA: USA (1983) 172.

[7-7] CHEN, Y., YANG, C., ZHANG, S., ZHAO, M., DU, K., An Experimental Study of Critical Flow of Water under near-critical and Supercritical Pressures (2009).

[7-8] FREDENHAGEN, A., Druckentlastung binärer Gemische aus Kohlendioxid und Stickstoff sowie Kohlendioxid und Wasser, Universität Hamburg-Harburg (2002).

[7-9] MIGNOT, G.P., ANDERSON, M.H., CORRADINI, M.L., Measurement of supercritical CO2 critical flow: effects of L/D and surface roughness. Nuclear Engineering and Design. 239(Copyright 2009, The Institution of Engineering and Technology) (2009) 949–55.

[7-10] STARKMAN, S., NEUSEN, K.F., et al. , Expansion of a very low quality two-phase fluid through a convergent-divergent nozzle. ASME Trans D, J Basic Engineering, 1964(82(2)) 247–256.

[7-11] MOODY, F.J., Maximum Flow Rate of a Single Component, Two-Phase Mixture. ASME Trans C, J Heat Transfer, 1965. 87(1) 134–142.

[7-12] HENRY, R.E., FAUSKE, H.K., The two-phase critical flow of one-component mixtures in nozzles, orifices, and short tubes. Transactions of the ASME. Series C, Journal of Heat Transfer, 1971. 93(Copyright 1971, IEE) 179–87.

[7-13] INTERNATIONAL ATOMIC ENERGY AGENCY, Thermohydraulic Relationships for Advanced Water Cooled Reactors, in Reactor technology, N. Askan, Editor May 2001, IAEA: IAEA Tecdoc Series No. 1203 (2001).

[7-14] WAGNER, W., et al., The IAPWS industrial formulation 1997 for the thermodynamic properties of water and steam. Journal of Engineering for Gas Turbines and Power, 2000. 122(1) (2000) 150–180.

[7-15] CHENG, X.T., SCHULENBERG, T., SOUYRI, A., SANCHEZ, V., AKSAN, N.,, Heat Transfer and Pressure Drop at Supercritical Pressure - Literature Review and Application to an HPLWR, H.D.D. (FIKI-CT-2000-00033), Editor (2001).

[7-16] FAUSKE, H.K., Some ideas about mechanism causing two-phase critical flow. Applied Scientific Research Section A, 13(2-3) (1964) 149–160.

[7-17] HENRY, R.E., FAUSKE, H.K., MCCOMAS, S.T., Two-phase critical flow at low qualities. II. Analysis. Nuclear Science and Engineering, 41(1) (1970) 92–98.

[7-18] HENRY, R.E., FAUSKE, H.K., MCCOMAS, S.T., Two-phase critical flow at low qualities. I. Experimental. Nuclear Science and Engineering, 41(1) (1970) 79–91.

[7-19] MOODY, F.J., A pressure pulse model for two-phase critical flow and sonic velocity. Transactions of the ASME. Series C, Journal of Heat Transfer, 91(Copyright 1970, IEE): (1969) 371–84.

[7-20] ISHII, M.A.H., T. , Thermo-Fluid Dynamics of Two-Phase Flow: Springer Science & Business Media, LLC, New York, USA (2006).

[7-21] RELAP/Mod 3.3 Code Manual, Volume I: Code Structure, System Models, and Solution methods, R. ISL, MD and Idaho Falls, Editor, March (2003).

[7-22] ARDRON, K.H., Two-fluid model for critical vapor-liquid flow, 4(3) (1978) 323–337.

[7-23] SCHULTZ, R.R., ERICSON, L., Marviken criical flow test program. Nuclear Safety, 22(6) (1981) 712–724.

[7-24] LEE, D.H., SWINNERTON. D., Critical discharge of sub-cooled water at very high pressure. in First U.K. National Conference on Heat Transfer, 3–5 July 1984, Rugby, UK: Instn. Chem. Eng. (1984).
[7-25] GEBBEKEN, B., EGGERS, R., Blowdown of carbon dioxide from initially supercritical conditions. Journal of Loss Prevention in the Process Industries, 9(4) (1996) 285–293.
[7-26] YUZHOU, C., et al., Heat transfer with water flowing upward in a tube for pressures up to supercritical region. Frontiers of Energy and Power Engineering in China, 4(3) (2010) 358–65.
[7-27] LIENHARD, J.H., ALAMGIR, M., TRELA, M., Early response of hot water to sudden release from high pressure. Journal of Heat Transfer, 100(3) (1978) 473–479.
[7-28] ALAMGIR, M., LIENHARD, J.H., Correlation of pressure undershoot during hot-water depressurization. Transactions of the ASME. Journal of Heat Transfer, 103(1) (1981) 52–5.
[7-29] MIGNOT, G., ANDERSON, M., CORRADINI, M., Supercritical CO2 critical flow. Transactions of the American Nuclear Society, 96(Copyright 2007, The Institution of Engineering and Technology) (2007) 568–569.
[7-30] HENRY, R.E., FAUSKE, H.K., The two-phase critical flow of one-component mixtures in nozzles, orifices, and short tubes. Transactions of the ASME. Series C, Journal of Heat Transfer, 93(2) (1971) 179–187.
[7-31] TEYSSEDOU, A., et al., Critical heat flux data in a vertical tube at low and medium pressures. in Sixth International Topical Meeting on Nuclear Reactor Thermal Hydraulics, 5-8 Oct. 1993, Netherlands (1994).
[7-32] OLEKHNOVITCH, A., TEYSSEDOU, A., TYE, P., Critical heat flux under choking flow conditions. Part II - maximum values of flow parameters attained under choking flow conditions. Nuclear Engineering and Design, 205(1-2) (2001) 175–190.
[7-33] OLEKHNOVITCH, A., SUN, J., A. TEYSSEDOU, A., A complex but accurate correlation for predicting critical heat flux in a round tube for low and medium pressures under circumferentially non-uniform heating conditions. International Journal of Heat and Mass Transfer, 51(7-8) (2008) 2041–54.
[7-34] OLEKHNOVITCH, A., et al., An empirical correlation for calculating steam-water two-phase pressure drop in uniformly heated vertical round tubes. International Journal of Multiphase Flow, 31(3) (2005) 358–370.
[7-35] LEUNG, L.K.H., et al., Pressure drops for steam and water flow in heated tubes. Nuclear Engineering and Design, 235(1) (2005) 53–65.
[7-36] OLEKHNOVITCH, A., et al., Critical heat flux under choking flow conditions. Part I - outlet pressure fluctuations. Nuclear Engineering and Design, 205(1-2) (2001) 159–173.
[7-37] PIORO, I.L., DUFFEY, R.B., Heat Transfer and Hydraulic Resistance at Supercritical Pressure in Power Engineering Applications: ASME Press, New York (2006).
[7-38] PIORO, I.L., DUFFEY, R.B., DUMOUCHEL, T.J., Hydraulic resistance of fluids flowing in channels at supercritical pressures (survey). Nuclear Engineering and Design, 231(2) (2004) 187–197.
[7-39] EDWARDS, A.R., O'BRIEN, T.P., Studies of phenomena connected with the depressurization of water reactors. Journal of the British Nuclear Energy Society, 9(2) (1970) 125–135.
[7-40] AKSAN, N.B., MARSAULT, D., ANTONI, P., MANERA, O., DAVITTILA, A., Safety for the HPLWR, in Deliverable D3-01-Y1, EC EURATOM FP6 High Performance Light Water Reactor Phase 22001.
[7-41] MARSAULT, P., et al., Pre-design studies of SCWR in fast neutron spectrum: Evaluation of operating conditions and analysis of the behaviour in accidental situations. in Proceedings of the 2004 International Congress on Advances in Nuclear Power Plants, ICAPP'04, June 13–17, 2004. Pittsburgh, PA, United States: American Nuclear Society (2004).
[7-42] DITTUS, W., BOELTER, L.M.K., *Heat transfer in automobile radiators of the tubular type.* University of California -- Publications in Engineering, **2**(13) (1930) 443–461.
[7-43] BISHOP, A.A., KRAMBECK, F.J., SANDBERG, D.R.O., Forced-convection heat transfer to superheated steam at high pressure and high Prandtl numbers. in ASME Meeting WA/HT-35,

Nov 7–11, 1965. New York, NY, United States: American Society of Mechanical Engineers (ASME) (1965).

[7-44] JACKSON, J.D., HALL, W.B., *Forced convection heat transfer to fluids at supercritical pressure*. Institution of Mechanical Engineers, Conference Publications, 1979. **2** (1979) 563–611.

[7-45] WATTS, M.J., CHOU, C.T., *Mixed convection heat transfer to supercritcal pressure water*. in Heat Transfer 1982, Proceedings of the 7th International Heat Transfer Conference. Volume 6: General Papers: Combined Heat and Mass Transfer, Particle Heat Transfer, Heat Exchangers, Industrial Heat Transfer, Heat Transfer in Energy Utilization. Munich, Ger: Hemisphere Publ Corp. (1982).

[7-46] CHEN, Y.Z., YANG, C.S., ZHANG, S.M., ZHAO, M.F., DU, K.W., An Experimental Study of Critical Flow of Water under Near-Critical and Supercritical Pressures, Proc. The 13th International Topical Meeting on Nuclear Reactor Thermal Hydraulics (NURETH-13), N13P1048, Japan (2009).

[7-47] CHEN, Y.Z., ZHAO, M.F., YANG, C.S., BI, K.M., DU, K.W., ZHANG, S.M., Research on Critical Flow of Water under Supercritical Pressures in Nozzles, Journal of Energy and Power Engineering.V.6, (2012) 201–208.

[7-48] CHEN, Y.Z., YANG, C.S., ZHANG, S.M., ZHAO, M.F., DU, K.W., CHENG, X., (2009)，Experimental study of critical flow of water at supercritical pressure，Front. Energy Power Eng. In China, Vol.3, No.2 (2009) 175–180.

[7-49] CHEN, Y.Z., YANG, C.S., ZHAO, M.F., DU, K.W., ZHANG, S.M., Experimental Studies on Critical Flow and Heat Transfer of Water for Near-critical and Supercritical pressures，Proc. the IAEA Technical Meeting on Heat Transfer, Thermal-Hydraulics and System Design for Supercritical Water-Cooled Reactors, Pisa, Italy (2010).

[7-50] CHEN, Y.Z., YANG, C.S., ZHANG, S.M., ZHAO, M.F., DU, K.W., An Experimental Study of Critical Flow of Water under Subcritical and Supercritical Pressures Proc. of the 4th International Symposium on Supercritical Water-Cooled Reactors, Germany, P-12 (2009).

[7-50] CHEN, Y.Z., ZHAO, M.F., YANG, C.S., BI, K.M., DU, K.W., ZHANG, S.M., Critical Flow of Water under Supercritical Pressures，Proc. the 14th International Heat Transfer Conference，USA，IHTC14-22156 (2010).

8. INSTABILITY AND NATURAL CIRCULATION IN SUPERCRITICAL PRESSURE SYSTEMS

8.1. INTRODUCTION

The design of supercritical water cooled reactors poses new challenges in relation to the prediction of some basic phenomena, whose characteristics are relatively well-known at subcritical pressure.

In particular, stability and natural circulation phenomena observed in single-phase conditions at subcritical pressures become more complex at supercritical pressures because of the strong variability of thermodynamic and thermophysical properties. Moreover, categories adopted for dealing with two-phase flow phenomena must be updated to deal with supercritical pressure flow regimes, having in principle a simpler structure than the corresponding two-phase flow ones, though they anyway involve uneven distributions of lighter and heavier fluids within the channel cross section.

Flow instabilities and natural circulation, being dealt with in this section, have been the subject of major experimental and modelling efforts at subcritical pressures. Some of these studies belong to both aspects, since a quite populated intersection of the two categories is represented by the interesting domain of natural circulation instabilities.

In single-phase flow, in particular, apart from turbulence and acoustic effects, which are beyond the scope of this section, instabilities mainly occur in natural circulation systems, being driven by a mechanism explained with effective elementary arguments by Welander in 1967 [8-1]. In that work, it was suggested that pockets of fluid with perturbed temperature may emerge from the heat source and/or the sink, affecting the fluid residence time along the loop and being damped or amplified as a consequence of the subsequent passages through the heater and the cooler. This mechanism was proposed on the basis of numerical computations and was confirmed later on by further experimental and computational studies, focusing on different interesting aspects affecting the phenomenon (see e.g., [8-2] - [8-22]). A remarkable feature of the observed behaviour is its chaotic character, mainly caused by the fact that the growth of flow perturbations frequently leads to flow reversal; as a consequence, the system is seen to continuously switch from clockwise to counter-clockwise flow directions and vice versa, showing a high sensitivity to initial conditions.

Two-phase flow instabilities are mainly connected with the behaviour of boiling channels that are recognized to be susceptible to different instability mechanisms, having a ‘static’ or a ‘dynamic’ nature (see e.g., [8-23]). The discrimination among the two categories of instabilities is introduced considering whether their occurrence can be explained on the basis of the static internal pressure drop vs. flow characteristic of the system. The Ledinegg ‘excursive’ instability mechanism [8-24] is representative of the category of static instabilities, while density-wave, pressure drop oscillations and thermal oscillations are mechanisms which belong to the second category. Of these instabilities, density waves represent the most relevant instability mechanism for nuclear reactor applications since, in combination with neutronic feedback, it is responsible for observed space and time oscillations of Boiling Water Reactor core power. These instabilities have been the subject of extensive studies, summarized in review papers and state of the art reports [8-25] - [8-31]. Basic experimental investigations (see e.g., [8-32] - [8-34] and [8-30] Section 3) allowed grasping the main features of involved phenomena, gaining the basic understanding necessary for analytical developments. An interesting body of information about reactor plant events is also available (see [8-30] Section 6). Models for predicting the unstable behaviour of boiling systems have been set up and qualified by applications ranging from the scale of experimental facilities to the full reactor scale (see e.g., [8-35] - [8-40], [8-26] and [8-30] Section 4). Both time-domain (i.e., transient) and frequency-domain (i.e., linearized) models are available to estimate the stability thresholds of even very complex systems.
Natural circulation phenomena have also been thoroughly studied at subcritical pressures, both in single-

and two-phase flow conditions. The relevance of this phenomenon for nuclear reactors is well known, since natural circulation involves several regimes of reactor operation. As previously mentioned, natural circulation and stability phenomena have an extensive intersection in single- and two-phase flows. A limited list of relevant aspects relating natural circulation at subcritical pressures is reported hereafter:

- different single- and two-phase natural circulation modes appear during start-up, under normal operating conditions and postulated light water reactor accidents, as observed in experiments and code predictions (see e.g., [8-41]);
- natural circulation is relied upon for decay heat removal from the nuclear reactor core and/or the containment system; in particular, passive decay heat removal by natural circulation represents one of the most important features in advanced (Gen III) and innovative (Gen IV) reactors;
- different modes of flow instabilities are recognized in natural circulation boiling systems, adding additional phenomena to be addressed to those already observed in boiling channels (see e.g., [8-42] - [8-43]);
- The vast body of information from experimental and theoretical researches on stability and natural circulation performed at subcritical pressures constitutes a useful background also for supercritical water reactor applications, at least in view of two main aspects:
    - the knowledge acquired on fundamental phenomena can be helpful in supporting the new developments required for supercritical pressure conditions, provided that analogies and differences between the two operating regions (subcritical and supercritical) are properly identified;
    - part of the operational and perturbed evolution of supercritical water reactors will occur at subcritical pressures, directly involving operating conditions for which previous knowledge is immediately applicable.

In the present section, as a specific contribution to the Coordinated Research Programme (CRP) in relation to flow stability and natural circulation at supercritical pressure systems, we are obviously mainly interested in extending previous knowledge to supercritical pressure conditions. Work has been already performed for decades in relation to both stability and natural circulation, but the related issues have recently acquired a greater relevance owing to the proposal of different supercritical reactor concepts.

In particular, stability has been addressed as an issue of great importance for SCWR design, owing to the fact that heated channels with supercritical pressure fluids are assumed to be susceptible to similar instability phenomena as observed in boiling channels. In fact, the transition across the pseudo-critical temperature can be considered as a sort of ‘pseudo-boiling’ phenomenon, leading to denser fluid at channel inlet and lighter one at the outlet. This is one of the reasons why the basic understanding and the numerical tools developed for two-phase flow instabilities are found immediately available for being converted for supercritical pressure instabilities. The scarcity of relevant experimental data on instabilities in supercritical pressure systems is presently a problem to be coped with in order to ascertain that this process of knowledge transfer from one research field to another is made without forgetting any important difference. On the other hand, natural circulation at supercritical conditions has been the subject of a number of experiments performed in past and recent times. Experimental facilities working at supercritical pressures, in particular, sometimes made use of natural circulation even when the primary focus was on different aspects (e.g., heat transfer). However, in these cases their data on natural circulation may be insufficiently detailed to allow for meaningful analytical conclusions. Though relevant experiments and modelling tools are already available in this field, there is still the need for further understanding and specific assessment.

In the following sections, after a short overview of the information available on stability and natural circulation at supercritical pressures, the contribution brought in this CRP to both the addressed research areas will be described. As it will be seen, this contribution mainly consists of:

- descriptions of experimental facilities where data are available to the present CRP, including:

    - an experimental facility addressing natural circulation and stability at the University of Manitoba in Canada;
    - an experimental facility addressing natural circulation and stability at the Bhabha Atomic Research Centre (BARC) in India;
    - an experimental facility operated with supercritical water at the China Institute for Atomic Energy (CIAE) in China;
- the description of new experimental data from:
    - the experimental loop at BARC;
    - the experimental loop at CIAE;
- code applications including:
    - stability analyses of supercritical VVER reactor assemblies, provided by Gidropress in the Russian Federation;
    - the application of codes available at BARC in relation to their own experimental data;
    - the application of CFD codes to the experimental CO_2 data obtained at BARC;
    - a short summary of a Code Testing Benchmark on flow stability (detailed results will be described in Section 9.2).

8.2. BACKGROUND ON STABILITY AND NATURAL CIRCULATION AT SUPERCRITICAL PRESSURES

8.2.1. Available information from models and experiments

Stability
The thorough review of the available literature on supercritical pressure systems by Pioro and Duffey [8-44] reports a list of early works on the subject of instabilities in supercritical and near-critical pressure systems. These works contain interesting information, collected starting from the sixties, regarding stability phenomena characterized by different time frequencies, ranging from system oscillations (at low frequencies) to acoustic ones. In this list, the number of works related to experimental observation is small (see e.g., [8-45] - [8-48]), and the applicability of the experimental data for the assessment of up-to-date models is unclear. A few examples from early experimental and theoretical works are reported hereafter.

In the article by Jones and Peterson [8-49], methods were developed to study the stability of supercritical helium cooling systems in the frequency range corresponding to density-wave instabilities. Though these methods have more common applications, they were developed in this work to study the cooling of superconducting power lines. A distinctive feature of this study is the application of helium thermodynamic properties determined by an exact equation of state and the consideration of compressibility effects. The classical linear control theory is used in the analysis, providing examples of typical parameters characterizing the power lines with helium coolers at some values of supercritical pressure. It is concluded that, though the occurrence of density-wave instability is quite possible in superconducting power lines, it is not difficult to design system characteristics to provide stable operating modes.

The article by Labuntzov and Mirozyan [8-50] reported the results of theoretical studies on stability of supercritical helium flow. An equation for determining stability conditions was derived. The presence of unstable operating regions was pointed out, where in addition to a principal mode, oscillations at higher frequencies might exist. The article contains comparison of experimental data from Daney et al. [8-51] and predictions from the methods of Jones and Peterson [8-49].

A description of an experimental facility and of experimental results for supercritical Freon-114 (symmetric dichlorotetrafluoroethane, critical pressure of 33.26 ata. and critical temperature of 145.7ºC) was reported in the article by Cornelius and Parker [8-52]. The experimental loop was intended to study

the unstable behaviour of the flow and was designed for operation in natural and forced convection conditions. The loop and test section were made of AISI-304 stainless steel pipes, with an outer diameter of 25.4 mm and an internal diameter 23.6 mm. The test section was 915-mm long and was electrically isolated from the rest of the circuit and heated up by alternating current, keeping constant the power input. In the experiments, pulsating behaviour was observed within a broad temperature range below the pseudo-critical temperature. The authors concluded that, apparently, the necessary requirement for the onset of unstable behaviour is that the liquid temperature on the heating surface is sufficiently higher than the pseudo-critical temperature, so that the boundary layer is in the gas-like state, while the bulk fluid is in the liquid-like region. The paper further expands on the acoustic character of pulsations and their occurrence as a consequence of pseudo-boiling.

In the article by Daney et al. [8-51], the boundary of flow stability against density waves was determined experimentally for supercritical helium flow in long heated channels with large length-to-diameter ratios. Oscillations of measured parameters were observed with amplitudes that reached large values at various temperatures and inlet flow rates. The increase of enthalpy (temperature) disturbance in the heated channels was confirmed experimentally. Experimental data about the onset of oscillations were correlated by parameters related to the rate of pressure drops and relative fluid expansion. According to measured results, in the presence of density-wave oscillations, the outlet temperature and inlet mass flow rate are in-phase and the oscillation period is approximately equal to twice the transit time. The experimental results were found in agreement with calculations performed by a simple model assuming incompressible flow. The paper also reported tables with experimental results.

Actually, retrieval of this early information for present use would be appropriate for code and model validations, in similarity with what was made in the field of heat transfer to supercritical fluids in the frame of this CRP. In fact, the first few works on this subject, produced well before the interest for supercritical water reactors became so widespread, contain basic concepts and observations that are still useful nowadays. Another relevant example of such early understanding of phenomena can be found in the report by Zuber [8-53] on thermally induced flow oscillations, which summarizes the knowledge acquired at the time on the subject of instabilities in near-critical fluids.

In view of the scarcity of experimental information on instabilities in supercritical pressure fluid systems, model applications flourished instead, based on the experience gained with previously developed tools for boiling channels instabilities. In particular, extensions of previous concepts and dimensionless numbers applicable to boiling channel stability appeared recently [8-54] - [8-57], aiming at establishing the rationale for setting up stability maps in a dimensionless form, trying to achieve some degree of universality. The main instability phenomena considered in these works are the oscillatory density-wave type and the excursive Ledinegg type; the latter was shown to be possible also in supercritical pressure systems [8-58] - [8-59], though at relatively low inlet channel temperatures for the upward flow, far enough from normal reactor operating conditions, being instead favoured by horizontal and downward flows.

Consideration of dimensionless parameters is also necessary for establishing effective theories for a fluid-to-fluid comparison to be adopted in downscaled experimental apparatuses, thus justifying the efforts recently made in this regard [8-60] - [8-62]. In particular, fluid-to-fluid modelling aspects have been studied by Marcel et al. (2009) [8-61] who observed that a 77.5%/22.5% mixture of refrigerants R-32 and R-125 simulates the supercritical water (SCW) conditions in HPLWR (High Performance Light Water Reactor). They also suggest that supercritical CO_2 cannot accurately simulate the HPLWR conditions with water because of the different dimensionless properties.
The models developed up to now are conceived for the analysis of simple systems, as single channels or natural circulation loops (see e.g., [8-54] - [8-56], [8-63] - [8-67]), as well as for more complex ones, up to the reactor scale (see e.g., [8-68] - [8-73]). In the case of reactor applications, it is quite evident the advantage resulting from the availability of analytical techniques set up for boiling water reactor systems,

capable to deal also with the coupling between thermal-hydraulics and neutronics. In fact, similar modelling techniques are now used to simulate supercritical water reactor phenomena, allowing for a suitable thermal-hydraulic description of the reactor, with multiple channels equipped with conductive rods and reactivity effects.

Linearization of the equations by perturbation and the application of control-theory principles to the obtained linear transfer functions is one of the adopted techniques for studying stability, in similarity with a methodology that has become popular for studying two-phase flow instabilities. The main result of these analyses is the evaluation of the decay ratio (DR) of oscillations for different reactor power-to-flow ratios; low values of DR are allowed for the normal operation (e.g., less than 0.25), while inadvertent occurrences may be considered, leading to power-to-flow ratios large enough to approach the stability threshold (DR=1).

In addition to linear analyses, the transient behaviour is also addressed by space and time discretization of balance equations using transient codes. As a consequence, also for supercritical pressure systems, a general categorization of models in 'frequency-domain' and 'time-domain' tools is applicable. Approaches making use of time and space discretization of balance equations for studying linear stability were also proposed (see e.g., [8-56]), pointing out the effect of numerical discretization on linear stability, as predicted using a given numerical scheme. Moreover, as it was in the past for boiling channels, simplified models are being developed for predicting flow stability [8-74].

With respect to previous applications concerning boiling systems, supercritical fluids, owing to the absence of phases and interfaces, allow an easier use of available transient CFD methodologies for addressing stability issues. In fact, single-phase CFD turbulence models can be directly applied to supercritical fluids, with due caution about their quantitative adequacy, adopting the usual approximation of pressure independent fluid properties at a fixed operating pressure. First applications addressed both 2D axi-symmetric conditions and 3D subchannel slices [8-75] - [8-76]. Though the calculations are much lengthier than with system codes, it must be considered that, in the absence of a reliable assessment of 1D models in front of experimental data, a diversification of computational tools is appropriate to highlight possible interesting behaviour that could be neglected by the one-dimensional approach. However, the analyses performed up to now seem to suggest that 1D models grasp the relevant dynamic features of instabilities, leaving to the CFD the role of highlighting details in relation to flow and temperature distribution effects.

Natural Circulation

Natural circulation with supercritical fluids was specifically studied considering simple loops, also with a limited experimental effort. In addition to study steady-state performances, the conditions for the occurrence of unstable behaviour were addressed by computational means in most studies. Few examples are reported hereafter.

Walker and Harden [8-46] made use of Freon-114 in a loop at a supercritical pressure (3.62 MPa). The stability data were successfully compared with predictions obtained with a model considering an approximate equation of state in a simplified loop geometry. The operating range of temperature of the performed runs is not reported in the paper. Harden and Boggs [8-77] conducted studies on Freon loops near the critical region; high and low frequency oscillations were observed when bulk fluid temperatures approached the pseudo-critical temperature.

Chatoorgoon [8-63] investigated a natural circulation loop with supercritical water at boundary conditions of imposed heating and cooling heat fluxes. A stability analysis of the system was performed, developing a theoretical stability criterion and also comparing the predictions using the nonlinear code SPORTS with those of an analytical model. An 'open loop' configuration was considered, with the flow entering at

constant temperature upstream of the heater and exiting downstream of the cooler. This kind of boundary conditions, in place of the actual periodicity of pressure, flow rate and temperature along the loop, is frequently used also in later studies. On the basis of some simplifications, a criterion for the onset of instability was suggested in the paper: the threshold of instability has been suggested to be the peak of steady-state mass flow rate versus power curve.

Lomperski et al. [8-78] performed experiments with supercritical CO_2 in a two-meter high natural-circulation loop. The test runs consisted of stepwise increases in input power followed by a waiting period to allow the system to stabilize at a new flow rate. The loop was operated in a base configuration that maximized flow rates and in a second configuration having an orifice in the hot leg. No flow instabilities were observed in these tests as the fluid was heated through the thermodynamic pseudo-critical point, though a model set up for comparison showed oscillations to occur in specific operating regions.

Jain and Corradini [8-79] performed the linear stability analysis of a supercritical water natural circulation loop; their results suggested that the instability behaviour of supercritical natural circulation loops is not strictly related to the peak of the steady-state flow rate versus power curve. Jain and Rizwan-uddin [8-80] investigated flow instabilities in a natural circulation loop with supercritical CO_2 using a computer code. In the paper, these authors studied the effects of numerical discretization parameters on the stability threshold. Also in this case, an open loop configuration was considered. In addition to study the effect of numerical discretization on stability predictions, the work discussed the location of the unstable region along the flow vs. power curve.

Sharma et al. [8-81] carried out linear stability analyses for supercritical water natural circulation loops using the SUCLIN code. The boundary conditions used in the analyses consisted again an imposed heat flux at the heater and at the cooler. Results were obtained also for loops addressed in previous works, showing the regions of instability as functions of heating power and heater inlet temperature. Moreover, Sharma et al. [8-82] compared the stability predictions of the in-house developed linear stability code (SUCLIN) and of the non-linear stability code (NOLSTA) for an open loop natural circulation with supercritical water. The results showed that the stability maps generated using these two codes agree qualitatively, but quantitatively there is a large difference which can be attributed to the difference in the two approaches.

Chen et al. [8-83] adopted a two-dimensional CFD model for a rectangular natural circulation loop utilizing supercritical CO_2 as working fluid at the pressure of 9 MPa. Convective boundary conditions were applied to both the heater and the cooler, while the rest of the piping was assumed to be adiabatic. Different patterns of oscillations were observed in the work as a function of the source and sink temperatures.

8.2.2. Areas requiring further efforts

The brief overview reported above shows that the renewed interest for reactor applications at supercritical pressures is presently producing increasingly sophisticated analytical tools, with a consequently large number of theoretical predictions, and a more limited number of experimental works.

The advantage of making use of the vast body of knowledge acquired for boiling water systems is quite clear in these developments. In fact, many concepts, ideas and tools applicable to two-phase flow phenomena are presently applied to the corresponding supercritical pressure phenomena by relatively minor changes, mainly regarding fluid properties and, in some cases, physical correlations. In fact, stability phenomena postulated (but seldom observed) to occur in supercritical pressure systems have many similarities with the ones occurring in subcritical conditions, sharing with them the nature of phenomena produced by the considerable expansion of a relatively dense fluid due to heating. As a consequence, density-wave as well as excursive unstable behaviour may be expected in supercritical

pressure systems, depending on the operating region considered.

Natural circulation at supercritical pressures is also expected to be characterized by phenomena similar to those observed at subcritical pressures. Buoyancy and frictional forces governing natural circulation in single- and two-phase flows are, in fact, presumably similar to those developed at supercritical pressures, except for those regimes specifically requiring the presence of separated phases to occur. Anyway, it must be considered that closure laws required to accurately predict these phenomena may be substantially different.

In particular, concerning the stability of natural circulation, it can be reasonably assumed that:

- mechanisms similar to those observed in single-phase (Boussinesq) fluids, e.g., the one described by Welander [8-1], may be operating also at supercritical pressures whenever a sufficient buoyancy is available to generate them;
- when the appropriate conditions occur, these mechanisms can be replaced or accompanied by density-wave oscillations or other instability mechanisms requiring large density changes, in similarity with what observed in two-phase natural circulation systems.

However, since the similarity between subcritical and supercritical pressure systems is obviously partial, a number of issues need to be clarified. As implied at several stages in these considerations, only experiments may provide reliable answers in this regard. Among these issues, the following should be considered:

- the need for accurate closure laws: as also demonstrated by the effort spent in this direction in the present CRP, phenomena like heat transfer enhancement and deterioration still need a proper treatment both at the level of engineering correlations and in CFD models; in addition, also friction factor correlations should be updated and carefully assessed for dealing with supercritical fluids, properly considering roughness effects; constitutive laws specifically developed for supercritical fluids are therefore needed for accurate predictions of flow stability and natural circulation phenomena;
- the possible interactions between flow and heat transfer regimes: the occurrence of heat transfer deterioration in heated channels results in a change in fluid properties close to the wall; this has the consequence of affecting also the hydraulic impedance of the channel, with effects on both stability and natural circulation;
- the effect of boundary conditions: the presence of heat structures as well as the use of closed loop or open loop boundary conditions in natural circulation can be in principle dealt with by presently available modelling tools; however, owing to the importance of these details on stability predictions, thorough sensitivity analyses and comparisons with experimental data are necessary.

Finally, as a lesson learned from the study of two-phase flow, the presence of strong differences in fluid density suggests the possibility that complex phenomena related to their interplay might occur, unless proper experimental evidence is accumulated showing the contrary. In this respect, considering the supercritical fluid as a more or less coherent fluid mixture, as it was for the two-phase flow in the early stage, may hide the multidimensional effect that could make the observed phenomena somehow different in comparison with expectations. This is an additional motivation to collect experimental information on supercritical fluids at conditions of interest for stability and natural circulation.

8.3. EXPERIMENTAL FACILITIES

8.3.1. Supercritical fluid flow facility at the University of Manitoba

A supercritical flow facility has been designed and built at the University of Manitoba. The facility was designed to operate with water, but the available budget did not yet allow operating with it. Hence, initially the facility is used to conduct flow instability studies with supercritical CO_2. In the future, the facility will be upgraded to conduct experiments with water.

The loop consists of three parallel channels connected by common inlet and outlet headers, on the lower horizontal tier, and a vertical rectangular piping arrangement with a micro-heat exchanger on the upper tier. The facility is applicable for both parallel-channel and natural-convection flow instability studies. A sketch showing the overall loop dimensions, without the three parallel channels, is shown in Fig. 8.1. The inlet assembly is shown in Fig. 8.2. The loop is designed for the following CO_2 operating conditions:

- System Pressure: 7.5-12 MPa;
- Maximum outlet CO_2 Temperature: 95^oC;
- Inlet CO_2 Temperature: 15-28^oC.

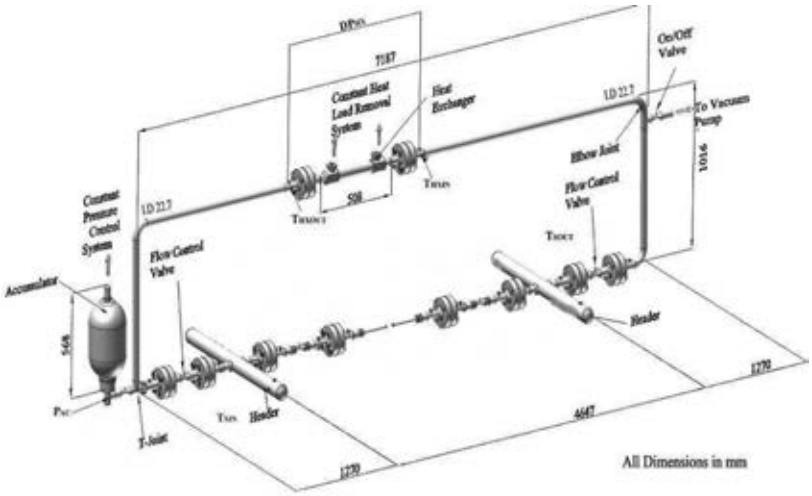

FIG. 8.1. University of Manitoba experimental loop without the inlet assembly (dimensions in mm)

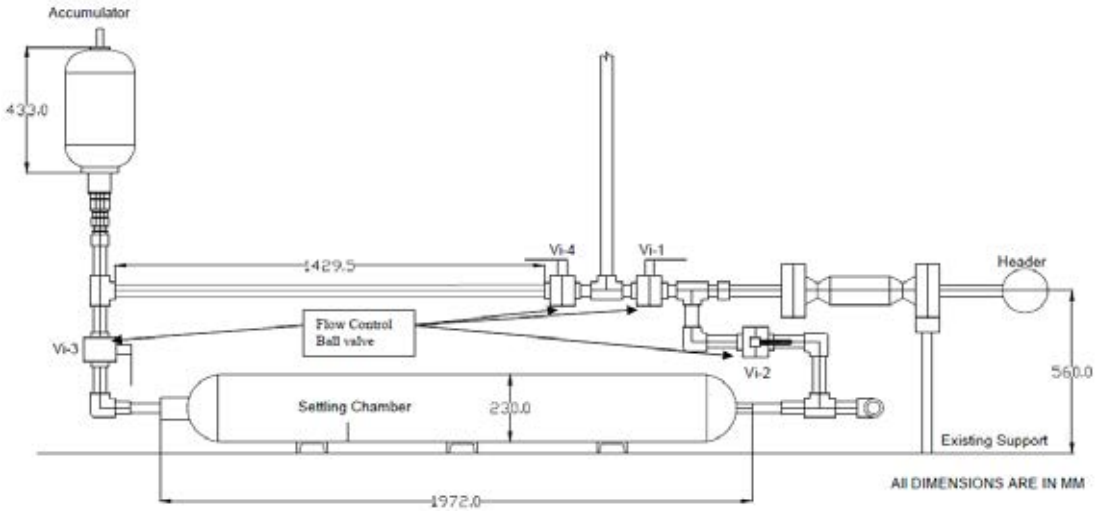

FIG. 8.2. Schematic drawing showing the settling chamber assembly of the University of Manitoba experimental loop.

The following loop components have been certified for the conditions noted above:

- Loop Piping;
- Accumulator & Pressure Control System;
- Settling Tank;
- Test Section;
- CO_2 Supply Line;
- Heat Exchanger;
- Power Supply;
- Thermocouples and Pressure Transducers;
- Safety Features.

Loop piping (excluding test section)
The loop piping is made of 1¼-in XXH stainless steel 316L pipes. Stainless steel 316L tees and 90° elbows were also used. Stainless steel flanges (XXH, 1¼ in and 1 in size) were used to join the various components of the loop. Flexitalic gaskets were used between the stainless steel flanges to make the facility pressure tight and leak proof. The ASME Code Section VIII Division 1 guidelines were used for determining the torque required to load the flanges for the required pressure rating.
Four H27 series Habonim® ball valves6 (Vi-1, Vi-2, Vi-3 and Vi-4) were welded to the loop. These ball valves are certified for 500°C and 25 MPa. Figure 8.2 shows a schematic diagram of the inlet assembly and the position of these valves. By controlling the valves opening, various flow rates can be obtained during experiments:

- Zero Loop configurations: in this configuration, valves Vi-4, Vi-2 are in the closed position and Vi-1 is in open position, thus eliminating the accumulator from the experiment;
- Non-Zero Loop Configuration with settling chamber: in this configuration, valves Vi-1 is in closed condition and valves Vi-2, Vi-3 and Vi-4 are in open position;
- Non-zero Loop Configuration without settling chamber: in this configuration, valves Vi-1, Vi-4 are in open position and valves Vi-2, Vi-3 are in the closed position.

Accumulator and pressure control system
A pressure control system was designed to help maintaining a constant loop pressure. The system consists of a single stage pressure regulator (PR-57 series, GO Regulator®) connected to a nitrogen gas bottle and to an accumulator (Hydac bladder accumulator). The pressure regulator can safely maintain inlet pressures up to 10000 psi. A grade 4.0 nitrogen gas cylinder (T style) at 2000 psi pressure, supplied by Praxair® was connected to the regulator. Nitrogen cylinders came with CGA-580 connections which are suitable for connecting with the pressure regulator through a flexible hose (high pressure flexible metal hose braided with stainless steel, 4100 psi working pressure). The bladder accumulator (11.0 Lts, Hydac®) consists of a fluid section (working fluid) and a gas (nitrogen gas) section where the bladder acts as a gas-proof screen in the accumulator. The allowable working pressure of this accumulator is 3000 psi at 200^{o}F and has been connected to the main loop through three different Swagelok® fittings.

Settling tank
The inlet assembly comprises the settling chamber, ball valves and piping. A gas bottle supplied by Parker® was chosen as a settling chamber. It is intended to reduce temperature fluctuations at the channel inlet. This settling chamber is a certified cylindrical vessel made out of carbon steel with a total internal volume of 56 liters (approximately three times the volume of the entire loop) and designed to withstand 3000 psi pressure at 200^{o}F. This settling chamber was coupled to the experimental facility by means of code 62-O' ring head adapter fittings.

Test-section
The horizontal test section was designed and fabricated by Stern Laboratories in accordance with ASME B31.1 with 750^{o}F and 3500 psi as the design temperature and pressure. The test section consists of an Inconel-625 tube (¾-in I.D. and 0.508-in thick); each tube is 2.5-m long. Inconel-625 was chosen because of its good electrical and thermal conducting properties. This channel is connected to inlet and outlet headers (316 SS XXH pipe with 2.3-in I.D.) by means of Swagelok® fittings, gasket and flange joints. Also, the fluid passing through the channel is heated by a DC current applied to the channel. The detailed schematic drawing of the test section and header assembly is shown in Fig. 8.3.

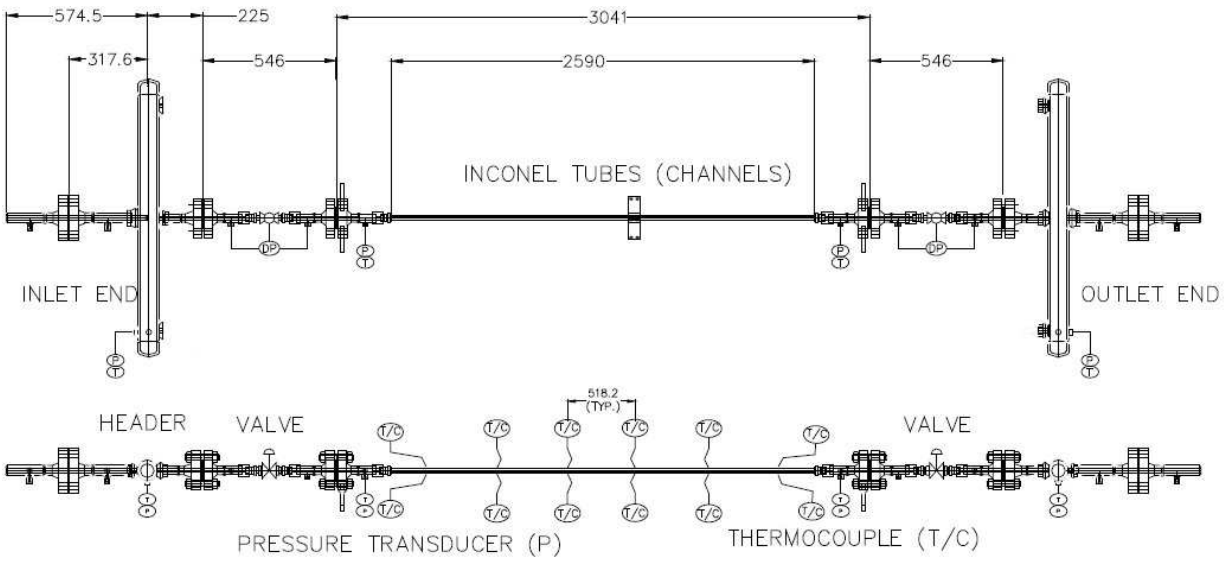

FIG. 8.3. Test section of the supercritical pressure experimental facility of the University of Manitoba (dimensions in mm).

An electro-pneumatic valve (1¼-in size) was installed upstream of the inlet header and downstream of the outlet header. Electro-pneumatic valves of the size ¾-in inlet and outlet of the channel. Each electro-

pneumatic valve assembly consists of a valve, pneumatically controlled actuator and a position controlling transducer. Swagelok® compression fittings were used in connecting these valves to the header and channel assembly.

Stern Laboratories pressure tested the test section with water at 25 MPa (~3600 psi) and issued a Certificate of Safety.

CO_2 supply line
Standard commercial carbon dioxide cylinders are available at 850-psi pressure. Grade 4.0 carbon dioxide supplied by Praxair® was used in filling the loop to the required pressure after repeated purging and evacuation procedures. But, they are not suitable to build up the required pressure (max. 1450 psi) inside the experimental facility. Hence, these gas cylinders cannot be used directly to pressurize the loop. To attain the required carbon dioxide pressure in the loop, a Maxpro® gas booster was selected. The gas booster will raise the pressure of the carbon dioxide gas from the cylinder to 1450 psi pressure inside the experimental facility. The single acting, single stage, gas booster has a compression ratio of 20:1 and is capable of generating up to a maximum pressure of 4540 psi.

Heat exchanger
Heat removal from the primary system is through a shell and tube micro-HX fabricated by Exergy. A programmable logic control (PLC) system controls the amount of heat to be removed from the test facility (by means of the heat exchanger) at any given time. An Exergy® 54 series shell and tube miniature heat exchanger was chosen; it consists of 127 stainless steel tubes (0.125-in O.D., 0.0125-in thick) and is rated for 1500 psi on tube side (and 500 psi on shell side) at a maximum operating temperature of 800^{o}F.

A PLC is used to measure the inlet and outlet temperatures of the secondary-side cooling water (via thermocouples) entering and leaving the Exergy HX. With these measured temperatures, and with a built-in program, the control system regulates a flow-control valve that controls the cooling system flow rate.

Power supply
An AC to DC converter (124KVA/600V/3φ rectifier, EMHP Power Supply®) is used to supply DC power to heat the test section by electrical induction. The output current (0 to 1500 Amps) and voltage (0 to 20 Volts) from the power source can be continuously varied during the experiments. The unit is rated to hold current fluctuations to within 0.1% of the full load current for the line voltage variations of 0.1%. A maximum of 30 kW can be supplied from the power supply source. Circuit breakers rated at 1500 A have been installed between the power supply and test section as per the electrical code. Using the control panel the power supplied to the three channels is controlled. The test facility is electrically isolated from the test section by using glass filled Teflon® gaskets between the stainless steel flanges and insulating sleeves to the flange bolts. These insulating measures are taken on the upstream side of the test section. As the voltage drops to zero, or near zero from the front end to back end of the test section, there is no need to electrically insulate the downstream side of the test section.

Thermocouples and pressure transducers
Twelve surface thermocouples (0.040-in O.D. x 12-in. LG, Type K, DeltaM®) were assembled on the outer surface of the channel. Six fluid thermocouples (1/8-in O.D. x 12-in, LG, Type K, DeltaM Corporation®) were also installed at various locations on the experimental facility to measure bulk fluid temperatures. DP 363 (Validyne®) differential pressure transducers are used to measure the pressure drop across four electro-pneumatic valves and two headers, and DP 303 (Validyne®) transducers are used to measure the pressure drop across the channel and across the heat exchanger. Three GP-50 (Dycor Technologies®) absolute pressure transducers are used to measure the absolute pressures in the accumulator and in the inlet and outlet headers of the test section. Swagelok® compression fittings are used in assembling the thermocouples and pressure transducers.

Safety features
As part of the safety requirements, the test facility was designed with the following features:

- Over-pressure relief system and rupture disk assembly;
- Safety shield;
- Carbon dioxide leak detection and activation system;
- Data acquisition system (DAS) with interlocks.

Over-pressure relief system
An over-pressure relief system is installed through a rupture disk assembly. A ½-in size rupture disk assembly is installed through a common union outlet, which is vented through the roof. The rupture disks will prevent the facility from any damage in the event of excess pressure build-up during experiments. The experimental facility is equipped with ½-in size PB series Inconel rupture disks rated for 1500-psi pressure at 200°F temperature. Swagelok® and Parker tube fitting are used in the assembly. The outlet tube (¾ in) from these ½-in rupture-disk tubes was routed away from the experimental facility and directed into a safe zone outside the building.

Safety shield
A protective safety shield was constructed around the experimental facility as a safety measure to protect against any accidental failure. Transparent polycarbonate sheets of thickness 9 mm and 6 mm are used for this purpose. Figure 8.4 shows the schematic drawing of the safety shield enclosure provided around the experimental facility.

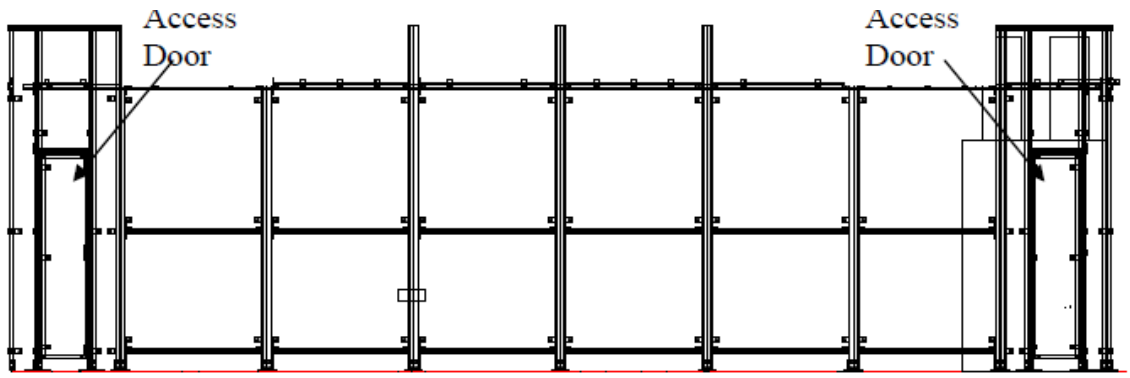

FIG. 8.4. Schematic drawing of the safety shield enclosure for the supercritical flow experimental facility of the University of Manitoba.

DAS with interlocks
The DAS has built-in interlocks designed to shut-down the electrical power to the loop if there is any inadvertent excursion in system pressure or maximum permitted temperature. The parameters to be measured and recorded are:

- Channel inlet and outlet temperatures;
- Pressure drop across each of the 4 control valves;
- Pressure drop across the heated channel;
- Flow rate (with a flow meter and through channel ΔT measurement);
- Channel wall temperatures;
- System pressure;
- Power to the channel.

8.3.2. Supercritical natural circulation loop at the Bhabha Atomic Research Centre

8.3.2.1. Introductory remarks

A supercritical natural circulation loop (SPNCL) has been set up and operated in Bhabha Atomic Research Centre (BARC). The experiments were conducted with carbon-dioxide at supercritical pressures. In comparison with water, carbon dioxide has analogous changes of properties, particularly density and viscosity, across the pseudo-critical point as shown in Fig. 8.5. The computer code NOLSTA (to be described in the following sections) was developed as an in-house tool for steady state and stability analyses of open- and closed-loop natural circulation.

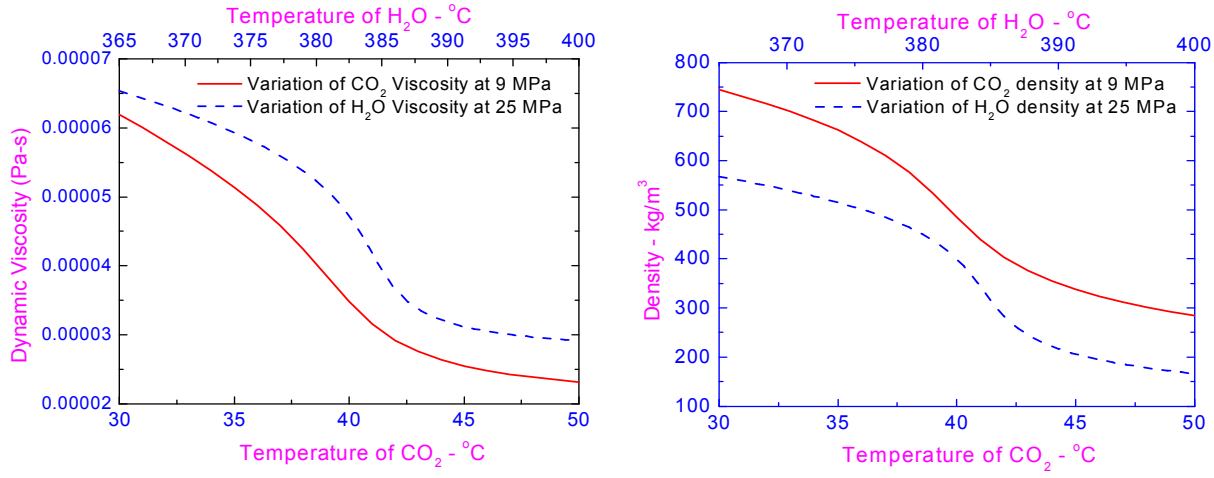

FIG. 8.5. Comparison of water and carbon-dioxide properties at supercritical conditions.

Supercritical water natural circulation loops are capable of generating density gradients comparable to two-phase natural circulation loops. Hence, supercritical water under natural circulation is being considered as a coolant in some advanced nuclear reactor designs (see e.g., [8-84] - [8-85]). Safety is a key issue in the design of advanced reactors and considerable emphasis is placed on passive safety. Natural circulation cooling instead of forced circulation in a reactor at full power is generally considered as enhancement of passive safety. Hence, the behaviour of steady state natural circulation with supercritical fluids is of interest for a number of new reactor systems. Operation with unstable natural circulation is undesirable as it can lead to power oscillations in natural circulation based supercritical water reactors. Moreover, it can also cause mechanical vibration of components and failure of control systems. Since supercritical water (SCW) or any other supercritical fluid experiences steep changes in its thermophysical properties (e.g., density) near the pseudo-critical temperature, supercritical water reactors may be susceptible to density-wave instability.

8.3.2.2. The experimental loop

Figure 8.6 shows the scheme of the experimental facility, which is a uniform diameter rectangular loop made of stainless steel pipe (SS-347) having 13.88-mm inner diameter and outside diameter of 21.34 mm. The loop has two heater and two cooler test sections, so that it can be operated in any one of the four orientations such as Horizontal Heater Horizontal Cooler (HHHC), Horizontal Heater Vertical Cooler (HHVC), Vertical Heater Horizontal Cooler (VHHC) and Vertical Heater Vertical Cooler (VHVC). The heater is made by uniformly winding Nichrome wire over a layer of fiberglass insulation. The cooler is of tube-in-tube type with chilled water as the secondary coolant flowing in the annulus. The outer tube forming the annulus has 77.9-mm inside diameter and 88.9-mm outside diameter. The loop has a

pressurizer connected at the bottom, which takes care of the thermal expansion besides accommodating the cover gas helium above the carbon dioxide. The safety devices of the loop (i.e., rupture disc and relief valve) are installed on top of the pressurizer. The entire loop is insulated with three inches of ceramic mat (k=0.06 W/(mK)).

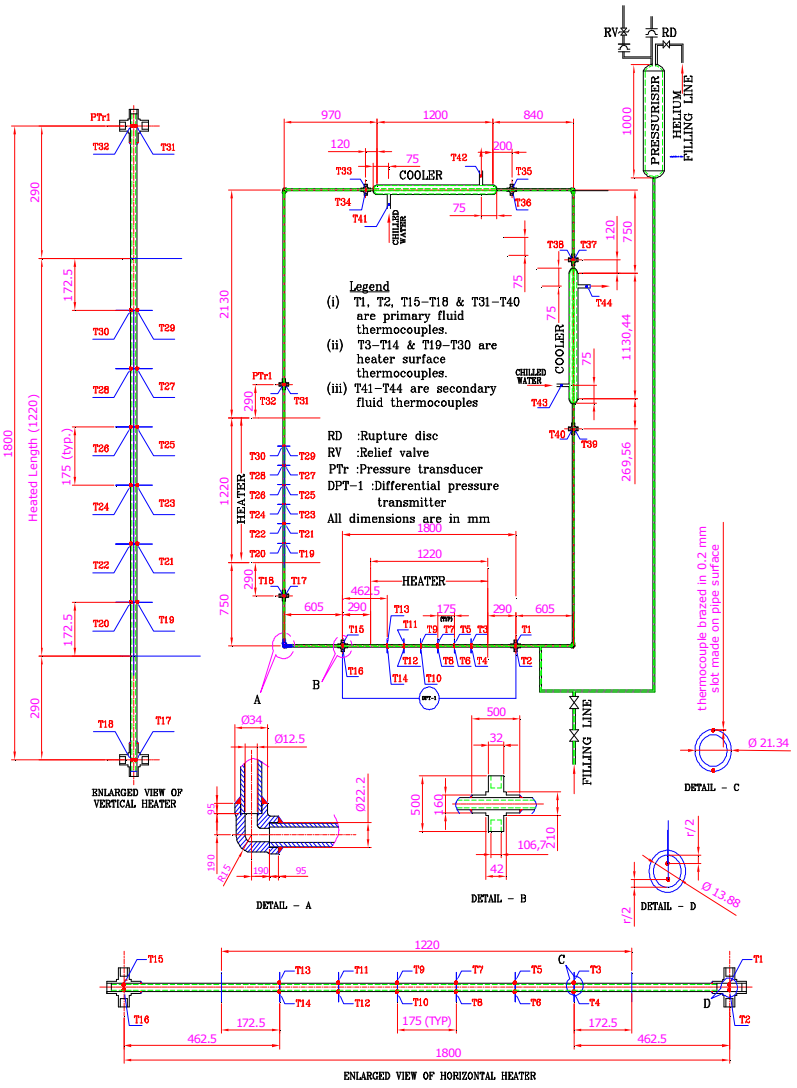

FIG. 8.6. BARC supercritical pressure natural circulation loop (SPNCL).

8.3.2.2.1. Instrumentation

The loop is instrumented with 44 calibrated K-type thermocouples to measure the primary fluid, secondary fluid and heater outside wall temperatures. Primary fluid temperatures at each location are measured as the average value indicated by two thermocouples inserted diametrically opposite at r/2 from the inside wall, whereas secondary fluid temperatures are measured by a single thermocouple located at the tube centre. This is adequate to obtain the average temperature as the temperature fluctuation in the secondary fluid is negligible. The thermocouples used to measure the outside wall temperature are installed flush with the outside surface. To enable this, a longitudinal slot of width equal to the diameter of the thermocouple is cut on the outside surface and the thermocouple is inserted in this groove and brazed. There are 12 thermocouples at six axial distances installed at diametrically opposite locations. The

system pressure is measured with two Kellar made pressure transducers located on the pressurizer as well as at the heater outlet. The pressure drop across the bottom horizontal tube and the level in the pressurizer are measured with two differential pressure transmitters. The power of each heater is measured with a Wattmeter. The secondary flow rate is measured with three turbine flow meters in parallel. All instruments are connected to a data logger with a user selectable scanning rate. For all the transient and stability tests the selected scanning period was 1 second.

The accuracy of the thermocouples is within ±1.5°C. Pressure and differential pressure measurements accuracy are within ±0.03 MPa and ±0.18 mm, respectively. The accuracy of the secondary flow as well as power measurement is ±0.5% of the reading. In addition, typical fluctuations of each instrument were also recorded during steady state with and without power. As seen from Table 8.1, there is hardly any difference in the fluctuations with and without power.

TABLE 8.1. FLUCTUATIONS OF MEASURED PARAMETERS

Parameter	Fluctuation without power	Fluctuation under steady state natural circulation at 1400 W
Heater inlet temperature (^oC)	± 0.28	± 0.44
Heater outlet temperature (^oC)	± 0.44	± 0.43
Pressure (MPa)	± 0.028	± 0.028
Pressure drop (mm WC)	± 0.21	± 0.21
Secondary inlet temperature (^oC)	± 0.1	± 0.07
Secondary outlet temperature (^oC)	± 0.035	± 0.47

8.3.2.2.2. Pressure drop characterization

The prssure drop characterization tests were carried out under forced flow conditions with the help of a pump in a separate facility using the same bottom horizontal pipe and one of the elbows installed horizontally. Apart from flow rate and pressure drop, the temperature was also measured at different flow rates in this facility. From the measured pressure drop across the bottom horizontal pipe and the flow rate, the friction factor for the pipe was evaluated using the following equation:

$$f = \frac{2D\rho A^2 \Delta p_m}{L W_m^2} \tag{8-1}$$

The experimental friction factor is plotted in Fig. 8.7; it is somewhat larger than that for smooth pipes due to the use of commercial pipes. The correlation fitted to the friction factor data is also shown in Fig. 8.7. From the measured pressure drop across the elbow and the flow rate, the loss coefficient was calculated as below.

$$K = \frac{2\rho A^2 \Delta p_m}{W_m^2} \tag{8-2}$$

The loss coefficients generated for the elbows at forced flow conditions are plotted in Fig. 8.8. A correlation has been derived to represent the experimental loss coefficients. The loss coefficient was found to be roughly constant at 0.55 for Reynolds numbers greater than 45,000.

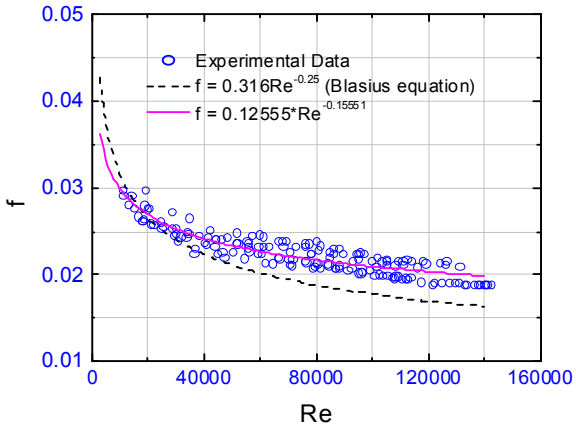

FIG. 8.7. Friction factor data for the tubes used in the construction of the BARC loop.

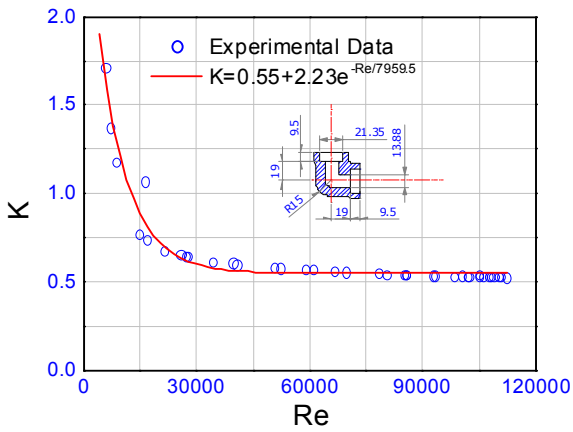

FIG. 8.8. Loss coefficient data for the 90° elbow used in the BARC loop.

8.3.2.2.3. Operation with supercritical CO_2

Before operatio with supercritical CO_2, the loop was flushed repeatedly with CO_2 at low pressures including all impulse, drain and vent lines. Subsequently the loop was filled with CO_2 up to 6 MPa pressure and the chilled water coolant system was started. This caused condensation of CO_2 and hence a decrease in loop pressure. The pressure decrease was compensated by admitting additional CO_2 from the cylinder and again allowing sufficient time for condensation. The process of filling and condensation was continued till there was no decrease in pressure. At this point the loop pressure was increased to the required value with the help of a helium gas cylinder. Once the required supercritical pressure was achieved, the helium cylinder was isolated. Sufficient time was allowed to reach a steady state. However, it was found difficult to attain completely stagnant conditions with a uniform temperature throughout the loop, as the higher ambient temperature allowed a small amount of heat absorption through the insulation into the loop, which was rejected at the cooler causing a small circulation rate. Once a steady state was achieved, the heater power was switched on and adjusted to the required value. Sufficient time was allowed to achieve the steady state. Once the steady state was achieved, power was increased and again sufficient time was provided to achieve the steady state. In case the system pressure increases beyond the set value by 0.1 MPa, a little helium was vented out to bring back the pressure to the original value. Similarly, during power decrease if the pressure decreases below the set point by 0.1 MPa, then the loop was pressurized by admitting additional helium into the pressurizer. The experiments were repeated for different pressures and different chilled water flow rates. Subsequently, the experiments were performed for different orientations of the heater and the cooler.

8.3.3. Supercritical fluid flow facility at CIAE

The natural circulation facility operated at CIAE is schematically shown in Fig. 8.9. It is a rectangular loop installed vertically with a width of 2.4 m and a height of 1.77 m. The heating section, located in a vertical side, is made of an Inconel-625 tube of 4.62-mm ID, 6.2-mm OD, and 1.37 m in heating length. An annular heat exchanger, located horizontally at the top side, is made of stainless-steel tubes with hot water flowing in the inner tube and cooling water in the annulus. The inner tube is 10-mm ID and 13-mm OD, and the outer tube is 16-mm ID, 20-mm OD, and 1.7 m in length. The other parts of the loop are made of stainless-steel tubes of 10-mm ID, except for a section of 4-mm ID and 300 mm in length at the bottom side for obtaining the flow rate by frictional pressure drop.

The loop is connected to a pressurizer. The heating section is supplied by a DC power with capacity of 70

V × 6750 A. It is thermally insulated by glass-fiber. An electric heating wire is wrapped in the insulation layer for compensation of heat losses. The loop is filled with de-ionized water, and the gas is released through the vent valve. The tap water is connected to the secondary side of the heat exchanger, and discharged to the environment.

The major measurements of parameters in the main loop include: the inlet and outlet water temperature and the wall temperatures of heating section by K-type thermocouples, the pressure by a pressure transducer (DCY1151), the pressure drop of the flow rate section by a differential pressure transducer (DCY1151) and the current and voltage across the heating section. In addition, the flow rate, the inlet and outlet water temperatures in the second side are measured.

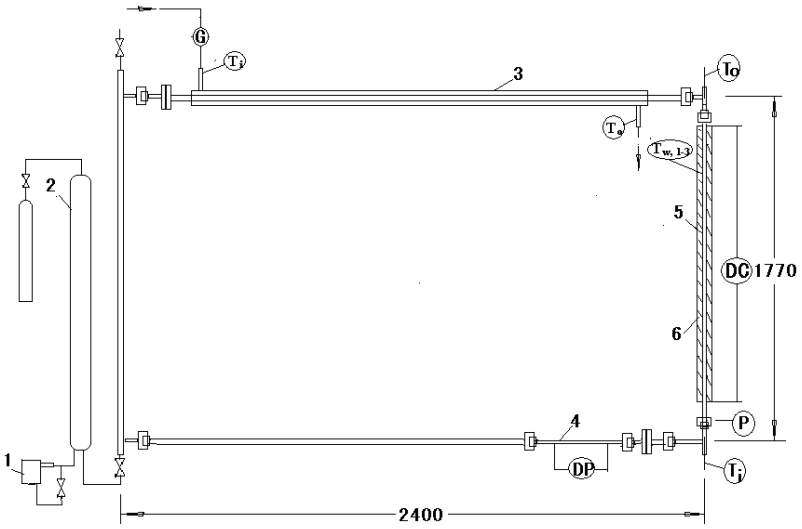

1. Piston pump,
2. Pressurizer,
3. Heat exchanger,
4. Flow rate,
5. Heating section,
6. Thermal insulation

FIG. 8.9. Schematic of the natural circulation loop at CIAE.

During the experiments the supercritical pressure is established by the piston pump. The flow rate of tap water to the secondary side of heat exchanger is not adjusted until later stage (after 7500 s). The heating power is initiated at 0 kW, and increased in small steps up to about 8600 s. At each step the power is kept constant and a stable condition is achieved. When the condition is close to the onset of flow instability the increment of power for each step is about 100 W. The measured parameters are recorded by a data acquisition system throughout the experiment with a frequency of 1 s.

8.4. EXPERIMENTAL DATA ON NATURAL CIRCULATION

8.4.1. Steady state natural circulation data for SPNCL at BARC

Steady state data on natural circulation flow rate and heat transfer were generated with supercritical CO_2 for various orientations of the source and sink. The data ranges for each orientation is given in Table 8.2. The range of parameters of all the steady state data is:

Orientations studied: HHHC, HHVC, VHHC and VHVC;
Pressure: 8 - 9.2 MPa;
Power: 0.1 - 2.4 kW;
Cold leg temperature: 17.5 - 57.7°C;
Hot leg temperature: 19.3 - 95.9°C;
Coolant flow rate: 29.6 - 56 lpm;
Coolant inlet temperature: 8.2 - 11.4°C;
Coolant outlet temperature: 9.0 - 12.5°C.

TABLE 8.2. RANGE OF PARAMETERS FOR STEADY STATE TESTS WITH SUPERCRITICAL CO_2

Orientation	Power (kW)	Loop conditions			Secondary coolant conditions		
		Pressure (MPa)	Temperature (°C)		Flow rate (lpm)	Temperature (°C)	
			Cold leg	Hot leg		Inlet	Outlet
HHHC	0.19-2.4	8.5-9.2	17.7-57.7	20.5-95.9	29.6-37	8.7-10.2	9.5-11.7
HHVC	0.3-2.2	8.5-8.8	20.2-49.3	24.2-93.1	33.5-34.8	8.2-9.3	9-10.4
VHHC	0.14-2.4	9-9.26	17.5-49.5	19.6-73.9	31.6-38	8.5-11.4	9.7-12.5
VHVC	0.1-2.0	8.1-9.1	17.5-41.3	19.3-66.8	36.2-56	8.6-9.5	8.8-9.7

8.4.1.1. Steady state natural circulation flow rate with supercritical CO_2

Steady state data for the different heater-cooler orientations (i.e., HHHC, HHVC, VHHC & VHVC) generated in the loop were compared with the NOLSTA code predictions [8-86]. The steady state mass flow rate for experimental conditions has been obtained as

$$W_{ss} = \text{Heater Power}/ (i_{out} - i_{in}) \quad (8\text{-}3)$$

Enthalpies at heater outlet (i_{out}) and heater inlet (i_{in}) were determined from the measured heater outlet and inlet temperatures and the operating pressure. The elbow loss coefficient has been taken to be 0.55 each (total 4 elbows) in predictions. Figure 8.10a shows the data for three different orientations (i.e., HHHC, HHVC and VHVC) at the pressure of 8.6 MPa. For the VHHC orientation, data were available only at the pressure of 9.1 MPa. The steady state data for VHHC and HHHC orientations at the pressure of 9.1 MPa are compared with NOLSTA predictions as shown in Fig. 8.10b. The data are found to be in close agreement with the code predictions.

8.4.1.2. Effect of pressure

The data on the effect of pressure on the steady state flow rate are presented in Fig. 8.11 along with the predictions of the NOLSTA code.

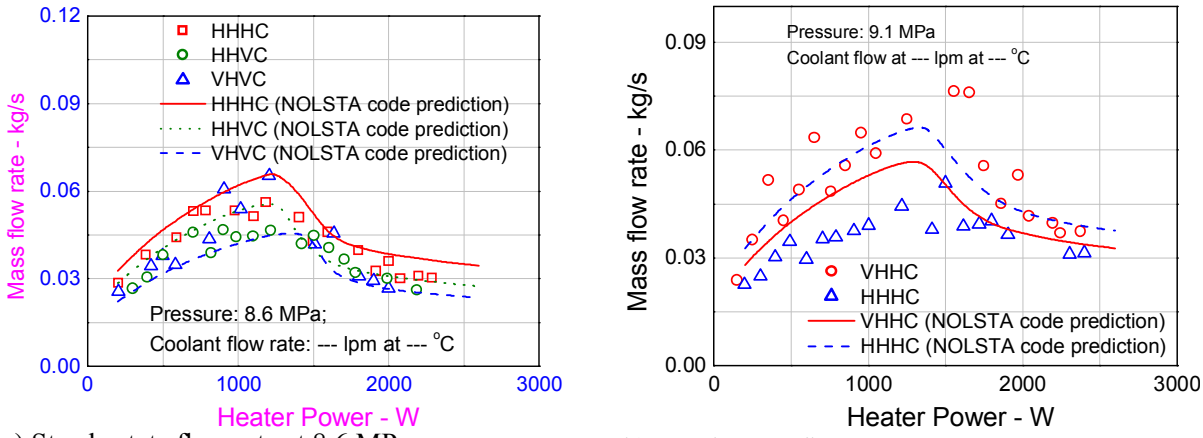

a) Steady state flow rate at 8.6 MPa

b) Steady state flow rate at 9.1 MPa

FIG. 8.10. Measured and predicted steady state flow rates for various orientations.

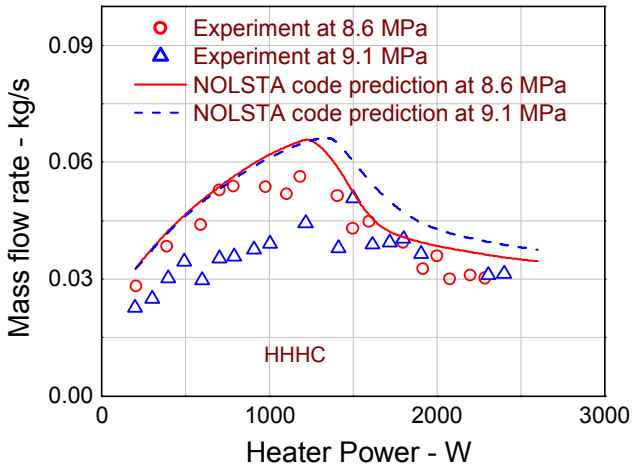

FIG. 8.11. Effect of pressure on the steady state flow rate for the HHHC orientation.

8.4.2. Experimental studies on instability for the SPNCL at BARC

Extensive natural circulation experiments were conducted in the test facility with supercritical carbon-dioxide as working fluid to observe instability. No instability was observed during the experiments conducted with high secondary side flow rate, i.e., 29.6 - 56 lpm. The instability has been observed for HHHC orientation only and with lower secondary side flow rates, i.e., 10-15 lpm. In particular, instability has been observed at an operating pressure of 9.06 MPa and 10.1 lpm secondary flow as shown in Fig. 8.12(a, b and c), showing the transient from 700 W to 500 W to 300 W. Figure 8.12a shows the pressure drop across the horizontal heater section, pointing out the development of instability during a power reduction from 700 W to 500 W, whereas instability diminishes with further reduction of power to 300 W. The instability is observed at 500 W with heater inlet temperature of about 27.1 °C (not exactly constant) and heater outlet temperature varying from 37 to 44.6 °C, as it can be seen from Fig. 8.12b. Figure 8.12c shows heater outlet temperature oscillations of equal amplitude in greater detail.

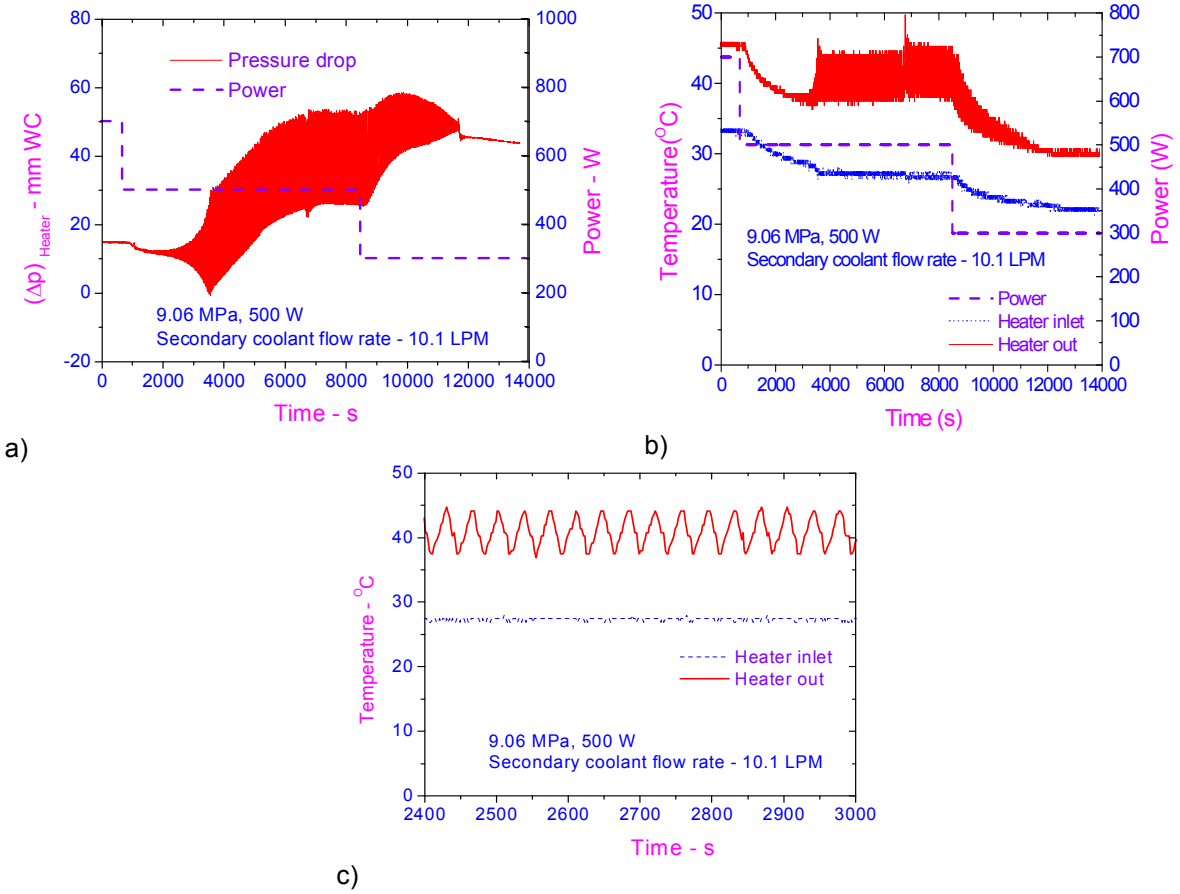

FIG 8.12. Typical unstable behaviour at 500 W for HHHC orientation.

With 15 lpm as secondary flow, the instability is observed at 800 W for the 9-MPa pressure, as shown in Fig. 8.13(a, b and c). It shows the transient from 600 W to 800 W and to 1000 W. Figure 8.13a shows the pressure drop across the horizontal heater section, which shows development of instability during the power rise from 600 W to 800 W, whereas the instability decreases with further increase of power to 1000 W. The instability is observed at 800 W with heater inlet temperature of about 31 °C and heater outlet temperature varying from 35 to 43 °C, as it can be seen from Fig. 8.13b. The heater outlet temperature oscillations are having consecutive larger and smaller peaks.

A similar type of instability is observed during the power transient from 925 W to 700 W and to 500 W, as shown in Fig. 8.14(a, b and c). The instability is observed at 700 W with a heater inlet temperature of about 31°C and heater outlet temperatures varying from 34 to 45 °C as can be seen from Fig. 8.14b. The loop is however stable at 925 W and 500 W. Figure 8.14c also shows repetitive large and small peaks in heater outlet temperature oscillations, whereas Fig. 8.12c shows only single peak oscillations. The typical characteristic of all these instabilities is that the only heater outlet temperature oscillates and heater inlet temperature is practically constant, which indicates open loop type of behaviour.

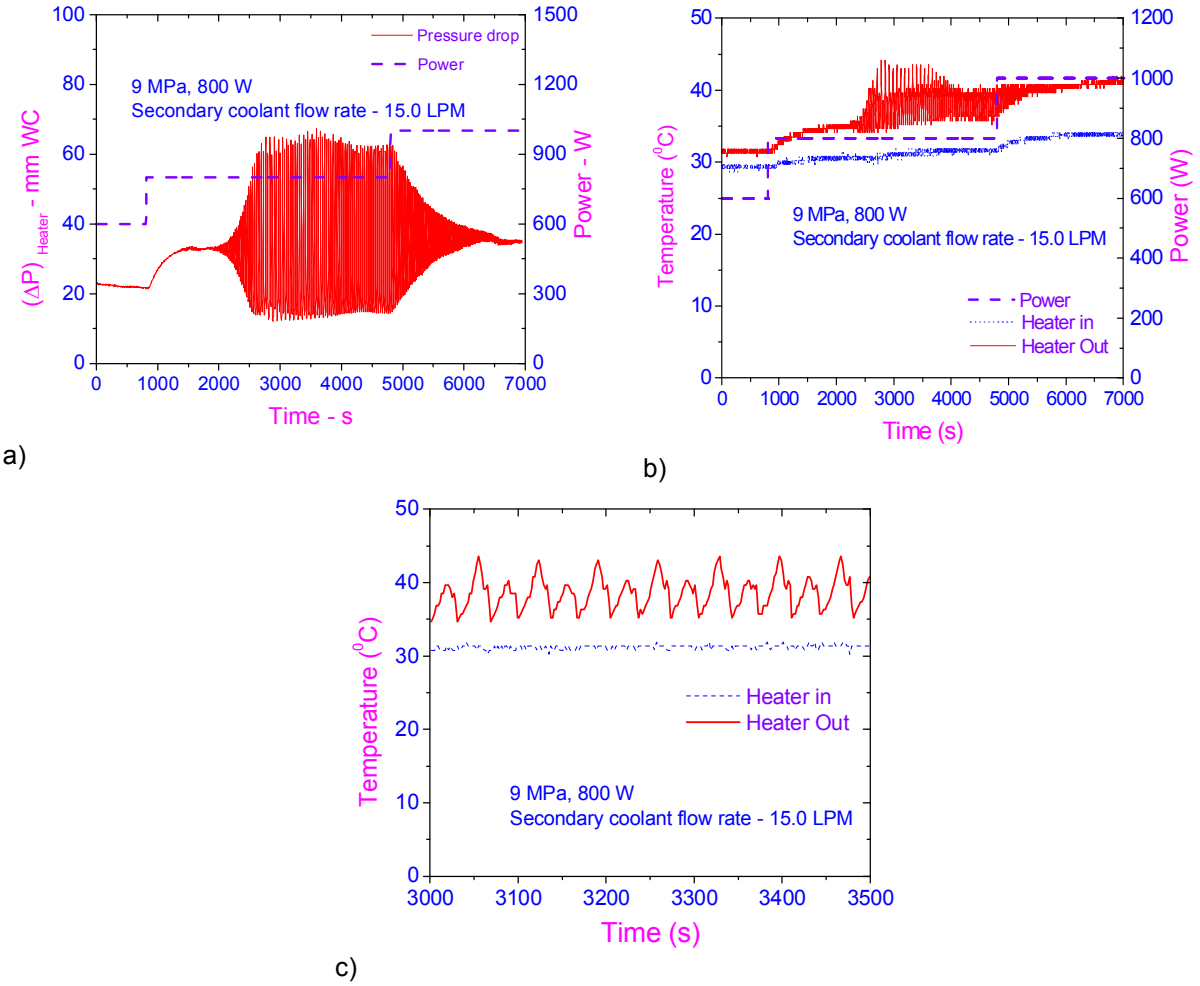

FIG. 8.13. Typical unstable behaviour at 800 W for HHHC orientation.

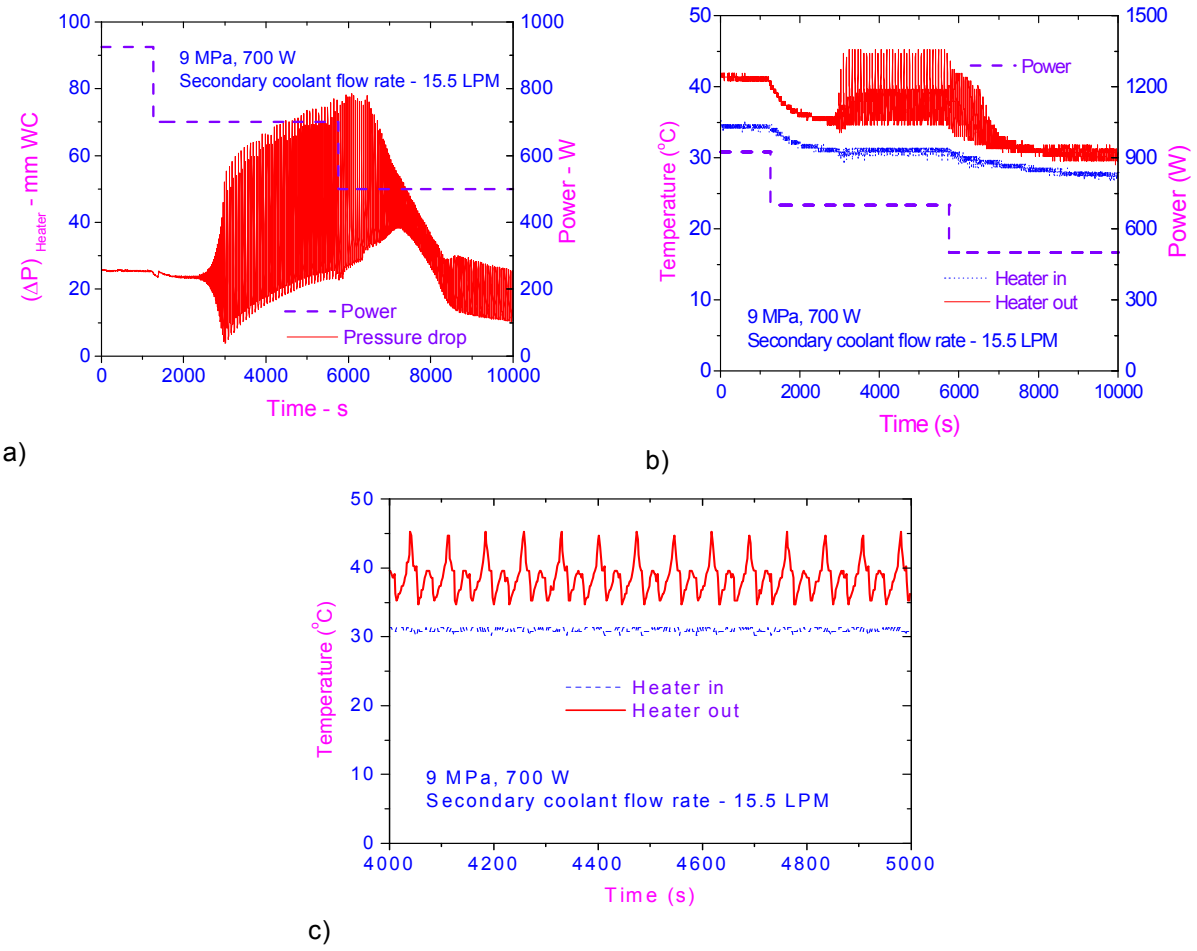

FIG. 8.14. Typical unstable behaviour at 700 W for HHHC orientation.

The instability was also observed during a power step down from 1900 W to 300 W at the pressure of 7.6 MPa and with secondary flow rate of 10 lpm, as shown in Fig. 8.15(a, b and c) showing some fluctuation in heater inlet temperature, as shown in Fig. 8.15c. Unstable behaviour has also been observed during start-up at 700 W at 8 MPa and secondary side flow rate of 10 lpm as shown in Fig. 8.16a and b; the instability decreases with further increasing power to 1100 W. Figure 8.16b shows uniform amplitude oscillations at 700 W.

The operating conditions, time period and amplitude of oscillations during experimentation have been reported in Table 8.3. The time period of the oscillation is in the order of loop circulation time. Sometimes, the instability could not be repeated during the experimentation. Actually, the instability is observed over a very narrow window of power and can be missed if the step change in power is high. In all the cases, the instability is observed when the heater inlet temperature is very near to the critical temperature (e.g., 31°C for CO_2) and the outlet temperature is oscillating even above the pseudo-critical temperature.

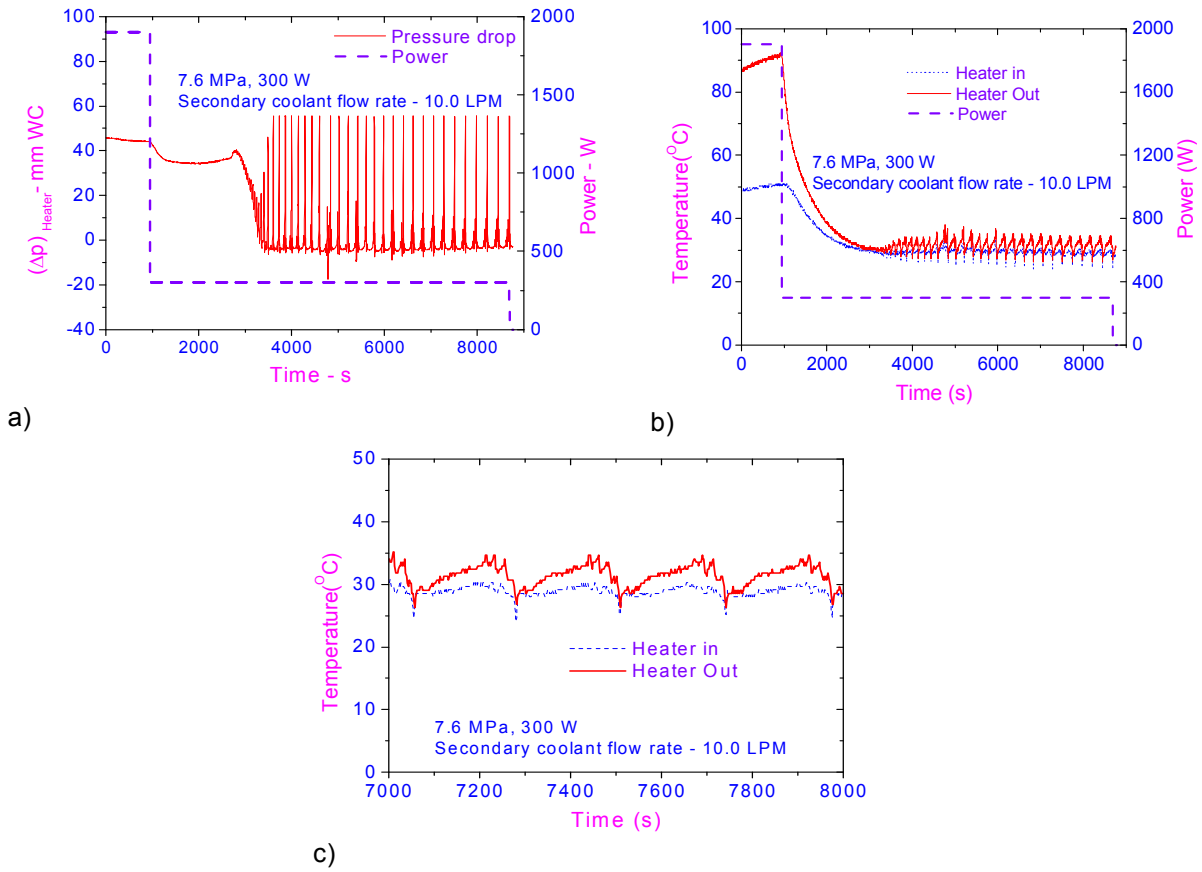

FIG. 8.15. Typical unstable behaviour at 300 W for HHHC orientation during power step down.

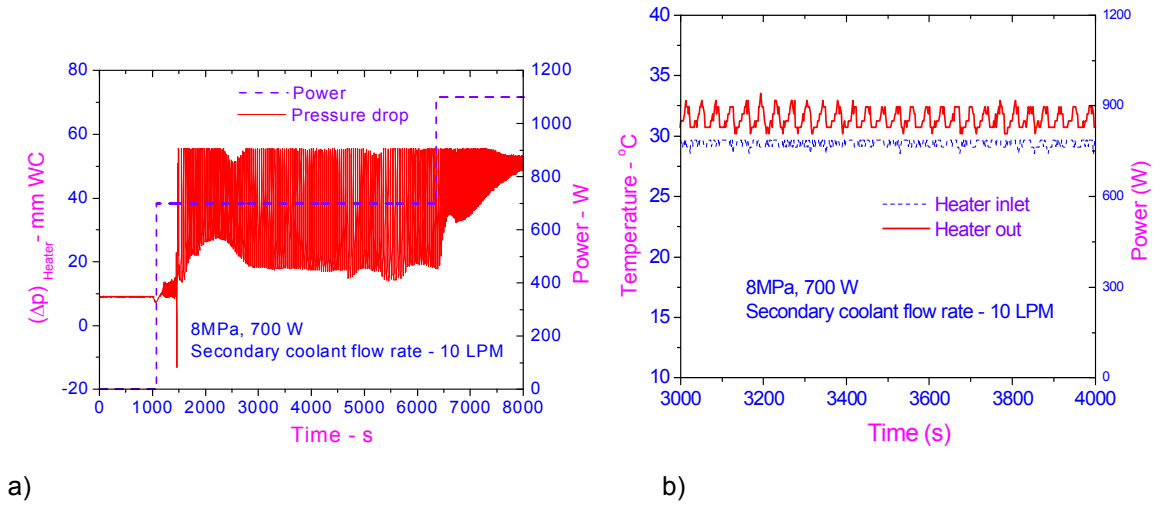

FIG 8.16. Typical unstable behaviour at 700 W for HHHC orientation during power step rise.

TABLE 8.3. OBSERVED OSCILLATORY CHARACTERISTICS

Power (W)	Pressure (MPa)	Secondary flow rate at 9°C inlet temperature (lpm)	Heater Inlet temperature (°C)	Range of heater outlet temperature oscillation (°C)	Amplitude of pressure drop oscillation (mm of WC)	Time period of heater outlet temperature oscillation (s)	Loop circulation time of steady state calculated by NOLSTA(s)
300	7.6	10.0	28.4	29.4 – 34.5	59.7	226.9	43.4
500	9.06	10.1	27.1	37 - 44.6	27.74	36	33.4
700	9.0	15.5	31	34 - 45	47.25	70.2	28.3
700	8.0	10.0	29.4	30.3 – 33.4	38.0	30.6	22.7
800	9.0	15.0	31	35 - 43	51.29	65	25.5

8.4.3. Experimental data from the CIAE facility

In the experiments performed by the CIAE facility, the pressure is kept in the range of 24.2 – 25.2 MPa, as shown in Fig. 8.17. The maximum heating power is 18 kW, as in Fig. 8.18 reporting the history of heating power throughout the experiment. The variations of inlet and outlet water temperatures of the heating section are shown in Fig. 8.19.

The flow rate is obtained from the measurement of frictional pressure drop, DP, on section 4, in combination with a curve of flow rate vs. DP, which has been established from a separate calibration test. It is also obtained by the heat balance equation with the measured heating power, Q, inlet temperature, T_i, and outlet temperature, T_o. For flow oscillation conditions both methods give oscillating characteristic around the average line, but they do not provide accurate instantaneous value of the flow rate. On the other hand, for stable conditions, because of the great temperature difference, T_o-T_i, the method by heat balance equation provides accurate flow rate. The flow rate throughout the experiment is shown in Fig. 8.20 reporting the flow rate against heating power. The evolution of inner wall temperature, $T_{w,i}$ is shown in Fig. 21, which is calculated from the heat conduction equation for estimation of the temperature drop across the wall and the average of outer wall temperatures measured by three thermocouples at 1.27 m from the beginning of heating length. At this location the local bulk water temperature, T_b, is evaluated by heat balance equation with the T_i and T_o, and is superimposed in Fig. 8.21.

As seen in Fig. 8.20, as the heating power increases the flow rate increases. At low powers, the flow is fairly stable. The onset of flow instability occurs when the power reaches about 11.6 kW with T_o = 370 °C. As the power increases further, the flow oscillates more severely, with some oscillation of pressure and outlet water temperature. When the power exceeds about 16 kW, the oscillation decreases considerably, and the flow rate exhibits a decreasing trend, accompanied by a rapid increase in the outlet water temperature and in the wall temperature.

It is observed from Fig. 8.21 that at power of about 8.3 kW the inner wall temperature (at z=1.27 m) reaches about 400 °C, and starts to increase sharply as the power increases slightly. This behaviour is typical of the pseudo-film boiling regime. After the oscillation occurs at Q = 11.6 kW, the wall temperature oscillates greatly, and exhibits a decreasing trend.

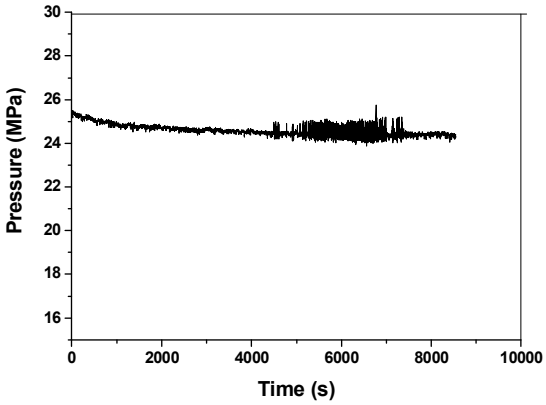

FIG. 8.17. The history of pressure.

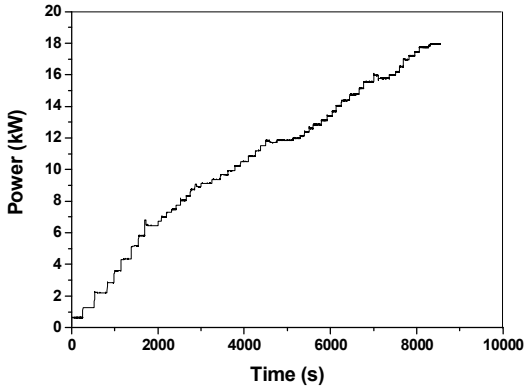

FIG. 8.18. The history of heating power.

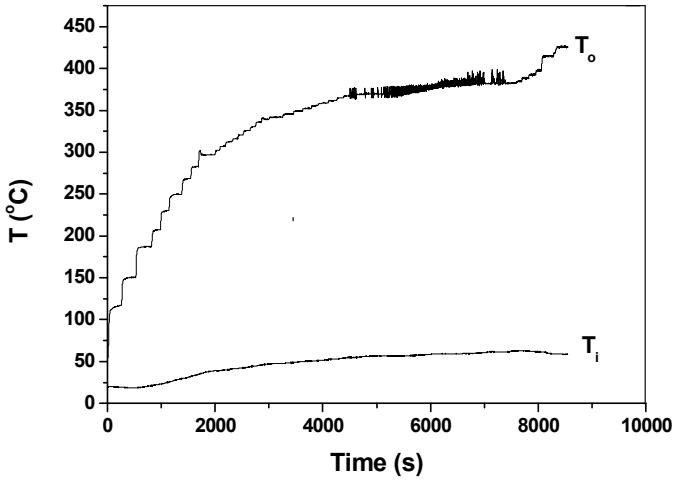

FIG. 8.19. The history of the inlet and outlet water temperatures.

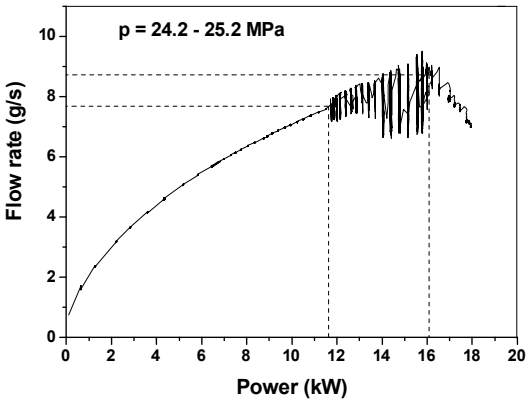

FIG. 8.20. Variation of the flow rate with power.

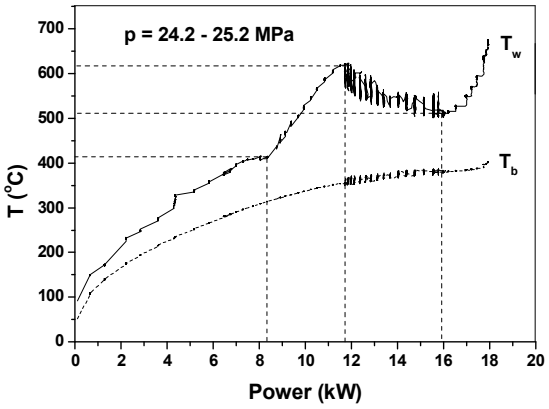

FIG. 8.21. Variation of $T_{w,i}$ and T_b with power (z=1.27 m).

8.5. CODE DEVELOPMENT AND APPLICATION

8.5.1. Stability analysis of coolant flow in fuel assemblies of VVER-SCP reactor

This section describes the thermal and hydrodynamic stability analysis of coolant flow in the fuel assemblies (FAs) of a VVER-SCP, with one-pass in the core. Two types of instabilities are considered in the analysis: the aperiodic (excursive) instability, caused by a multivalued hydrodynamic pressure drop vs. flow rate characteristic of the channel, with the potential for a sudden change of mass coolant flow rate, and the oscillatory instability, that may occur in heated channels when the coolant has strongly variable thermodynamic and thermophysical properties. The latter type of instability is also called 'channel instability' or 'density-wave oscillations'. The calculations were performed using the computer code TEMPA-SC [8-87], being developed in OKB GIDROPRESS to study heat and mass transfer processes in FAs of reactors with water at supercritical pressures.

Stability of coolant flow against aperiodic behaviour

The thermal-hydraulic calculations were performed by the computer code TEMPA-SC to study the aperiodic (excursive) instability of coolant flow through FAs having different relative powers (Kq = 0.4, Kq = 1.0 and Kq = 1.4, where $Kq=Q_{FA}/Q_{avg.FA}$). The range of flow rate through the FAs was selected to provide values of coolant temperature at the outlet ranging from 390 to 755°C, with an inlet coolant temperature of 290 °C. The results of the calculations are presented in Fig. 8.22.

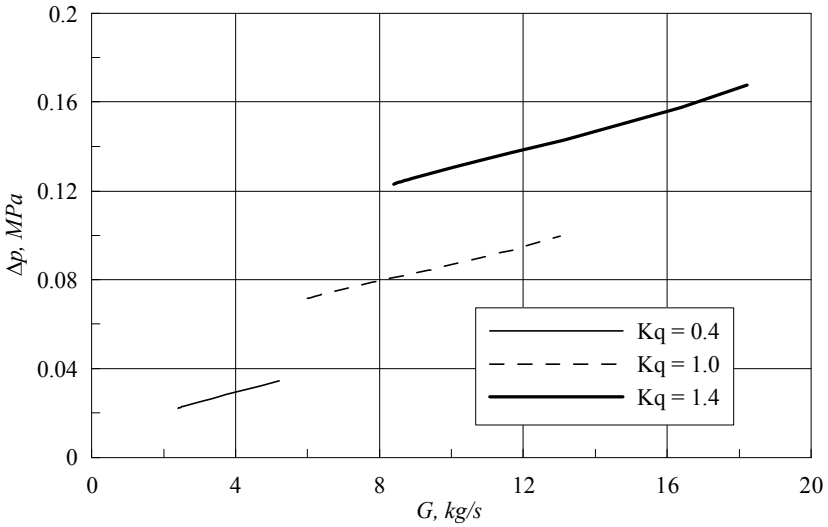

FIG. 8.22. Pressure differences in FAs as a function of flow rate.

As it can be noted, all three curves are monotonic showing that there are no multivalued hydrodynamic characteristics for the examined conditions and, therefore, aperiodic (excursive) instability of the coolant flow is not predicted.

An analysis of the influence of spacer grids (SG), lower grid and FA cap on the hydraulic resistance was also made. The thermal-hydraulic calculations were performed with a relative power Kq = 1.4, and a range of flow rates through FAs resulting in a coolant temperature at FA outlet ranging from 390 to 755°C (at the same inlet coolant temperature of 290°C). Three variants of FA singular pressure drop coefficients are examined:

- variant 1, with minimum coefficient of hydraulic resistance of FA cap and maximum coefficient of hydraulic resistance of grids;

- variant 2, with minimum coefficient of hydraulic resistance of FA cap and minimum coefficient of hydraulic resistance of grids;
- variant 3, with maximum coefficient of hydraulic resistance of FA cap and maximum coefficient of hydraulic resistance of grids.

The results of the calculations are presented in Fig. 8.23. Again, it can be noted that there is no multivalued hydrodynamic characteristic for the examined conditions and therefore aperiodic instability of the coolant flow is not predicted.

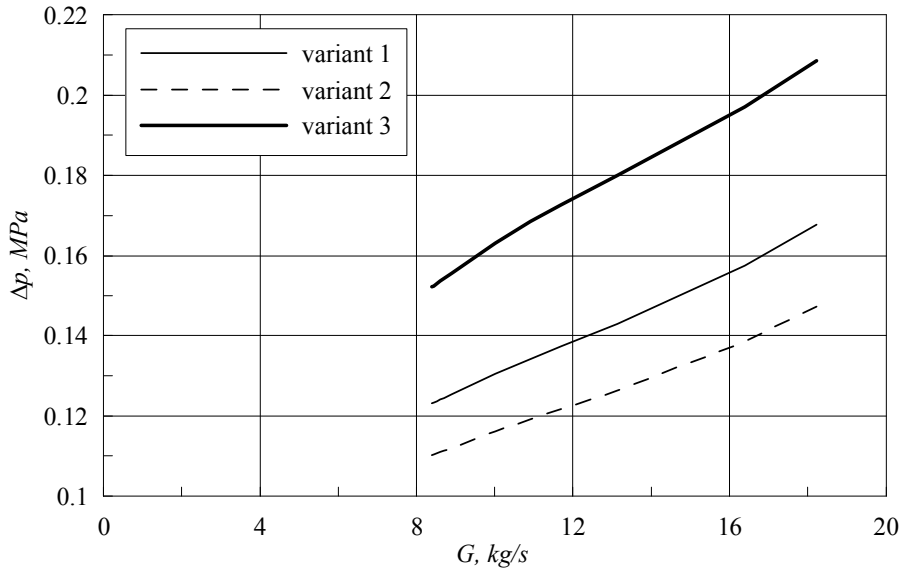

FIG. 8.23. Pressure differences in FAs with Kq = 1.4 as a function of flow rate for the different fuel assembly variants.

Stability of coolant flow against oscillatory behaviour

Thermal-hydraulic calculations of coolant flow through FAs with relative power of Kq = 1.22 were performed for analysing stability against oscillatory behaviour. The pressure difference across the FAs was 110 kPa and a FA inlet coolant temperature at the inlet ranging from 220 to 380°C. The results of the calculations were translated into dimensionless form using the trans-pseudo-critical (N_{TPC}) and the sub-pseudo-critical (N_{SPC}) numbers [8-56] (see Section9.2). The coolant flow instability region and the area of operating parameters of VVER-SCP were plotted in Fig. 8.24. As it can be noted, the area of unstable coolant flow has an intersection with the operating area of VVER-SCP.

To avoid the possibility of oscillatory instabilities, inlet throttling of FAs is used. The value of the coefficient of hydraulic resistance at the throttling device is determined by the results of variant calculations. The coolant flow stability map obtained with the use of the throttling device is shown in Fig. 8.25; the area of unstable coolant flow has now no intersection with the area of the operating parameters of the VVER-SCP; therefore, oscillatory thermal-hydrodynamic instability is not predicted when the inlet throttling device is used.

Conclusion

The stability analysis of coolant flow in FAs was performed for the VVER-SCP concept, with one-pass coolant system in the core. Two types of instabilities were considered in the analysis: aperiodic (excursive) instabilities and oscillatory instabilities. The analysis of stability against aperiodic behaviour has shown that there are no multivalued hydrodynamic characteristics of the FAs for the examined conditions; therefore, there is no aperiodic instability of coolant flow. The stability analysis against

oscillatory behaviour has shown that it is necessary to use an inlet throttling device to achieve stability of the coolant flow and its coefficient of hydraulic resistance was determined.

Further research is necessary to investigate the possibility of aperiodic and oscillatory instabilities in other conditions of core operation. The research for resonance effects in the system is also necessary [8-88]. An important area of further research is the coupled thermal-hydraulic and neutronic instability analysis; this requires the implementation of a reactor kinetic model in the computer code TEMPA-SC.

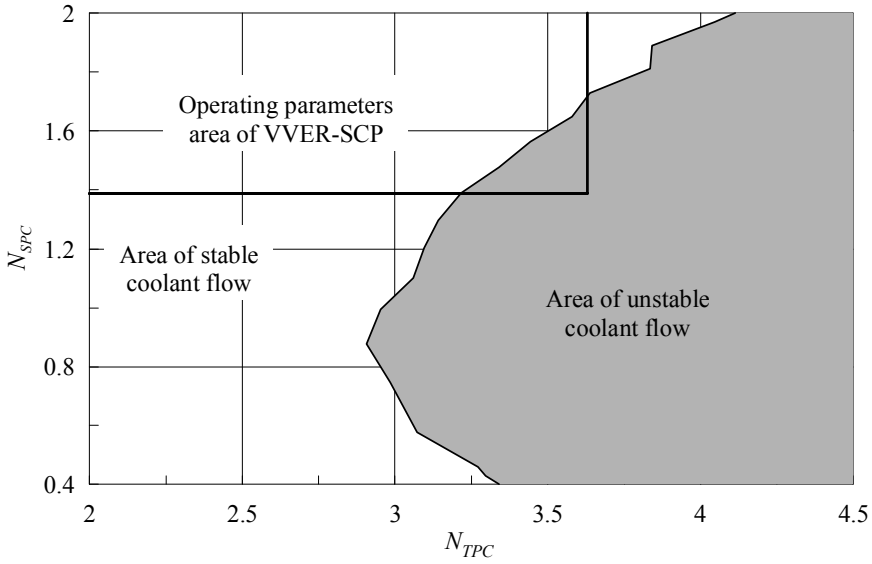

FIG. 8.24. Coolant flow stability map for the base case.

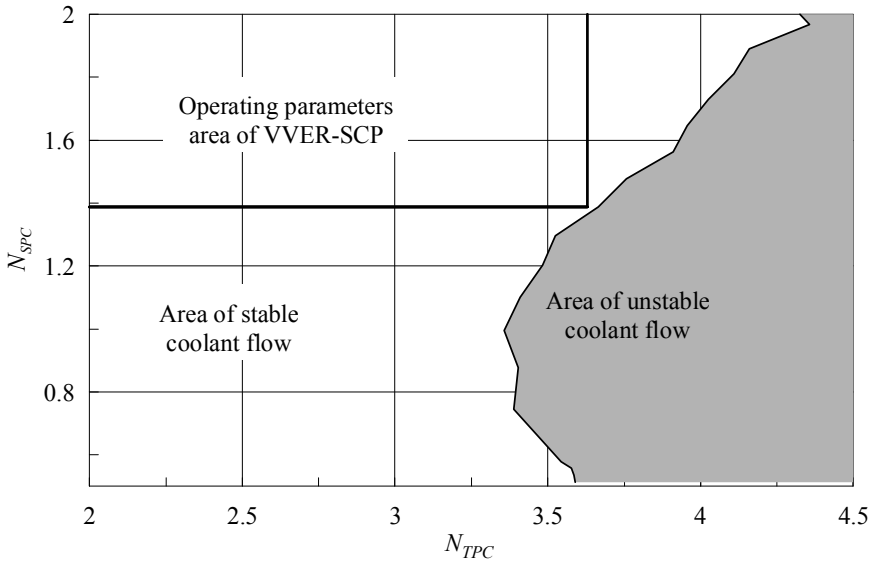

FIG. 8.25. Coolant flow stability map with additional inlet throttling.

8.5.2. NOLSTA code development and application at BARC

8.5.2.1. Code development

A NOn-Linear Stability Analysis (NOLSTA) code has been developed to analyse the stability of natural circulation loops operating with supercritical fluids with open as well as closed-loop boundary conditions.

8.5.2.2. Open loop

The NOLSTA code was initially developed for natural circulation with open loop boundary conditions [8-82]. In an open loop, the fluid temperature at the heater inlet is fixed irrespective of the heater power. For the analysis of an open loop, the heat supplied to the heater is entirely rejected at the cooler, keeping the heater inlet temperature constant. In this case, the operating pressure of the loop, the inlet fluid temperature to the heater and the heater power are specified along with the entire geometry of the loop (hydraulic diameter, flow area and length of each pipe).

Governing equations

In one dimensional analysis, the co-ordinate x runs around the loop with origin at the inlet of the heater. The governing continuity, momentum and energy equations for one dimensional flow can be written as:
Continuity:

$$\frac{\partial \rho}{\partial t}+\frac{\partial(\rho u)}{\partial x}=0 \tag{8-4}$$

Momentum:

$$\frac{\partial(\rho u)}{\partial t}+\frac{\partial(\rho u^2)}{\partial x}+\frac{\partial p}{\partial x}+\left(\frac{f}{D}+K\right)\frac{\rho u^2}{2}+\rho g\cos\phi=0 \tag{8-5}$$

Energy:

$$\frac{\partial(\rho i)}{\partial t}+\frac{\partial(\rho u i)}{\partial x}=q''' \tag{8-6}$$

In addition an equation of state is required for the density, given by:

$$\rho = f(p,i) \tag{8-7}$$

The set of mass, momentum and energy conservation equations is therefore closed by the equation of state for the supercritical fluid.

The steady state solution can be obtained by dropping the time derivatives from the above equations, obtaining

$$\frac{\partial(\rho u)}{\partial x}=0 \tag{8-8}$$

$$\frac{\partial(\rho u^2)}{\partial x} + \frac{\partial p}{\partial x} + \left(\frac{f}{D} + K\right)\frac{\rho u^2}{2} + \rho g \cos\phi = 0 \tag{8-9}$$

$$\frac{\partial(\rho u i)}{\partial x} = \begin{cases} q_h''' \text{ or } -q_c''' & \text{for heater or cooler region,} \\ 0 & \text{adiabatic region.} \end{cases} \tag{8-10}$$

A control volume discretization in space using an upwind scheme is employed to derive the difference equations for mass, momentum and energy conservation. In deriving the difference equations, the effect of integrating across a computational cell is analogous to averaging the field variables in that section and leads to better accuracy compared to first order difference schemes for the spatial derivatives [8-89].

Discretization of governing equations for steady state solution

Integrating the steady-state mass, momentum and energy equations (8-8), (8-9) and (8-10) across the control volume from *j* to *j+1* (where *j* and *j+1* are grid points at inlet and outlet face of the control volume) leads to the following set of discretized equations:

Continuity:

$$(\rho u)_{j+1} = (\rho u)_j \tag{8-11}$$

Momentum:

$$p_{j+1} = p_j - \left(1 + \frac{1}{4}\left(\frac{f}{D}\Delta x + K\right)\right)(\rho u^2)_{j+1} + \left(1 - \frac{1}{4}\left(\frac{f}{D}\Delta x + K\right)\right)(\rho u^2)_j - \left(\frac{\rho_j + \rho_{j+1}}{2}\right) g\, \Delta z \tag{8-12}$$

Energy:

$$i_{j+1} = i_j + \frac{(q_h''' or - q_c''')\,\Delta x}{(\rho u)_j} \tag{8-13}$$

for the heater or the cooler. The equation of state is rewritten as:

$$\rho_{j+1} = f(p_{j+1}, i_{j+1}) \tag{8-14}$$

Boundary conditions:

- The heat coming from the heater is rejected in the cooler with an imposed heat flux;
- The pressure in the first control volume should be equal to the pressure calculated by equation (8-12) in the last control volume (i.e. $\Sigma\Delta P = 0$).

While the density at any axial distance is known from equation (8-7), the friction factor in the single-phase region (sub-critical or supercritical), is obtained from the local Reynolds number as follows.

$$f_{laminar} = 64/Re \tag{8-15}$$

for laminar flow

$$f_{turbulent} = 0.316/Re^{0.25} \tag{8-16}$$

for turbulent flow. The friction factor used in the calculations is selected as the maximum value calculated by the two equations above, i.e.:

$$f = maximum\ of\ (f_{laminar}\ ,\ f_{turbulent}) \tag{8-17}$$

This formulation is used to avoid discontinuities in the friction factor at the transition from laminar to turbulent flow.

Discretization for time dependent solution

Integrating the time dependent conservation equations (8-4), (8-5) and (8-6) across the control volume from j to $j+1$ leads to following set of discretized equations:

Continuity:

$$(\rho u)_{j+1}^{n+1} = (\rho u)_{j}^{n+1} - \left(\rho_{j+1}^{n+1} - \rho_{j+1}^{n} + \rho_{j}^{n+1} - \rho_{j}^{n}\right) \frac{\Delta x}{2\,\Delta t} \tag{8-18}$$

Momentum:

$$p_{j+1}^{n+1} = p_{j}^{n+1} - \left(1 + \frac{1}{4}\left(\frac{f}{D}\Delta x + K\right)\right)\left(\rho u^2\right)_{j+1}^{n} + \left(1 - \frac{1}{4}\left(\frac{f}{D}\Delta x + K\right)\right)\left(\rho u^2\right)_{j}^{n} - \left(\frac{\rho_{j}^{n} + \rho_{j+1}^{n}}{2}\right) g\,\Delta z$$
$$- \left((\rho u)_{j+1}^{n+1} - (\rho u)_{j+1}^{n} + (\rho u)_{j}^{n+1} - (\rho u)_{j}^{n}\right) \frac{\Delta x}{2\,\Delta t} \tag{8-19}$$

Energy:

$$i_{j+1}^{n+1} = \frac{q'''\,\Delta x + \left((\rho i)_{j+1}^{n} + (\rho i)_{j}^{n} - (\rho i)_{j}^{n+1}\right) \frac{\Delta x}{2\,\Delta t} + (\rho u i)_{j}^{n+1}}{(\rho u)_{j+1}^{n+1} + \frac{\Delta x}{2\,\Delta t}\rho_{j+1}^{n+1}} \tag{8-20}$$

NOLSTA has been validated for open loop analysis with experimental data available in literature. Lomperski et al. (2004) [8-78] have reported experimental natural circulation data for carbon-dioxide at supercritical pressure for constant heater inlet temperature irrespective of power. The loop orientation is HHHC having ID of 13.88 mm and height of 2 m. The code predicts the steady state mass flow rate and heater outlet temperature appreciably well as shown in Fig. 8.26. The code predicts the threshold of instability as 9.8 kW (see Fig. 8.27) for Lomperski's loop, whereas no instability has been observed during experiments. This is in agreement with predictions of other one-dimensional stability codes [8-78].

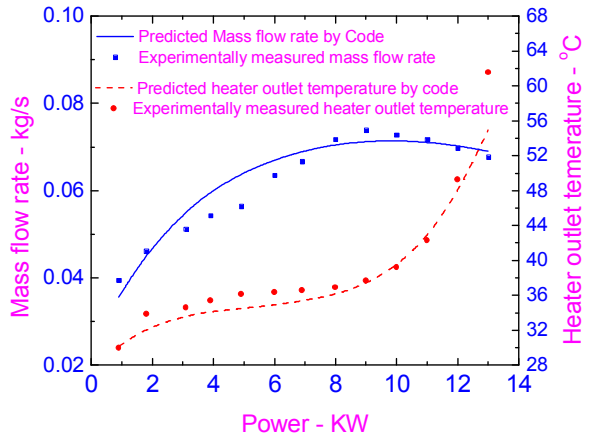

FIG. 8.26. Comparison of experimental data with theoretical predictions for Lomperski's loop at 8 MPa and 24°C heater inlet temperature.

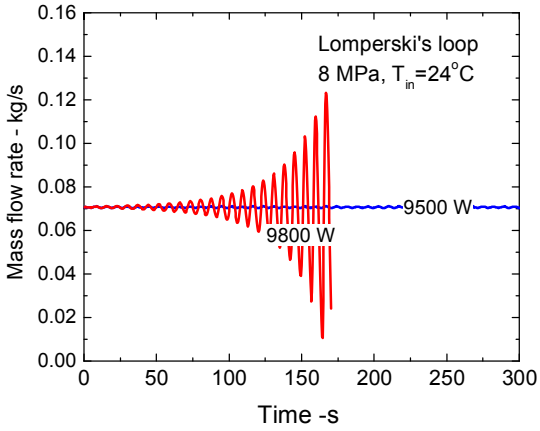

FIG. 8.27. Prediction of instability for Lomperski's loop at 8 MPa and 24 °C heater inlet temperature.

8.5.2.3. Closed loop

The SPNCL of BARC is actually a closed loop, where heater inlet temperature is not controlled and only chilled water mass flow rate and inlet temperature on the secondary side of the cooler is maintained constant. Hence NOLSTA code was modified for closed loop boundary conditions and results compared with experimental data [8-90]. In a closed loop, the coolant mass flow rate on the secondary side of the cooler (i.e., chilled water in SPNCL) is kept constant as the heater power is increased. The heater inlet temperature is not fixed and increases with an increase in the-heater power. For the analysis of closed loops, the rate of heat rejection in the cooler is evaluated basing on the calculation of the overall heat transfer coefficient for the cooler and the temperature difference between the primary and the secondary fluid. In this case, the operating pressure of the loop, the coolant mass flow rate and the inlet temperature for the secondary side of the cooler and the heater power are specified along with the entire geometry of the loop (hydraulic diameter, flow area and length of each pipe). The procedure to achieve steady-state mass flow rate is explained below:

- assume an inlet temperature to the heater and calculate the steady state mass flow rate of SPNCL for a given power, by assuming total heat rejection in cooler, i.e., open loop;
- taking this flow rate and temperature distribution on primary side of cooler, evaluate UA x LMTD for the cooler, where:

$$\frac{1}{UA} = \frac{1}{h_i A_i} + \frac{\ln(d_o/d_i)}{2\pi L k_w} + \frac{1}{h_o A_o} \tag{8-21}$$

and

$$LMTD = \frac{\Delta T_{out} - \Delta T_{in}}{\ln\left(\frac{\Delta T_{out}}{\Delta T_{in}}\right)} \tag{8-22}$$

where, ΔT_{in} is the temperature difference between the primary and the secondary fluid at the inlet of the cooler and ΔT_{out} is the temperature difference between the primary and the secondary fluid at the outlet of the cooler;

- if the product (UA x LMTD) is less than the power given to the heater, then increase the heater inlet temperature, else reduce the heater inlet temperature; the iterations converge if UA x LMTD is closer than 99.9% to the power given to the heater.

The governing equations for closed loop analysis remain the same as shown for the open-loop case.

Moreover, to calculate UA, the evaluation of the inside primary heat transfer coefficient (h_i) and the outside secondary heat transfer coefficient (h_o) for the cooler is required. The Dittus-Boelter correlation has been used for the evaluation of the heat transfer coefficient on primary/secondary side of the cooler under turbulent conditions. Thus, inside and outside heat transfer coefficients are evaluated as follows:

$$h_{laminar} = 3.66\ k/D \tag{8-23}$$

for laminar flow,

$$h_{turbulent} = 0.023\ Re^{0.8}\ Pr^{0.3}\ k/D \tag{8-24}$$

for turbulent flow. The heat transfer coefficient (inside or outside the flow ducts) used in the calculations is selected as the maximum value calculated by the above two equations, i.e.:

$$h = maximum\ of\ (h_{laminar}\ ,\ h_{turbulent}) \tag{8-25}$$

8.5.2.4. Analysis of instabilities by the NOLSTA code

Open loop boundary conditions

Considering the nature of the instabilities, with no perturbation observed in the heater inlet temperature, the SPNCL stability map was generated for HHHC orientation considering it as an open loop. The stability map, reported in Fig. 8.28, shows that the loop should have been completely stable for all the operating powers for HHHC orientation. The stability threshold for open loop boundary conditions has been found to be weakly sensitive to the number of control volumes used in the analysis, hence 28 control volumes have been used for generating the stability map [8-82].

Typical stable and unstable cases considering constant heater inlet temperature for HHHC orientation at 9 MPa pressure are shown in Fig. 8.29 (a and b). In particular, Fig. 8.29b shows the temperature oscillations for the unstable case, which indicates the ever increasing amplitude of temperature oscillation at the heater outlet leading to flow reversal, whereas the heater inlet temperature remains constant. The NOLSTA code at present cannot handle flow reversal. However, the heater outlet temperature oscillations observed during experiment achieve a limit cycle without any flow reversal (see Fig. 8.12c, Fig. 8.13c, Fig. 8.14c, Fig. 8.15c and Fig. 8.16b).

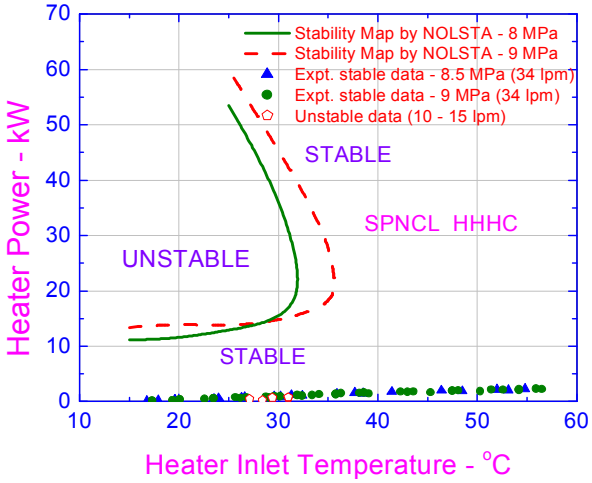

FIG. 8.28. Comparison of experimental data with the stability maps generated by NOLSTA code considering SPNCL as open loop for HHHC orientation.

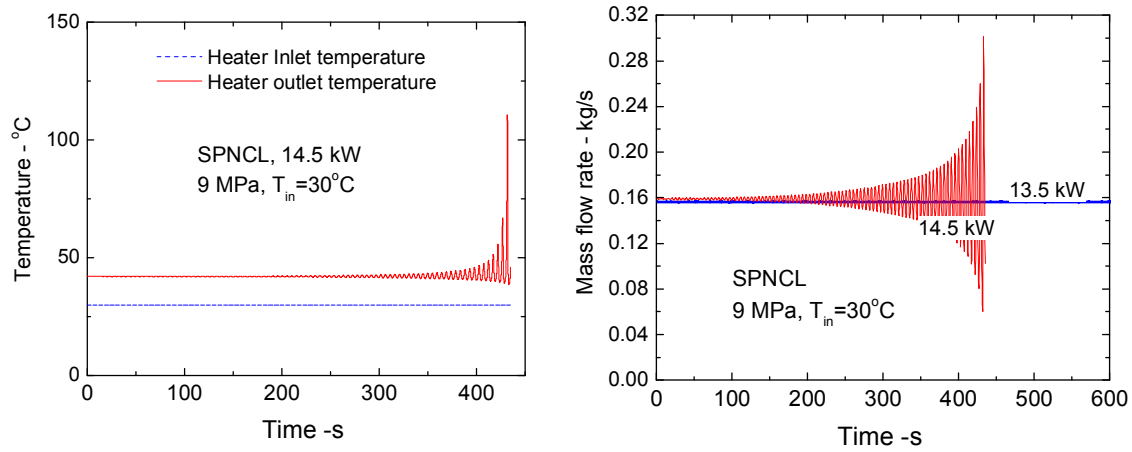

a) b)

FIG. 8.29. Typical unstable behaviour at 14.5 kW for open loop SPNCL with HHHC orientation.

Closed loop boundary conditions

The analysis was carried out for HHHC orientation considering a closed loop behaviour in which the heater inlet temperature was allowed to fluctuate with time. The results of the analysis are shown in Fig. 8.30 (a and b). The loop is found to be stable at 600 W, becomes unstable at 800 W and continues to be unstable till 1400 W and again becomes stable at 2100 W, as shown in Fig. 8.30a. The instability is predicted for the heater inlet temperature varying from 29 °C to 63 °C (a spread of 40 °C across the pseudo-critical temperature at 9 MPa) as shown in Fig. 8.30b. Thus, the code is predicting larger unstable zone than that observed in the experiment. The stability threshold for closed loop boundary conditions has been found to be sensitive to the number of control volumes used in the analysis (i.e., using 28 control volumes predicts instability from 900 W – 1800 W). Hence, 100 control volumes have been used in the present analysis with closed loop boundary conditions.

The typical unstable behaviour predicted by the NOLSTA code at 800 W is shown in greater detail in Fig.

8.31a and Fig. 8.31b. Figure 8.31a shows a continuously increasing amplitude of flow oscillations up to the flow reversal. Figure 8.31b shows increasing amplitudes for both heater inlet and outlet temperature oscillations, having a time period of 22.3 s (the steady state loop circulation time period is 25.5 s) which indicates development of instability by the Welander mechanism [8-1]. The Welander mechanism is observed for instability development from steady state conditions for SPNCL, as also shown in Fig. 8.12a, Fig. 8.13a, Fig. 8.14a and Fig. 8.15a. This is a typical phenomenon of development of instability during single-phase natural circulation at sub-critical conditions, which mostly leads to a flow reversal. However, no flow reversal was observed during the experiments.

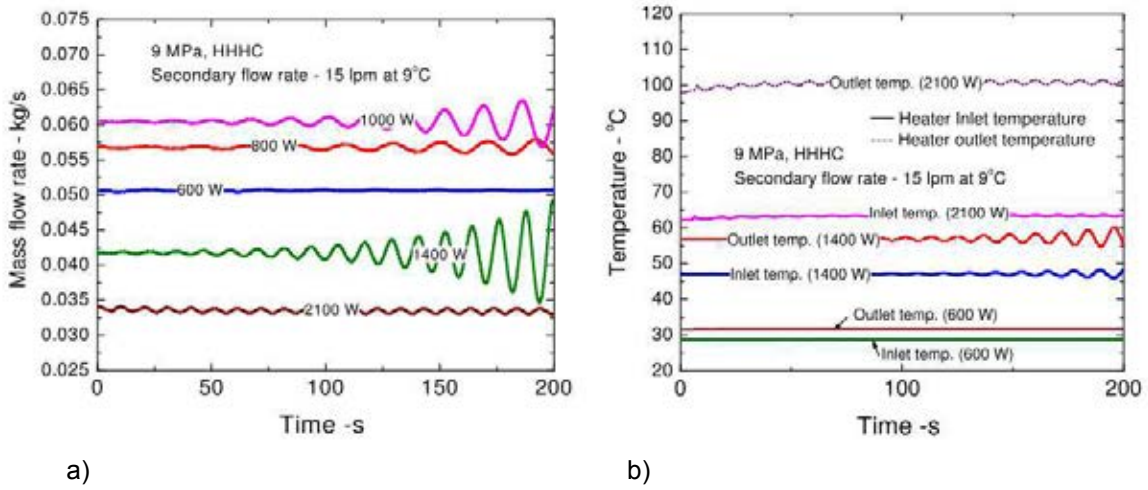

a) b)

FIG. 8.30. Stability predictions for closed loop SPNCL with HHHC orientation.

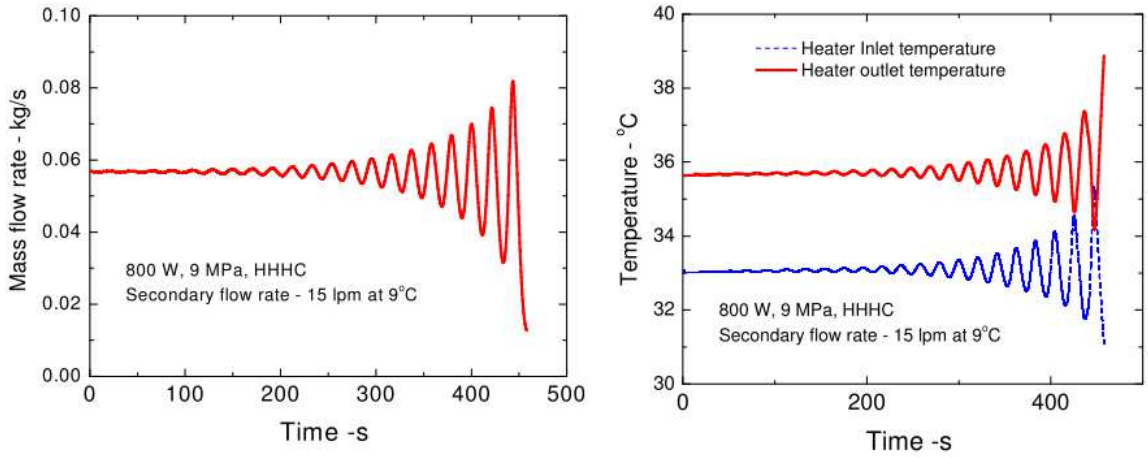

a) b)

FIG. 8.31. Detail of the prediction of instability at 800 W by the NOLSTA code.

The threshold of instability was predicted in this way for different secondary coolant flow rates and the obtained stability map is given in Fig. 8.32 along with the stable and unstable natural circulation data. The predicted pseudo-critical and critical lines are also plotted in the figure which shows that the instability is predicted only for a narrow range of power around the pseudo-critical point in agreement with the experimental observations. Besides, the instability is not predicted for high coolant flow rates as observed in the experiments. However, there is significant difference in the value of coolant flow rate at which the instability disappears between the prediction and data which could be attributed to the neglect of heat

losses, multi-dimensional effects and possibly wall thermal capacitance effects.

In fact, the NOLSTA code at present does not simulate the effect of thermal capacitance of pipe wall and heat losses from the insulation which may play a significant role in the development of instabilities under closed loop boundary conditions. Moreover, three-dimensional effects may play an important role in instability behaviour of supercritical natural circulation loops. Hence 3D-CFD codes may be a helpful tool in understanding the mechanism of instability at supercritical fluid conditions for closed loop thermosyphon.

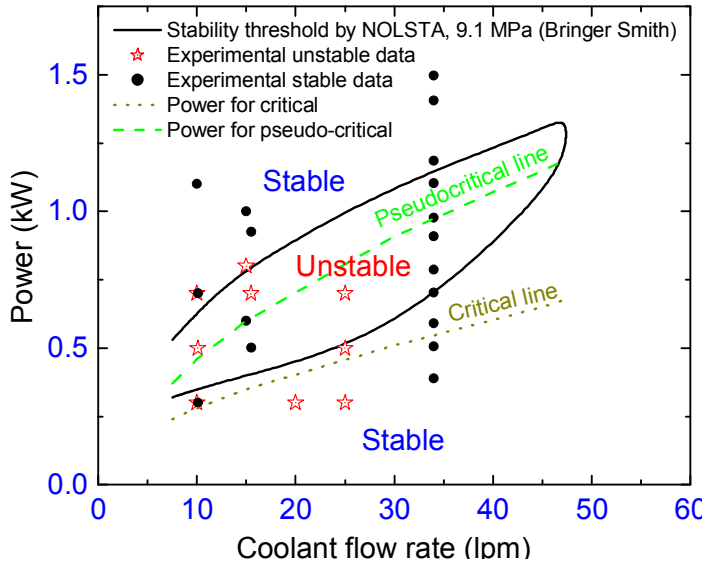

FIG. 8.32. Stability map predicted by the NOLSTA code.

8.5.3. RELAP5 application to the CIAE facility experimental tests

The previously reported experiment in the CIAE facility was simulated with RELAP5/MOD3.3 and the calculation was performed at the pressure of 25 MPa with power as Q = 1.034 t (Q in W and t in s) and the requested time step of $\Delta t = 0.1$ s. Figure 8.33 compares the predictions and the experimental results. As seen in Fig. 8.33a, the calculated flow rate increases as the power increases, and it reaches a maximum of about 8.6 g/s at Q = 14 kW with outlet water temperature of $T_o = 390$ °C. Afterwards, it decreases with increasing power. The onset of oscillations occurs at Q = 16.7 kW with the flow rate of 7.9 g/s and $T_o = 450$ °C, as in Fig. 8.33b. The oscillations become more severe as the power increases further, leading to a failure of calculation due to the property out of range.

Compared to the experimental results, RELAP5 gives a slight over-prediction of the flow rate and a delay of the onset of oscillations. It is noted that the inlet water temperature is greatly over-predicted, associated with an over-prediction of the outlet water temperature. For instance, at Q = 11.6 kW, when the onset of oscillation occurs, the measured inlet and outlet water temperatures are 55 °C and 370 °C, respectively, versus 159 °C and 384 °C in the calculation.

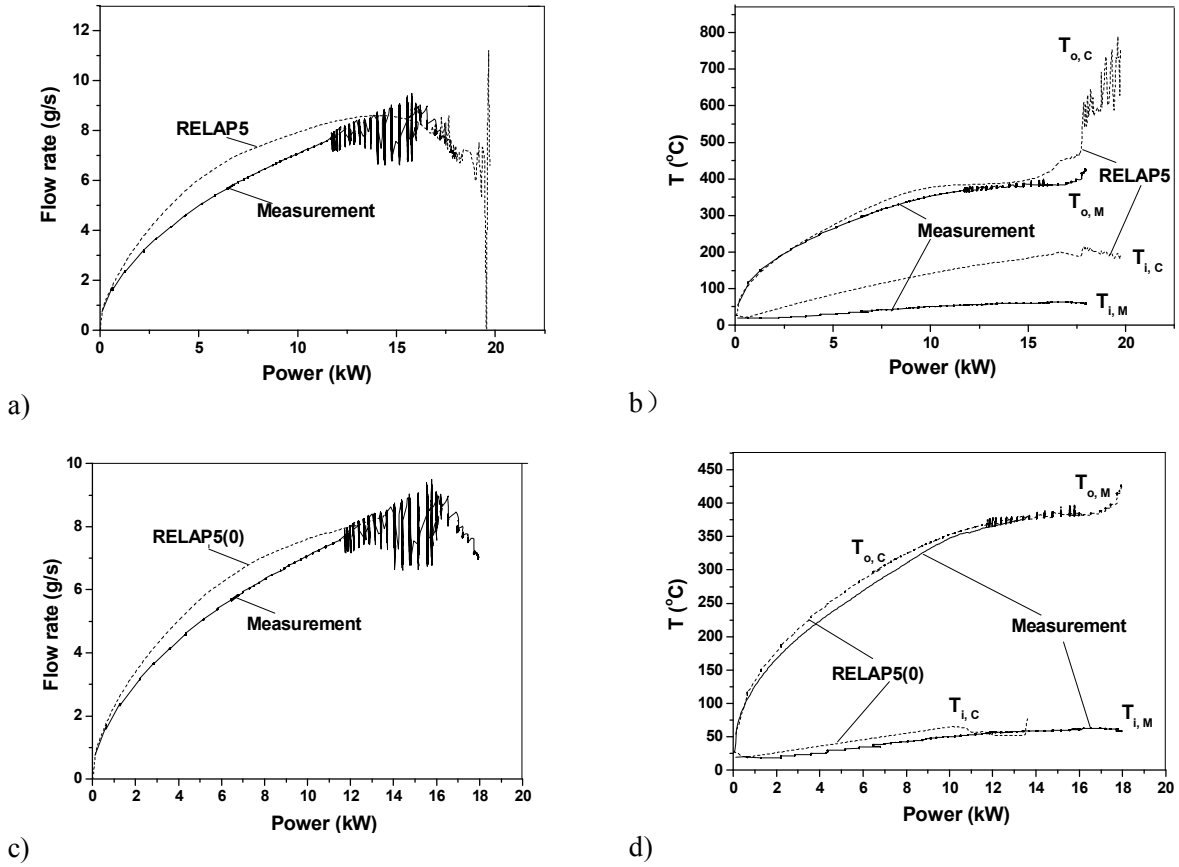

FIG. 8.33. Comparison of the calculation by RELAP5 with experiment (RELAP5 original simulation, RELAP5(0) — input with increased heat transfer area of heat exchanger).

This over-prediction of the water temperatures can be attributed to the underestimation of the heat transfer coefficient in the primary side of the heat exchanger. By artificially increasing the heat transfer area to catch the evolution of water temperatures, the calculation, denoted by RELAP5(0), is made with the same requested time step of 0.1 s. As seen in c) and d), the calculated flow rate is closer to the experiment. The onset of oscillations is calculated at Q =13.5 kW with the flow rate of 8.3 g/s and T_o = 376 °C. The oscillation leads to the failure of calculation immediately.

In the latter calculation, the flow rate is slightly lower than in the former one, as seen in Fig. 8.34. The outlet water temperature is appreciably lower (i.e., 376 °C versus 450 °C) and is close to the experimental temperature (370 °C) and below the pseudo-critical temperature (383 °C).

The calculation (RELAP5(0)) is also made with a requested time step of t = 0.02 s. It is terminated at the power of 16 kW when the oscillation occurs, leading to failure of calculation. It occurs slightly after the peak of flow rate. The results of two calculations with Δt = 0.1 and 0.02 s are compared in Fig. 8.35. As seen, the flow rates of the two calculations are nearly the same for stable flow period, but the conditions at the onset of oscillation are appreciably different, e.g., Q = 18 kW and T_o = 398 °C for Δt = 0.02 s, versus 13.5 kW and T_o = 376 °C for Δt = 0.1 s.

The time steps of 0.1 s and 0.02 s correspond to an increase in the heating powers of 0.1 W and 0.02 W, respectively, for each step. It is evident that the oscillation could occur in a small region of peak flow rate

with the derivative of flow rate/power near zero, in which a small variation of flow rate corresponds to an appreciable difference in Q or T_o, depending on the nature of disturbance. In view of the mechanism of flow instability associated with the sharp variation of fluid density in the near pseudo-critical region, the condition for the onset of oscillation is also closely related to the distribution of the flow resistances in the natural circulation loop.

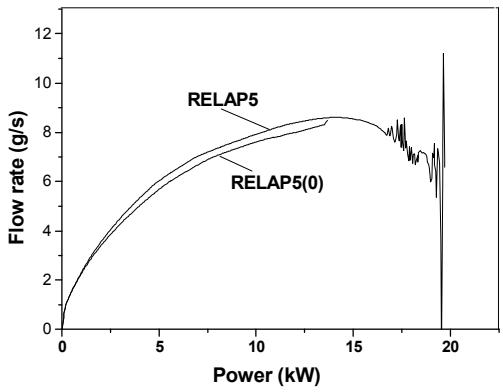

FIG. 8.34. Calculation results with different heat transfer area of heat exchanger.

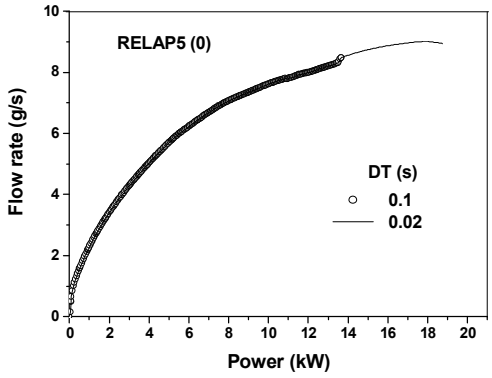

FIG. 8.35. The effect of time step on the calculation results.

In conclusion, flow instability is observed in natural circulation of water and the results are compared with the calculations of RELAP5. It is concluded that the flow instability is associated with the sharp variation of fluid density near the pseudo-critical region and it occurs in a small region of peak flow rate and could be induced by a minor disturbance. The condition for the onset of instability is closely related to the nature of the disturbance and the distribution of flow resistances in the natural circulation loop.

8.5.4. Application of CFD codes to CO_2 natural circulation experiments by BARC

In a joint work performed by BARC and University of Pisa [8-91], the experiments on natural circulation performed in the NSPCL facility with CO_2 were simulated by the STAR-CCM+ [8-92] and the FLUENT [8-93] commercial CFD codes.

The experimental facility was discretized with the meshing tools available for the two codes, taking into account the symmetry with respect to a vertical plane passing through the pipe axes; this allowed reducing the number of nodes by half for a reasonably fine discretization. Figures 8.36 and 8.37 report the obtained discretization for the two CFD codes, showing that also the conductive pipe walls were considered in the analysis by a conjugated heat transfer approach. For the FLUENT code a structured mesh was adopted: 28 non uniform cells were defined on the diameter and 20 azimuthal cells are used along the outer circumference. Of the overall 230 cells present in the cross section, 150 are used to mesh the fluid region and 80 for the solid region, making use of a conjugated heat transfer approach. For the STAR-CCM+ code, the generation of the mesh was automatically obtained by the built-in mesher of the code, after selecting appropriate models (polyhedral nodes in the core and prism layers at the wall) with a target size of 2 mm. The result was a polyhedral mesh in the center of the fluid region, 5 prism layers near the wall, and 3 layers adopted to discretize the solid region.

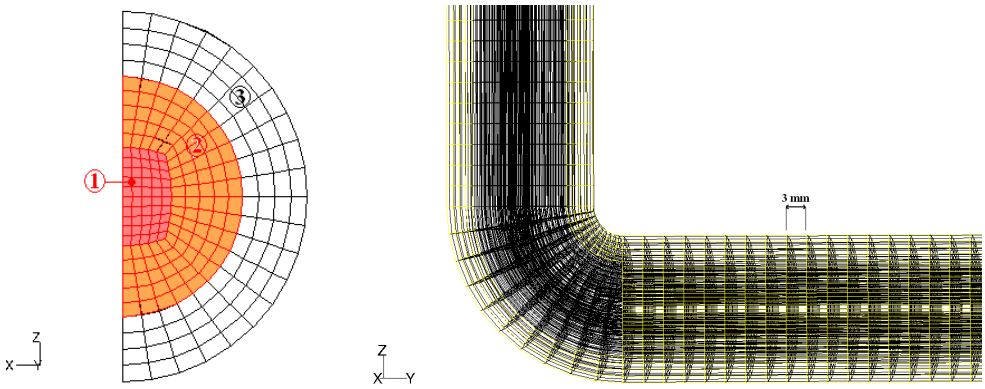

FIG. 8.36. Spatial discretization adopted for the FLUENT code.

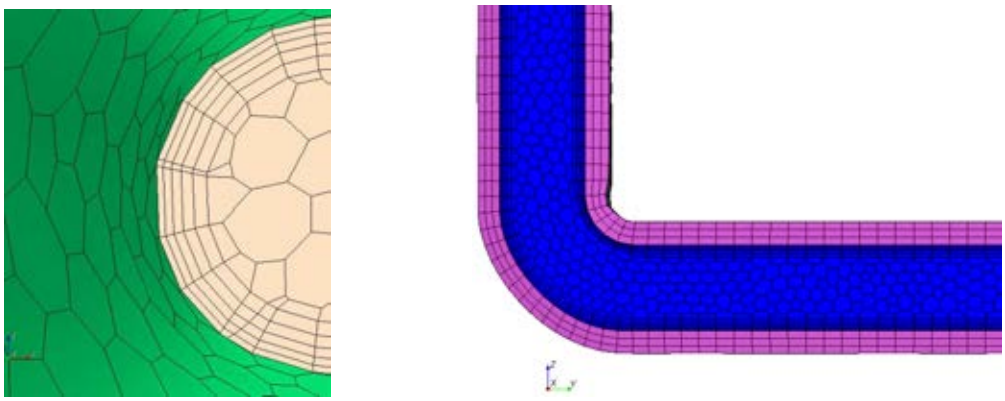

FIG. 8.37. Spatial discretization adopted for the STAR-CCM+ code.

Fluid properties were assigned in FLUENT by a piece-wise linear approximation of data obtained by the NIST package [8-94]. In the case of STAR-CCM+, cubic spline polynomials were generated also starting from the NIST database.

The turbulence models adopted in both cases were of the k-ε type, making use of wall functions for dealing with near-wall conditions. Adequate mesh refinement close to the walls was anyway provided in order to better describe the changes in fluid properties occurring close to the solid walls.

The HHHC configuration was addressed in the calculations, applying the corresponding boundary conditions at the outer surface of the solid region, in order to simulate heated and cooled parts. An operating pressure of 8.6 MPa was selected for analysing steady-state behaviour. Heat losses were evaluated assigning an outer pipe surface heat transfer coefficient equal to 2 W/(m^{2}K) to all the surfaces not involved in heating or cooling, also taking into account the presence of insulating material. The heat transfer coefficient to the secondary coolant was imposed at 850 W/(m^{2}K); this value was anyway subjected to sensitivity analyses. Rough walls were also assumed, assigning an absolute roughness height of 25 μm.

The results obtained in the analyses are compared with experimental data and the NOLSTA code predictions by BARC in Fig. 8.38. The good agreement with the observed experimental trends can be noted, though differences appear in the steady-state flow rate calculated by the two CFD codes, accounting for the effect of slightly different assumptions adopted in the models. It is interesting to note

the sharp decrease in flow rate predicted by the CFD codes when the temperature in both legs approaches the pseudo-critical value; this sharp decrease is caused by the interplay of the reduced heat transfer on the primary side of the cooler section, due to the presence of a transition to a 'gas-like' fluid, and of the greater pressure drops along the loop caused by this transition. Figure 8.38b shows clearly the achievement of pseudo-critical conditions almost simultaneously in the heater and the cooler inlets and the subsequent steep increase of fluid temperature with increasing power, owing to the degradation of the overall heat rejection capability to the secondary coolant.

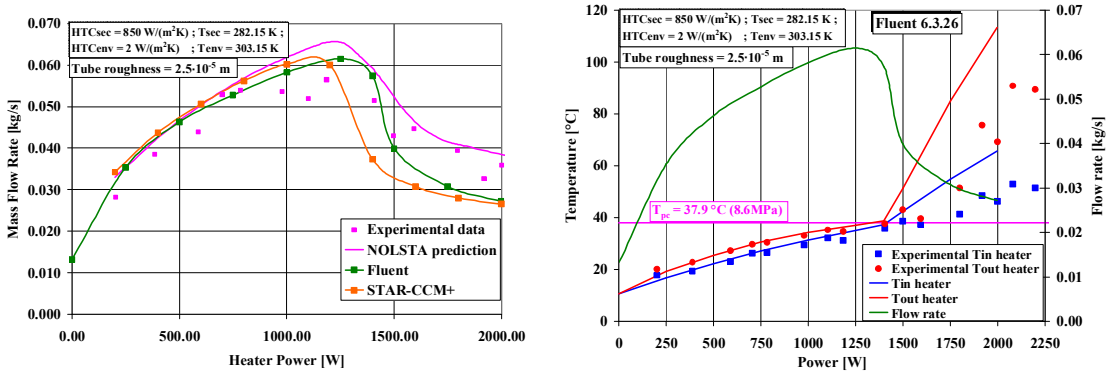

a) flow rate b) fluid temperatures

FIG. 8.38. Steady-state flow rate and fluid temperatures vs. heating power as predicted by the FLUENT and the STAR-CCM+ codes.

Sensitivity analyses were performed on different parameters to be considered somehow uncertain in the analyses, as reported in Fig. 8.39. As it can be noted, the effects of the secondary coolant temperature and of the assumed secondary heat transfer coefficients have a role in determining the value of power at which the transition through the pseudo-critical temperature occurs (Fig. 8.39 a and b), also suggesting the reasons for possible differences in the results obtained by the two codes in this regard (Fig. 8.38). The assumptions made to estimate heat losses provide a similar effect (Fig. 8.39c), while pipe roughness has both an impact on the value of flow rate and on the power level at which flow rate starts decreasing (Fig. 8.39d).

Though the prediction of steady-state conditions was rather satisfactory, also providing useful suggestions about the reasons for the slight discrepancies with respect to data, the transient analysis was not able to provide data in agreement with the observed unstable behaviour. Reasons to justify this discrepancy may be identified in the representation of the heat capacitance of pipe walls with a few radial nodes, as well as in possible effects related to numerical diffusion of the adopted discretization schemes. A careful analysis of these aspects will be made in the future.

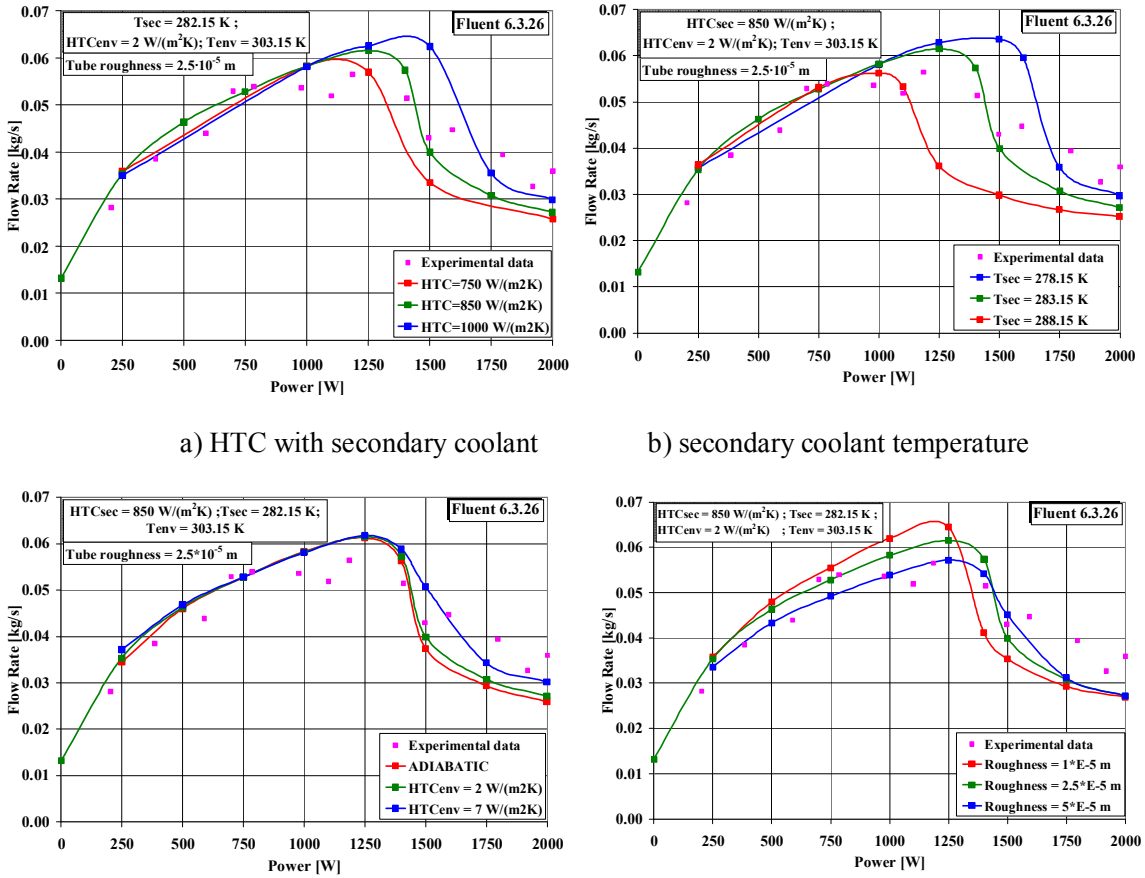

a) HTC with secondary coolant

b) secondary coolant temperature

c) HTC with the environment

d) pipe roughness

FIG. 8.39. Sensitivity analyses concerning the effect of different parameters on the flow rate vs. power curve performed by the FLUENT code.

8.5.5. Summary from the code testing benchmark exercise on flow stability

Section 9.2 of this Report describes a Code Testing Benchmark Exercise on flow stability that was planned since the start of the CRP as a useful code-to-code comparison.

The reference data for this exercise were generated by the University of Pisa making use of in-house codes and RELAP5. Submissions were received by:

- VTT with the APROS code;
- the University of Manitoba and AECL, making use of in-house tools developed by Prof. Chatoorgoon;
- the Bhabha Atomic Energy Research Centre, making use of the in-house codes SUCLIN and NOLSTA;
- the JRC-IE Petten, making use of the RELAP5 code;
- Gidropress, making use of the TEMPA code;
- McMaster University and the Gruppo di Ricerca Nucleare di San Piero a Grado (GRNSPG), making use of both RELAP5 and TRACE codes.

The results obtained by the Participants in the exercise were in reasonable qualitative agreement with the reference data. In particular, the predictions by the JRC-IE with RELAP5 and by BARC with the NOLSTA code were very close to the reference data, but different levels of quantitative discrepancies were noted for some of the other submissions (see Fig. 8.40).

As discussed in Section 9.2, the submission by VTT and the following interesting discussions and further submissions were particularly revealing of the impact that the use of different friction-factor correlations may have on the prediction of stability at supercritical pressures. In fact, the reference data, as well as most of the submitted results, were obtained with standard rough tube friction-factor correlations available in codes for subcritical pressure water systems, while the applications by VTT made use of different correlations for supercritical pressure fluids in smooth tubes. This allowed interesting reflections about the need to qualify friction-factor models specifically suitable for rough tubes at supercritical pressure conditions.

The Benchmark Exercise achieved its goal to provide an overall picture of the challenges presently faced by system codes in predicting the stability of flows at supercritical pressures.

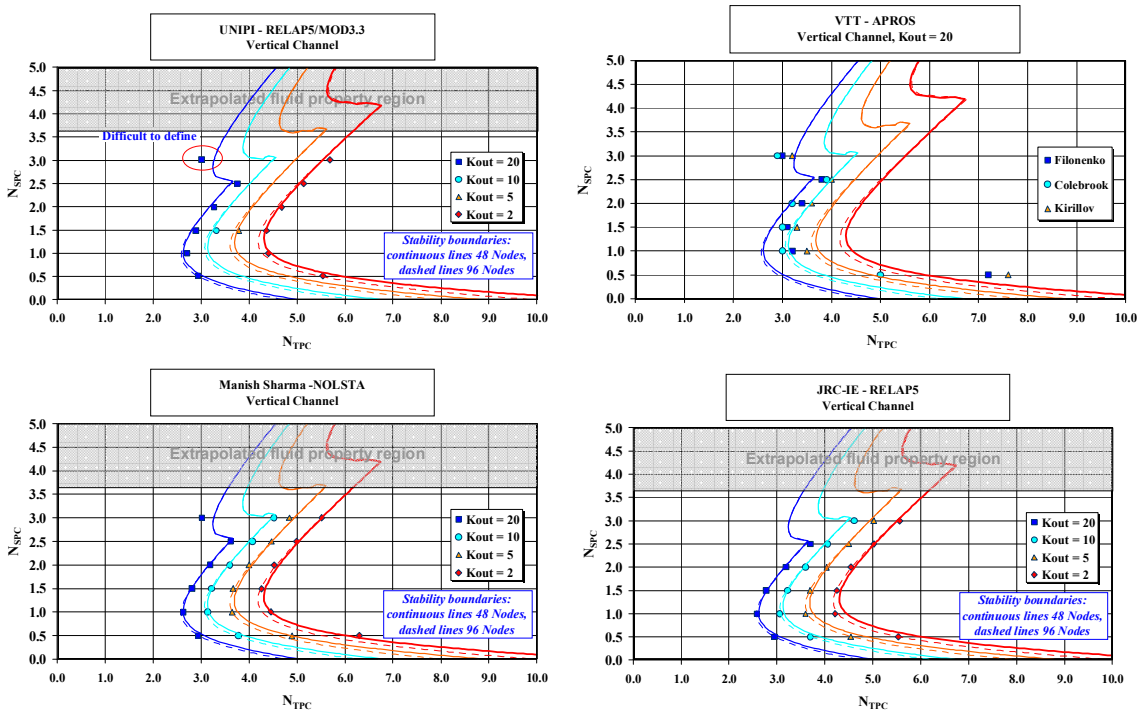

FIG. 8.40. Selected results from the flow stability benchmark exercise for a vertical channel.

The present section collected and described contributions by Participants in the CRP about the relevant issues of stability and natural circulation with fluids at supercritical pressure. In particular, the following considerations can be made in relation to the presented material.

- The experimental facilities available at the University of Manitoba, at the Bhabha Atomic Research Centre and at the China Institute for Atomic Energy testify for activities planned or already in progress for collecting experimental data in relation to natural circulation in simple loop configurations. As it can be noted, efforts are spent in particular to establish the boundaries of stable operation of the loops, trying to answer fundamental questions about the causes of instabilities. In this regard, unstable behaviour was observed only in the horizontal heater and horizontal cooler configuration (HHHC) for the BARC facility, confirming the known conclusion that vertical heater and/or cooler tend to favour stability, at least against a Welander's type instability mechanism. On the other hand, the unstable behaviour observed in the CIAE facility with vertical heater suggests that at sufficiently high power-to-flow ratios also such configurations may undergo unstable behaviour;
- In this perspective, considering the available literature on the subject of natural circulation stability, it appears that there is no complete consensus about the location of the unstable operating regions in the parameter space for a closed loop, except for a generic indication that instabilities are often predicted or observed close to the maximum of the flow vs. power curve. Since this maximum occurs mostly simultaneously with the transition through the pseudo-critical temperature, when a considerable density difference is produced, this transition could be considered at the root of the most probable unstable behaviour. This observation must be anyway contrasted by the consideration that Welander's type instability mechanisms occur also in single-phase loops, where the density difference between hot and cold fluid regions is so small that the Boussinesq fluid model can be safely adopted;
- On the basis of the above considerations it can be concluded that a thorough investigation about

the mechanisms leading to instability must be made, e.g. to distinguish between possible different unstable modes. In this regard, the presented model results are partly encouraging, showing that system codes and in-house models are able at least to mimic the observed unstable behaviour. However, at the time of writing the role of some plant features, as the heating and passive structures, is not completely clear, being mostly disregarded in simulations; in turn, the effect of heating structures on stability calls into play the prediction of fluid-to-wall heat transfer phenomena, which decide the extent of dynamic coupling between fluid and structures. In this respect, the inability of the reported CFD analysis to predict the unstable behaviour observed in rather specific conditions in the BARC loop does not support firm conclusions about model suitability in predicting instabilities;

- On the other hand, the reported work mainly concerns natural circulation stability, giving no experimental contribution to the discussion about the prediction of the stability of simple heated channels containing fluids at supercritical pressures. This issue, discussed in detail in Section 9.2, whose main conclusions were summarized at the end of this section, indeed requires specific investigations, allowing for a step forth with respect to simple model prediction as those reported in the related code-to-code benchmarking activities.

In summary, the results collected in the frame of this CRP on natural circulation and stability are extremely helpful in indicating the potential that experimental activities have in contributing to clarify these phenomena. This happens to be the case also because the presented data, though indicating possible explanations for the addressed mechanisms, clearly show that phenomena occurring in even simple experimental apparatuses are not amenable to too simplistic interpretations, requesting for more in depth analyses to be soundly explained. These analyses are already going on in cooperation between CRP Participants and may constitute a future long lasting product of the above described efforts.

LIST OF SYMBOLS FOR SECTION 8

Latin Letters

A	Area (m^2)
D	Hydraulic diameter (m)
DAS	Data Acquisition System
c_p	Specific heat (J/kg/k)
d	diameter (m)
f	Friction factor
FA	Fuel assembly
g	Acceleration due to gravity (m/s^2)
h	Heat transfer coefficient ($W/m^2/k$)
i	Specific enthalpy (J/kg)
k	Thermal conductivity (W/m/k)
K	Local loss coefficient
L	Length of a section (m)
lpm	Liter per minute
N_{TPC}	trans-pseudocritical number (see section 9.2)
N_{SPC}	sub-pseudocritical number (see section 9.2)
P	Pressure (Pa)
PB	
Pr	Prandtl No. ($\mu c_p/k$)
PLC	Powerline communications
q'''	Heat applied/unit volume of coolant (W/m^3)
Re	Reynolds number ($\rho uD/\mu$)

t	Time (s)
T	Temperature (°C)
u	Velocity (m/s)
U	Overall heat transfer coefficient (W/m^2/K)
W	Mass flow rate (kg/s)
WC	Water column
x	Axial distance (m)
z	Elevation (m)

Greek Symbols

ρ	Density (kg/m^3)
μ	Dynamic viscosity of fluid (Pa-s)
ϕ	Inclination angle of the pipe with respect to vertical direction

Subscripts

c	cooler
env	environment
h	heater
i	inside
in	inlet
o	outside
out	outlet
sec	secondary
ss	steady state
w	wall

Superscripts

n	Previous time step
n+1	Current time step

REFERENCES FOR SECTION 8

[8-1] WELANDER, P., 1967, On the Oscillatory Instability of a Differentially Heated Fluid Loop*, J. Fluid Mech.,* Vol. 29, part 1, (1967) 17–30.

[8-2] CREVELING, H.F., DE PAZ, J.F., BALADI, J.Y., SCHOENALS, R.J., 1975, Stability Characteristics of a Single-Phase Free Convection Loop, J. Fluid Mech., Vol. 67, part 1 (1975) 65–84.

[8-3] ZVIRIN, Y., 1979, The Effect of Dissipation on Free Convection Loops, Int. J. Heat Mass Transfer, Vol. 22 (1979) 1539–1545.

[8-4] GREIF, R., ZVIRIN, Y., MERTOL, A., 1979, The Transient and Stability Behaviour of a Natural Convection Loop, J. Heat Transfer, Transactions of the ASME, Vol. 101, November (1979) 684–688.

[8-5] ZVIRIN, Y., GREIF, R., 1979, Transient Behaviour of Natural Circulation Loops: Two Vertical Branches with Point Heat Source and Sink, Int. J. Heat Mass Transfer, Vol. 22 (1979) 499–504.

[8-6] BAU, H.H., TORRANCE, K.E., 1981, Transient and Steady Behaviour of an Open, Symmetrically Heated, Free convection Loop, Int. J. Heat Mass Transfer, Vol. 24, (1981) 597–609.

[8-7] CHEN, K., 1985, On the Oscillatory Instability of Closed Loop Thermosyphons, J. Heat Transfer, Transactions of the ASME, Vol. 107, November (1985) 826–832.

[8-8] HART, J. E., 1984, A New Analysis of the Closed Loop Thermosyphon, Int. J. Heat Mass Transfer, Vol. 27, No. 1 (1984) 125–136.

[8-9] HART, J.E., 1985, A Note on the Loop Thermosyphon with Mixed Boundary Conditions, Int. J. Heat Mass Transfer, Vol. 28, No. 5 (1985) 939–947.
[8-10] SEN, M., RAMOS E., TREVIÑO, C., 1985, The Toroidal Thermosyphon with Known Heat Flux, Int. J. Heat Mass Transfer, Vol. 28, No. 1 (1985) 219–233.
[8-11] MISALE, M., TAGLIAFICO, L., 1987, The Transient and Stability Behaviour of Single-Phase Natural Circulation Loops, Heat and Technology, Vol. 5, No. 1-2 (1987).
[8-12] VIJAYAN, P.K., DATE, A.W., 1990, Experimental and Theoretical Investigations on the Steady-State and Transient Behaviour of a Thermosyphon with Throughflow in a Figure-of-Eight Loop , Int. J. Heat Mass Transfer, Vol. 33, No. 11 (1990) 2479–2489.
[8-13] VIJAYAN, P.K., DATE, A.W, 1992, The Limits of Conditional Stability for Single-Phase Natural Circulation With Throughflow in a Figure-of-Eight Loop, Nuclear Engineering and Design, 136, (1992) 361–380.
[8-14] BAU, H.H., WANG, Y.Z., 1992, Chaos: a heat transfer perspective, in 'Annual Review of Heat Transfer', Volume 4, Edited by L. Tien, Hemisphere Publishing Co. (1992).
[8-15] VIJAYAN, P. K., Austregesilo, H., 1994, Scaling Laws for Single-Phase Natural Circulation Loops, Nuclear Engineering and Design, 155 (1994), 331–347.
[8-16] VELAZQUEZ, J.J, 1994, On the Dynamics of a Closed Thermosyphon, SIAM J.Appl. Math., Vol. 54, December (1994) 1561–1593.
[8-17] VENKAT RAJ, V., 1994, Experimental Studies Related to Thermosyphon Cooling of Nuclear Reactors - A Review, Proceedings of the First ISHMT-ASME Heat and Mass Transfer Conference and Twelfth National Heat and Mass Transfer Conference, January 5–7, 1994, Bhabha Atomic Research Centre, Bombay, India (1994).
[8-18] RODRIGUEZ-BERNAL, A., 1995, Attractors and inertial manifolds for the dynamics of a closed thermosyphon, Journal of Mathematical Analysis and Applications, 193 (1995) 942–965.
[8-19] VIJAYAN, P.K., AUSTREGESILO, H., TESCHENDORFF, V., 1995, Simulation of the Unstable Behavior of Single-Phase Natural Circulation with Repetitive Flow Reversals in a Rectangular Loop Using the Computer Code ATHLET, Nuclear Engineering and Design, 155, (1995), 623–641.
[8-20] FROGHERI, M., MISALE, M., D'AURIA, F., Experiments in Single-Phase Natural Circulation, 15th UIT National Heat Transfer Conference 1997, Torino, June 19-20, 1997 (1997).
[8-21] MISALE, M., FROGHERI, M., D'AURIA, F., Experiments in Natural Circulation: Influence of Scale Factor on the Stability Behavior, Eurotherm Seminar No. 63 on Single and Two-Phase Natural Circulation, September 6-8 1999, Genoa, Italy (1999).
[8-22] VIJAYAN, P.K., Experimental Observations on the General Trends of the Steady State and Stability Behaviour of Single-Phase Natural Circulation Loops, Invited Lecture at the Eurotherm Seminar No. 63 on Single and Two-Phase Natural Circulation, September 6-8 1999, Genoa, Italy (1999).
[8-23] LAHEY, R.T., MOODY, F.J., The thermalhydraulics of a boiling water reactor, American Nuclear Society (1993).
[8-24] LEDINEGG, M., Instability during Natural and Forced Circulation, Die Wärme, Vol. 16, (1938).
[8-25] BOURÈ, J.A., BERGLES, A.E., TONG, L.S., Review of Two-Phase Flow Instability, Nuclear Engineering and Design, 25, (1973), 165–192.
[8-26] YADIGAROGLU, G., CHAN, K.C., Analysis of Flow Instabilities, Proc. Japan-U.S. Seminar on Two-Phase Flow Dynamics, July 31-August 3, Kobe, Japan (1979).
[8-27] VEZIROGLU, T.N., LEE, S.S., KAKAÇ, S., Fundamentals of two-phase oscillations and experiments in single-channel systems, in: S. Kakac, F. Mayinger (Eds.), Two-Phase Flows and Heat Transfer, vol. 1, Hemisphere Publishing Corp., Washington, DC (1977).
[8-28] YADIGAROGLU, G., Two-phase flow instabilities and propagation phenomena, in: J.M. Dehaye, M. Giot, M.L. Riethmuller (Eds.), Thermohydraulics of Two-phase Flow Systems for Industrial Design and Nuclear Engineering, Mc Graw-Hill, New York (1981) 353–404.

[8-29] MARCH-LEUBA, J., REY, J.M., Coupled Thermohydraulic-Neutronic Instabilities in Boiling Water Nuclear Reactors: A Review of The State of the Art, Nuclear Engineering and Design, 145, (1993), 97–111.
[8-30] D'AURIA, F., (Editor) et al., State of the art Report on Boiling Water Reactor Stability, NEA/CSNI/R(96)21, OCDE/GD(97)13, OECD/NEA Paris (1997).
[8-31] KAKAÇ, S., BON, B., A Review of two-phase flow dynamic instabilities in tube boiling systems, International Journal of Heat and Mass Transfer 51 (2008) 399–433.
[8-32] BECKER, K. M., J. FLINTA, O. NYLUND, Dynamic and Static Burnout Studies for the Full Scale 36-Rod Marviken Fuel Element in the 8 MW Loop FRIGG, Paper presented at the Symposium on Two-Phase Flow Dynamics, Eindhoven, Sept. (1967).
[8-33] SAHA, P., ISHII, M., ZUBER, N., 1976, An experimental Investigation of Thermally Induced Flow Oscillations in Two-Phase Systems, J. Heat Transfer, 98 (1976) 616–622.
[8-34] LIU, H.T., KAKAÇ, S., An experimental investigation of thermally induced flow instabilities in a convective boiling upflow system, Waerme- und Stoffuebertragung 26 (1991) 365–376.
[8-35] WALLIS, G.B., HEASLEY, J.H., Oscillations in Two-Phase Flow Systems, J. Heat Transfer, Trans. ASME, 83 (1961) 363–369.
[8-36] LAHEY, R.T., JR., YADIGAROGLU, G., A Lagrangian analysis of two-phase hydrodynamic and nuclear-coupled density-wave oscillations, in: Proceedings of the 5th International Heat Transfer Conference, Tokyo, Vol. A (1974) 225–229.
[8-37] PENG, S.J., PODOWSKI, M.Z., LAHEY, R.T., JR., M. BECKER, 1984, NUFREQ-NP: A Computer Code for the Stability Analysis of Boiling Water Nuclear Reactors, Nucl. Sci. Eng., 88, (1984) 404–411.
[8-38] PENG, S.J., PODOWSKI, M.Z., LAHEY, R.T., JR., 1986, BWR Linear Stability Analysis, Nucl. Eng. Des., 93, (1986) 25–37.
[8-39] ROHATGI, U.S., NEYMOTIN, L.Y., WULFF, W., Assessment of RAMONA-3B Methodology with FRIGG Dynamic Tests, Proc. International Workshop on BWR Stability, Holtsville, NY, USA, October 17-19, 1990, CSNI Report 178 (1990) 412–432.
[8-40] ROHATGI, U.S., ARONSON, A.L., CHENG, H.S., KHAN, H.J., MALLEN, A.N., 1993, RAMONA-4B development for SBWR safety studies, BNL-NUREG--60148; CONF-931079—23.
[8-41] D'AURIA, F., FROGHERI, M., Use of a natural circulation map for assessing PWR performance, Nuclear Engineering and Design 215 (2002) 111–126.
[8-42] FUKUDA, K., KOBORI, T., Classification of two-phase flow instability by density wave oscillation model. J. Nucl. Sci. Technol. 16 (2) (1979) 95–108.
[8-43] VAN DER HAGEN, T.H.J.J., VAN BRAGT, D.D.B., VAN DER KAA, F.J., KARUZA, J., KILLIAN, D., NISSEN, W.H.M., STEKELENBURG, A.J.C., WOUTERS, J.A.A., Exploring the Dodewaard Type-I and Type-II Stability; From Start-Up to Shut-Down, from Stable to Unstable, Ann. Nucl. Energy, Vol. 24, No. 8 (1997) 659–69.
[8-44] PIORO, I.L., DUFFEY, R.B., Heat Transfer and Hydraulic Resistance at Supercritical Pressure in Power Engineering Applications, ASME Press, New York (2007).
[8-45] CORNELIUS, A.J., PARKER, J.D., Heat Transfer Instabilities near the thermodynamic critical point, Proceedings of the 1965 Heat Transfer and Fluid Mechanics Institute, Stanford University Press (1965) 317 and 329.
[8-46] WALKER, B.J., HARDEN, D.G., The 'density effect' model: prediction and verification of the flow oscillation threshold in a natural circulation loop operating near the critical point, ASME, Paper No. 67-WA/HT-23 (1967) 9 pages.
[8-47] TRESCHEV, G.G., SUKHOV, V.A., SHEVCHENKO, G.A., Flow auto-oscillations in a heated channel at the supercritical state parameters, Transactions of the IVth all-Union Conference on Heat Transfer and Hydraulics at Movement of Two-Phase Flow Inside Elements of Power Engineering Machines and Apparatuses, Leningrad, Russia (1971) 167–175.

[8-48] CHAKRYGIN, V.G., AGAFONOV, M.B., LETYAGIN, I.P., Experimental determination of the limits of aperiodic instability at very high and supercritical pressures, Thermal Engineering, 21 (1), (1974) 17–22.
[8-49] JONES, M.C., PETERSON, R.G., A Study of Flow Stability in Helium Cooling Systems, ASME conference 17–22 November 1975 (In Russian: Journal 'Heat transfer', No.4 (1975) 26–34).
[8-50] LABUNTZOV, D. A., MIROZYAN, P. A., The analysis of boundaries of stable flow move of helium at supercritical parameters in heated channel, (In Russian), Heat-power engineering, №3 (1983) 2–4.
[8-51] DANEY, D. E., LUDTKE, P. R., JONES, M. C., An Experimental Study of Thermally-Induced Flow Oscillations in Supercritical Helium, ASME 1978 (In Russian: Journal 'Heat transfer', 1979, v.101, No.1 (1979) 7–15).
[8-52] CORNELIUS, A.J., PARKER, D., Instability of heat exchange near critical point, Proceedings of the 1965 Heat Transfer and Mechanics Institute, Stanford, California (1965) 317–329, (In Russian: Achievements in heat exchange. Collected articles. Moscow: 'MIR', 1970).
[8-53] ZUBER, N., An analysis of thermally induced flow oscillation in the near-critical and supercritical thermal-dynamic region, Report no. NASA-CR-80609, General Electric Co., NY, USA (1966).
[8-54] ZHAO, J., SAHA, P., KAZIMI, M.S., Stability of supercritical water-cooled reactor during steady-state and sliding pressure start-up. The 11th International Topical Meeting on Nuclear Reactor Thermal-Hydraulics (NURETH-11), Paper: 106, Popes' Palace Conference Center, Avignon, France, October 2-6, 2005 (2005).
[8-55] ORTEGA GÓMEZ, T., CLASS, A., LAHEY, R.T., JR., SCHULENBERG, T., 2008, Stability analysis of a uniformly heated channel with supercritical water, Nuclear Engineering and Design 238 (2008) 1930–1939. Also published in 2006 at ICONE-14.
[8-56] AMBROSINI, W., SHARABI, M., Dimensionless parameters in stability analysis of heated channels with fluids at supercritical pressures, Nucl. Eng. Des. 238, (2008) 1917–1929. Also published in 2006 at ICONE-14.
[8-57] CHATOORGOON, V., YEYLAGHI, S., LEUNG L., Benchmarking Study of Non-Dimensional Parameters For Supercritical Flow Instability, Submitted for the IAEA Benchmark on Flow Stability (2010).
[8-58] AMBROSINI, W., On the analogies in the dynamic behaviour of heated channels with boiling and supercritical fluids, Nuclear Engineering and Design, Vol. 237/11 (2007) 1164–1174.
[8-59] CHATOORGOON, V., Static Instability in Supercritical Parallel-Channel Systems, Proceedings of Int. Conf. of Nuclear Engineering, ICONE 16-48068, May 11-15, Orlando, Florida (2008).
[8-60] MARCEL, C.P., ROHDE, M., VAN DER HAGEN, T.H.J.J., Fluid-to-fluid modeling of natural circulation boiling loops for stability analysis, Int. J. Heat Mass Transfer 51 (2008) 566–575.
[8-61] MARCEL, C.P., ROHDE, M., MASSON, V.P., VAN DER HAGEN, T.H.J.J., Fluid-to-fluid modeling of supercritical water loops for stability analysis, International Journal of Heat and Mass Transfer 52 (2009) 5046–5054.
[8-62] ROHDE, M., MARCEL, C.P., T'JOEN, C., CLASS, A.G., VAN DER HAGEN, T.H.J.J., Downscaling a supercritical water loop for experimental studies on system stability, International Journal of Heat and Mass Transfer 54 (2011) 65–74.
[8-63] CHATOORGOON, V., Stability of supercritical fluid flow in a single-channel natural-convection loop. Int. J. Heat Mass Trans. 44 (2001) 1963–1972.
[8-64] CHATOORGOON, V., UPADHYE, P., Analytical Studies of Two-Phase Flow Stability in Natural-Convection Loops, 11th International Topical Meeting on Nuclear Reactor Thermal-Hydraulics (NURETH-11), Avignon, France, Oct 2-6, paper #165 (2005).
[8-65] CHATOORGOON, V., VOODI, A., FRASER, D., The Stability Boundary for Supercritical Flow in Natural Convection Loops, Part I: H2O Studies, Nucl. Eng. & Design 235 (2005) 2570–2580.

[8-66] CHATOORGOON, V. VOODI, A., UPADHYE, P., The Stability Boundary for Supercritical Flow in Natural Convection Loops, Part II: CO2 and H2 Studies, Nucl. Eng. & Design 235 (2005) 2581–2593.
[8-67] CHATOORGOON, V., Supercritical Flow Stability in Two Parallel Channels, Proceedings of ICONE14, International Conference on Nuclear Engineering, July 17-20, 2006, Miami, Florida, USA (2006).
[8-68] YI, T.T., KOSHIZUKA, S., OKA, Y., A linear stability analysis of supercritical water reactors, (I) thermal–hydraulic stability. Journal of Nuclear Science and Technology 41, 1166–1175 (2004).
[8-69] YI, T.T., KOSHIZUKA, S., OKA, Y., A linear stability analysis of supercritical water reactors, (II) coupled neutronic thermal–hydraulic stability. Journal of Nuclear Science and Technology 41 (2004) 1176–1186.
[8-70] ZHAO, J., SAHA, P., KAZIMI, M.S., 2008, Core-wide (in-phase) stability of supercritical water-cooled reactors - I: Sensitivity to design and operating conditions, Nuclear Technology Volume 161, Issue 2, February (2008) 108–123.
[8-71] ZHAO, J., SAHA, P., KAZIMI, M.S., Core-wide (in-phase) stability of supercritical water-cooled reactors - II: Comparison with boiling water reactors, Nuclear Technology, Vol. 161, Issue 2, February (2008) 124–139
[8-72] ZHAO, J., SAHA, P., KAZIMI, M.S., Coupled neutronic and thermal-hydraulic out-of-phase stability of supercritical water-cooled reactors, Nuclear Technology, Volume 164, Issue 1, October (2008) 20–33.
[8-73] CAI, J., ISHIWATARI, Y., IKEJIRI, S., OKA, Y., Thermal and stability considerations for a supercritical water-cooled fast reactor, with downward-flow channels during power-raising phase of plant startup, Nuclear Engineering and Design 239 (2009) 665–679.
[8-74] CHENG, X., YANG, Y.H., A point-hydraulics model for flow stability analysis, Nuclear Engineering and Design 238 (2008) 188–199.
[8-75] SHARABI, M.B., AMBROSINI, W., HE, S., Prediction of unstable behaviour in a heated channel with water at supercritical pressure by CFD models, Annals of Nuclear Energy, 35 (2008) 767–782.
[8-76] SHARABI, M., AMBROSINI, W., HE, S., JIANG, P.-X., ZHAO, C.-R., Transient Three-Dimensional Stability Analysis of Supercritical Water Reactor Rod Bundle Subchannels by a Computational Fluid Dynamics Code, J. Eng. Gas Turbines Power, March 2009, Volume 131, Issue 2, 022903, DOI:10.1115/1.3032437 (2009)
[8-77] HARDEN, D., BOGGS, J., Transient flow characteristics of a natural circulation loop operated in the critical region, Proc. Heat transf. Fluid mech. Inst., 38 (1964).
[8-78] LOMPERSKI, S., CHO, D., JAIN, R., CORRADINI, M.L., Stability of a natural circulation loop with a fluid heated through the thermodynamic pseudo-critical point. In: Proceedings of ICAPP'04, Pittsburgh, PA, USA, June 13–17, Paper 4268 (2004).
[8-79] JAIN, R., CORRADINI, M.L., 2006, A linear stability analysis for natural-circulation loops under supercritical conditions, Nuclear Technology, Vol. 155, September (2006) 312–323.
[8-80] JAIN, P.K., RIZWAN-UDDIN, Numerical analysis of supercritical flow instabilities in a natural circulation loop, Nuclear Engineering and Design 238 (2008) 1947–1957.
[8-81] SHARMA, M., PILKHWAL, D.S., VIJAYAN, P.K., SAHA, D., SINHA, R.K., Steady state and linear stability analysis of a supercritical water natural circulation loop, Nuclear Engineering and Design 240 (2010) 588–597.
[8-82] SHARMA M., VIJAYAN, P.K., PILKHWAL, D.S., SAHA, D., SINHA, R.K., Linear and non-linear stability analysis of a supercritical natural circulation loop, ASME Journal of Engineering for Gas Turbines and Power, October 2010, Vol. 132 / 102904-1 (2010).
[8-83] CHEN, L., ZHANG, X-R., YAMAGUCHI, H., LIU, Z-S, Effect of heat transfer on the instabilities and transitions of supercritical CO_2 flow in a natural circulation loop, International Journal of Heat and Mass Transfer 53 (2010) 4101–4111.

[8-84] SILIN V.A., VOZNESENSKY, V.A., AFROV, A.M., The light water integral reactor with natural circulation of the coolant at supercritical pressure B:500 SKDI, Nuclear Engineering and Design 144 (1993) 327–336.
[8-85] BUSHBY, S.J., DIMMICK, G.R., DUFFEY, R.B., SPINKS, N.J., BURRILL, K.A., CHAN, P.S.W., Conceptual designs for advanced, high-temperature CANDU reactors, SCR-2000, Nov.6–8, 2000, Tokyo, Paper 103 (2000).
[8-86] SHARMA M., PILKHWAL, D.S., VIJAYAN, P.K., SAHA, D., SINHA, R.K., Steady state behaviour of natural circulation loops operating with supercritical fluids for open and closed loop boundary conditions, available online in Heat Transfer Engineering Journal, Taylor and Francis group, Dec. (2011).
[8-87] CHURKIN, A.N., YAGOV, P.V., "Computer code TEMPA-SC: Simulation of Thermo-Hydraulic Processes in the Core of VVER SCP Reactor", 4th International Symposium on Supercritical Water-Cooled Reactors, March 8–11, 2009, Heidelberg, Germany, Paper No. 02, http://www.hplwr.eu/public/Symposium/Proceedings_01-20.zip
[8-88] CHURKIN, A.N., MAKHIN, V.M., SHCHEKIN, I.G., YAGOV, P.V., Flow stability investigation in the core of reactors with supercritical water, Seminar 'THERMALPHYSICS-2008', 15-17 October 2008, IPPI, Obninsk, Collected abstracts (2008) 72–74.
[8-89] DOGAN, T., KAKAC, S., VEZIROGLU, T.N., Analysis of forced-convection boiling flow instabilities in a single- channel upflow system, Int. J. Heat and fluid flow 4 (1983) 145
[8-90] SHARMA, M., VIJAYAN, P.K., PILKHWAL, D.S., SAHA, D., Experimental and Theoretical investigations on the steady state and stability behaviour of natural circulation systems operating with supercritical fluid, Technical meeting on Heat Transfer, thermal hydraulics and system design for supercritical pressure water cooled reactors, TM22, 5–8 July 2010, Pisa, Italy.
[8-91] MOLFESE, E., AMBROSINI, W., FORGIONE, N., VIJAYAN, P.K., SHARMA, M., Study of Supercritical Carbon Dioxide Natural Circulation by The Use of CFD Codes, The 14th International Topical Meeting on Nuclear Reactor Thermal Hydraulics (NURETH-14), Log Number: 560, Hilton Toronto Hotel, Toronto, Ontario, Canada, September 25–29, 2011.
[8-92] STAR-CCM+, web-site http://www.cd-adapco.com/products/STAR-CCM_plus/
[8-93] Fluent, FLUENT 6.3.26 User Guide (2006).
[8-94] NIST, Reference Fluid Thermodynamic and Transport Properties – REFRPROP. Lemmon, E.W., McLinden, M.O., Hurber, M.L. (Eds.), NIST Standard Reference Database 23 (Software and Source), V. 7.0, U.S. Department of Commerce (2002).

9. THERMOHYDRAULICS CODE TESTING FOR SCWR CONDITIONS

The development and verification of thermal-hydraulic codes is one of the most urgent tasks to prepare design tools for Super-Critical Water Cooled Reactors (SCWRs). The knowledge of temperature of fuel rod cladding and of the reactor structures in different operational states and accident conditions is essential for evaluating reactor design and safety and choosing existing materials or developing new ones for application in supercritical water. Needless to say, these aspects considerably affect the feasibility of proposed SCWR projects.

Within this CRP, it was proposed to make the first step in thermal-hydraulic code testing, starting with codes adopted or developed by CRP participants. The testing was aimed at comparing the results of different codes and computational methods, with the purpose to reveal the effect of differences in modeling assumptions on the obtained results.
In particular, two Code Testing Benchmarks (CTBs) were prepared:

- CTB No.1 'Steady state Flow in a Heated Pipe', aimed at assessing the code capabilities in the prediction of heat transfer against experimental data;
- CTB No.2 'Flow Stability', aimed at performing a code-to-code comparison of flow stability predictions in a simple heated channel.

These Code Testing Benchmarks had not the purpose to be qualified as Standard Problems, e.g., as specified in OECD-CSNI International Standard Problem Procedures (CSNI report No. 17 - Rev. 4, March 2004). In particular, the two Code Testing Benchmarks performed within the CRP had limitations especially in the short time allowed for the activity and in the difficulty to organize specific meetings to discuss the results of the calculations. Nevertheless, they provided interesting information on code predictions, resulting very valuable for future developments and fulfilling the intended goal of letting the Participants compare their own codes and models and discuss the obtained results.

This Section describes the specifications of the Code Testing Benchmarks, the results obtained by the Participants with different code and models and the main conclusions obtained by the work.

9.1. CODE TESTING BENCHMARK NO.1 'STEADY STATE FLOW IN A HEATED PIPE'

9.1.1. Participants and codes

Ten participants took part in the computation of CTB No.1:

AECL – Atomic Energy of Canada Limited, Canada;
BARC – Bhabha Atomic Research Centre, India;
CIAE – China Institute of Atomic Energy, China;
GP – Experimental and Design Organization GIDROPRESS (OKB GIDROPRESS), Russia;
JRC – European Commission DG Joint Research Centre, the Netherlands;
KAERI – Korea Atomic Energy Research Institute, Republic of Korea;
MP – cooperation of the University of Pisa and McMaster University;
SJTU – Shanghai Jiao Tong University, China;
UMAP – cooperation of the University of Manchester, the University of Aberdeen and the University of Pisa;
VTT – VTT Technical Research Centre of Finland, Finland.

The above abbreviations of test problem participants are used subsequently in the legend of the figures.

Participants	Name of Participants	Codes	
AECL	T. Beuthe, B. Hanna	CATHENA	Subchannel and system codes
GP	P.V. Yagov, A.N. Churkin	TEMPA-SC	
JRC	L. Ammirabile	COBRA-EN	
MP	F. Fiori, D. R. Novog, A. Petruzzi	TRACE5.0	
		RELAP5/Mod3.3	
VTT	J. Kurki, M. Hänninen	APROS	
BARC	A.M. Vaidya, P.K. Vijayan, N.K. Maheshwari	NAFA	CFD codes
CIAE	Z. Minfu, Y. Chen	ANSYS CFX	
KAERI	B.-H. Cho	Fluent	
SJTU	H. Gu, X. Cheng	Fluent	
		SIMPLE2D	
UMAP	M. Mucci, W. Ambrosini, J.D. Jackson, S. He	SWIRL	

After the completion of computational step, JAEA (Japan) joined the Benchmark in the stage of preparation of Section 9.1. The results presented by Dr. Kazuyuki Takase are represented by separate figures at the end of Sub-section 9.1.4.

9.1.2. Specifications for the code testing benchmark[5]

9.1.2.1. Objective of the benchmark

An important objective of the IAEA CRP on Heat Transfer Behaviour and Thermohydraulics Code Testing for SCWRs is to test analysis methods for SCWR thermohydraulic behaviour and to identify code development needs. The benchmark problem in this proposal consists of a simple steady-state flow of water in a heated pipe at supercritical conditions. While the intention of the CRP is to define and perform new tests, it is useful to use one of the numerous tests that are reported in the open literature to test certain analysis methods and codes. Two cases are proposed for which adequate experimental data exist:
Case 1 – Upward flow in a heated pipe;
Case 2 – Upward and downward flow in a heated pipe of a different geometry.

9.1.2.2. Case 1: Upward flow in a heated pipe

The data for this case consist of heat transfer measurements (wall temperature) in a vertical circular pipe with uniform heating and are reported in [9-1]. A schematic of the test section is shown in Fig. 9.1. The geometric parameters and boundary conditions are presented in Table 9.1. Figure 9.2 shows the experimental results.

The purpose of this exercise is to compare code predictions to the experimental measurements. 'Tweaking' of the modelling approach (e.g., turbulence model used in CFD codes) is permitted to get the best agreement with test data.

[5] Prepared by OKB "GIDROPRESS" (Russia) and AECL (Canada)

9.1.2.3. Case 2: upward and downward flow in a heated pipe

It was a 'blind' exercise in which the same modelling approach that is chosen in Case 1 was applied without any modification or tweaking. This exercise uses test data where deteriorated heat transfer is observed only in the upward direction and should provide a good challenge for the modelling approach that was chosen for Case 1. The test Section schematic is shown in Fig. 9.3 while the geometric and test parameters are shown in Table 9.2.

9.1.2.4. Computational parameters adopted for comparison

For both test cases, the following parameters were presented:

$\Delta p(l) = (p(l) - p_{out})$	pressure difference axial distribution, Pa;
$T_b(l)$	bulk water temperature axial distribution, ºC;
$\rho_b(l)$	bulk water density axial distribution, kg/m³;
$h_b(l)$	bulk water enthalpy axial distribution, J/kg;
$T_w(l)$	inner pipe temperature axial distribution, ºC;
α	heat transfer coefficient axial distribution, W/(m² K).

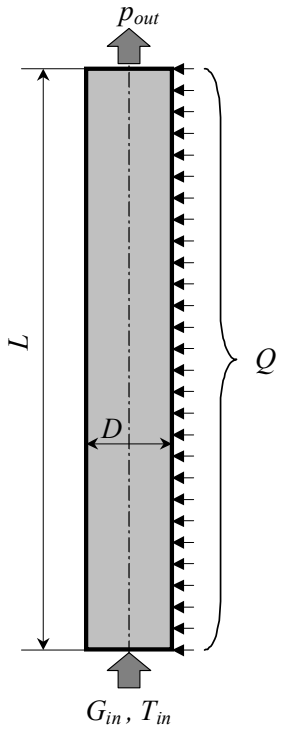

Nomenclature:

D – inner pipe diameter, m
G – mass flow rate, kg/s
L – pipe length, m
p – pressure, Pa
Q – heat power, W
T – temperature, ºC

Indexes:

in – inlet
out – outlet

FIG. 9.1. Test section schematic for Case 1.

TABLE 9.1. CASE 1 GEOMETRIC AND TEST PARAMETERS

Parameter	Value*
Pipe diameter, m	0.01
Pipe length, m	4.0
Inlet mass flow rate, kg/s (Inlet mass flux, kg/m^{2}s)	$1.178 \cdot 10^{-1}$ (1500)
Inlet temperature, ºC	352
Outlet pressure, MPa	24.05
Heat flux, kW/m²	884

* - from [9-1]

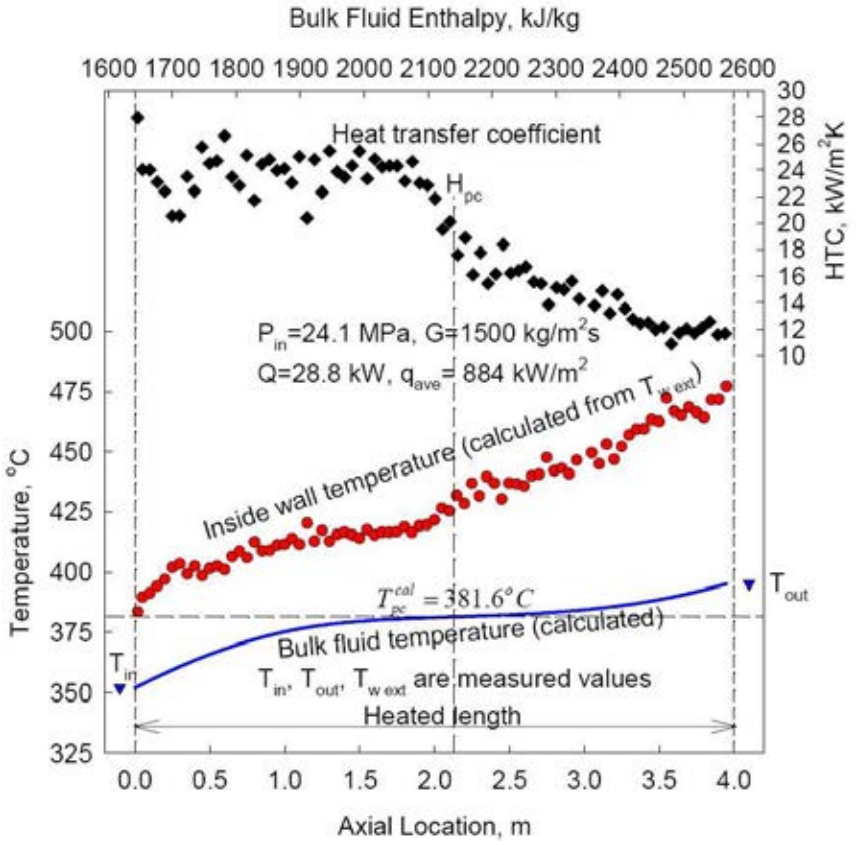

FIG. 9.2. Experimental data for Case 1 [9-1].

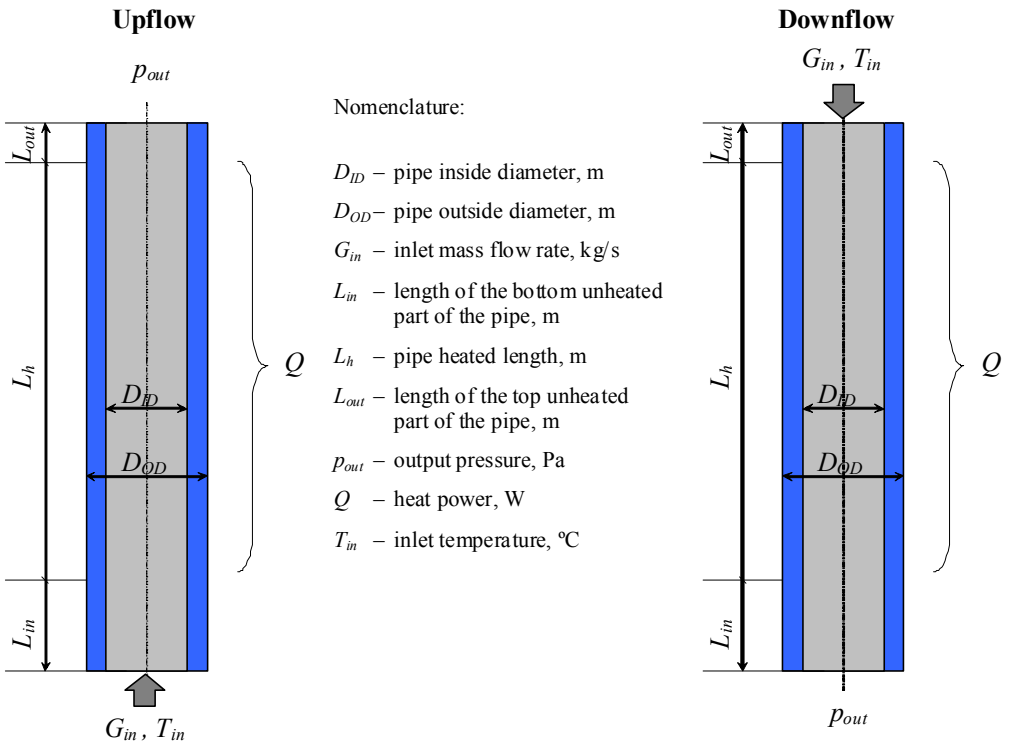

FIG. 9.3. Test section schematic for Case 2.

TABLE 9.2. CASE 2 GEOMETRIC AND TEST PARAMETERS

Parameter	Value*	
	Upflow	Downflow
Pipe inside diameter, mm	25.4	
Pipe outside diameter, mm	38.1	
Pipe inlet length, m	0.63	
Pipe heated length, m	2	
Pipe outlet length, m	0.16	
Inlet mass flux, kg/m^{2}s	820 (380 for variant 2)**	892 (380 for variant 2)
Inlet temperature, ºC	250 (200 for variant 2)	
Outlet pressure, MPa	25	
Heat flux, kW/m²	400	

* In accordance with [9-2].
** Variant 1 – for the core design; variant 2 – flow direction effect on heat transfer in a vertical tube. The test section was lagged with 63.5 mm (2½ inch) thick mineral-wool insulation.

Two variants were considered in Case 2. Variant 1 was chosen for the reason that parameters of experimental conditions were mostly similar to those expected in proposed SCWR projects. Variant 2 was chosen for addressing a condition in which there is a well-defined area with deteriorated heat transfer during upward flow in comparison with downward flow.

9.1.3. Description of the computer codes

9.1.3.1. Subchannel and system codes

9.1.3.1.1. AECL. CATHENA code

The CATHENA code was developed by Atomic Energy of Canada Limited (AECL). The acronym CATHENA stands for Canadian Algorithm for THErmalhydraulic Network Analysis. The thermalhydraulic code CATHENA was developed primarily for the analysis of postulated upset conditions in CANDU reactors; however, the code has been qualified for a wider range of applications for the modeling of experimental thermalhydraulic test facilities. CATHENA uses a transient, one-dimensional two-fluid representation of two-phase flow in piping networks. An overview of the CATHENA thermalhydraulic code numerical methods and constitutive relations is given in [9-3].

The CATHENA code includes thermophysical properties for both light water (H_2O) and heavy water (D_2O). The standard thermophysical property functions in CATHENA are based on functional fits [9-4] to generate functions for H_2O and D_2O. For the latest code version (MOD-3.5d/Rev 3), an alternative set of light water property fits have been included extending their application into the supercritical pressure region (to 100 MPa). The extended thermodynamic property functions for light water included in the MOD-3.5d/Rev 3 code version are based on the International Standard generating functions [9-5], using the same fitting methodology.

The code uses a staggered-mesh, one-step, semi-implicit, finite-difference solution method, which is not transit time limited. In the numerical solution method used, a linear system of finite-difference equations is constructed as a result of the time and spatial integration of the partial differential mass, momentum and energy conservation equations over finite time steps and finite space (nodes or links). In the CATHENA numerical method, the time step is selected based on the rates of change of a set of thermalhydraulic and numerical solution parameters.

The CATHENA code also includes system models for components such as pumps, valves, emergency coolant injection (ECI) accumulator, user definable junction resistances, and separators. Also included in the set of system models is a point reactor kinetics model, a break-discharge model, and separators. An extensive control system modeling capability is also provided for complete loop simulations and a general code interface to external executable programs is provided through the PVM (Parallel Virtual Machine) data passing software.

The code holder of CATHENA is the Thermalhydraulics Branch at Chalk River Laboratories, AECL.

9.1.3.1.2. GP. TEMPA-SC code

Computer code TEMPA-SC [9-6] and [9-7] has been developed in OKB GIDROPRESS for steady-state and transient thermal-hydraulic analyses of supercritical water cooled FA. The code is based on the TEMPA-1F code [9-8].

TEMPA-SC mathematical model is based on the 3D conservation equations written in an integral form for the sets of control volumes fixed in the space. These equations are: mass conservation, energy conservation and momentum conservation.

Discretization is typical of the sub-channel analysis. The cross section of the FA is divided into sets of parallel channels. The set of main channels (Fig. 9.4a) is used for the mass, energy and longitudinal momentum conservation equations. The set of link channels (Fig. 9.4b) is used for a transverse momentum conservation equation. A link channel connects two main channels. For example, the link channel ij connects main channel i and main channel j (Fig. 9.4).

In the longitudinal direction the channels are divided into layers (Fig. 9.5). The set of main layers is used for mass, energy and transverse momentum conservation equations. The set of link layers, placed between main layers, is used for a longitudinal momentum equation.

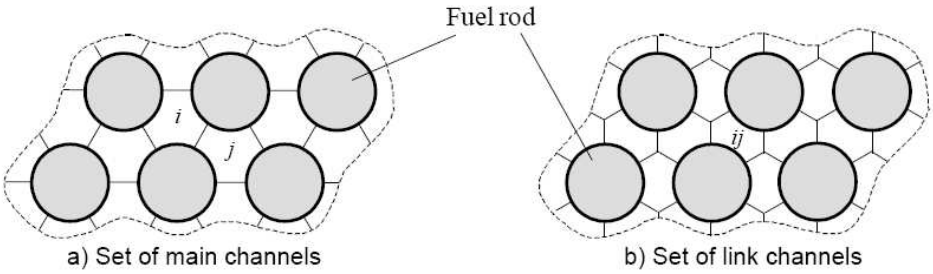

FIG. 9.4. Fragmentation of FA cross-section.

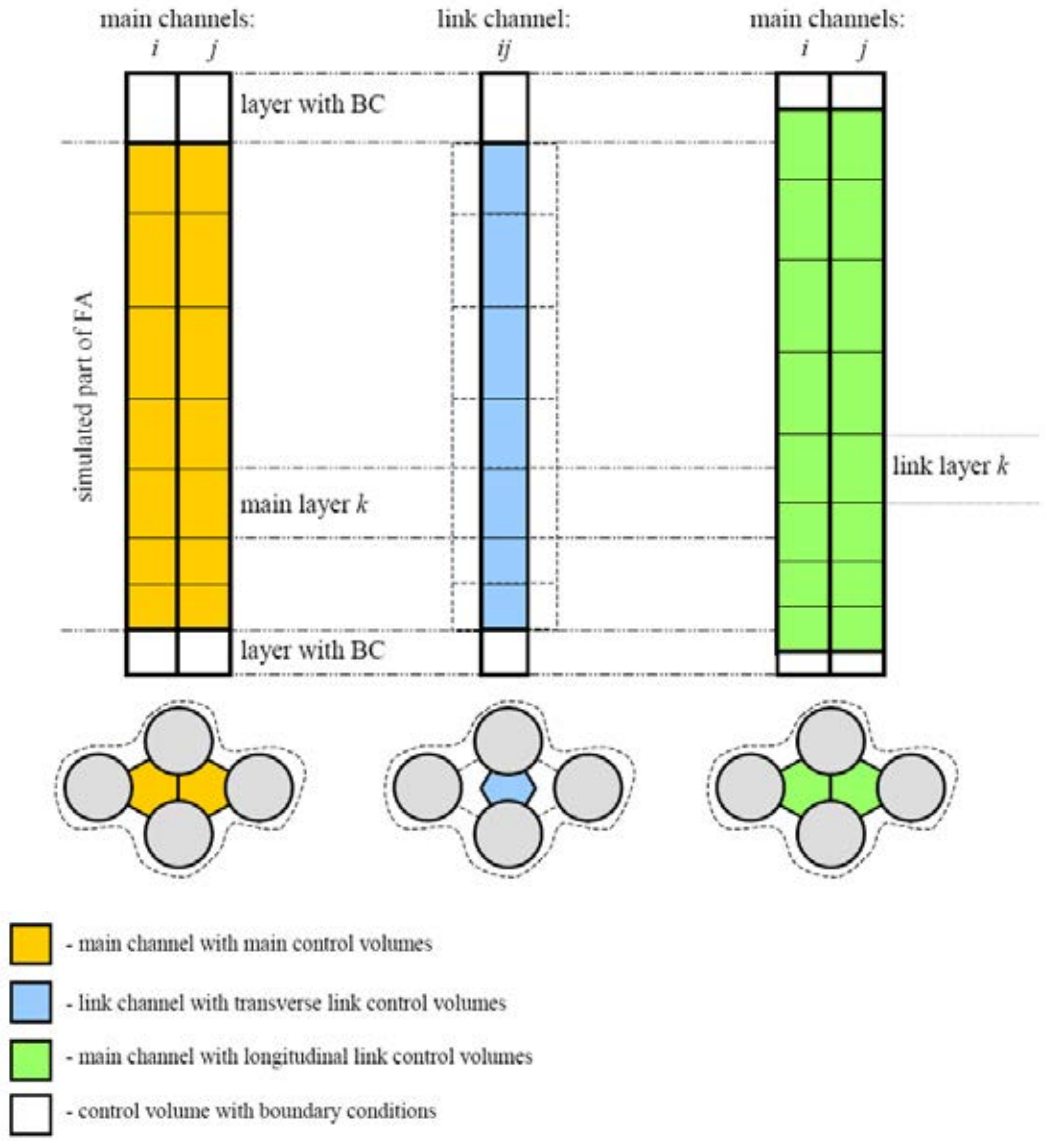

FIG. 9.5. Fragmentation of the FA in longitudinal direction.

The intersections of the channels and layers form three sets of control volumes:

$\{V_n\}$ - set of control volumes for mass and energy conservation equations;

$\{\tilde{V}_n\}$ - set of control volumes for longitudinal momentum conservation equation;

$\{\hat{V}_n\}$ - set of control volumes for transverse momentum conservation equations.

Inlet boundary conditions are:

- pressure or flowrate;
- enthalpy or temperature.

Outlet boundary conditions are:

- pressure;
- enthalpy or temperature.

The user can select different correlations for the calculation of the friction factor and heat transfer coefficients (HTC). Five correlations of HTC were used For the Benchmark:
HTC_0[6]: Dittus-Boelter:

$$Nu = 0.023\,\mathrm{Re}_{\mathrm{f}}^{0.8}\,\mathrm{Pr}_{\mathrm{f}}^{0.4} \tag{9-1}$$

HTC_1: Kirillov et al. [9-9]:

$$Nu = Nu_0\left(\frac{\bar{c}_{\mathrm{p}}}{c_{\mathrm{pf}}}\right)^{\mathrm{n}} \cdot \left(\frac{\rho_{\mathrm{w}}}{\rho_{\mathrm{f}}}\right)^{\mathrm{m}} \cdot \varphi(\mathrm{K}) \tag{9-2}$$

where $\mathrm{K} = \left(1 - \frac{\rho_{\mathrm{w}}}{\rho_{\mathrm{f}}}\right)\mathrm{Gr}\,\mathrm{Pr}^{-2}$;

HTC_2: Jackson and Fewster [9-10]:

$$Nu = 0.0183\,\mathrm{Re}_{\mathrm{f}}^{0.82}\,\overline{\mathrm{Pr}}^{0.5}\left(\frac{\rho_{\mathrm{w}}}{\rho_{\mathrm{f}}}\right)^{0.3} \tag{9-3}$$

HTC_3: Jackson [9-11]:

$$Nu = 0.0183\,\mathrm{Re}_{\mathrm{f}}^{0.82}\,\overline{\mathrm{Pr}}^{0.5}\left(\frac{\rho_{\mathrm{w}}}{\rho_{\mathrm{f}}}\right)^{0.3}\left(\frac{\overline{c_{\mathrm{p}}}}{c_{\mathrm{pf}}}\right)^{n}, \tag{9-4}$$

HTC_4: Krasnoshchekov and Protopopov [9-12]:

$$Nu = Nu_0\left(\frac{\mu_{\mathrm{f}}}{\mu_{\mathrm{w}}}\right)^{0.11}\left(\frac{\lambda_{\mathrm{f}}}{\lambda_{\mathrm{w}}}\right)^{-0.33}\left(\frac{\overline{c_{\mathrm{p}}}}{c_{\mathrm{pf}}}\right)^{0.35} \tag{9-5}$$

HTC_5: Krasnoshchekov et al. [9-13]:

$$Nu = Nu_0\left(\frac{\rho_{\mathrm{w}}}{\rho_{\mathrm{f}}}\right)^{0.3}\left(\frac{\overline{c_{\mathrm{p}}}}{c_{\mathrm{pf}}}\right)^{n} \tag{9-6}$$

[6] The number of HTC correlation ID is used to identify the OKB "Gidropress" run of the test. The last numerical digit in the run ID (for example: GP2101) is the ID of HT correlation.

For the calculation of the friction factor the Kirillov [9-9] correlation was used:

$$\xi/\xi_0 = \left(\frac{\bar{\rho}}{\rho_f} \right)^{0.74} \tag{9-7}$$

where ξ_0 is the isothermal friction factor.

Two thermophysical properties of water ρ and h are solutions of the balance equations. Two different methods can be used to calculate p and T. The first method uses tables of properties ρ=ρ(p,T) and h=h(p,T). This method applies a special algorithm for finding p and T on the basis of the known values of ρ and h. The ranges of key parameters are: 23 MPa < p < 49 MPa; 0 < T < 800 ºC. This method has high accuracy, but significantly increases the calculation time.

A second method is based on approximation of the thermophysical properties of water. This method is faster than the first method, but its ranges of key parameters are narrower: 23.5 MPa < p < 26 MPa; 20º C < T < 800 ºC. The second method is also less accurate than the first method.

9.1.3.1.3. JRC. COBRA-EN Code

The benchmark exercise was analysed using the subchannel thermalhydraulic code COBRA-EN [9-14].

The COBRA-EN code belongs to the series of the COBRA (COolant Boiling in Rod Arrays) subchannel analysis computer programs which were originally developed by Pacific Northwest Laboratories (PNL). It derives from the COBRA-3C/MIT code and was upgraded according to more refined and consistent features of other computer codes (COBRA-IV-I and, mainly, VIPRE-01), evolved from the original COBRA-3C sub-channel analysis code.

The COBRA-EN code is based on a two-phase homogeneous model which includes the conservation equations of the mixture mass, energy and momentum vector in axial and lateral directions, i.e., three balance equations.

Two solution schemes are available for the three-equation homogeneous model: an implicit (iterative) algorithm called 'pressure gradient' solution (similar to the 'cross-flow' solution of COBRA-3C and COBRA-IV-I) and an implicit solution based on a Newton-Raphson iteration for nonlinear systems. In the former scheme, limited to positive axial flows, the axial and lateral momentum equations are combined into a single equation containing the axial pressure gradients instead of the cross-flows. The Newton-Raphson scheme adjusts, through the local pressures, the axial flows and the cross-flows to force continuity of the mixture mass.

Temperature-dependent physical properties of both fuel and clad materials are possible.

A variable axial mesh size and the choice between the American Engineering (AE) and International (SI) unit systems for both input and output are allowed.

The code can perform two kinds of analyses: the (core) analysis of an assembly of open or separated coolant channels, each containing a bundle of fuel rods and represented by lumped thermal-hydraulic parameters and by an 'average' fuel pin, and the (sub-channel) analysis of an array of individual fuel rods which partition the coolant flow area into small sub-channels.

COBRA-EN is also equipped with a Heat Transfer Model which consists of a heat conduction model inside the rod and of a heat transfer model between rod and coolant. The fuel rod heat conduction model computes the temperature distribution in the cylindrical fuel rod at each axial level. Axial heat conduction is neglected.

Heat transfer and friction factor correlation for supercritical water conditions

Several experimental studies have reported the inadequacy of the Dittus-Boelter correlation above the critical pressure of water and have proposed alternative correlations. The heat-transfer correlations for water above the critical point available in the literature are derived empirically based essentially on experimental results with circular tubes. A literature review of those correlations was performed in the framework of the European High Performance Light Water Reactor (HPLWR) project [9-15]. The correlations appear generally as a modified Dittus-Boelter equation in the general form:

$$Nu = C \cdot \mathrm{Re}_X^m \cdot \mathrm{Pr}_X^n \cdot F \tag{9-8}$$

where:

- the coefficient C and both the exponents n and m are determined using experimental data;
- Nu, Re, Pr are the Nusselt, Reynolds and Prandtl numbers defined at different reference temperatures X;
- F is a correction factor.

Among the different correlations, the Bishop correlation [9-15] seems to be the most suitable for safety design studies of the HPLWR. It is based on experiments conducted with supercritical water flowing upward inside tubes and annuli within the range of flow and operating parameters which are expected during normal plant working conditions (Table 9.3).

TABLE 9.3. RANGE OF VALIDITY OF BISHOP'S CORRELATION [9-15]

Pressure	22.8÷27.6 MPa
bulk-fluid temperature	282÷527 ºC
mass flux	651÷3662 kg/m^{2}s
heat flux	0.31÷3.46 MW/m^2

The data for heat transfer in tubes were generalized using the following correlation:

$$Nu = 0.0069 \cdot \mathrm{Re}_B^{0.9} \cdot \mathrm{Pr}_B^{0.66} \cdot \left(\frac{\rho_w}{\rho_B}\right)^{0.43} \cdot \left(\frac{\overline{C}_P}{C_P}\right)^{0.66} \cdot \left(1 + \frac{2.4 \cdot D}{x}\right) \tag{9-9}$$

where x is axial location along the heated length and the subscript B stands for bulk flow.

The Bishop correlation can predict heat transfer well in the whole range of flow and operating parameters of the HPLWR. In addition it can also compute conservatively the conditions near the pseudo-critical point [9-15].

Based on these considerations, the Bishop correlation was selected to be implemented in COBRA-EN.

Based on the review study of Cheng and Schulenberg [9-15], the following equation was implemented in COBRA-EN for the friction factor in turbulent flow at supercritical pressures:

$$f = f_0 \cdot \left(\frac{\rho_w}{\rho_B} \right)^{0.4} \tag{9-10}$$

where:

$$f_0 = \left(1.82 \cdot \ln\left(\frac{\mathrm{Re}}{8} \right) \right)^{-2} \tag{9-11}$$

9.1.3.1.4. MP. RELAP5/Mod3.3 and TRACE5.0

The RELAP5 [9-17] and TRACE5.0 [9-18] are light water reactor transient analysis codes developed for the U.S. Nuclear Regulatory Commission (NRC) for use in rulemaking, licensing calculations, evaluation of operator guidelines, and as a basis for nuclear plant analyser. Both codes are capable to perform LOCA, SBLOCA and a wide range of operational transient calculations.

Moreover, both codes are one-dimensional and use transient hydrodynamic models, with unequal temperature and unequal velocity assumption for vapour/gas and liquid phase. The two-fluid balance equations are formulated in terms of volume and time-averaged parameters of the flow, phenomena such as heat transfer and wall drag are formulated in terms of bulk properties using empirical transfer coefficient formulations. The system model is solved numerically using a semi-implicit finite-difference technique.

9.1.3.1.5. VTT. APROS code

APROS [9-19] is a general-purpose process system analysis code, including multiple thermal-hydraulic solvers among other calculation models (see also http://www.apros.fi/). For the benchmark under discussion, the one-dimensional separate two-fluid model (the six-equation model) was utilized.

The six-equation model is based on the one-dimensional conservation principles of mass, momentum and energy, separately for both phases. The solved variables are phase velocities, phase total enthalpies, void fraction and pressure, which is assumed constant over the cross-sectional flow area. At supercritical pressures, a numerical ‘pseudo phase transition’ is modelled, causing the numeric void fraction to change from zero to unity as the enthalpy passes the pseudo-critical line. This transition is done in order to ensure that the fluid is assigned to the correct numeric phase when the pressure drops below the critical point.

9.1.3.2. CFD codes

9.1.3.2.1. BARC. NAFA code

NAFA [9-20] is an acronym for Numerical Analysis of Flows in Axi-symmetric Geometries. NAFA is indigenously developed at BARC for computational investigation of heat transfer and pressure drops in a wide variety of fluid flows in pipe. NAFA can solve an axi-symmetric laminar/ turbulent flow with/ without heat transfer. For turbulent flows, the standard k-ε model is implemented with standard wall functions and default model constants. Full Navier-Stokes equations are solved so that the formulation becomes valid for variable properties. The thermophysical properties, i.e. density, specific heat, conductivity and viscosity can be given in the tabular form as a function of temperature. Piece-wise linear interpolation is used for all the properties. A control volume based discretization scheme is used for

discretizing the equations (which are (i) pressure correction equation, (ii) momentum equations in radial and axial directions, (iii) energy equation and (iv) equations for turbulent kinetic energy and its dissipation rate). To solve the set of equations, the segregated solution procedure, according to *S*emi *I*mplicit Method for Pressure Linked Equations (SIMPLE) algorithm, is used. Alternating direction Tri Diagonal Matrix Algorithm (TDMA) solver is used for solving the implicit equations. Power law as well as 2nd order upwind scheme is used for convection modelling.

The code incorporates four boundary conditions namely 'VELOCITY INLET', 'WALL', 'AXIS' and 'PRESSURE OUTLET' as shown in Fig. 9.6. For laminar flow, at WALL boundary, the no-slip condition is used for axial momentum equation. For turbulent flow, at WALL boundary, standard wall functions are implemented. A gravity term is incorporated in momentum equation.

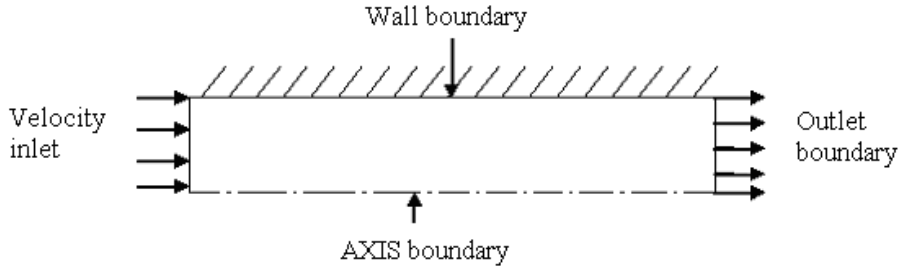

FIG. 9.6. Computational domain and boundary conditions.

To test the adequacy of the code to predict supercritical heat transfer, it was validated with Yamagata's experimental data. The thermophysical property variation with temperature is obtained from NIST website (http://webbook.nist.gov/chemistry/fluid/).

9.1.3.2.2. CIAE. ANSYS CFX code

The general purpose Computational Fluid Dynamics (CFD) software CFX developed by ANSYS Inc. was used in dealing the benchmark problem 'Pipe with heating' was solved.

The Shear-Stress-Transport (SST) model was selected to simulate the flow features. Through many calculations using various grids, it was found that the SST model is able to reproduce the heat transfer behaviour of supercritical water, but it is sensitive to the grid, and needs a suitable grid to match experimental data. In the grid which provide the best result, the first layer spacing near the wall was between 1~5 y^+, as shown in Fig. 9.7.

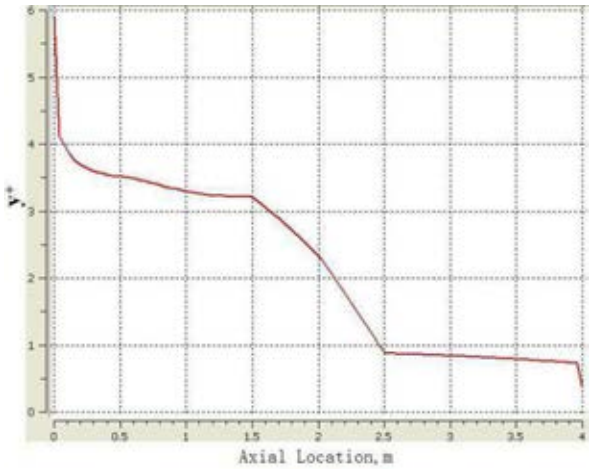

FIG. 9.7. Variation curve of y+ .

Comparing Fig. 9.7 with Fig. 9.8, it can be seen that the value of y^+ is related to the state of supercritical water: when it is subcooled water, $y^+ \approx 3.5$; when it is superheated steam, $y^+ \approx 1$; and when it round the pseudo-critical temperature, y^+ decreases rapidly from 3 to 1.

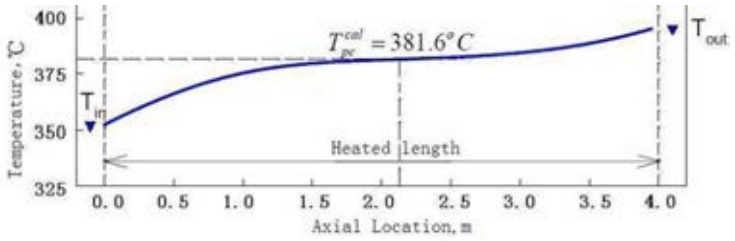

FIG. 9.8. Variation curve of bulk fluid temperature.

9.1.3.2.3. KAERI. Fluent Ver. 6.3 code

The commercial CFD code, Fluent v. 6.3 [9-21] has been used for the computation. A steady and 2D axi-symmetric flow field was assumed for computational simplicity. The grid sizes in the axial and radial directions were small enough to achieve grid independency. Grid sensitivity has been tested with nodes numbers ranging from 77000 to 212300. The total cell numbers for the case 1 and 2 were 85000 and 193000, respectively. The distance between the first calculating node and the wall was chosen to be small enough to have y^+ nearly equal to 0.5 in order to meet the requirements of the low-Reynolds number turbulence models. Isobaric fluid properties of supercritical water from the NIST table have been incorporated in Fluent as a user defined function. To obtain a fully developed flow field before the heated region, an additional unheated length of 50 cm was added to the domain before and after the heated region. The heated wall was defined as a constant heat flux and the unheated wall as an adiabatic wall. Constant mass flow with a uniform temperature was used for the inlet boundary condition and a fixed outlet pressure for the outlet boundary condition.

Among the turbulence models which are embedded in the Fluent code, the following models were selected for the calculations: ReNormalization Group k-ε model with an enhanced wall treatment (RNG), Reynolds Stress Model with an enhanced wall treatment (RSM), standard k-ω model (SKW), shear-stress-transport k-ω model (SST), six low-Reynolds number models such as Abid (ABD), Lam-

Bremhorst (LB), Launder-Sharma (LS), Yang-Shih (YS), Abe-Kondo-Nagano (AKN) and Chang-Hsieh-Chen (CHC), and V^2-f (V2F) model.

9.1.3.2.4. SJTU. Fluent and SIMPLE2D code description

The Fluent and an in-house CFD code named SIMPLE2D were used in this application. Fluent is a well known commercial CFD program; it is applied in a wide range of industrial applications. The SIMPLE2D is an in-house CFD code which is based on the finite control volume method. The QUICK scheme is used to discretize the convection terms. And the central differencing is used for the diffusion terms. The SIMPLE algorithm is used to solve the pressure-velocity coupling equation system. The algebraic equations are solved with the Alternating Direction Implicit (ADI) method. The code calculates the thermal physical property through lookup table. The SIMPLE2D have a flexible structure which allows for further development. However, currently it is only capable to deal with steady-state 2D flows.

9.1.3.2.5. UMAP. SWIRL code

The 'in-house' CFD code SWIRL [9-22] has been used to carry out the simulations for the benchmark 'Pipe with heating'. The code was set up to solve the discretized RANS equations for an axi-symmetric geometry. The equations are discretized using on the conservative finite volume method with a *staggered mesh* arrangement and a *coupled solver*. The energy equation is expressed in terms of *enthalpy*.

Convergence is checked on the value of the residual of each transport equation: these terms should progressively decrease until annihilate. The iterations are stopped when each residual is lower than a selected value. The scheme adopted for generation of control volumes is *grid point centred*; i.e. the control volume faces are first defined and then the grid points are placed at the centre of the control volume. The QUICK scheme is used to approximate the convection terms in the momentum equations and the UPWIND scheme is used for the other transport equations for reasons of numerical stability.

The *Semi-Implicit Method for Pressure-Linked Equations* SIMPLE scheme was used for coupling the pressure and the velocity fields involved in momentum equation. The resulting five-point coefficient matrix system is solved iteratively using the line-by-line direct method *Tri Diagonal Matrix Algorithm* TDMA.

9.1.4. Results of calculations

9.1.4.1. System codes

9.1.4.1.1. Case 1

Figures 9.9–9.14 show computational results of the subchannel and system codes: CATHENA (AECL), TEMPA-SC (GP), COBRA-EN (JRC), RELAP5/Mod3.3 (MP), TRACE5.0 (MP) and APROS (VTT). Results of only two OKB GIDROPRESS runs (GP1101 and GP1104), which better describe the experimental data on heat-transfer coefficient and wall temperature, are presented in Fig. 9.10 and Fig. 9.11. The list of the compared results is given in Table 9.4.

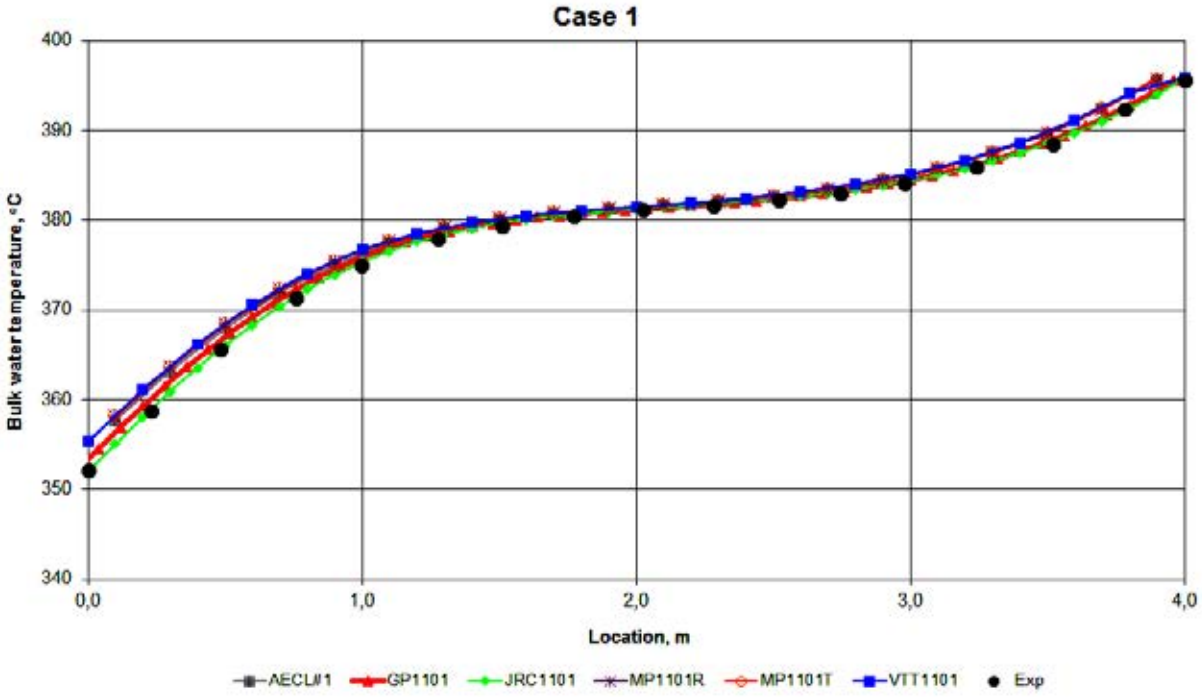

FIG. 9.9. Bulk water temperature axial distribution.

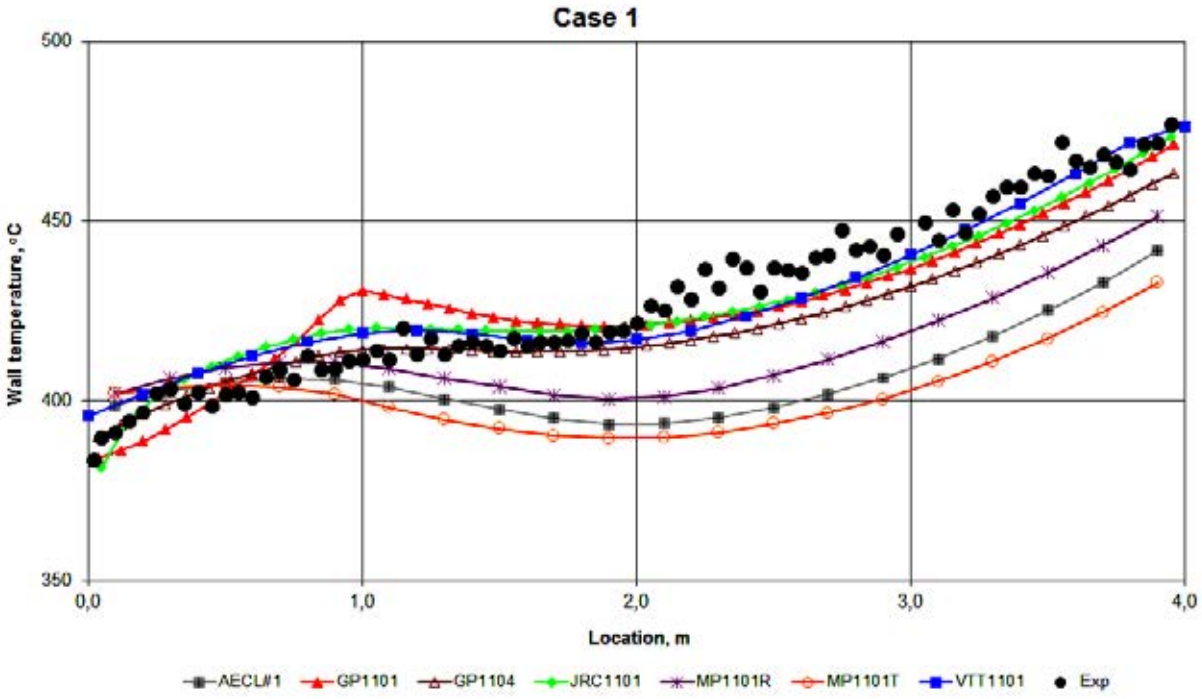

FIG. 9.10. Wall temperature axial distribution.

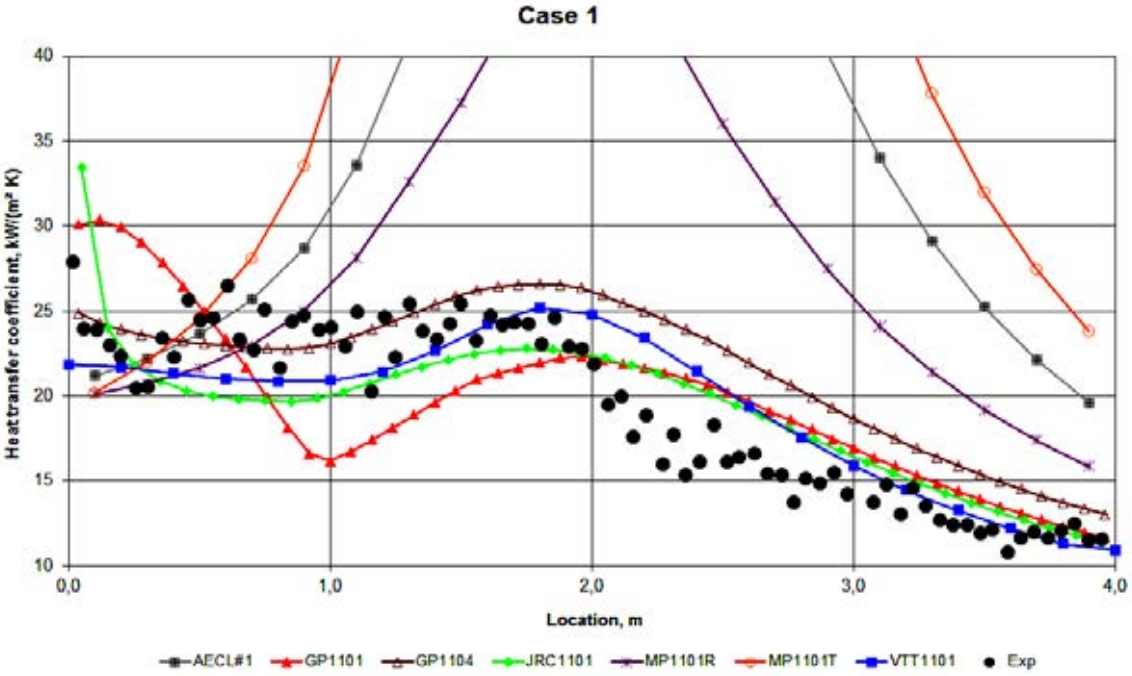

FIG. 9.11. Heat transfer coefficient axial distribution.

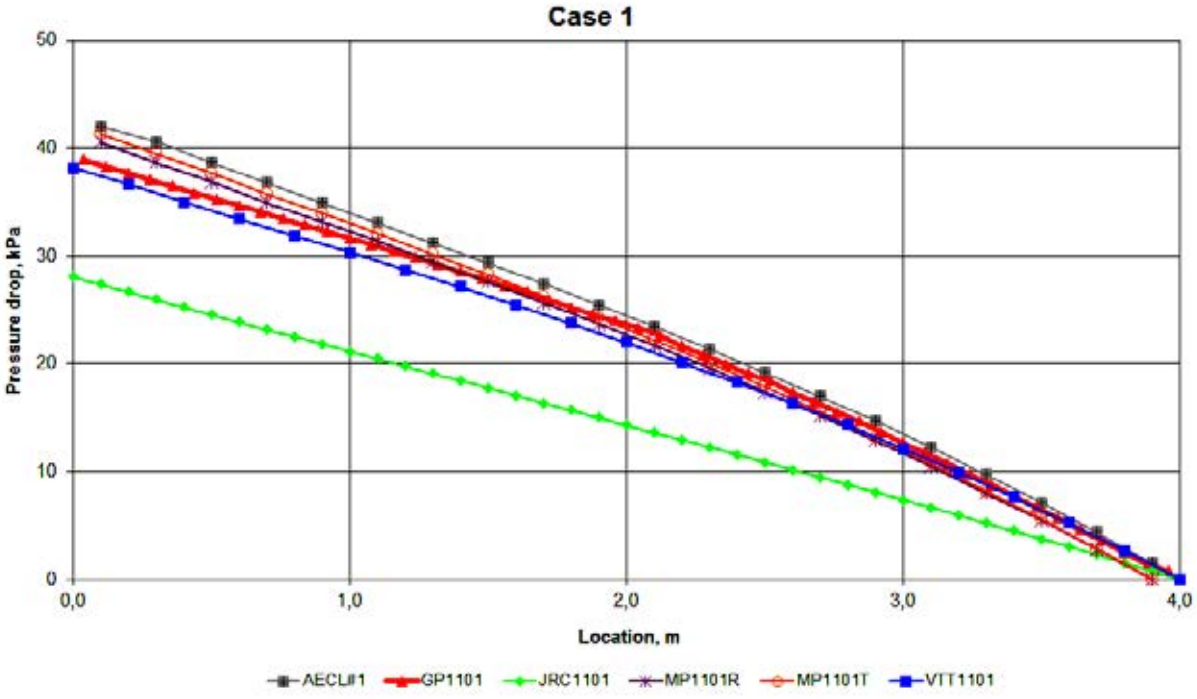

FIG. 9.12. Pressure drop axial distribution.

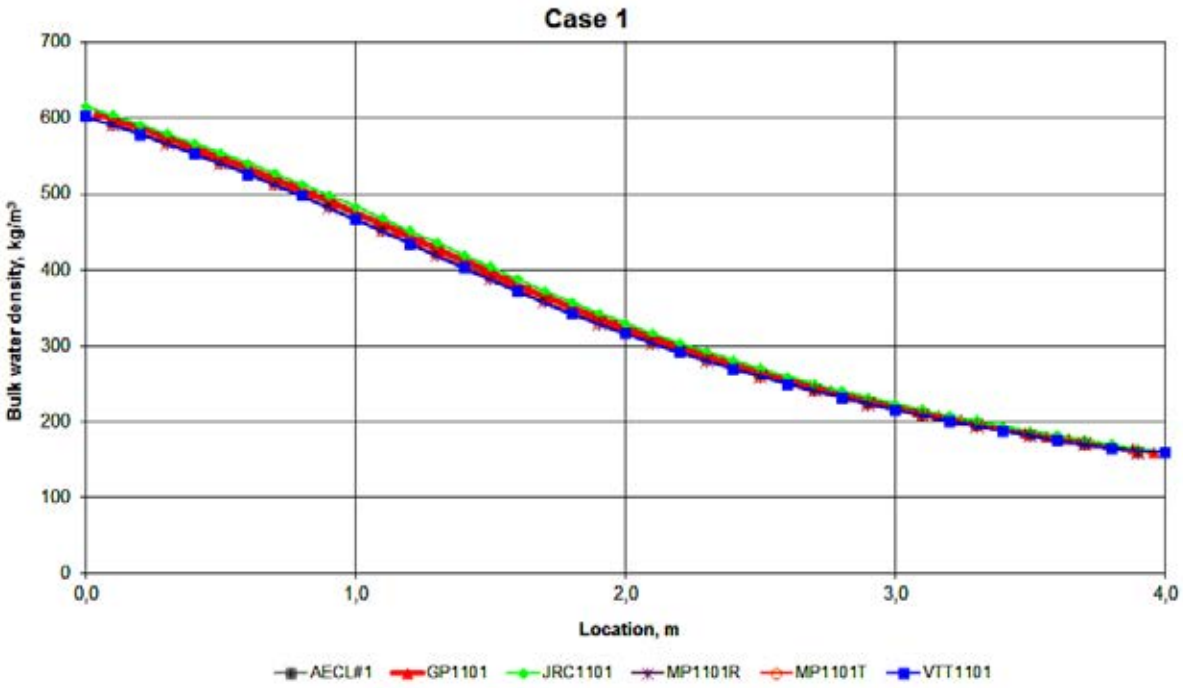

FIG. 9.13. Bulk water density axial distribution.

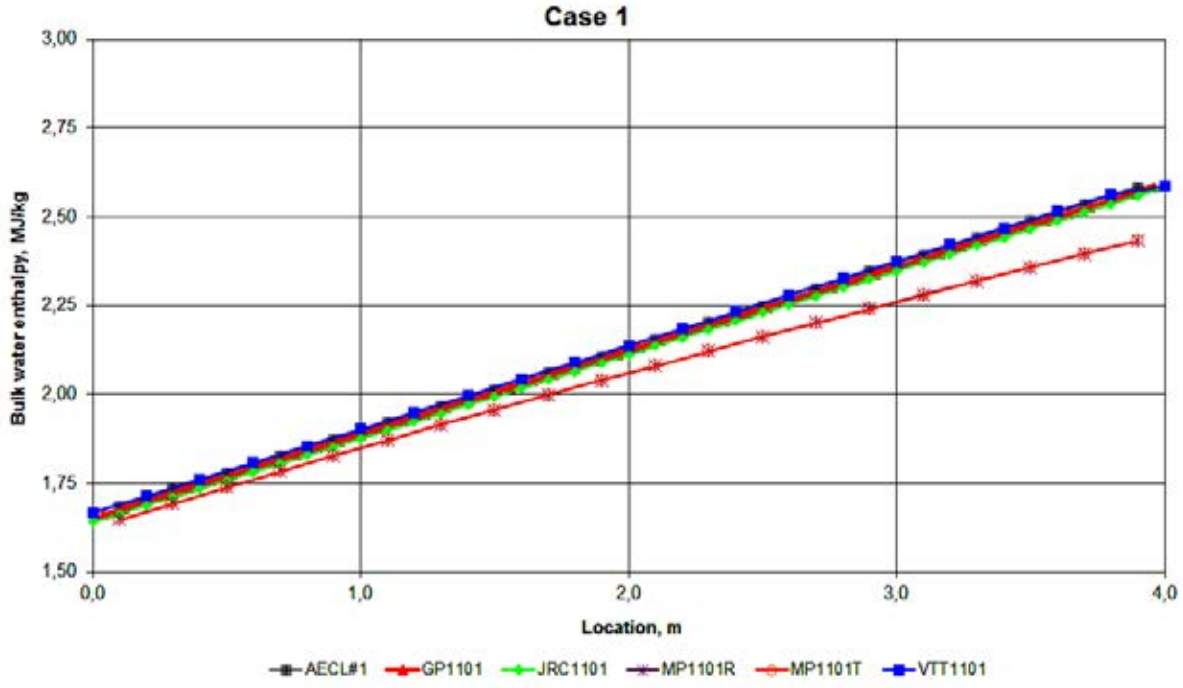

FIG. 9.14. Bulk water enthalpy axial distribution.

TABLE 9.4. LIST OF THE COMPARED RESULTS FOR S&S CODES

Participant ID	Task ID: Case/Variant/Direction of flow (U- up; D-down)	Code	HT correlation	Label ID
AECL	1 / - / U	CATHENA	Dittus-Boelter	AECL#1
	2 / 1 / U			AECL#UPV1
	2 / 1 / D			AECL#DNV1
	2 / 2 / U			AECL#UPV2
	2 / 2 / D			AECL#DNV2
GP	1 / - / U	TEMPA-SC	Kirillov et al.	GP1101
	2 / 1 / U			GP2101
	2 / 1 / D			GP2101D
	2 / 2 / U			GP2201
	2 / 2 / D			GP2201D
	1 / - / U		Krasnoshchekov and Protopopov	GP1104
	2 / 1 / U			GP2104
	2 / 1 / D			GP2104D
	2 / 2 / U			GP2204
	2 / 2 / D			GP2204D
JRC	1 / - / U	COBRA-EN	Bishop	JRC1101
	2 / 1 / U			JRC2101
	2 / 1 / D			JRC2102
	2 / 2 / U			JRC2201
	2 / 2 / D			JRC2202
MP	1 / - / U	TRACE5.0	Dittus-Boelter	MP1101T
	2 / 1 / U			MP2101T
	2 / 1 / D			MP21D01T
	2 / 2 / U			MP2201T
	2 / 2 / D			MP22D01T
	1 / - / U	RELAP5/Mod3.3		MP1101R
	2 / 1 / U			MP2101R
	2 / 1 / D			MP21D01R
	2 / 2 / U			MP2201R
	2 / 2 / D			MP22D01R
VTT	1 / - / U	APROS	Jackson and Hall	VTT1101
	2 / 1 / U			VTT2101
	2 / 1 / D			VTT2102
	2 / 2 / U			VTT2201
	2 / 2 / D			VTT2202

9.1.4.1.2. Case 2

9.1.4.1.2.1. VARIANT 1

The experimental results for the Case 2, Variant 1 for up-flow are presented in Fig. 9.15 (see Fig. 510 of Reference [9-2]).

Figures 9.16–9.21 show computational results of the sub-channel and system codes for the up-flow: CATHENA (AECL), TEMPA-SC (GP), COBRA-EN (JRC), RELAP5/Mod3.3 (MP), TRACE5.0 (MP) and APROS (VTT). In Figs 9.17 and 9.18 results of the two OKB GIDROPRESS runs (GP2101 and

GP2104), with best results for the Case 1, are presented.

The experimental results for the Case 2, Variant 1, down-flow, are presented in Fig. 9.22 (see Fig. 5.24 of Reference [9-2]).

Figures 9.23–9.28 show computational results of the sub-channel and system codes for the down-flow: CATHENA (AECL), TEMPA-SC (GP), COBRA-EN (JRC), RELAP5/Mod3.3 (MP), TRACE5.0 (MP) and APROS (VTT).

In constructing the graphs, it is assumed that the direction of the pipe axis coincides with the direction of the coolant flow. The inlet of the pipe heated section, defined considering the flow direction, was assumed as the zero coordinate.

The following changes of data submitted by participants had to be done in order to prepare the plots:

JRC:
- the zero coordinate is shifted to the beginning of the heated section;
- the pressure drop is counted from the value of pressure at the heated section outlet;

MP:
- the zero coordinate is shifted to the beginning of heated section;
- the pressure drop is counted from the value of pressure of the heated section outlet (along the flow);
- for down-flow the direction of the pipe axis was changed;

VTT:
- for down-flow the direction of the pipe axis was changed.

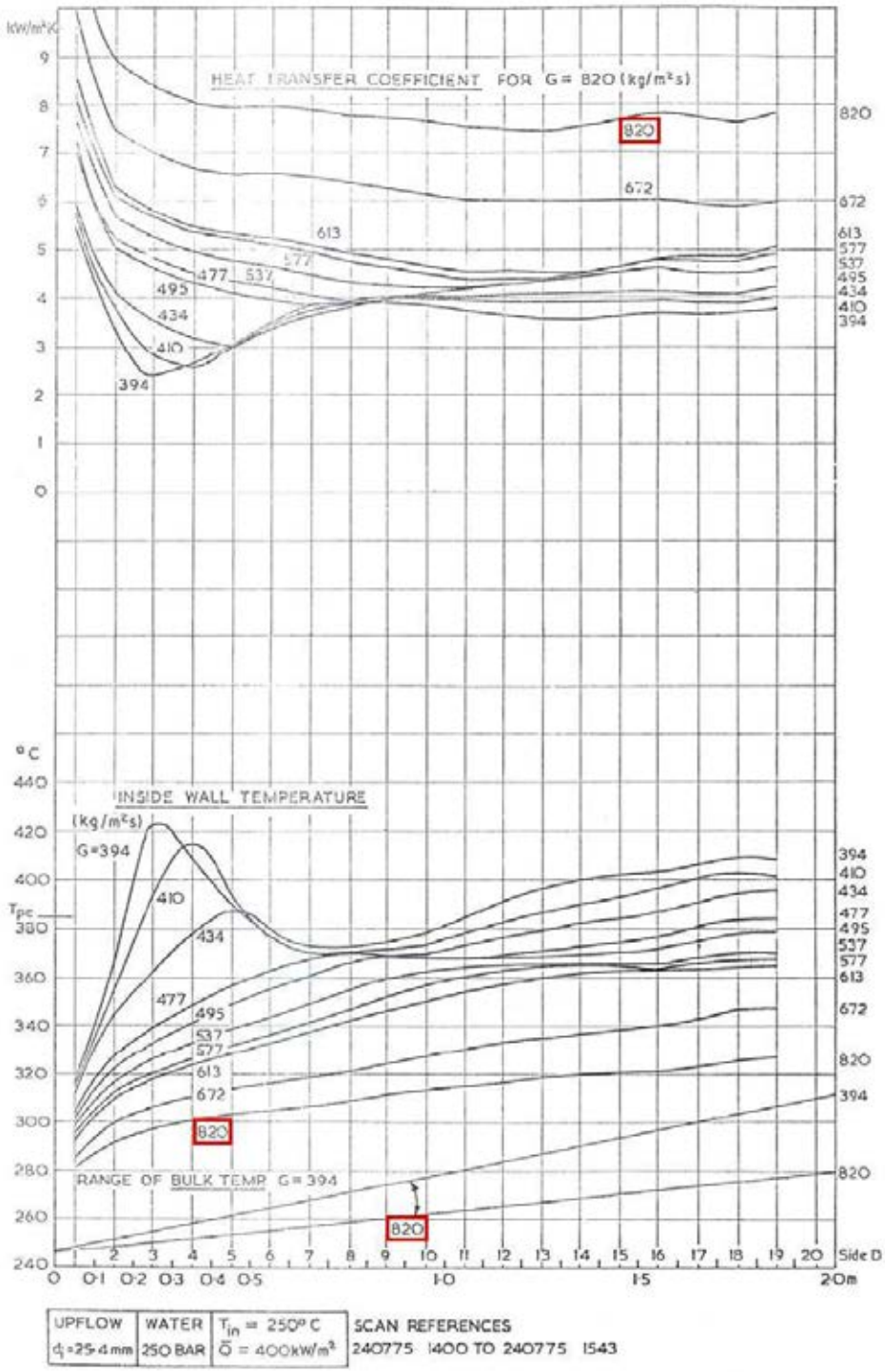

FIG. 9.15. Experimental results of the Case 2, Variant 1, up-flow.
(see page 64, Fig. 5.10 of the reference [9-2])

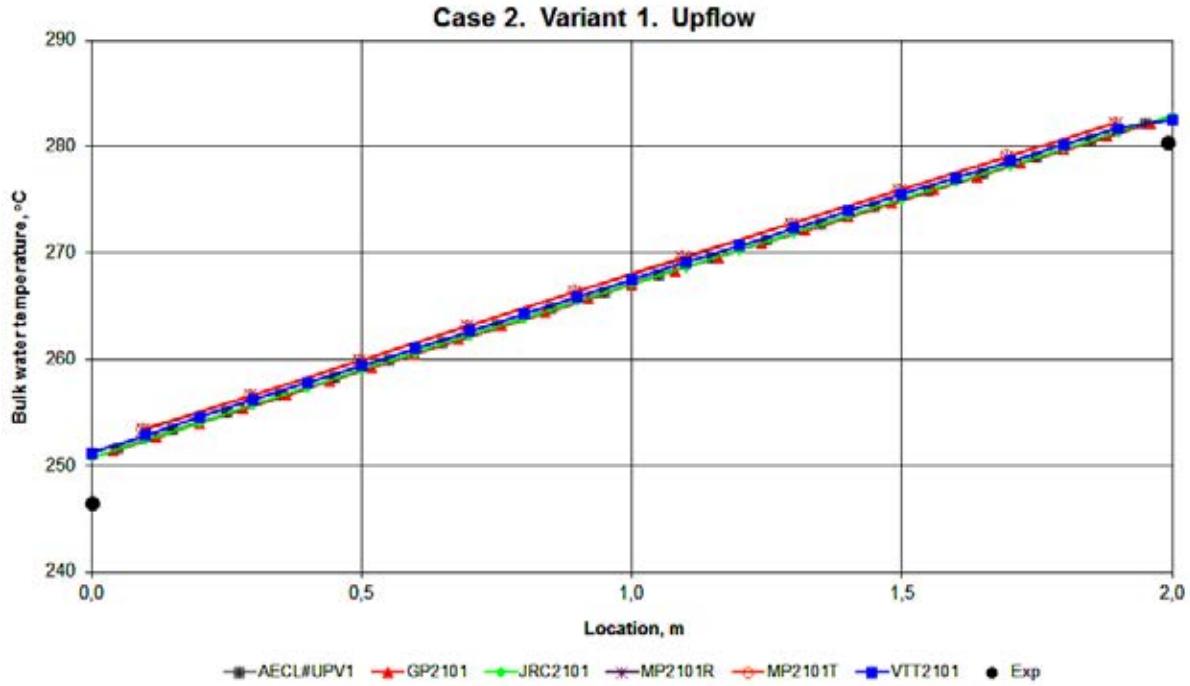

FIG. 9.16. Bulk water temperature axial distribution.

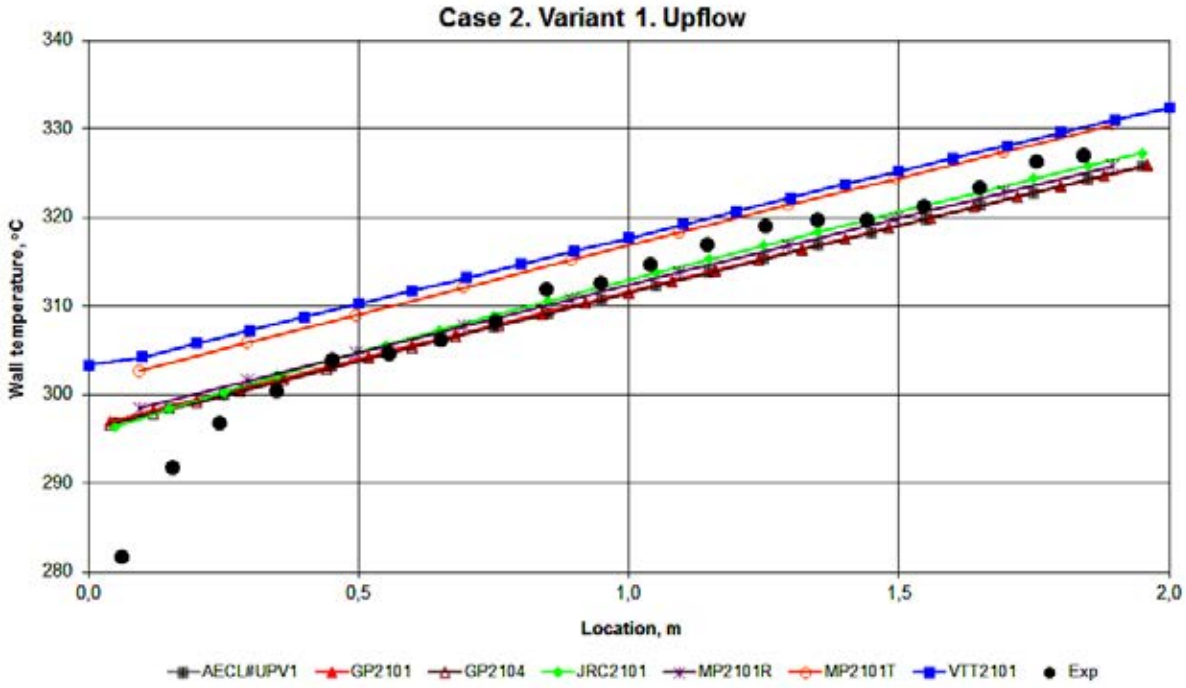

FIG. 9.17. Wall temperature axial distribution.

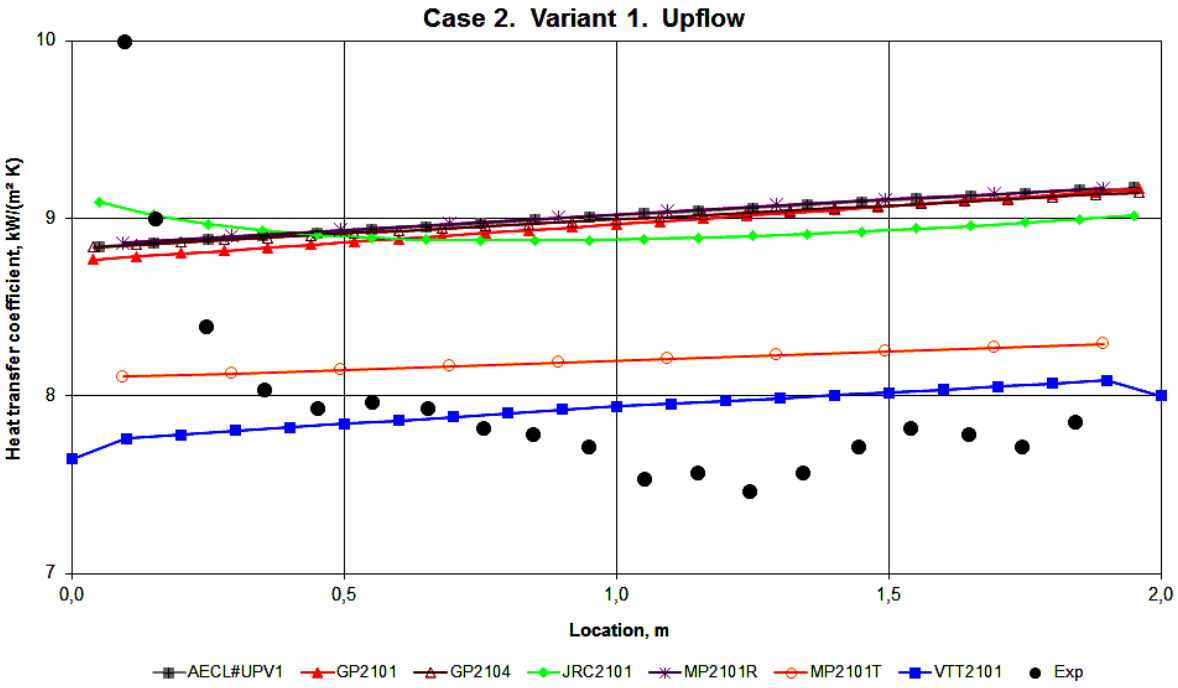

FIG. 9.18. Heat transfer coefficient axial distribution.

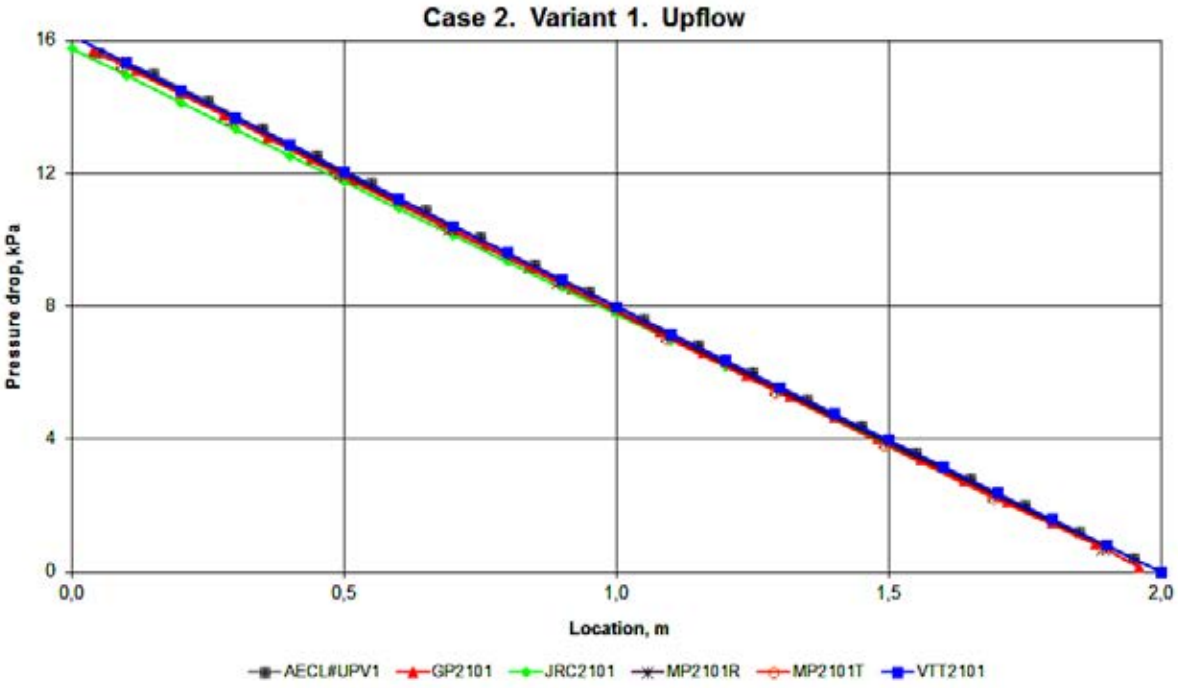

FIG. 9.19. Pressure drop axial distribution.

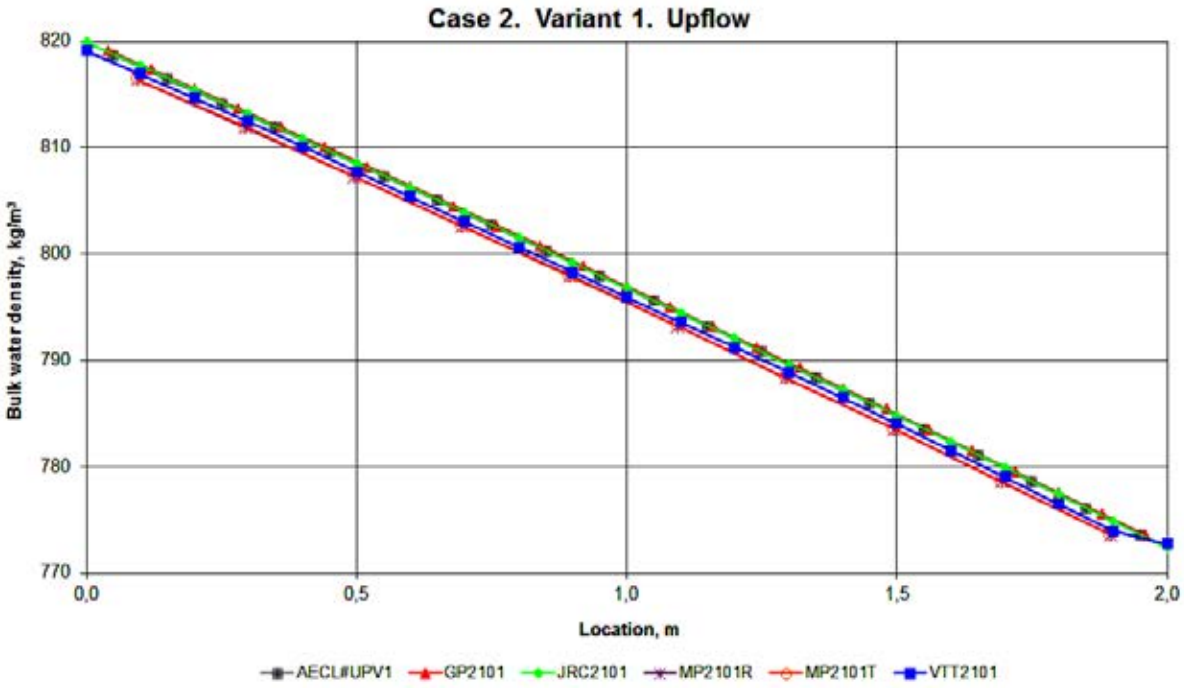

FIG. 9.20. Bulk water density axial distribution.

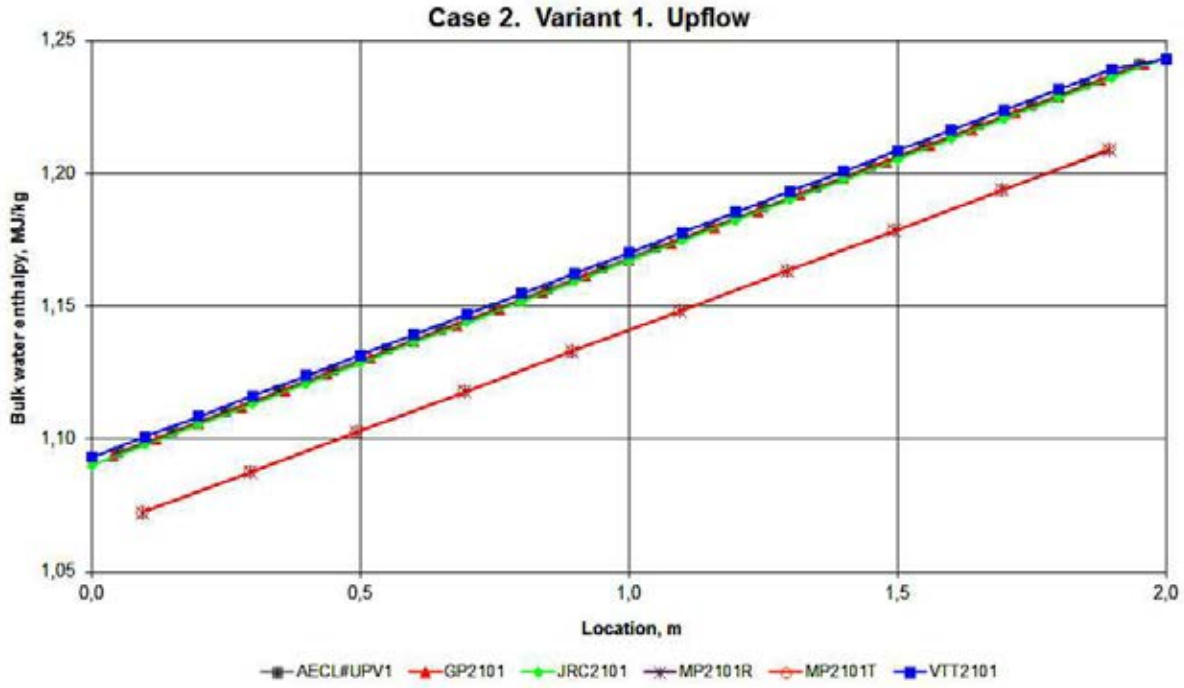

FIG. 9.21. Bulk water enthalpy axial distribution.

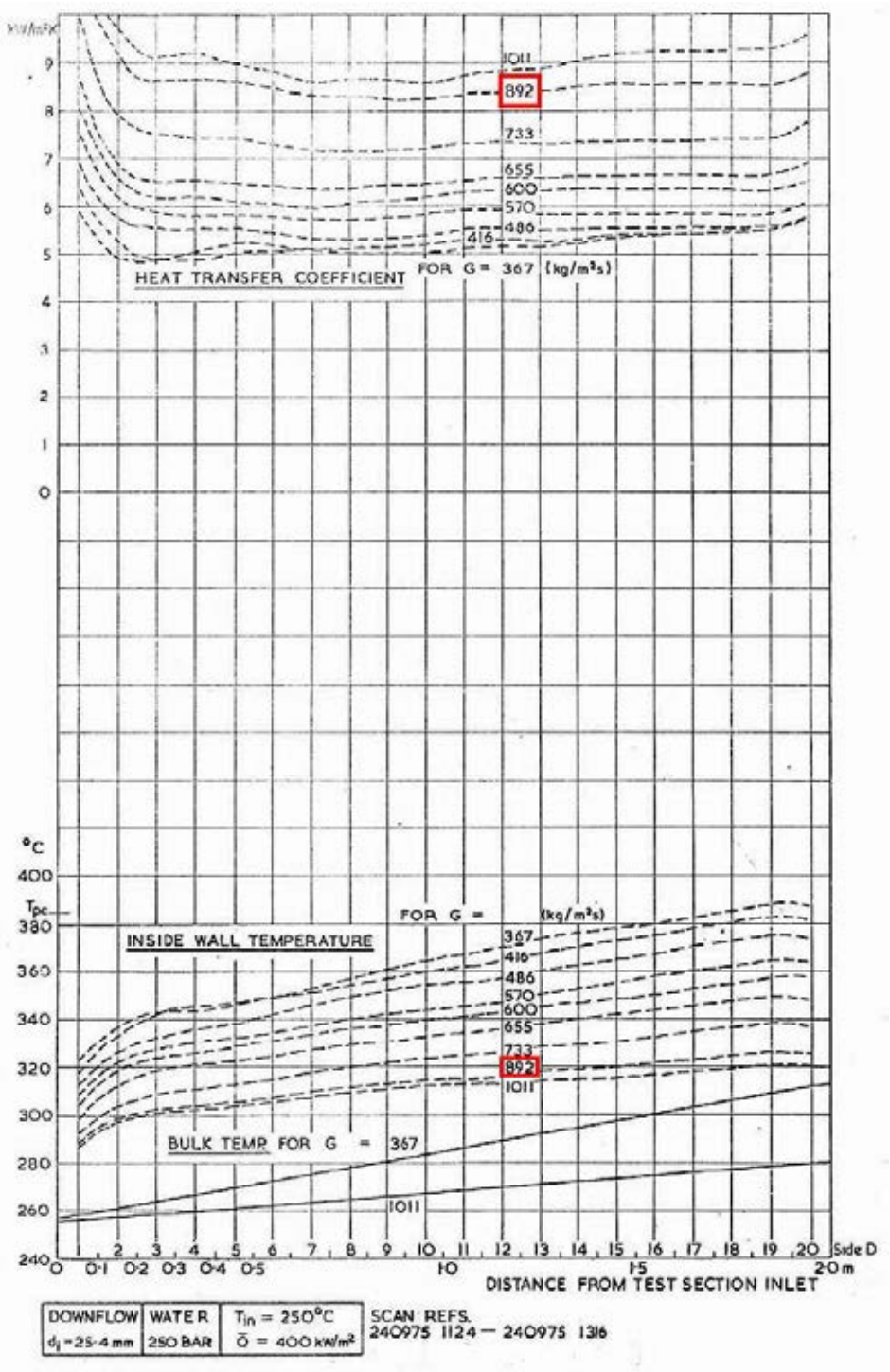

FIG. 9.22. Experimental results of the Case 2, Variant 1, downflow.
(see page 79, Fig. 5.24 of the reference [9-2])

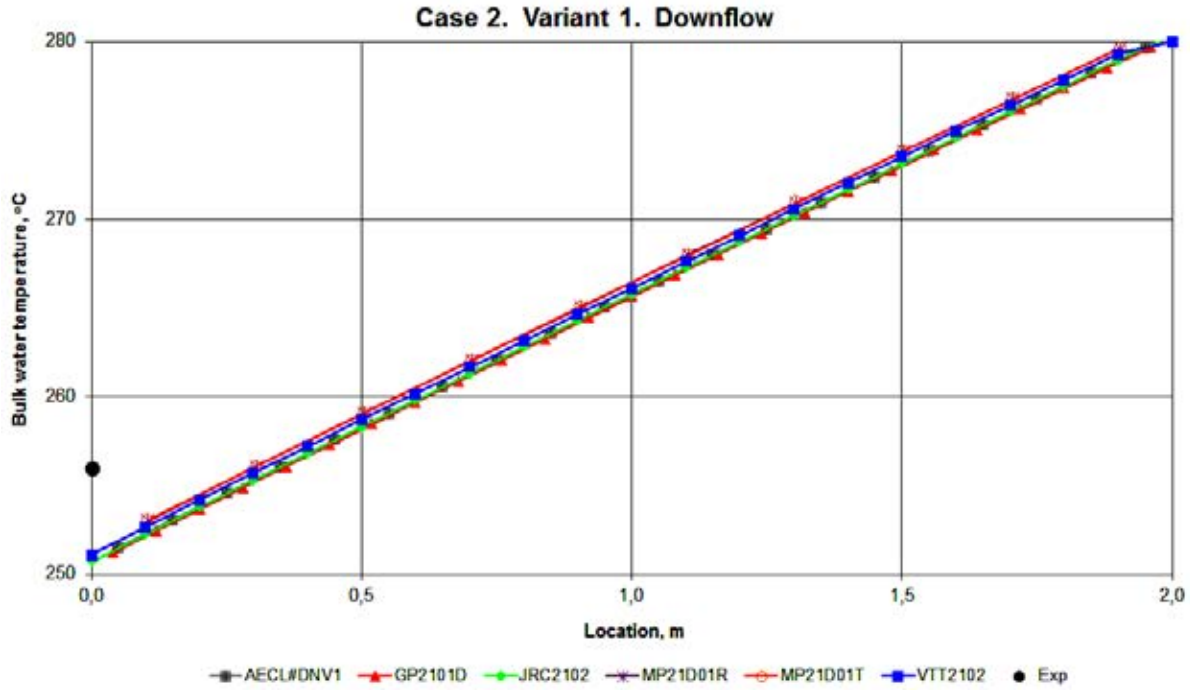

FIG. 9.23. Bulk water temperature axial distribution.

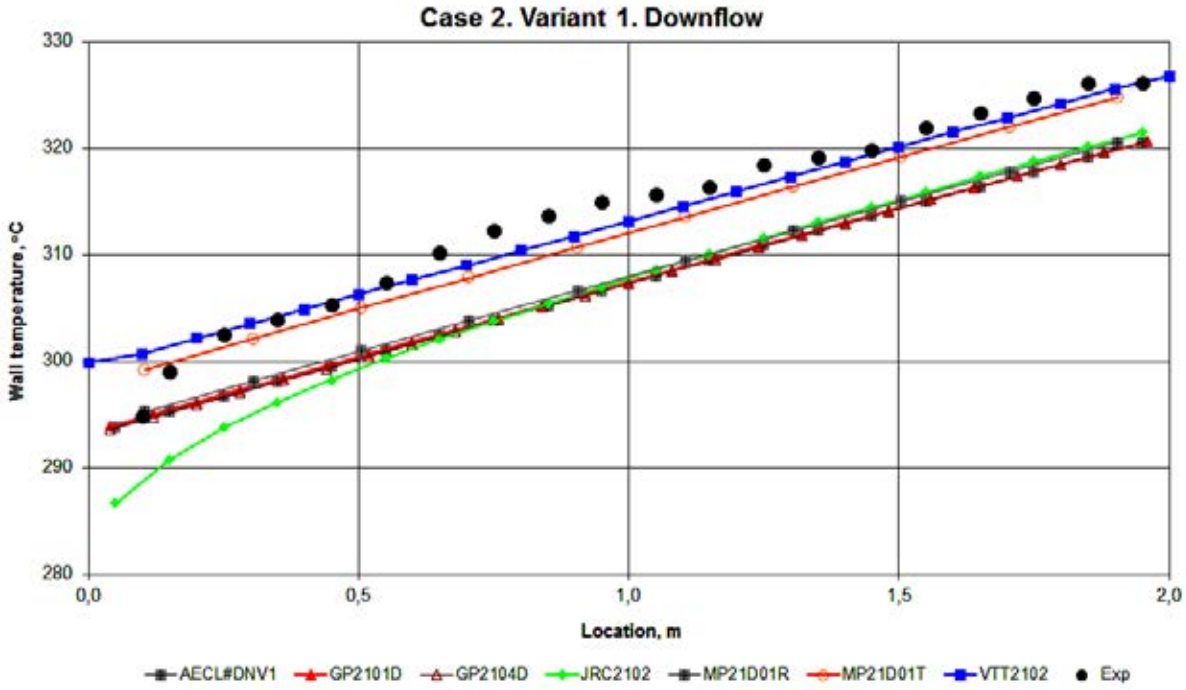

FIG. 9.24. Wall temperature axial distribution.

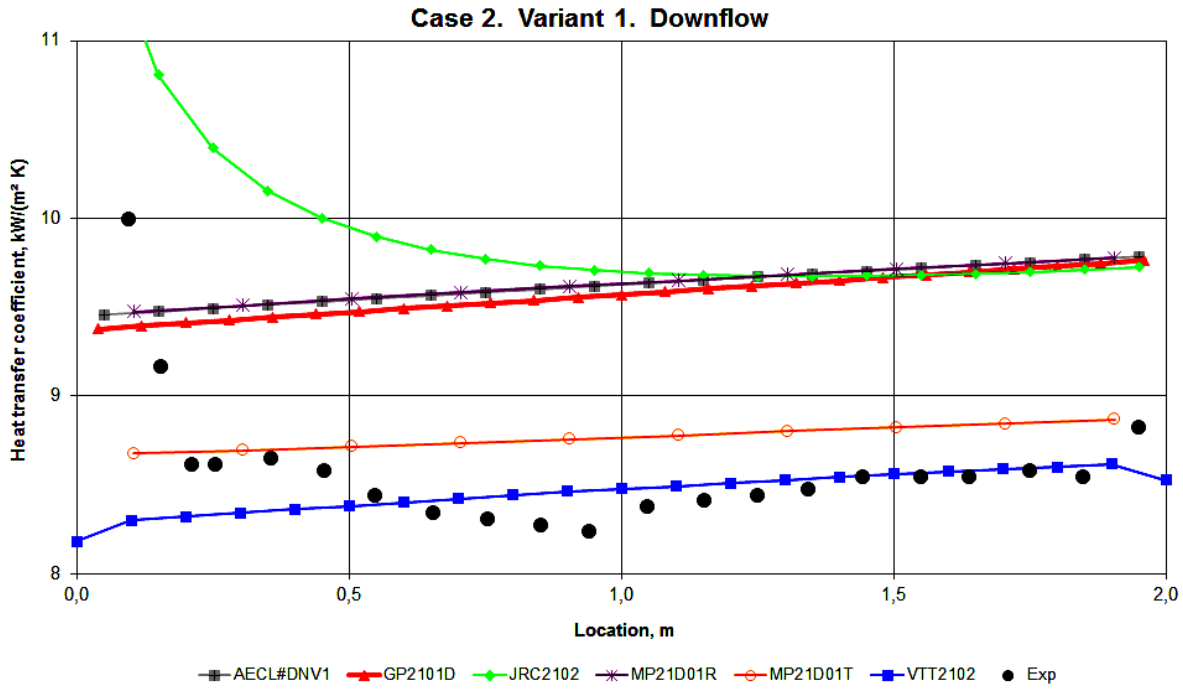

FIG. 9.25. Heat transfer coefficient axial distribution.

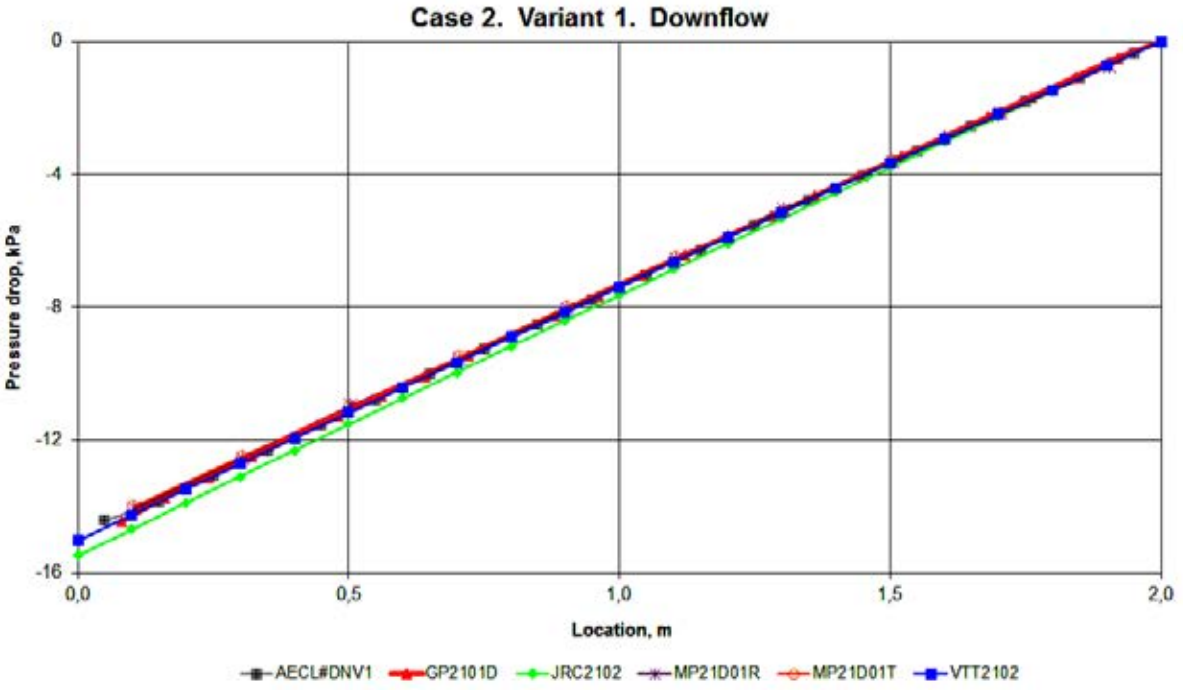

FIG. 9.26. Pressure drop axial distribution.

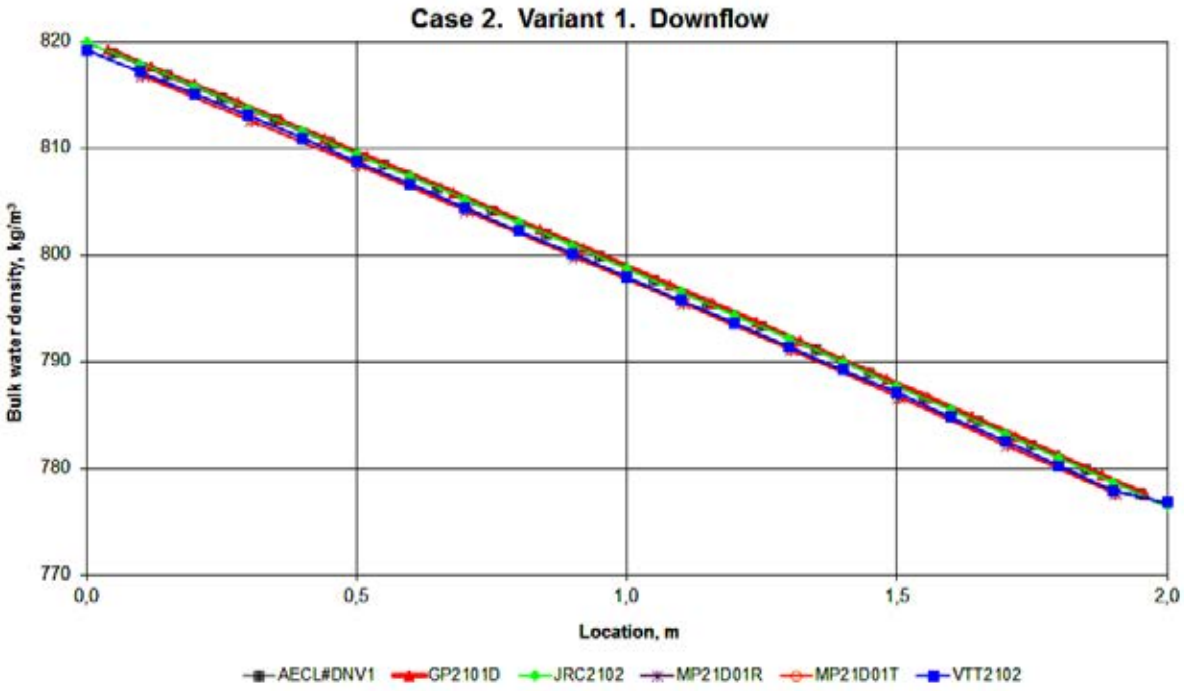

FIG. 9.27. Bulk water density axial distribution.

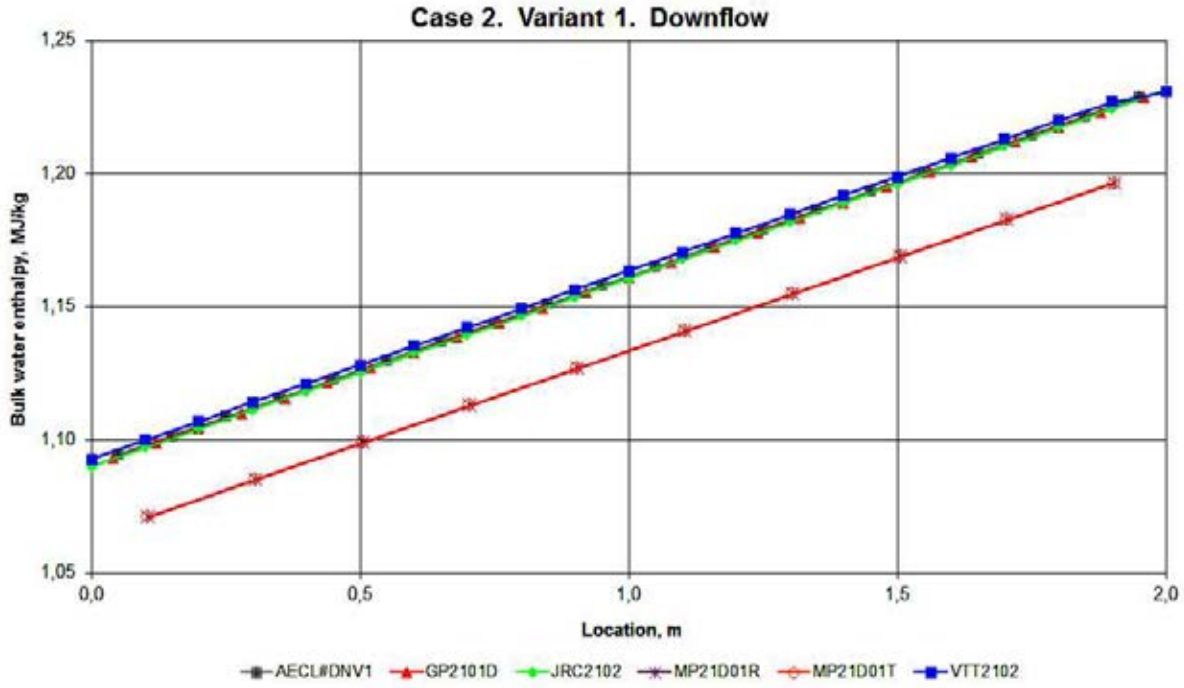

FIG. 9.28. Bulk water enthalpy axial distribution.

9.1.4.1.2.2. VARIANT 2

The experimental results for the Case 2, Variant 2 for up- and down-flow are presented in Fig. 9.29 (see Fig. 5.31 of Reference [9-2]).

Figures 9.30–9.41 show computational results of the sub-channel and system codes for up- and down-flow: CATHENA (AECL), TEMPA-SC (GP), COBRA-EN (JRC), RELAP5/Mod3.3 (MP), TRACE5.0 (MP) and APROS (VTT).

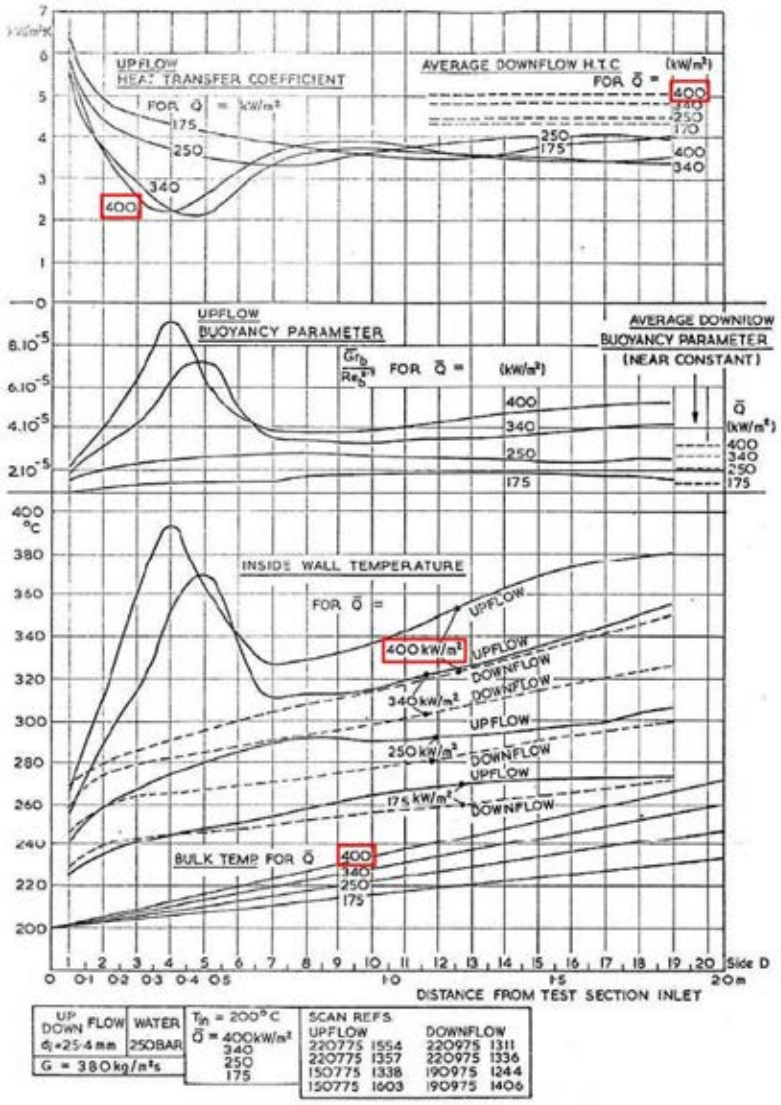

FIG. 9.1. Experimental results of the Case 2, Variant 2, up- and downflow.

(see page 86, Fig. 5.31 of the reference [9-2])

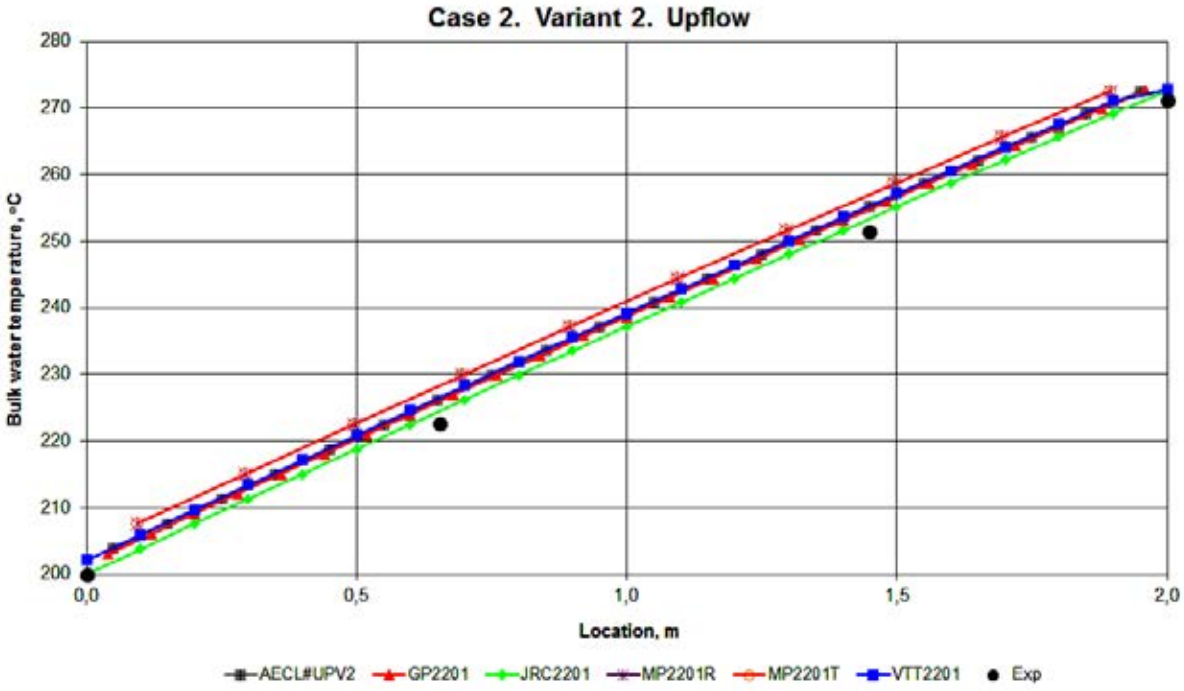

FIG. 9.30. Bulk water temperature axial distribution.

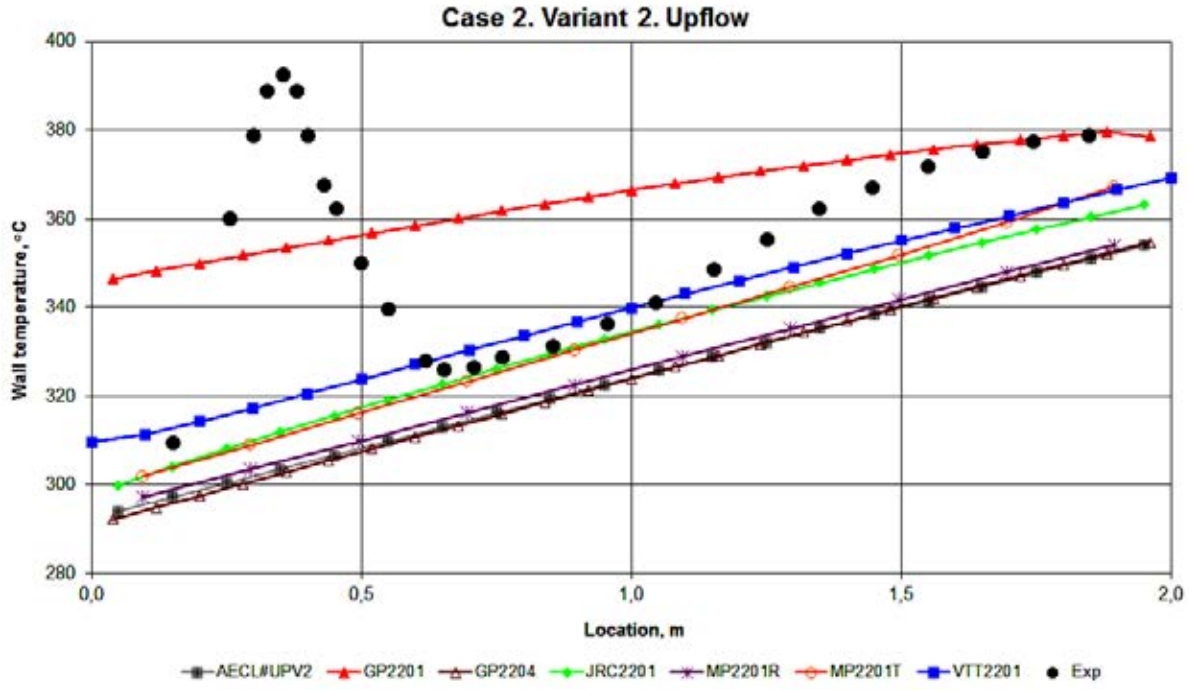

FIG. 9.31. Wall temperature axial distribution.

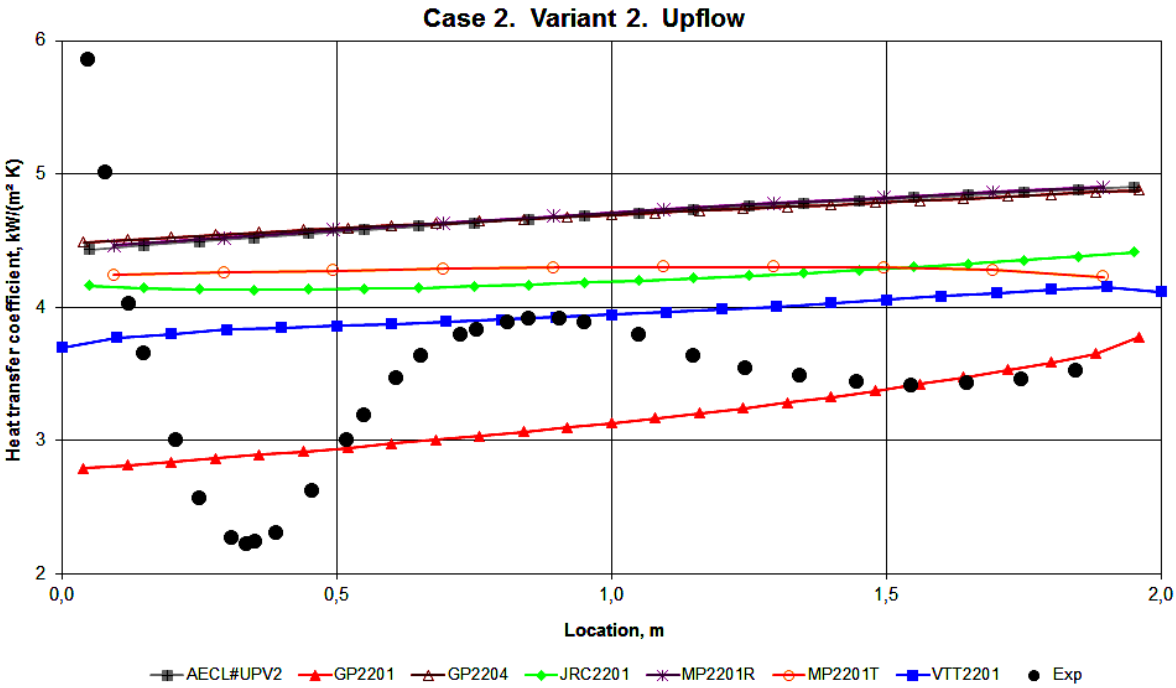

FIG. 9.32. Heat transfer coefficient axial distribution.

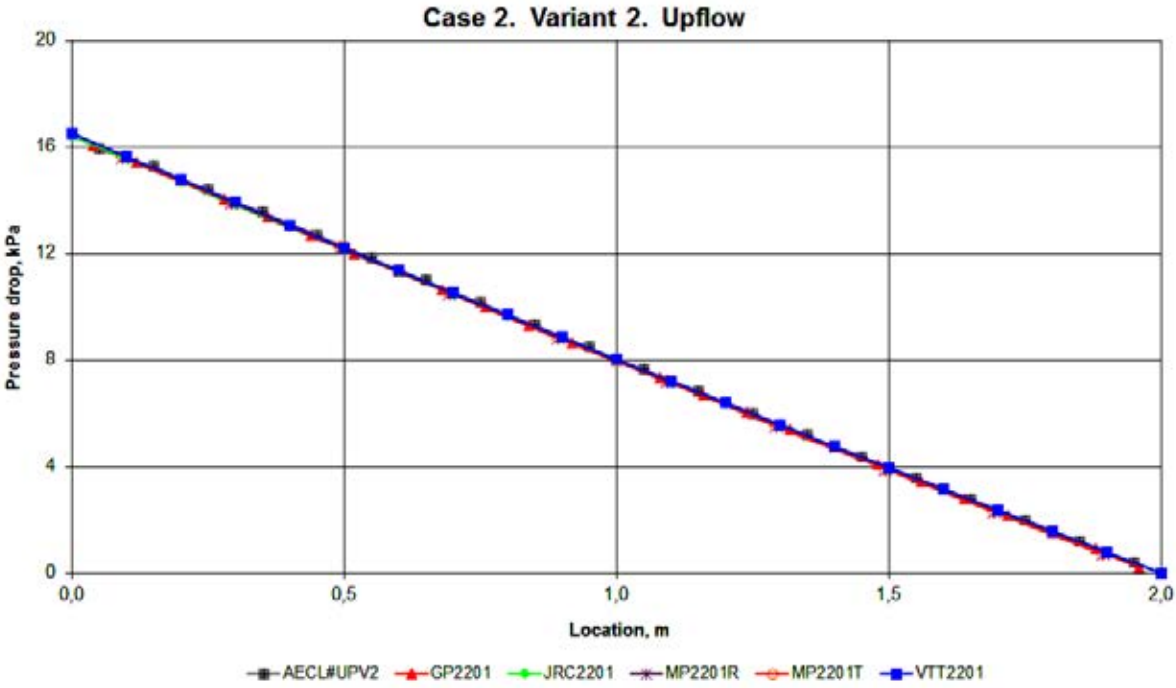

FIG. 9.33. Pressure drop axial distribution.

FIG. 9.34. Bulk water density axial distribution.

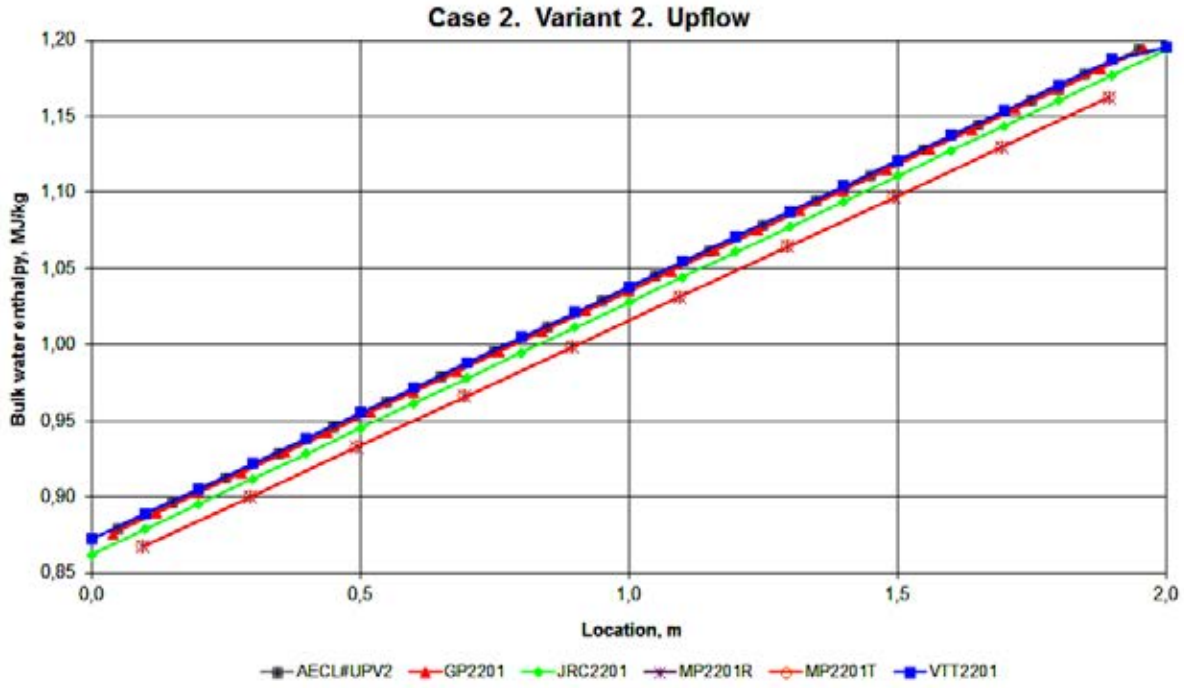

FIG. 9.35. Bulk water enthalpy axial distribution.

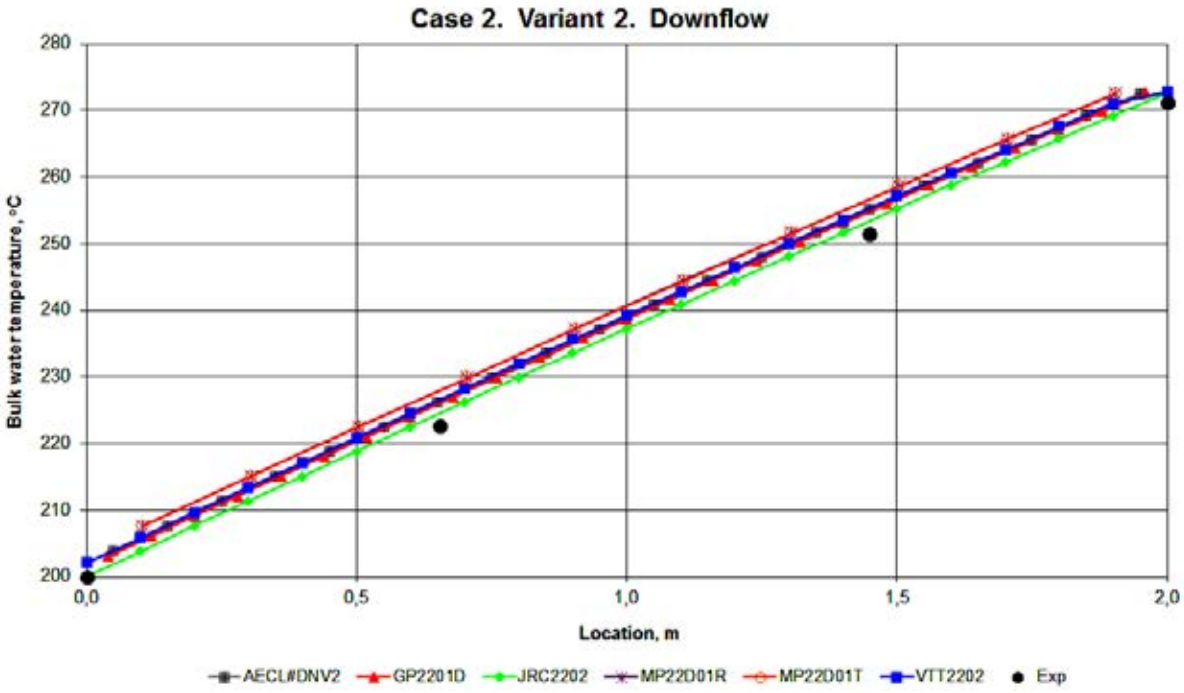

FIG. 9.36. Bulk water temperature axial distribution.

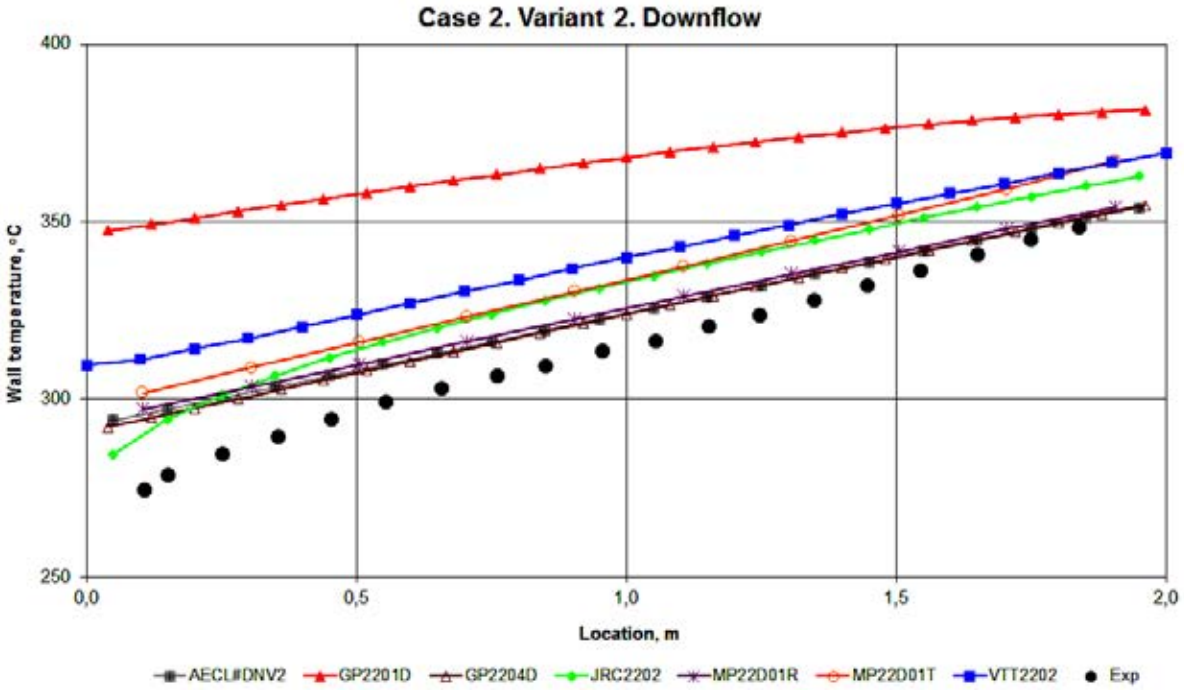

FIG. 9.37. Wall temperature axial distribution.

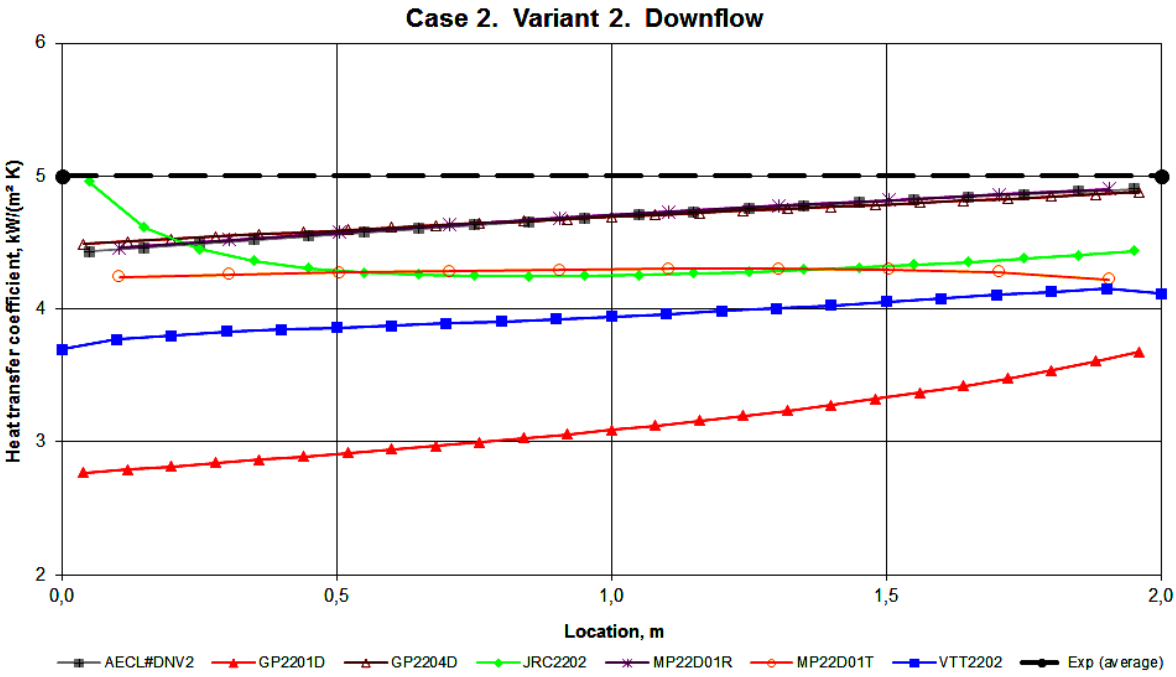

FIG. 9.38. Heat transfer coefficient axial distribution.

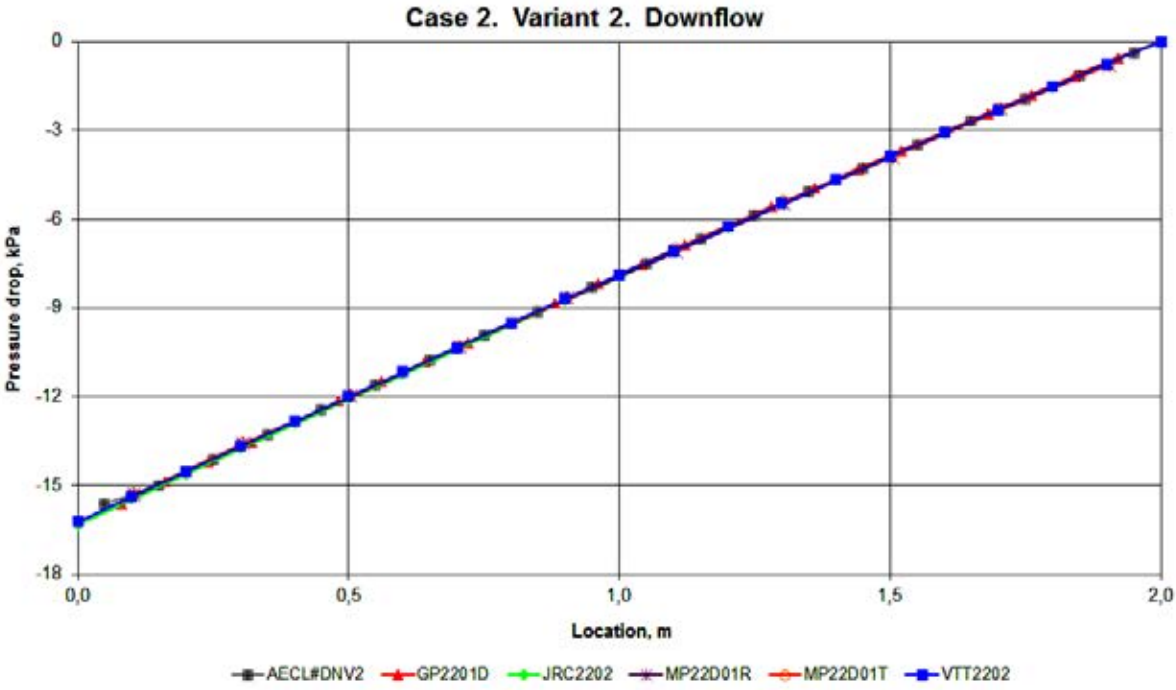

FIG. 9.39. Pressure drop axial distribution.

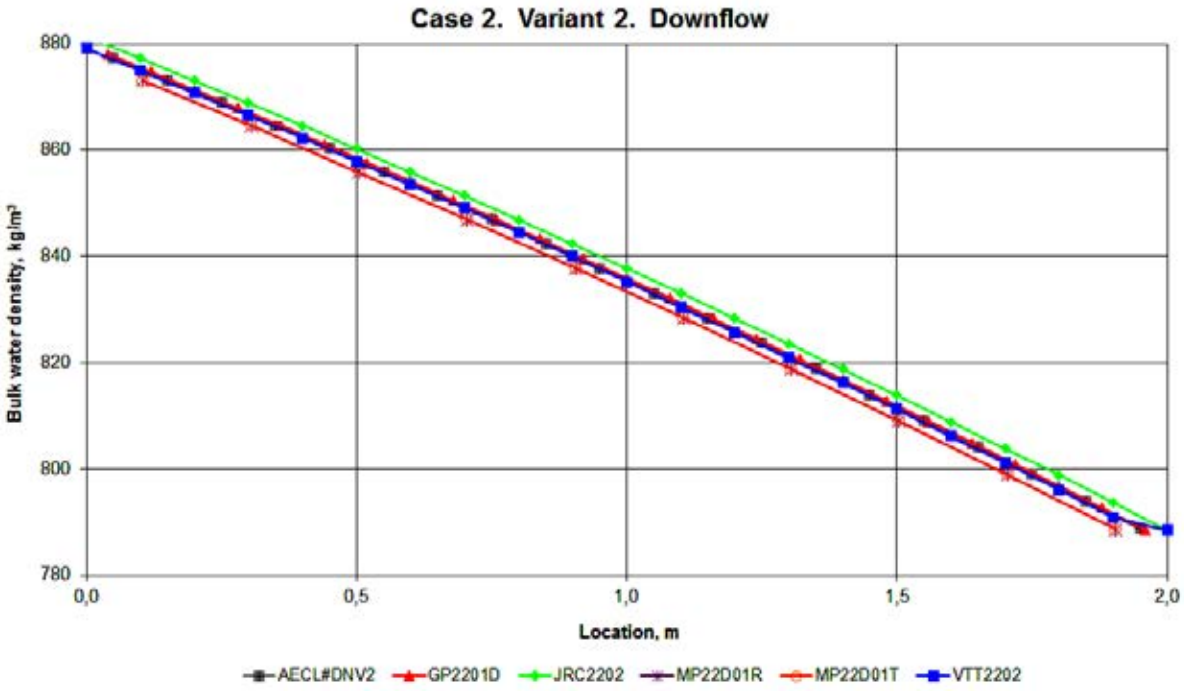

FIG. 9.40. Bulk water density axial distribution.

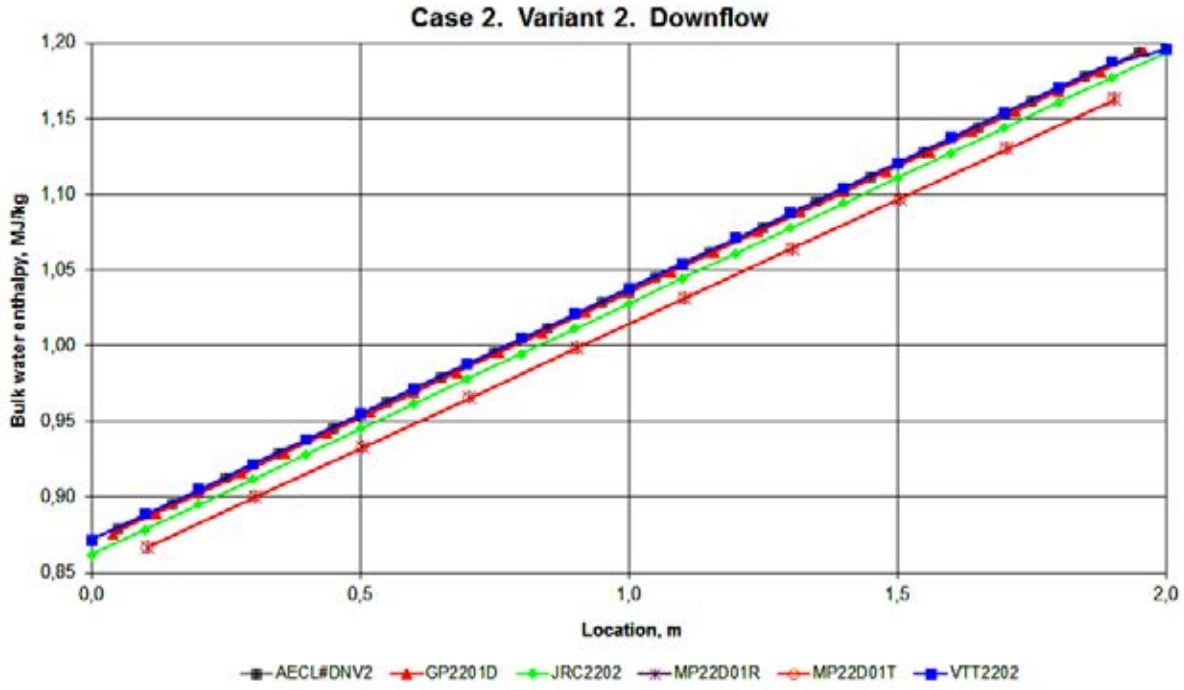

FIG. 9.41. Bulk water enthalpy axial distribution.

9.1.4.2. CFD codes

9.1.4.2.1. Case 1

Figures 9.42– 9.50 show the computational results of the CFD codes: NAFA (BARC), ANSYS CFX (CIAE), Fluent Ver. 6.3 (KAERI), Fluent (SJTU), SIMPLE2D (SJTU), SWIRL (UMAP). Of all the variants of SJTU calculations, only three of them (turbulence models: CH, SKW, SST) are presented, which better describe the experimental data (see Fig. 9.2). Wall temperature axial distributions for the all variants of SJTU calculations are shown in Fig. 9.51, separately. The list of the compared results is given in Table 9.5.

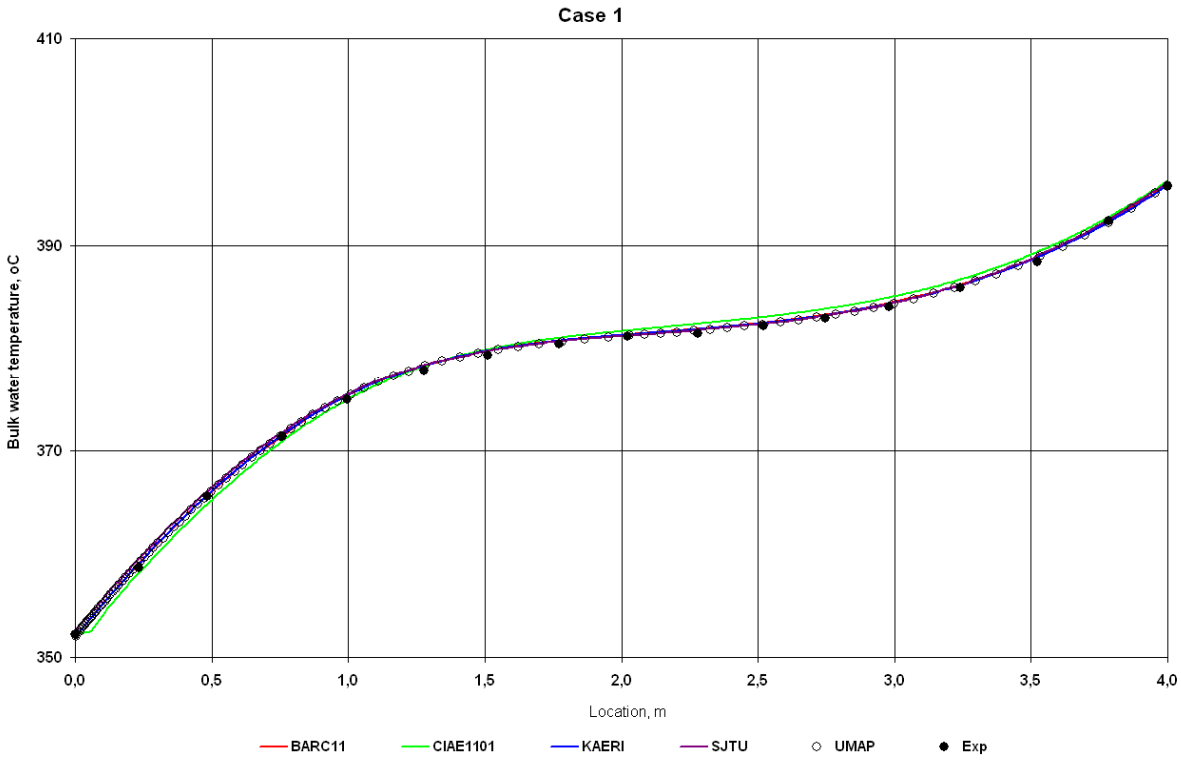

FIG. 9.42. Bulk water temperature axial distribution.

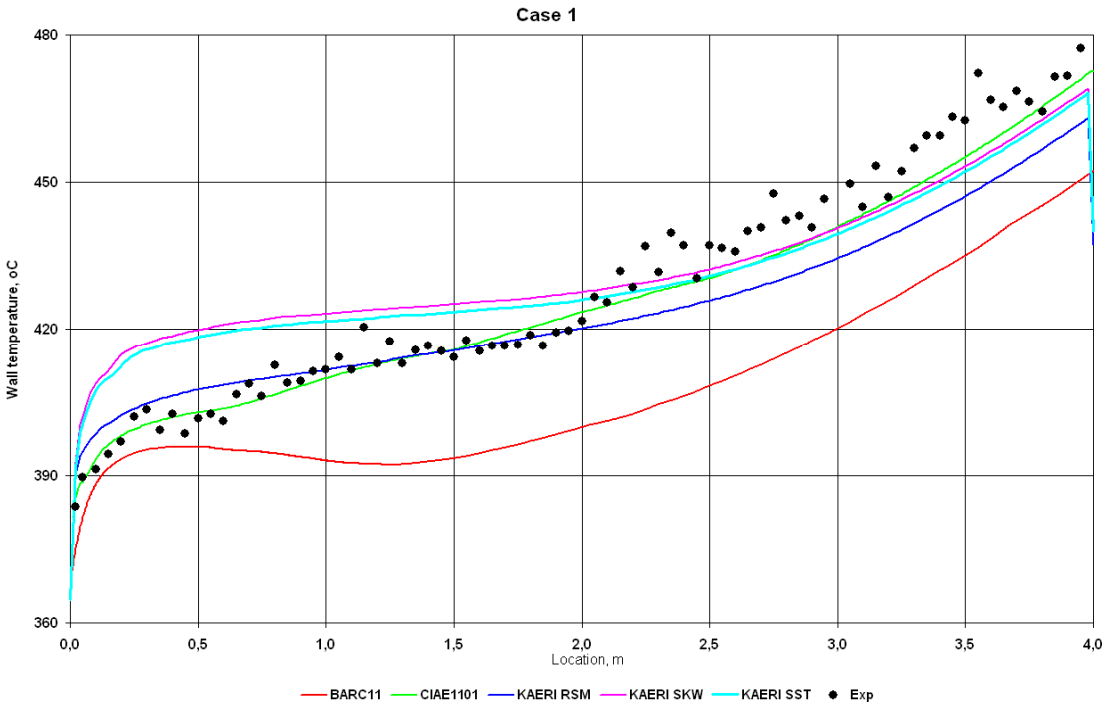

FIG. 9.43. Wall temperature axial distribution.

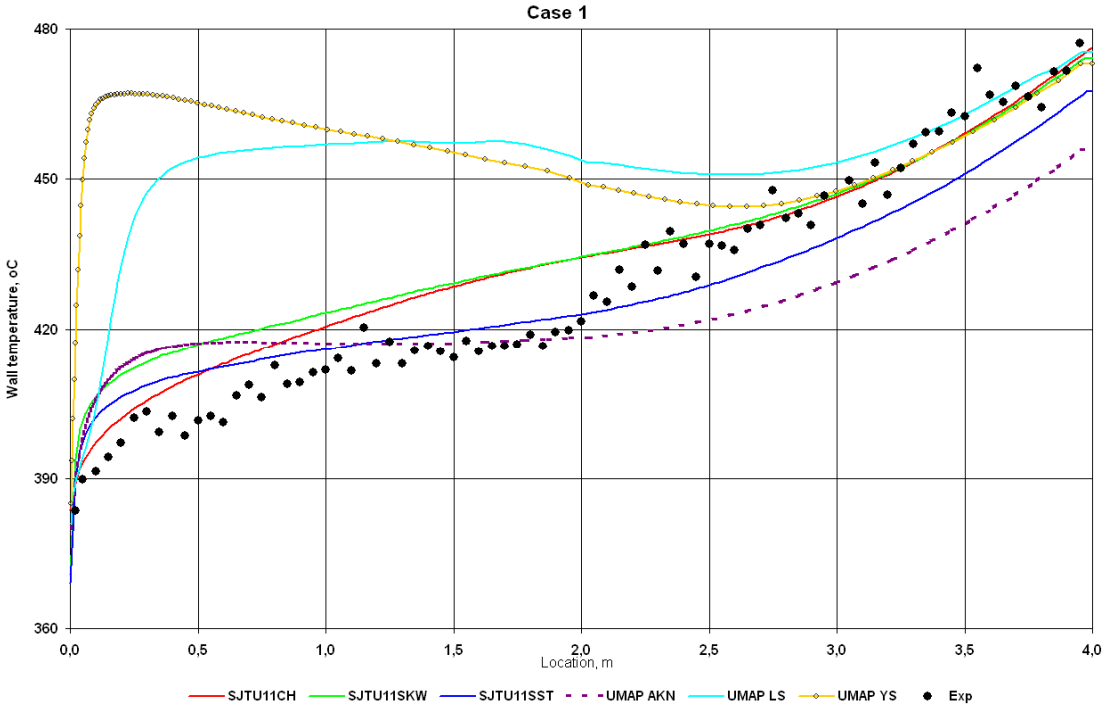

FIG. 9.44. Wall temperature axial distribution.

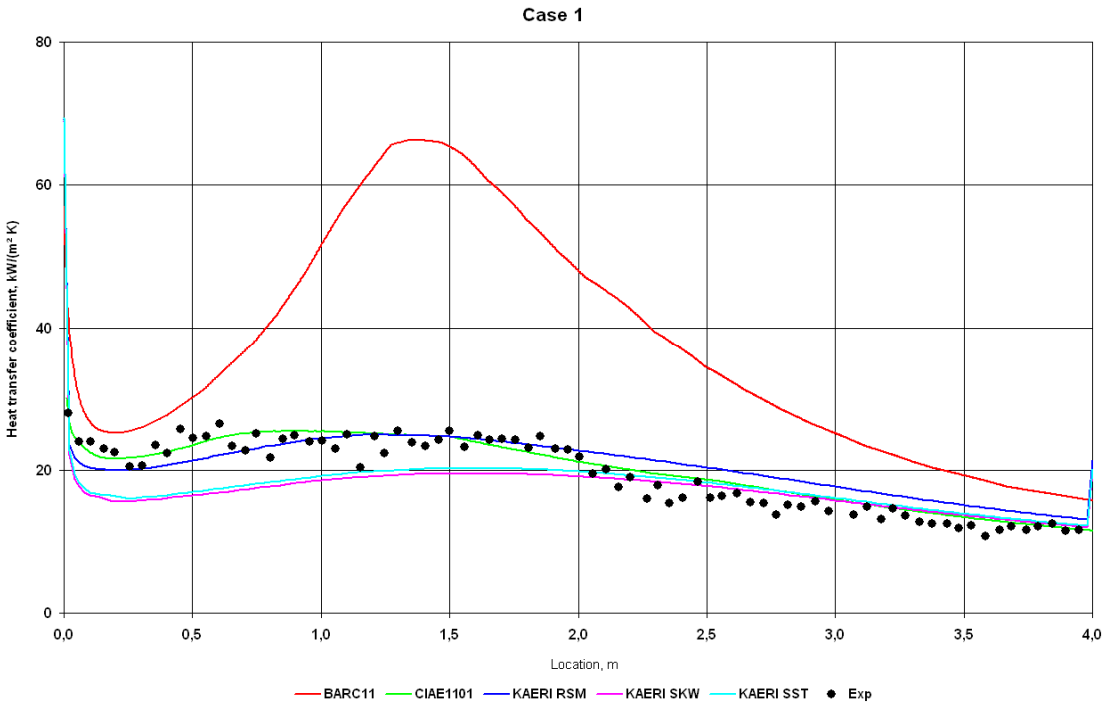

FIG. 9.45. Heat transfer coefficient axial distribution.

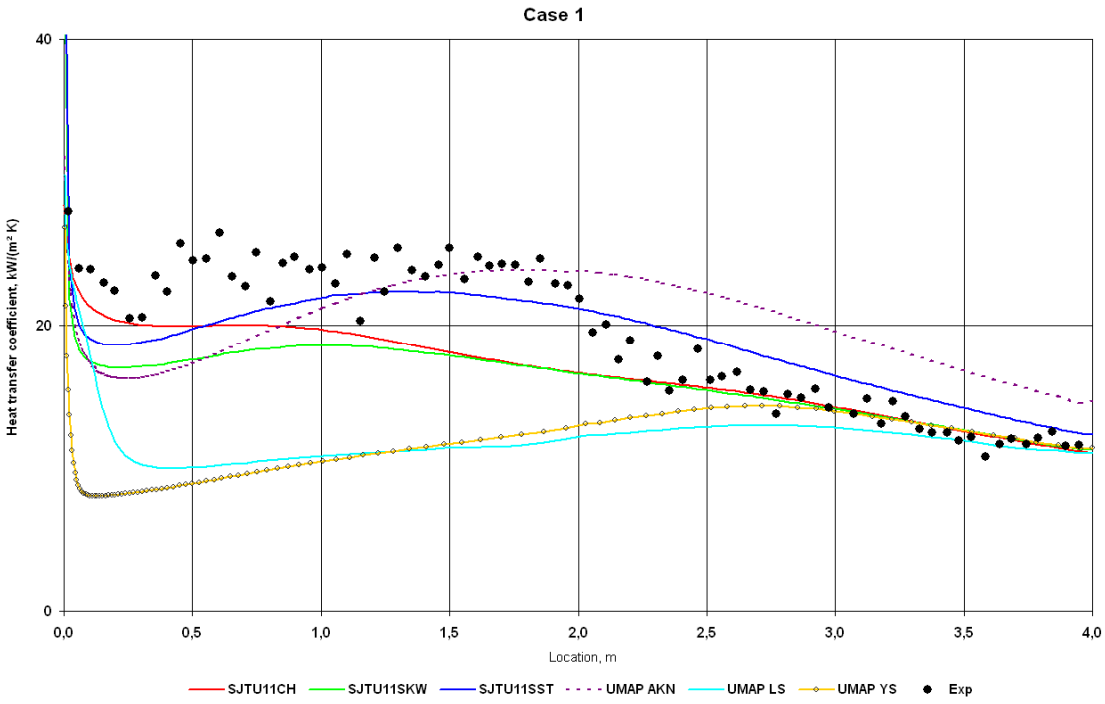

FIG. 9.46. Heat transfer coefficient axial distribution.

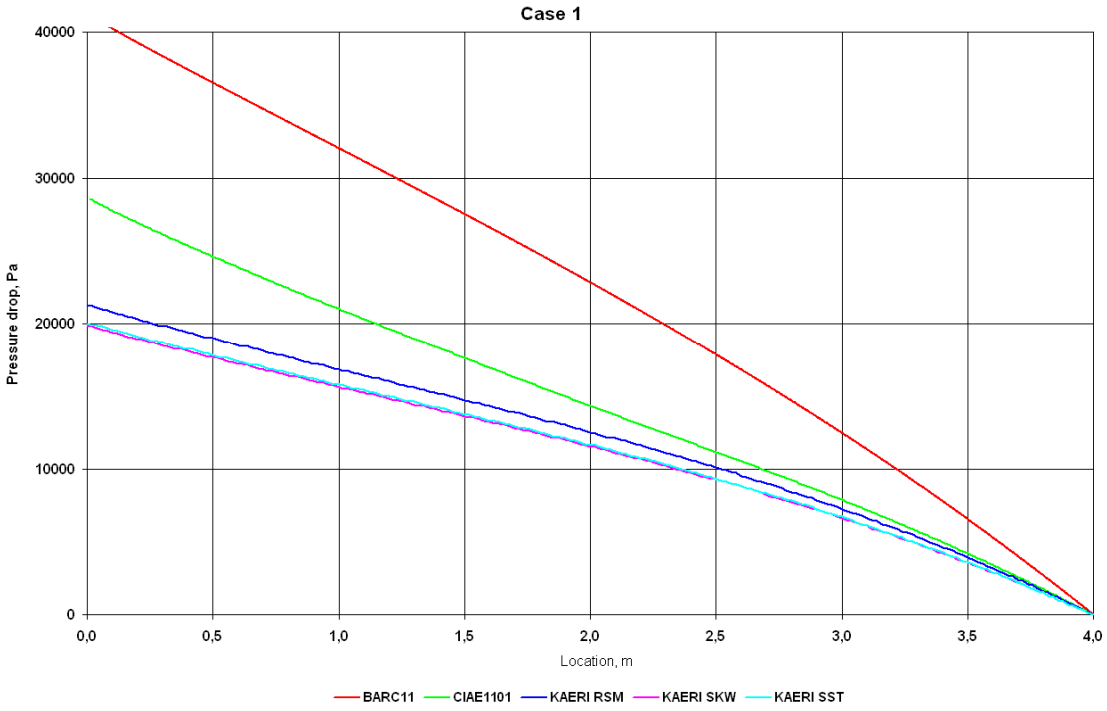

FIG. 9.47. Pressure drop axial distribution.

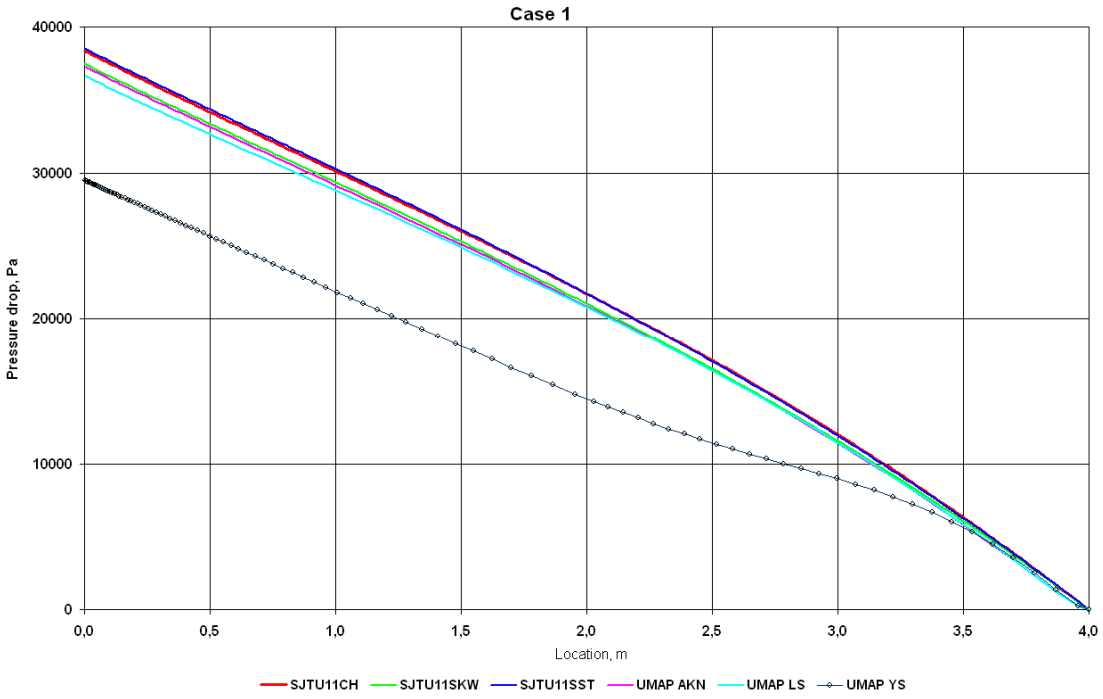

FIG. 9.48. Pressure drop axial distribution.

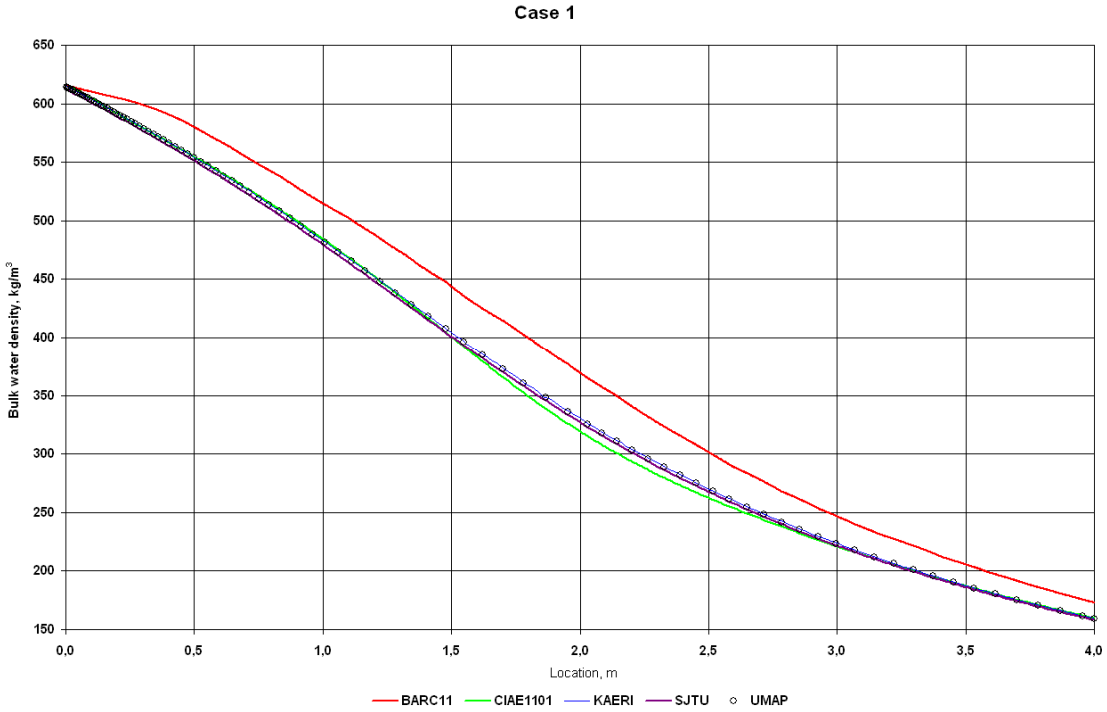

FIG. 9.49. Bulk water density axial distribution.

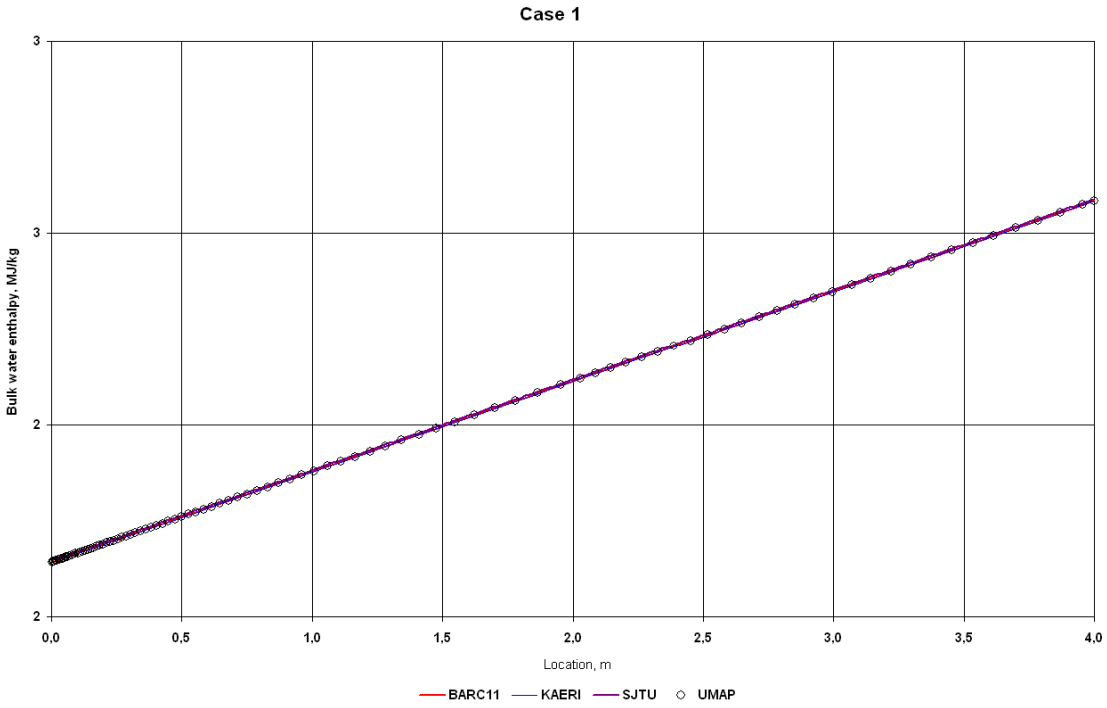

FIG. 9.50. Bulk water enthalpy axial distribution.

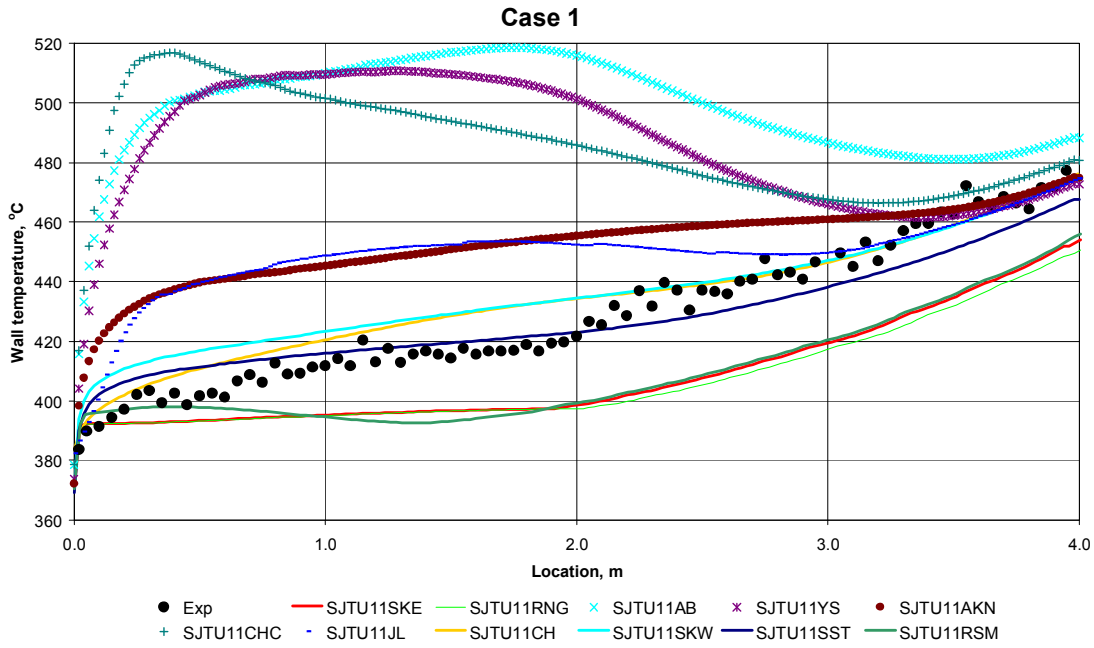

FIG. 9.61. Wall temperature axial distribution (all variants of SJTU).

TABLE 9.5. LIST OF THE COMPARED RESULTS FOR CFD CODES

Participant ID	Task ID: Case/Variant/Direction of flow (U- up; D-down)	Code	Turbulence model	Label ID[7]
BARC	1 / - / U	NAFA	Standard k-ε (SKE)	BARC11
	2 / 1 / U			BARC
	2 / 1 / D			
	2 / 2 / U			
	2 / 2 / D			
CIAE	1 / - / U	ANSYS CFX	Shear-Stress-Transport K-ω (SST)	CIAE1101
	2 / 1 / U			CIAE2101
	2 / 1 / D			CIAE2101
	2 / 2 / U			CIAE2201
	2 / 2 / D			CIAE2202
KAERI	1 / - / U	Fluent	Reynolds Stress Model (RSM);	KAERI RSM
			Standard K-ω (SKW);	KAERI SKW
			SST	KAERI SST
	2 / 1 / U		Results for different turbulence models are presented on the individual Figures 9.60, 9.69, 9.78, 9.87	
	2 / 1 / D			
	2 / 2 / U			
	2 / 2 / D			
SJTU	1 / - / U	Fluent	SKW; SST	SJTU11SKW (SST)
	2 / 1 / U			
	2 / 1 / D			
	2 / 2 / U			
	2 / 2 / D			
	1 / - / U	SIMPLE2D	Chien low Re models (CH)	SJTU11CH
	2 / 1 / U			
	2 / 1 / D			
	2 / 2 / U			
	2 / 2 / D			
UMAP	1 / - / U	SWIRL	Low Re models: AKN, LS, YS	UMAP AKN (LS, YS)
	2 / 1 / U			UMAP2101AKN (LS, YS)
	2 / 1 / D			
	2 / 2 / U			UMAP2201AKN (LS, YS)
	2 / 2 / D			

9.1.4.2.2. Case 2

9.1.4.2.2.1. VARIANT 1

Experimental results of the Case 2, Variant 1 for up-flow are presented in Fig. 9.15 (see Fig. 5.10 of the reference [9-2]).

[7] If legend of figure has only Participant ID instead of Label ID it means that the change of applicable parameters (usually – water properties) are equal for the all variants of calculations (turbulence models).

Computational results of the CFD codes NAFA (BARC), ANSYS CFX (CIAE), Fluent (SJTU), SIMPLE2D (SJTU), SWIRL (UMAP) are shown in Fig. 9.52–9.59. Of all the variants of SJTU calculations, only three of them (turbulence models: CH, SKW, SST) are presented, which better describe the Case 1 experimental data. Wall temperature axial distributions for the all variants of KAERI calculations (Fluent Ver. 6.3 code) are shown in Fig. 9.60.

Experimental results of the Case 2, Variant 1, down-flow, are presented in Fig. 9.22 (see Fig. 5.24 of Reference [9-2]).

Figures 9.61–9.68 show computational results of the CFD codes NAFA (BARC), ANSYS CFX (CIAE), Fluent (SJTU), SIMPLE2D (SJTU), SWIRL (UMAP). Wall temperature axial distributions for the all variants of KAERI calculations (Fluent Ver. 6.3 code) are shown in Fig. 9.69.

The following changes of initial data of BARC had to be done in order to prepare graph:

- the pressure drop is counted from pressure of the heated section outlet (along the flow).

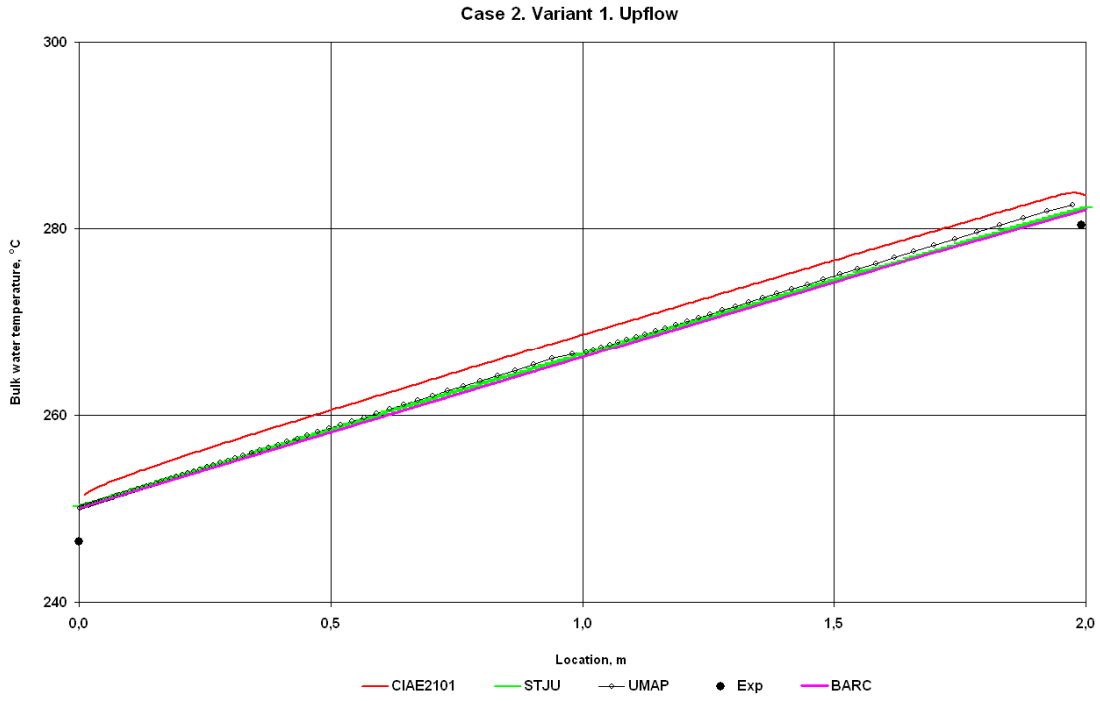

FIG. 9.52. Bulk water temperature axial distribution.

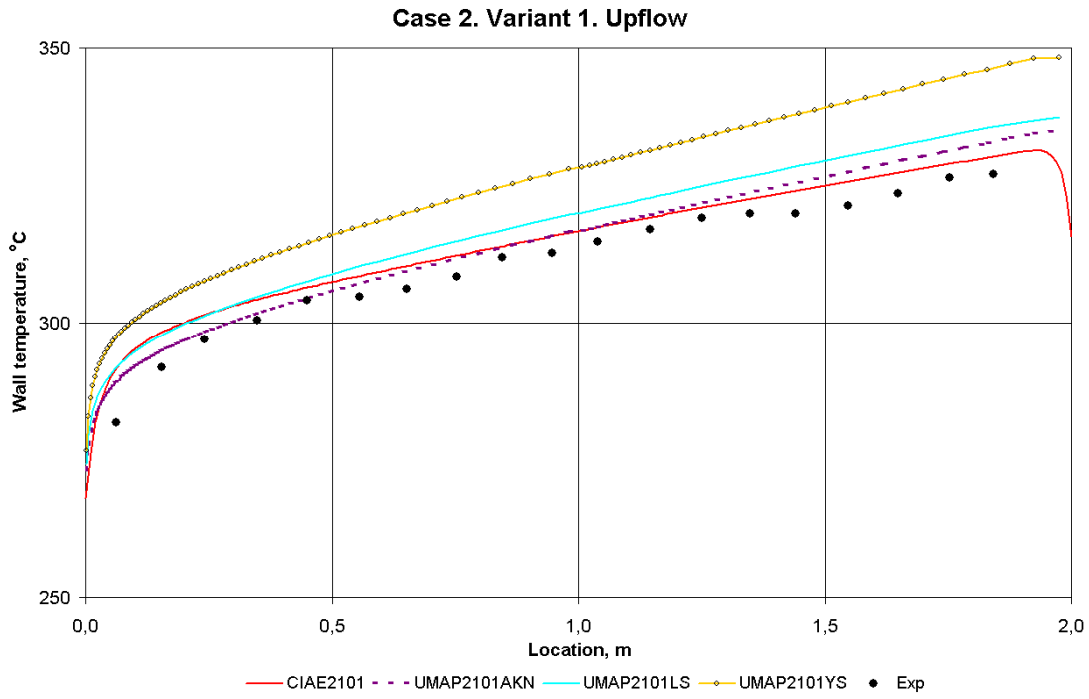

FIG. 9.53. Wall temperature axial distribution.

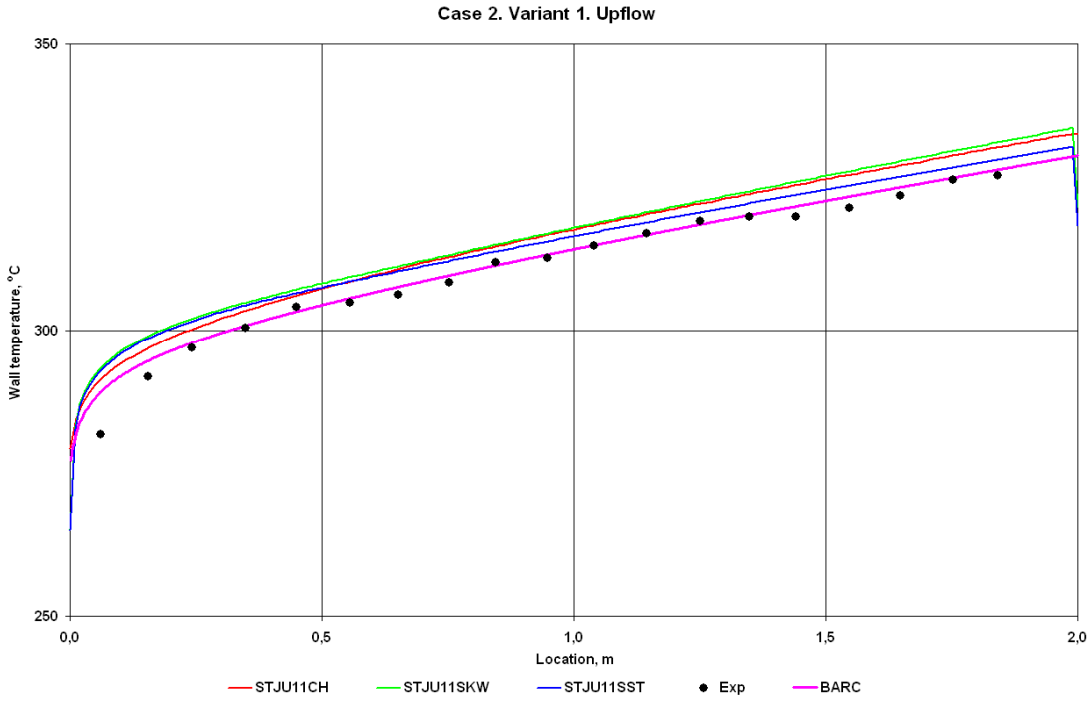

FIG. 9.54. Wall temperature axial distribution.

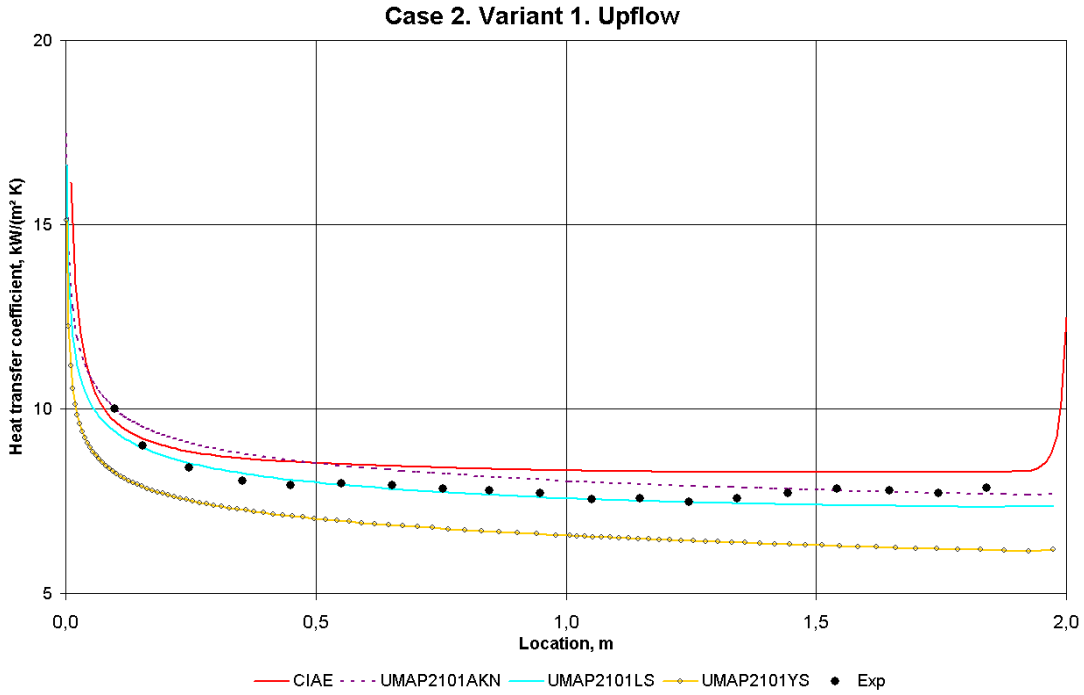

FIG. 9.55. Heat transfer coefficient axial distribution.

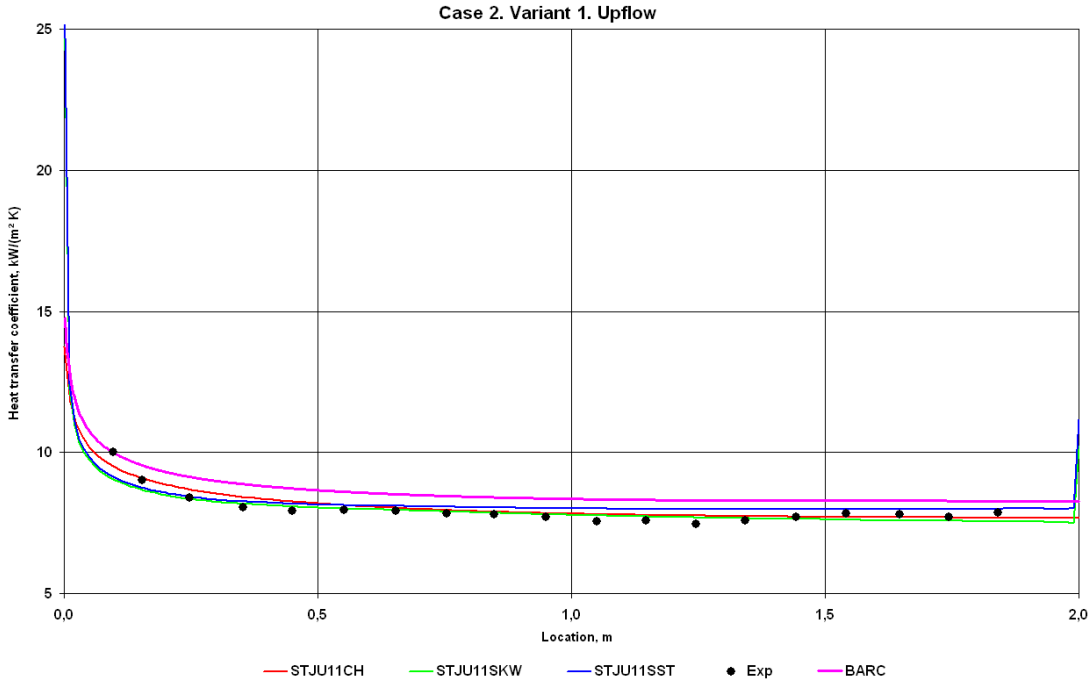

FIG. 9.56. Heat transfer coefficient axial distribution.

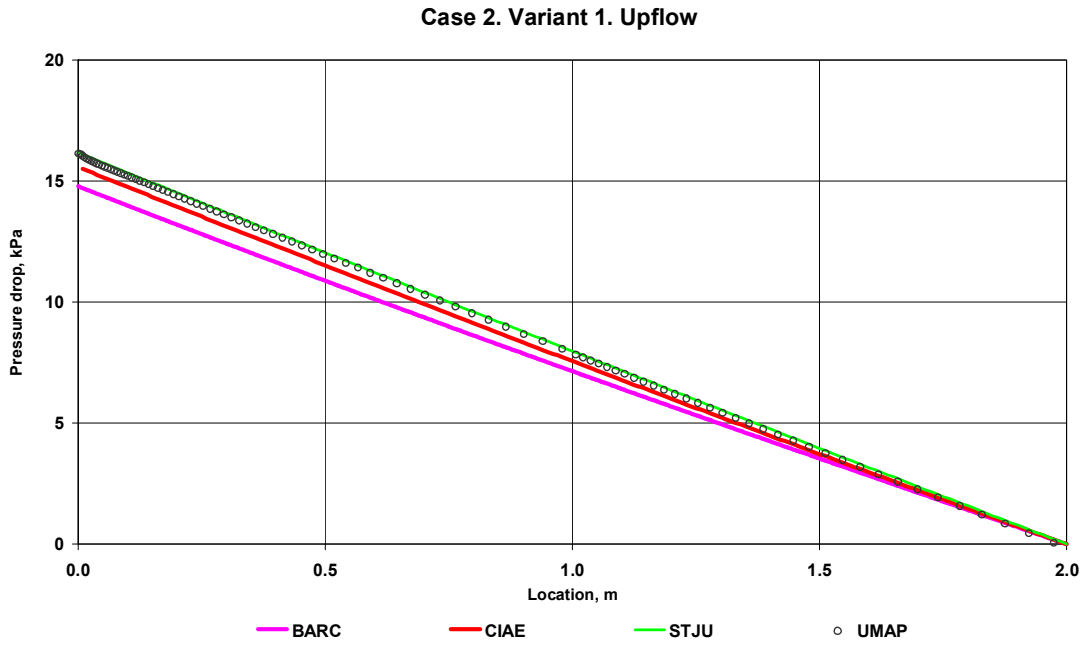

FIG. 9.57. Pressure drop axial distribution.

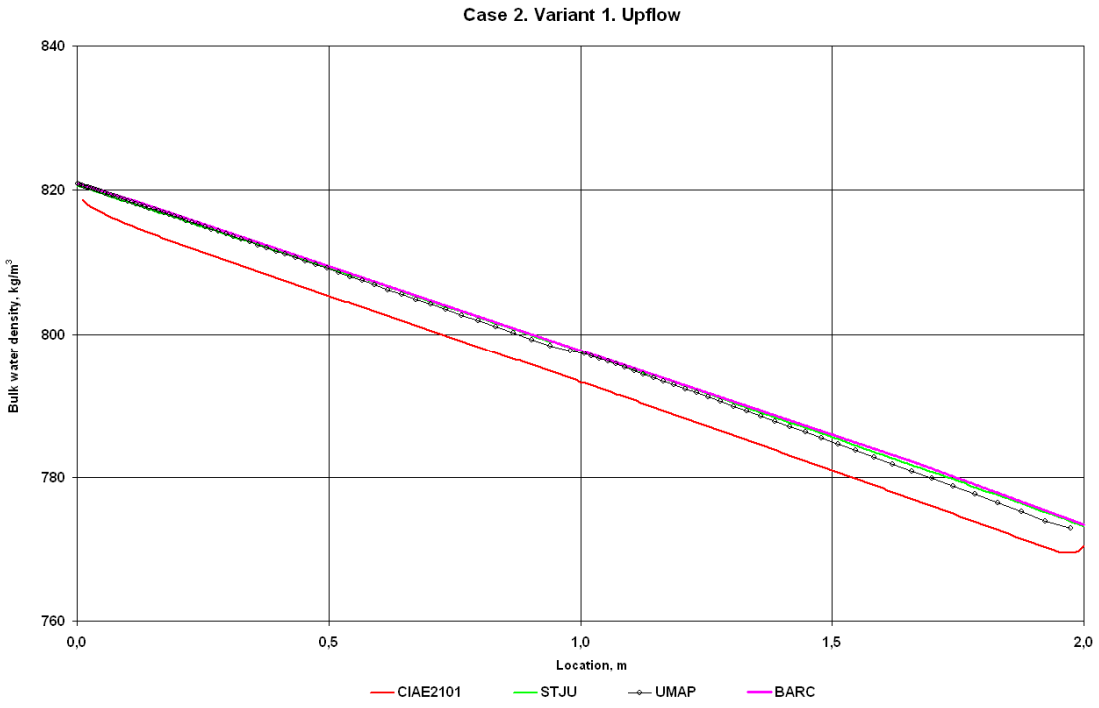

FIG. 9.58. Bulk water density axial distribution.

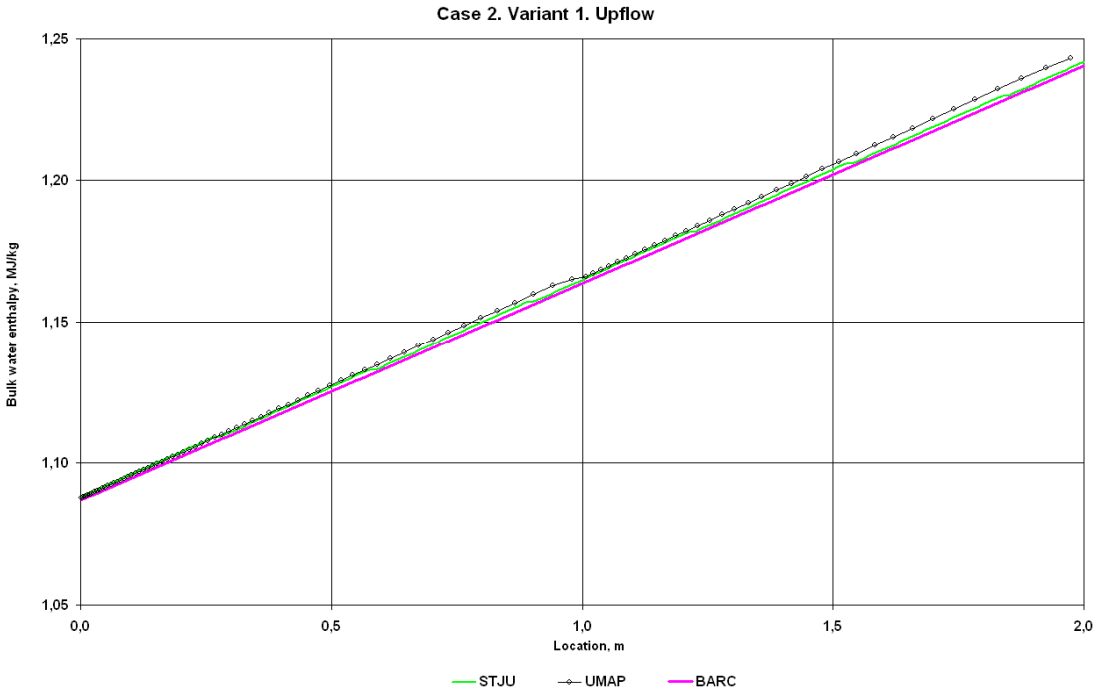

FIG. 9.59. Bulk water enthalpy axial distribution.

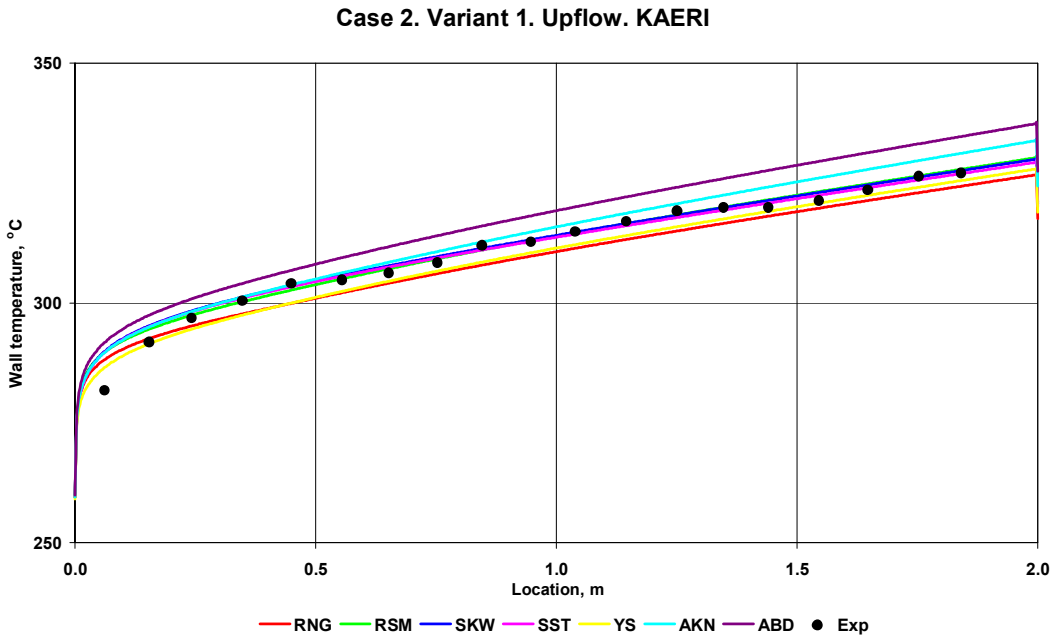

FIG. 9.60. Wall temperature axial distribution (variants of KAERI).

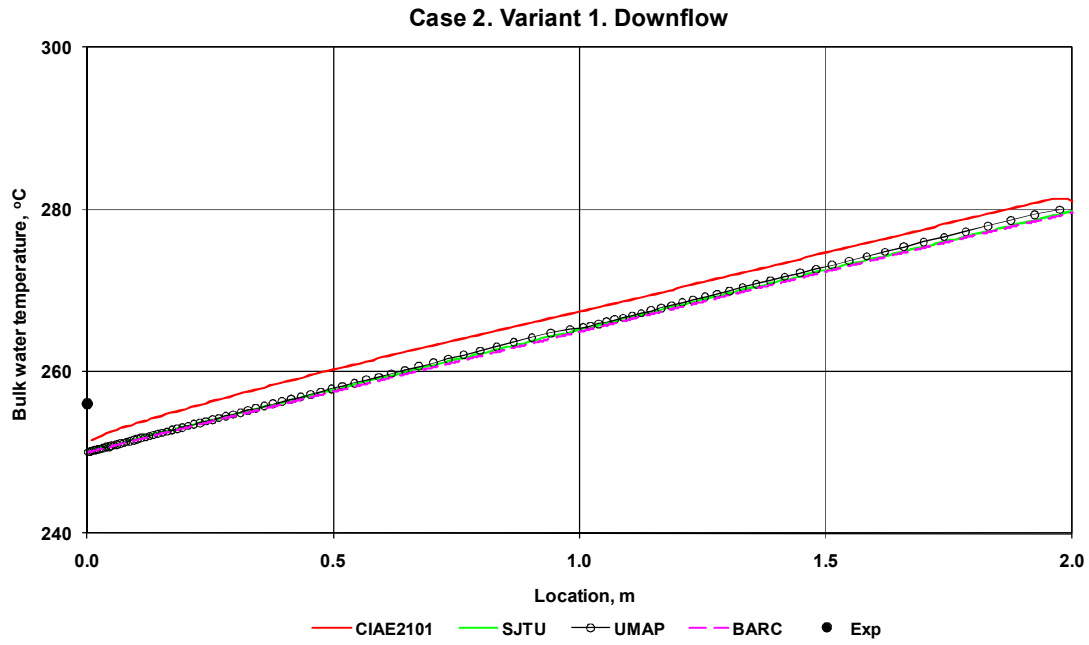

FIG. 9.61. Bulk water temperature axial distribution.

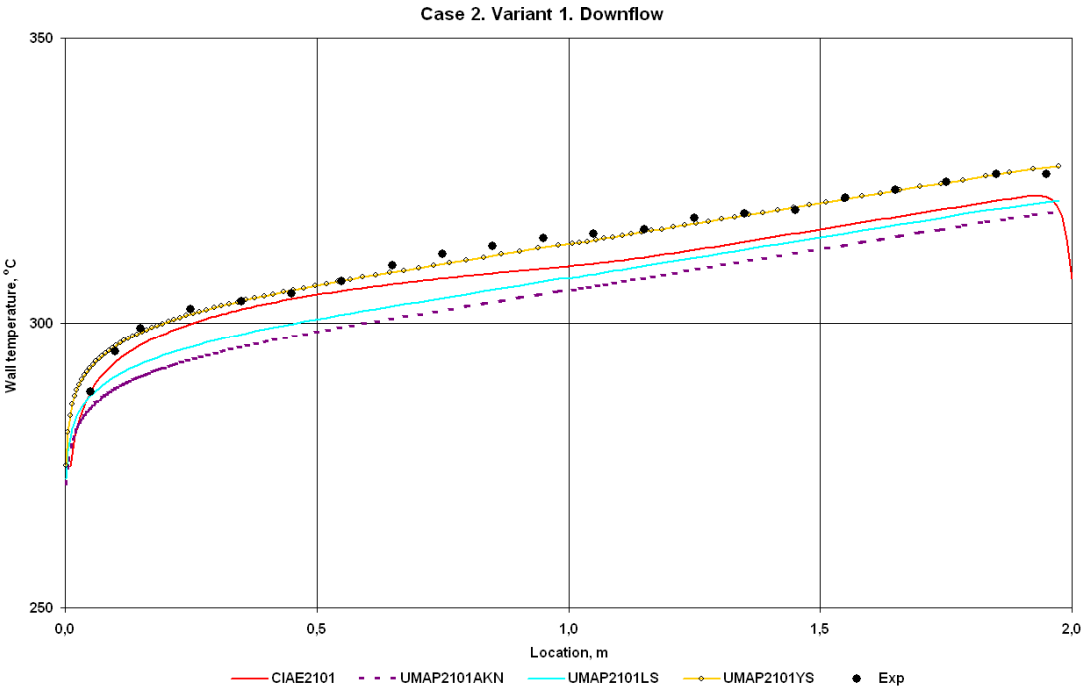

FIG. 9.62. Wall temperature axial distribution.

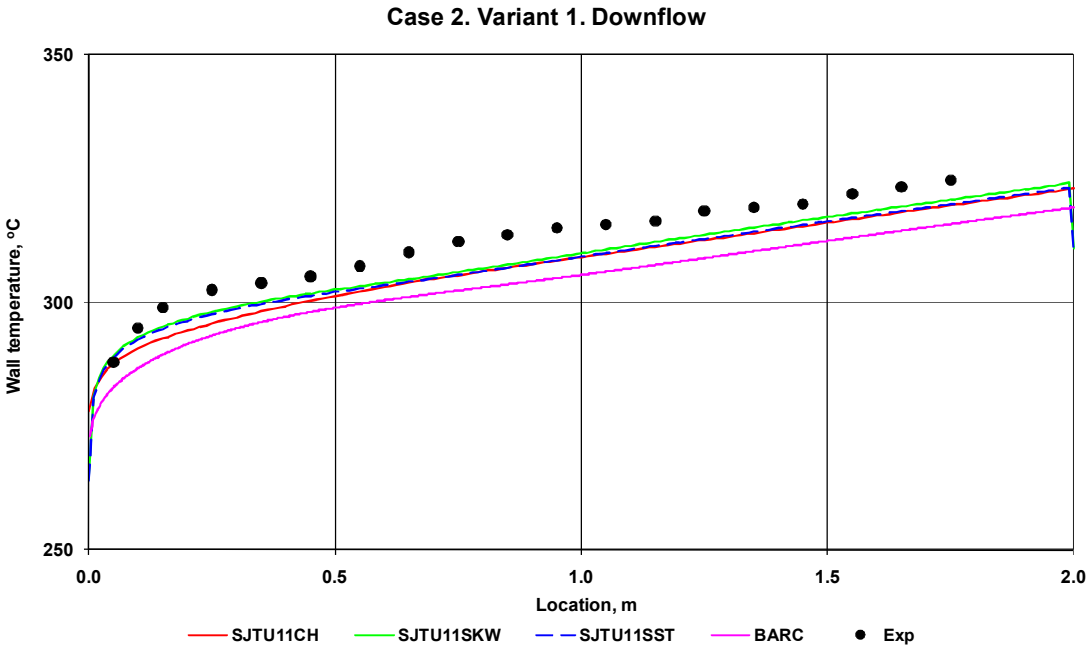

FIG. 9.63. Wall temperature axial distribution.

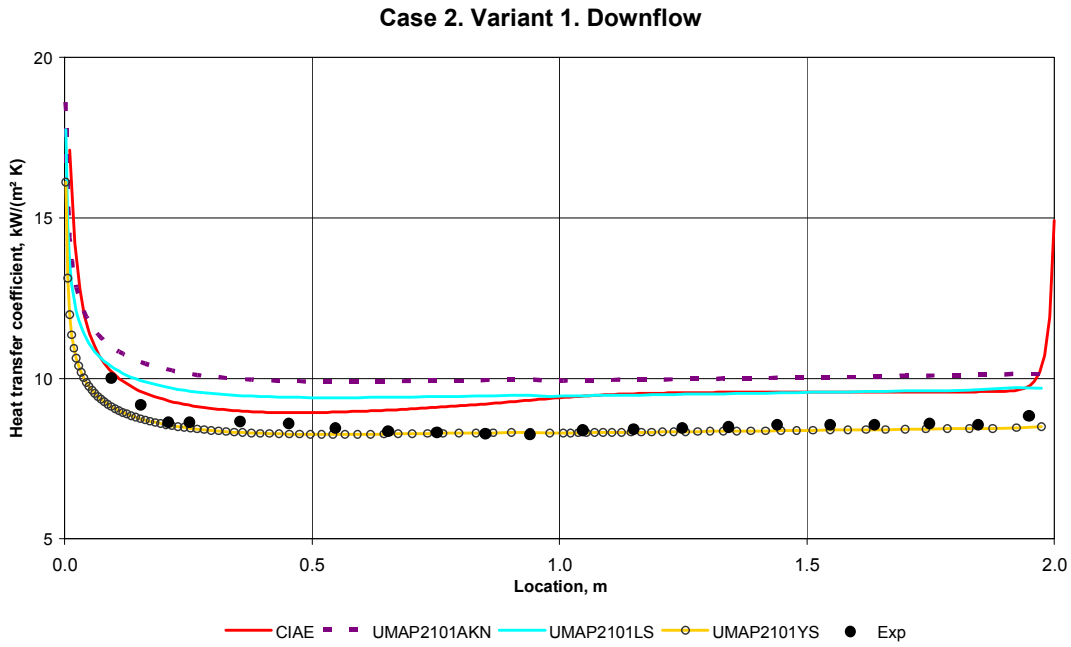

FIG. 9.64. Heat transfer coefficient axial distribution.

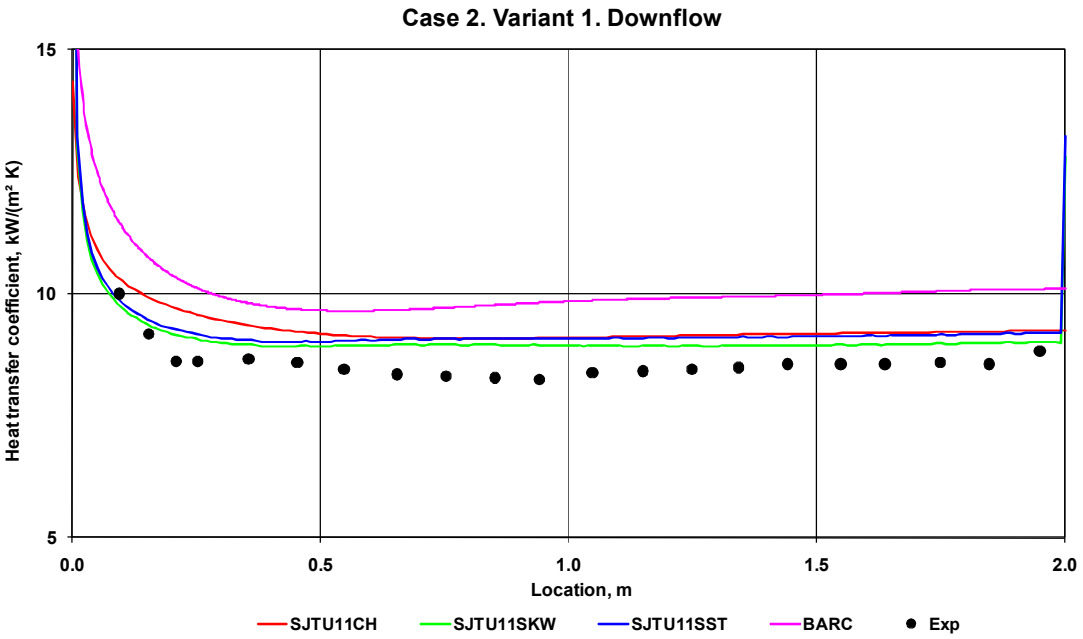

FIG. 9.65. Heat transfer coefficient axial distribution.

FIG. 9.66. Pressure drop axial distribution.

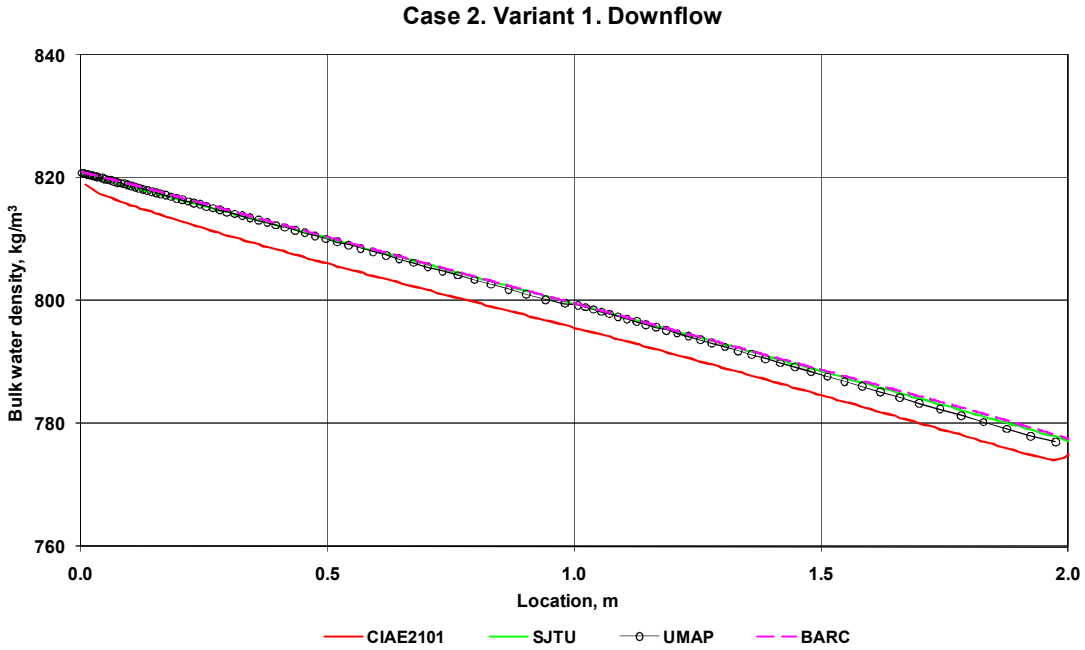

FIG. 9.67. Bulk water density axial distribution.

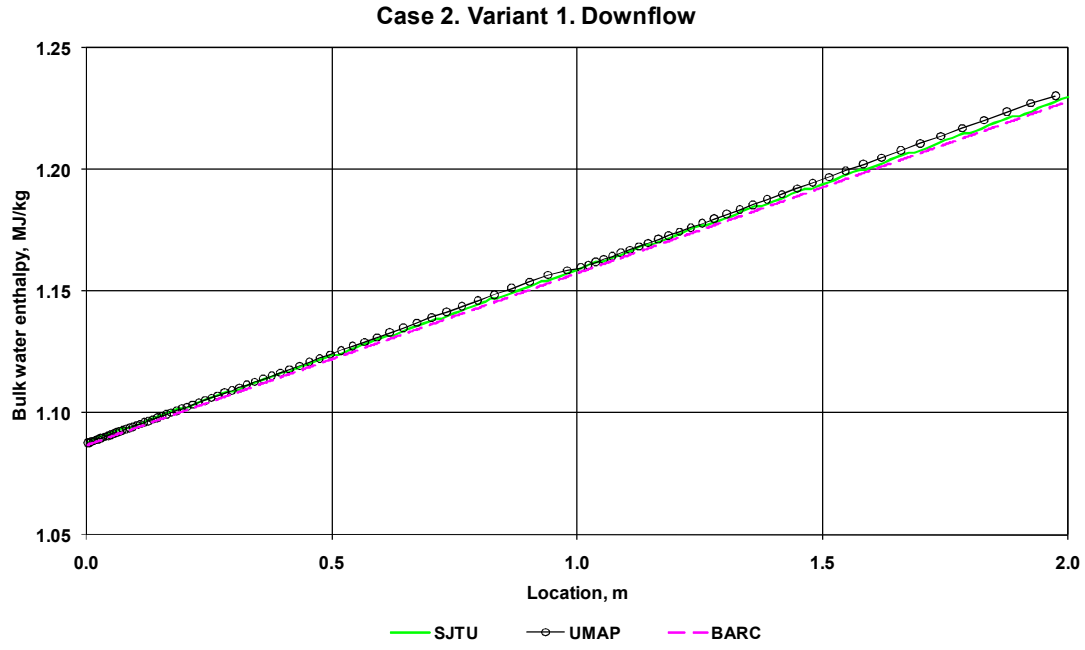

FIG. 9.68. Bulk water enthalpy axial distribution.

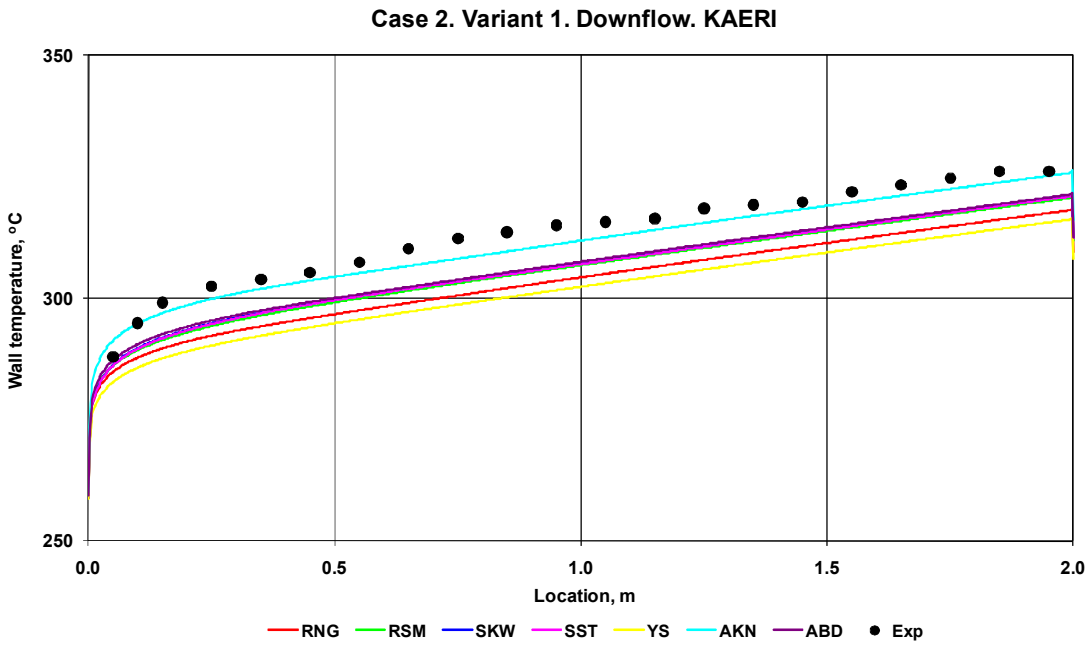

FIG. 9.69. Wall temperature axial distribution (variants of KAERI).

9.1.4.2.2.2. VARIANT 2

Experimental results of the Case 2, Variant 2 for up- and down-flow are presented in Fig. 9.29 (see Fig. 5.31 of Reference [9-2]).

Computational results of the CFD codes NAFA (BARC), ANSYS CFX (CIAE), Fluent (SJTU), SIMPLE2D (SJTU), SWIRL (UMAP) are shown in Figs 9.70–9.77. Of all the variants of SJTU calculations, only three of them (turbulence models: CH, SKW, SST) are presented, which better describe the Case 1 experimental data. Wall temperature axial distributions for the all variants of KAERI calculations (Fluent Ver. 6.3 code) are shown in Fig. 9.78.

Experimental results of the Case 2, Variant 1, downflow, are presented in Fig. 9.22 (see Fig. 5.24 of Reference [9-2]).

Figures 9.79–9.86 show computational results of the CFD codes NAFA (BARC), ANSYS CFX (CIAE), Fluent (SJTU), SIMPLE2D (SJTU), SWIRL (UMAP). Wall temperature axial distributions for the all variants of KAERI calculations (Fluent Ver. 6.3 code) are demonstrated in Fig. 9.87.

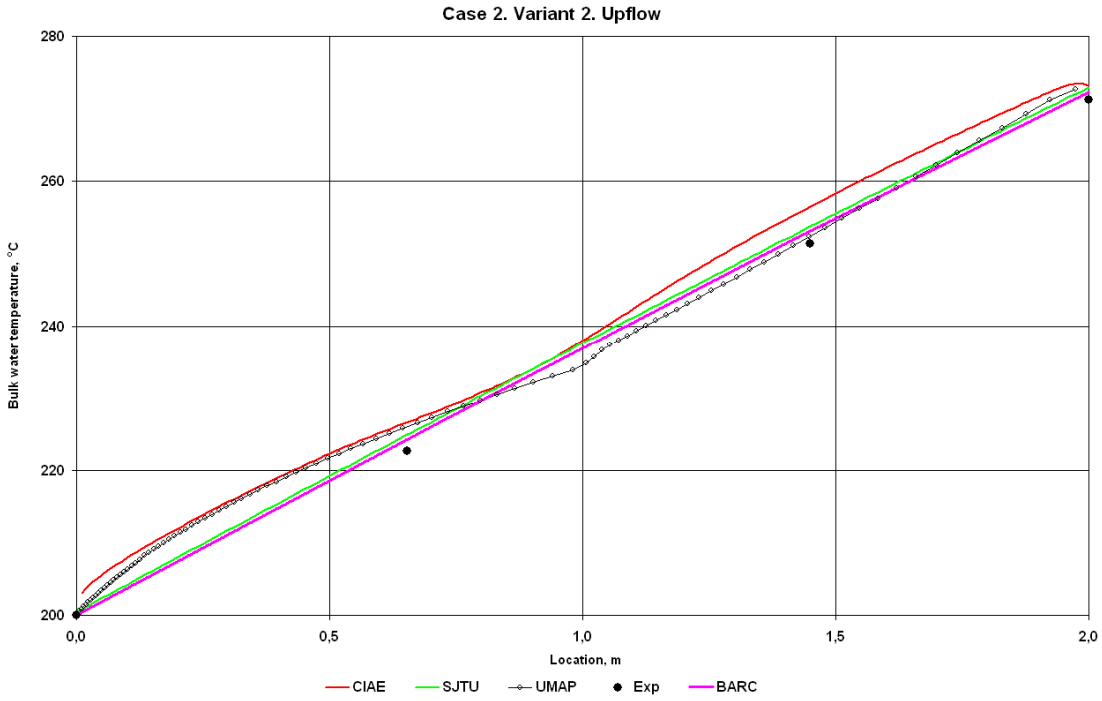

FIG. 9.70. Bulk water temperature axial distribution.

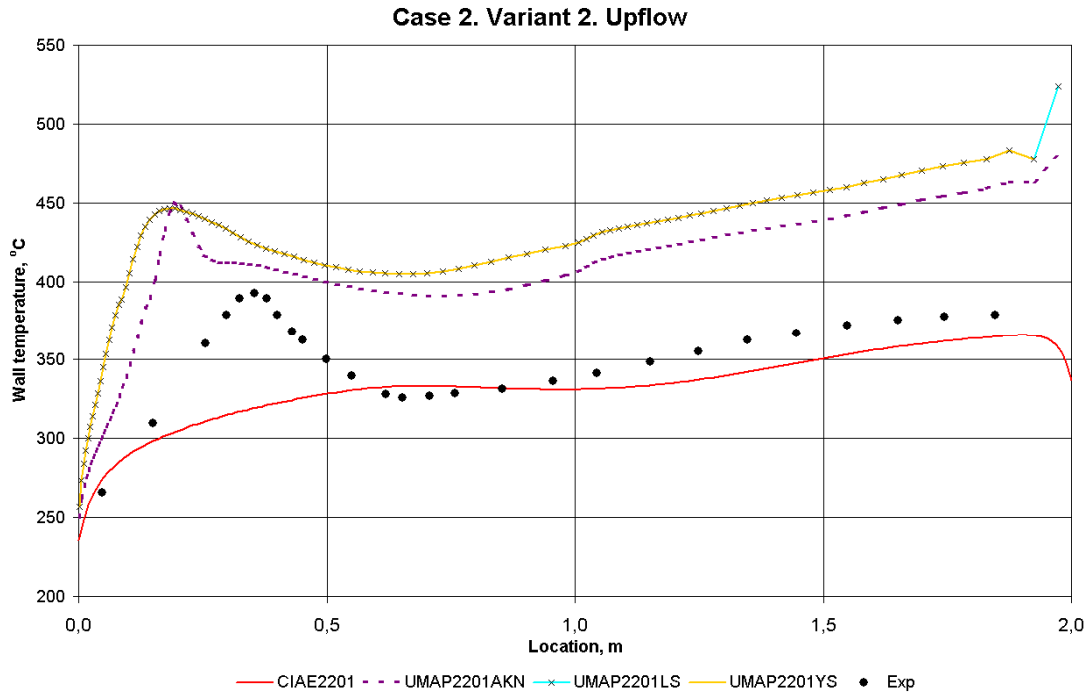

FIG. 9.71. Wall temperature axial distribution.

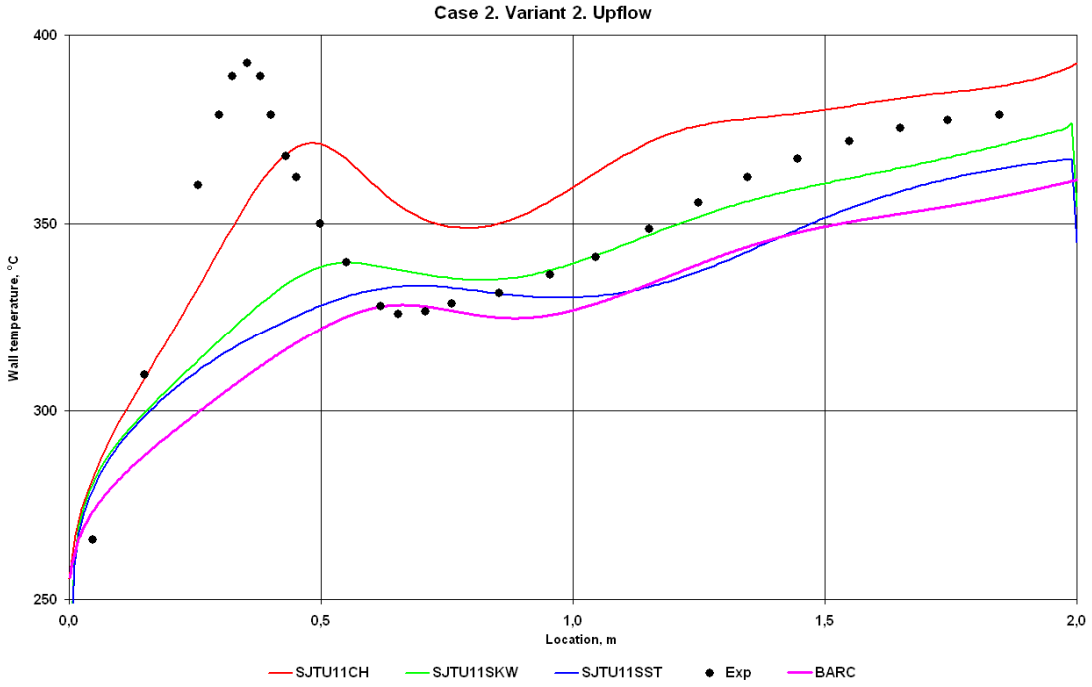

FIG. 9.72. Wall temperature axial distribution.

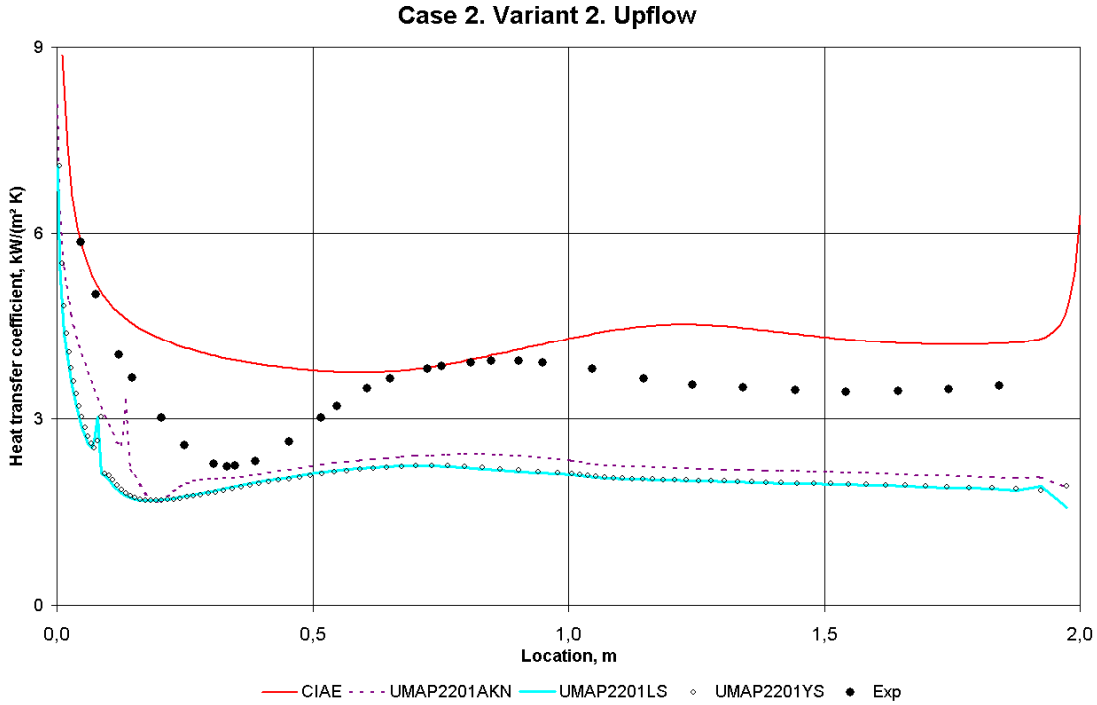

FIG. 9.73. Heat transfer coefficient axial distribution.

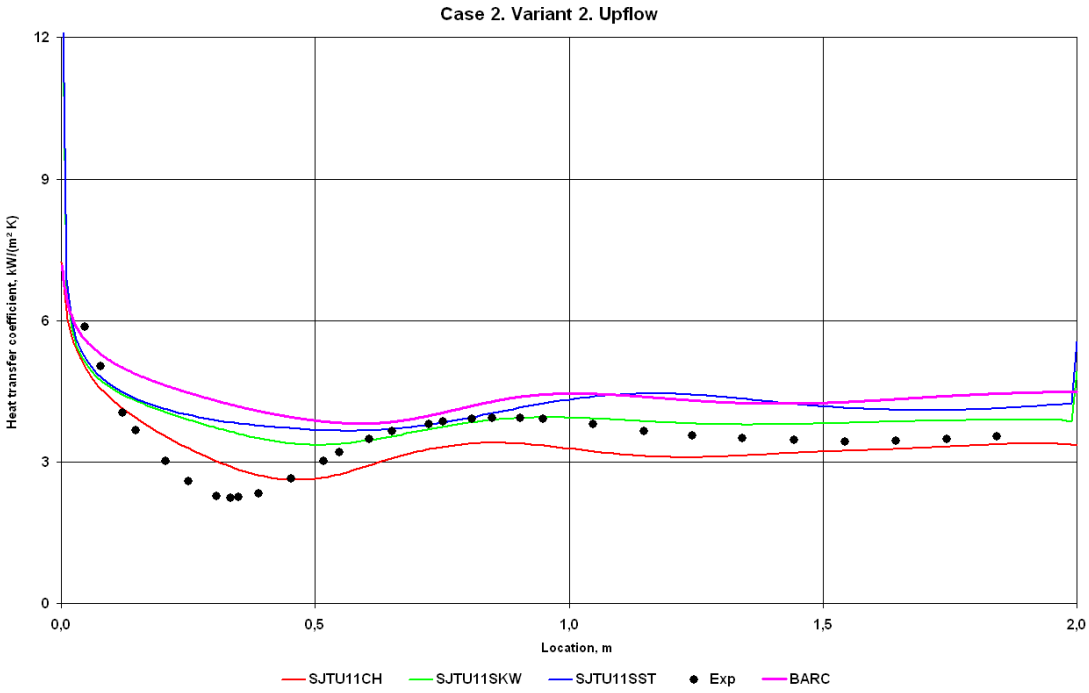

FIG. 9.74. Heat transfer coefficient axial distribution.

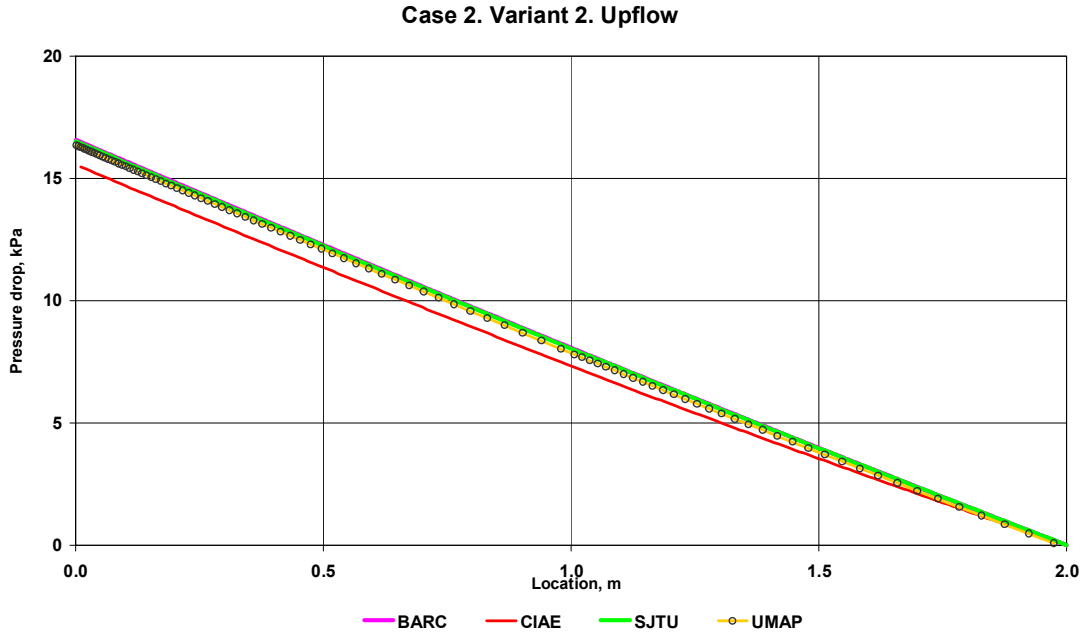

FIG. 9.75. Pressure drop axial distribution.

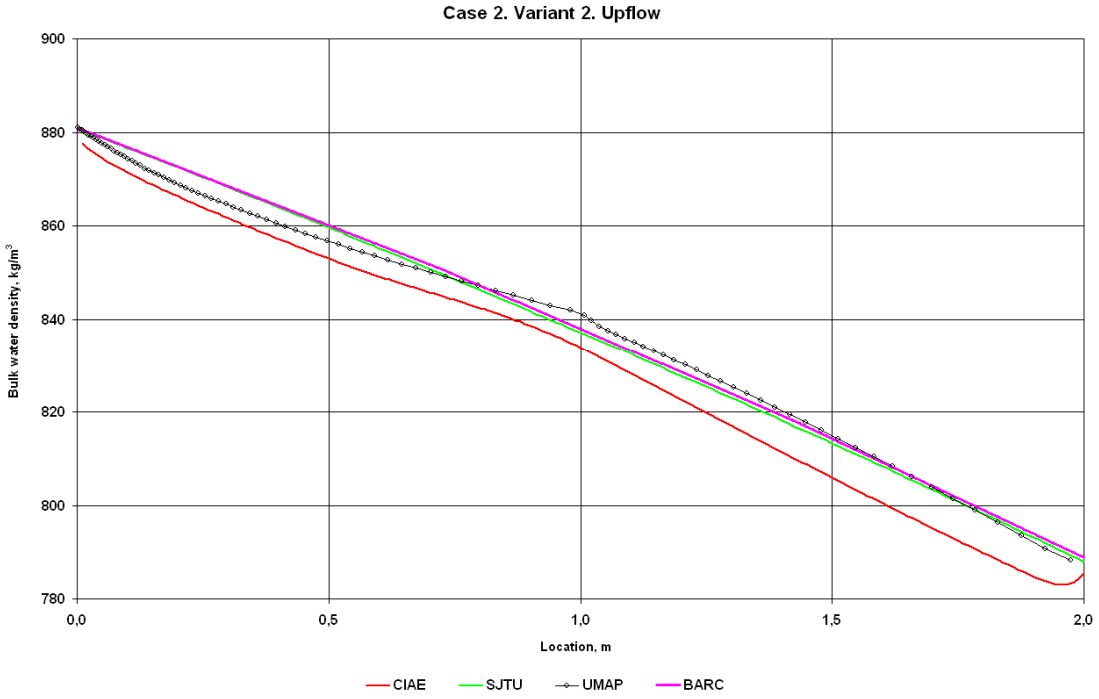

FIG. 9.76. Bulk water density axial distribution.

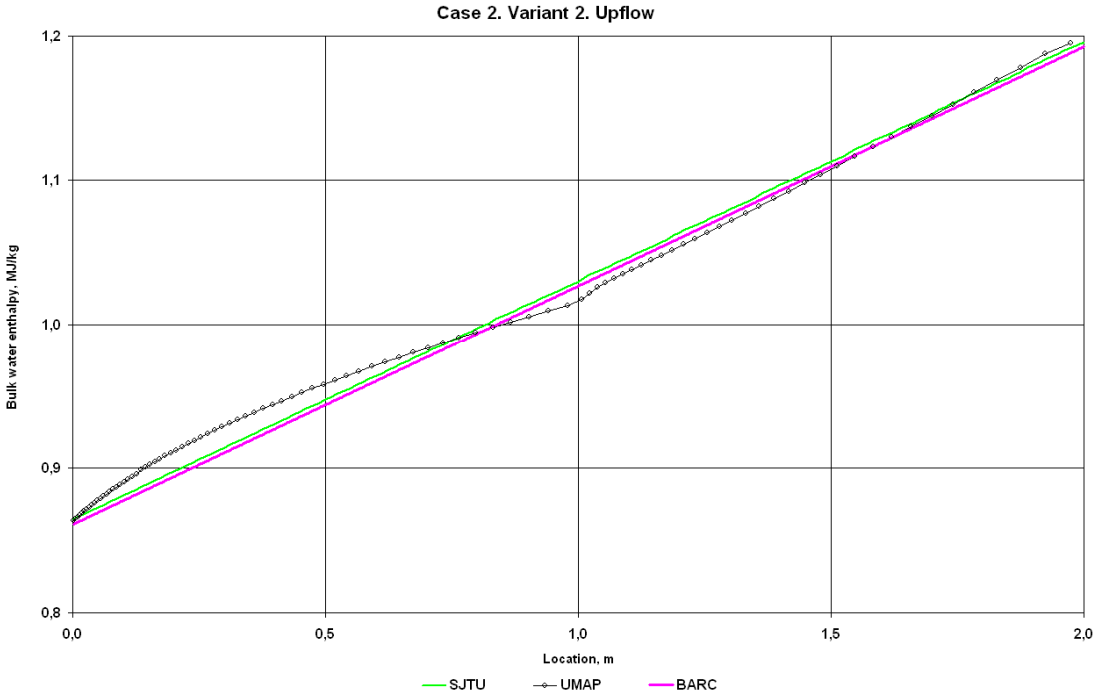

FIG. 9.77. Bulk water enthalpy axial distribution.

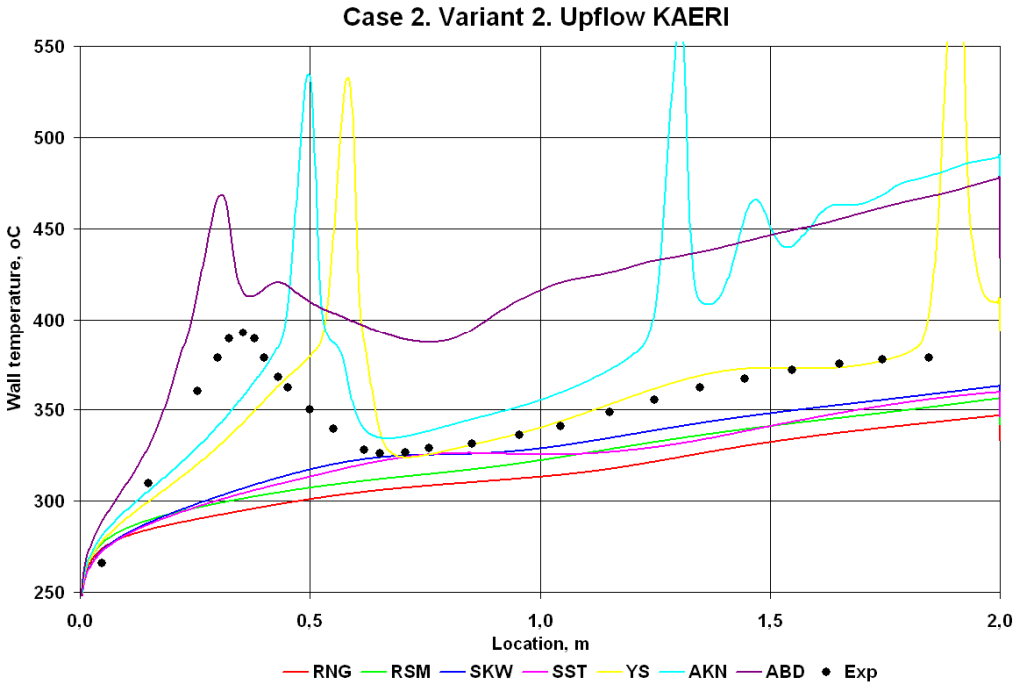

FIG. 9.78. Wall temperature axial distribution (variants of KAERI).

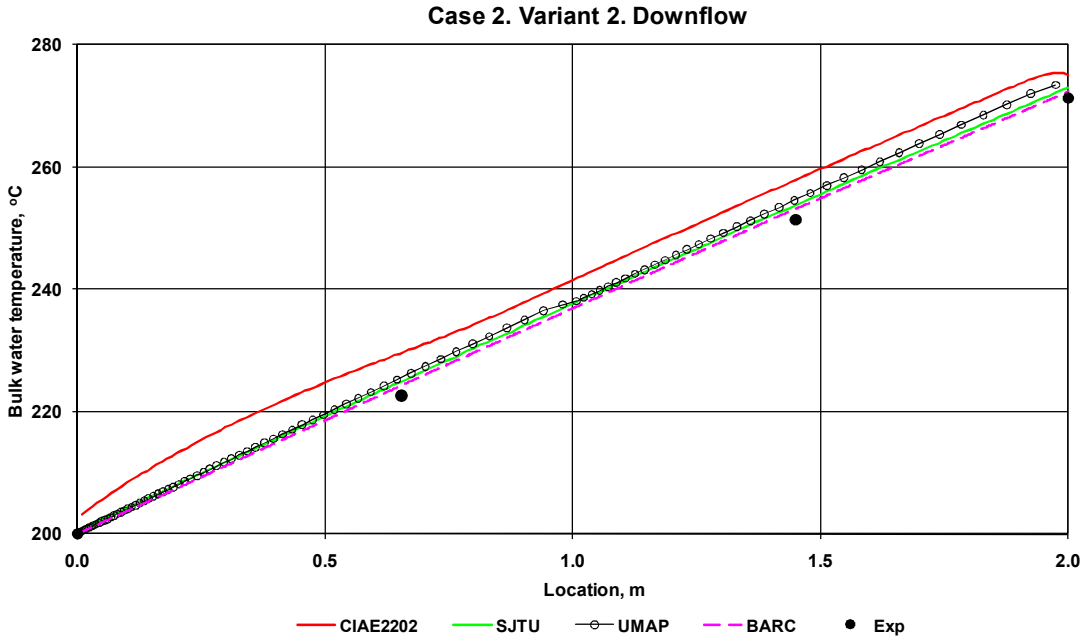

FIG. 9.79. Bulk water temperature axial distribution.

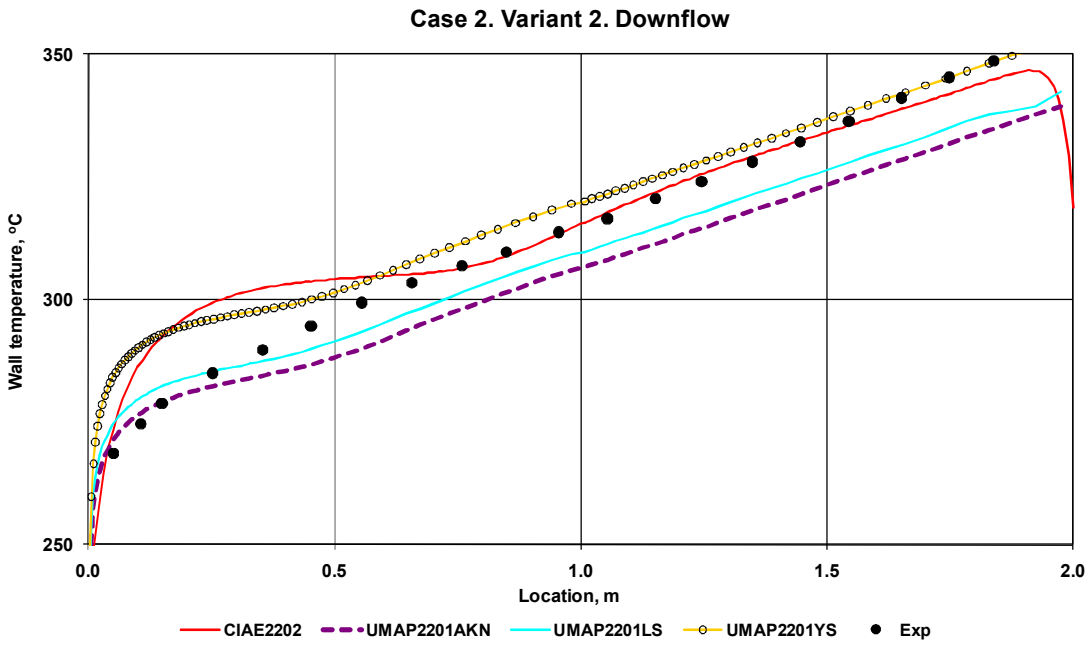

FIG. 9.80. Wall temperature axial distribution.

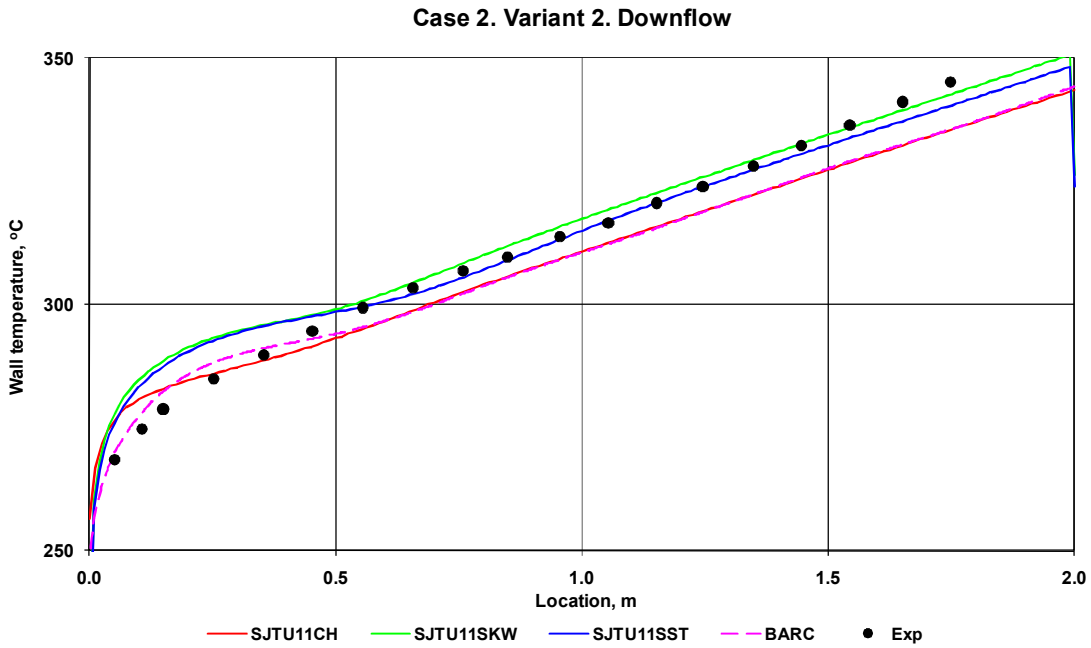

FIG. 9.81. Wall temperature axial distribution.

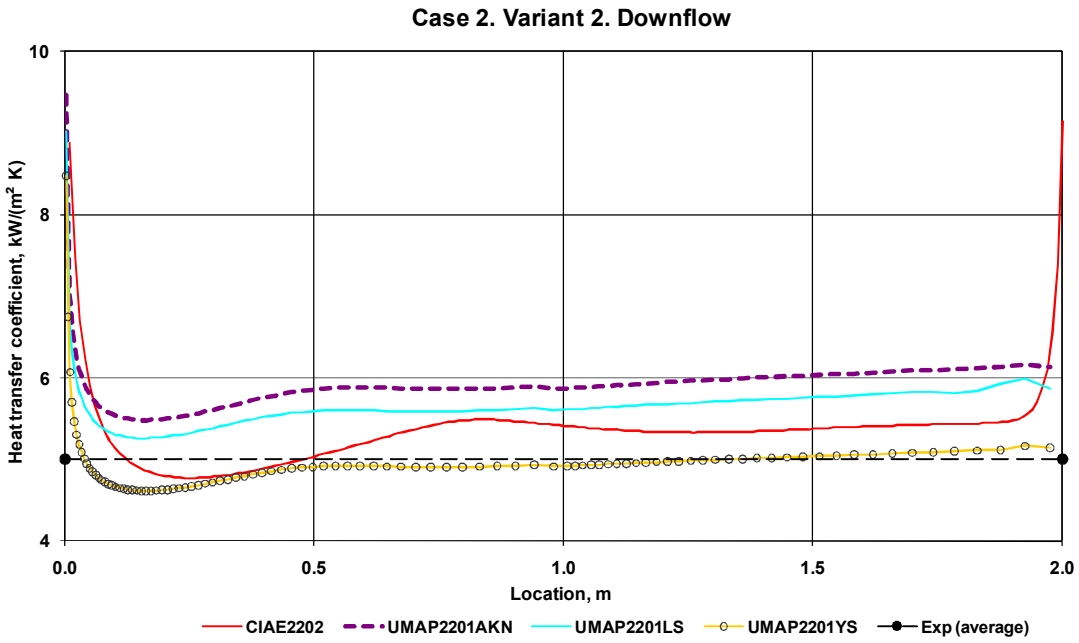

FIG. 9.82. Heat transfer coefficient axial distribution.

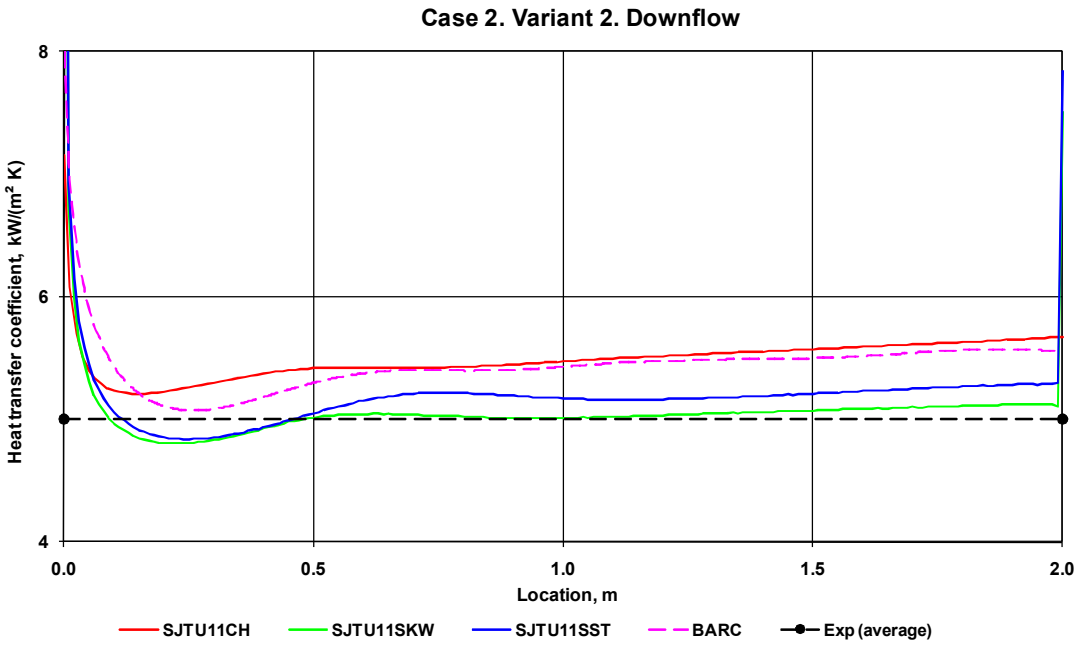

FIG. 9.83. Heat transfer coefficient axial distribution.

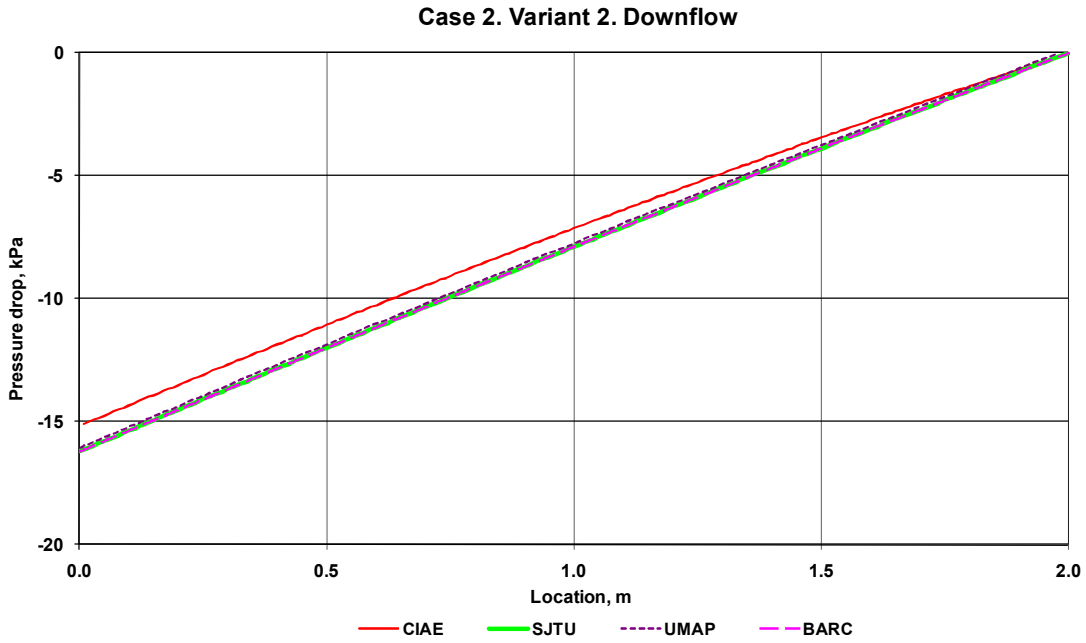

FIG. 9.84. Pressure drop axial distribution.

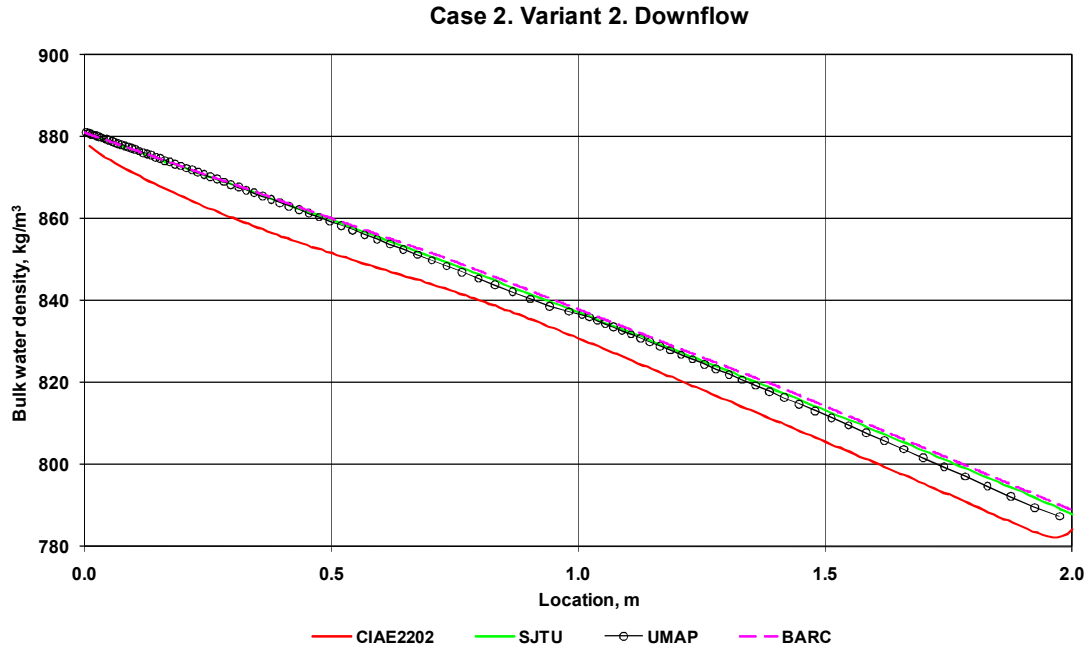

FIG. 9.85. Bulk water density axial distribution.

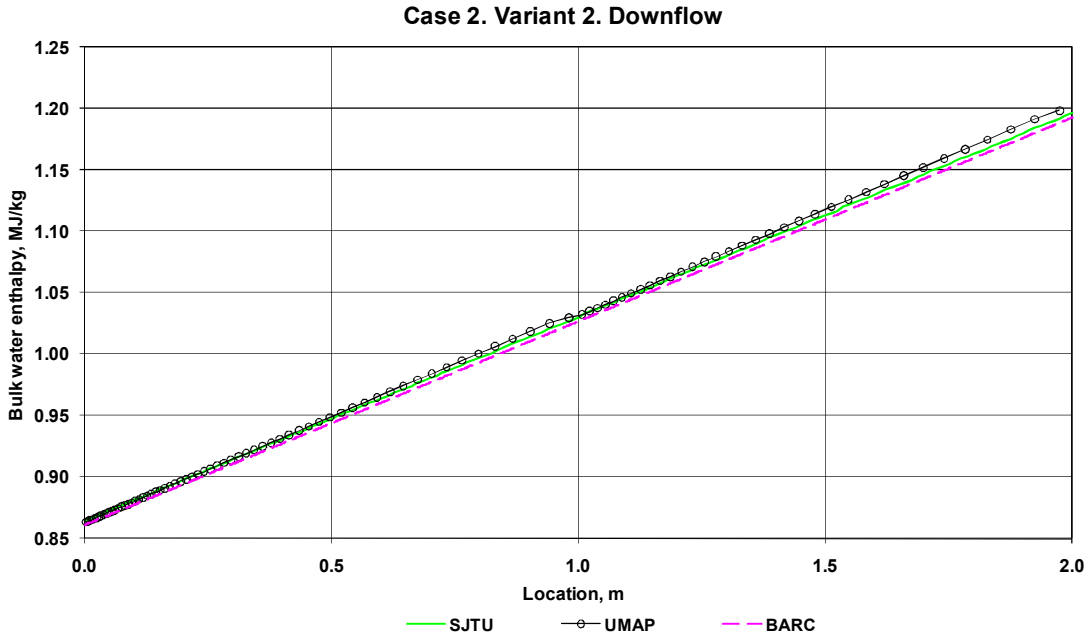

FIG. 9.86. Bulk water enthalpy axial distribution.

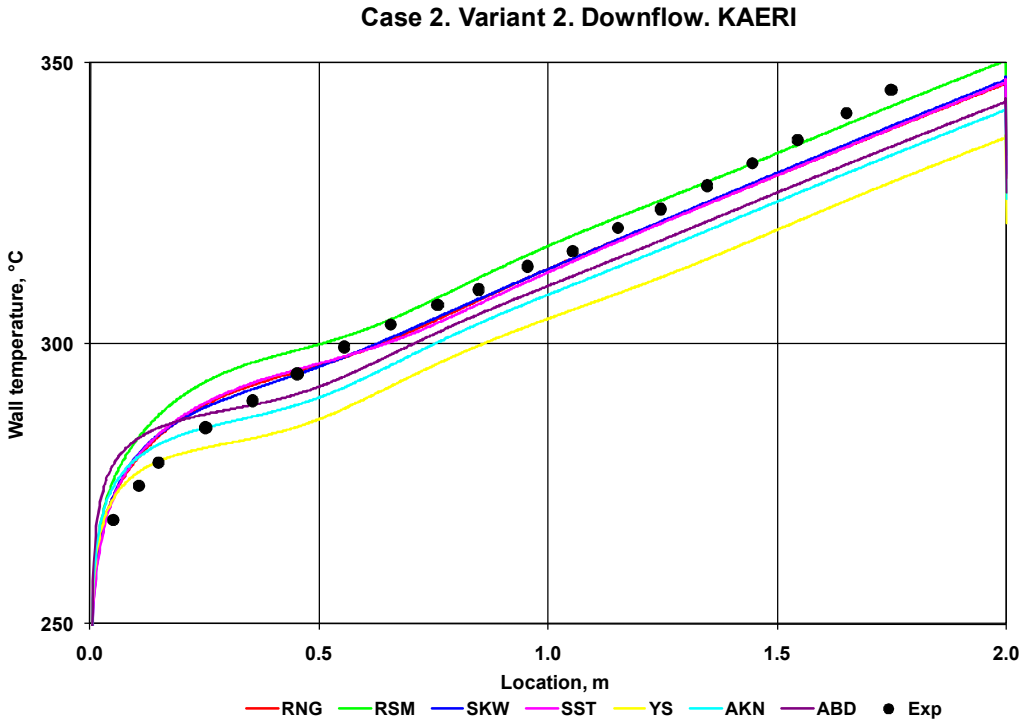

FIG. 9.87. Wall temperature axial distribution (variants of KAERI).

Some calculation results obtained at JAEA (Japan) are presented in Figs 9.88–9.92. The calculations were performed using the ACE-3D [9-23] code.

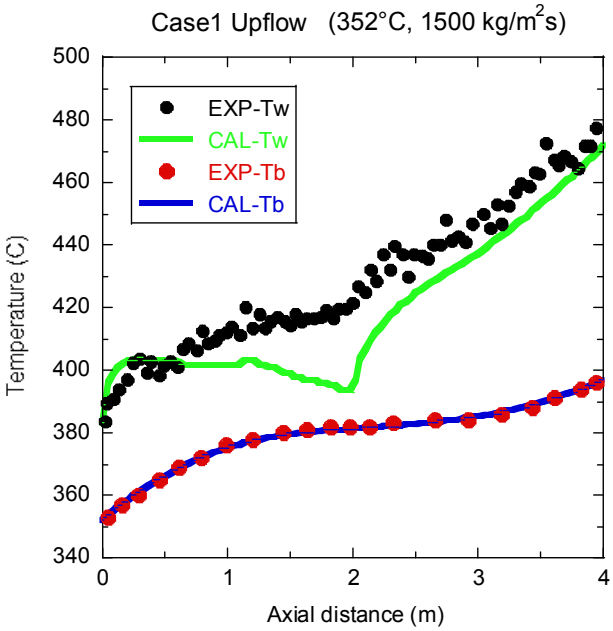

FIG. 9.88. Calculated results of wall temperature (T_w) and bulk temperature (T_b) distributions for Case 1, obtained by the ACE-3D code developed by JAEA.

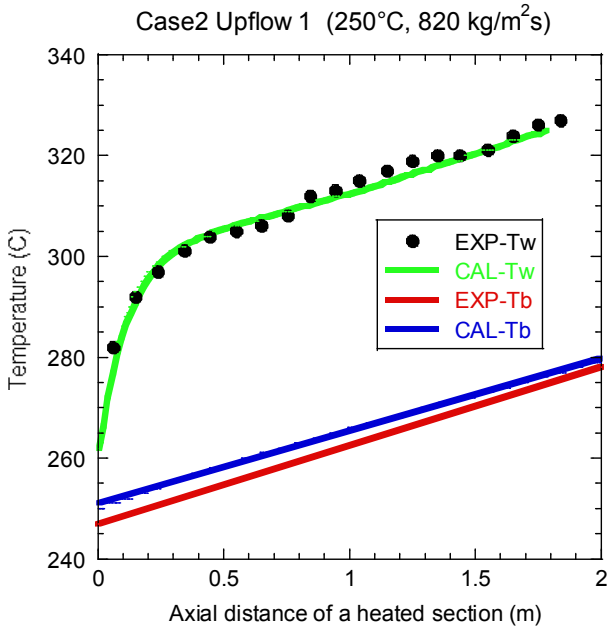

FIG. 9.89. Calculated results of wall temperature (T_w) and bulk temperature (T_b) distributions for Case 2 upflow Variant 1 obtained by the ACE-3D code developed by JAEA.

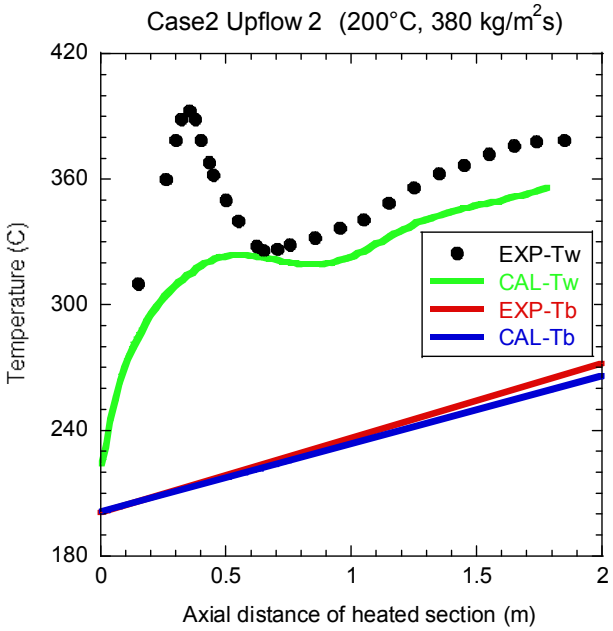

FIG. 9.90. Calculated results of wall temperature (T_w) and bulk temperature (T_b) distributions for Case 2 upflow Variant 2 obtained by code ACE-3D code developed by JAEA.

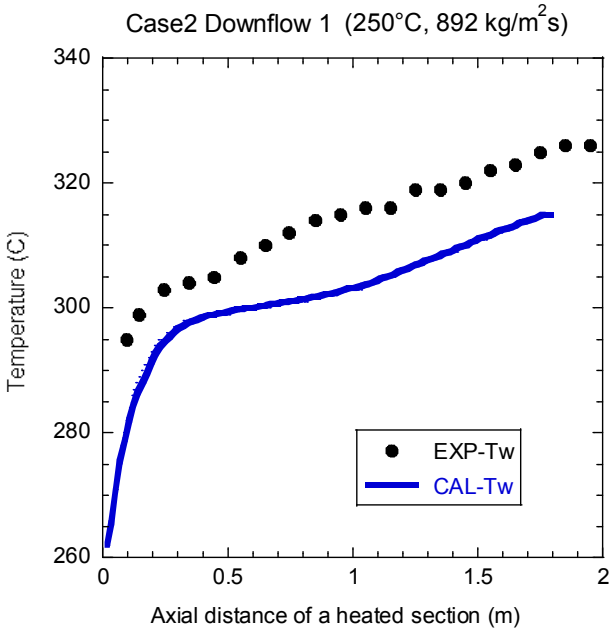

FIG. 9.91. Calculated results of wall temperature (T_w) and bulk temperature (T_b) distributions at Case 2 downflow Variant 1 obtained by the ACE-3D code developed by JAEA.

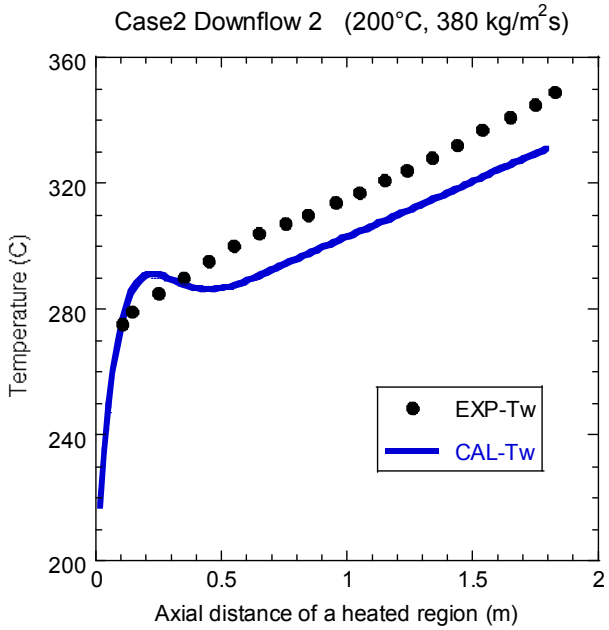

FIG. 9.92. Calculated results of wall temperature (T_w) and bulk temperature (T_b) distributions for Case 2 downflow Variant 2, which were obtained by the ACE-3D code developed by JAEA.

9.1.5. Comparison of the experimental and computational results

This section contains quantitative comparisons of experimental and computational results. Arithmetic means of the relative difference between computational and experimental results of pipe wall temperature, and standard deviations are given in Table 9.6. The computation of the relative difference between experimental and computational values of pipe wall temperature was obtained by the formula:

$$\delta T_w = \frac{\hat{T}_w^{com} - T_w^{\exp}}{T_w^{\exp}},$$

where $T_w^{\exp}$ is the experimental value of wall temperature in °C and $\hat{T}_w^{com}$ is the computational value of wall temperature in thermocouple location pointin °C. The value $\hat{T}_w^{com}$ was calculated under the assumption of linear temperature change between two nearby computational temperature values to the thermocouple location points.

The next two sections include figures with experimental wall temperature vs. computational one.

The comparison of calculation results using pressure difference across the test section and water parameters is presented in Table 9.7 (for S&S codes) and Table 9.8 (for CFD codes).

TABLE 9.6. COMPARISON OF EXPERIMENTAL AND COMPUTATIONAL VALUES OF WALL TEMPERATURE

Participants	Codes	Variants of calculations	Relative difference of wall temperature δT_w, %									
			AM [1]	SD [2]	AM	SD	AM	SD	AM	SD	AM	SD
			Case 1		Case 2 Variant 1				Case 2 Variant 2			
System and subchannel codes			Upflow		Upflow		Downflow		Upflow		Downflow	
AECL	CATHENA	-	−4.7	3.6	0.0	1.6	−1.9	1.1	−13.3	19.0	3.5	2.3
GP	TEMPA-SC	HTC_1	−0.1	2.1	0.0	1.6	−1.8	1.1	3.1	8.6	17.9	5.7
		HTC_4	−1.4	1.8	−0.1	1.6	−1.9	1.0	−9.7	7.7	3.3	2.1
JRC	COBRA-EN	-	0.0	1.7	0.3	1.4	−2.1	0.6	−6.3	8.3	5.2	0.9
MP	TRACE5.0	-	−5.7	4.2	1.4	0.9	−0.7	0.4	−10.7	19.6	8.9	1.7
	RELAP5/Mod3.3	-	−2.9	3.2	−0.1	0.9	−2.0	0.4	−12.8	19.1	6.3	2.2
VTT	APROS	-	−0.1	1.7	2.0	1.7	0.0	1.2	−5.1	8.1	8.5	2.8
CFD codes												
BARC	NAFA	-	−4.8	1.8	0.4	0.6	−2.8	0.3	−7.8	7.3	−1.1	1.3
CIAE	ANSYS CFX	-	−0.6	1.0	1.2	0.7	−1.2	0.5	−6.2	6.7	1.2	2.0
KAERI	Fluent	RSM	−1.1	1.8	0.3	0.7	−2.4	0.5	−10.1	7.2	0.9	1.3
		SKW	0.9	2.4	0.4	0.7	−2.2	0.5	−8.2	7.4	−0.3	1.2
		SST	0.6	2.3	0.2	0.7	2.3	0.5	9.2	7.4	0.4	1.3
SJTU	SIMPLE2D	CH	1.2	1.5	1.4	0.6	−1.7	0.5	2.0	6.0	−1.0	1.6
	Fluent	SKW	1.7	1.7	1.7	0.7	−1.3	0.5	−4.1	6.8	1.0	1.4
		SST	−0.2	1.8	1.2	0.8	−1.5	0.5	−6.1	6.9	0.4	1.5
UMAP	SWIRL	AKN	−1.0	3.0	1.2	0.6	−2.6	0.5	16.3	5.9	−2.4	1.5
		LS	6.1	4.7	2.1	0.6	−2.0	0.5	21.4	7.5	−1.3	1.6
		YS	6.6	6.3	4.7	0.8	−0.1	0.4	21.4	7.5	2.0	1.8

1) AM – arithmetic mean of δT_w.
2) SD – standard deviation of δT_w.

TABLE 9.7. COMPARISON OF COMPUTATIONAL RESULTS FOR S&S CODES

Parameter	Maximum difference of calculation results (relative difference)					Comments
	Case 1	Case 2 Var. 1 Up	Case 2 Var. 1 Down	Case 2 Var. 2 Up	Case 2 Var. 2 Down	
Pressure drop, kPa	14 (50%) **4 (10%)** *)	1.0 (6%)	1.5 (10%)	0.9 (6%)	1.0 (6%)	*) values without taking JRC results into consideration in comparison
Water bulk enthalpy, kJ/kg	0.16 (6%) **0.03 (1.6%)** *)	0.03 (2%) **0.003 (0.3%)***)	0.03 (3%) **0.003 (0.3%)***)	0.02 (2%) **0.010 (1.3%)***)	0.02 (2%) **0.016 (1.9%)***)	*) values without taking MP results into consideration in comparison
Water bulk temperature, °C	4 (1%)	1.3 (0.5%)	1.0 (0.4%)	4 (2%)	4 (2%)	
Water bulk density, kg/m^3	12 (2%)	1.8 (0.2%)	1.3 (0.2%)	5.3 (0.7%)	4.9 (0.6%)	

TABLE 9.8. COMPARISON OF COMPUTATIONAL RESULTS FOR CFD CODES

Parameter	Maximum difference of calculation results (relative difference)					Comments
	Case 1	Case 2 Var. 1 Up	Case 2 Var. 1 Down	Case 2 Var. 2 Up	Case 2 Var. 2 Down	
Pressure drop, kPa	21 (110%)	1.4 (10%)	0.8 (6%)	1.1 (7%)	7 (50%)	
Water bulk enthalpy, kJ/kg	0.005 (0.3%)	0.003 (0.2%)	0.0014 (0.11%)	0.004 (0.5%)	0.005 (0.4%)	
Water bulk temperature, °C	0.8 (0.2%)	1.5 (0.5%)	1.4 (0.5%)	2.2 (1.1%)	2.7 (1.0%)	
Water bulk density, kg/m^3	50 (16%) **11 (3%)** *)	5 (0.6%)	3 (0.4%)	3 (0.4%)	5 (0.6%)	*) values without taking BARC results into consideration in comparison

9.1.5.1.1. Subchannel and system codes

9.1.5.1.1.1. AECL

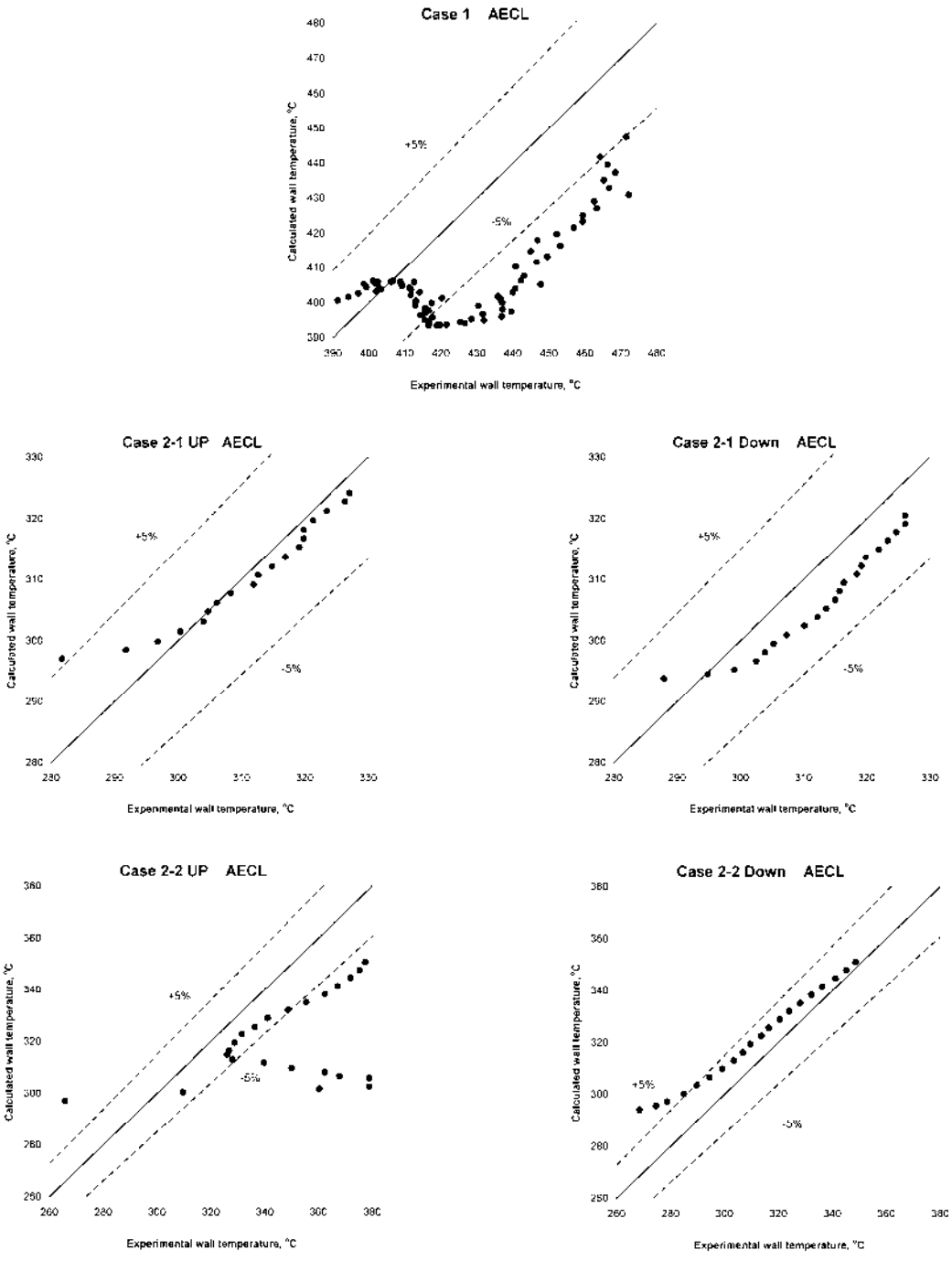

FIG. 9.93. Comparison of the experimental and computational results of AECL.

9.1.5.1.1.2. GP

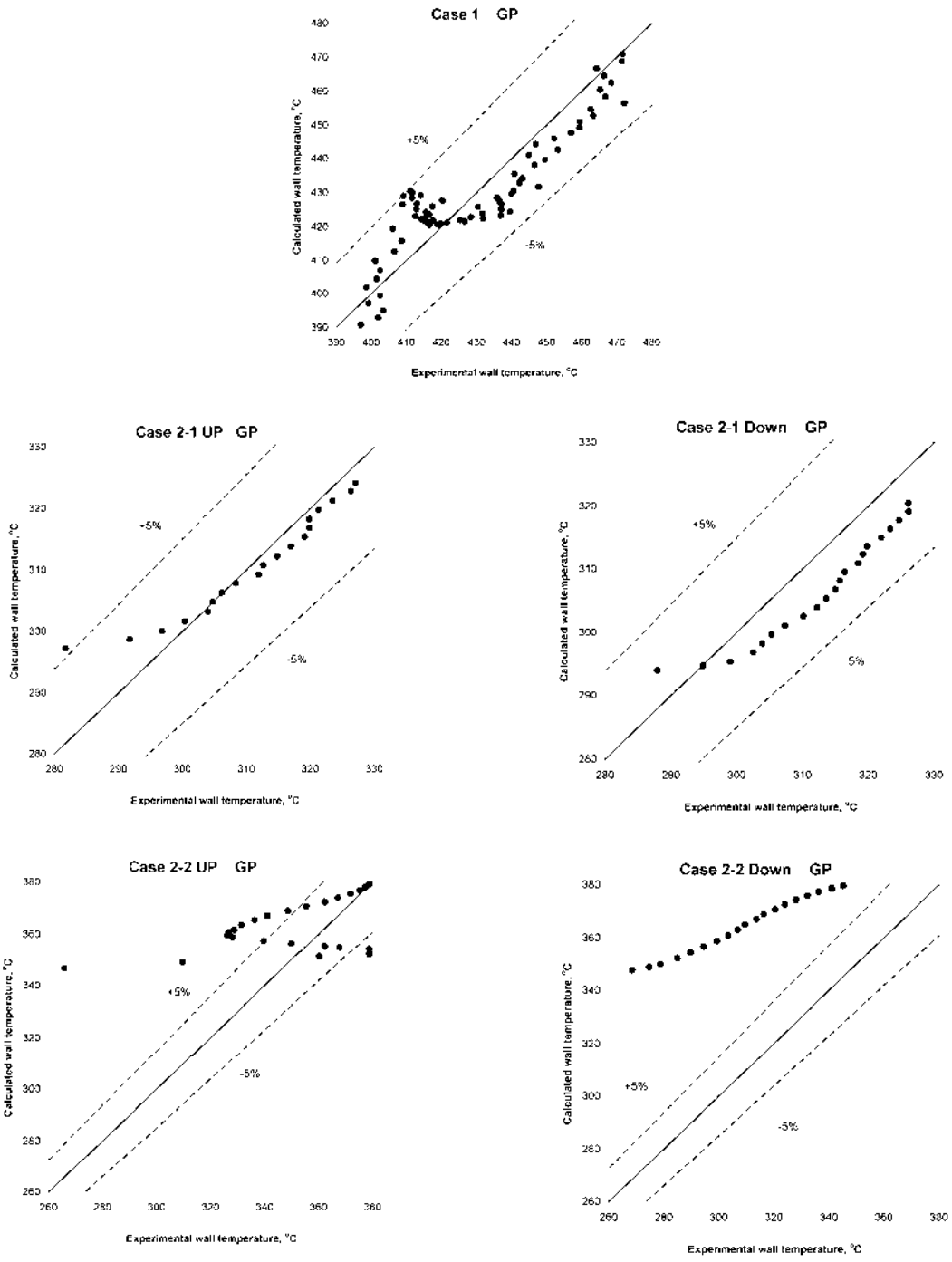

FIG. 9.94. Comparison of the experimental and computational results of Gidropress (variant GP1101).

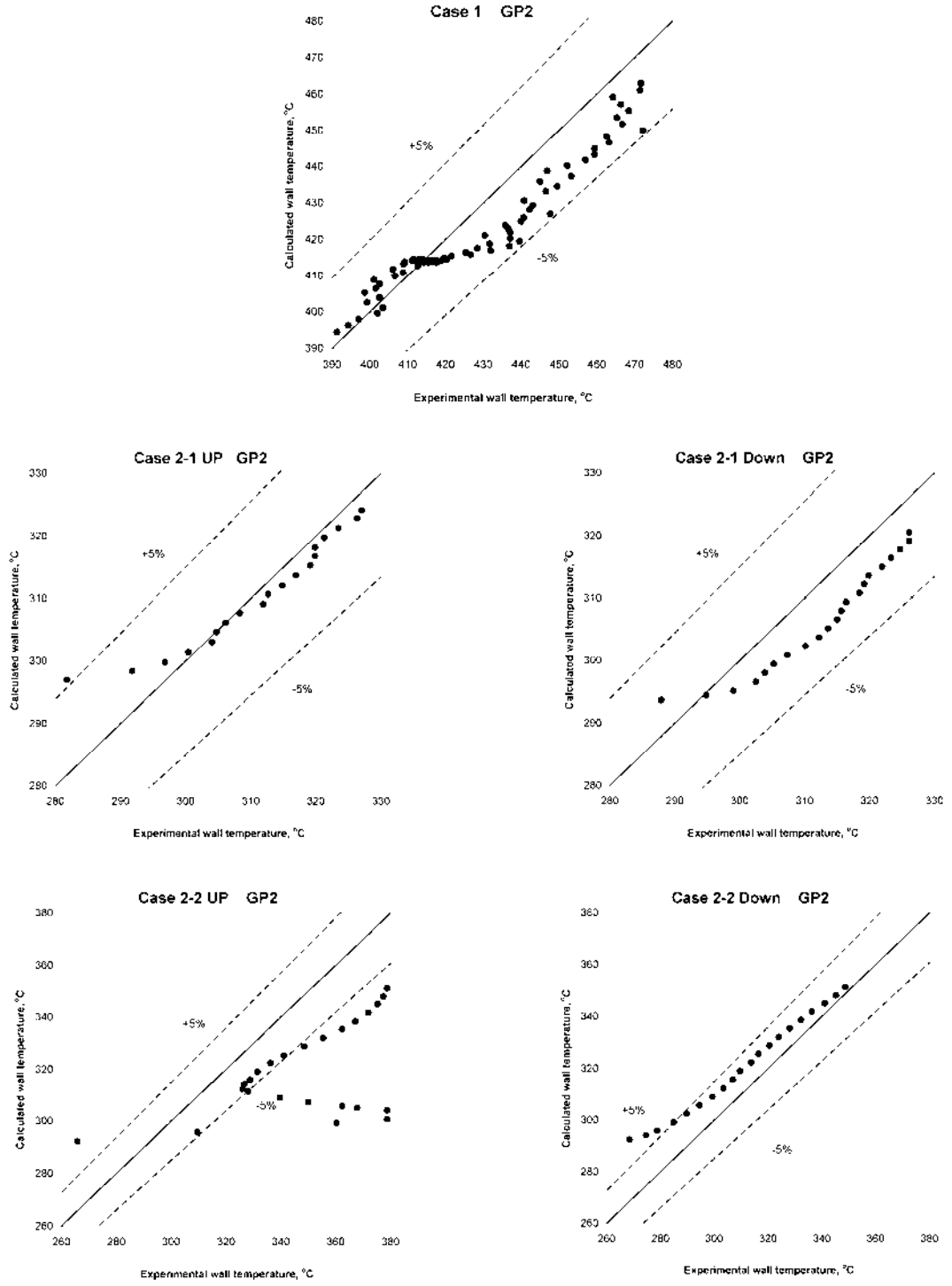

FIG. 9.95. Comparison of the experimental and computational results of Gidropress (variant GP1104).

9.1.5.1.1.3. JRC

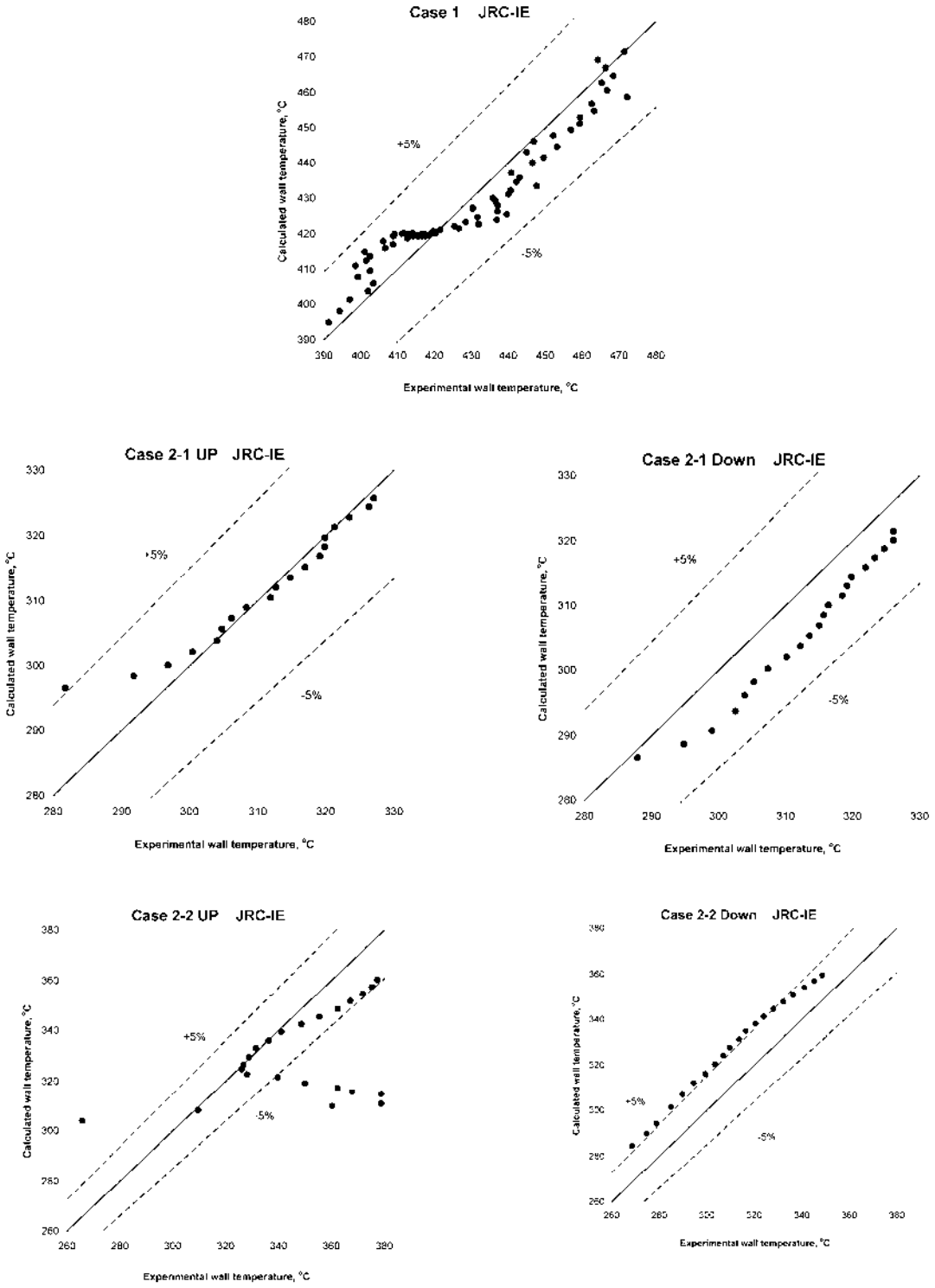

FIG. 9.96. Comparison of the experimental and computational results of JRC.

9.1.5.1.1.4. MP

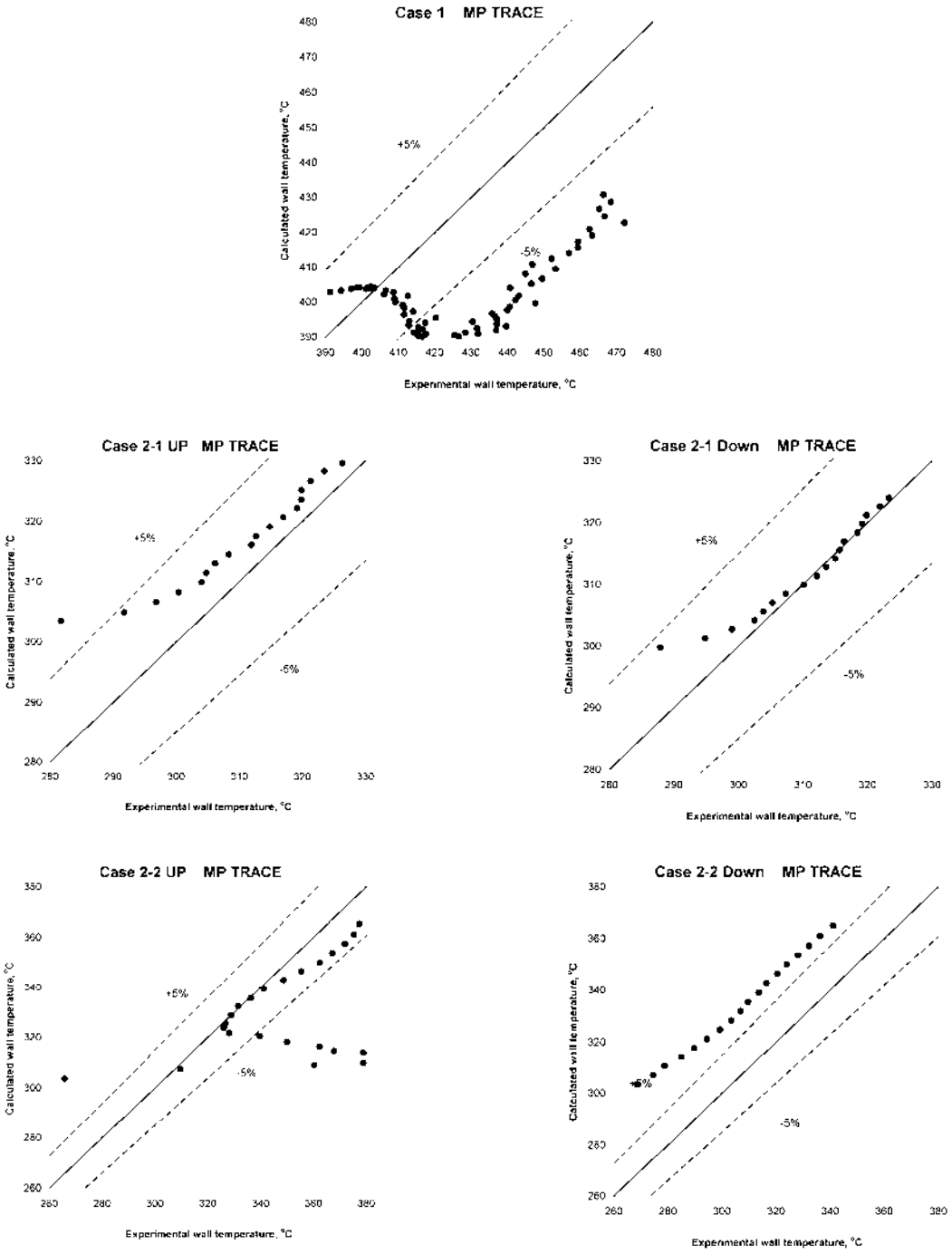

FIG. 9.97. Comparison of the experimental and computational results of MP (code TRACE).

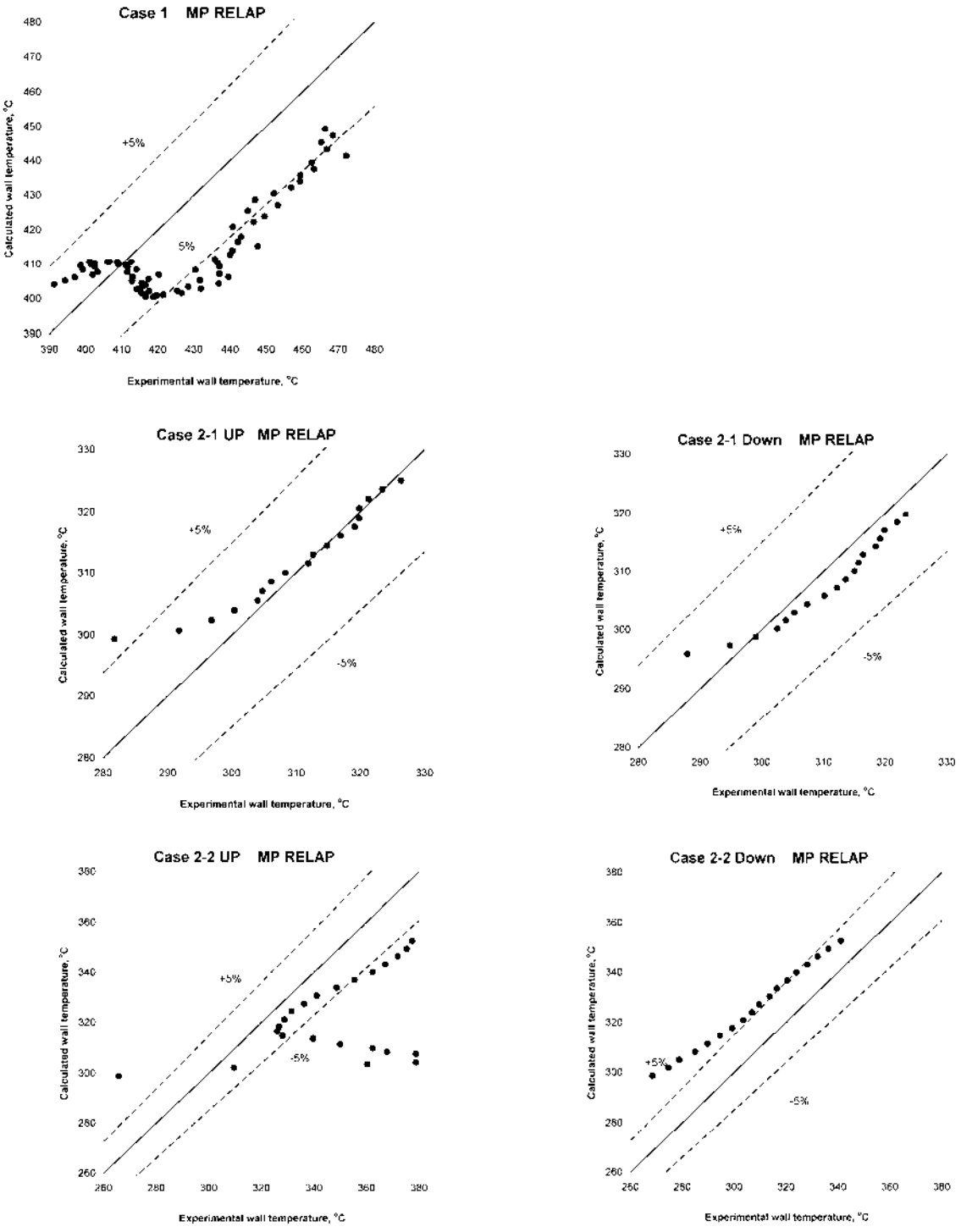

FIG. 9.98. Comparison of the experimental and computational results of MP (code RELAP).

9.1.5.1.1.5. VTT

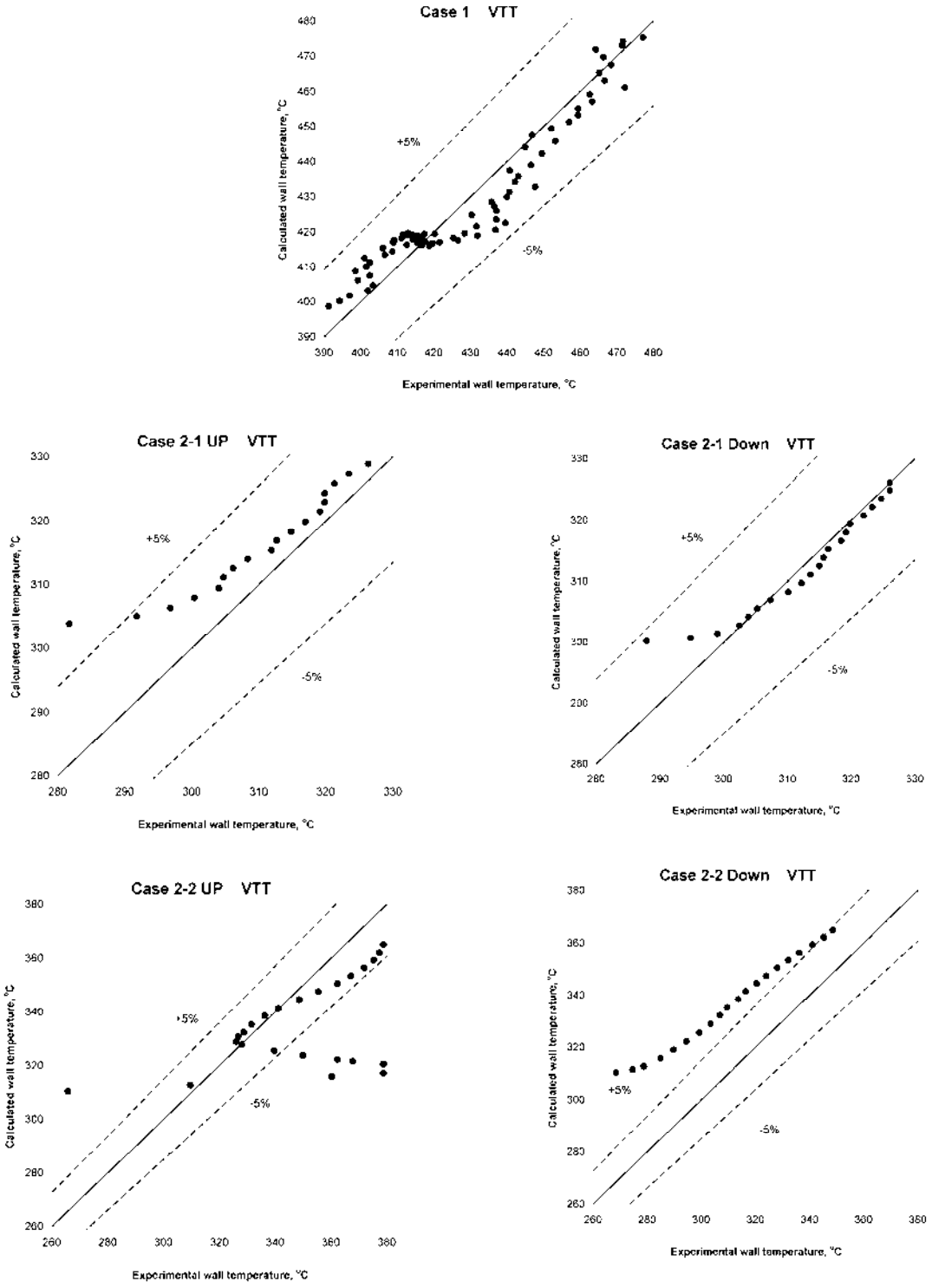

FIG. 9.99. Comparison of the experimental and computational results of VTT.

9.1.5.1.2. CFD codes

9.1.5.1.2.1. BARC

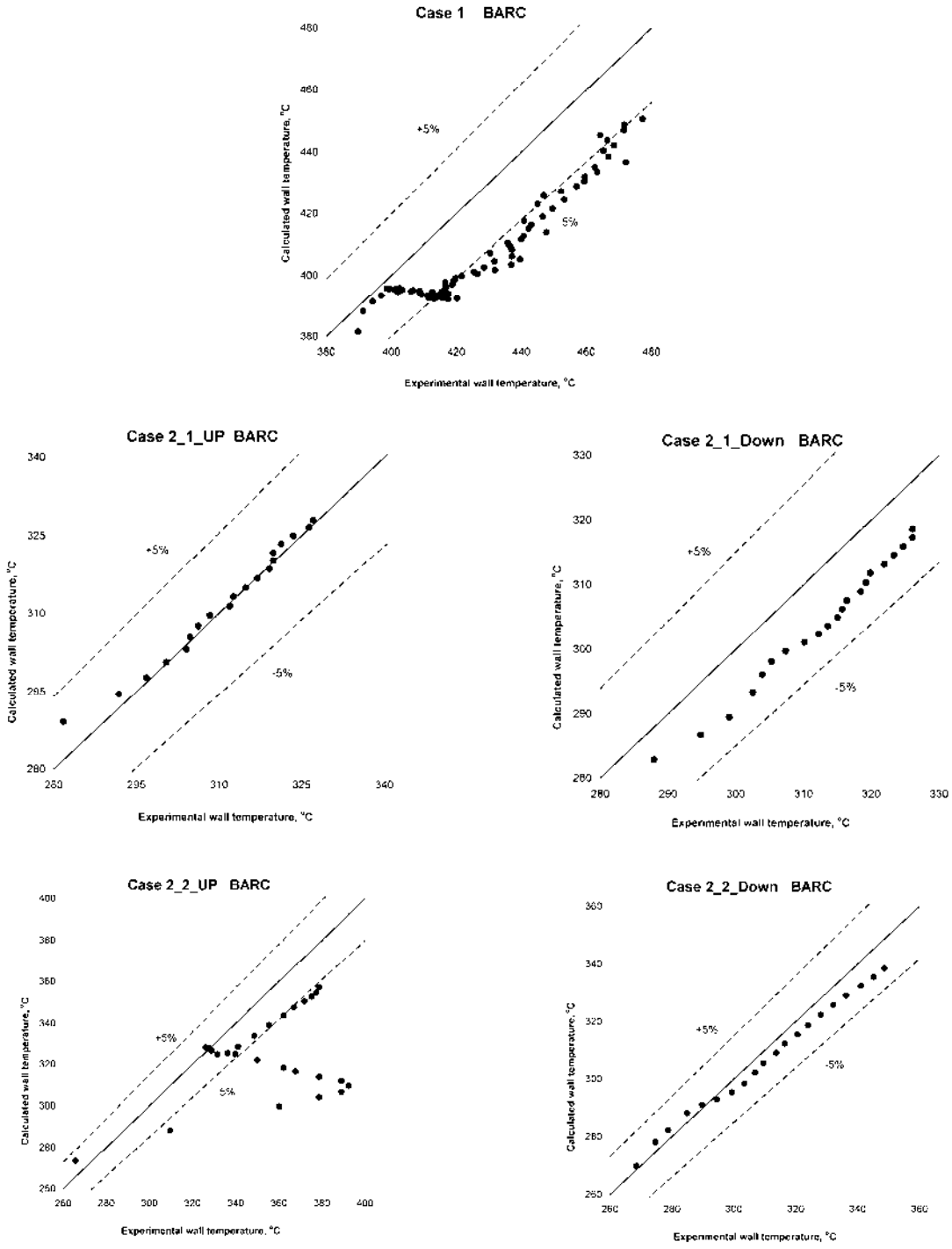

FIG. 9.100. Comparison of the experimental and computational results of BARC.

9.1.5.1.2.2. CIAE

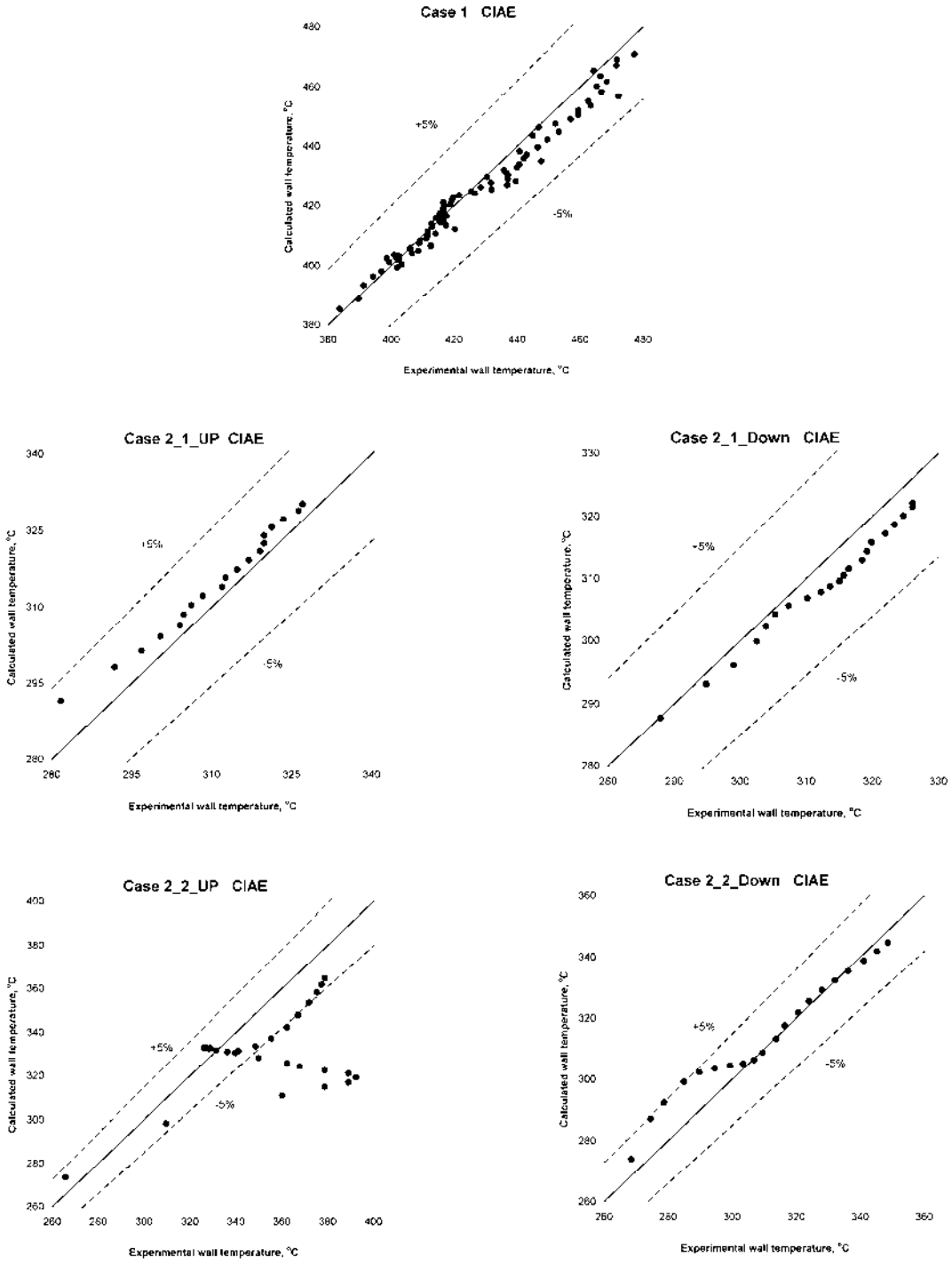

FIG. 9.101. Comparison of the experimental and computational results of CIAE.

9.1.5.1.2.3. KAERI

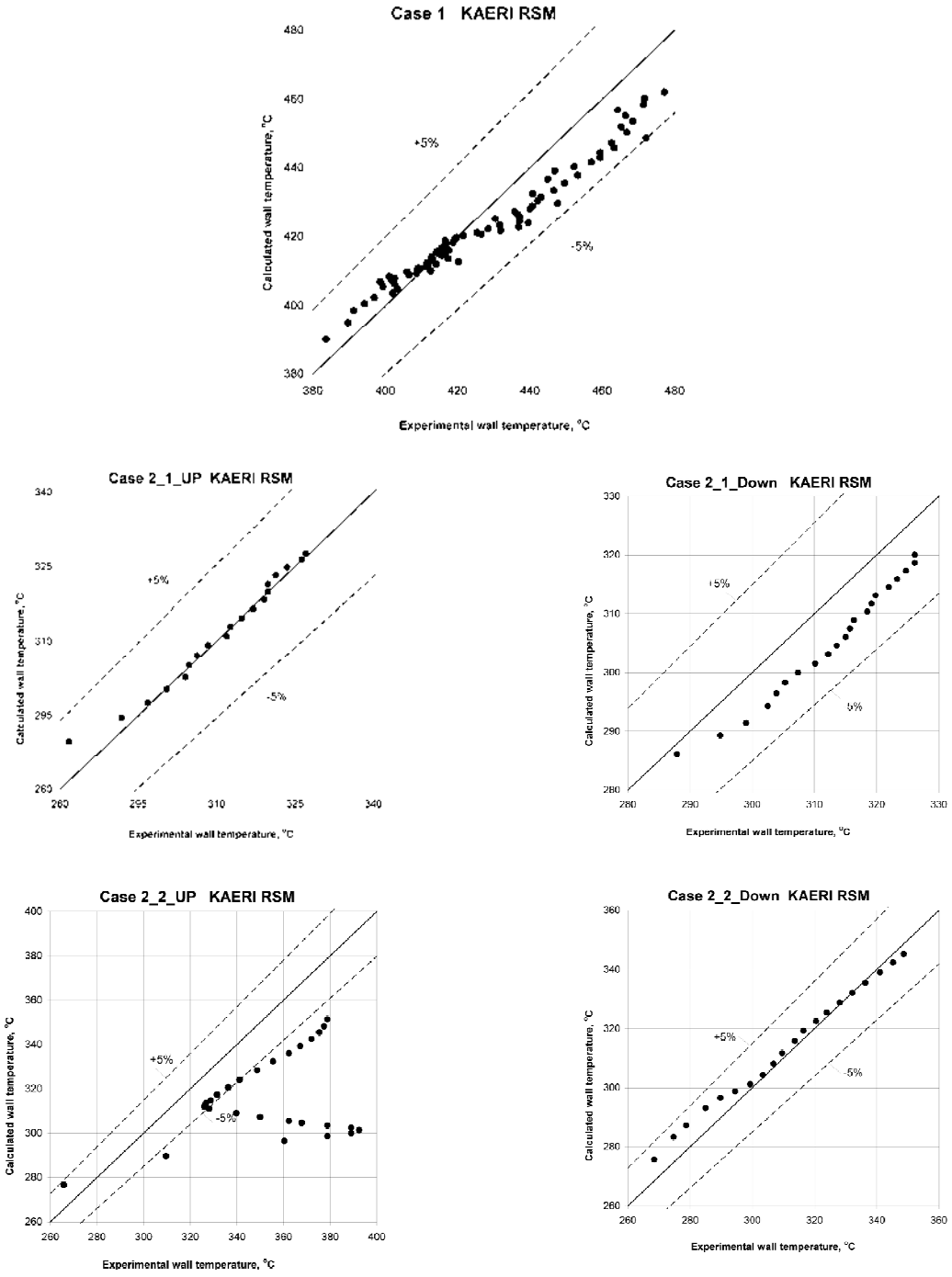

FIG. 9.102. Comparison of the experimental and computational results of KAERI (variant RSM).

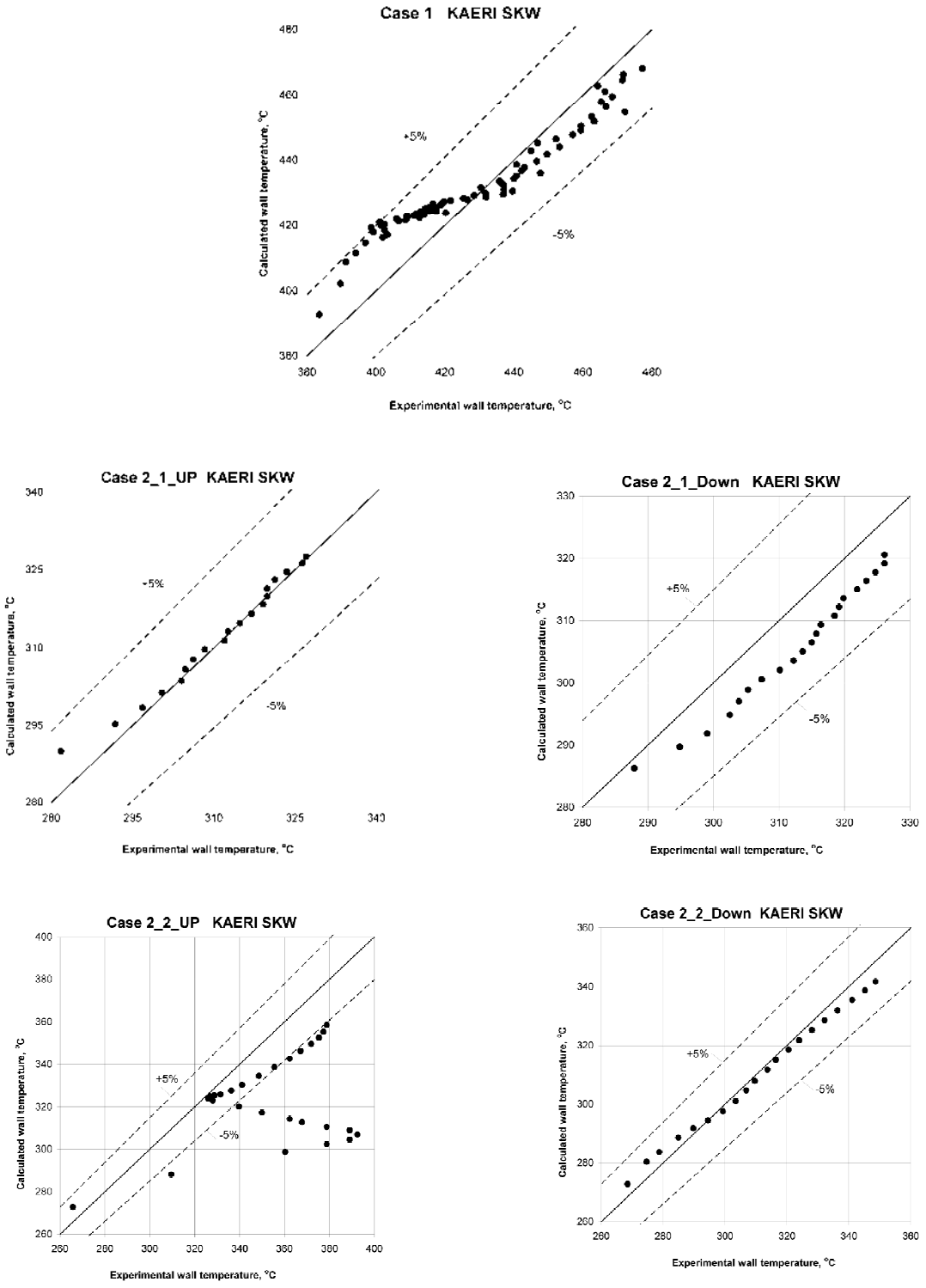

FIG. 9.103. Comparison of the experimental and computational results of KAERI (variant SKW).

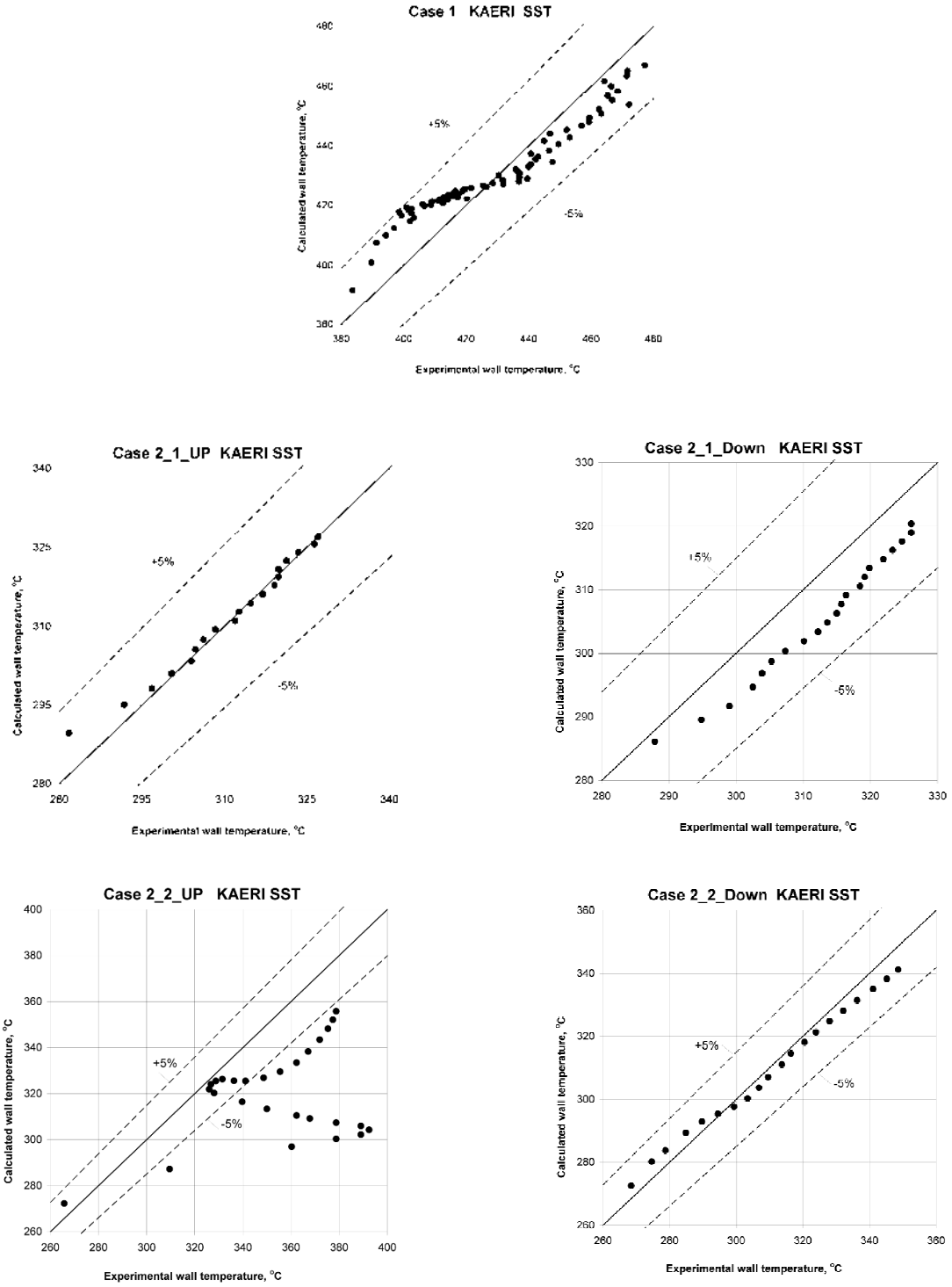

FIG. 9.104. Comparison of the experimental and computational results of KAERI (variant SST).

9.1.5.1.2.4. SJTU

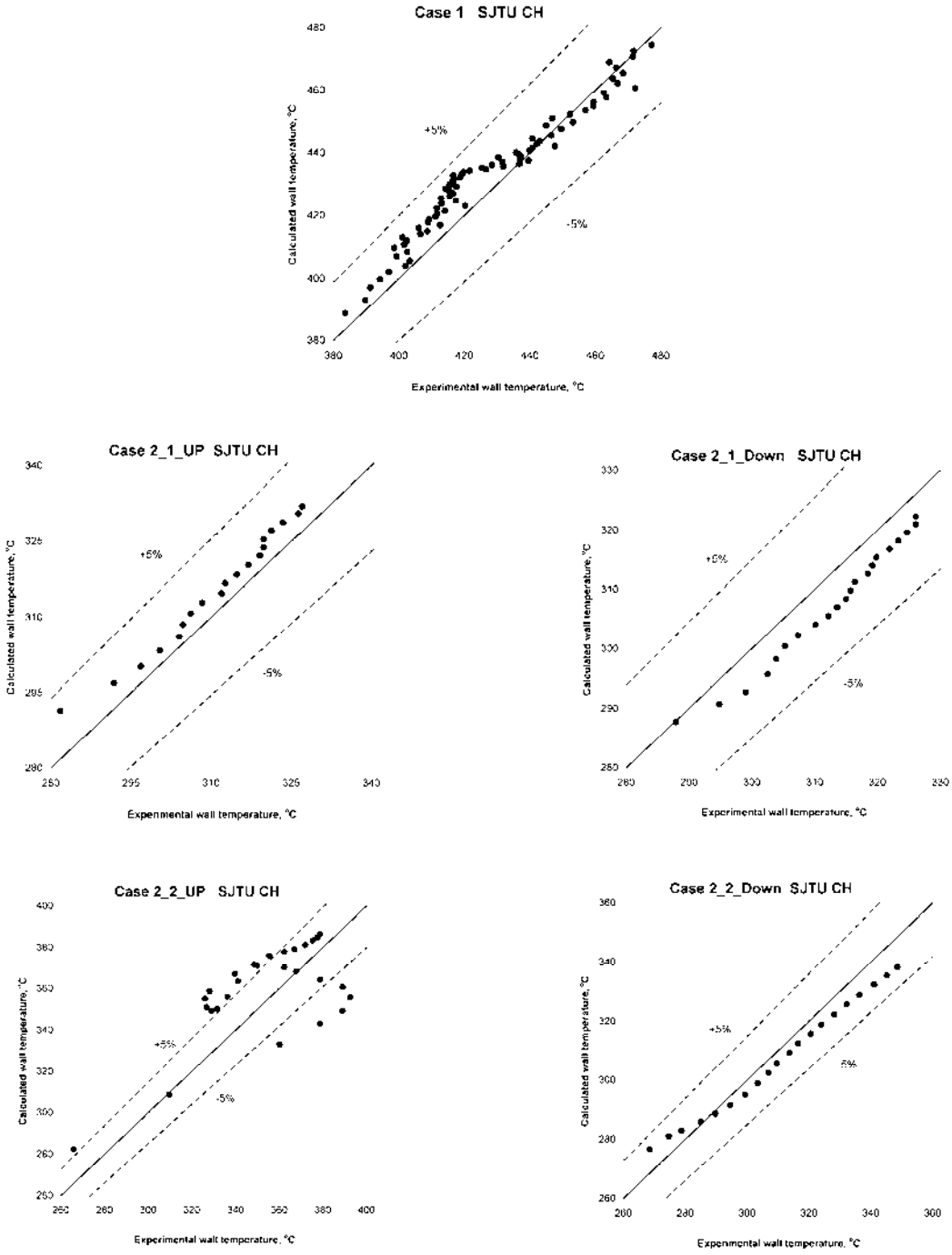

FIG. 9.105. Comparison of the experimental and computational results of SJTU (variant CH).

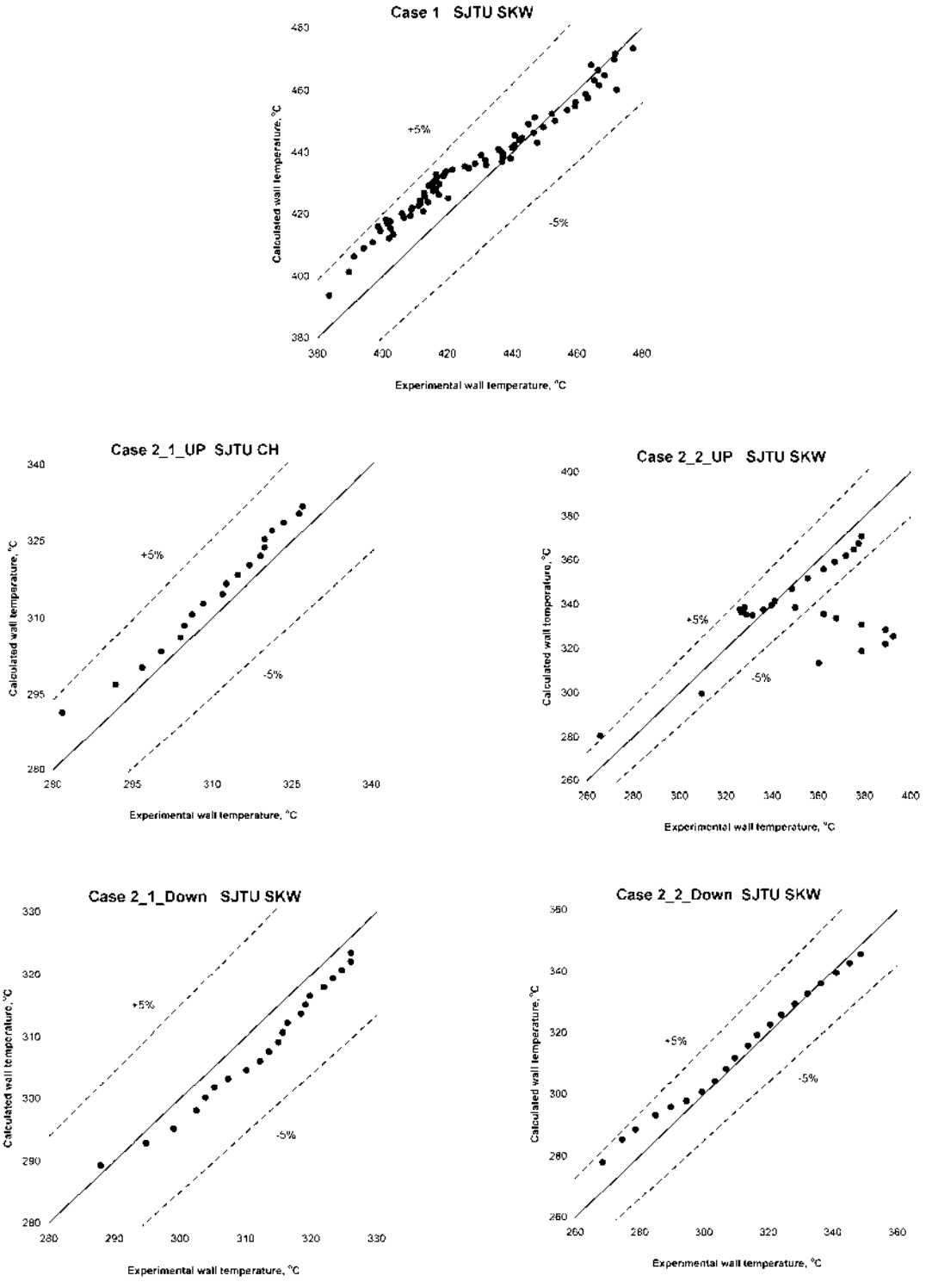

FIG. 9.106. Comparison of the experimental and computational results of SJTU (variant SKW).

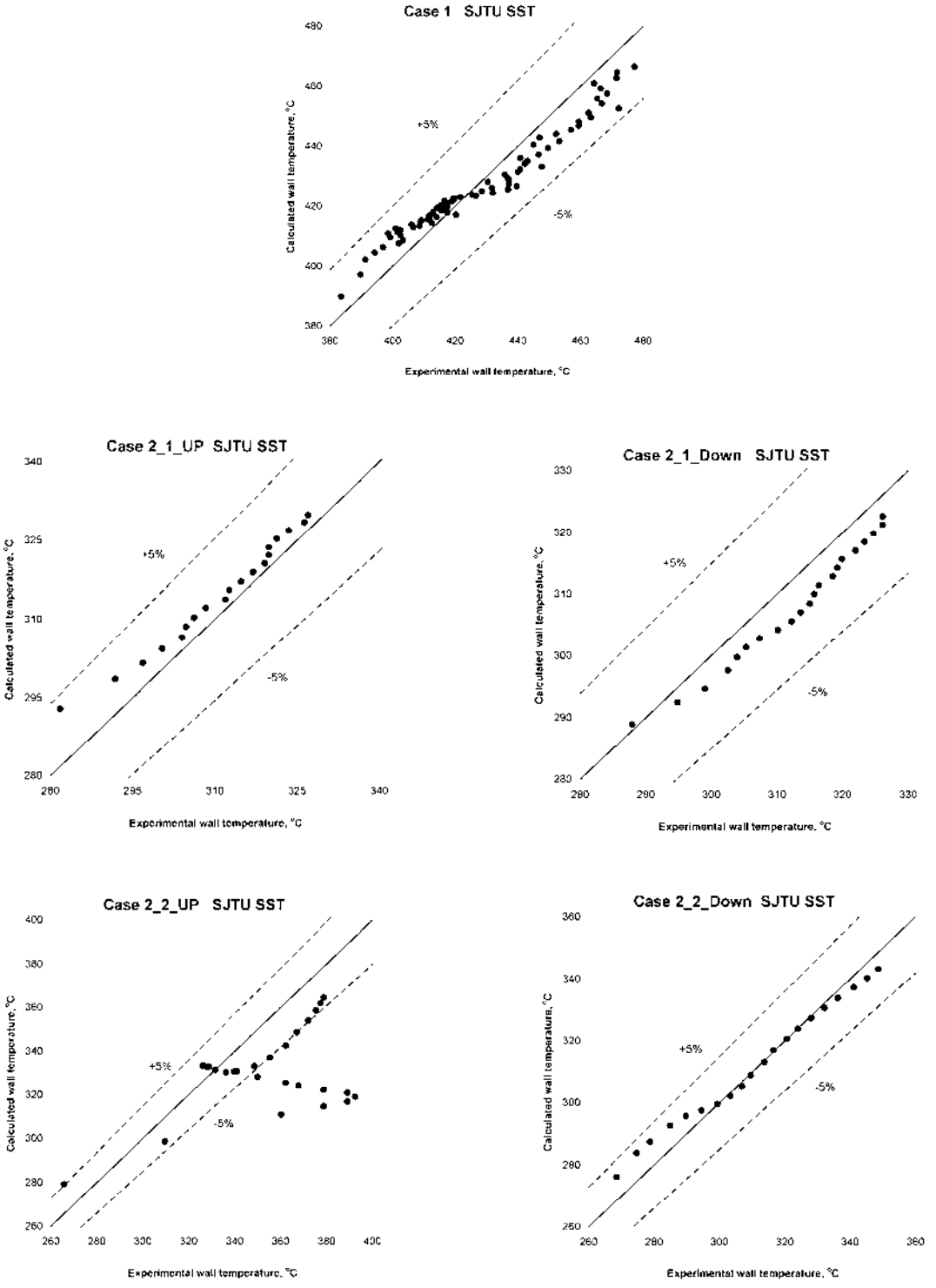

FIG. 9.107. Comparison of the experimental and computational results of SJTU (variant SST).

9.1.5.1.2.5. UMAP

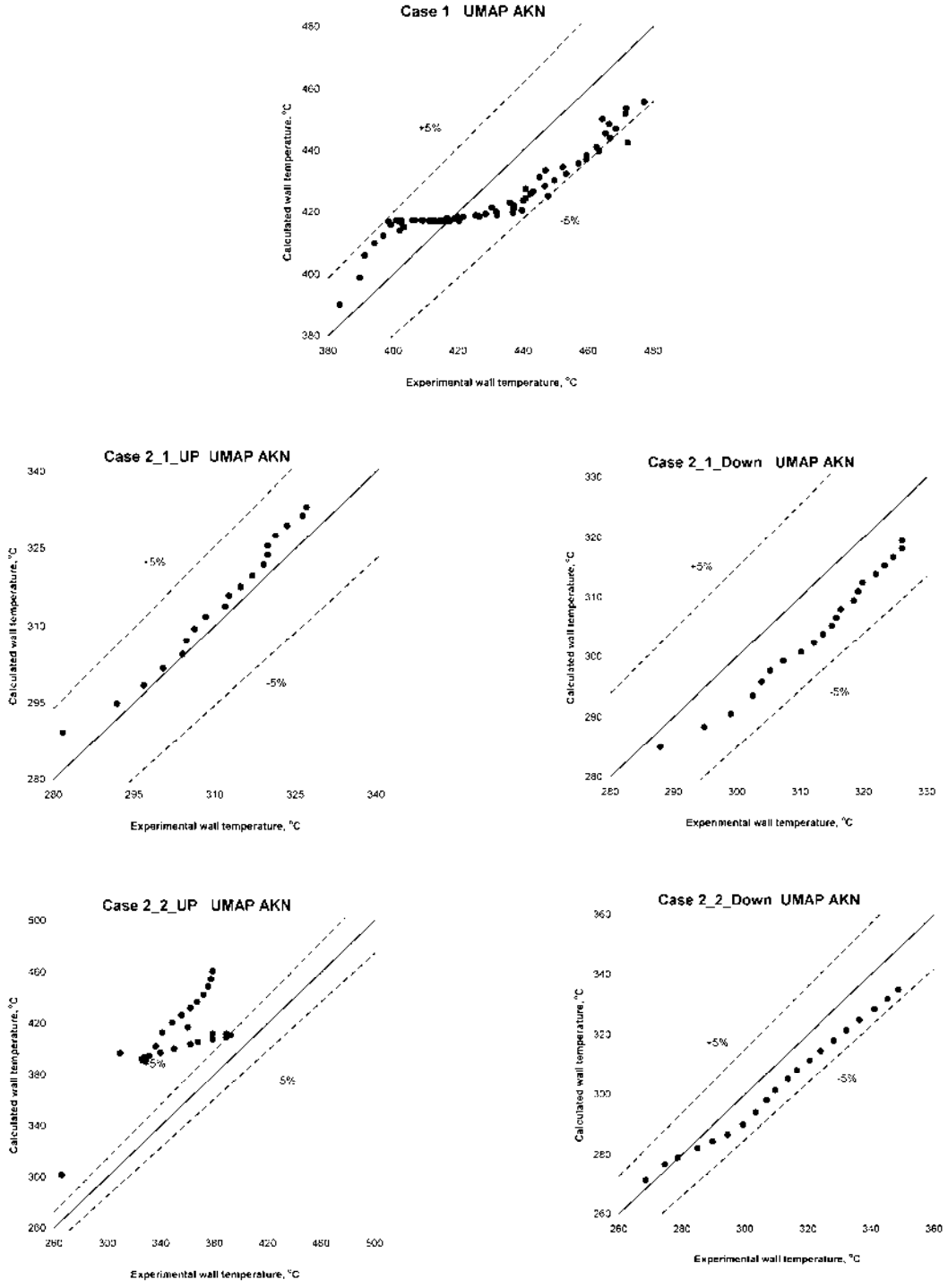

FIG. 9.108. Comparison of the experimental and computational results of UMAP (variant AKN).

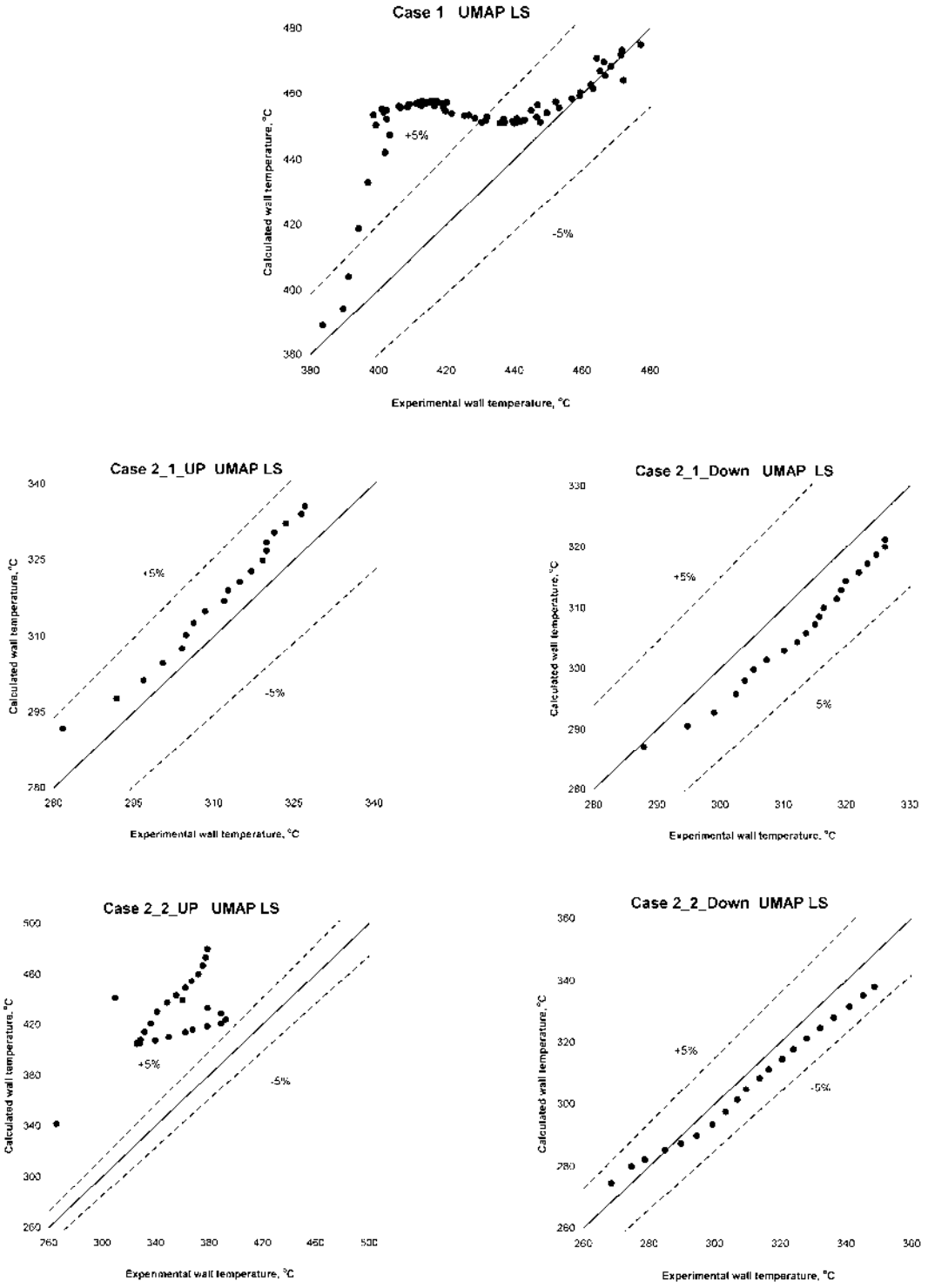

FIG. 9.109. Comparison of the experimental and computational results of UMAP (variant LS).

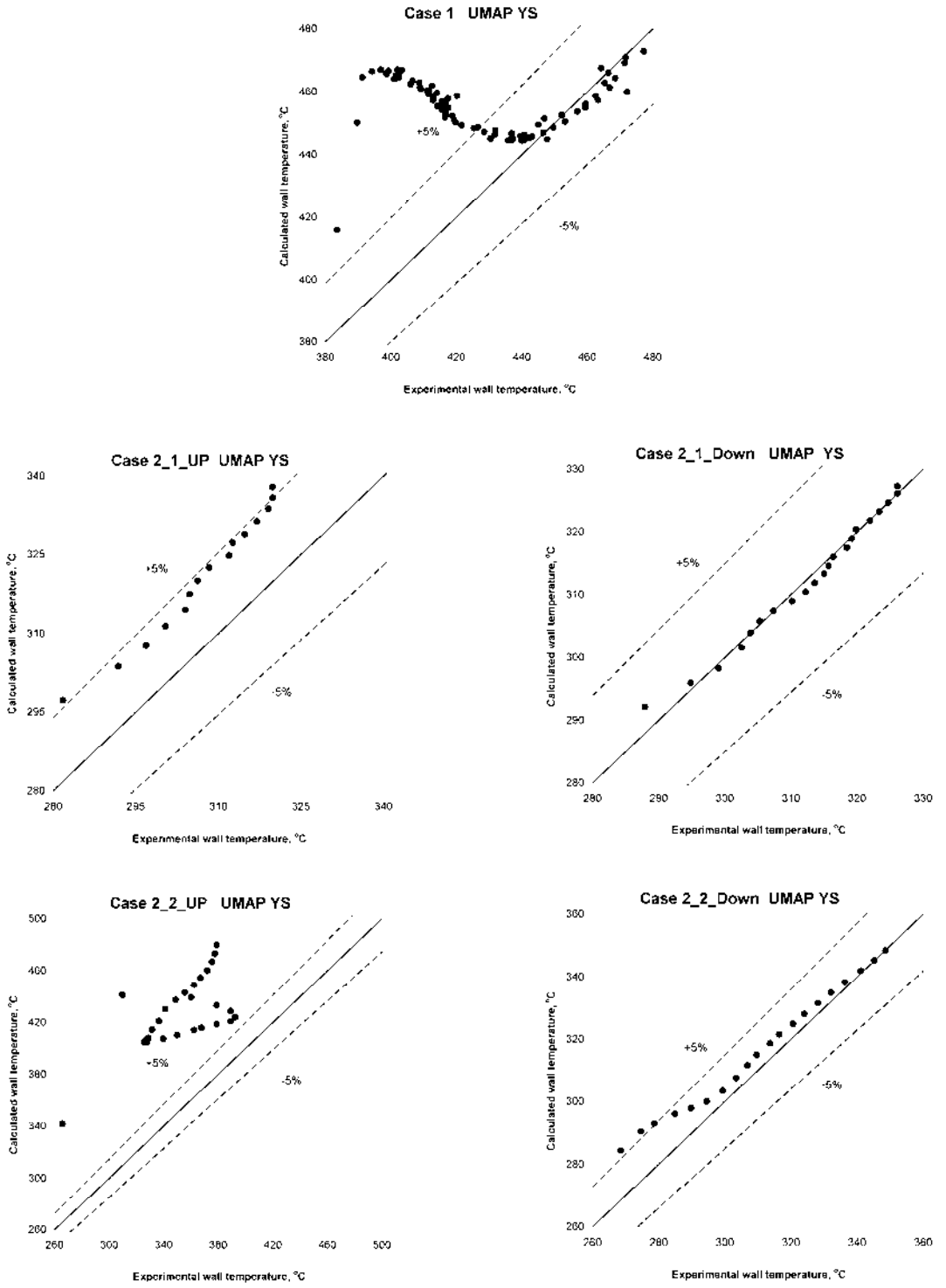

FIG. 9.110. Comparison of the experimental and computational results of UMAP (variant YS).

9.1.6. Discussion

9.1.6.1. AECL[8]

CATHENA is a one-dimensional, two-fluid system thermalhydraulics code. As a result, it requires empirical wall heat transfer and wall shear correlations to provide model closure. The MOD-3.5d/Rev 3 code version used in this exercise is the first production code version that includes supercritical fluid properties. From a preliminary examination of the supercritical heat transfer literature no constitutive relations with a wide range of applicability were apparent. As a result, simple extensions of the single-phase liquid heat transfer and wall shear have been included in this code version. The well-known Colebrook-White and Dittus-Boelter correlations were used to calculate the wall friction factor and heat transfer coefficient respectively for supercritical conditions. It is understood that both of these correlations do not account for the potentially large density gradient near a heated/cooled surface for supercritical pressure conditions.

The CATHENA results for the Case 1 show that the simple extensions for supercritical flow used in CATHENA provide reasonable agreement for conditions towards the pipe inlet; however, the simulation results diverge from the experiment as the coolant temperature passes through the 'pseudo-critical' enthalpy region further along the pipe. This level of agreement is to be expected given the heat transfer coefficient that was chosen for supercritical conditions in this code version. It is acknowledged that this heat transfer correlation has limited applicability; however, it was chosen for simplicity while further research is being performed to include a correlation (or correlation set) with a wider range of applicability. The CATHENA results show good agreement with the bulk water and wall temperatures shown in Figs 9.9 and 9.10. The agreement in fluid temperature is expected since these values are inferred from the fluid enthalpy. Figure 9.11 shows the heat transfer coefficient calculated. The calculated peak near the middle of the heated channel is a result of the property variation (primarily the Prandtl number) as the fluid passes through the pseudo-critical condition along the heated section. This calculated peak is not observed in the heat transfer coefficient inferred from the experiment. The CATHENA calculated pressure drop, enthalpy and density results shown in Figs 9.12–9.14 are in good agreement with those calculated by other codes. Since CATHENA is a qualified code (under N286.7 standard), implementing a new correlation or modifying the existing correlations to mimic the experimental trend must follow a strict protocol and/or procedure. Therefore, no adjustment has been introduced to improve the agreement between code predictions and experimental data.

The CATHENA results for both variants of the Case 2 up-flow simulation indicate that although the overall trends are modelled, the simulations do not necessarily capture the details of the experimental results. The simulated results show reasonable agreement with the experimental results for the bulk water temperatures shown in Figs 9.16 and 9.30, although the predicted temperatures tend to be too high. The modelled wall temperatures shown in Figs 9.17 and 9.31 agree better in the middle of the heated section than near the ends, but overall, the simulated wall temperatures tend to be lower than the experimentally measured wall temperatures in Variant 1, and higher in Variant 2. Consistent with the trends shown in the wall temperatures, the predicted heat transfer coefficients agree better with the experimental results in the middle of the heated section than at the ends, and tend to be larger than the experiment in Variant 1 and smaller than the experimental in Variant 2. The differences in the predicted versus the experimentally measured wall temperatures and heat transfer coefficients near the ends of the heated section tend to point to details in the experimental results that are not captured with the currently implemented correlations. For example, the current code version correlations are not influenced by the fluid density gradient near the wall. As a result, a localized excursion of the heat transfer like that seen in the lower portion of the heated segment in Fig. 9.18 or Fig. 9.32 is not captured by the simulations. The CATHENA calculated pressure drop, enthalpy and density results shown in Figs 9.19–9.21 and Figs 9.33–9.35 are in good

[8] Thomas Beuthe, Bruce Hanna, Thermalhydraulics Branch, Chalk River Laboratories, AECL, Canada.

agreement with those calculated by other codes.
The CATHENA results for both variants of the Case 2 down-flow simulation are in reasonable agreement with the experimental results. In these cases, the axial position begins at the top (i.e., the flow entrance). The simulated bulk water temperature is in good agreement with the experimental results as shown in Fig. 9.23 and Fig. 9.36, although the lack of experimental data in Fig. 9.23 makes comparison difficult. The predicted wall temperatures are lower than the experimental results in Variant 1 (Fig. 9.24) and higher in Variant 2 (Fig. 9.37). As a result, the predicted heat transfer coefficients are higher in Variant 1 (Fig. 9.25) and lower in Variant 2 (Fig. 9.38). Overall, however, both the predicted wall temperature and heat transfer coefficient compare well in trend and magnitude to the experimental results. The CATHENA calculated pressure drop, enthalpy and density results shown in Figs 9.26–9.28 and Figs 9.39–9.41 are in good agreement with those calculated by other codes.

Correlations for supercritical heat-transfer coefficient are being developed for tubes and bundles. These correlations will be implemented into the CATHENA code to provide improved prediction accuracy of the wall temperature in safety analyses for the CANDU-SCWR.

9.1.6.2. GP[9]

9.1.6.2.1. Summary of the chosen experiments for testing

When Code Testing Benchmark No.1 was organized, experiments and conditions were chosen to be those that are the most similar to conditions of different SCWR concepts. Among chosen exercises Case 1 is the most similar to SCWR parameters (long pipe, high mass velocity and heat flux). In Case 2 Variant 2 the experiment parameters correspond less to SCWR parameters, but this variant was chosen specifically to examine the sensitivity of the codes to flow direction influence on the deterioration of heat transfer.

The main reason for heat transfer deterioration in supercritical fluid is a strong dependence of fluid density on temperature across the pseudo-critical temperature. In the presence of temperature variation over the cross-section of the channel, it causes the occurrence of secondary forces, related to flux acceleration and buoyancy near the hotter wall. It causes the change of velocity profiles and turbulent diffusion coefficient on the cross-section of the channel.

A well-known criterion for heat transfer deterioration conditions connect heat flux with mass velocity, for example, Yamagata criterion [9-24], [9-16]:

$$q/G^{1.2} > 0.2 \tag{9-12}$$

and Styrikovich – Miropol'skii criterion [9-25]:

$$q/G > 0.6 \tag{9-13}$$

where q is in kW/m² and G is in kg/(m² s).

Professor Jackson suggested [9-28] two parameters that allow estimating the power influence on fluid acceleration and buoyancy effects:

[9] Andrey Churkin, OKB "GIDROPRESS", Russia.

$$Ac_b^* = Q_b^* / \left(Re_b^{1.625} \, Pr_b \right) \text{ – acceleration parameter;} \quad (9\text{-}14)$$

$$Bo_b^* = Gr_b^* / \left(Re_b^{3.425} \, Pr_b^{0.8} \right) \text{ – buoyancy parameter,} \quad (9\text{-}15)$$

where $Q_b^* = \beta_b q_w d / k_b$ – thermal expansion parameter.

If $Ac_b^* < 2 \cdot 10^{-6}$ or/and $Bo_b^* < 2 \cdot 10^{-7}$, then fluid acceleration or/and buoyancy effects are negligible (less than 1%) [9-28].

Parameters (1) – (4) are calculated for the variants with upward flow considered in CTB No.1 (Table 9.9). The parameters Ac_b^* and Bo_b^* are shown as graphs (Figs 9.111 and 9.112) for Case 1. Parameter changes along the pipe are slight for Case 2.

TABLE 9.9. ACCELERATION AND BUOYANCY PARAMETERS FOR CASE 1 AND CASE 2

Parameter		Value			Condition for effect neglect (absence of HT deterioration)
		Case 1	Case 2, var. 1	Case 2, var. 2	
Ac_b^*	min	$0.21 \cdot 10^{-06}$	$0.09 \cdot 10^{-06}$	$0.28 \cdot 10^{-06}$	$< 2 \cdot 10^{-06}$
	max	$0.37 \cdot 10^{-06}$	$0.10 \cdot 10^{-06}$	$0.30 \cdot 10^{-06}$	
Bo_b^*	min	$0.04 \cdot 10^{-07}$	$2.4 \cdot 10^{-07}$	**$33 \cdot 10^{-07}$**	$< 2 \cdot 10^{-07}$
	max	$0.49 \cdot 10^{-07}$	$2.4 \cdot 10^{-07}$	**$34 \cdot 10^{-07}$**	
$q/G^{1.2}$		0.14	0.13	**0.32**	< 0.2
q/G		0.59	0.49	**1.05**	< 0.6

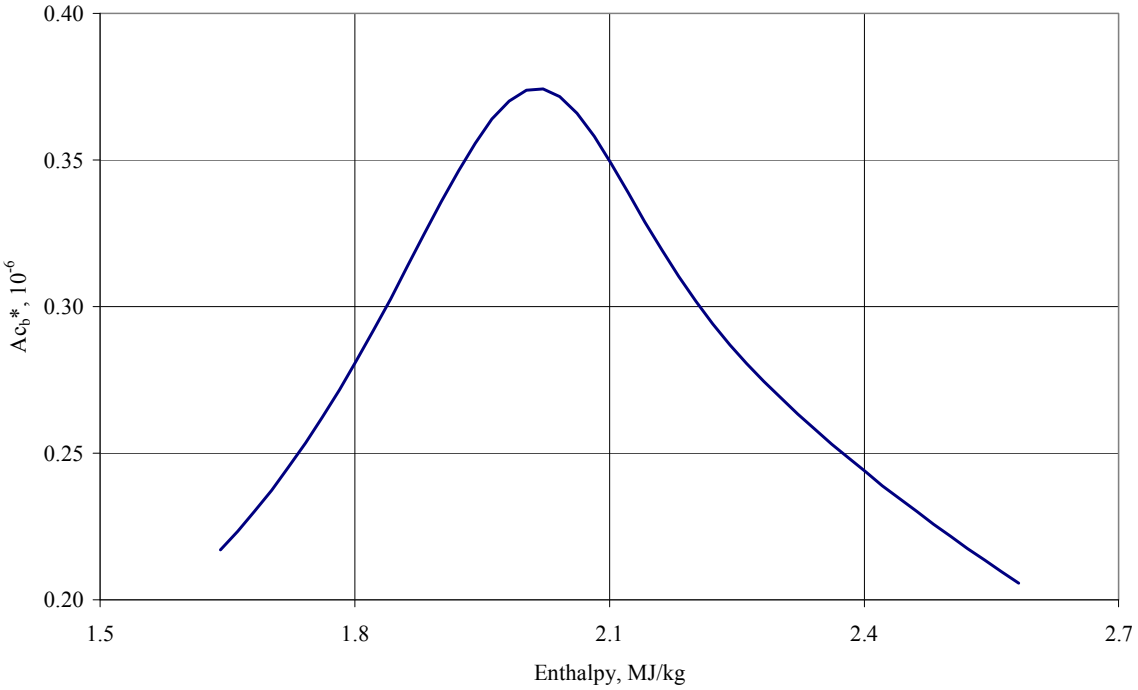

FIG. 9.111. Change of acceleration parameter depending on water enthalpy in pipe (Case 1).

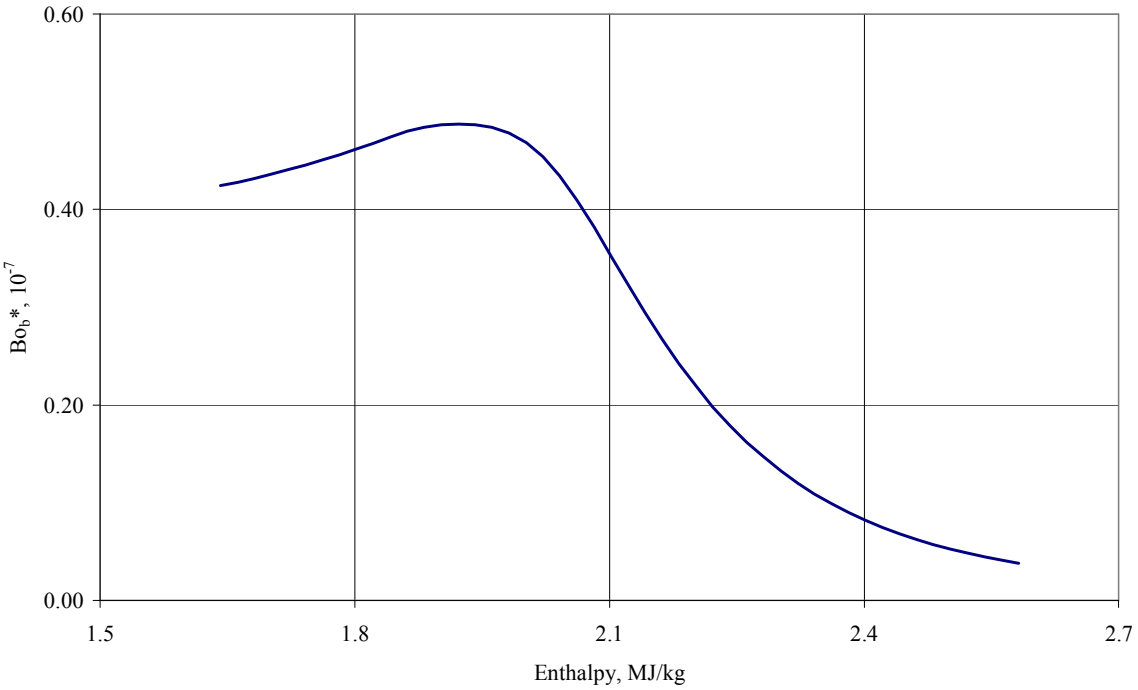

FIG. 9.112. Change of buoyancy parameter depending on water enthalpy in pipe (Case 1).

As shown in Table 9.1, according to all criteria in Case 2 Variant 2 deteriorated or enhanced (depending on flow direction) heat transfer conditions should be observed. It is proved by the experiments (see Figs 9.29, 9.32, 9.38). The obtained values of the parameters Ac_b^* and Bo_b^* indicate that heat transfer deterioration (for the upward flow) or enhancement (for the downward flow) occurs owing to the buoyancy effect.

Analyzing the experimental parameters and criteria (3) and (4), it may be concluded that Case 1 was not adequate for the task of tuning thermal-hydraulic codes before performing Case 2, since the differences between Case 1 and Case 2 are considerable.

9.1.6.2.2. Summary of the performed calculations by sub-channel and system codes

The participants' calculations made by sub-channel and system codes showed very close values of integral parameters that are defined by balance equations. Only MP results of the enthalpy of water differ from the results of other participants. The mathematical model and computer code should be analysed to determine the reasons for the differences.

Noticeable differences are observed in local parameters that are defined by correlations: pressure drop and heat transfer coefficient. It emphasizes one more time the necessity to design heat transfer and wall friction standard correlations for supercritical fluids.

Comparing the distribution of wall temperature along the pipe in the calculations and experiments (Table 9.6), it may be concluded that the most similar results for Case 1 were obtained by JRC, VTT and GP (variant GP1101). AECL and MP results that possibly used Dittus-Boelter correlation, show overestimation of the heat transfer coefficient at water temperature near pseudocritical point and higher.

In Case 2 Variant 1 with upward coolant flow the results of VTT and MP (variant MP2101T) show overestimation of the pipe wall temperature (Fig. 9.17 and Table 9.6); however, if one compares the heat transfer coefficients, it is seen that these two calculations predicted the values of heat transfer coefficients closest to the experimental data. Probably, this disagreement is caused by temperature differences of inlet water that were presented in the tables with experiment data [9-2] and obtained in the experiment (Fig. 9.15). This disagreement was retained in the specification for CTB No.1 (Fig. 9.16). As a result, if one offsets the graphs of water temperature down by 5 ºC and, respectively, wall temperatures, the results of VTT and MP (variant MP2101T) best predict the experiment data.

A good coincidence with experimental values of heat transfer coefficients for VTT and MP (variant MP21D01T) results is also observed in Case 2 Variant 1. In this variant, it is also observed discrepancy of inlet water temperature that is written in the tables with experiment data and is realized in the experiment (Fig. 9.22). If we apply the method similar to that which was described in the previous paragraph, and displace all wall temperature values by 5 ºC, VTT and MP results will exceed the experiment data. Unlike in the previous case, this is difficult to explain taking into account good value coordination of heat transfer coefficients.

Unfortunately, none of the sub-channel and system codes could predict heat transfer deterioration for Case 2 Variant 2 with upward flow.

As a preliminary conclusion, it can be observed that there are correlations that predict quite well heat transfer coefficient and wall temperature of round pipe for supposed conditions of SCWR normal operation. The revision of the computational methods and codes is necessary for the conditions where acceleration and buoyancy effects influence is significant.

Computational codes testing in pressure drop experiments on pipe is required, as the CTB No.1 showed a

considerable discrepancy of computational results. In addition, it is necessary to perform experiments in the bundles of fuel rods and to test codes for these geometries.

9.1.6.3. JRC[10]

The benchmark exercise was performed at JRC-IE using the sub-channel thermal-hydraulic code COBRAEN. The Bishop correlation was adopted for the computation of the heat transfer coefficient, while the friction factor correlation was taken from a review on the subject performed by Chen and Schulenberg (see Section 9.1.3.1).

Case 1
The first calculations for Case 1 showed a strong over-prediction of the heat transfer coefficient computed using the Bishop formula. This was due to heat transfer deterioration conditions which affected the experiment and that could not be computed by the Bishop correlation.

In order to have a better agreement a 25% reduction in the computed value of the heat transfer coefficient was considered (N.B. No reduction was applied for the other cases of the benchmark). The results for Case 1 are in excellent agreement for what concerns the fluid thermal-hydraulic properties. A good agreement in the wall temperature was also obtained.

A large discrepancy is observed instead in the axial pressure drop with respect to other codes. Since no experimental data are available on the pressure drop along the channel only a code-to-code comparison is possible here. This discrepancy is probably due to the adopted friction factor correlation that computes a lower the friction pressure drop in correspondence to strong density changes. It must be noted that the CFD results from CIAE and UMAP show similar pressure drops for this case.

Case 2
The fluid bulk thermal-hydraulic properties are overall in very good agreement with the experimental results in all four tests. Due to the absence of strong density gradients the computed pressure drops along the channel are also in agreement with the values computed by the other codes. The fluid model demonstrates to be consistent with the experimental results. The same cannot be said for the wall temperature and heat transfer coefficient.

Case2 Variant1 Down-flow
The overall trend of the heat transfer coefficient is qualitatively very well predicted but it consistently remains 10% higher than the experimental value. The wall temperature is, in line with the heat transfer coefficient, qualitatively correct but under-predicted.

Case 2 Variant2 Down-flow
Similar observations on the qualitative aspects of the heat transfer coefficient and wall temperature can be made for the second down-flow test. However the simulated wall temperatures are lower than the experimentally measured wall temperatures in variant 1, and higher in variant 2 with the heat transfer coefficient higher in variant 1 and lower in variant 2.

Case 2 Variant 1 Up-flow
The Bishop correlation is not able to capture the high heat transfer coefficient at the inlet of the channel while it predicts a 10% constantly higher heat transfer coefficient along the channel. Consequently the wall temperature is over-predicted at the inlet and it is in reasonable agreement for the rest of the test section.

[10] L. Ammirabile, European Commission DG Joint Research Centre, the Netherlands

Case 2 Variant 2 Up-flow
The heat transfer deterioration at the inlet of the test section is totally missed in the simulation. The wall temperature calculated by COBRA-EN is about 90 ºC lower that the experimental value and remains 20 ºC lower along the rest of the test section.

As a general conclusion the COBRA-EN results for both the wall temperatures and heat transfer coefficients show that the code is not able to reproduce the details of the tests, while the overall trends are captured reasonably well.

9.1.6.4. MP[11]

The RELAP5/Mod3.3 and TRACE5.0 have been applied to characterize the flow behaviour in two simple problems. The simulation of a simple pipe with uniform heating on the wall highlights the necessity of improve the codes capability in addressing the HTC value, phenomena of deteriorated or enhanced heat transfer do not occur with sub-critical water, so far, the results of the two correlations used by the codes in fully developed flow regime give results that are higher than the experimental data.

The lesson learned from this study is the need to improve and/or adjust the capability of the computational tools that the scientific community has developed until nowadays in order to improve their accuracy in predicting the phenomena that arise from the use of supercritical water. The implementation of heat transfer correlation, developed specifically for supercritical water flowing in bare tubes and possibly bundles, in RELAP5/Mod3.3 and in TRACE5.0 is the first step that the authors would like to accomplish. Among the many correlations developed in the last fifty years [9-1], [9-26], [9-27] the authors are working to implement the Mokry correlation [9-26], specifically developed for vertical bare tube, due to the wide range of applicability. An assessment of the modified codes against more experimental data is also part of the planned work.

9.1.6.5. VTT[12]

The case 1 was first calculated with APROS using three different supercritical pressure forced convection heat transfer correlations. The correlations applied were the correlations of Jackson & Hall, Bishop et al. and Watts & Chou. Results obtained with the Watts & Chou correlation best reproduced the behaviour observed in the experimental data, and so it was selected as the correlation to be used in the exercise.

The bulk water temperature axial distribution computed with APROS (Fig. 9.9) is seemingly shifted left by half a mesh thickness. This is due to the rather coarse nodalization and the cell-centered nodalization scheme applied in APROS. In general, APROS reproduces the observed heat transfer behaviour adequately in the case 1.

In case 2 variant 1, both the up-flow and down-flow experiments, the computational results coincide quite well with the experimental data, with the exception of the very beginning of the pipe, at which APROS gives qualitatively wrong values for the heat transfer coefficient. However, this has a limited effect as can be seen from the graphs of the wall temperature (Figs 9.17 and 9.24).

In case 2 variant 2, up-flow experiment, where heat transfer deterioration is observed in the beginning of the pipe (Fig. 9.31), APROS produces quantitatively good results, but fails to predict the deterioration. In the down-flow experiment on the other hand, the shape of the wall temperature distribution is

[11] F. Fiori, A. Petruzzi, Gruppo di Ricerca Nucleare San Piero a Grado, Università di Pisa, Italy,
D. R. Novog, Department of Engineering Physics, McMaster University, Hamilton, Canada
[12] Joona Kurki, Markku Hänninen, VTT Technical Research Centre of Finland.

qualitatively correct (Fig. 9.37), but the values of the heat transfer coefficient are clearly under-predicted, leading in to too high estimates of the wall temperatures.

9.1.6.6. BARC[13]

Trend of heat transfer coefficient variation for Case 1
In case 1, the inlet temperature is 352 ^{o}C, outlet temperature is 392 ^{o}C. Since the operating pressure is 24.05 MPa, the pseudo-critical temperature is 382 ^{o}C. In this situation, at the location at which the bulk temperature is slightly below 382 ^{o}C the heat transfer coefficient shows the maximum value. The BARC results show this trend. The experimental data does not show such a trend.

Under supercritical conditions, at a given mass flux, beyond a certain heat flux, heat transfer deterioration is reported to start [9-24]. As per Yamagata's correlation q (kW/m^2) = 0.2 G$^{1.2}$, where G is in kg/m^2-s and q is heat flux beyond which deterioration starts. In the present case, mass flux is 1500 kg/m^{2}s and heat flux is 884 kW/m^2. The limiting heat flux, at which heat transfer deterioration occurs, as per Yamagata's correlation, is 0.2 x 1500$^{1.2}$ = 1295 kW/m^2. Since the present heat flux is much less than deterioration heat flux, the peak in heat transfer coefficient predicted by NAFA code (of BARC) is justifiable.

Variation of bulk quantities for case 1
The computation of bulk enthalpy does not depend on the computation of other flow parameters by a CFD code. Also bulk temperature and bulk density are directly related to bulk enthalpy. Hence all codes should predict the same bulk enthalpy, bulk temperature and bulk density. But even in these parameters, there is variation by different codes. The variation of bulk temperature over the length computed by CIAE and BARC only match with experimental data (see Fig. 9.42). It is important to understand why this is happening. It may be because some of the codes are computing mean quantities (based on some averaging procedure) and not bulk values. In case of NAFA, bulk enthalpy at a given location is computed from inlet enthalpy and energy addition (due to surface heating) to that location. The bulk temperature, bulk density which correspond to that bulk enthalpy are then computed using tabulated properties data. This also agreed with the bulk enthalpy computed from the mean temperature from the code results.

Pressure drop variation in Case 2 variant 1 up-flow
In case 2 variant 1 up-flow, pressure drop is due to friction, elevation and acceleration. The results provided by BARC account for all these effects. The pressure drop reported by BARC is very close other computed results like e.g. SJTU (Fig. 9.57). In this particular case, sub-critical flow is encountered and hence the density does not vary much from inlet to outlet. Therefore, a linear pressure profile is expected. BARC and others' results show a linear profile. The pressure drop is proportional to the elevation and is very close to that given by $\Delta p = \rho g \Delta h$ since friction and acceleration pressure drop are small.

Wall temperature variation in Case 2 variant 2 up-flow
In Case 2 – Variant 2 - upward flow, at x = 0.4 m, wall temperature is peaking in experimental data (Fig. 9.29). The BARC results also show a qualitatively similar trend, though the peak wall temperature value and its location are different from experimental data. Most of the other codes show results very close to BARC result.

[13] A. M. Vaidya, P. K. Vijayan, and N. K. Maheshwari, RED, Bhabha Atomic Research Centre, Trombay, Mumbai 400085, India.

Pressure drop variation in Case 2 variant 2 up-flow
In Case 2 – Variant 2 - upward flow, the pressure variation should be linear and proportional to elevation i.e. $\Delta p = \rho g \Delta h$ because density is only slightly reducing. The BARC result shows this trend (Fig. 9.75).

9.1.6.7. KAERI[14]

Trend of wall temperature variation for Case 1
Yamagata et al. [9-24] suggested a criterion for deterioration of heat transfer (DHT), $q/G^{1.2} > 0.2$, where G is mass flux in kg/m^{2}s and q is heat flux in kW/m^2. Pioro [9-16] suggested a modified criterion, as q/G>0.4.

In the present case, the mass flux was 1500 kg/m^{2}s and the heat flux was 884 kW/m^2. The values of the ratios in the above two criteria were 0.14 and 0.59 respectively. These values fell within or at the boundary of the deteriorated heat transfer regime, based on the Yamagata's and Pioro's DHT criterion.

At this operating condition, the wall temperature variation predicted by using the RNG, RSM and the two k-ω models (SKW and SST) showed a better performance than the low-Reynolds turbulence models, when compared with the experimental data as shown in Fig. 9.113. Currently, among the several turbulence models, the RSM and the k-ω models (SKW and SST) are recommended for the prediction of the case 1 problem.

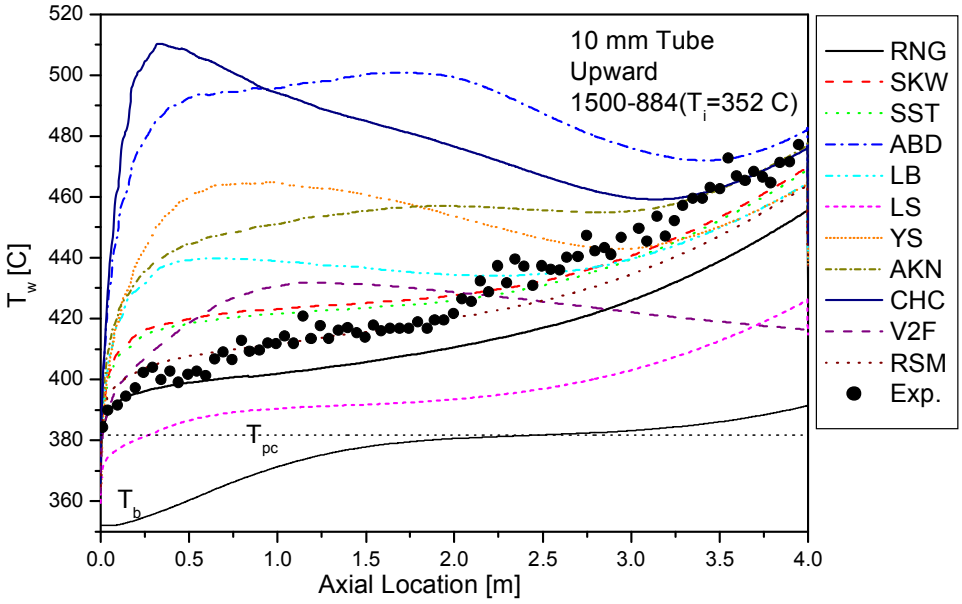

FIG. 9.113. Prediction of wall temperature (Case 1).

Wall temperature variation in Case 2 variant 1
In this case, the values of the ratios in the two criteria are ranged about 0.12-0.13 and 0.45-0.49, respectively. These values are a little bit higher but still very close to those for the case 1.

[14] B. H. Cho and Y. Y. Bae. Korea Atomic Energy Research Institute, Daejeon, Korea.

At this operating condition, all the turbulence models, without exception, predicted the increasing wall temperature very gently for both the upward and downward flow as shown in Figs 9.114 and 9.115. The predicted wall temperatures for downward flow were lower than those for the upward flow by about 10 ºC.

Wall temperature variation in Case 2 variant 2
In the present case, the values of the ratios in the two criteria were 0.32 and 1.05, respectively. These values corresponded to the deteriorated heat transfer regime.

For the downward flow, all turbulence models predicted the wall temperature similarly as shown in Fig. 9.117. But, for the upward flow, two groups (AKN and YS) were clearly different from others as shown in Fig. 9.116. The low-Reynolds turbulence models showed sharp peaks of wall temperature (DHT characteristics). The RNG, RSM and the two k-ω models (SKW and SST) did not show such a wall temperature peak.

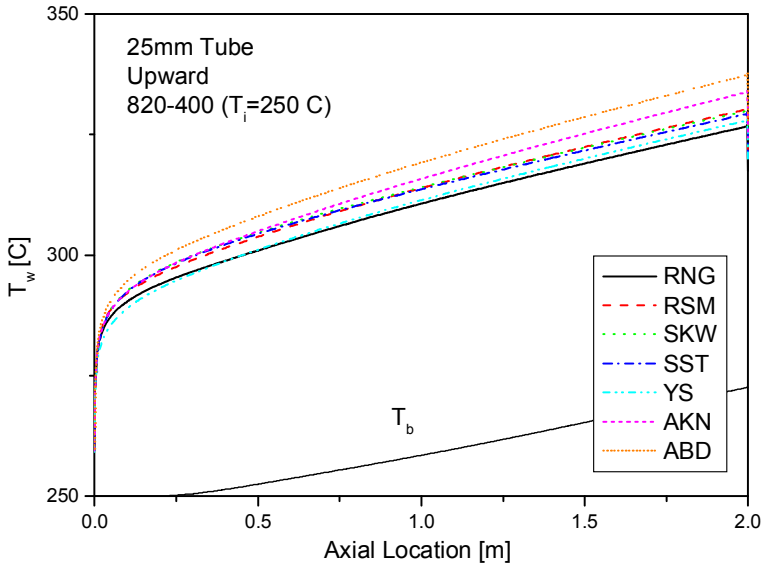

FIG. 9.114. Prediction of wall temperature (Case 2, var. 1, upward).

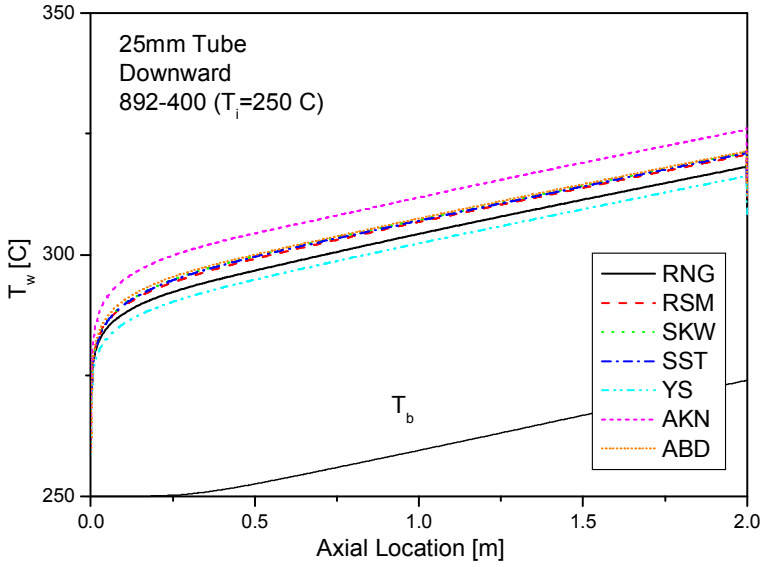

FIG. 9.115. Prediction of wall temperature (Case 2, var. 1, downward).

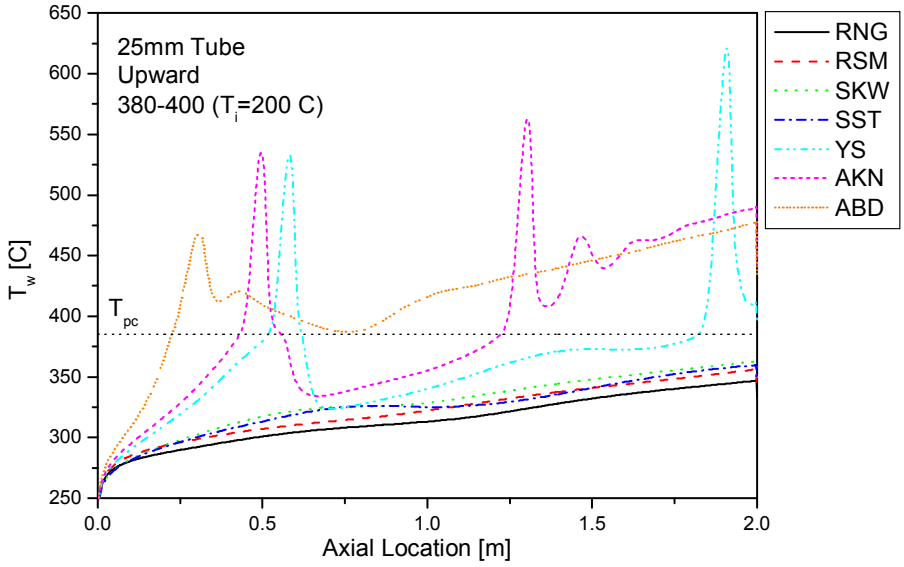

FIG. 9.116. Prediction of wall temperature (Case 2, var. 2, upward).

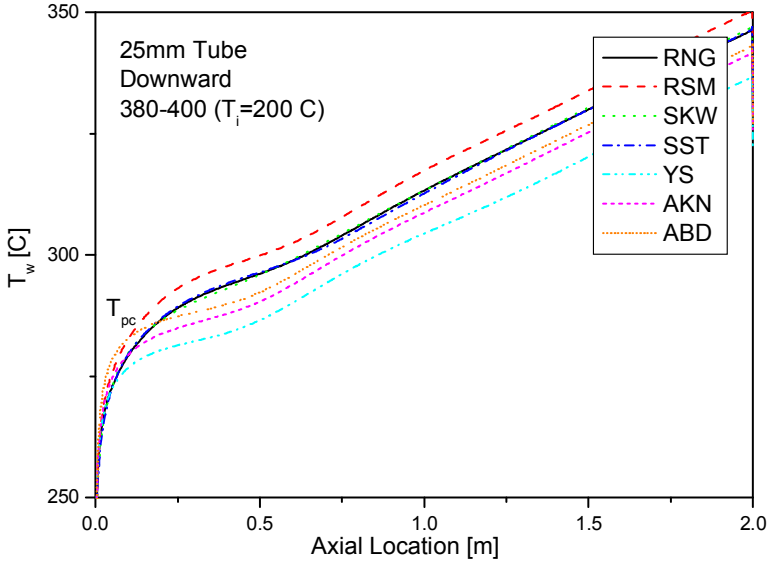

FIG. 9.117. Prediction of wall temperature (Case 2, var. 2, downward).

Comments on the results for Code Testing Benchmark No.1
Case 1
Figure 9.43 shows that KAERI's RSM and the two k-ω models (SKW and SST) predict the wall temperature relatively well. Figure 9.45 also shows the similar results of a heat transfer coefficient.

The bulk temperature was used for the calculation of the local heat transfer coefficient. In the KAERI's work, the bulk temperature of the fluid was calculated assuming that the specific enthalpy was linearly increased along the flow direction, which was started from the inlet enthalpy, since the heat flux was uniform. Figure 9.42 shows that the bulk temperatures plotted the most of the codes are identical. In Figs 9.50 and 9.49 all predictions of the bulk enthalpy and the bulk density by the various codes were plotted against the axial location. They showed almost identical values.

KAERI predicted the cross section averaged total pressure much lower, about half, compared to BARC results as shown in Fig. 9.47. We can assume that the dynamic head at the flow inlet and the outlet will be the same as far as the mean flow velocity is not changed. The roughly estimated gravity head for the 4m-long supercritical pressure water column is about 23 kPa. The deviation between the KAERI and BARC results seems to arise by the gravity head.

Case 2. Variant 1 – Up-flow
Among the turbulence models, RNG, RSM, SKW, SST, and three low-Reynolds number models such as YS, ABD and AKN were chosen for the Case 2 calculations.

As shown in Fig. 9.60, the wall temperatures predicted by RSM and the two k-ω models (SKW and SST) matched very well with the experimental data.

Case 2. Variant 1 – Down-flow
Among the selected models, the wall temperatures predicted by AKN matched relatively well with the experimental data as shown in Fig. 9.69.

Case 2. Variant 2 – Up-flow
Under the condition of the deteriorated heat transfer, two groups are clearly different from others for the upward flow as shown in Fig. 9.78. The low-Reynolds turbulence models showed rapid peaks of wall temperature (DHT characteristics), but the RNG, RSM and the two k-ω models(SKW and SST) did not show such a wall temperature peak.

The wall temperature predicted by YS model matched well with the experimental data.

Case 2. Variant 2 – Down-flow
As shown in Fig. 9.87, the wall temperatures predicted by the RSM and the two k-ω models (SKW and SST) matched very well with the experimental data.

9.1.6.8. SJTU[15]

In this study, the heat transfer under supercritical pressure is numerically studied using several turbulence models including k-ε, k-ω and Reynolds stress model. The main conclusions obtained are as follows:

- Standard k-ε, RNG and Reynolds stress model over-predict heat transfer capability. Most low Reynolds number models under-predict heat transfer capability. Standard k-ω, SST and CH perform best among these models, they have acceptable prediction ability;
- When the flow rate is large, the buoyancy effect is negligible. So, the influence of flow direction is slight. No heat transfer impairment is found in this case. The wall temperature and heat transfer coefficient predicted by models is similar;
- When the flow rate is small, the great buoyancy effect influences heat transfer. When flow direction is upward, most models predict heat transfer impairment appears. But these models give different wall temperature and heat transfer coefficient distribution. When flow direction is downward, the wall temperature and heat transfer coefficient predicted by models are similar, and no heat transfer impairment appear.

9.1.6.9. UMAP[16]

For the downward flow cases, the experimental wall temperature distribution did not show any sign of deterioration and the predicted wall temperature is very close to the measurement using all turbulence models. In all the downward cases analysed, the velocity field is similar to a standard forced convection velocity profile and the overall level of turbulence kinetic energy is low. Moreover, the turbulence kinetic energy reduces sharply near the wall and decreases towards the end of the pipe.

For the upward flow cases all the low-Reynolds number k-ε turbulence models used in this study are able to respond to the influence of buoyancy and to predict both heat transfer enhancement and deterioration phenomena seen in experimental data. The turbulence models are not able to predict quantitatively the wall temperature, but are able to capture qualitatively the general behaviour: the selected turbulence models tend to overestimate the effect of laminarization, predicting wall temperature profile higher than measurements.

Analysing the velocity field, it is possible to note two different types if behaviours:
- Case 1 and Case 2 - Variant 1 are similar to the standard forced convection (same consideration of downward cases);
- Case 2 - Variant 2 present a distorted velocity field. It can be seen that beyond the axial position of

[15] X. Cheng, SJTU

[16] W. Ambrosini, University of Pisa, S. He, University of Aberdeen.

maximum impairment of heat transfer, the velocity profile starts to present the characteristic M-shape: the velocity decreases in the core flow region. The progressive deformation of the axial velocity component profile, occurring along the heated section, reduces the value of the turbulent kinetic energy peak close to the wall.

The simulations show that the SWIRL CFD code used in conjunction with the three turbulence models chosen is able to describe the wall temperature profile reasonably, especially for the conditions in Case 2.

In particular, for the analysis of case 1 it can be noted the large mass flux results in a standard forced convection velocity profile; so, buoyancy effects are minimal. Nevertheless, only the AKN turbulence model gives a wall temperature prediction which is reasonably close to the experimental data, while LS and YS turbulence models show an over-prediction of wall temperature. This may be due to the large variation of density when temperature passes through the *pseudo-critical* value; the predicted effect of buoyancy is much greater than suggested by the value of the buoyancy parameter based on bulk temperature.

Regarding the heat transfer phenomena, only the upward Case 2 – Variant 2 exhibits a behaviour different from the other cases: in this case, buoyancy causes the deformation of the radial velocity profile and the consequent reduction of turbulent kinetic energy which leads to the flow laminarization and heat transfer deterioration.

9.1.7. Conclusion for the code testing benchmark on heat transfer

9.1.7.1. Sub-channel and system codes

The participants' calculations showed very close values of water bulk thermophysical properties (see Table 9.7). The maximum difference of calculation results for enthalpy does not exceed 1.9%. Only MP results for enthalpy differ from the results of other participants of 4 – 6%. The maximum difference of calculated results for bulk water temperature and density are about 2%.

Noticeable differences are observed in local parameters that are defined by correlations: pressure drop and heat transfer coefficient. The maximum difference in calculated results for pressure drop is about 10% (see Table 9.7). For Case 1, only JRC results of pressure drop differ from the results of other participants at 40 – 50%. Local differences in calculated data from experimental ones for the heat transfer coefficient can reach hundreds percent for Case 1 and Case 2 Variant 2 Up-flow. This emphasizes even more the need to design heat transfer and wall friction correlations for supercritical fluids.

Comparing the distribution of wall temperature along the pipe in calculations and experiments (Table 9.4), it may be concluded that similar results for Case 1 were obtained by JRC, VTT and GP (variant GP1101). AECL and MP results, that possibly were obtained using the Dittus-Boelter correlation, show overestimates of the heat transfer coefficient at water temperatures near the pseudo-critical point and higher.

In Case 2 Variant 1 with upward coolant flow the results of VTT and MP (variant MP2101T) show overestimates of pipe wall temperature; however, comparing the heat transfer coefficients, it is seen that these two calculations predicted the most accurate heat transfer coefficient. Probably, this disagreement is caused by differences in inlet water temperature reported in the tables with respect to experimental data [9-2]. As a result, displacing the curves of water and wall temperature down by 5 ºC and, respectively, the results of VTT and MP (variant MP2101T) are found to best predict the experimental data.

A good coincidence with experimental values of heat transfer coefficients for VTT and MP (variant MP21D01T) results is also observed in Case 2 Variant 1 down-flow.

Unfortunately, none of the sub-channel and system codes could predict heat transfer deterioration for Case 2 Variant 2 with upward flow.

9.1.7.2. CFD codes

The participants used different turbulence models, listed in Table 9.9 to perform calculations by CFD codes.

The participants' calculations showed very close values of water bulk thermophysical properties (see Table 9.8). The maximum difference of calculation results for enthalpy does not exceed 0.5%. The maximum difference of calculated results for bulk water temperature is about 1.1%. The difference of calculated values of water density for Case 2 does not exceed 0.6%. This difference amounts to 3% for Case 1 and only the results of BARC differ from the results of other participants at 11 – 16%.

Great differences are observed in pressure drop. Maximum difference of calculation results is about 110% (see Table 9.8).

The comparison of calculated and experimental values of wall temperature for different Cases is presented below.

For Case 1, SST model of CFX (CIAE) and SKW model of Fluent (SJTU) were found to predict closest to the experimental data in comparison with other codes/models. Fluent's RSM was found to predict well up to x = 2 m. SKE model of NAFA (BARC) is found to under-predict the wall temperature.

TABLE 9.10. TURBULENCE MODELS USED FOR CFD ANALYSIS

Institute	Code	Turbulence Model (Abbreviation)
BARC	NAFA	Standard k-ε (SKE)
CIAE	CFX	Shear-Stress-Transport K-ω (SST)
KAERI	Fluent	ReNormalization Group k-ε (RNG); Reynolds Stress Model (RSM); Standard K-ω (SKW); SST; V^2-f (V2F); Low Re models: ABD, AKN, CHS, LB, LS, YS[17]
SJTU	Fluent, SIMPLE2D	SKE; RNG; SKW; SST; RSM; Low Re models: ABD, AKN, CH, CHC, JL, YS
UMAP	SWIRL	Low Re models: AKN, LS, YS

Conclusions for Case 1 – all models, except low Re models, YS and LS models, predict the experimental data quite well. SST and SKW models were found to perform better than other models.

The analysis of the experimental data for Case 2 Variant 1 up-flow shows that these conditions are much simpler than for Case 1. The bulk temperature varies from 250 ºC to 283 ºC (from inlet to outlet). It is much less than the pseudo-critical temperature of 387ºC at 25 MPa. For this case, results of SKE, SKW, SST models and low Re variants like AKN, LS, YS are available. SKE model in NAFA (BARC), SST model of Fluent (KAERI) and SKW model of Fluent (KAERI) predicted closest to the experimental data.

[17] Abbreviations of the low Re models: AKN – Abe-Kondoh-Nagano; ABD – Abid; CH – Chien; CHC – Chang-Hsieh-Chen; JL – Jones-Launder; LB – Lam-Bremhorst; LS – Launder-Sharma; YS – Yang-Shih.

Low Re model (variant YS) over-predicted the wall temperature. Heat transfer coefficient predicted by all models except YS, was close to the coefficient obtained experimentally.

Conclusions for Case 2 Variant 1 up-flow – all models, except low Re model (variant YS), predicted results close to the experimental data for Case 2 Variant 1 up-flow (especially SKE, SKW and SST models were more accurate).

In this Case 2 Variant 1 down-flow sub-pseudo-critical conditions are encountered as the bulk temperature is much less than the pseudo-critical temperature. Hence, qualitatively all models have given the same result as the experimental data. However, an interesting trend is obtained in the results. The YS and AKN variant of low Re model implemented in SWIRL (UMAP) and Fluent respectively show excellent match with the experimental data. However, the YS variant in Fluent (KAERI) and AKN variant of SWIRL show maximum deviation from the experimental data. Thus, different codes using the same models have shown different results. All other models/codes predict results in between the deviations of the above mentioned ones. Further predictions with SST and SKW models by different codes are all found to match closely with the experimental data.

Conclusion for Case 2 Variant 1 down-flow – in this case also SST and SKW models predict results close to the experimental data.

For Case 2 Variant 2 up-flow only BARC and SJTU results of bulk temperature match well with the experimental data. Regarding wall temperature variation, none of the models/codes was able to predict the experimental data accurately over the entire range. The low Re variants like AKN, YS, LS, CH (all UMAP) and ABD (KAERI) are qualitatively the same as the experimental data in the initial heated part, i.e. up to $x = 0.5$ m, beyond which wall temperature is over-predicted. The high Re versions (i.e. SKE (BARC), SST (SJTU), SKW (SJTU and KAERI)) are close to the experimental data beyond $x = 0.5$ m.

Conclusion for Case 2 Variant 2 up-flow – though none of the models predicts the experimental data accurately, in general, SKW model was found to perform better than other models.

The analysis of various results for Case 2 Variant 2 down-flow shows that in this case none of the models predicted accurately the experimental data. The models which predict in the initial region (up to $x = 0.5$ m), under-predict in the next part. The models which properly predict in the next part ($x > 0.5$ m), over-predict in the initial part.

Conclusion for Case 2 Variant 2 down-flow – in general, predictions of SST and SKW were found to be better than other models. These models show the least average deviation from the experimental data.

Overall conclusion for CFD codes – in all cases, SST, SKW and CH were found to perform better than other models (like low Re models, other high Re models and RSM).

As a preliminary conclusion, it can be stated that there are correlations and turbulence models that predict heat transfer coefficient and wall temperature of circular pipe quite well for supposed conditions of SCWR normal operation (i.e. for conditions without deteriorated heat transfer). A revision of the computational methods and codes is necessary for the conditions where acceleration and buoyancy effects have a considerable influence.

Computational codes testing in pressure drop experiments in pipe is required, as the Benchmark Exercise No.1 showed a considerable discrepancy of computational results. In addition, it is necessary to perform experiments in the bundles of fuel rods and to test codes for these geometries.

9.2. CODE TESTING BENCHMARK NO. 2: 'FLOW STABILITY'

9.2.1. Purpose of the exercise

As discussed in Section 8, stability is a relevant issue to be coped with in designing reactors cooled by supercritical water. In fact, the presence of a dense fluid at the inlet of heated channels, which is subjected to a substantial expansion along its length, is likely to produce instability phenomena similar to those observed in boiling systems. In this regard, it must be considered that though experimental observation of instabilities in heated channels with supercritical fluids is mostly lacking, there is a general consensus about the relevance of this phenomenon for future SCWRs, as testified by the several works published on these aspects addressing the issue also in a reactor design perspective (see, e.g., [9-30] to [9-34]). Such a belief is mainly supported by the present understanding of the involved phenomena, assumed to occur in close similarity with those observed in the case of boiling systems, and by model prediction based on the properties of supercritical fluids.

On one hand, this situation motivates performing experimental studies aiming to ascertain the way in which the phenomena envisaged in computational analyses really occur in practical systems; on the other hand, the need is felt to compare the postulated unstable behaviour predicted by different models, in order to get greater insight into the expected physical mechanisms of instabilities. In this regard, making use of different computational tools, adopting rather independent and diverse models, represents a prudent strategy to critically discuss the obtained predictions, trying to quantify their reliability while waiting for experimental confirmation. Moreover, comparing results obtained by different codes and code users for an undisclosed set of reference data is a well-known methodology for evaluating the potential agreement in the prediction of unknown physical behaviour.

This latter aspect motivated the proposal of benchmark exercises, in a code-to-code comparison perspective, in the frame of the IAEA Coordinated Research Programme on Heat Transfer Behaviour and Thermohydraulics Codes Testing for SCWRs. The present benchmarking activity, in particular, was decided at the 1st Research Coordination Meeting of the CRP (Vienna, 22-25 July, 2008) and the action was assigned for coordination to the AECL and the University of Pisa.

This code testing benchmark exercise was aimed at comparing the results of linear and non-linear stability codes and models in the application to a simple reference geometrical condition. A very simplified problem was initially proposed at the 2nd Research Coordination Meeting (Vienna, 25-28 August, 2009), conceived to allow for the application of both one-dimensional and CFD models of different complexity. However, remarks raised during the Meeting suggested modifying the initial proposal, addressing only the capabilities of system codes, in order to consider a more realistic problem. The final version of the specifications [9-35] was set up considering these observations; the main change with respect to the initial proposal consisted in the introduction of throttling (i.e., singular pressure drops) at the inlet and at the outlet of the channel and of distributed wall roughness. The results of the analyses by Participants had to be proposed both in dimensional and in dimensionless form, possibly adopting different definitions in order to check their suitability to represent stability thresholds. Both dynamic and static instabilities were addressed.

As it will be shown in the following, the activity, though limited to system codes, involved sufficiently diverse models to stimulate useful discussions about the suitability of the different approaches in identifying the thresholds of instabilities in the parameter space [9-36]. In this perspective, the exercise completely reached the goal to highlight the present potential for accurate stability predictions, also indicating the areas in which the present models should be better customized once relevant experimental data will be made available.

9.2.2. Specifications for code testing benchmark No.2

The addressed geometrical configuration is represented in Fig. 9.118 [9-35]. It consists of a circular pipe with uniform heating along the axis. The length is assumed to be 4.2672 m (14 ft) and the ID is 8.36 mm. This diameter was selected in a previous work [9-37] in order to keep the same cross section and the same length of a previously addressed SCWR subchannel, though the geometry was simplified in order to allow for 2D axi-symmetric CFD calculations.

Inlet and outlet pressure drops represented by (irreversible) singular pressure drop coefficients (K_{in} = 20 and K_{out} variable from 2 to 20) were assumed and a uniform value of the roughness parameter, $\varepsilon = 2.5\times10^{-5}$ m, was assigned for the pipe wall. In considering the inlet and outlet singular pressure drop coefficients, it must be assumed the existence of inlet and outlet plena (that it is not necessary to simulate explicitly in detail) of comparatively very large area, where it was assumed to assign pressure. The reversible pressure changes due to restriction and enlargement effects in the plena had to be accounted for separately with respect to the assigned irreversible pressure drop coefficients.

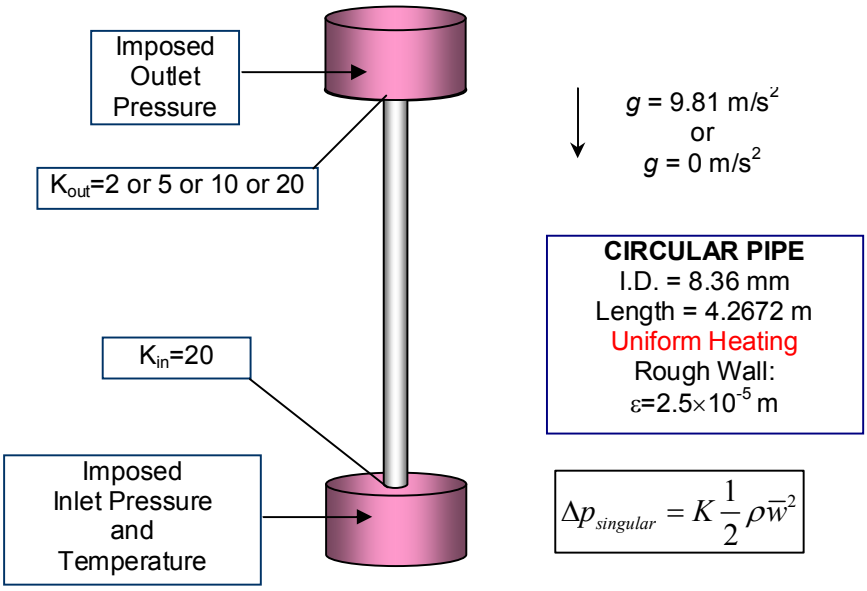

FIG. 9.118. Sketch of the addressed system.

Distributed friction factors had to be evaluated according to applicable constitutive laws (e.g., the Moody diagram and its suitable approximations). It must be mentioned that this aspect resulted to be quite relevant, since specific constitutive friction laws exist for supercritical fluids which may give results different enough with respect the ones obtained by the classical Moody diagram.

Whenever it was needed to represent the wall from the thermal point of view, negligible heat capacitance and very high heat conductance had to be assumed, in order to closely simulate axially uniform and constant heating by an assigned power source.
Different boundary conditions were suggested to address the proposed calculation cases; in particular:
in the case of steady-state calculations, aiming at defining the initial conditions for a transient evolution or frequency domain analysis, *imposed inlet mass flow rate and temperature and imposed outlet pressure* should be assumed in order to avoid as far as possible the occurrence of flow instabilities along the channel at any power level; mass flow rate was suggested to be selected in the range 0.04 – 0.08 kg/s for all the fluids, though the role of its value should be relatively immaterial for evaluating the stability

threshold in dimensionless form; in a later phase, upon request by Participants, a reference pressure drop of 0.12 MPa was suggested as an alternative, in order to define the flow rate in compliance with this requirement;

- in the case of transient or frequency domain calculations aiming at defining the stability threshold, *imposed inlet pressure and temperature and imposed outlet pressure* must be assumed; this specifies a minimum of constraint to the system that should be free of oscillating, either because of purposely introduced perturbations or because of round-off errors occurring in calculations; the value of pressure drop should be taken constant at the value identified in steady-state calculations (or at 0.12 MPa, as suggested above);
- Gravity was assumed to be downward directed (vertical upward flow) or to be absent (horizontal flow). The comparison between these two cases is meaningful in understanding their differences in the dynamic behaviour of the system. It was explicitly suggested that Participants wishing to perform a more complete analysis also consider downward flow.

The proposed exercise was subdivided into two parts:

- the first was related to water at 25 MPa with vertical channel, in consideration of the great interest that this fluid and this operating condition have for SCWR reactor applications;
- the second addressed fluid-to-fluid comparison with vertical upward or horizontal flow.

Since many codes have not the possibility to use fluids other than water, the first part was expectedly the primary common basis for code-to-code comparison.

The fluids considered in the two parts of the proposed exercise are those reported in Table 9.11 and already used as a basis for discussion in a previously published paper [9-38]. In the case in which the adopted code did not allow for the use of any fluid other than water, Participants interested in a more in depth analysis of the effect of fluid properties were suggested to make use of water at additional operating pressures (e.g., 30 and 40 MPa), in order to highlight possible similarities in terms of dimensionless numbers. Both routes were intended for assessing the effect of changes in fluid properties on stability thresholds at different extents. Obviously, the use of different fluid property packages by Participants might introduce some variability in the obtained results to be considered. Sensitivity analyses on other parameters, e.g, concerning channel length and inlet throttling, were also suggested.

TABLE 9.11. CONSIDERED FLUIDS AND OPERATING PRESSURES

Fluid	$p[MPa]$
Water	25.0, (30.0, 40.0)
CO_2	8.0
R23	5.7
Ammonia	15.0

For the purpose of defining the operating conditions in a compact way for different fluids and operating pressures, the following dimensionless definitions were adopted:

$$N_{SPC} = \frac{\beta_{pc}}{C_{p,pc}}\left(h_{pc} - h_{in}\right) \tag{9-16}$$

$$N_{TPC} = \frac{\dot{Q}_{heating}}{W_{in}}\frac{\beta_{pc}}{C_{p,pc}} \tag{9-17}$$

The above *sub-pseudocritical* number and *trans-pseudocritical* number, as introduced in previous work [9-39] and [9-40], were used respectively to specify inlet fluid thermodynamic conditions (e.g., inlet specific enthalpy) and for representing the stability threshold. In using these definitions, it is necessary to consider that:

- pseudo-critical parameters (subscript 'pc') are evaluated for each fluid and at each pressure at the maximum of the specific heat at constant pressure, following a common definition;
- the sub-pseudocritical number was mainly used to specify the inlet specific enthalpy (i.e., temperature), according to the straightforward inverse relationship:

$$h_{in} = h_{pc} - \frac{C_{p,pc}}{\beta_{pc}} N_{SPC} \tag{9-18}$$

- the trans-pseudocritical number was mainly used to define the observed threshold of instability at constant N_{SPC}; different routes were proposed, as summarized below, for defining the critical value of N_{TPC} at which the start of unstable oscillations or of excursive behaviour was observed;
- The use of other dimensionless numbers in representing the obtained results in addition to those proposed for this benchmark, e.g., as proposed by Zhao et al., (2005) [9-41] and by Ortega Gomez et al. (2008) [9-42], or those ones elaborated for this benchmark by Chatorgoon et al. (2010) [9-43] on the basis of previous work [9-44] and [9-45], was encouraged. In such a way, the benchmark exercise would have had as a useful by-product an improved understanding of the presently available proposals to define stability thresholds in dimensionless form.

The proposed stability analyses were aimed at establishing the thresholds for instability at assigned values of the number quantifying pseudo-subcooling, N_{SPC}, in terms of a threshold value of N_{TPC} at the start of oscillatory or excursive behaviour. As mentioned, the boundary conditions to be used in studying the dynamics of the system were the imposed inlet and outlet pressure and the inlet fluid temperature.

Suitable procedures for obtaining information on stability thresholds could be different depending on the specific adopted model. In particular, the following examples were proposed:

- for linear stability codes: whether a characteristic equation is obtained or the eigenvalues of a matrix are discussed for considering stability, the relevant information can be expressed in different forms, including the threshold power needed to reach unstable behaviour with an assigned flow rate or the threshold flow rate at an assigned power; this basic information had to be translated in terms of the dimensionless power-to-flow ratio N_{TPC} and the specific way followed for obtaining the threshold had to be clearly declared; linear stability is generally studied only after a steady-state calculation is performed: as already pointed out above, the imposed pressure drop boundary condition had to be therefore determined as the one observed in the steady-state analyses by imposing the flow rate in a range that is suggested to be 0.04 - 0.08 kg/s for water and the other fluids (or taken as 0.12 MPa);
- for non-linear stability codes: it was suggested that, whenever a steady-state algorithm was available, the transient calculation was initialized at a stationary condition in the suggested operating region; in this case, at least two-possible strategies of calculations could be adopted:
  - running repeated steady-state calculations at increasing power levels, followed by free evolutions

in which the pressure drop across the channel and the inlet pseudo-subcooling are kept constant at the steady-state values; the evolution may be started by introducing an initial small perturbation (e.g., in velocity or pressure) or just relying on the effects of discretization error and round-off; observing the damping or amplification of perturbations will give information on stability, to be translated in terms of a threshold value of N_{TPC};

- starting from an arbitrary condition and slowly increasing in time the power at constant pressure drop and inlet pseudo-subcooling up to the point at which oscillations are observed; this route must be considered less accurate than the previous one, because of its transient nature, but it is also suitable to identify the N_{TPC} threshold at unstable behaviour; in fact, if the rate of power increase is limited, the results can be considered reliable enough, especially when a sensitivity analysis on this parameter demonstrated that the rate of power increase is low enough to only marginally affect the results;
- as a variant of the above route, the calculation can be started from an arbitrary condition, slowly decreasing the pressure drop across the channel at constant power and inlet pseudo-subcooling, up to the point in which oscillations are observed; this route is similar to the above one and affected by similar possible inaccuracies in evaluating the threshold of N_{TPC} at unstable behaviour, because of the introduction of some degree of unsteadiness.

Any other means to obtain the critical dimensionless power-to-flow ratio were obviously considered acceptable, provided that a clear explanation of the related rationale was given in the model description. Additional information on the ratio between the fluid transit time in the channel and the period of oscillations had to be provided (from here on named T_{trans}/T), whenever available.

In addition to the basic data about the stability thresholds, further information was asked to the Participants; e.g.:

- in the case of linear stability codes:
  - linear stability maps, whenever available, in any dimensional or dimensionless format;
  - frequency of oscillations or character of the unstable bifurcation (e.g., complex conjugated roots or single real root with positive real part);
  - rate of increase of the amplification factor as a function of the quantity $N_{TPC} - N_{TPC,threshold}$ at constant N_{SPC} beyond the stability threshold;
- non-linear stability codes:
  - in case of repeated steady-state calculations at different N_{SPC} and N_{TPC} followed by free evolutions after perturbation, plots of inlet and outlet flow rate as a function of time at different values of N_{SPC} should be provided, to show the basis for the selection of the threshold value;
  - in case of increasing power at constant pressure drop or decreasing pressure drop at constant power in time:
    - plots of inlet and outlet flow rate as a function of time;
    - plots of N_{TPC}, evaluated on the basis of power and of the inlet flow rate, as a function of time.

Different calculation matrices were proposed for the two phases of the exercise, as reported below in Table 9.12 to Table 9.15. The tables were supplied to the Participants in the form of template Excel files to be filled with the required information, shown in unified format plots.

TABLE 9.12. MATRIX OF THE BASE CALCULATION CASES FOR SUPERCRITICAL WATER AT 25 MPA

Participant name – Code Name			Kout=20	Kout=20	Kout=10	Kout=10	Kout=5	Kout=5	Kout=2	Kout=2
Case	Channel orientation	Nspc	Ntpc, threshold	Type of instability	Ntpc, threshold	Type of instability	Ntpc, threshold	Type of instability	Ntpc, threshold	Type of instability
Label				Oscillatory or Excursive		Oscillatory or Excursive		Oscillatory or Excursive		Oscillatory or Excursive
D0.5V-K20 to K2	Vertical	0.5	1	Oscillatory					3	Oscillatory
D1.0V-K20 to K2	Vertical	1	1	Excursive					3	Excursive
D1.5V-K20 to K2	Vertical	1.5	1	Oscillatory	1.5	Oscillatory	2.5	Excursive	3	Oscillatory
D2.0V-K20 to K2	Vertical	2	1	Excursive					3	Excursive
D2.5V-K20 to K2	Vertical	2.5	1	Oscillatory					3	Oscillatory
D3.0V-K20 to K2	Vertical	3	1	Excursive					3	Excursive

TABLE 9.13. ADDITIONAL DIMENSIONLESS INFORMATION ON THE PERIOD OF OSCILLATIONS FOR SUPERCRITICAL WATER AT 25 MPA

Participant name – Code Name			Kout=20	Kout=10	Kout=5	Kout=2
Case	Channel orientation	Nspc	Ratio of Transit Time to the Period of Oscillations	Ratio of Transit Time to the Period of Oscillations	Ratio of Transit Time to the Period of Oscillations	Ratio of Transit Time to the Period of Oscillations
Label						
D0.5V-K20 to K2	Vertical	0.5	1			1
D1.0V-K20 to K2	Vertical	1	1			1
D1.5V-K20 to K2	Vertical	1.5	1	1	1	1
D2.0V-K20 to K2	Vertical	2	1			1
D2.5V-K20 to K2	Vertical	2.5	1			1
D3.0V-K20 to K2	Vertical	3	1			1

TABLE 9.14. MATRIX FOR THE CALCULATIONS FOR FLUID-TO-FLUID COMPARISON

Participant name – Code Name			Water	Water	CO2	CO2	R23	R23	NH3	NH3
Case	Channel orientation	Nspc	Ntpc. threshold	Type of instability	Ntpc. threshold	Type of instability	Ntpc. threshold	Type of instability	Ntpc. threshold	Type of instability
Label				Oscillatory or Excursive		Oscillatory or Excursive		Oscillatory or Excursive		Oscillatory or Excursive
F0.5V	Vertical	0.5	1	Oscillatory	2	Oscillatory	3	Oscillatory		
F1.0V	Vertical	1	1	Excursive	2	Excursive	3	Excursive	4	Oscillatory
F1.5V	Vertical	1.5	1	Oscillatory	2	Oscillatory	3	Oscillatory	4	Excursive
F2.0V	Vertical	2	1	Excursive	2	Excursive	3	Excursive	4	Oscillatory
F2.5V	Vertical	2.5	1	Oscillatory			3	Oscillatory		
F3.0V	Vertical	3	1	Excursive			3	Excursive		
F0.5H	Horizontal	0.5	1.5	Oscillatory	2.5	Oscillatory	3.5	Oscillatory		
F1.0H	Horizontal	1	1.5	Excursive	2.5	Excursive	3.5	Excursive	4.5	Oscillatory
F1.5H	Horizontal	1.5	1.5	Oscillatory	2.5	Oscillatory	3.5	Oscillatory	4.5	Excursive
F2.0H	Horizontal	2	1.5	Excursive	2.5	Excursive	3.5	Excursive	4.5	Oscillatory
F2.5H	Horizontal	2.5	1.5	Oscillatory			3.5	Oscillatory		
F3.0H	Horizontal	3	1.5	Excursive			3.5	Excursive		

TABLE 9.15. ADDITIONAL DIMENSIONLESS INFORMATION ON THE PERIOD OF OSCILLATIONS FOR FLUID-TO-FLUID COMPARISON

Participant name – Code Name			Water	CO2	R23	NH3
Case Label	Channel orientation	Nspc	Ratio of Transit Time to the Period of Oscillations	Ratio of Transit Time to the Period of Oscillations	Ratio of Transit Time to the Period of Oscillations	Ratio of Transit Time to the Period of Oscillations
F0.5V	Vertical	0.5	1	1	1	
F1.0V	Vertical	1	1	1	1	1
F1.5V	Vertical	1.5	1	1	1	1
F2.0V	Vertical	2	1	1	1	1
F2.5V	Vertical	2.5	1		1	
F3.0V	Vertical	3	1		1	
F0.5H	Horizontal	0.5	1	1	1	
F1.0H	Horizontal	1	1	1	1	1
F1.5H	Horizontal	1.5	1	1	1	1
F2.0H	Horizontal	2	1	1	1	1
F2.5H	Horizontal	2.5	1		1	
F3.0H	Horizontal	3	1		1	

9.2.3. Reference data

The reference data prepared on behalf of the IAEA for comparison with Participant submissions are described in a specific report [9-46]. As in previous published work [9-38], the codes and models adopted by the University of Pisa in the purpose of generating the reference data were:

- an in-house code making use of linearized and dimensionless forms of the space and time discretized governing equations, adopted to set up stability maps;
- an in-house transient code, used for dealing with the cases of different fluids in dimensional form;
- the RELAP5/MOD3.3 code [9-47], used in transient mode only in the case of water.

Since all the adopted models are based on discretized equations, a discussion on the effects of truncation errors was included, making use of the interesting possibility to set up stability maps affected by discretization in similarity with what happens for many available transient codes.

The **linearized program (named ISHII-SUP)** is based on dimensionless definitions introduced in previous works [9-39] and [9-40] in which the model is described in detail. The dimensionless definitions are as follows:

$$\rho^* = \frac{\rho}{\rho_{pc}} \qquad h^* = \frac{\beta_{pc}}{C_{p,pc}}\left(h - h_{pc}\right) \qquad w^* = \frac{w}{w_0} \qquad t^* = \frac{t\, w_0}{L} \tag{9-19}$$

$$z^* = \frac{z}{L} \qquad p^* = \frac{p}{\rho_{pc}\, w_0^2} \qquad G^* = \rho^*\, w^* \qquad Fr = \frac{w_0^2}{g\, L} \tag{9-20}$$

$$\Lambda = \frac{f\, L}{2\, D_h} \qquad N'_{TPC} = \frac{q''_0\, \Pi_h\, L}{\rho_{pc}\, w_0\, A}\frac{\beta_{pc}}{C_{p,pc}} \qquad N_{SPC} = \frac{\beta_{pc}}{C_{p,pc}}\left(h_{pc} - h_{in}\right) \tag{9-21}$$

$$N_{TPC} = \frac{\dot{Q}_{channel}}{W_{channel}}\frac{\beta_{pc}}{C_{p,pc}} = N'_{TPC} \big/ \rho^*_{in} \tag{9-22}$$

The mass, momentum and energy balance equations on which the model is based are as follows:

$$\frac{\partial \rho^*}{\partial t^*} + \frac{\partial \rho^* w^*}{\partial z^*} = 0 \tag{9-23}$$

$$\frac{\partial G^*}{\partial t^*} + \frac{\partial}{\partial z^*}\left(\frac{G^{*2}}{\rho^*}\right) + \frac{\partial p^*}{\partial z^*} = -\frac{\rho^*}{Fr} - \left[\Lambda + \frac{1}{2}K_{in}\delta^*(z^*) + \frac{1}{2}K_{out}\delta^*(z^* - 1)\right]\frac{G^{*2}}{\rho^*} \tag{9-24}$$

$$\frac{\partial \rho^* h^*}{\partial t^*} + \frac{\partial \rho^* w^* h^*}{\partial z^*} = N'_{TPC} f_q^*(z^*) \tag{9-25}$$

In the development of these equations, it was assumed that the flow is one-dimensional, the fluid expands because of heating but it can be considered incompressible, the flow work can be neglected and heating because of viscous dissipation is also negligible.

The boundary conditions imposed to evaluate the steady-state conditions whose stability is the objective of the study were:

$$h^*_{in} = -N_{SPC} \tag{9-26}$$

$$G^* = \rho^*_{in} \tag{9-27}$$

The latter condition follows from the fact that w_0 is assumed to be the inlet velocity, w_{in}, so that $w_{in}^* = 1$ and $G_{in}^* = \rho_{in}^* w_{in}^* = \rho_{in}^*$.

As a consequence of the boundary conditions, also considering that a unique relationship $\rho^*\left(h^*\right)$ is found for different supercritical pressures and, at a lower extent, for different fluids, given any set of parameters Λ, K_{in}, K_{out}, Fr, N_{SPC} and N_{TPC} the overall steady-state dimensionless pressure drop across the channel in steady-state conditions, $\Delta p_{channel}^*$, is completely specified. Also the distribution of dimensionless fluid density along the channel is therefore completely specified, since the dimensionless enthalpy distribution is specified.

In the stability analyses, the value of the pressure drop obtained by the steady-state calculation is imposed across the channel, letting flow rate to freely oscillate. The dynamics of the system is in fact fully defined, including the threshold value of N_{TPC} leading to unstable behaviour as a function N_{SPC} when all the other parameters are assumed to be constant.

The above balance equations are discretized in space and time by a classical semi-implicit numerical scheme. The linearization by perturbation of the obtained algebraic equations is followed by the evaluation of the eigenvalues of a matrix representing at each steady-state condition the linearized dynamics of the system, providing the following parameters:

- z_R, being a dimensionless amplification parameter that is negative for stable conditions and positive for unstable ones;
- z_I, being a dimensionless angular frequency of oscillations.

While z_R is used to set up contour plots used as quantitative stability maps, allowing for identifying the stability boundary in the $N_{TPC} - N_{SPC}$ plane, z_I is used to evaluate the dimensionless period of oscillations that can be conveniently compared with the dimensionless fluid transit time along the channel producing interesting contour plots of their ratio.

The discretization method adopted for the balance equations, making use of staggered meshes and of a classical donor cell principle (upwind differencing), has a first order truncation error. A reasonable compromise between computational efficiency and accuracy is to run the program making use of 48 nodes in the heated channel and a maximum Courant number as large as 0.9; however, stability maps obtained with 96 nodes are also considered, in order to clearly point out the level of convergence reached in the addressed conditions.

The dimensionless equation of state adopted in the code represents an approximation of the mentioned unique relationship between dimensionless density and dimensionless enthalpy, $\rho^*\left(h^*\right)$, that was observed to hold for different supercritical pressures and, at a reasonable extent, also for different fluids.

RELAP5/MOD3.3 [9-47] (version RBIC/3.3gl) is a well-known system code adopted for the safety analysis of LWRs. In the previous works, it was noted that the code does not show numerical problems in being used for water at supercritical pressures, at least if no trans-critical condition is considered. On the contrary, it always showed reasonable agreement with the stability maps obtained by the dimensionless linearized code.

The main reason for using the code in this frame is to adopt a completely 'diverse', independent and well verified tool whose results can be compared with those of the in-house codes. In fact, both these codes

were derived by a similar root in terms of balance equations and discretization methods: an independent check was considered useful.

Obviously, the use of the RELAP5 code is limited to water, since this is the single fluid among the ones addressed in this exercise to be available in the adopted version of RELAP5. The nodalization set up for the analysis was also very simple, including two 'time-dependent volumes' used, to impose the pressure drop, connected by two single-junctions to a pipe with 48 nodes. A very thin and highly conductive heat structure is introduced to simulate the conditions of imposed heat flux.

A maximum time step of 0.1 s was used in all the calculations in which, anyway, the built-in Courant number limitation of the code was automatically applied putting an upper bound to the actually adopted time step. In the case of RELAP5, the strategy for achieving the stability threshold consisted in running calculations at constant boundary conditions with increasing the heating power up to the point in which flow oscillations or an excursion were observed. The value of the power-to-flow ratio at the threshold of stability was then converted into a corresponding value of N_{TPC}, as in the case of the in-house transient program, to be compared with the stability boundary generated by the linearized code.

The adopted **transient program in dimensional form (named TRANSDIM)** is based on the semi-implicit discretization of the original mass, momentum and energy balance equations, whose dimensionless form was used in the previous described program. These balance equations are:

$$\frac{\partial \rho}{\partial t}+\frac{\partial \rho w}{\partial z}=0 \tag{9-28}$$

$$\frac{\partial \rho w}{\partial t}+\frac{\partial \rho w^2}{\partial z}+\frac{\partial p}{\partial z}=-\rho g-\left[\frac{f}{D_h}+K_{in}\delta_d(z)+K_{ex}\delta_d(z-L)\right]\frac{\rho w^2}{2} \tag{9-29}$$

$$\frac{\partial \rho h}{\partial t}+\frac{\partial \rho h w}{\partial z}=q''_0\frac{\Pi_h}{A}f_q(z) \tag{9-30}$$

The adopted numerical discretization method is just the same as the one adopted for the linearized code, except for the fact that in this case a transient solution is obtained and stability is checked by simply running the code with a constant pressure drop at constant operating conditions (namely, pressure drop and inlet enthalpy), with a continuous increase in the heating power imposed to the channel. This increase, kept very slow to avoid introducing unwanted transient effects, brings eventually the system to show oscillations or an excursion, thus allowing to identify the corresponding stability threshold.

The critical value of the power-to-flow ratio observed at the threshold of instability is then translated into dimensionless form obtaining a corresponding value of N_{TPC}. With due caution in relation to the differences in the adopted boundary conditions, this value can be directly compared with the stability boundary obtained by the dimensionless program.

The equation of state required for closing the balance equations is introduced in the program in the form of very detailed tables of values of density as a function of enthalpy; a technique of direct access to the tables and a linear interpolation allow obtaining at the same time a reasonable computational effort in running the calculations and a good accuracy. Four different tables were generated from the NIST

package [9-48] for the fluids addressed in the problem (water, carbon dioxide, refrigerant R23 and ammonia) at the specific operating pressures listed in Table 9.11. As a consequence, in the calculations the variation of fluid properties as a function of the local value of pressure was not accounted for. Also TRANSDIM was used with 48 nodes, providing the basis for a direct comparison with the stability maps generated by the dimensionless code.

Figures 9.119 to 9.121 report the basic reference information provided by the linear stability program for the vertical and horizontal channel cases proposed in the present benchmark exercise. In particular:

- Figs 9.119 and 9.120 report information on the distributions of z_R and of T_{trans}/T (i.e., of the ratio between the fluid transit time along the channel and the period of oscillations) applicable to the vertical channel cases with upward flow of water proposed in the first part of the exercise**,** mainly devoted to the effect of channel throttling; Figure 9.121 reports information on the distributions of z_R and of T_{trans}/T applicable to the vertical and horizontal channel cases proposed in the second part of the exercise, mainly devoted to the fluid-to-fluid comparison.

Considerations about the values adopted for some calculation parameters are in order:

- the value of the friction parameter, Λ**,** that must be specified in the linearized program is assumed constant and roughly equal to the value that it is assumed to hold in the addressed conditions; since the friction factor is a function of the Reynolds number, this represents an approximation introduced in the calculation, though the Reynolds number in the addressed cases is large enough to be in a region in which the friction factor mostly depends on pipe roughness;
- the value 0.03 of the Froude number for vertical channel corresponds to an inlet velocity equal to $w_{in} = \sqrt{Fr\, g\, L} \approx 1.12\ m/s$ with the geometrical data of the present problem; however, the exercise, as assigned in the specifications, does not refer to a single value of inlet velocity, on which a certain freedom was left to the Participants in selecting the flow rate to initialize the calculations; as shown hereafter, this aspect does not pose relevant problems in establishing the stability threshold in terms of N_{TPC} in the density-wave instability region, though it may change the value of the ratio T_{trans}/T; this has the consequence that while the comparison of the stability margin with the data of the transient program is fully meaningful (with a few possible exception), the comparison of the values of T_{trans}/T will be affected by some degree of indeterminacy: both these aspects will be clarified hereafter;
- a value 10^5 of the Froude number is adopted to identify a horizontal channel.

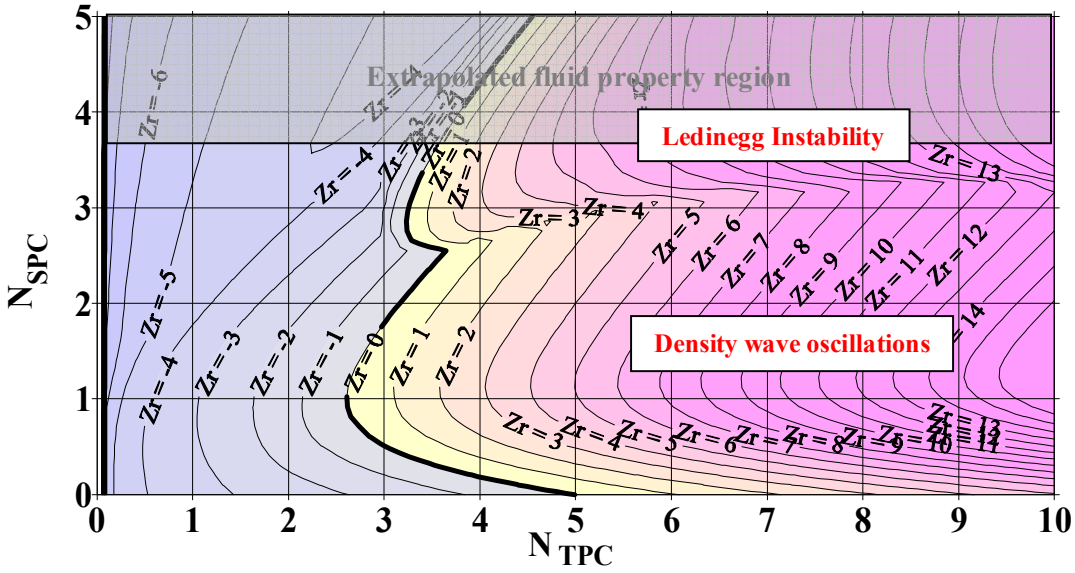

a) stability map

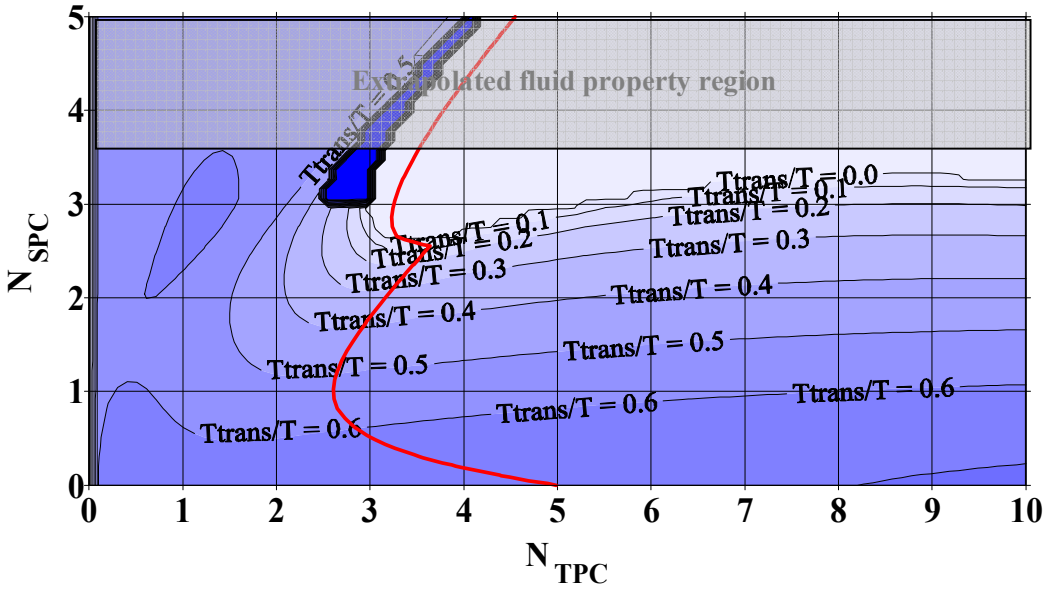

b) contour plot of T_{trans}/T

FIG. 9.119. Reference stability map and contour plot of T_{trans}/T for the case of vertical channel with K_{in}=K_{out}=20 ($\Lambda = 7, Fr = 0.03, C_{\max} = 0.9, N_{nodes} = 48$).

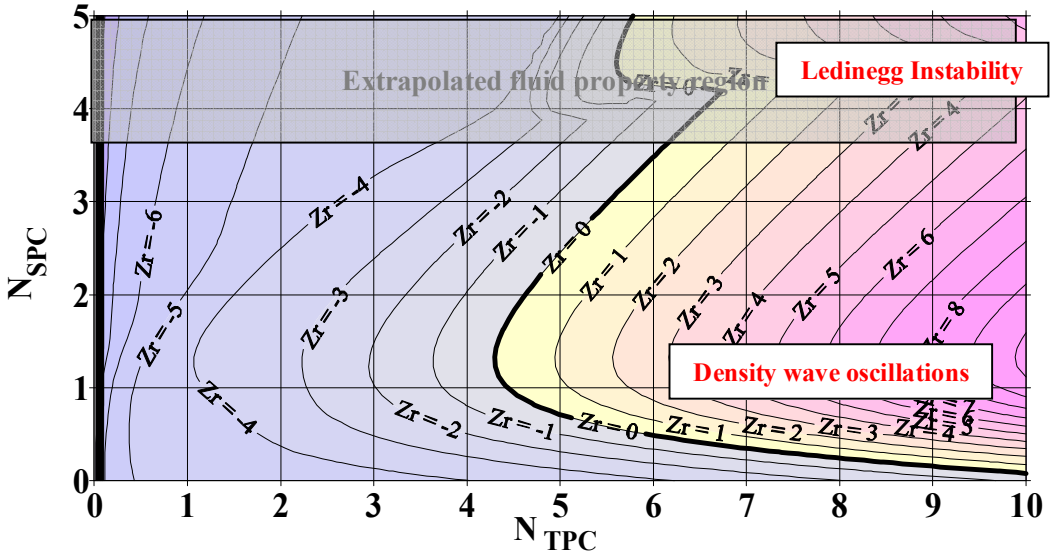

a) stability map

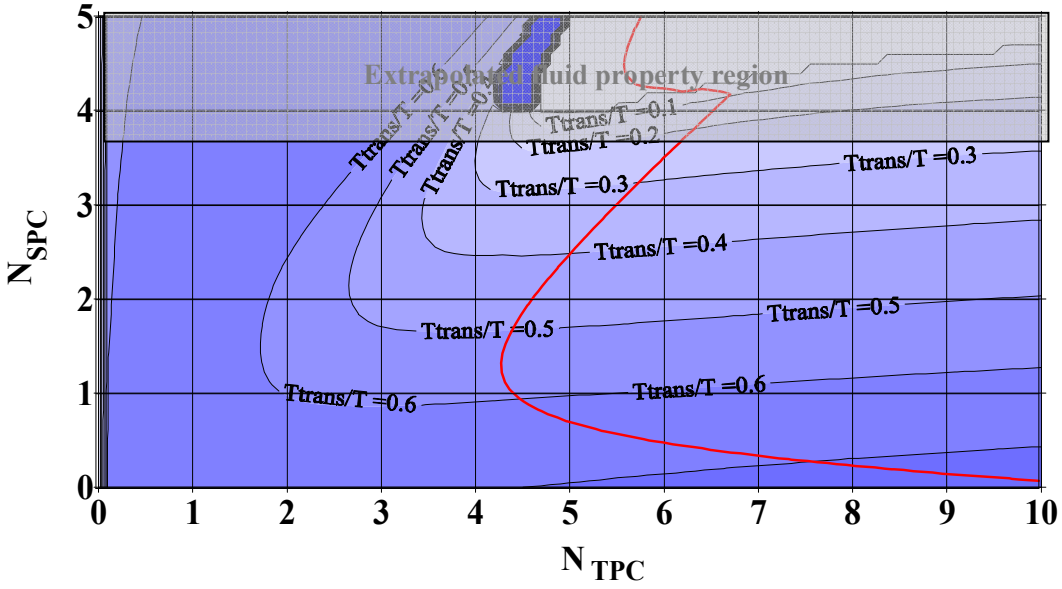

b) contour plot of T_{trans}/T

FIG. 9.120. Reference stability map and contour plot of T_{trans}/T for the case of vertical channel with K_{in}=20 and K_{out}=2 ($\Lambda = 7, Fr = 0.03, C_{\max} = 0.9, N_{nodes} = 48$).

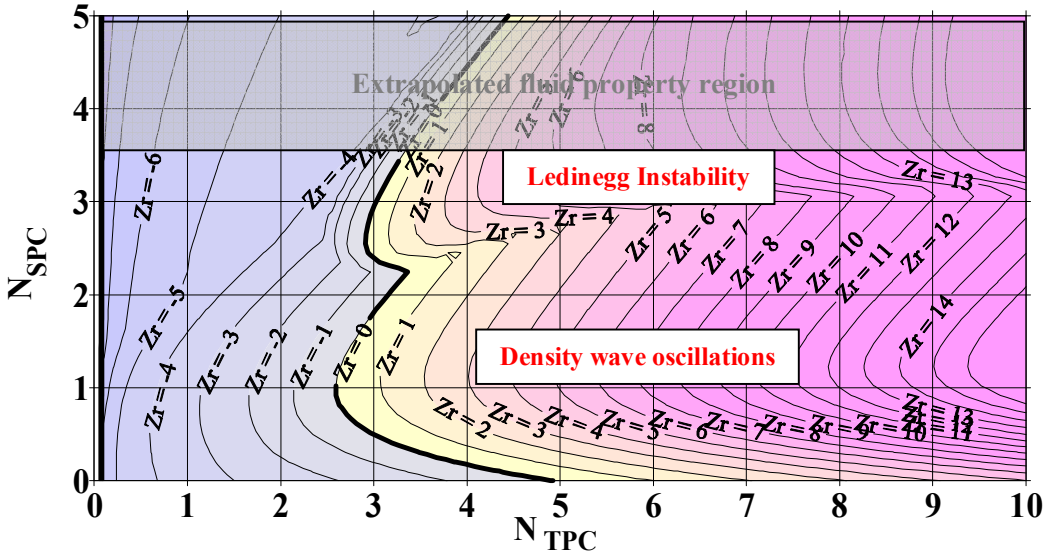

a) stability map

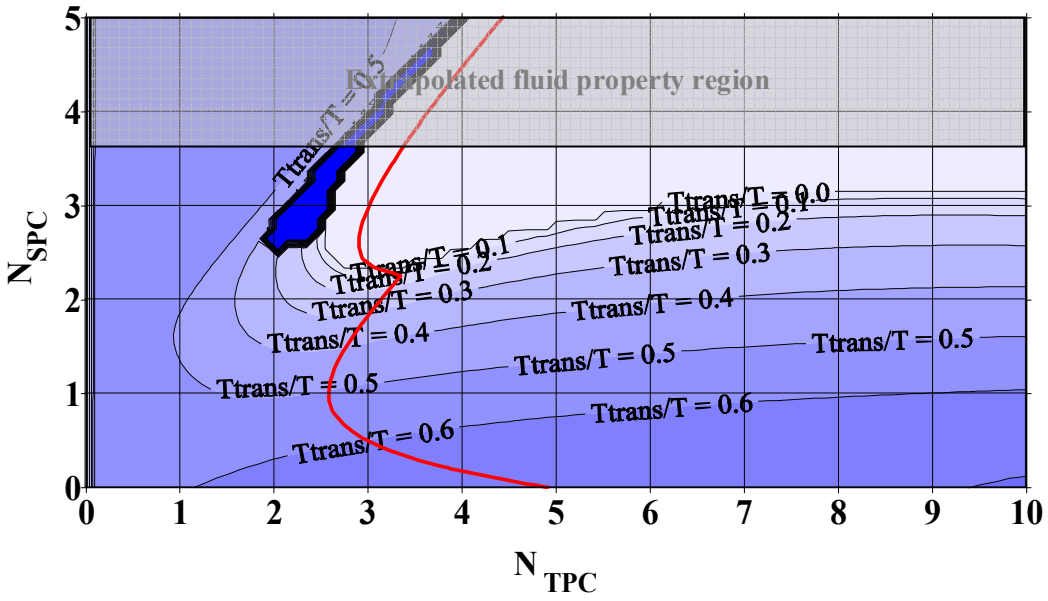

b) contour plot of T_{trans}/T

FIG. 9.121. Reference stability map and contour plot of T_{trans}/T for the case of horizontal channel with K_{in}=K_{out}=20 ($\Lambda = 7, Fr = 10^5, C_{\max} = 0.9, N_{nodes} = 48$).

Figure 9.122 and 9.123 show the differences appearing in the stability margin as a function of the Froude number ranging from the average values that can be considered somehow applicable in the present case for a vertical channel (Fr=0.03) to very large values characterising the horizontal channel (Fr=10^5), also considering a case of lower inlet velocity (Fr=0.01). In addition, Figs 9.124 and 9.125 report the full information about the additional two cases at Fr=0.01. From the observation of these figures, it can be noted that:

- the changes observed in the stability boundary related to density wave oscillations (lower lobe of the map) are negligible;
- in the addressed range of parameters, the Froude number seriously affects only the location of the region of Ledinegg instability (upper lobe of the map);
- owing to the fact that in the density-wave region the ratio T_{trans}/T decreases with increasing the pseudo-subcooling (i.e., N_{SPC}), becomig zero in the Ledinegg region, the effect of a change of the Froude number in the density-wave region is mainly to affect the ratio T_{trans}/T, leaving almost unchanged the stability boundary.

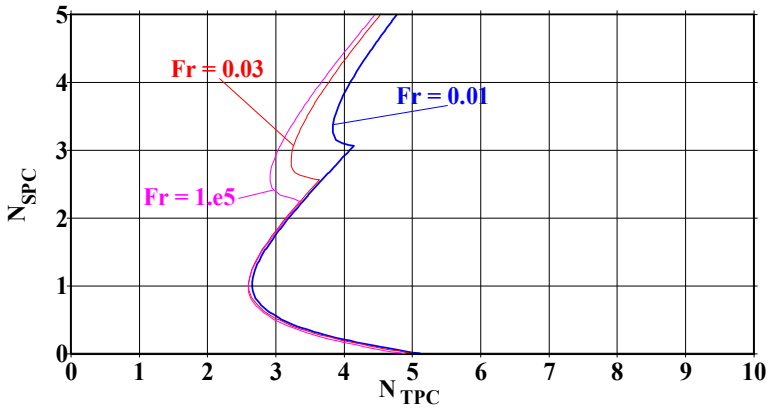

FIG. 9.122. Effect of the Froude number on the stability margin in the case with K_{in}=K_{out}=20 ($\Lambda = 7, C_{\max} = 0.9, N_{nodes} = 48$).

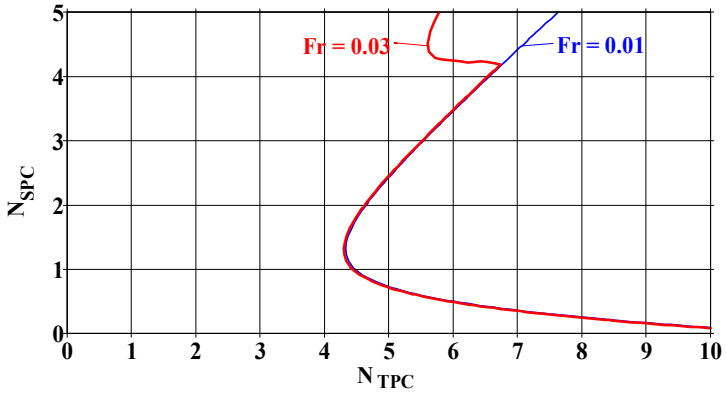

FIG. 9.123. Effect of the Froude number on the stability margin in the case with K_{in}=20 and K_{out}=2 ($\Lambda = 7, C_{\max} = 0.9, N_{nodes} = 48$).

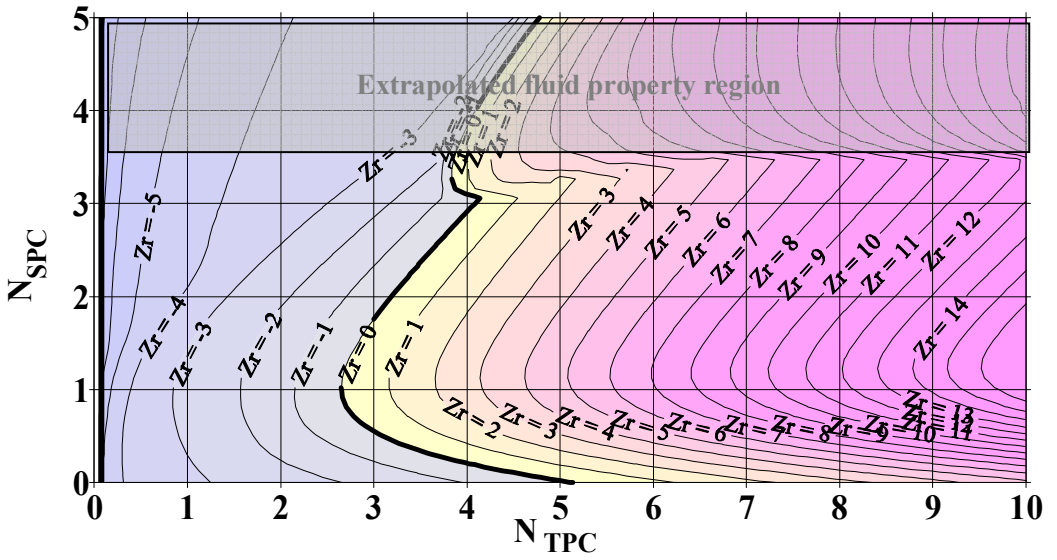

a) stability map

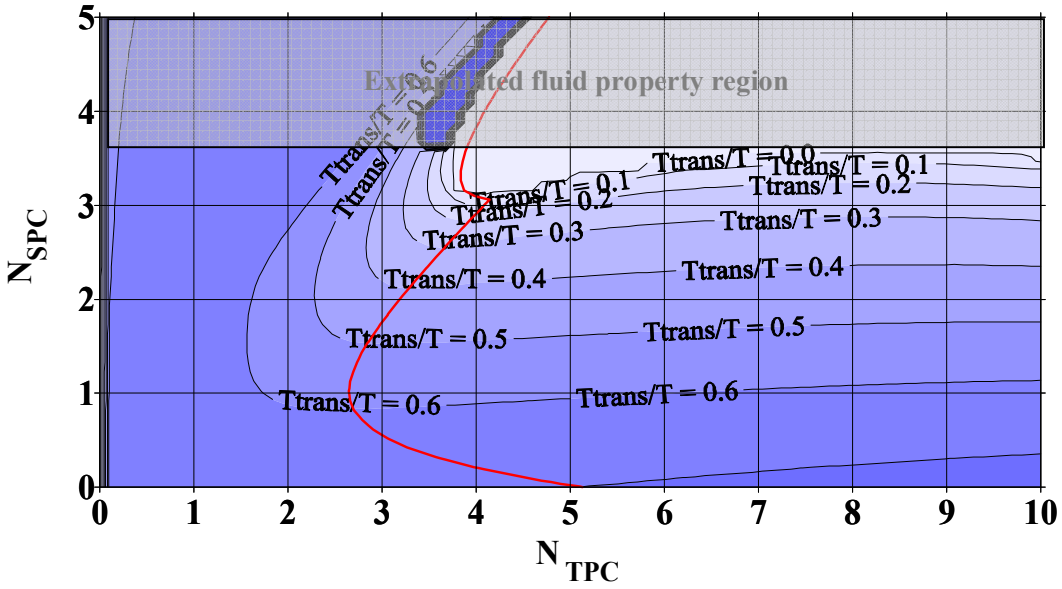

b) contour plot of T_{trans}/T

FIG. 9.124. Additional stability map and contour plot of T_{trans}/T for the case of horizontal channel with K_{in}=K_{out}=20 ($\Lambda = 7, Fr = 0.01, C_{\max} = 0.9, N_{nodes} = 48$).

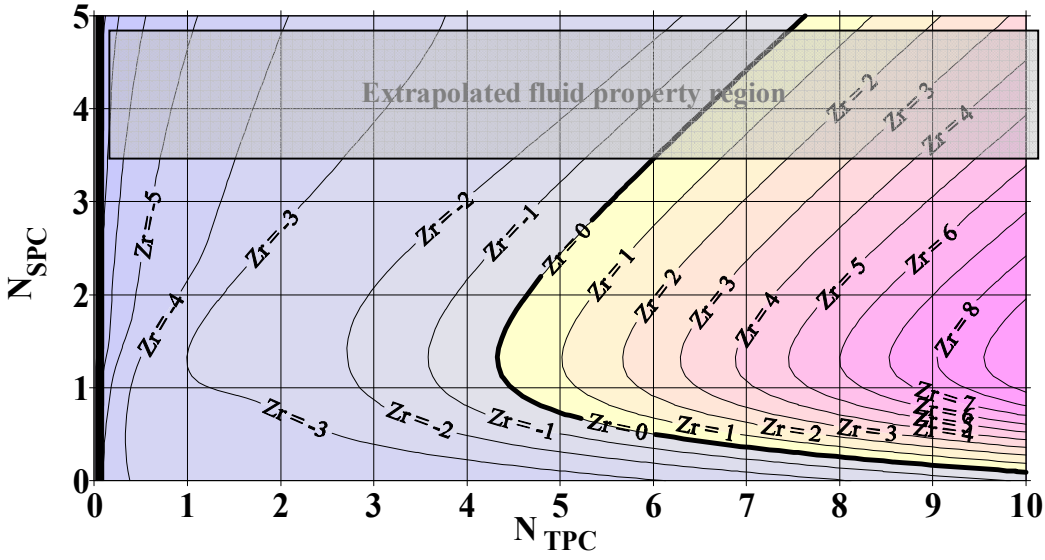

a) stability map

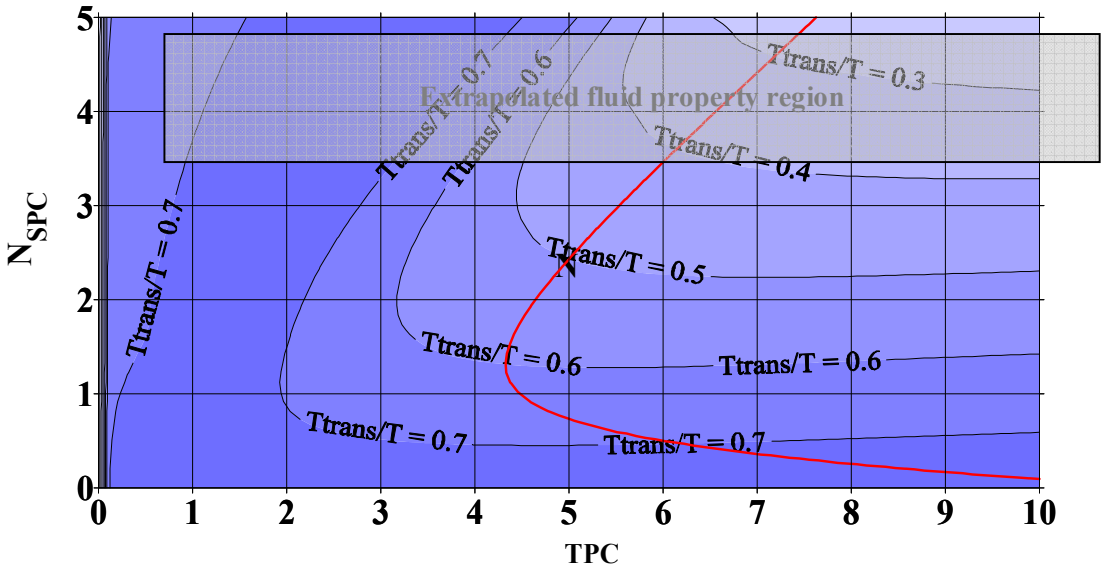

b) contour plot of T_{trans}/T

FIG. 9.125. Additional stability map and contour plot of T_{trans}/T for the case of horizontal channel with K_{in}=20 and K_{out}=2 ($\Lambda = 7, Fr = 0.01, C_{\max} = 0.9, N_{nodes} = 48$).

As a general consideration on the above described stability maps, it can be recognized that the Ledinegg and the density-wave instability regions, though they are characterized by different dynamic behaviour ('excursive', the former, and 'oscillating', the latter), are anyway neighbouring and form somehow a continuum. In particular, it can be noted that the period of oscillations increases with pseudo-subcooling from values in the order of twice the transit time to longer and longer durations, becoming infinite for Ledinegg-type behaviour. Correspondingly, the calculations show that the two complex conjugated eigenvalues characterising instabilities in the density wave region progressively decrease their imaginary part with increasing pseudo-subcooling being transformed into two real roots.

Further interesting considerations on the reported data are related to:

- the presence of a region of extrapolated properties; in fact, requesting a pseudo-subcooling as large as 4 or 5, is unrealistic for all the considered fluids: this was highlighted in the dimensionless stability maps;
- the effect of truncation error; numerical diffusion affects the presented results; in fact, as shown in Fig. 9.126, reporting the stability boundaries for the cases with K_{out}=2, 5, 10 and 20, the curves obtained with 96 nodes are slightly different with respect to those obtained with 48 nodes; a more quantitative impression of the degree of convergence reached with different numbers of nodes is obtained observing Fig. 9.127.

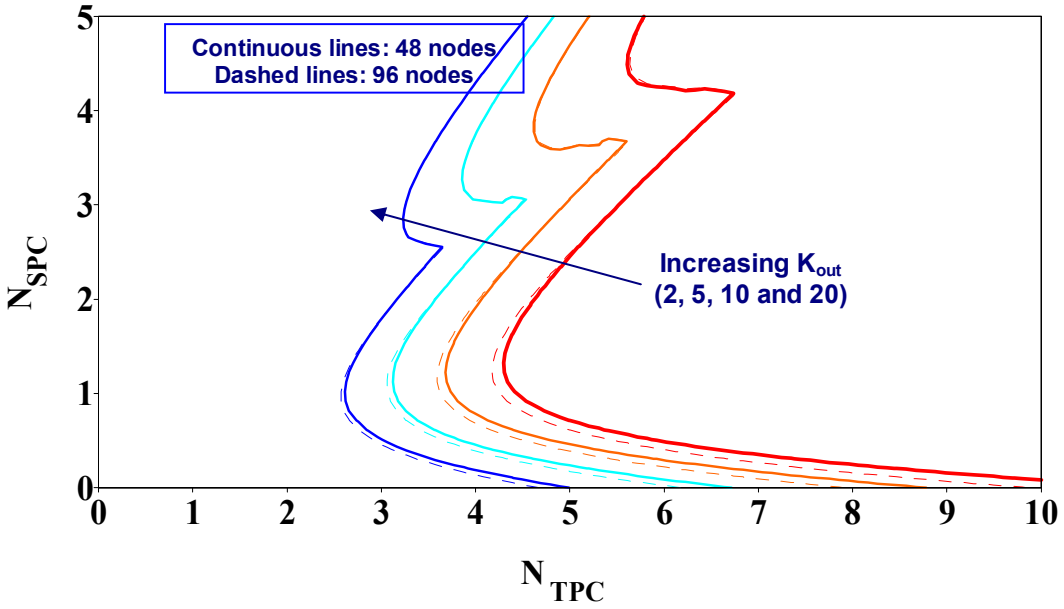

FIG. 9.126. Stability boundaries for the case of vertical channel with K_{in}=20 and K_{out}=2, 5, 10 and 20 ($\Lambda = 7, Fr = 0.03, C_{max} = 0.9$) at two different values of the number of axial nodes.

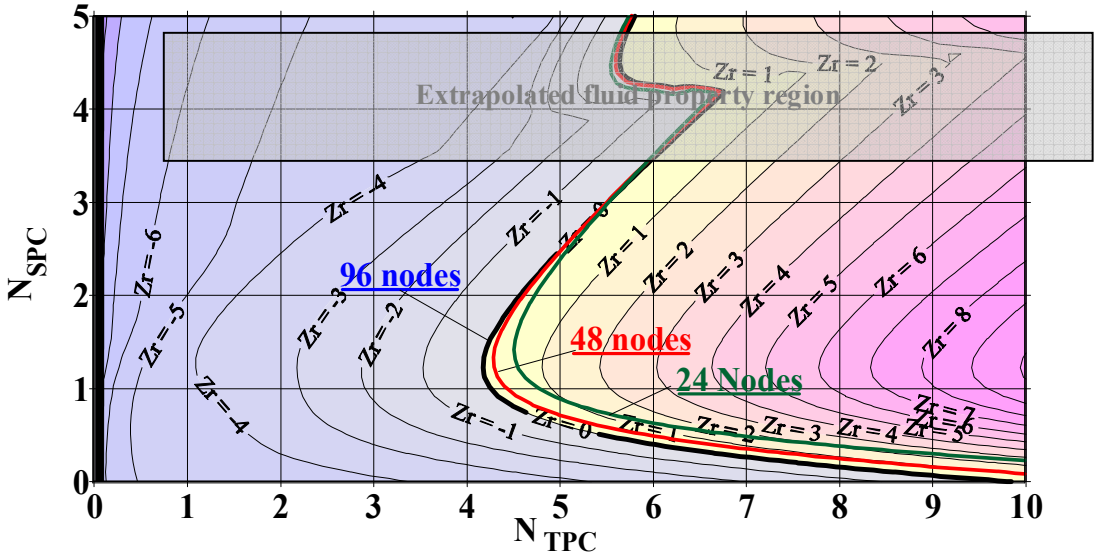

FIG. 9.127. Sensitivity to channel nodalization in the case of vertical channel with K_{in}=20 and K_{out}=2 ($\Lambda = 7, Fr = 0.03, C_{max} = 0.9$).

The RELAP5/MOD3.3 code was adopted for addressing the first part of the exercise related to the vertical channel containing water with different outlet throttling degrees. An overall pressure drop around 0.12 MPa across the channel was adopted in these calculations irrespective of the particular inlet enthalpy conditions resulting in different values of the Froude number. The value of N_{TPC} at the stability threshold was evaluated by graphical means highlighting the value of this parameter close to the onset of instability, as shown in the trends on N_{TPC} vs. time reported in the Appendix of [9-46]. Similarly, the evaluation of the period of oscillations was obtained by looking in detail at the oscillating trends and evaluating their period for small enough amplitude to assume that the system is behaving in a linear fashion.

Figure 9.128 reports a comparison of the stability boundaries calculated by the linear stability program for the cases addressed for water in the vertical channel at different outlet throttling with the threshold values of N_{TCP} calculated by RELAP5 for the proposed calculation cases. Table 9.16 reports the related numerical results and the observed character of the oscillations. The curves obtained with both 48 nodes and 96 nodes are reported for purpose of showing the possible effect of numerical diffusion; the curves were obtained with reference to a Froude number equal to 0.03. The good match observed between the data of the two completely independent models testifies for the substantial correctness of the assumptions adopted in both cases.

Figures 9.129a and 9.129b report two sample trends of N_{TCP} as a function of time as obtained by post-processing the results of the code calculations. It can be noted that the value of N_{TCP} estimated for the excursive instability case (N_{SCP}=3.0, K_{out}=20) is quite difficult to determine in the plots of the transient behaviour (see e.g. Fig. 9.129b) and its definition involves therefore some degree of arbitrariness. Nevertheless, the existence of the excursive behaviour at the considered pseudo-subcooling is confirmed.

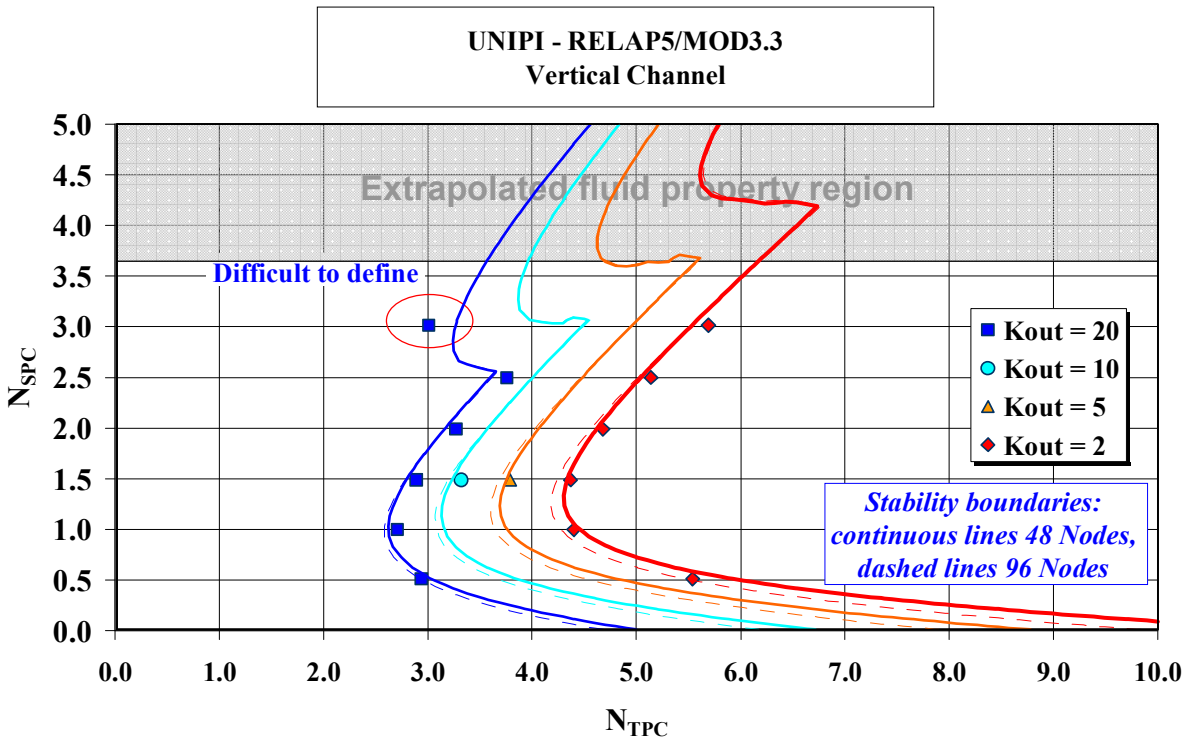

FIG. 9.128. Comparison of RELAP5/MOD3.3 data for vertical channel and water with the stability boundaries obtained with $\Lambda = 7, Fr = 0.03, C_{max} = 0.9$.

TABLE 9.16. NUMERICAL RESULTS FOR THE THRESHOLD VALUES OF N_{TPC} OBTAINED BY RELAP5/MOD3.3 FOR VERTICAL CHANNEL AND WATER AT DIFFERENT OUTLET THROTTLING

UNIPI – RELAP5/MOD 3.3			Kout=20	Kout=20	Kout=10	Kout=10	Kout=5	Kout=5	Kout=2	Kout=2
Case	Channel orientation	Nspc	Ntpc. threshold	Type of instability	Ntpc. threshold	Type of instability	Ntpc. threshold	Type of instability	Ntpc. threshold	Type of instability
Label				Oscillatory or Excursive		Oscillatory or Excursive		Oscillatory or Excursive		Oscillatory or Excursive
D0.5V-K20 to K2	Vertical	0.51	2.94	Oscillatory					5.54	Oscillatory
D1.0V-K20 to K2	Vertical	1.00	2.71	Oscillatory					4.4	Oscillatory
D1.5V-K20 to K2	Vertical	1.49	2.89	Oscillatory	3.32	Oscillatory	3.79	Oscillatory	4.37	Oscillatory
D2.0V-K20 to K2	Vertical	1.99	3.27	Oscillatory					4.68	Oscillatory
D2.5V-K20 to K2	Vertical	2.50	3.76	Oscillatory					5.14	Oscillatory
D3.0V-K20 to K2	Vertical	3.01	3.01	Excursive					5.69	Oscillatory

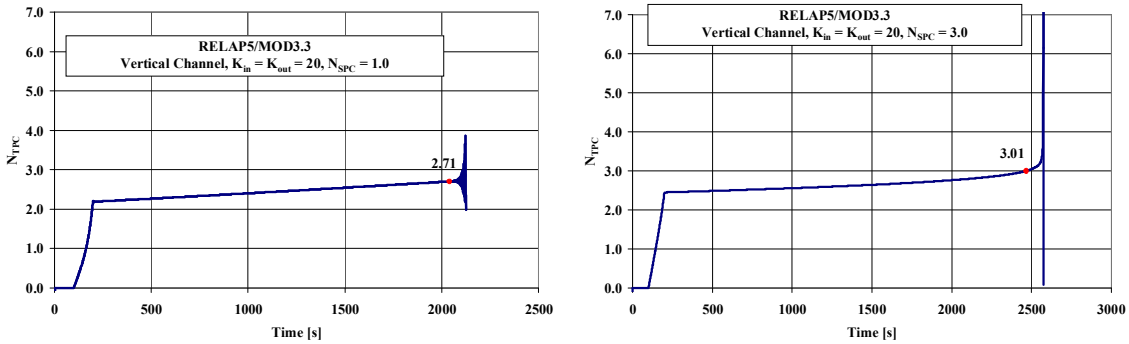

a) sample oscillatory case *b) sample excursive case*

FIG. 9.129. Sample trends of N_{TPC} as a function of time as calculated by RELAP5.

Table 9.17 reports the values of the ratio of the transit time to the period of oscillations as evaluated by RELAP5. This information can be compared to the one presented in Figs 9.130 and 9.131 obtained by the linear stability program. It can be noted that:

- the match is not perfect, probably due to the variability of the Froude number in the RELAP5 calculations that, as already noted, affects mainly the period of oscillations and the location of the Ledinegg instability region;
- despite of this imperfect match, the general qualitative trend of the ratio T_{trans}/T is confirmed: in particular, the ratio decreases with increasing pseudo-subcooling towards the Ledinegg instability region and its values are included in the range (0, 0.7).

TABLE 9.17. NUMERICAL RESULTS FOR THE VALUES OF T_{TRANS}/T AT THE THRESHOLD OF INSTABILITY OBTAINED BY RELAP5/MOD3.3 FOR VERTICAL CHANNEL AND WATER AT DIFFERENT OUTLET THROTTLING

UNIPI – RELAP5/MOD 3.3			Kout=20	Kout=10	Kout=5	Kout=2
Case Label	Channel orientation	Nspc	Ratio of Transit Time to the Period of Oscillations	Ratio of Transit Time to the Period of Oscillations	Ratio of Transit Time to the Period of Oscillations	Ratio of Transit Time to the Period of Oscillations
D0.5V-K20 to K2	Vertical	0.51	0.63			0.71
D1.0V-K20 to K2	Vertical	1.00	0.53			0.60
D1.5V-K20 to K2	Vertical	1.49	0.47	0.48	0.51	0.52
D2.0V-K20 to K2	Vertical	1.99	0.35			0.46
D2.5V-K20 to K2	Vertical	2.50	0.22			0.40
D3.0V-K20 to K2	Vertical	3.01	0.00			0.34

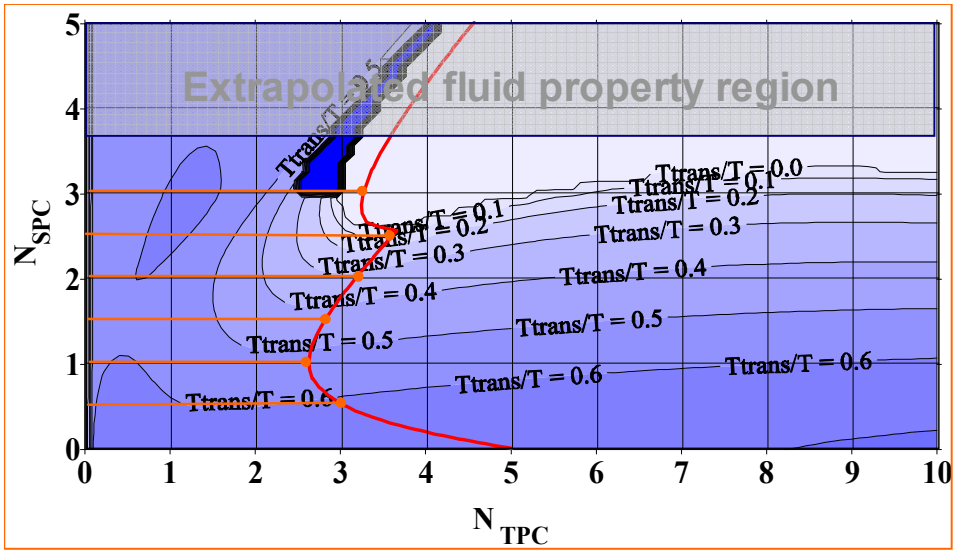

FIG. 9.130. Contour plot of T_{trans}/T for the case of the vertical channel and $K_{in} = K_{out} = 20, \Lambda = 7, Fr = 0.03, C_{\max} = 0.9$ with indication of the selected operating points.

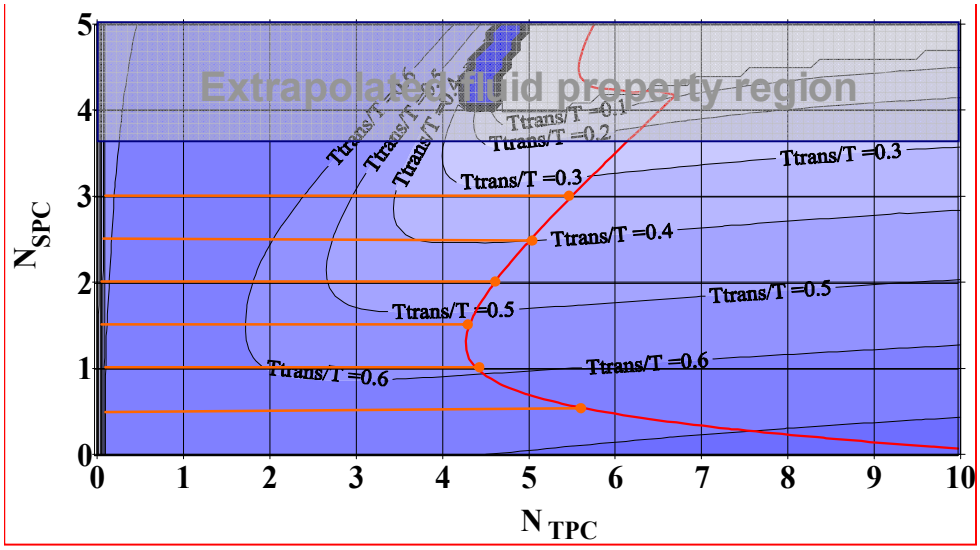

FIG. 9.131. Contour plot of T_{trans}/T for the case of the vertical channel and $K_{in} = 20, K_{out} = 2, \Lambda = 7, Fr = 0.03, C_{\max} = 0.9$ with indication of the selected operating points.

Figures 9.132 and 9.133 compare the results obtained by the TRANSDIM program in relation to the cases proposed for fluid-to-fluid comparison with stability boundaries obtained by the linear stability program. Table 9.18 reports the corresponding numerical values.

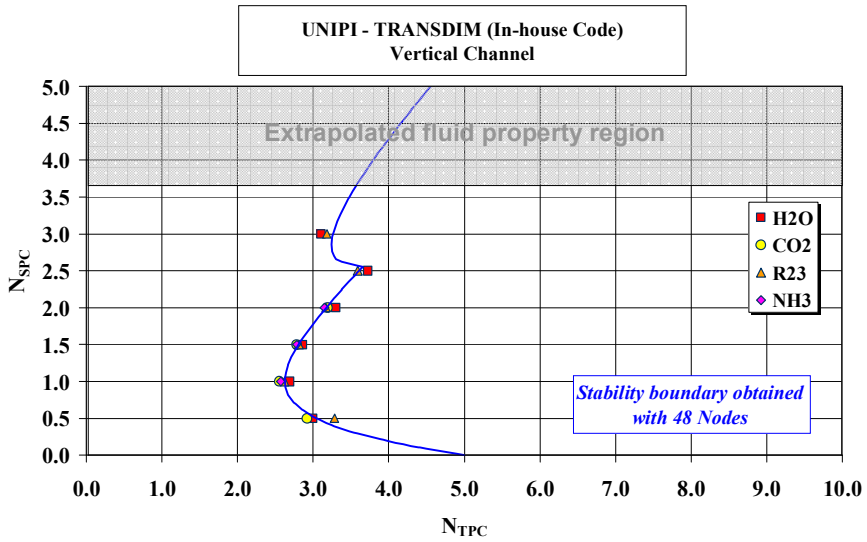

FIG. 9.132. Comparison of TRANSDIM data for vertical channel and the fluid-to-fluid comparison with the stability boundaries obtained with $\Lambda = 7, Fr = 0.03, C_{\max} = 0.9$.

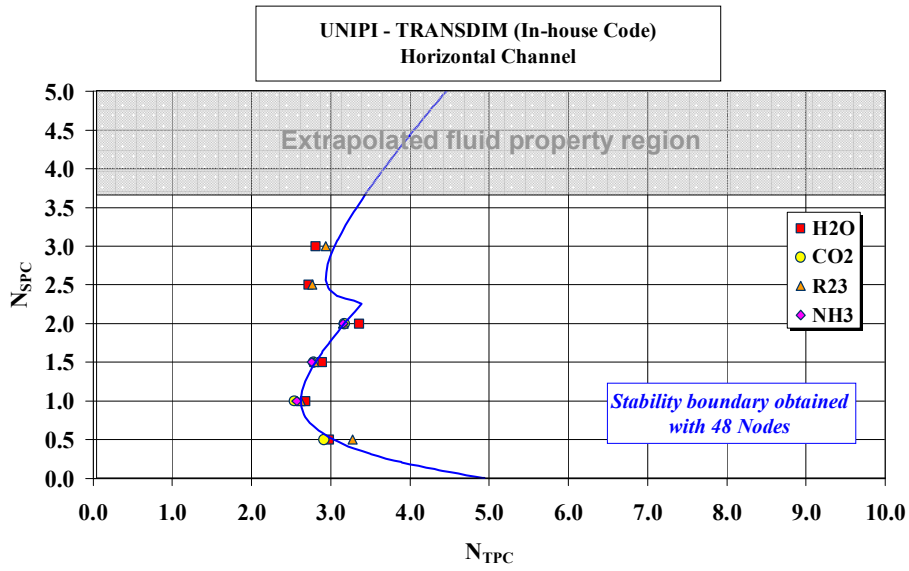

FIG. 9.133. Comparison of TRANSDIM data for horizontal channel and the fluid-to-fluid comparison with the stability boundaries obtained with $\Lambda = 7, Fr = 0.03, C_{\max} = 0.9$.

TABLE 9.18. NUMERICAL RESULTS FOR THE THRESHOLD VALUES OF N_{TPC} OBTAINED BY TRANSDIM FOR THE FLUID-TO-FLUID COMPARISON

UNIPI – Transdim (in-house code)			Water	Water	CO2	CO2	R23	R23	NH3	NH3
Case	Channel orientation	Nspc	Ntpc. threshold	Type of instability	Ntpc, threshold	Type of instability	Ntpc, threshold	Type of instability	Ntpc, threshold	Type of instability
Label				Oscillatory or Excursive		Oscillatory or Excursive		Oscillatory or Excursive		Oscillatory or Excursive
F0.5V	Vertical	0.5	2.99	Oscillatory	2.92	Oscillatory	3.28	Oscillatory		
F1.0V	Vertical	1	2.69	Oscillatory	2.55	Oscillatory	2.62	Oscillatory	2.57	Oscillatory
F1.5V	Vertical	1.5	2.86	Oscillatory	2.78	Oscillatory	2.81	Oscillatory	2.78	Oscillatory
F2.0V	Vertical	2	3.3	Oscillatory	3.19	Oscillatory	3.17	Oscillatory	3.15	Oscillatory
F2.5V	Vertical	2.5	3.72	Oscillatory			3.59	Oscillatory		
F3.0V	Vertical	3	3.1	Excursive			3.18	Excursive		
F0.5H	Horizontal	0.5	2.98	Oscillatory	2.91	Oscillatory	3.28	Oscillatory		
F1.0H	Horizontal	1	2.68	Oscillator	2.54	Oscillatory	2.62	Oscillatory	2.57	Oscillatory
F1.5H	Horizontal	1.5	2.89	Oscillatory	2.78	Oscillatory	2.79	Oscillatory	2.76	Oscillatory
F2.0H	Horizontal	2	3.36	Oscillator	3.17	Oscillatory	3.16	Oscillatory	3.16	Oscillatory
F2.5H	Horizontal	2.5	2.72	Excursive			2.77	Excursive		
F3.0H	Horizontal	3	2.81	Excursive			2.94	Excursive		

As it can be noted, there is a good match between the trends of the stability thresholds observed for different fluids and the curve proposed by the linearized program operating in the dimensionless space. In particular:

- as it follows from the character of reasonable universality observed at different supercritical pressures for different fluids in the equation of state $\rho^*\left(h^*\right)$, the results obtained by TRANSDIM are crowded along the linear stability boundary lines for all the fluids;
- the oscillatory or excursive behaviour of the system observed by the transient code is completely coherent with what predicted by the linear stability analysis;
- in particular, the differences obtained between the horizontal and the vertical channel cases mainly concern the high pseudo-subcooling cases, where excursive or oscillatory behaviour can be observed.

On the other hand, comparing the values of the ratio of the fluid transit time to the period of oscillations reported in Table 9.19 with the contour plots reported in Figs 9.134 and 9.135, in similarity with what observed for the water cases, a general agreement is noted, with some quantitative deviation. This confirms the sensitivity of the period of oscillations to the exact location of the Ledinegg instability region that, as shown in the contour plots, largely determines the distribution of T_{trans}/T. It is anyway necessary to recognize that the values of this ratio reported in the table may be affected by some inaccuracy due to the difficulty involved in evaluating the period of oscillations at their onset by visual inspection of the observed oscillating trends.

Figures 9.136, 9.137 and 9.138 report the values of the ratio between the fluid transit time to the period of oscillations as obtained by the transient programs, RELAP5 and TRANSDIM, for the different considered cases. The effect of throttling for the vertical channel and the substantial agreement between the values predicted for the different fluids, showing just little differences, also as a consequence of the slightly

different values of the Froude number, can be noted.

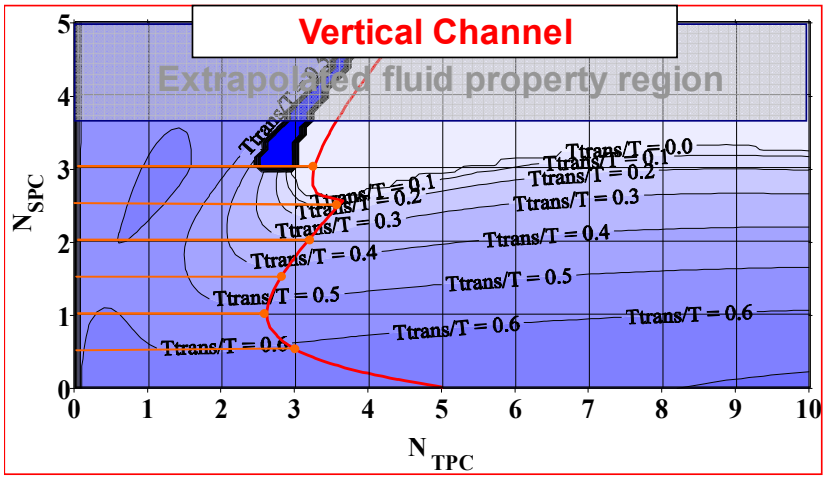

FIG. 9.134. Contour plot of T_{trans}/T for the case of the vertical channel and $K_{in} = K_{out} = 20, \Lambda = 7, Fr = 0.03, C_{\max} = 0.9$ with indication of the selected operating points.

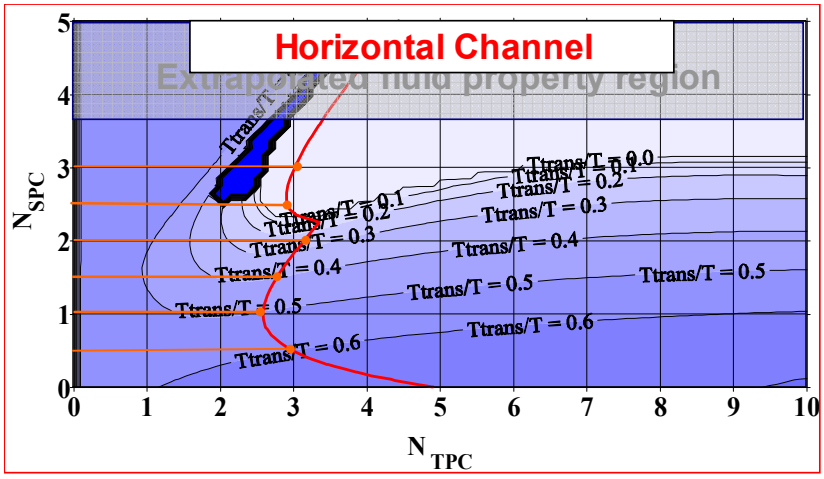

FIG. 9.135. Contour plot of T_{trans}/T for the case of the horizontal channel and $K_{in} = K_{out} = 20, \Lambda = 7, Fr = 10^5, C_{\max} = 0.9$ with indication of the selected operating points.

TABLE 9.19. NUMERICAL RESULTS FOR THE VALUES OF T_{TRANS}/T OBTAINED BY TRANSDIM

UNIPI – Transdim (in-house code)			Water	CO2	R23	NH3
Case Label	Channel orientation	Nspc	Ratio of Transit Time to the Period of Oscillations	Ratio of Transit Time to the Period of Oscillations	Ratio of Transit Time to the Period of Oscillations	Ratio of Transit Time to the Period of Oscillations
F0.5V	Vertical	0.5	0.61	0.64	0.68	
F1.0V	Vertical	1	0.52	0.53	0.56	0.53
F1.5V	Vertical	1.5	0.48	0.44	0.48	0.43
F2.0V	Vertical	2	0.35	0.34	0.40	0.32
F2.5V	Vertical	2.5	0.21		0.31	
F3.0V	Vertical	3	0.00		0.00	
F0.5H	Horizontal	0.5	0.61	0.63	0.68	
F1.0H	Horizontal	1	0.51	0.52	0.55	0.53
F1.5H	Horizontal	1.5	0.40	0.41	0.45	0.42
F2.0H	Horizontal	2	0.28	0.30	0.35	0.38
F2.5H	Horizontal	2.5	0.00		0.00	
F3.0H	Horizontal	3	0.00		0.00	

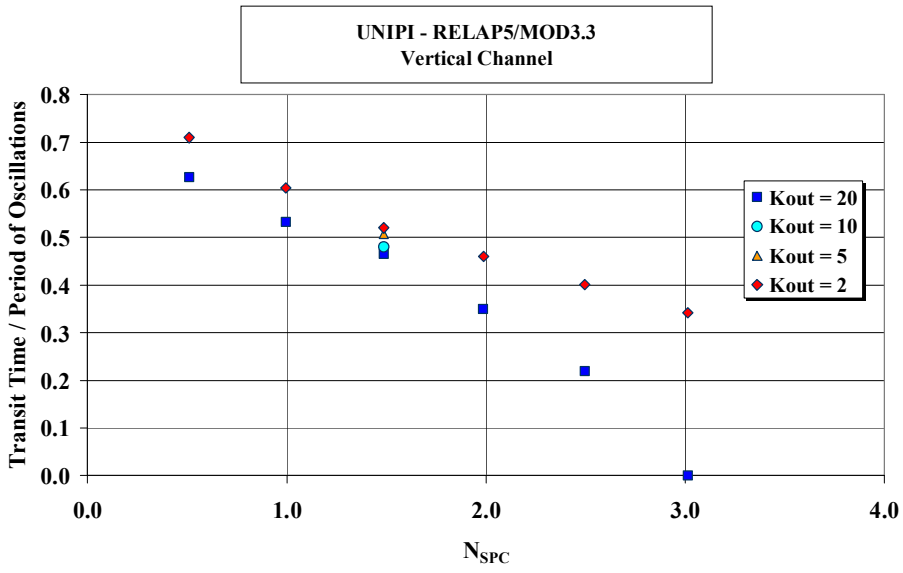

FIG. 9.136. Values of T_{trans}/T for the case of the vertical channel obtained by RELAP5 at different inlet throttling.

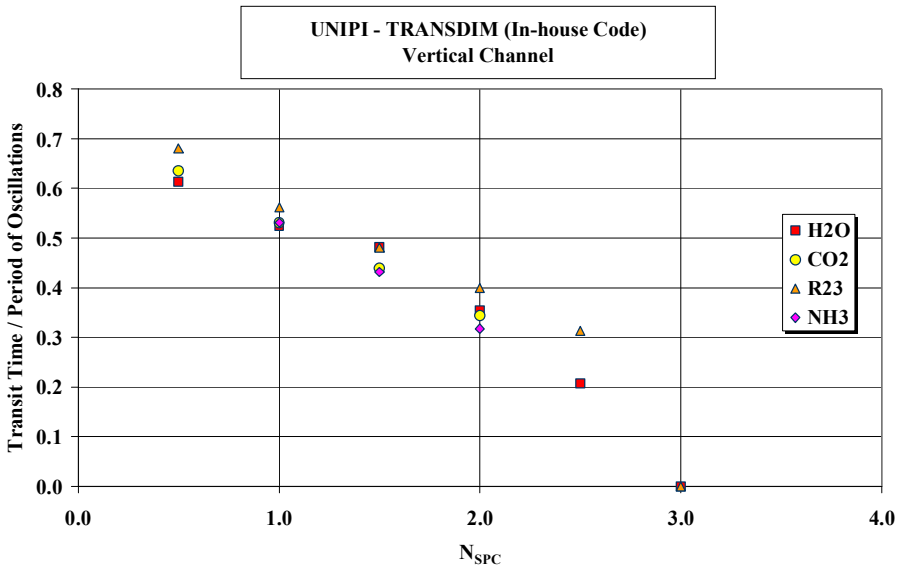

FIG. 9.137. Values of T_{trans}/T for the case of the vertical channel obtained by TRANSDIM for different fluids.

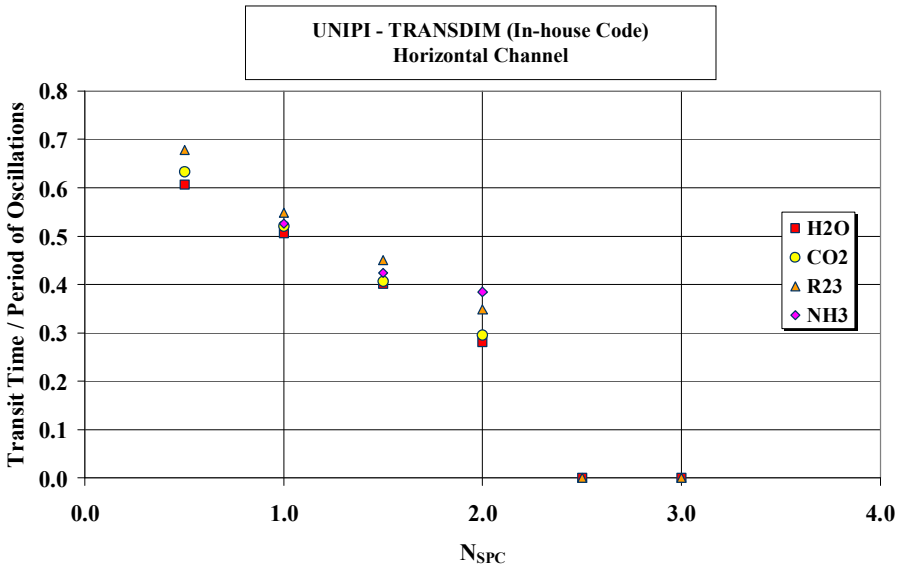

FIG. 9.138. Values of T_{trans}/T for the case of the horizontal channel obtained by TRANSDIM for different fluids.

9.2.4. Received submissions

9.2.4.1. First submission by VTT

In a first submission [9-49], VTT made use of the transient two-phase flow APROS code, adopting a nodal staggered mesh technique for solving the governing equations. A channel with 40 nodes was used for simulating the problem and the heated structure was made very thin, as suggested in the specifications, in order to avoid any undue inertia due to energy storage in the walls. The case of supercritical fluids is

treated making the void fraction to change from 0 to 1 across the pseudo-critical temperature. Specific correlations for heat transfer are adopted.

Only water data at 25 MPa for the vertical channel were considered. Figure 9.139 compares the results obtained by VTT with the reference stability boundaries, while Table 9.20 reports the numerical values of the stability thresholds; two cases at low pseudo-subcooling were not calculated.

As it can be noted, a greater stability is observed in all conditions with respect to the reference data. The greater stability is possibly the cause for the impossibility to evaluate the two conditions at low pseudo-subcooling with $K_{out} = 2$; in fact, at such large values of N_{TPC}, the physical temperature of the outlet fluid is rather high.

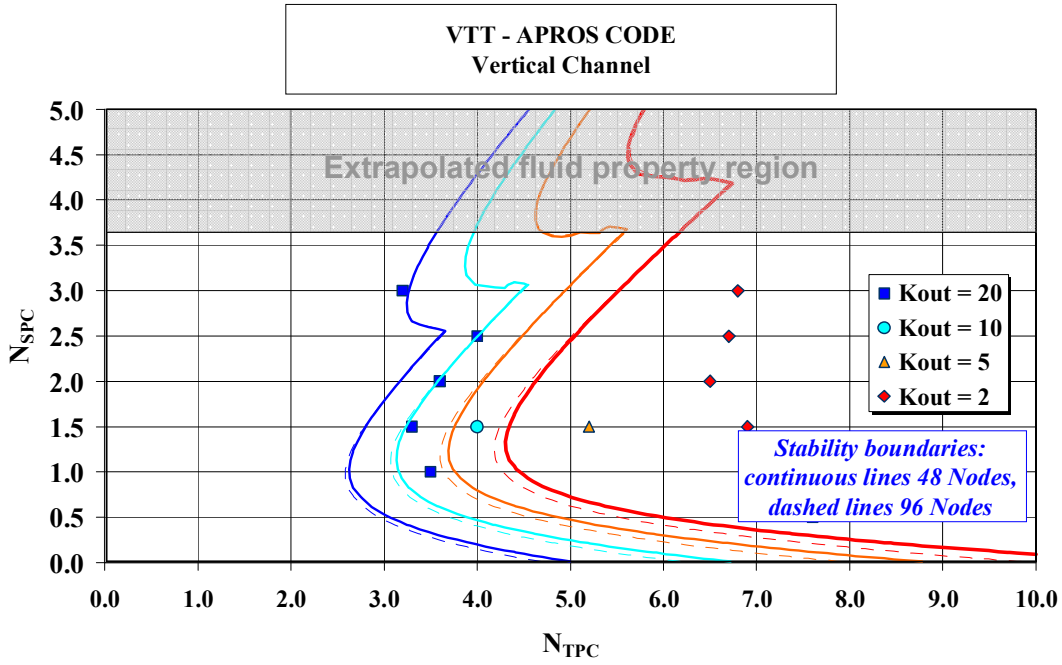

FIG 9.139. Comparison of the results obtained by VTT against the reference stability boundaries for water in the vertical channel with the friction correlation by Kirillov.

TABLE 9.20. RESULTS OBTAINED BY VTT FOR THE INSTABILITY THRESHOLD

VTT APROS			Kout=20	Kout=20	Kout=10	Kout=10	Kout=5	Kout=5	Kout=2	Kout=2
Case	Channel orientation	Nspc	Ntpc. threshold	Type of instability	Ntpc. threshold	Type of instability	Ntpc. threshold	Type of instability	Ntpc. threshold	Type of instability
Label				Oscillatory or Excursive		Oscillatory or Excursive		Oscillatory or Excursive		Oscillatory or Excursive
D0.5V-K20 to K2	Vertical	0.5	7.6	Oscillatory						Not obtained
D1.0V-K20 to K2	Vertical	1	3.5	Oscillatory						Not obtained
D1.5V-K20 to K2	Vertical	1.5	3.3	Oscillatory	4	Oscillatory	5.2	Oscillatory	6.9	Oscillatory
D2.0V-K20 to K2	Vertical	2	3.6	Oscillatory					6.5	Oscillatory
D2.5V-K20 to K2	Vertical	2.5	4	Oscillatory					6.7	Oscillatory
D3.0V-K20 to K2	Vertical	3	3.2	Excursive					6.8	Oscillatory

9.2.4.2. Comments by VTT on the first submission

The results calculated with the VTT APROS program show in general too large stability compared to the reference results. The form of the instability threshold shown as N_{TCP} - N_{SPC} plots preserve the same form as the reference curves, especially when K_{out} is 20. However, with small K_{out} values the instability was obtained with very high N_{TCP} or was not reached at all.

In the standard APROS code, the wall friction was calculated with the Kirillov wall friction correlation:

$$f_{kir} = \left(1.82 \log_{10} \mathrm{Re}_b - 1.64\right)^{-2} \left(\frac{\rho_w}{\rho_b}\right)^{0.4} \tag{9-31}$$

This correlation is intended also for the supercritical pressure region, since it takes into account the fast density change near the heated wall. However, it does not take into account the roughness of the wall, which was defined to be 2.5×10^{-5} in this exercise. The other aspect which may affect the results of APROS is that the water properties in the program were accurate up to 800 ºC. Above that temperature the material property values are extrapolated. Especially in case of small K_{out}, the temperature at the outlet was much above 800 ºC.

9.2.4.3. Additional submissions by VTT

The intention of the additional calculations was to clarify how much the wall friction affects the threshold of instability. The vertical channel water cases were recalculated using various wall friction correlations; the cases were calculated, in addition to the Kirillov correlation, also with the Filonenko and the Colebrook correlations; their form is as follows:

- Kirilllov

$$f_{kir} = \left(1.82 \log_{10} \mathrm{Re}_b - 1.64\right)^{-2} \left(\frac{\rho_w}{\rho_b}\right)^{0.4} \tag{9-32}$$

- Filonenko

$$f_{kir} = \left(1.82 \log_{10} \mathrm{Re}_b - 1.64\right)^{-2} \tag{9-33}$$

- Colebrook

$$\frac{1}{\sqrt{f_{col}}} = 1.74 - 2\log\left(\frac{1}{\sqrt{f_{col}}}\frac{18.7}{\mathrm{Re}} + \frac{2\varepsilon}{D_h}\right) \tag{9-34}$$

The case with K_{out} = 20 was calculated with N_{SPC} = 3.0, 2.5, 2.0, 1.5, 1.0 and 0.5. In addition, the case where N_{SPC} was 1.5 was calculated with K_{out} = 20, 10, 5 and 2. Figures 9.140, 9.141 and 9.142 summarize the obtained results.

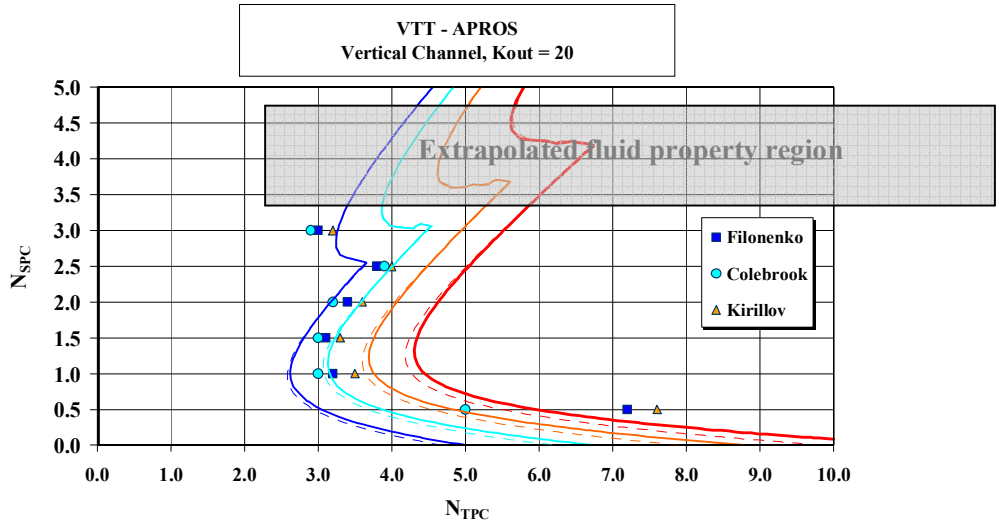

FIG. 9.140. Results of the sensitivity analysis performed by VTT with different correlations for friction for the cases with K_{out} = 20.

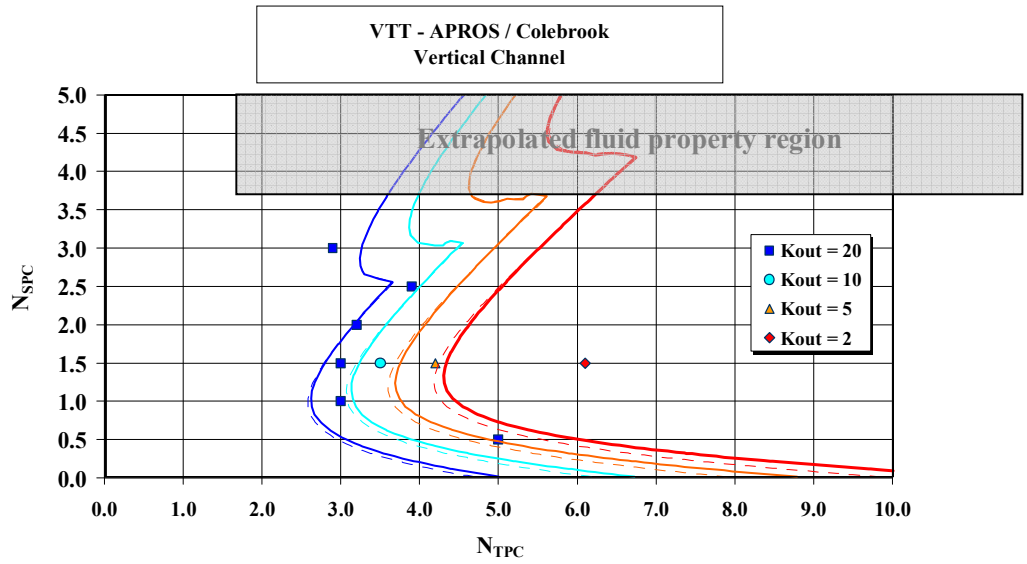

FIG. 9.141. Results of the sensitivity analysis performed by VTT with the Colebrook friction correlation for cases with different outlet throttling.

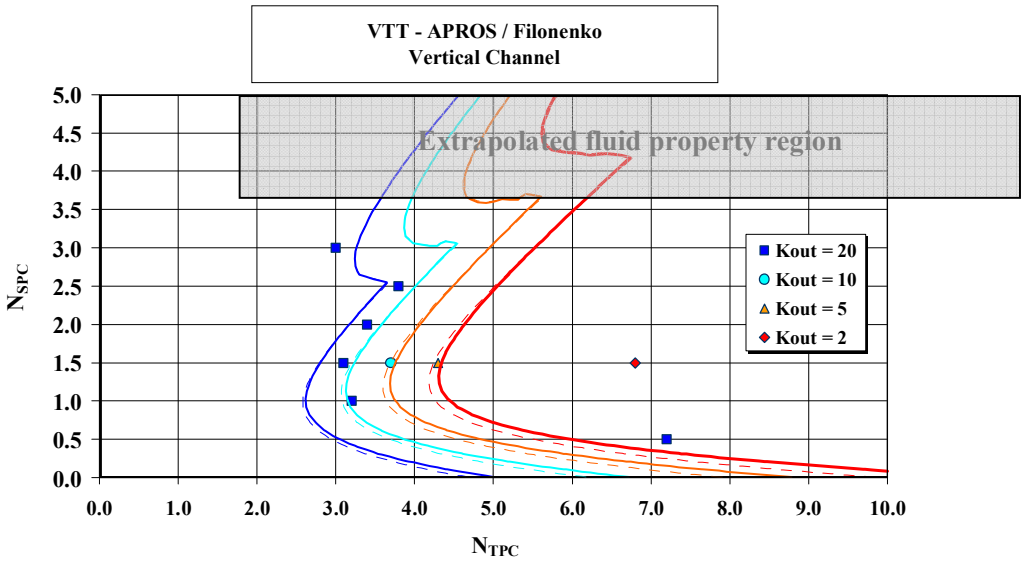

FIG. 9.142. Results of the sensitivity analysis performed by VTT with the Filonenko friction correlation for cases with different outlet throttling.

The results obtained with the Filonenko correlation are clearly closer to the reference values than those with the Kirillov correlation. The instability threshold values obtained with the Colebrook correlation were quite close to the reference values. However, the Colebrook result with K_{out} = 2 was still far from the reference value.

As shown in Fig. 9.143, the friction factor distributions along the pipe in case K_{out} = 5 and N_{SPC} = 1.5 indicate that the Filonenko and Kirillov correlations give quite similar distributions at the onset of instability. In the case of the Filonenko correlation, the instability starts when N_{TPC} was 4.3 and in the case of the Kirillov correlation the instability starts when N_{TPC} was 5.2. The friction factor distribution with the Colebrook correlation is larger compared to the Filonenko or Kirillov cases. The instability in the Colebrook case started when N_{TPC} was 4.2.

The correlations of Filonenko and Kirillov differ from each other only because of the term $(\rho_w/\rho_b)^{0.4}$, which is missing in the Filonenko correlation. This term has a minimum value near the pseudocritical point; thus, it affects the location of the minimum in the friction factor itself. When N_{TPC} increases, the minimum position of the friction factor in the Kirillov case approaches the pipe inlet. This can be seen in Fig. 9.144, where the friction factor distributions with the Kirillov correlation as a function of N_{TPC} are shown. The same minimum position with the Kirillov correlation as in the Filonenko case is achieved at larger N_{TPC} values and this happens when the flow in both cases turns unstable.

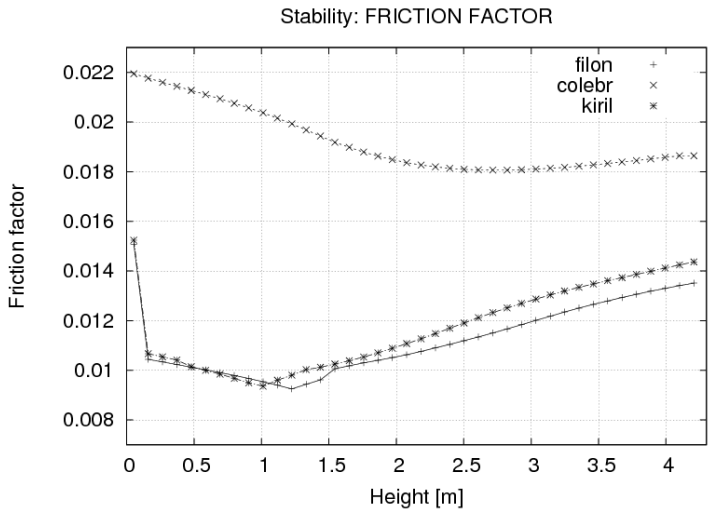

FIG. 9.143. Friction factor distributions along the pipe at start of instability calculated with various wall friction correlations (N_{SPC} = 1.5, K_{out} =5, N_{TPC}: Kirillov = 5.2, Filonenko = 4.3, Colebrook = 4.2).

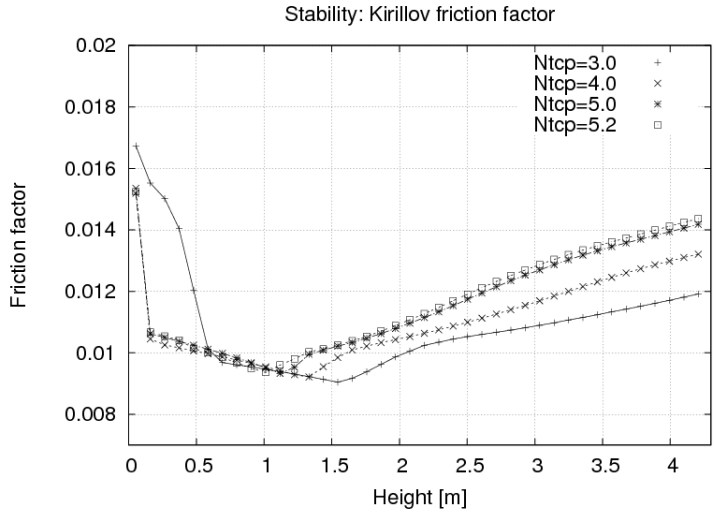

FIG. 9.144. Kirillov friction factor distributions at with different N_{TPC}, for K_{out} = 5 and N_{SPC}=1.5.

9.2.4.4. Submission by the University of Manitoba and AECL

The University of Manitoba and AECL investigators [9-43] report finding the instability boundary flow rate to be close to the flow rate corresponding to $\frac{\partial^2 \Delta p}{\partial \dot{m}^2} = 0$, where Δp is the steady-state channel frictional pressure drop and $\dot{m}$ is the flow-rate. Assuming this as a hypothesis, they developed a simple criterion for the instability boundary which they state will correlate all the instability boundary data, irrespective of fluid, system pressure, K factors, inlet temperature, power, channel length or diameter. This criterion naturally defines non-dimensional parameters that they feel may aptly describe the instability boundary in supercritical oscillatory flow. Their parameters, however, would not be valid for static instabilities, or when gravity effects dominate the K factor effect.

In the application, both water at three different pressures (24 cases) and CO_2 (12 cases) were considered. Figures 9.145 and 9.146 summarize the data obtained in the exercise. The compact form of the adopted stability criterion represents a very interesting feature of the application.

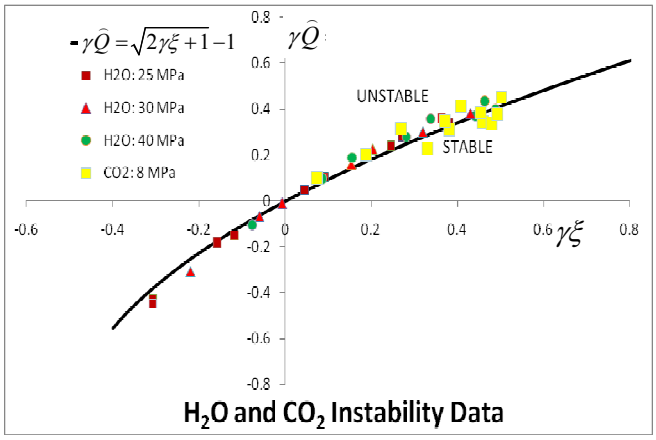

FIG. 9.145. Comparison of the results obtained by the University of Manitoba and AECL by the stability analysis with those of the simplified criterion.

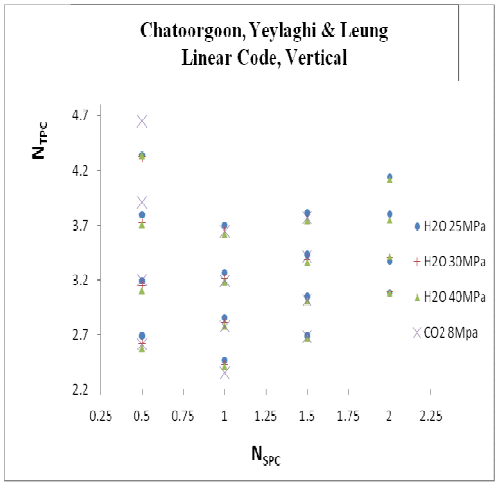

FIG. 9.146. Results obtained by the University of Manitoba and AECL expressed in the suggested dimensionless formalism.

In Fig. 9.147 the obtained results are compared with the reference stability boundaries, showing some differences. An interesting feature shown in the plot, that was implied in writing the specifications, is that the results weakly depend on water pressure and just a bit more on the specific fluid.

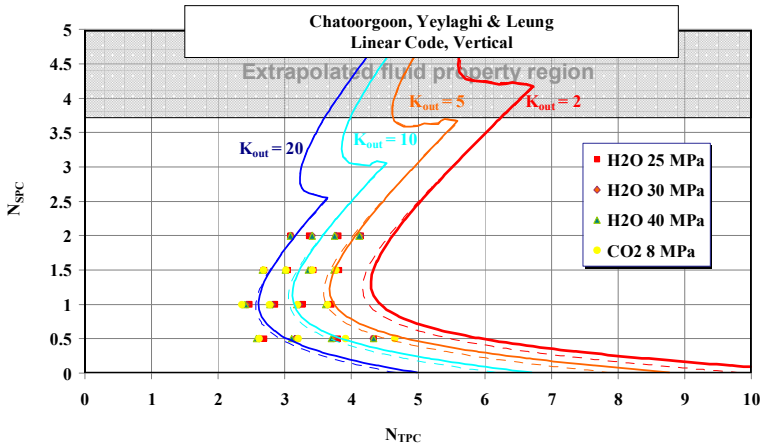

FIG. 9.147. Comparison of the results by the University of Manitoba and AECL in the suggested stability map.

9.2.4.5. Comments by V. Chatoorgoon on the University of Manitoba and AECL submission

Chatoorgoon proposed non-dimensional parameters based on certain (numerically) observed effects and although these parameters were still in an unfolding state at the time of writing. Non-dimensional parameters were developed for both oscillatory and static instabilities. The non-dimensional parameters developed for the oscillatory instability mode in supercritical flow were formulated from the observed effect that the instability boundary flow rate lay very close to the flow rate corresponding to $\frac{\partial^2 \Delta p}{\partial \dot{m}^2} = 0$ where Δp is the channel steady-state frictional pressure drop. This yielded the following non-dimensional parameters for oscillatory instability (obtained at the time of this study): $\hat{Q}$, γ and ξ, where

$$\hat{Q} = \frac{\dot{Q}\theta}{\dot{m}} \tag{9-35}$$

$$\gamma = -\left(1 + \frac{1}{\theta^2}\frac{\partial \theta}{\partial h_e}\right) \tag{9-36}$$

$$\theta = -\frac{1}{\rho_e}\left(\frac{\partial \rho_e}{\partial h_e}\right)_p \tag{9-37}$$

$$\xi = \left(1 - \frac{\rho_e}{\rho_i}\right) + \frac{\rho_e A^2}{2}\left(\frac{\partial^2 p_e}{\partial \dot{m}^2}\right) \tag{9-38}$$

In particular, Q is the applied power and $\dot{m}$ is the steady mass flow rate, ρ_i and ρ_e are the channel inlet and outlet densities respectively, h_e and p_e are the channel outlet enthalpy and pressure respectively, and A is the flow area.

A universal curve, defined by the relation $\gamma\hat{Q}=\sqrt{2\gamma\xi+1}-1$, was produced that correlates well, with less than 10% error, the system pressure, fluid, K factors, inlet temperature, flow rate, geometry and flow orientation for oscillatory instability. The study undertaken also developed parameters for static instability, but that is excluded here as that development, though began during this study, was finalized after this study. The hypothesis used here for oscillatory instability is believed to be 'new' but the hypothesis used for static instability is 'old', as it has been commonly used for static instability in two-phase flow instability.

The non-dimensional parameters proposed here have an explicit dependence on inlet and outlet K factors through the ξ term and all the oscillatory data for up-flow, horizontal flow and down-flow, generated for this study with in-house instability codes, fall within 90 - 100% of the universal curve.

A final word about the codes used in this study. The SPORTS non-linear instability program was developed while the author was in industry at AECL about 27 years ago and it has a built-in suite of correlations for calculating friction pressure drop based on Reynolds number and roughness factor. The linear code, developed at University of Manitoba, uses only the SPORTS front end to calculate the system steady-state parameters, but employs otherwise standard control-theory principles. Both codes give closely similar predictions of the flow instability boundary, but it is worthy to note that we did not alter in any way the built-in correlations for friction pressure drop. Thus, any difference in instability predictions between our codes and other code results may likely be due to the different friction formulae used.

9.2.4.6. Submissions by BARC

The data submitted by the Bhabha Atomic Research Centre of Mumbai [9-50] were obtained by the linear stability SUCLIN code, modified for the application to supercritical conditions, and by the transient NOLSTA code.

Concerning the application of SUCLIN, the document accompanying the submission describes in detail the adopted models and fluid properties, including the adopted polynomial representation of them. A classical technique of linearization by perturbation of the partial differential equations, followed by the search for a complex exponential time trend, is adopted to translate the problem from the time to the frequency domain. The analytic solution of the resulting ordinary differential equations in the spatial variable and the use of the boundary conditions lead finally to the characteristic equations, whose roots are numerically calculated to discuss the value of their real part. The Nyquist criterion is adopted to establish the stability thresholds. The dominant root of the characteristic equation is used to evaluate the period of oscillations.

The analysis was made in dimensional form and the thresholds of instability were converted to the suggested dimensionless numbers. One of the meaningful proposed stability maps is reported hereafter in Fig. 9.148, showing that both excursive and density wave oscillation instabilities are identified by the SUCLIN code, applied only to water cases. No instability was obtained for the case with the lowest exit pressure drop coefficient.

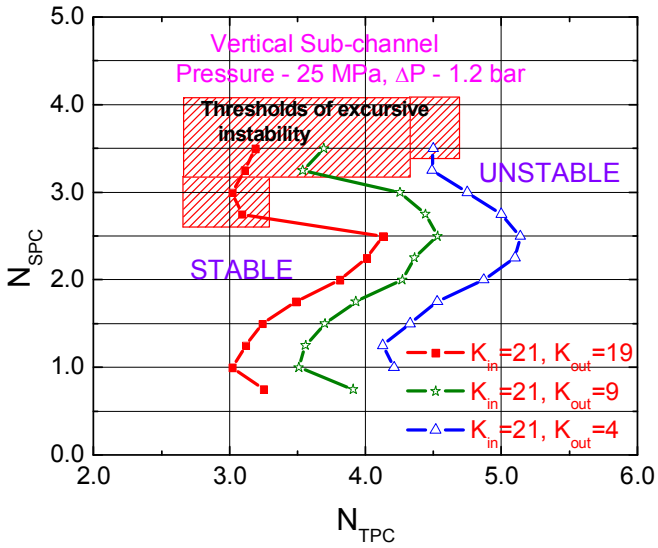

FIG. 9.148. Stability boundaries identified by the SUCLIN code for water and vertical channel.

A comparison between the cases with vertical and horizontal channel is made in Fig. 9.149, confirming the greater extension of the region of excursive instability in the latter case, as pointed out in the data by the University of Pisa.

Quantitative comparisons between the results of SUCLIN and the reference stability boundaries are reported in Figs 9.150 and 9.151. As it can be noted, while there is agreement in relation to the Ledinegg instability, a greater stability seems to be predicted by SUCLIN with respect to the reference data in the case of density waves. Also the values of the ratio of the transit time to the period of oscillations, as reported in tabular form in the submitted data, are in the same range as for the reference data.

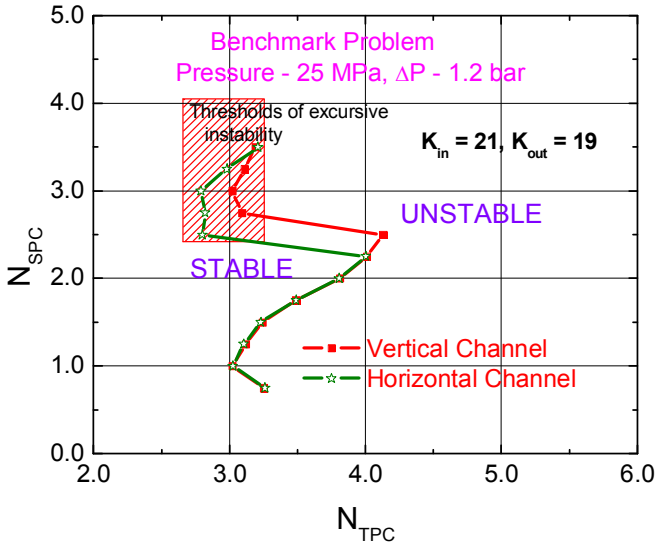

FIG. 9.149. Comparison of the stability boundaries identified by the SUCLIN code for water with vertical channel and horizontal channel.

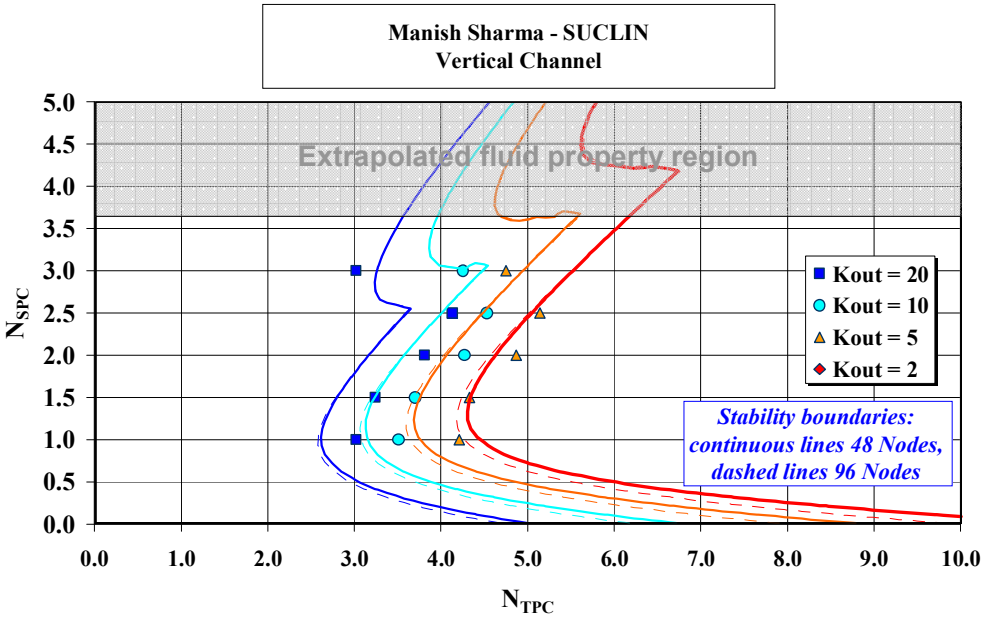

FIG. 9.150. Comparison of the stability boundaries identified by the SUCLIN code for water and vertical channel with the reference stability boundaries.

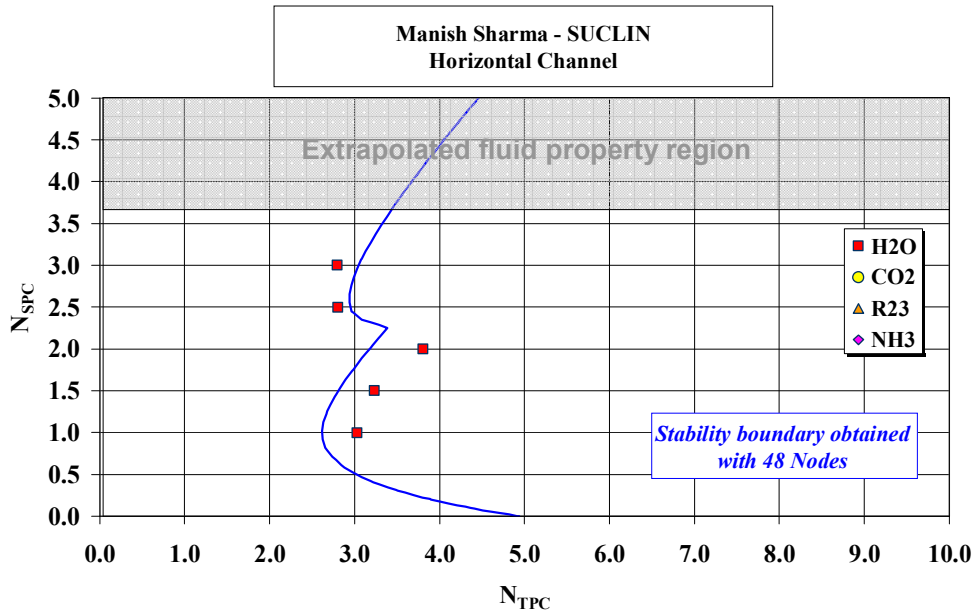

FIG. 9.151. Comparison of the stability boundaries identified by the SUCLIN code for water and horizontal channel with the reference stability boundaries.

The data obtained by the NOLSTA code, making use of time and space discretization, are somehow different from those of the SUCLIN one. Figures 9.152 and 9.153 report the stability boundaries obtained by the code for the horizontal and the vertical channel and Figs 9.154 and 9.155 compare them with the reference stability boundaries, showing very good agreement with the reference data. Table 9.21 to Table 9.24 and Figs 9.156 and 9.157 report the values of the instability thresholds and of the ratio T_{trans}/T as calculated by both the SUCLIN and the NOLSTA codes.

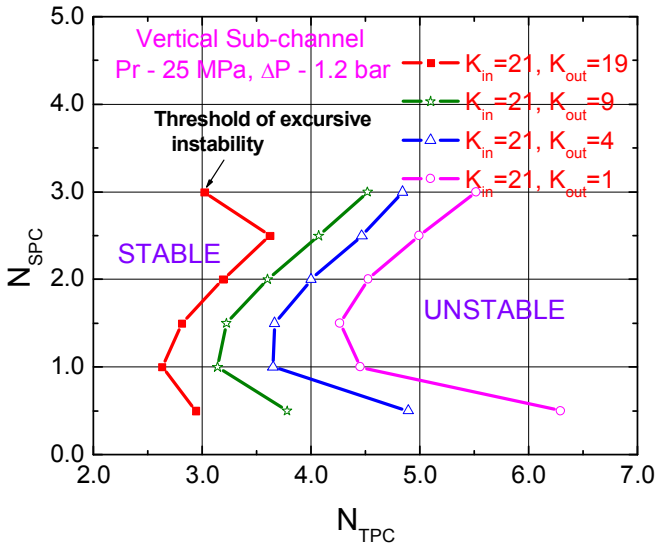

FIG.9.152. Comparison of the stability boundaries identified by the NOLSTA code for water and vertical channel with the reference stability boundaries.

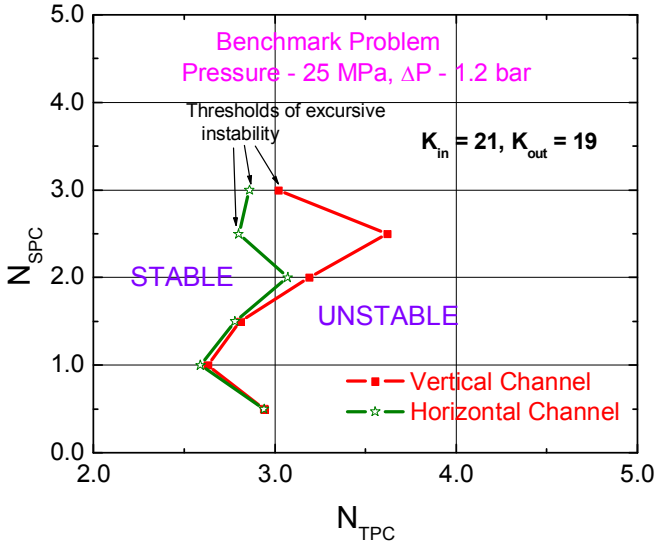

FIG. 9.153. Comparison of the stability boundaries identified by the NOLSTA code for water and horizontal channel with the reference stability boundaries.

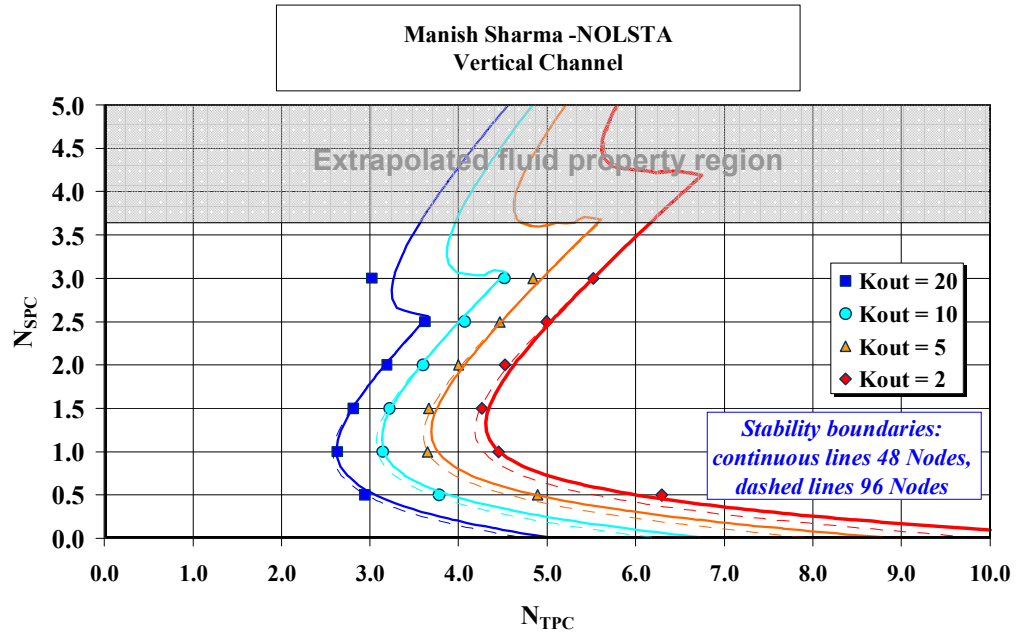

FIG. 9.154. Comparison of the stability boundaries identified by the NOLSTA code for water and vertical channel with the reference stability boundaries.

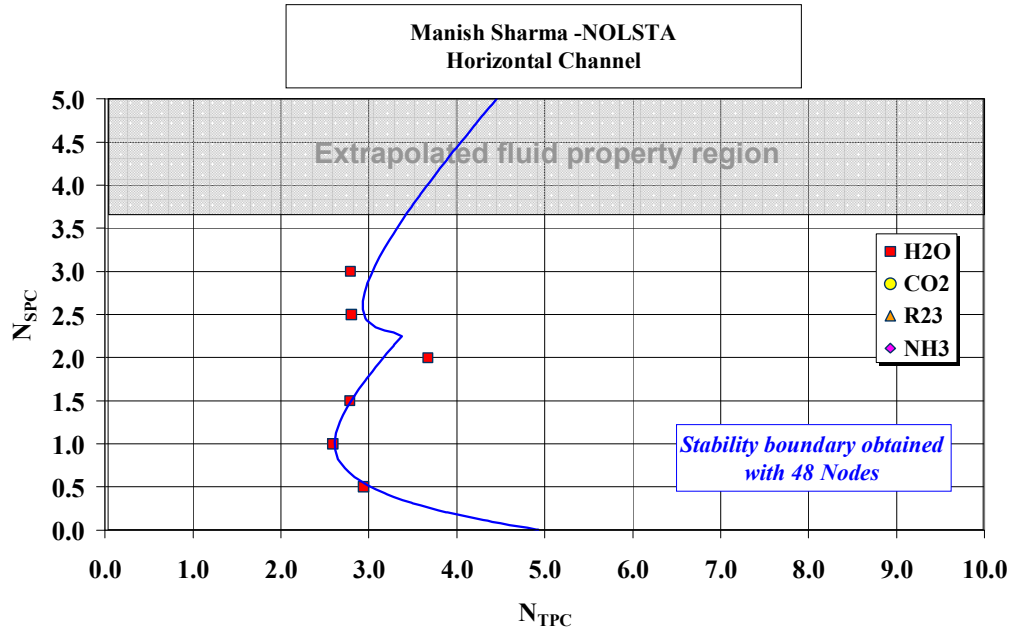

FIG. 9.155. Comparison of the stability boundaries identified by the NOLSTA code for water and horizontal channel with the reference stability boundaries.

TABLE 9.21. RESULTS OBTAINED BY BARC FOR THE INSTABILITY THRESHOLD AND THE RATIO T_{TRANS}/T WITH THE SUCLIN CODE FOR THE CASE OF VERTICAL CHANNEL WITH DIFFERENT THROTTLING

Manish Shama - SUCLIN			Kout=20	Kout=20	Kout=10	Kout=10	Kout=5	Kout=5	Kout=2	Kout=2
Case	Channel orientation	Nspc	Ntpc. threshold	Type of instability	Ntpc. threshold	Type of instability	Ntpc. threshold	Type of instability	Ntpc. threshold	Type of instability
Label				Oscillatory or Excursive		Oscillatory or Excursive		Oscillatory or Excursive		Oscillatory or Excursive
D0.5V-K20 to K2	Vertical	0.5		No instability		No instability		No instability		No instability
D1.0V-K20 to K2	Vertical	1	3.02	Oscillatory	3.51	Oscillatory	4.21	Oscillatory		No instability
D1.5V-K20 to K2	Vertical	1.5	3.24	Oscillatory	3.7	Oscillatory	4.329	Oscillatory		No instability
D2.0V-K20 to K2	Vertical	2	3.81	Oscillatory	4.27	Oscillatory	4.87	Oscillatory		No instability
D2.5V-K20 to K2	Vertical	2.5	4.13	Oscillatory	4.53	Oscillatory	5.14	Oscillatory		No instability
D3.0V-K20 to K2	Vertical	3	3.02	Excursive	4.253	Oscillatory	4.75	Oscillatory		No instability

Manish Shama - SUCLIN			Kout=20	Kout=10	Kout=5	Kout=2
Case	Channel orientation	Nspc	Ratio of Transit Time to the Period of Oscillations	Ratio of Transit Time to the Period of Oscillations	Ratio of Transit Time to the Period of Oscillations	Ratio of Transit Time to the Period of Oscillations
Label						
D0.5V-K20 to K2	Vertical	0.5				No instability
D1.0V-K20 to K2	Vertical	1	1.434	1.434	1.445	No instability
D1.5V-K20 to K2	Vertical	1.5	2.47	2.461	1.369	No instability
D2.0V-K20 to K2	Vertical	2	2.418	2.408	2.405	No instability
D2.5V-K20 to K2	Vertical	2.5	3.438	2.359	3.428	No instability
D3.0V-K20 to K2	Vertical	3		3.372	3.342	No instability

TABLE 9.22. RESULTS OBTAINED BY BARC FOR THE INSTABILITY THRESHOLD AND THE RATIO T_{TRANS}/T WITH THE SUCLIN CODE FOR THE CASES OF VERTICAL AND HORIZONTAL CHANNEL

Manish Sharma - SUCLIN			Water	Water	CO2	CO2	R23	R23	NH3	NH3
Case Label	Channel orientation	Nspc	Ntpc. threshold	Type of instability Oscillatory or Excursive	Ntpc. threshold	Type of instability Oscillatory or Excursive	Ntpc. threshold	Type of instability Oscillatory or Excursive	Ntpc. threshold	Type of instability Oscillatory or Excursive
F0.5V	Vertical	0.5		No instability		Oscillatory		Oscillatory		
F1.0V	Vertical	1	3.02	Oscillatory		Excursive		Excursive		Oscillatory
F1.5V	Vertical	1.5	3.24	Oscillatory		Oscillatory		Oscillatory		Excursive
F2.0V	Vertical	2	3.81	Oscillatory		Excursive		Excursive		Oscillatory
F2.5V	Vertical	2.5	4.13	Oscillatory		Oscillatory		Oscillatory		
F3.0V	Vertical	3	3.02	Excursive				Excursive		
F0.5H	Horizontal	0.5		No instability		Oscillatory		Oscillatory		
F1.0H	Horizontal	1	3.025	Oscillatory		Excursive		Excursive		Oscillatory
F1.5H	Horizontal	1.5	3.23	Oscillatory		Oscillatory		Oscillatory		Excursive
F2.0H	Horizontal	2	3.806	Oscillatory		Excursive		Excursive		Oscillatory
F2.5H	Horizontal	2.5	2.8	Excursive		Oscillatory		Oscillatory		
F3.0H	Horizontal	3	2.79	Excursive				Excursive		

Manish Sharma – SUCLIN			Water	CO2	R23	NH3
Case Label	Channel orientation	Nspc	Ratio of Transit Time to the Period of Oscillations	Ratio of Transit Time to the Period of Oscillations	Ratio of Transit Time to the Period of Oscillations	Ratio of Transit Time to the Period of Oscillations
F0.5V	Vertical	0.5				
F1.0V	Vertical	1	1.434			
F1.5V	Vertical	1.5	2.47			
F2.0V	Vertical	2	2.418			
F2.5V	Vertical	2.5	3.438			
F3.0V	Vertical	3				
F0.5H	Horizontal	0.5				
F1.0H	Horizontal	1	1.433			
F1.5H	Horizontal	1.5	2.467			
F2.0H	Horizontal	2	2.413			
F2.5H	Horizontal	2.5				
F3.0H	Horizontal	3				

TABLE 9.23. RESULTS OBTAINED BY BARC FOR THE INSTABILITY THRESHOLD AND THE RATIO T_{TRANS}/T WITH THE NOLSTA CODE FOR THE CASE OF VERTICAL CHANNEL WITH DIFFERENT THROTTLING

Manish Shama - NOLSTA			Kout=20	Kout=20	Kout=10	Kout=10	Kout=5	Kout=5	Kout=2	Kout=2
Case Label	Channel orientation	Nspc	Ntpc. threshold	Type of instability Oscillatory or Excursive	Ntpc. threshold	Type of instability Oscillatory or Excursive	Ntpc. threshold	Type of instability Oscillatory or Excursive	Ntpc. threshold	Type of instability Oscillatory or Excursive
D0.5V-K20 to K2	Vertical	0.5	2.94	Oscillatory	3.78	Oscillatory	4.896	Oscillatory	6.295	Oscillatory
D1.0V-K20 to K2	Vertical	1	2.63	Oscillatory	3.14	Oscillatory	3.649	Oscillatory	4.453	Oscillatory
D1.5V-K20 to K2	Vertical	1.5	2.81	Oscillatory	3.22	Oscillatory	3.665	Oscillatory	4.265	Oscillatory
D2.0V-K20 to K2	Vertical	2	3.19	Oscillatory	3.6	Oscillatory	4	Oscillatory	4.526	Oscillatory
D2.5V-K20 to K2	Vertical	2.5	3.62	Oscillatory	4.07	Oscillatory	4.467	Oscillatory	4.993	Oscillatory
D3.0V-K20 to K2	Vertical	3	3.02	Excursive	4.52	Oscillatory	4.842	Oscillatory	5.518	Oscillatory

Manish Shama - NOLSTA			Kout=20	Kout=10	Kout=5	Kout=2
Case Label	Channel orientation	Nspc	Ratio of Transit Time to the Period of Oscillations	Ratio of Transit Time to the Period of Oscillations	Ratio of Transit Time to the Period of Oscillations	Ratio of Transit Time to the Period of Oscillations
D0.5V-K20 to K2	Vertical	0.5	0.628	0.655	0.712	0.714
D1.0V-K20 to K2	Vertical	1	0.535	0.539	0.566	0.589
D1.5V-K20 to K2	Vertical	1.5	0.442	0.48	0.5	0.517
D2.0V-K20 to K2	Vertical	2	0.339	0.395	0.427	0.427
D2.5V-K20 to K2	Vertical	2.5	0.184	0.3	0.36	0.392
D3.0V-K20 to K2	Vertical	3	Excursive	0.314	0.274	0.327

TABLE 9.24. RESULTS OBTAINED BY BARC FOR THE INSTABILITY THRESHOLD AND THE RATIO T_{TRANS}/T WITH THE NOLSTA CODE FOR THE CASES OF VERTICAL AND HORIZONTAL CHANNEL

Manish Sharma - NOLSTA			Water	Water	CO2	CO2	R23	R23	NH3	NH3
Case Label	Channel orientation	Nspc	Ntpc. threshold	Type of instability Oscillatory or Excursive	Ntpc. threshold	Type of instability Oscillatory or Excursive	Ntpc. threshold	Type of instability Oscillatory or Excursive	Ntpc. threshold	Type of instability Oscillatory or Excursive
F0.5V	Vertical	0.5	2.94	Oscillatory		Oscillatory		Oscillatory		
F1.0V	Vertical	1	2.63	Oscillatory		Excursive		Excursive		Oscillatory
F1.5V	Vertical	1.5	2.81	Oscillatory		Oscillatory		Oscillatory		Excursive
F2.0V	Vertical	2	3.19	Oscillatory		Excursive		Excursive		Oscillatory
F2.5V	Vertical	2.5	3.62	Oscillatory		Oscillatory		Oscillatory		
F3.0V	Vertical	3	3.02	Excursive				Excursive		
F0.5H	Horizontal	0.5	2.94	No instability		Oscillatory		Oscillatory		
F1.0H	Horizontal	1	2.59	Oscillatory		Excursive		Excursive		Oscillatory
F1.5H	Horizontal	1.5	2.78	Oscillatory		Oscillatory		Oscillatory		Excursive
F2.0H	Horizontal	2	3.67	Oscillatory		Excursive		Excursive		Oscillatory
F2.5H	Horizontal	2.5	2.8	Excursive		Oscillatory		Oscillatory		
F3.0H	Horizontal	3	2.79	Excursive				Excursive		

Manish Sharma – NOLSTA			Water	CO2	R23	NH3
Case Label	Channel orientation	Nspc	Ratio of Transit Time to the Period of Oscillations	Ratio of Transit Time to the Period of Oscillations	Ratio of Transit Time to the Period of Oscillations	Ratio of Transit Time to the Period of Oscillations
F0.5V	Vertical	0.5	0.628			
F1.0V	Vertical	1	0.535			
F1.5V	Vertical	1.5	0.442			
F2.0V	Vertical	2	0.339			
F2.5V	Vertical	2.5	0.184			
F3.0V	Vertical	3	Excursive			
F0.5H	Horizontal	0.5	0.616			
F1.0H	Horizontal	1	0.512			
F1.5H	Horizontal	1.5	0.402			
F2.0H	Horizontal	2	0.26			
F2.5H	Horizontal	2.5	Excursive			
F3.0H	Horizontal	3	Excursive			

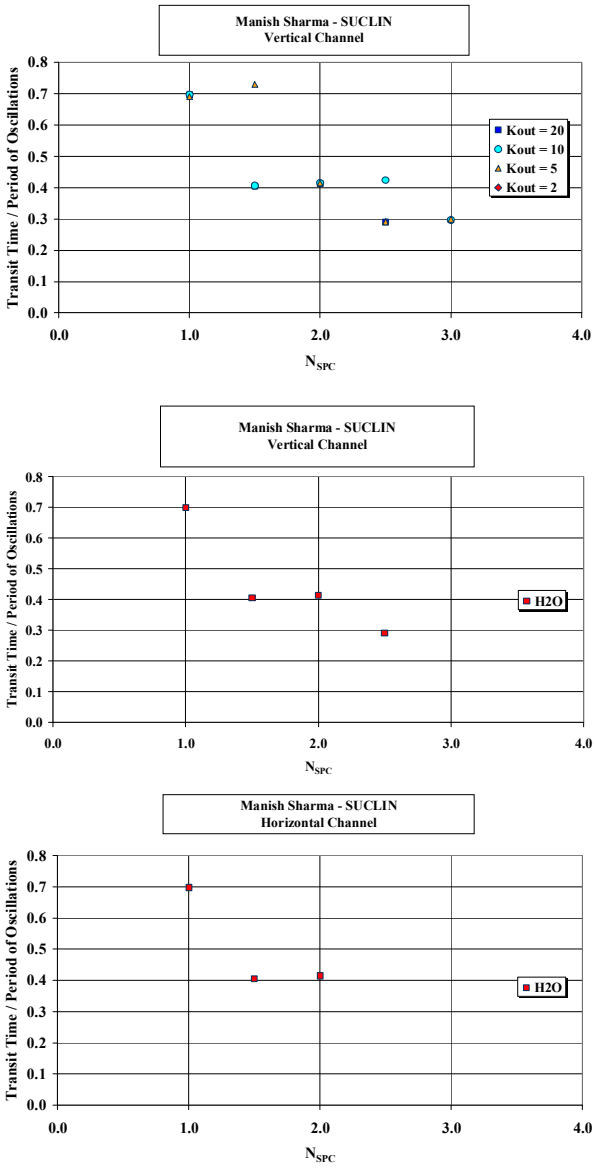

FIG. 9.156. Ratio of the transit time to the period of oscillations evaluated by the SUCLIN code.

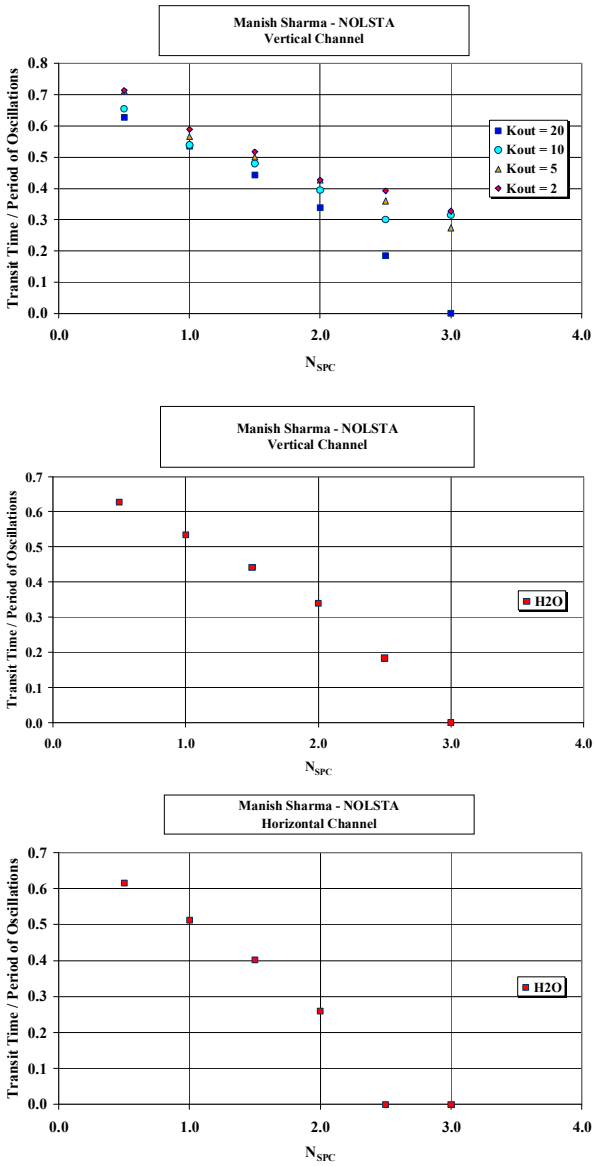

FIG. 9.157. Ratio of the transit time to the period of oscillations evaluated by the NOLSTA code.

9.2.4.7. Comments by BARC

BARC has made two submissions for the benchmark problem, one using linear stability code (SUCLIN) and the other using non-linear stability code (NOLSTA). The predictions by NOLSTA code are in very good agreement with reference stability boundaries for the oscillatory density wave instability, whereas SUCLIN code predicts greater stability for the same cases. The NOLSTA code uses only 28 nodes which can contribute to some amount of numerical diffusion. Apart from numerical diffusion, there are other differences which can also contribute to the mismatch as specified below:

- All the fluid properties (including viscosity) are perturbed in the nonlinear analysis (i.e. NOLSTA analysis), whereas only enthalpy and specific volume perturbations are considered in linear stability analysis (i.e. SUCLIN analysis);
- The friction factor perturbation is not considered in linear stability analysis, whereas nonlinear analysis accounts for it;
- The perturbation induced in specific volume due to perturbations in enthalpy has been considered in the SUCLIN code, whereas perturbations in specific volume due to perturbation in pressure have been neglected. The NOLSTA code accounts for both.

Similar differences were also observed in the stability analysis of natural circulation in a rectangular open loop with supercritical water by NOLSTA and SUCLIN codes as reported in Sharma et al. (2010) [9-51].

9.2.4.8. Submission by JRC-IE Petten

The submission by JRC-IE [9-52] was made closely following the specifications and provided results in excellent agreement with the reference data for the computed stability thresholds and in close agreement also for the values of the ratio of the transit time to the period of oscillations. As in previously published work by the University of Pisa, the RELAP5 code was used for simulating a channel with 48 nodes.

The exercise was carried out using water as fluid, whose properties are in agreement with the IAPWS 97 standard. An attempt was made to perform the exercise with other fluids than water, namely CO_2 and NH_3; however, it is reported that the code was not able to handle these fluids in supercritical conditions. The submitted data report the trends of flow rate, power and N_{TPC}, as suggested in the specifications. The resulting stability thresholds are shown in Fig. 9.158 in comparison with the reference stability boundaries; as it can be noted, the results represent a sort of independent confirmation of the reference data. Table 9.25 and Fig. 9.159 report the numerical values of the instability thresholds and of the ratio T_{trans}/T.

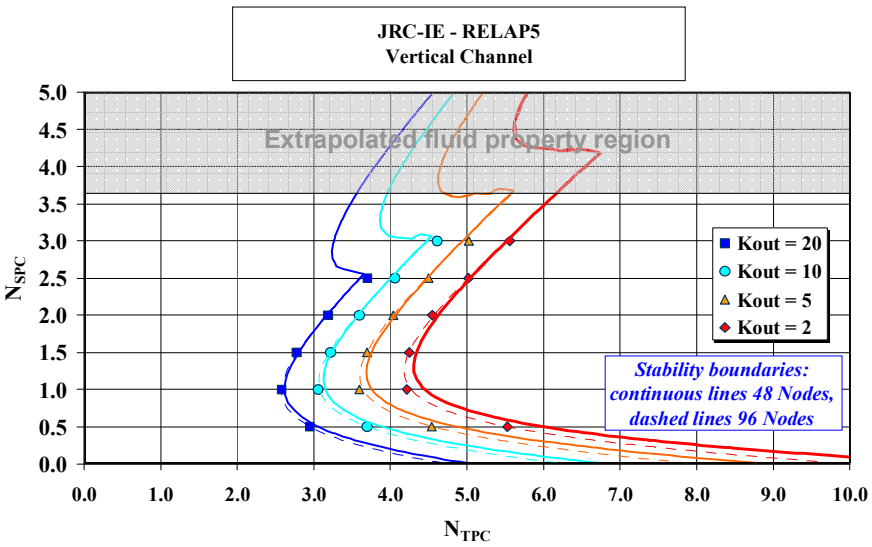

FIG. 9.158. Comparison of the stability boundaries identified by the RELAP code for water and vertical channel with the reference stability boundaries.

TABLE 9.25. RESULTS OBTAINED BY JRC-IE FOR THE INSTABILITY THRESHOLD AND THE RATIO T_{TRANS}/T

JRC-IE – RELAP5			Kout=20	Kout=20	Kout=10	Kout=10	Kout=5	Kout=5	Kout=2	Kout=2
Case	Channel orientation	Nspc	Ntpc. threshold	Type of instability	Ntpc. threshold	Type of instability	Ntpc. threshold	Type of instability	Ntpc. threshold	Type of instability
Label				Oscillatory or Excursive		Oscillatory or Excursive		Oscillatory or Excursive		Oscillatory or Excursive
D0.5V-K20 to K2	Vertical	0.5	2.949	Oscillatory	3.6972	Oscillatory	4.5399	Oscillatory	5.5291	Oscillatory
D1.0V-K20 to K2	Vertical	1	2.5789	Oscillatory	3.0585	Oscillatory	3.5985	Oscillatory	4.2168	Oscillatory
D1.5V-K20 to K2	Vertical	1.5	2.7792	Oscillatory	3.2196	Oscillatory	3.6946	Oscillatory	4.2494	Oscillatory
D2.0V-K20 to K2	Vertical	2	3.1888	Oscillatory	3.5971	Oscillatory	4.0389	Oscillatory	4.5497	Oscillatory
D2.5V-K20 to K2	Vertical	2.5	3.6999	Excursive (?)	4.0615	Oscillatory	4.5001	Oscillatory	5.0196	Oscillatory
D3.0V-K20 to K2	Vertical	3		Excursive	4.61	Excursive (?)	5.0214	Oscillatory	5.5583	Oscillatory

JRC-IE – RELAP5			Kout=20	Kout=10	Kout=5	Kout=2
Case	Channel orientation	Nspc	Ratio of Transit Time to the Period of Oscillations	Ratio of Transit Time to the Period of Oscillations	Ratio of Transit Time to the Period of Oscillations	Ratio of Transit Time to the Period of Oscillations
Label						
D0.5V-K20 to K2	Vertical	0.5	0.6323	0.6168	0.7551	0.6430
D1.0V-K20 to K2	Vertical	1	0.5010	0.5922	0.4883	0.5843
D1.5V-K20 to K2	Vertical	1.5	0.4619	0.4910	0.4080	0.5193
D2.0V-K20 to K2	Vertical	2	0.3576	0.3444	0.4804	0.4095
D2.5V-K20 to K2	Vertical	2.5	0.2015	0.2782	0.3273	0.3498
D3.0V-K20 to K2	Vertical	3		0.1275	0.2611	0.3140

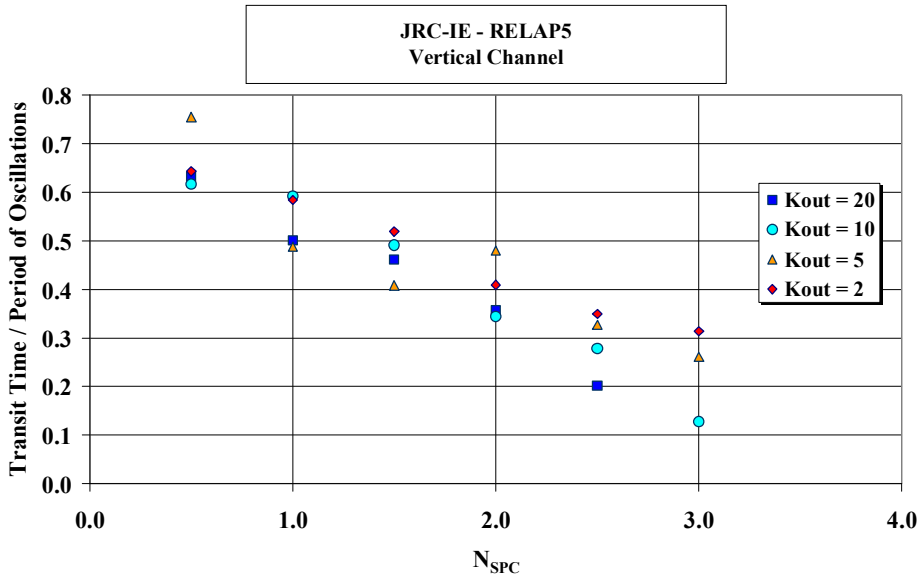

FIG. 9.159. Ratio of the transit time to the period of oscillations evaluated by JRC-IE with the RELAP5 code.

9.2.4.9. Comments by JRC-IE Petten

The results are in excellent agreement with the reference data for the computed stability thresholds. The exercise was done with the use of the same RELAP5 code, a close follow-up of specifications and with the attentive review of previous work [9-39] and [9-40].

Particular attention was given to the power ramp in proximity of the instability range. In the first 100 seconds no power is imposed in the channel. From 100 until 500 seconds the power increases from zero to a value high enough to quickly approach the unstable region, and then the increased rate is lowered to 2 W/s to slowly cross the instability boundary. The flow rate follows power with a continuous trend, since the initial pressure drop of 0.12 MPa is imposed across the channel. This is followed by a sharp reduction in flow rate due to the increase in power. The rate of reduction in flow rate becomes then lower when the final power ramp of 2 W/s is attained. The power needed to reach the instability threshold increases with increasing sub-pseudocritical number N_{SPC}. This is evident since a higher N_{SPC} implies a higher sub-cooling at the inlet. For the same N_{SPC}, a lower local pressure drop (K_{out}) requires a higher power to attain instability.

The onset of instabilities was detected by the presence of increasing oscillations in the computed values of the flow rate. The code then computed the flow rate and power to convert them into a corresponding evolution of the trans-pseudocritical number N_{TPC}. It must be noted that both the trans-pseudocritical number N_{TPC} and the sub-pseudocritical number N_{SPC} are directly computed by RELAP5 without using external tables; this allows a more consistent procedure (Fig. 9.158). No automatic procedure was defined to evaluate the threshold value of N_{TPC}. Over a printing frequency of 1.0 s, the threshold value was manually detected whenever the pseudo-critical number presented an oscillation higher than third decimal digit.

For some trends it was quite easy to estimate the threshold value of N_{TPC}. In some cases oscillations showed a first onset of instability followed by a second occurrence (e.g., for N_{SPC}=0.5, K_{out}=2). Very often, the calculation was abruptly aborted after the onset of instabilities, because of numerical problems. While the values of the period of oscillations have been manually detected from the calculated trends, the transit time has been automatically evaluated by taking the ratio of the instantaneous channel mass to the instantaneous inlet mass flow. As already noted [9-53] and [9-54], the ratio decreases with increasing sub-cooling throughout the region of density-wave instability up to the boundary with the Ledinegg instability region. It can be therefore argued that the period of oscillations increases with increasing sub-cooling much more than the transit time does as a consequence of the lower average velocity of the fluid along the channel. In particular, the oscillation period becomes very long in the proximity of the Ledinegg instability region, in which an excursive behaviour is expected.

The regions of stable and unstable behaviour are clearly shown in Fig. 9.158. The effect of outlet pressure drop coefficients on stability is also evident. The stability boundaries show a shift to the right with decreasing values of K_{out}, indicating the stabilizing effect of reducing the throttling at the exit.

9.2.4.10. Further studies by JRC-IE Petten

The excellent results obtained in the benchmark incited to extend the analysis to a more realistic power profile than the uniform shape proposed in the benchmark exercise. The work done by Tsige-Tamirat et al. (2009) [9-55] was taken as reference to define the hypothetical axial power profile of the first core pass of a High Performance Light Water Reactor (HPLWR).

A three dimensional MCNP geometry model (Fig. 9.160) of the HPLWR assembly was set up based on the data from the current HPLWR design. The thermal-hydraulic analysis was performed using an upgraded version of the sub-channel code COBRA-EN [9-56] for supercritical water conditions. For reactivity coefficient calculations, temperature-dependent continuous-energy cross section data based on JEFF3.1 were used. The calculated axial power profile is shown in Fig. 9.161.

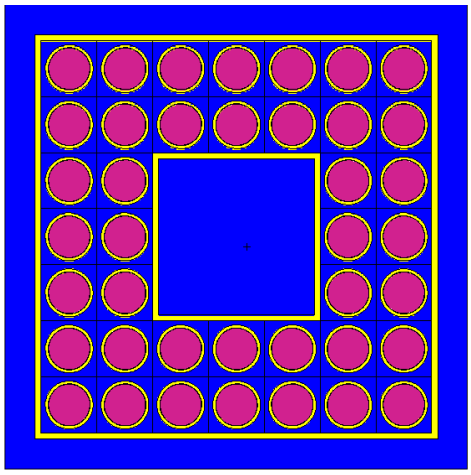

FIG. 9.160. Horizontal section of the HPLWR assembly MCNP model.

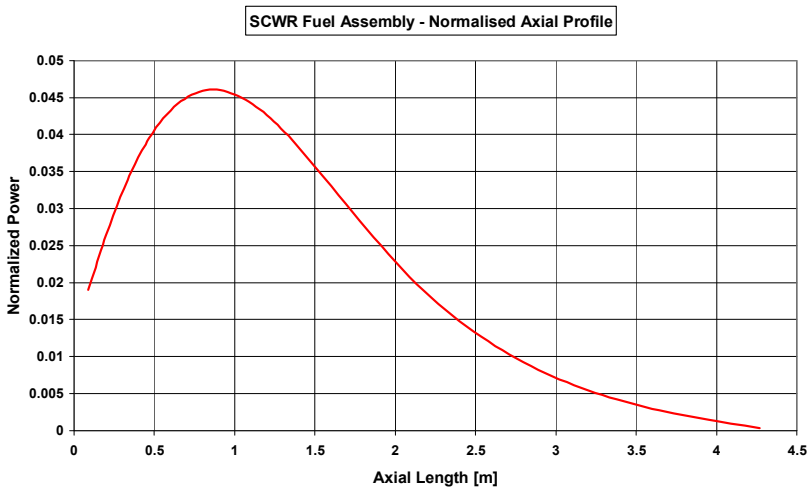

FIG. 9.161. Axial neutron flux distribution in HPLWR with oxide and hydride assemblies.

The axial flux distribution achieves its maximum in the lower part of the assembly. This is due to the higher coolant density and, therefore, to the higher moderation and neutron flux in this part as shown from the thermal-hydraulic analysis (Fig. 9.162).

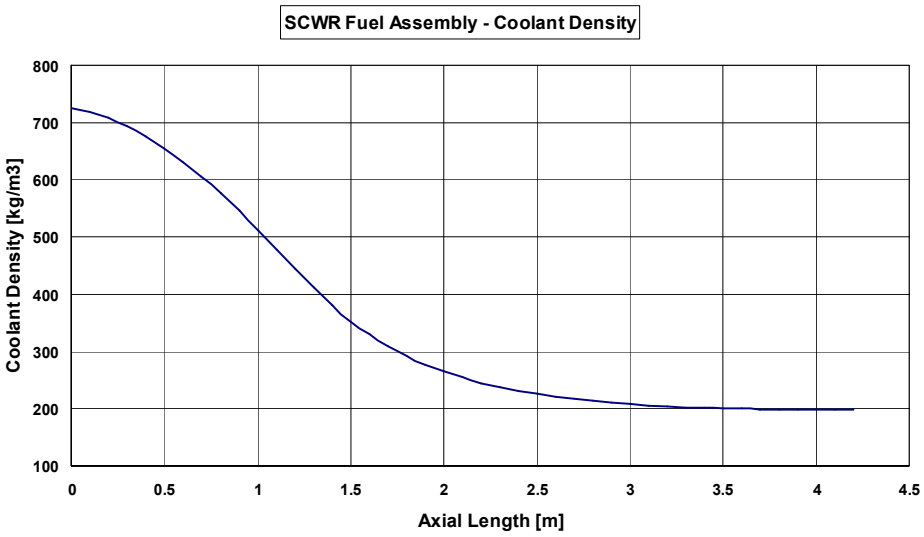

FIG. 9.162. Average axial density profile in HPLWR oxide assembly.

The benchmark exercise was performed again using the same model and the same values for N_{SPC} and K_{out} but with the new axial power profile. Some preliminary considerations were made on the general stability behaviour of the new system. In analogy with the theory of stability in boiling channels, the large density change takes place closer to the channel inlet causing the onset of instability to occur at a lower power for the same N_{SPC}. This shifts towards the left the stability curves and essentially depicts a less stable system under the same physical conditions.

This was indeed confirmed by the calculations whose results are shown in Table 9.26 and graphically in Fig. 9.163. The stabilizing effect of reducing the throttling at the exit was confirmed with the stability boundaries that show a shift to the right with decreasing values of K_{out}.

TABLE 9.26. RESULTS OBTAINED FOR THE INSTABILITY THRESHOLD FOR THE BOTTOM SKEWED PROFILE CASES

Participant Name – Code Name			Kout=20	Kout=20	Kout=10	Kout=10	Kout=5	Kout=5	Kout=2	Kout=2
Case	Channel orientation	Nspc	Ntpc. threshold	Type of instability	Ntpc. threshold	Type of instability	Ntpc. threshold	Type of instability	Ntpc. threshold	Type of instability
Label				Oscillatory or Excursive		Oscillatory or Excursive		Oscillatory or Excursive		Oscillatory or Excursive
D0.5V-K20 to K2	Vertical	0.5	1.9204	Oscillatory	2.561	Oscillatory	3.5011	Oscillatory	5.2279	Oscillatory
D1.0V-K20 to K2	Vertical	1	1.5	Oscillatory	1.9034	Oscillatory	2.3975	Oscillatory	2.9225	Oscillatory
D1.5V-K20 to K2	Vertical	1.5	1.601	Oscillatory	1.8589	Oscillatory	2.238	Oscillatory	2.6611	Oscillatory
D2.0V-K20 to K2	Vertical	2	1.9264	Oscillatory	2.1071	Oscillatory	2.373	Oscillatory	2.7501	Oscillatory
D2.5V-K20 to K2	Vertical	2.5	2.3661	Oscillatory	2.4657	Oscillatory	2.7354	Oscillatory	3.0133	Oscillatory
D3.0V-K20 to K2	Vertical	3	2.8415	Oscillatory	2.9091	Oscillatory	3.0489	Oscillatory	3.3795	Oscillatory

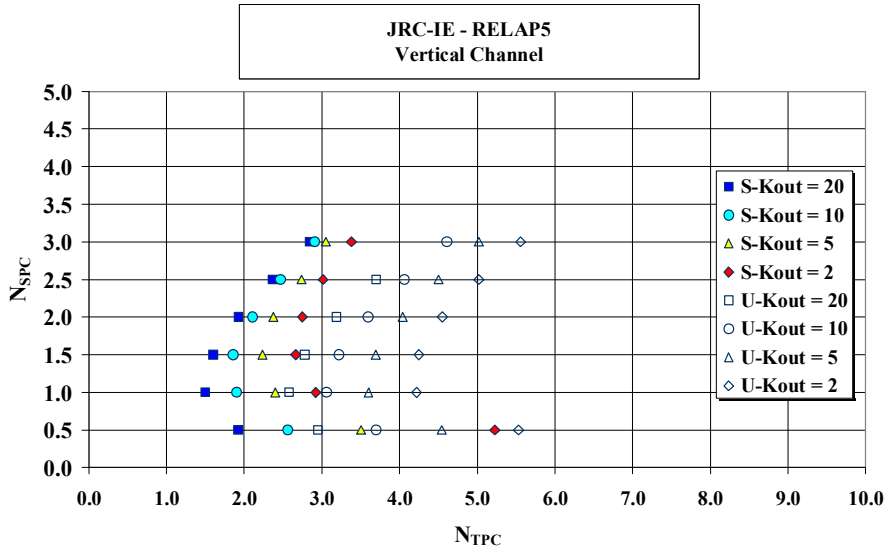

FIG.9.163. Comparison of the stability boundaries identified by the RELAP code for skewed axial power and vertical channel with the uniform power stability boundaries.

9.2.4.11. Submission by Gidropress

TEMPA is a transient subchannel code based on 3D conservation equations [9-57]. The number of nodes adopted for the analysis was 61 and the increasing power strategy was adopted to identify stability. A specific criterion for automatically detecting the onset of instabilities was adopted. The stability thresholds calculated by the TEMPA-SC code for the addressed cases are reported in Fig. 9.164. The match with the reference stability lines is only approximate, especially concerning the effect of outlet throttling. The values of the ratio of the transit time to the period of oscillations reported in Table 9.27 show the expected trend. In particular, interesting plots of the period of oscillations and of the ratio of the fluid transit time to this quantity as a function of N_{SPC} are proposed in the submission (Figs 9.165 and 9.166).

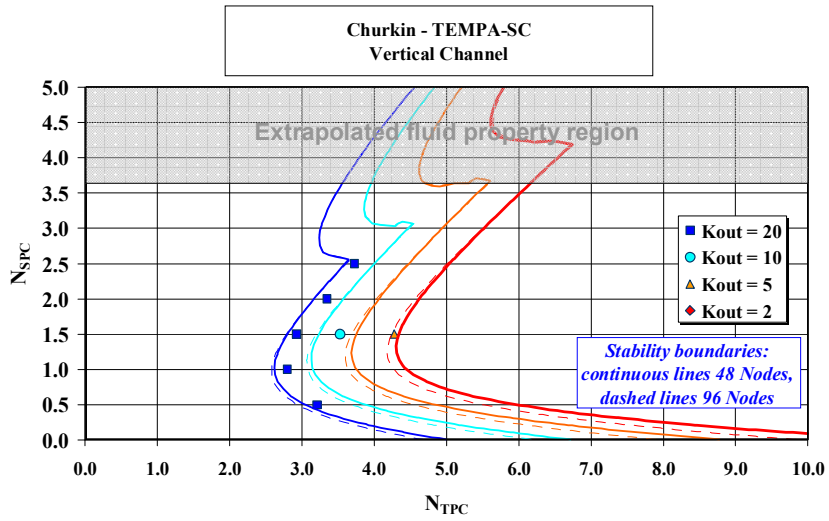

FIG. 9.164. Comparison of the stability boundaries identified by the TEMPA-SC code for water and vertical channel with the reference stability boundaries.

TABLE 9.27. RESULTS OBTAINED BY GIDROPRESS FOR THE INSTABILITY THRESHOLD AND THE RATIO T_{TRANS}/T

Churkin – TEMPA-SC			Kout=20	Kout=20	Kout=10	Kout=10	Kout=5	Kout=5	Kout=2	Kout=2
Case	Channel orientation	Nspc	Ntpc. threshold	Type of instability	Ntpc. threshold	Type of instability	Ntpc. threshold	Type of instability	Ntpc. threshold	Type of instability
Label				Oscillatory or Excursive		Oscillatory or Excursive		Oscillatory or Excursive		Oscillatory or Excursive
D0.5V-K20 to K2	Vertical	0.5	3.21	Oscillatory						(Code limitation)
D1.0V-K20 to K2	Vertical	1	2.8	Oscillatory						(Code limitation)
D1.5V-K20 to K2	Vertical	1.5	2.93	Oscillatory	3.53	Oscillatory	4.28	Oscillatory		(Code limitation)
D2.0V-K20 to K2	Vertical	2	3.35	Oscillatory						(Code limitation)
D2.5V-K20 to K2	Vertical	2.5	3.73	Oscillatory						(Code limitation)
D3.0V-K20 to K2	Vertical	3		Oscillatory						(Code limitation)

Churkin – TEMPA-SC			Kout=20	Kout=10	Kout=5	Kout=2
Case	Channel orientation	Nspc	Ratio of Transit Time to the Period of Oscillations	Ratio of Transit Time to the Period of Oscillations	Ratio of Transit Time to the Period of Oscillations	Ratio of Transit Time to the Period of Oscillations
Label						
D0.5V-K20 to K2	Vertical	0.5	0.65			
D1.0V-K20 to K2	Vertical	1	0.54			
D1.5V-K20 to K2	Vertical	1.5	0.46	0.48	0.50	
D2.0V-K20 to K2	Vertical	2	0.37			
D2.5V-K20 to K2	Vertical	2.5	0.24			
D3.0V-K20 to K2	Vertical	3				

Churkin – TEMPA-SC			Kout=20	Kout=10	Kout=5	Kout=2
Case	Channel orientation	Nspc	Ratio of Transit Time to the Period of Oscillations	Ratio of Transit Time to the Period of Oscillations	Ratio of Transit Time to the Period of Oscillations	Ratio of Transit Time to the Period of Oscillations
Label						
D0.5V-K20 to K2	Vertical	0.5	1.1/1.7			
D1.0V-K20 to K2	Vertical	1	1.4/2.6			
D1.5V-K20 to K2	Vertical	1.5	1.8/3.9	1.5/3.1	1.2/2.4	
D2.0V-K20 to K2	Vertical	2	2.1/5.7			
D2.5V-K20 to K2	Vertical	2.5	2.3/9.5			
D3.0V-K20 to K2	Vertical	3				

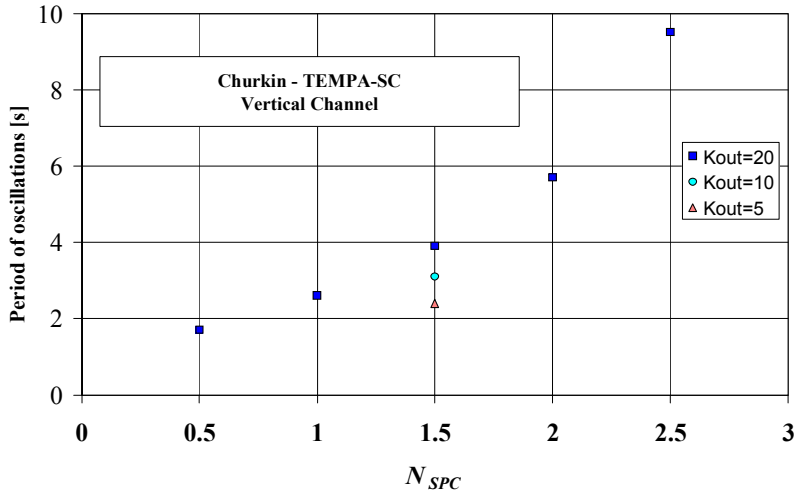

FIG. 9.165. Period of oscillations evaluated by the TEMPA-SC code.

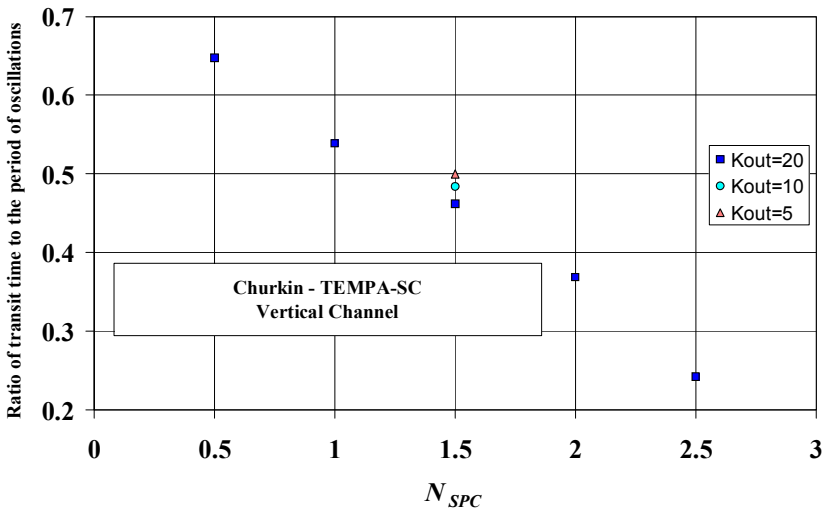

FIG. 9.166. Ratio of the transit time to the period of oscillations evaluated by the TEMPA-SC code.

9.2.4.12. Comments by Gidropress

In order to analyse the differences between the computational results of Gidropress and the reference data, sensitivity analyses are presently being performed. The influence on the stability threshold of the following parameters is being checked:

- heat transfer correlations;
- friction factor correlations;
- nodalization;
- rate of heating power increase adopted for reaching unstable behaviour;
- local hydraulic resistance coefficients.

In particular, a significant influence of the heating power increasing rate for reaching unstable behaviour is being revealed. At high heating rate a 'retardation' of instability occurs, that was also mentioned in previous literature. The submitted results were obtained with dQ/dt=21.3 W/s; it was then observed that, for the case with K_{out}=20 and NSPC=1.5, the Gidropress results obtained with dQ/dt=3.6 W/s are equal to the reference results.

Other relevant parameters (especially for low values of K_{out}) are the inlet and outlet local hydraulic resistance coefficients. If the corrections to local hydraulic resistance coefficients recommended in the specifications when inlet and outlet plena (+1 at the inlet and –1 at the outlet) are not taken into account, the Gidropress results are found very close to the reference data for K_{out}=5.

9.2.4.13. Submission by McMaster University and GRNSPG

This submission was twofold, making use of the RELAP5 and the TRACE codes, adopted with very similar choices [9-58] and [9-59]. Both the vertical and the horizontal channels with water were addressed calculating many more working conditions than specified.

The models for RELAP5 and TRACE are similar, including a pipe discretized with 23 nodes and two branches (upstream and downstream) to simulate the plena, in addition to two time-dependent volumes needed to impose inlet and outlet pressures. The procedure adopted for reaching the instability threshold is the one suggested in the specifications for transient codes and used by other Participants, i.e., a progressive increase of channel power at imposed pressure drop across the channel.

The results of the two codes in terms of stability thresholds are compared with the continuous stability boundaries in Figs 9.167, 9.168, 9.169 and 9.170. A greater stability with respect to the reference data is observed. However, also in this submission the presence of the excursive instability seems confirmed at low enough inlet temperature, though the tables of results do not point out this effect (see Table 9.28 and Table 9.29). In considering these results, the effect of numerical diffusion on the obtained results should be assessed: in fact, 23 nodes are expected to involve substantial truncation error when a first order numerical scheme is used; moreover, the effect of the explicit introduction of inlet and outlet plena should be also considered, since it may also include compressibility effects that were out of the scope of the exercise.

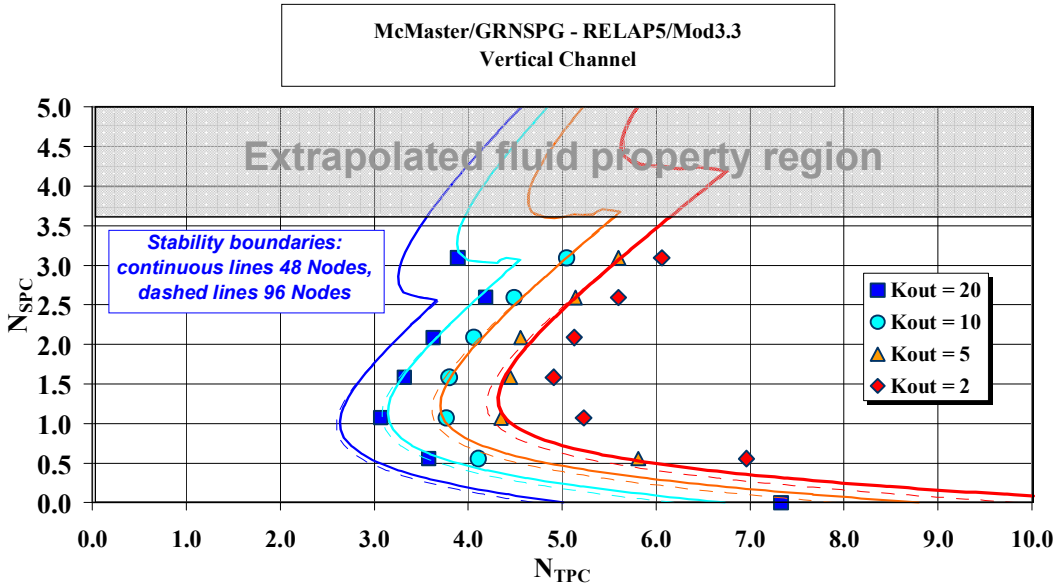

FIG. 9.167. Comparison of the stability boundaries identified by the RELAP5 code for water and vertical channel with the reference stability boundaries.

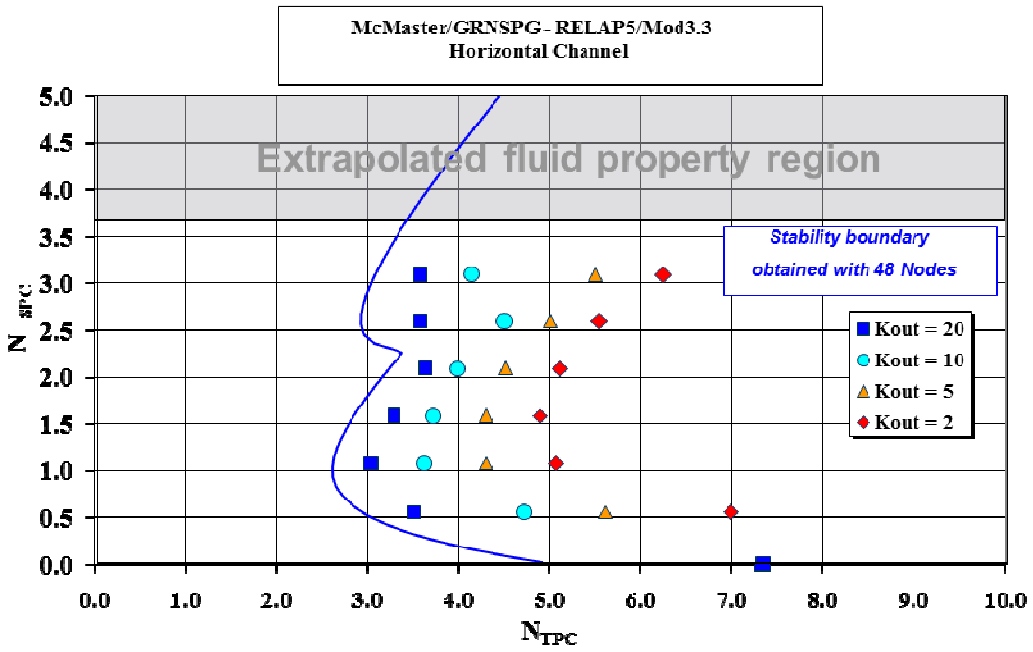

FIG. 9.168. Comparison of the stability boundaries identified by the RELAP5 code for water and horizontal channel with the reference stability boundaries.

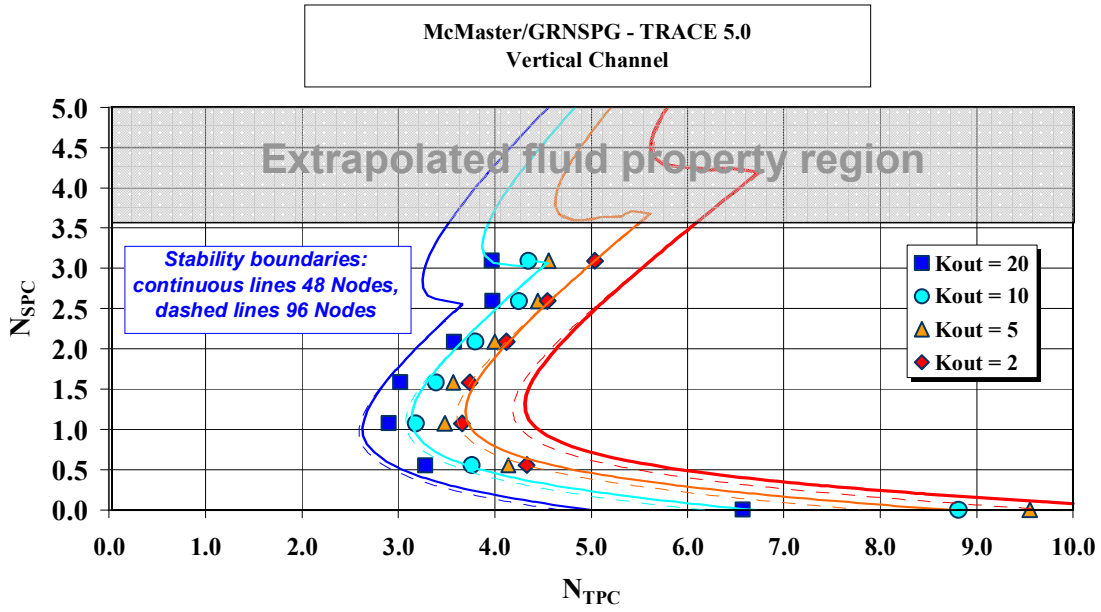

FIG. 9.169. Comparison of the stability boundaries identified by the TRACE code for water and vertical channel with the reference stability boundaries.

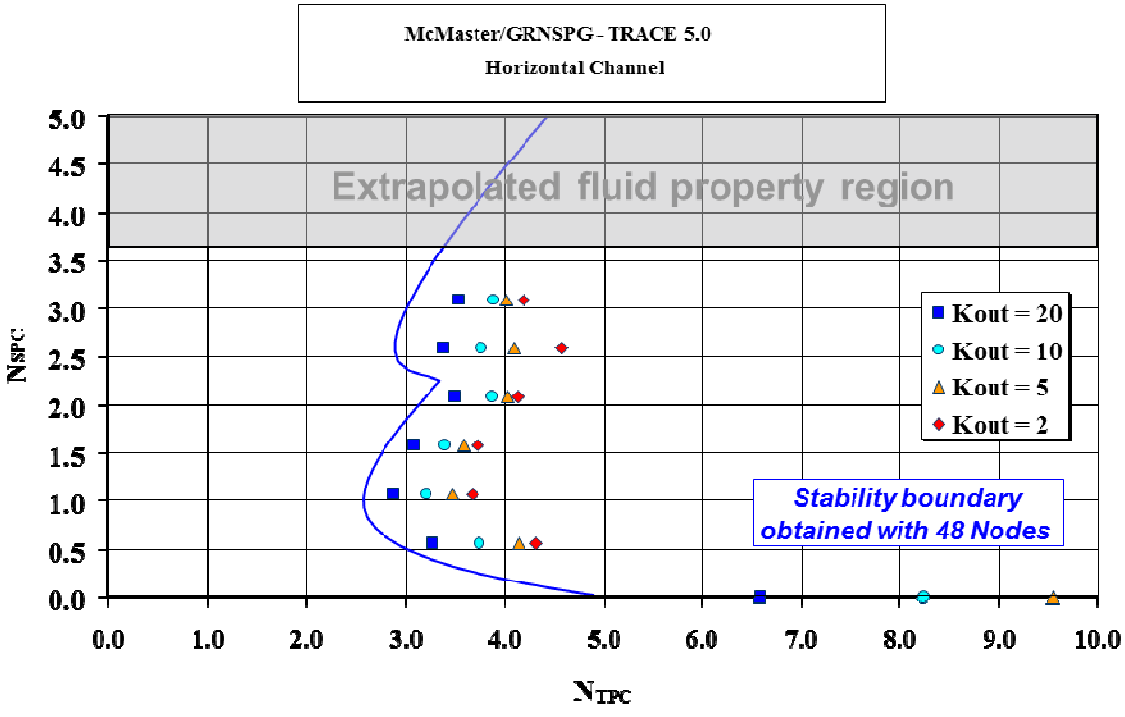

FIG. 9.170. Comparison of the stability boundaries identified by the TRACE code for water and horizontal channel with the reference stability boundaries.

TABLE 9.28. RESULTS OBTAINED BY MCMASTER UNIVERSITY AND GRNSPG WITH TRACE FOR THE INSTABILITY THRESHOLD

McMaster-GRNSPG-TRACE 5.0			Kout=20	Kout=20	Kout=10	Kout=10	Kout=5	Kout=5	Kout=2	Kout=2
Case	Channel orientation	Nspc	Ntpc. threshold	Type of instability	Ntpc. threshold	Type of instability	Ntpc. threshold	Type of instability	Ntpc. threshold	Type of instability
Label				Oscillatory or Excursive		Oscillatory or Excursive		Oscillatory or Excursive		Oscillatory or Excursive
D0.0V-K20 to K2	Vertical	0	6.57	Oscillatory	8.81	Oscillatory	9.55	Oscillatory	10.55	Oscillatory
D0.5V-K20 to K2	Vertical	0.555	3.28	Oscillatory	3.76	Oscillatory	4.14	Oscillatory	4.33	Oscillatory
D1.0V-K20 to K2	Vertical	1.0733	2.9	Oscillatory	3.18	Oscillatory	3.48	Oscillatory	3.66	Oscillatory
D1.5V-K20 to K2	Vertical	1.5825	3.02	Oscillatory	3.39	Oscillatory	3.57	Oscillatory	3.74	Oscillatory
D2.0V-K20 to K2	Vertical	2.088	3.58	Oscillatory	3.8	Oscillatory	4	Oscillatory	4.12	Oscillatory
D2.5V-K20 to K2	Vertical	2.592	3.98	Oscillatory	4.25	Oscillatory	4.45	Oscillatory	4.55	Oscillatory
D3.0V-K20 to K2	Vertical	3.0932	3.97	Oscillatory	4.35	Oscillatory	4.56	Oscillatory	5.04	Oscillatory

McMaster-GRNSPG-TRACE 5.0			Kout=20	Kout=20	Kout=10	Kout=10	Kout=5	Kout=5	Kout=2	Kout=2
Case	Channel orientation	Nspc	Ntpc. threshold	Type of instability	Ntpc. threshold	Type of instability	Ntpc. threshold	Type of instability	Ntpc. threshold	Type of instability
Label				Oscillatory or Excursive		Oscillatory or Excursive		Oscillatory or Excursive		Oscillatory or Excursive
D0.0H-K20 to K2	Horizontal	0	6.59	Oscillatory	8.23	Oscillatory	9.54	Oscillatory	No Oscillation	
D0.5H-K20 to K2	Horizontal	0.555	3.28	Oscillatory	3.75	Oscillatory	4.14	Oscillatory	4.32	Oscillatory
D1.0H-K20 to K2	Horizontal	1.0733	2.88	Oscillatory	3.21	Oscillatory	3.47	Oscillatory	3.67	Oscillatory
D1.5H-K20 to K2	Horizontal	1.5825	3.09	Oscillatory	3.4	Oscillatory	3.59	Oscillatory	3.73	Oscillatory
D2.0H-K20 to K2	Horizontal	2.088	3.5	Oscillatory	3.88	Oscillatory	4.03	Oscillatory	4.13	Oscillatory
D2.5H-K20 to K2	Horizontal	2.592	3.39	Oscillatory	3.77	Oscillatory	4.09	Oscillatory	4.57	Oscillatory
D3.0H-K20 to K2	Horizontal	3.0932	3.54	Oscillatory	3.89	Oscillatory	4.02	Oscillatory	4.19	Oscillatory

TABLE 9.29. RESULTS OBTAINED BY MCMASTER UNIVERSITY AND GRNSPG WITH RELAP5 FOR THE INSTABILITY THRESHOLD

McMaster/GRNSPG-RELAP5/Mod3.3			Kout=20	Kout=20	Kout=10	Kout=10	Kout=5	Kout=5	Kout=2	Kout=2
Case	Channel orientation	Nspc	Ntpc. threshold	Type of instability	Ntpc. threshold	Type of instability	Ntpc. threshold	Type of instability	Ntpc. threshold	Type of instability
Label				Oscillatory or Excursive		Oscillatory or Excursive		Oscillatory or Excursive		Oscillatory or Excursive
D0.0V-K20 to K2	Vertical	0	7.33	Oscillatory	No Oscillation	Oscillatory	No Oscillation		No Oscillation	
D0.5V-K20 to K2	Vertical	0.555	3.58	Oscillatory	4.11	Oscillatory	5.81	Oscillatory	6.96	Oscillatory
D1.0V-K20 to K2	Vertical	1.0733	3.07	Oscillatory	3.77	Oscillatory	4.35	Oscillatory	5.23	Oscillatory
D1.5V-K20 to K2	Vertical	1.5825	3.32	Oscillatory	3.8	Oscillatory	4.45	Oscillatory	4.91	Oscillatory
D2.0V-K20 to K2	Vertical	2.088	3.63	Oscillatory	4.06	Oscillatory	4.56	Oscillatory	5.13	Oscillatory
D2.5V-K20 to K2	Vertical	2.592	4.19	Oscillatory	4.49	Oscillatory	5.14	Oscillatory	5.6	Oscillatory
D3.0V-K20 to K2	Vertical	3.0932	3.89	Oscillatory	5.05	Oscillatory	5.6	Oscillatory	6.06	Oscillatory

McMaster/GRNSPG-RELAP5/Mod3.3			Kout=20	Kout=20	Kout=10	Kout=10	Kout=5	Kout=5	Kout=2	Kout=2
Case	Channel orientation	Nspc	Ntpc. threshold	Type of instability	Ntpc. threshold	Type of instability	Ntpc. threshold	Type of instability	Ntpc. threshold	Type of instability
Label				Oscillatory or Excursive		Oscillatory or Excursive		Oscillatory or Excursive		Oscillatory or Excursive
D0.0H-K20 to K2	Horizontal	0	7.33	Oscillatory	No Oscillation		No Oscillation		No Oscillation	
D0.5H-K20 to K2	Horizontal	0.555	3.51	Oscillatory	4.71	Oscillatory	5.61	Oscillatory	6.98	Oscillatory
D1.0H-K20 to K2	Horizontal	1.0733	3.04	Oscillatory	3.62	Oscillatory	4.3	Oscillatory	5.07	Oscillatory
D1.5H-K20 to K2	Horizontal	1.5825	3.29	Oscillatory	3.71	Oscillatory	4.29	Oscillatory	4.89	Oscillatory
D2.0H-K20 to K2	Horizontal	2.088	3.63	Oscillatory	3.99	Oscillatory	4.51	Oscillatory	5.11	Oscillatory
D2.5H-K20 to K2	Horizontal	2.592	3.58	Oscillatory	4.5	Oscillatory	5.01	Oscillatory	5.54	Oscillatory
D3.0H-K20 to K2	Horizontal	3.0932	3.58	Oscillatory	4.14	Oscillatory	5.5	Oscillatory	6.24	Oscillatory

9.2.4.14. Comments by McMaster University and GRNSPG

The proposed results qualitatively match with the Reference data. The small number of axial cells can be the limiting factor that affects more the discrepancies between the results and the reference data, due to the truncation error. To verify this statement the same procedure followed for this analysis should be repeated for RELAP5.33 and TRACE5.0 using a model with 48 cells as used in the preparation of the reference data. The compressibility effect that could arise by using inlet and outlet plena should be also addressed performing the calculations with a different volume of the two components. Notwithstanding the discrepancies between our and the reference results, the adopted non-dimensional parameters look promising to assess the stability boundaries for this kind of problems.

9.2.5. Conclusions for the code testing benchmark on flow stability

9.2.5.1. Significance of the exercise and of the reference data

The results generated by the University of Pisa, being obtained by models whose performance is affected by specific choices in the basic assumptions and modelling techniques, in similarity with those adopted by Participants, cannot be considered exact. Nevertheless, the use of three relatively independent codes and the sensitivity analyses performed in relation to different aspects provided a reasonable assurance about data adequacy, as a consequence of the good match obtained among their results. Moreover, the predictions by JRC-IE with RELAP5 and by BARC with NOLSTA actually provided additional confirmation of the reference data.

It must be anyway considered that the three codes adopted by the University of Pisa to generate the reference data make use of the standard closure relationships normally available in present system codes for single-phase fluid and specifically qualified for water at subcritical pressures. This represents an unavoidable limitation of the present exercise, which has therefore the significance of a code-to-code comparison.

In this regard, among the various submissions showing different degrees of agreement with respect to the reference data, the ones by VTT allowed interesting reflections about the applicability of general models implemented nowadays in system codes to the specific case of supercritical pressure fluids, with main regard to friction correlations. As the two applications and the interesting sensitivity studies by VTT clearly showed, correlations for friction with supercritical fluids do exist in literature, though they are presently not available in many codes, being purposely implemented in APROS. Unavoidably, different friction correlations provide different stability results, posing the problem of the applicability of the reference data to real supercritical fluid conditions.

On the other hand, heat transfer correlations should have in principle little role in the present exercise, since heat flux at the wall is assigned no matter the wall and fluid temperature. However, it must be recognized that the local heat transfer coefficient determines the wall temperature which has, in turn, an effect on friction factors through the property ratios appearing in many correlations accredited for supercritical fluids.

In this respect, a study on friction factor correlations for supercritical fluids developed at the University of Pisa, also using a CFD code, highlighted interesting problems [9-60]. In particular, the following considerations from this study are relevant for the present discussion:

- the application of correlations for friction with supercritical fluids requires an accurate evaluation of wall temperature and, therefore, of heat transfer; considering the present difficulty in correctly predicting heat transfer deterioration with engineering correlations or CFD models, estimating friction can be therefore regarded as a relatively challenging task;

- on the other hand, most of the available correlations for friction at supercritical conditions are developed with reference to smooth tube conditions, where the dependence on the Reynolds number is considerable; little information is instead available on rough tubes that at large Reynolds number should be characterized by friction factors relatively independent of fluid properties;
- finally, it is suggested that in the liquid-like and the gas-like conditions, where property variations are milder, classical relationships for friction factor (e.g., the mentioned Colebrook one) are applicable, while major discrepancies occur in the region across the pseudo-critical temperature.

This situation makes the evaluation of friction factors in supercritical pressure conditions still uncertain on the basis of present knowledge and, considering the influence of this parameter on stability, it is expected that a corresponding uncertainty is induced in stability predictions. It is therefore clear that only experimental data may provide the further assessment that is necessary to decide about the physical adequacy of code predictions about stability, in the light of the specific constitutive laws that should be included in system codes to make them effectively applicable to fluids at supercritical pressure.

Another interesting aspect is pointed out by the additional analyses performed by JRC-IE on the effect of a bottom-skewed power profile similar to those that could be observed in a real reactor under some operating conditions. Expectedly, stability is decreased in similarity with what happens in boiling channels, since the length of the channel at higher fluid speed is increased, giving greater importance to delays in the effect of inlet flow on the overall pressure drop. This highlights another simplification included in generating the reference data that must be attentively considered.

Another important aspect to be considered in practical applications, which was neglected in the present analysis, is the effect of heating structure capacitance on dynamic stability mechanisms. This suggests prudence in extrapolating results of this and similar analyses on stability to reactor conditions.

In summary, though the performed exercise cannot have the pretence to propose data having an absolute physical reliability, it clearly showed what standard models presently available in codes can propose when reasonably free from too heavy simplifying assumptions or numerical effects. The effort of the Participants made possible the success of the exercise in joining the efforts to obtain a first code-to-code comparison in relation to the important issue of SCWR stability.

9.2.5.2. Code-to-code comparison aspects

As a whole, the received submissions show a general capability of the adopted codes in predicting the stability thresholds coherently with the reference data. The observed discrepancies can be mostly justified on the basis of the assumptions adopted in the models.

Some features that are common to most of the submissions and to the reference data are related to the following aspects:

- the presence of oscillating as well as excursive instabilities, the latter occurring at relatively low inlet temperature, in regions that would be hopefully of little interest to nuclear reactor operation; in particular, the results of most of the submissions in the benchmark exercise agree qualitatively in the fact that there is a lower lobe of density wave instability and an upper lobe of excursive instability in the $N_{TPC} - N_{SPC}$ plane;
- the well-known effect of outlet throttling in determining lower stability of heated channels with strong density differences, that is clearly observed in all the submissions; in particular, outlet throttling increases the extension of the region of density wave instabilities and also enhances the chances of incurring into excursive instability;
- the substantial equality of the stability threshold for density wave instability in vertical and

horizontal channels, whereas horizontal channels are found more prone to excursive instabilities;
- the larger stable zone predicted by many codes in the density wave region;
- the decreasing value of the ratio of the transit time to the period of oscillations with increasing pseudo-subcooling.

9.2.5.3. Fluid-to-fluid comparison

Only a limited application to the fluid-to-fluid part of the exercise was performed by Participants. This is mainly due to the unavailability of versions of the adopted codes addressing fluids other than water. Nevertheless, the interesting application by the University of Manitoba and AECL actually considered water at different pressures, as suggested in the problem specifications, and also CO_2, showing similar stability thresholds in the proposed dimensionless formalism, as predicted by the reference data.

9.2.5.4. Dimensionless parameters for stability analyses

Two of the presently available proposals for dimensionless numbers to be adopted in stability analyses for supercritical fluids were adopted in data presentation.

In particular, the formulations proposed by [9-39] and [9-38] were suggested for use in the benchmark and all the submissions made use of them to represent data. Moreover, the formalism adopted by the University of Manitoba and AECL represented a very interesting contribution, owing to the unique trend found for the stability threshold for very different operating conditions.
Both the proposals look promising and further study is required to clarify the potential of each proposed set of parameters and its possible optimization.

9.2.5.5. Future developments

The present Code Testing Benchmark represents a first step in the activities related to flow stability analysis that the Participants in the CRP have the potential to jointly perform. The lesson learned from this first step will be certainly valuable in coordinating further efforts that, in a possible extension of the present CRP, should be devoted to analyse experimental data that will be hopefully made available from ongoing studies.

LIST OF SYMBOLS FOR SECTION 9

Latin Letters

A	cross section area [m^2]
Ac^*	acceleration parameter
Bo^*	buoyancy parameter
C_p	specific heat at constant pressure [J/(kgK)]
C_{max}	maximum Courant number
D_h	hydraulic diameter [m]
f	Darcy-Weisbach friction factor
$f_q(z)$	normalized distribution of heat flux
Fr	Froude number
g	gravity [m/s^2]
G	mass velocity [$kg/(m^2s)$] or mass flow rate [kg/s]
Gr^*	Grashof number
h	fluid specific enthalpy [J/kg]
j	volumetric flux [m/s]
K_{in}	localized pressure drop coefficient at the channel inlet
K_{out}	localized pressure drop coefficient at the channel outlet
L	channel length [m]
$\dot{m}$	mass flow rate [kg/s]
N_{nodes}	number of nodes
N_{SPC}	sub-pseudo-critical number
N'_{TPC}, N_{TPC}	apparent and true trans-pseudo-critical numbers
p	pressure [Pa]
Pr	Prandtl number
q or q''	heat flux [W/m^2]
$\dot{Q}$	power [W]
$\widehat{Q}$	dimensionless parameter defined by Chatoorgoon (see the definintion in the text)
Q_b^*	thermal expansion parameter
Re	Reynolds number
t	time [s]
T	period of oscillations [s]
T_{trans}	transit time [s]
T_w^{exp}	experimental value of wall temperature [°C]
$\hat{T}_w^{com}$	computed value of wall temperature in thermocouple location point [°C]
v	specific volume [m^3/kg]
w	velocity [m/s]
W	mass flow rate [kg/s]
x or z	axial coordinate along the channel [m]
z_I	imaginary part of a complex exponent

z_R	real part of a complex exponent

Greek Letters

β	isobaric thermal expansion coefficient [K^{-1}]
γ	dimensionless parameter defined by Chatoorgoon (see the definintion in the text)
δ_d	dimensional Dirac delta function [m^{-1}]
δ^*	dimensionless Dirac delta function
δT_w	relative difference between experimental and computed values of pipe wall temperature.
ε	surface roughness [m]
θ	dimensionless parameter defined by Chatoorgoon (see the definintion in the text)
ξ	dimensionless parameter defined by Chatoorgoon (see the definintion in the text)
Λ	friction dimensionless group (Euler number)
Π_h	heated perimeter [m]
ρ	density [kg/m^3]

Subscripts

b	bulk
channel	channel
com	computed
e	exit
exp	experimental
f	saturated liquid
g	saturated vapour (steam)
fg	difference between saturated vapour and saturated liquid
heating	heating
i	inlet
in	inlet
out	outlet
p	constant pressure
pc	pseudo-critical
w	wall
0	reference value

Superscripts

*	starred variables indicate dimensionless values

REFERENCES FOR SECTION 9

[9-1] KIRILLOV, P., POMET'KO, R., SMIRNOV, A., GRABEZHNAIA, V., PIORO, I., DUFFEY, R., KHARTABIL, H., Experimental Study on Heat Transfer to Supercritical Water Flowing in 1- and 4-m-Long Vertical Tubes. Proceedings of GLOBAL 2005, Tsukuba, Japan, Oct. 9–13, 2005, Paper No. 518 (2005).

[9-2] WATTS, M.J., "Heat Transfer to Supercritical Pressure Water: Mixed Convection With Upflow or Downflow in a Vertical Tube" *PhD Thesis*, University of Manchester (1980).

[9-3] HANNA, B.N., CATHENA: A thermalhydraulic code for CANDU analysis, Nuclear Engineering and Design (180) (1998) 113–131.

[9-4] LINER, Y., HANNA, B.N., RICHARDS, D.J., Piecewise Hermite Polynomial Approximation of Liquid-Vapour Thermodynamic Properties, In Fundamentals of Gas-Liquid Flow, 72, (1988) 99–102.

[9-5] WAGNER, W., PRUß, A., The IAWPS Formulation 1995 for the Thermodynamic Properties of Ordinary Water Substance for General and Scientific Use, Journal of Physical and Chemical Reference Data, Vol. 31, No. 2 (2002) 387–535.

[9-6] YAGOV, P.V., CHURKIN, A.N., MOKHOV, V.A., Computer code TEMPA-SC and first experience of its application // Scientific and Technical Seminar on Reactors With Supercritical Parameters of Water, 6-7 September 2007, IPPI, Obninsk (2007) 151–160.

[9-7] CHURKIN, A.N., YAGOV, P.V., MOKHOV, V.A., SHCHEKIN, I.G., Computer code TEMPA-SC: simulation of thermal-hydraulic processes in the core of VVER-SCP reactor // 4th International Symposium on Supercritical Water-Cooled Reactors, March 8–11, 2009, Heidelberg, Germany, Paper No. 02 (http://www.hplwr.eu/public/Symposium/Proceedings_01-20.zip) (2009).

[9-8] CHURKIN, A.N., Mathematical simulation of processes of heat-and-mass transfer in the heating rods bundle, Abstract of Ph.D. Thesis, OKB GIDROPRESS (2006).

[9-9] KIRILLOV, P.L., YUR'EV, YU.S., BOBKOV, V.P., Handbook of Thermal-Hydraulics Calculations, (In Russian), Energoatomizdat Publishing House, Moscow, Russia (1990).

[9-10] JACKSON, J.D., Fewster, J., Forced Convection Data for Supercritical Pressure Fluids. HTFS 21540 (1975).

[9-11] JACKSON, J.D., Consideration of Heat Transfer Properties of Supercritical Pressure Water in Connection with the Cooling of Advanced Nuclear Reactors. Proc. of the 13th Pacific Basin Nuclear Conf., Shenzhen City, China, Oct. 21–25 (2002).

[9-12] KRASNOSHCHEKOV, E.A., PROTOPOPOV, V.S., 1960. About heat transfer in flow of carbon dioxide and water at supercritical region of state parameters, (In Russian), Thermal Engineering (Теплоэнергетика, стр. 94), No. 10 (1960) 94.

[9-13] KRASNOSHCHEKOV, E.A., PROTOPOPOV, V.S., VAN, F., KURAEVA, I.V., 1967. Experimental investigation of heat transfer for carbon dioxide in the supercritical region, Proceedings of the 2nd All-Soviet Union Conference on Heat and Mass Transfer, Minsk, Belarus', May, 1964, Published as Rand Report R-451-PR, Edited by C. Gazley, Jr., J.P. Hartnett and E.R.C. Ecker, Vol. 1 (1967) 26–35.

[9-14] BASILE, D., BEGHI, M., CHIERICI, R., SALINA, E., BREGA, E., 1999. COBRA-EN: an Upgraded Version of the COBRA-3C/MIT Code for Thermal Hydraulic Transient Analysis of Light Water Reactor Fuel Assemblies and Cores. Report 1010/1, ENELCRTN, Milano.

[9-15] CHENG, X., SCHULENBERG, T., Heat transfer at supercritical pressures—literature review and application to an HPLWR, Scientific report FZKA 6609, FzK (2001).

[9-16] PIORO I., DUFFEY R., Experimental Heat Transfer to Supercritical Water Flowing inside Channels (Survey), Nuclear Engineering and Design, 235(22) (2005) 2407–2430.

[9-17] RELAP5/MOD3.3 Code Manual, Volume I: Code Structure, System models and Solution Methods. Nuclear Safety Analysis Division, Rockville, Maryland, March (2003).

[9-18] TRACE V5.0 Theory Manual: Field Equations, Solution Methods and Physical Models. Division of Safety Analysis, Office of Nuclear Regulatory Commission, Washington DC 20555-0001.
[9-19] HÄNNINEN, M. & YLIJOKI, J., The one-dimensional separate two-phase flow model of APROS, VTT Research Notes 2443, VTT Technical Research Centre of Finland (2008).
[9-20] VAIDYA, A.M., MAHESHWARI, N.K., VIJAYAN, P.K., SAHA, D., Development, validation and application of NAFA 2D-CFD code, BARC/2010/E/001, Bhabha Atomic Research Centre Mumbai, India (2010).
[9-21] FLUENT INC., Fluent 6.3 User's Guide, Fluent Incorporated, Lebanon, NH (2006).
[9-22] HE, S., KIM, W.S., JIANG, P.X., JACKSON, J.D., Mixed convection heat transfer to carbon dioxide at supercritical pressure comparisons between experiments and computational simulations using advanced turbulence models, Proceedings of the 7th UK National Heat Transfer Conference, Oxford, 9–10 September (2003).
[9-23] NAKATSUKA, T., EZATO, K., MISAWA, T., SEKI, Y., YOSHIDA, H., DAIRAKU, M., SUZUKI, S., ENOEDA, M., TAKASE, K., Assessment of Applicability of Two-Fluid Model Code ACE-3D to Heat Transfer Test of Supercritical Water Flowing in an Annular Channel, Journal of Nuclear Science and Technology, Vol. 47, Issue 12 (2010) 1118–1123.
[9-24] YAMAGATA, K., NISHIKAWA, K., HASEGAWA, S., FUJII, T., YOSHIDA, S., Forced Convective Heat Transfer to Supercritical Water Flowing in Tubes, International Journal of Heat and Mass Transfer, Vol. 15 (1972) 2575–2593.
[9-25] STYRIKOVICH, M.A., MORGULOVA, T.H., MIROPOL'SKII, Z.L., Vital problems of development of Supercritical boiler (in Russian), J. of Thermal physics of high temperature, v.16, No.4 (1978) 778–790.
[9-26] MOKRY, S., FARAH, A., KING, K., GUPTA, S., PIORO, I., Development of Supercritical Water Heat-Transfer Correlation for Vertical Bare Tubes, International Conference Nuclear Energy for New Europe, Bled, Slovenia, September (2009).
[9-27] CHENG, X., SCHULENBERG, T., Heat Transfer at Supercritical Pressures – Literature Review and Application to an HPLWR, FZKA 6609, Forschungszentrum Karlsruhe GmbH, Karlsruhe 2001.
[9-28] JACKSON, J.D., Validation of an extended heat transfer equation for fluids at supercritical pressure, 4th International Symposium on Supercritical Water-Cooled Reactors, March 8–11, 2009, Heidelberg, Germany, Paper No. 24 (2009).
[9-29] STYRIKOVICH, M.A., MARGULOVA, T.KH., MIROPOL'SKII, Z.L., Problems in the Development of Designs of Supercritical boilers, Thermal Engineering, volume 14, No 6 (1967) 5–9.
[9-30] YI, T.T., KOSHIZUKA, S., OKA, Y., A Linear Stability Analysis of Supercritical Water Reactors, (I) Thermal-Hydraulic Stability, Journal of Nuclear Science and Technology, 41 (2004) 1166–1175 (2004).
[9-31] YI, T.T., KOSHIZUKA, S., OKA, Y., 2004, A Linear Stability Analysis of Supercritical Water Reactors, (II) Coupled Neutronic Thermal-Hydraulic Stability, Journal of Nuclear Science and Technology, 41 (2004) 1176–1186.
[9-32] ZHAO, J., SAHA, P., KAZIMI, M.S., 2008, Core-wide (in-phase) stability of supercritical water-cooled reactors - I: Sensitivity to design and operating conditions, Nuclear Technology Volume 161, Issue 2, February (2008) 108–123.
[9-33] ZHAO, J., SAHA, P., KAZIMI, M.S., 2008, Core-wide (in-phase) stability of supercritical wayer-cooled reactors - II: Comparison with boiling water reactors, Nuclear Technology, Volume 161, Issue 2, February (2008) 124–139.
[9-34] ZHAO, J., SAHA, P., KAZIMI, M.S., Coupled neutronic and thermal-hydraulic out-of-phase stability of supercritical water-cooled reactors, Nuclear Technology, Volume 164, Issue 1, October 2008 (2008) 20–33.

[9-35] AMBROSINI, W., Specifications for a Benchmark Exercise on Flow Stability in Heated Channels with Supercritical Fluids, University of Pisa, Italy, DIMNP RL 1214(2009) Rev. 3, Pisa, March 16th 2010 (2009).
[9-36] AMBROSINI, W., 2010, Quick Look Report on the Results of the Flow Stability Benchmark, IAEA Coordinated Research Programme on Heat Transfer Behaviour and Thermohydraulics Codes Testing for SCWRs, University of Pisa, Italy, DIMNP RL 1251(2010), Pisa, May 14th, (2010).
[9-37] SHARABI, M.B., AMBROSINI, W., He, S., Prediction of unstable behaviour in a heated channel with water at supercritical pressure by CFD models, Annals of Nuclear Energy, 35 (2008) 767–782.
[9-38] AMBROSINI, W., Discussion on the Stability of Heated Channels with Different Fluids at Supercritical Pressures, Nuclear Engineering and Design, 239 (2009) 2952–2963.
[9-39] AMBROSINI, W., SHARABI, M., Dimensionless Parameters in Stability Analysis of Heated Channels with Fluids at Supercritical Pressures, Proceedings of ICONE 14, 14th International Conference on Nuclear Engineering, July 17–20, 2006, Miami, Florida USA (2006).
[9-40] AMBROSINI, W., SHARABI, M., Dimensionless Parameters in Stability Analysis of Heated Channels with Fluids at Supercritical Pressures, Nuclear Engineering and Design 238 (2008) 1917–1929.
[9-41] ZHAO, J., SAHA, P., KAZIMI, M.S., Stability of supercritical water-cooled reactor during steady-state and sliding pressure start-up. In: Proceedings of NURETH-11, Avignon, France (2005).
[9-42] ORTEGA GÓMEZ, T., CLASS, A., LAHEY JR., R.T., SCHULENBERG, T., Stability analysis of a uniformly heated channel with supercritical water, Nuclear Engineering and Design 238 (2008) 1930–1939.
[9-43] CHATOORGOON, V., YEYLAGHI, S., (UNIVERSITY OF MANITOBA), LEUNG L., (AECL), Benchmarking Study of Non-Dimensional Parameters For Supercritical Flow Instability, Submitted for the IAEA Benchmark on Flow Stability (2010).
[9-44] CHATOORGOON, V., Supercritical Flow Stability in Two Parallel Channels, Proceedings of ICONE 14, 14th International Conference on Nuclear Engineering, July 17–20, 2006, Miami, Florida USA (2006).
[9-45] CHATOORGOON, V, Static Instability in Supercritical Parallel-Channel Systems, Proceedings of Int. Conf. of Nuclear Engineering, ICONE 16-48068, May 11–15, Orlando, Florida (2008).
[9-46] AMBROSINI, W., Reference Data for a Benchmark Exercise on Flow Stability in Heated Channels with Supercritical Fluids for the IAEA Coordinated Research Programme on Heat Transfer Behaviour and Thermohydraulics Codes Testing for SCWRs, University of Pisa, Italy, DIMNP RL 1246(2010), March 16th (2010).
[9-47] SCIENTECH. Inc., Code structure system models and solution methods. RELAP5/Mod3 Code Manual, June 1999, vol. 1. The Thermal Hydraulics Group, Idaho (1999).
[9-48] NIST 2002, REFPROP, NIST Standard Reference Database 23, Version 7.0.
[9-49] HÄNNINEN, M., KURKI, J., Computational benchmark 'Exercise on Flow Stability in Heated Channels with Supercritical Fluids' with APROS, VTT Technical Research Center of Finland, Submitted for the IAEA Benchmark on Flow Stability (2010).
[9-50] SHARMA, M., VIJAYAN, P.K., PILKHWAL, D.S., SAHA, D., Benchmark Exercise on Flow Stability in Heated Channels with Supercritical Fluids, Reactor Engineering Division, Bhabha Atomic Research Centre, Trombay, Mumbai, 40085, India, Submitted for the IAEA Benchmark on Flow Stability (2010).
[9-51] SHARMA, M., VIJAYAN, P.K., PILKHWAL, D.S., SAHA, D., SINHA, R.K., Linear and non-linear stability analysis of a supercritical natural circulation loop, ASME Journal of Engineering for Gas Turbines and Power, October 2010, Vol. 132 / 102904-1 (2010).
[9-52] AMMIRABILE, L., IAEA CRP on Heat Transfer Behaviour and Thermohydraulics Codes Testing for SCWRs Benchmark Exercise #2, 'Benchmark Exercise on Flow Stability in Heated

Channels with Supercritical Fluids', JRC-IE Report, Submitted for the Benchmark on Flow Stability (2010).
[9-53] AMBROSINI, W., DI MARCO, P., FERRERI, J.C., Linear and Non-Linear Analysis of Density-Wave Instability Phenomena, International Journal of Heat and Technology, Vol. 18, No. 1, 2000, pp. 27–36 (2000).
[9-54] AMBROSINI, W., FERRERI J.C., Analysis of Basic Phenomena in Boiling Channel Instabilities with Different flow Models and Numerical Schemes, Proceedings of ICONE 14, 14th International Conference on Nuclear Engineering, July 17–20, Miami, Florida USA (2006).
[9-55] TSIGE-TAMIRAT, H., AMMIRABILE, L., FÜTTERER, M.A., On use of hydride fuel in HPLWR, Proc. 4th International Symposium on Supercritical Water-Cooled Reactors, March 8-11, Heidelberg, Germany (2009).
[9-56] AMMIRABILE L., Studies on supercritical water reactor fuel assemblies using the sub-channel code COBRA-EN. Nuclear Engineering and Design 240 (2010) 3087–3094.
[9-57] CHURKIN, A.N., Computer code TEMPA-SC: Computational results of the Benchmark Exercise on Flow Stability in Heated Channels with Supercritical Fluids, OKB GIDROPRESS, Ordzhonikidze st., 21, Podolsk, Russian Federation, 142103, Submitted for the IAEA Benchmark on Flow Stability.
[9-58] FIORI, F., NOVOG, D.R., PETRUZZI, A. , 2010a, Benchmark Exercise on Flow Stability in Heated Channels with Supercritical Fluid: TRACE5.0 patch1.0 results report, Submitted for the Benchmark on Flow Stability (2010).
[9-59] FIORI, F., NOVOG, D.R., PETRUZZI, A. , 2010b, Benchmark Exercise on Flow Stability in Heated Channels with Supercritical Fluid: RELAP5/Mod3.3 results report, Submitted for the Benchmark on Flow Stability (2010).
[9-60] ANGELUCCI, M., Perdite di carico per attrito in fluidi a pressione supercritica: analisi bibliografica e applicazioni di CFD, Tesi di Laurea in Ingegneria della Sicurezza Nucleare e Industriale, Anno Accademico (2010) 2010–2011.

10. CONCLUDING REMARKS

In view of the high interest in a number of Member States in the Supercritical Water Cooled Reactor (SCWR) concept, the IAEA has established this Coordinated Research Project (CRP) on Heat Transfer Behaviour and Thermohydraulics Code Testing for Supercritical Water Cooled Reactors (SCWRs) to exchange and share information on thermal-hydraulics of SCWRs and foster research and development in Member States. A key outcome is the publication of this Technical Document (TECDOC) synthesizing the results and technology advancements achieved under the framework of the CRP. The content is based on work done and related activities carried out between July 2008 to September 2012 by fourteen (14) institutes from 9 Member States and two international organizations participating in the CRP.

The two key objectives of the CRP are:

1) To establish a base of accurate data of heat transfer, pressure drop, blowdown, natural circulation and stability for conditions relevant to supercritical fluids; and
2) To test analysis methods for SCWR thermohydraulic behaviour, and identify code development needs.

Detailed conclusions and recommendations are provided in each of the related sections. A short summary is provided in generic form in this section.

A considerable amount of experimental data has been contributed to establish a database of thermal-hydraulics for supercritical fluids. This database is hosted by the OECD/NEA and has facilitated data exchange among the participating institutes, fostered collaboration and accelerated research and development.

Design parameters of several SCWR design concepts under development are collected and shared to identity the ranges of interest. One of these concepts evolves from the pressurized heavy-water reactor design and others from the light water reactor designs, but the thermal-hydraulics parameter ranges are found to be almost similar. All design concepts utilize the once-through reactor coolant system and the direct thermal cycle that leads to design simplification and cost reduction. Their thermal efficiencies are higher than 43%.

Existing heat transfer data for supercritical pressure fluids are collected, shared and analysed. Accurate predictions of heat transfer coefficient are necessary to estimate fuel cladding temperatures of the SCWR core, which will exceed 700 deg C. Large amounts of experimental data are available for vertical upward flow of water and surrogate fluids in tubes. These data cover a wide range of flow conditions. However, the amount of data is still limited for conditions relevant to current SCWR design concepts.

In addition, existing pressure drop data of supercritical pressure fluids are collected, shared and analysed. Pressure drop calculations are needed in design and safety analyses, which could be difficult in the SCWR core region due to the steep changes of fluid properties in the vicinity of the pseudo-critical point. A number of friction factor equations have been reported in literature, but information about surface roughness effects is not available.

Information on available test facilities for supercritical fluid heat transfer experiments has been collected and shared. Most of these facilities have relatively small capacity and hence are only suitable for experiments with simple test sections and small bundle subassemblies. A new water test facility and two surrogate-fluid test facilities have recently been constructed. Data from these facilities will be essential for validating subchannel and computational fluid dynamics codes.

Several new heat transfer prediction methods have recently been developed and are described in this report. The heat transfer database has been utilized for the assessment of correlations and the development

of a look-up table. One of the new correlations combines simplicity of structure and explicit connection with physically-based phenomena. An evaluation is presented of four mixed convection heat transfer correlations. Two physically-based, semi-empirical models are presented.

An overview on critical flow during depressurization from supercritical conditions is provided. Depressurization transients from supercritical to subcritical water conditions represent a challenge for system codes in terms of physics and numerical methods. Two experiments have been performed and the data have been incorporated into the database. Additional experiments have been planned to expand the database. There is a need for further work in this area to validate the models against the new experimental data near and above the pseudo-critical point.

Flow stability and natural circulation with fluids at supercritical pressure were studied. Supercritical pressure fluid flow can be unstable due to the drastic change of density across the pseudo-critical point, in straight channels and in natural circulation loops. Experiments on natural circulation of supercritical water have been performed in two participating institutes. The experimental data show that complex phenomena occur even in simple geometries, requiring the improvement of prediction techniques.

Two code-testing benchmark (CTB) excercises were prepared and have been performed under the framework of this CRP. The title of CTB No. 1 is 'Steady State Flow in a Heated Pipe' and it is aimed at assessing code capabilities in the prediction of heat transfer against experimental data. The title of CTB No. 2 is 'Flow Stability' and it is aimed at performing a code-to-code comparison of flow stability predictions. Relatively simple cases were considered as benchmark conditions; however, the results obtained provided a clear perspective of the present capabilities and challenges of currently available codes.

In addition, further activities have been initiated or supported:

- A Technical Meeting on Heat transfer, Thermal-hydraulics and System Design for SCWRs was held in 2010 and attended by 54 participants from 17 Member States;
- The IAEA training courses on Science and Technology of Supercritical Water-cooled Reactors were held in 2011 and 2012 with major contributions from several experts participating in the CRP.

Many joint papers by CRP participants were presented at international conferences and published in journals.

The objectives of the CRP have been fully met. However, international collaboration established by this CRP needs to be continued in light of excellent perspectives for future works identified in the CRP. Several bi-lateral or multi-lateral collaborations are already in progress as a result of the cooperation between CRP participants in several areas and may constitute a valuable future product of the efforts.

ABBREVIATIONS

ABWR	advanced boiling water reactor
AC	alternate current
ACC	accumulator
ADS	automatic depressurization system
AFS	auxiliary feedwater system
APC	average pressure cylinder
APROS	advanced process simulator
ATWS	anticipated transient without scram
BN	fast sodium (type of reactors)
BNA	burnable neutron absorber
BOC	beginning of cycle
BOP	balance of plant
BRU	steam dump valve
BWR	boiling water reactor
CAMP	code application and maintenance program
CANDU®	Canada deuterium uranium (a registered trademark of Atomic Energy of Canada Limited)
CANFLEX	CANDU flexible (a registered trademark of AECL and KAERI)
CATHARE	code for analysis of thermal hydraulics during an accident of reactor and safety evaluation
CECS	containment external cooling system
CFD	computational fluid dynamics
CHF	critical heat flux
CL	cold leg
CPS CR	control and protection system control rod
CR	control rod
CSS	containment spray system
CTB	code testing benchmarks
D	deaerator
DAS	data acquisition system
DC	direct current
D_2O	heavy water
DVI	direct vessel injection
ECCS	emergency core cooling system

EOC	end of cycle
ESBWR	economic simplified boiling water reactor
FA	fuel assembly
FR	fuel rod
FW	feedwater
FWP	feedwater pump
Gd	Gadolinium
Gd_2O_3	Gadolinia
GDCA	gravity driven cooling system
GIF	Generation-IV International Forum
H_2O	light water
HA	hydro-accumulator
HEC	high efficiency channel
HEM	homogeneous equilibrium model
Hg	mercury
HL	hot leg
HP	high pressure
HP/LP-FWH	high pressure and low pressure feedwater heater
HPC	high pressure cylinder
HP-CP	high pressure condensate pump
HPH	high pressure heater
HPL	high pressure loop
HPLWR	high performance light water reactor
HPT	high pressure turbine
HTP	high temperature pump
HTS	heat transport system
HWR	heavy water reactor
HX	heat exchanger
ICCS	ICS cooling system
ICS	isolation condenser system
ID	inside diameter
IP	intermediate pressure
IPT	intermediate pressure turbine
IRP	integrated research plan
JSCWR	Japan SCWR
LER	linear element rating

LMZ	Leningrad engineering plant
LOCA	loss of coolant accident
LP	low pressure
LPC	low pressure cylinder
LPCI	low pressure core injection
LP-CP	low pressure condensate pump
LPH	low pressure heater
LPT	low pressure turbine
LWR	light water reactor
M-HEM	modified homogeneous equilibrium model
MOC	middle of cycle
MOX	mixed oxide
MPL	medium pressure loop
MSIV	main steam isolation valve
MSR	moisture separator reheater
MSV	main steam valve
NCL	natural convection loop
NU	natural uranium
ODS	oxide dispersion strengthened
PCFS	passive core flooding system
PH	preheater
PHRS	passive heat removal system
PHWR	pressurized heavy water reactor
PMB	project management board
POAK	prototype-of-a-kind
PORV	pilot-operated relief valve
PPDS	passive pressure decrease system
PPF	power peaking factor
PSV	pressure relieve valve
PT	pressure tube
Pu	plutonium
PV	pressure vessel
PWR	pressurized water reactor
R&D	research and development
RB	reactor building
RCCA	rod cluster control assembly

RELAP5	reactor leak analysis program
RFP	reactor feedwater pump
RFSP	reactor fuelling simulation program
RHR	residual heat removal
RP	reactor plant
RPV	reactor pressure vessel
RRC	Russian research center
RSW	reactor service water
RTD	resistance temperature detectors
S	separator
SCF	supercritical fluid
SCHT	supercritical pressure heat transfer
S-CO_2	supercritical CO_2
SCP	supercritical pressure
SCW	supercritical water
SCWR	supercritical water cooled reactor
SH	superheater
SLCS	standby liquid control system
SMOFTH	supercritical model fluids thermal hydraulics
SPCS	suppression pool cooling system
SPHINX	supercritical pressure heat transfer investigation for next generation
SPSS	suppression pool spray system
SRP	system research plan
SRV	safety relieve valve
SS	stainless steel
SWAMUP	supercritical water multi purpose
TCW	turbine building cooling water system
Th	thorium
TS	temperature - entropy
TSW	turbine building sea water system
TVS-2M	identifier of FA design
TWG	technical working group
TYP	type
UO_2	uranium oxide
USC	ultra-super-critical
VHP	very high pressure

VVER	water cooled, water moderated power reactor
VVER-SCP	water cooled, water moderated power reactor at supercritical pressures
WIMS	Winfrith improved multigroup scheme
YSZ	yttrium-stabilized zirconia
ZrH, ZrH_2	zirconium hydride

CONTRIBUTORS TO DRAFTING AND REVIEW

Aksan, N.	Paul Scherrer Institute, Switzerland
Ambrosini, W.	Universitá di Pisa, Italy
Ammirabile, L	European Commission - Joint Research Centre (EC-JRC), Netherlands
Anderson, M.	University of Wisconsin – Madison, USA
Bae, Y.-Y.	Korea Atomic Energy Research Institute (KAERI), Republic of Korea
Chen, Y.	China Institute of Atomic Energy (CIAE), China
Churkin, A.	OKB GIDROPRESS, Russian Federation
Haenninen, M.J.	VTT Research Centre of Finland, Finland
Jackson, J.D.	The University of Manchester, UK / Tsinghua University, China
Kirillov, P.L.	Institute for Physcis & Power Engineering (IPPE), Russian Federation
Leung, L.	Atomic Energy of Canada Ltd. (AECL), Canada
Novog, D.	McMaster University, Canada
Pioro, I.	University of Ontario Institute of Technology, Canada
Razumovskiy, V.	National Technical University of Ukraine, Ukraine
Vijayan, P.	Bhabha Atomic Research Centre (BARC), India
Xiaojing, L.	Shanghai Jiao Tong University (SJTU), China
Yamada, K.	International Atomic Energy Agency (IAEA)

LIST OF MEETINGS

- 1st Research Coordination Meeting: 22–23 July 2008, Vienna, Austria;
- 2nd Research Coordination Meeting: 25–28 August 2009, Vienna, Austria;
- 3rd Research Coordination Meeting: 23–27 August 2010, Obninsk, Russian Federation;
- Consultancy Meeting: 17–18 March 2011, Vancouver, Canada;
- 4th Research Coordination Meeting: 19–23 September 2011, Mississauga, Canada;
- Consultancy Meeting: 21–22 June 2012, Madison, Wisconsin, USA;
- 5th Research Coordination Meeting: 3–6 September 2012, Beijing, China.

IAEA
International Atomic Energy Agency

No. 23

ORDERING LOCALLY

In the following countries, IAEA priced publications may be purchased from the sources listed below or from major local booksellers.

Orders for unpriced publications should be made directly to the IAEA. The contact details are given at the end of this list.

AUSTRALIA
DA Information Services
648 Whitehorse Road, Mitcham, VIC 3132, AUSTRALIA
Telephone: +61 3 9210 7777 • Fax: +61 3 9210 7788
Email: books@dadirect.com.au • Web site: http://www.dadirect.com.au

BELGIUM
Jean de Lannoy
Avenue du Roi 202, 1190 Brussels, BELGIUM
Telephone: +32 2 5384 308 • Fax: +32 2 5380 841
Email: jean.de.lannoy@euronet.be • Web site: http://www.jean-de-lannoy.be

CANADA
Renouf Publishing Co. Ltd.
5369 Canotek Road, Ottawa, ON K1J 9J3, CANADA
Telephone: +1 613 745 2665 • Fax: +1 643 745 7660
Email: order@renoufbooks.com • Web site: http://www.renoufbooks.com

Bernan Associates
4501 Forbes Blvd., Suite 200, Lanham, MD 20706-4391, USA
Telephone: +1 800 865 3457 • Fax: +1 800 865 3450
Email: orders@bernan.com • Web site: http://www.bernan.com

CZECH REPUBLIC
Suweco CZ, spol. S.r.o.
Klecakova 347, 180 21 Prague 9, CZECH REPUBLIC
Telephone: +420 242 459 202 • Fax: +420 242 459 203
Email: nakup@suweco.cz • Web site: http://www.suweco.cz

FINLAND
Akateeminen Kirjakauppa
PO Box 128 (Keskuskatu 1), 00101 Helsinki, FINLAND
Telephone: +358 9 121 41 • Fax: +358 9 121 4450
Email: akatilaus@akateeminen.com • Web site: http://www.akateeminen.com

FRANCE
Form-Edit
5 rue Janssen, PO Box 25, 75921 Paris CEDEX, FRANCE
Telephone: +33 1 42 01 49 49 • Fax: +33 1 42 01 90 90
Email: fabien.boucard@formedit.fr • Web site: http://www.formedit.fr

Lavoisier SAS
14 rue de Provigny, 94236 Cachan CEDEX, FRANCE
Telephone: +33 1 47 40 67 00 • Fax: +33 1 47 40 67 02
Email: livres@lavoisier.fr • Web site: http://www.lavoisier.fr

L'Appel du livre
99 rue de Charonne, 75011 Paris, FRANCE
Telephone: +33 1 43 07 50 80 • Fax: +33 1 43 07 50 80
Email: livres@appeldulivre.fr • Web site: http://www.appeldulivre.fr

GERMANY
Goethe Buchhandlung Teubig GmbH
Schweitzer Fachinformationen
Willstätterstrasse 15, 40549 Düsseldorf, GERMANY
Telephone: +49 (0) 211 49 8740 • Fax: +49 (0) 211 49 87428
Email: s.dehaan@schweitzer-online.de • Web site: http://www.goethebuch.de

HUNGARY
Librotade Ltd., Book Import
PF 126, 1656 Budapest, HUNGARY
Telephone: +36 1 257 7777 • Fax: +36 1 257 7472
Email: books@librotade.hu • Web site: http://www.librotade.hu

INDIA
Allied Publishers
1st Floor, Dubash House, 15, J.N. Heredi Marg, Ballard Estate, Mumbai 400001, INDIA
Telephone: +91 22 2261 7926/27 • Fax: +91 22 2261 7928
Email: alliedpl@vsnl.com • Web site: http://www.alliedpublishers.com

Bookwell
3/79 Nirankari, Delhi 110009, INDIA
Telephone: +91 11 2760 1283/4536
Email: bkwell@nde.vsnl.net.in • Web site: http://www.bookwellindia.com

ITALY
Libreria Scientifica "AEIOU"
Via Vincenzo Maria Coronelli 6, 20146 Milan, ITALY
Telephone: +39 02 48 95 45 52 • Fax: +39 02 48 95 45 48
Email: info@libreriaaeiou.eu • Web site: http://www.libreriaaeiou.eu

JAPAN
Maruzen Co., Ltd.
1-9-18 Kaigan, Minato-ku, Tokyo 105-0022, JAPAN
Telephone: +81 3 6367 6047 • Fax: +81 3 6367 6160
Email: journal@maruzen.co.jp • Web site: http://maruzen.co.jp

NETHERLANDS
Martinus Nijhoff International
Koraalrood 50, Postbus 1853, 2700 CZ Zoetermeer, NETHERLANDS
Telephone: +31 793 684 400 • Fax: +31 793 615 698
Email: info@nijhoff.nl • Web site: http://www.nijhoff.nl

Swets Information Services Ltd.
PO Box 26, 2300 AA Leiden
Dellaertweg 9b, 2316 WZ Leiden, NETHERLANDS
Telephone: +31 88 4679 387 • Fax: +31 88 4679 388
Email: tbeysens@nl.swets.com • Web site: http://www.swets.com

SLOVENIA
Cankarjeva Zalozba dd
Kopitarjeva 2, 1515 Ljubljana, SLOVENIA
Telephone: +386 1 432 31 44 • Fax: +386 1 230 14 35
Email: import.books@cankarjeva-z.si • Web site: http://www.mladinska.com/cankarjeva_zalozba

SPAIN
Diaz de Santos, S.A.
Librerias Bookshop • Departamento de pedidos
Calle Albasanz 2, esquina Hermanos Garcia Noblejas 21, 28037 Madrid, SPAIN
Telephone: +34 917 43 48 90 • Fax: +34 917 43 4023
Email: compras@diazdesantos.es • Web site: http://www.diazdesantos.es

UNITED KINGDOM
The Stationery Office Ltd. (TSO)
PO Box 29, Norwich, Norfolk, NR3 1PD, UNITED KINGDOM
Telephone: +44 870 600 5552
Email (orders): books.orders@tso.co.uk • (enquiries): book.enquiries@tso.co.uk • Web site: http://www.tso.co.uk

UNITED STATES OF AMERICA
Bernan Associates
4501 Forbes Blvd., Suite 200, Lanham, MD 20706-4391, USA
Telephone: +1 800 865 3457 • Fax: +1 800 865 3450
Email: orders@bernan.com • Web site: http://www.bernan.com

Renouf Publishing Co. Ltd.
812 Proctor Avenue, Ogdensburg, NY 13669, USA
Telephone: +1 888 551 7470 • Fax: +1 888 551 7471
Email: orders@renoufbooks.com • Web site: http://www.renoufbooks.com

United Nations
300 East 42nd Street, IN-919J, New York, NY 1001, USA
Telephone: +1 212 963 8302 • Fax: 1 212 963 3489
Email: publications@un.org • Web site: http://www.unp.un.org

Orders for both priced and unpriced publications may be addressed directly to:

IAEA Publishing Section, Marketing and Sales Unit, International Atomic Energy Agency
Vienna International Centre, PO Box 100, 1400 Vienna, Austria
Telephone: +43 1 2600 22529 or 22488 • Fax: +43 1 2600 29302
Email: sales.publications@iaea.org • Web site: http://www.iaea.org/books

14-28061

International Atomic Energy Agency
Vienna
ISBN 978–92–0–107614–4
ISSN 1011–4289